BIOCHEMISTRY AND CLIMATE CHANGE



Henry Jakobowski
College of St. Benedict/St. John's University

LibreTexts™

Biochemistry and Climate Change

This text is disseminated via the Open Education Resource (OER) LibreTexts Project (https://LibreTexts.org) and like the thousands of other texts available within this powerful platform, it is freely available for reading, printing, and "consuming."

The LibreTexts mission is to bring together students, faculty, and scholars in a collaborative effort to provide an accessible, and comprehensive platform that empowers our community to develop, curate, adapt, and adopt openly licensed resources and technologies; through these efforts we can reduce the financial burden born from traditional educational resource costs, ensuring education is more accessible for students and communities worldwide.

Most, but not all, pages in the library have licenses that may allow individuals to make changes, save, and print this book. Carefully consult the applicable license(s) before pursuing such effects. Instructors can adopt existing LibreTexts texts or Remix them to quickly build course-specific resources to meet the needs of their students. Unlike traditional textbooks, LibreTexts' web based origins allow powerful integration of advanced features and new technologies to support learning.



LibreTexts is the adaptable, user-friendly non-profit open education resource platform that educators trust for creating, customizing, and sharing accessible, interactive textbooks, adaptive homework, and ancillary materials. We collaborate with individuals and organizations to champion open education initiatives, support institutional publishing programs, drive curriculum development projects, and more.

The LibreTexts libraries are Powered by NICE CXone Expert and was supported by the Department of Education Open Textbook Pilot Project, the California Education Learning Lab, the UC Davis Office of the Provost, the UC Davis Library, the California State University Affordable Learning Solutions Program, and Merlot. This material is based upon work supported by the National Science Foundation under Grant No. 1246120, 1525057, and 1413739.

Any opinions, findings, and conclusions or recommendations expressed in this material are those of the author(s) and do not necessarily reflect the views of the National Science Foundation nor the US Department of Education.

Have questions or comments? For information about adoptions or adaptions contact info@LibreTexts.org or visit our main website at https://LibreTexts.org.

This text was compiled on 05/19/2026

TABLE OF CONTENTS

Licensing

1: The Basics of Climate Change

2: Back to the Present and Future of Climate Change

3: Use of Isotope Analysis in Measuring Climate Change

4: Climate Change - The Carbon Cycle and Carbon Chemistry

5: Biofuels A - Corn and Sugar Cane Ethanol

6: Biofuels B - Cellulosic Ethanol

7: Algae - an Introduction

8: Biodiesel, Syngas and Bioaviation fuels

9: Biohydrogen - An Introduction

10: Biohydrogen - Hydrogenases

11: A Warmer World- Temperature Effects On Chemical Reactions

12: A Warmer World- Temperature Effects On Proteins

13: Biochemistry, Climate Change and Human Health

14: Pandemic Diseases and Drug Discovery - Under Construction

15: Fixing Carbon Fixation

16: Fixing Nitrogen Fixation

17: Turning Trees into Plexiglass - Synthetic Biology For Production of Green Foods and Products

Index

Glossary

Detailed Licensing

Detailed Licensing

Licensing

*A detailed breakdown of this resource's licensing can be found in **Back Matter/Detailed Licensing**.*

1: THE BASICS OF CLIMATE CHANGE

Search Fundamentals of Biochemistry

LEARNING GOALS

(Learning Goals written by Claude, Anthropic)

By the end of this chapter, students should be able to:

The Greenhouse Effect and Earth's Energy Balance

- Explain how greenhouse gases — especially CO_2, CH_4, and N_2O — trap infrared radiation emitted by Earth, using IR spectroscopy and blackbody radiation principles to connect molecular properties to planetary warming, and calculate the Earth Energy Imbalance (~1 W/m²) to appreciate its magnitude.
- Define Global Warming Potential (GWP_{100}), compare the values, atmospheric lifetimes, and climate contributions of CO_2, CH_4, and N_2O, and explain why CO_2 remains the primary long-term concern despite methane's higher per-molecule potency.
- Rebut the argument that "CO_2 absorption is saturated" using three lines of evidence: spectral line broadening at higher pressures and Doppler effects, continued absorption in the upper troposphere and stratosphere, and direct satellite measurements showing decreased outgoing IR radiation at CO_2 absorption wavelengths.

Climate History: Ice Ages, Orbital Forcing, and CO_2

- Interpret ice core and ocean sediment proxy data to describe the synchronous relationship between atmospheric CO_2 and temperature over 800,000 years, explain what the Milankovitch cycles (eccentricity, obliquity, precession) do and do not explain, and identify why present CO_2 levels are unprecedented in at least 3 million years.
- Explain how small orbital temperature increases trigger deglaciation through AMOC slowdown, Southern Ocean warming, and CO_2 release from ocean stores — making CO_2 the driver of the bulk of subsequent warming — and rebut the skeptic argument that "temperature rises before CO_2."
- Describe the role of dust, iron deposition, and phytoplankton primary production as feedback mechanisms that amplify or dampen glacial cycles through their effects on ocean CO_2 uptake.

Deep-Time Climate: Key Events and Sensitivity

- Describe the Paleocene–Eocene Thermal Maximum (PETM, ~56 MYA) and the Eocene–Oligocene Transition (EOT, ~33 MYA) as case studies in rapid CO_2-driven climate change, comparing PETM CO_2 release rates (~1.5 Pg/year) to present emissions (~25 Pg/year).
- Distinguish equilibrium climate sensitivity (ECS, ~3.4°C per CO_2 doubling) from Earth System Sensitivity (ESS, ~5–8°C), explain what each includes, and connect the higher ESS value to the long-term consequences of sustained CO_2 elevation.
- Explain why AMOC weakening (projected ~50% by 2100) represents a major climate risk, describing its consequences for European weather, North American sea levels, tropical precipitation, ocean carbon uptake, and atmospheric CO_2.

INTRODUCTION

We've known for a long time that burning fossil fuels and releasing CO_2 into the atmosphere would warm our climate. Perhaps the first paper addressing this, Circumstances affecting the Heat of the Sun's Rays, was published in 1856, before the US Civil War, by a woman scientist, Eunice Foote. John Tyndall (of the Tyndall effect) published more comprehensively on greenhouse gases in 1859. Given the complexity of the biosphere's climate, it was not until the 1980s that climate models became sophisticated enough for scientists like James Hansen to become convinced and alarmed enough to discuss, in Congressional hearings, the role of anthropogenic (human-caused) CO_2 released into the atmosphere as a cause of ever-worsening global warming. The knowledge of human-induced climate change has been politicized and subjected to an orchestrated campaign of misinformation and disinformation by fossil fuel companies and their political contributors. We have delayed global action for so long that we must act immediately and aggressively to address climate change before we reach climatic conditions so austere for humans that parts of the world become uninhabitable. Homo sapiens evolved in a world dominated by repetitive glaciation and deglaciation. Hans Joachim Schellnhuber, an atmospheric physicist, climatologist, and founding director of the Potsdam Institute for Climate Impact Research, has stated that humans have so affected the world that we have eliminated the possibility of the next glaciation cycle.

Many readers might not be familiar with the data and models supporting human-caused climate change. They may not be aware that climate scientists are almost unanimous in supporting climate data and models. As in any field, however, you will find outliers who don't and whose ideas carry disproportionate weight among climate change skeptics. Hence, we provide basic data to show the relationships among increasing atmospheric CO_2 levels, global warming, drought and flooding, ocean acidification, and biodiversity loss. We also provide supportive information, allowing users to address questions from those who question the reality of present human-induced climate change. We don't shy away from using basic physics either, since most students studying biochemistry at the level covered in this book have also studied physics and biology. In subsequent sections, we will address the biochemical consequences of climate change and how biochemistry can help mitigate it.

GREENHOUSE EFFECT

Before the advent of the Industrial Revolution, the Earth's climate was fairly constant since the last ice age, which peaked about 22,000 years ago (YA) and ended about 12,000 YA. There have been short (on a geological time scale) cooling periods since the end of the last ice age. Humans evolved around 200,000 years ago, with modern civilizations arising about 4000 BCE, so it could be said that humans are ice-age peoples (a distinctly Northern Hemisphere perspective). Humans have benefited from a fairly stable climate since then.

The sun's energy warms the Earth. If the Earth did not radiate back into space an amount of energy equal to what it receives, it would slowly and continually warm. The Earth reflects energy as light. In addition, as the Earth is heated by the sun, it emits infrared radiation (as do all warm objects). Earth's temperatures are stable when the energy it emits equals the energy it receives from the sun. This is illustrated in Figure **1.1**.

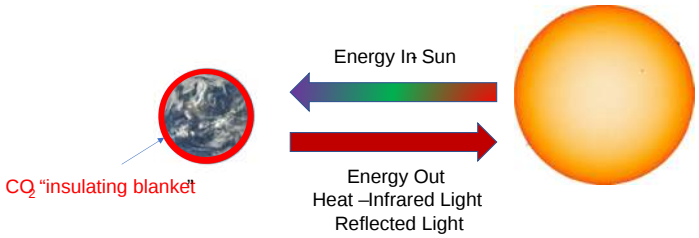


Figure 1.1: Energy balance for Earth as it adsorbs and emits solar radiation

Relatively constant levels of atmospheric CO_2 have enabled our stable climate, a trace atmospheric gas, which has hovered around 280 parts per million (ppm) until the start of the Industrial Revolution in 1770. CO_2 is a greenhouse gas, which, as anyone who has run an IR spectrum knows, absorbs in the infrared. CO_2 in the atmosphere absorbs some of the infrared radiation emitted by the Earth, allowing the Earth to be warmer than it would be in its absence. The CO_2 effectively acts as an insulating blanket. In fact, without CO_2 or other "greenhouse" gases, the Earth would be completely covered by snow.

Other greenhouse gases in the atmosphere include methane and nitrous oxide. The IR spectra of these gases are shown in Figure 1.2. Students who have taken organic chemistry labs and obtained IR spectra of samples always blank the instrument to remove spectral signals from both CO_2 and H_2O.

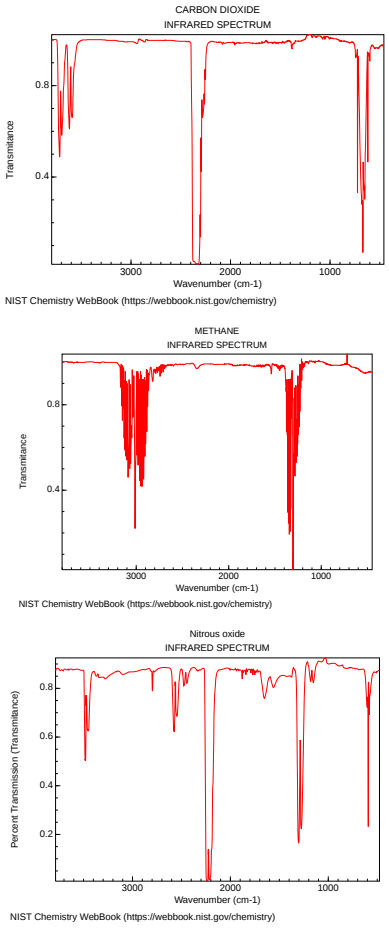


Figure 1.2: IR spectra of some greenhouse gases. NIST (ex: https://webbook.nist.gov/cgi/cbook.c...ndex=1#IR-SPEC)

Let's look at the relationship between the IR spectra of CO_2 and the spectra emitted by the sun and the Earth. You have probably heard of a blackbody radiator in introductory physics classes. It is a hypothetical object that absorbs 100% of all electromagnetic radiation that falls on it without transmitting or reflecting it (hence it appears black). In addition, it emits light energy that depends only on its temperature, not on its chemical composition.

The surface of the sun is about 5778 K. The peak of blackbody radiation for a body at that temperature is at approximately 0.5 μm (500 nm), which falls in the middle of the visible spectrum. The Earth, with an average temperature of 288 K, emits at a peak of about 10-15 μM in the IR region. The blackbody radiation curves emitted by the sun and the Earth are shown in the Figure 1.3 PHET simulation below. Move the blackbody temperature slider to see the effect on the emitted blackbody radiation. You will have to change the -/+ icons to see the Earth's IR spectra in comparison to the sun.

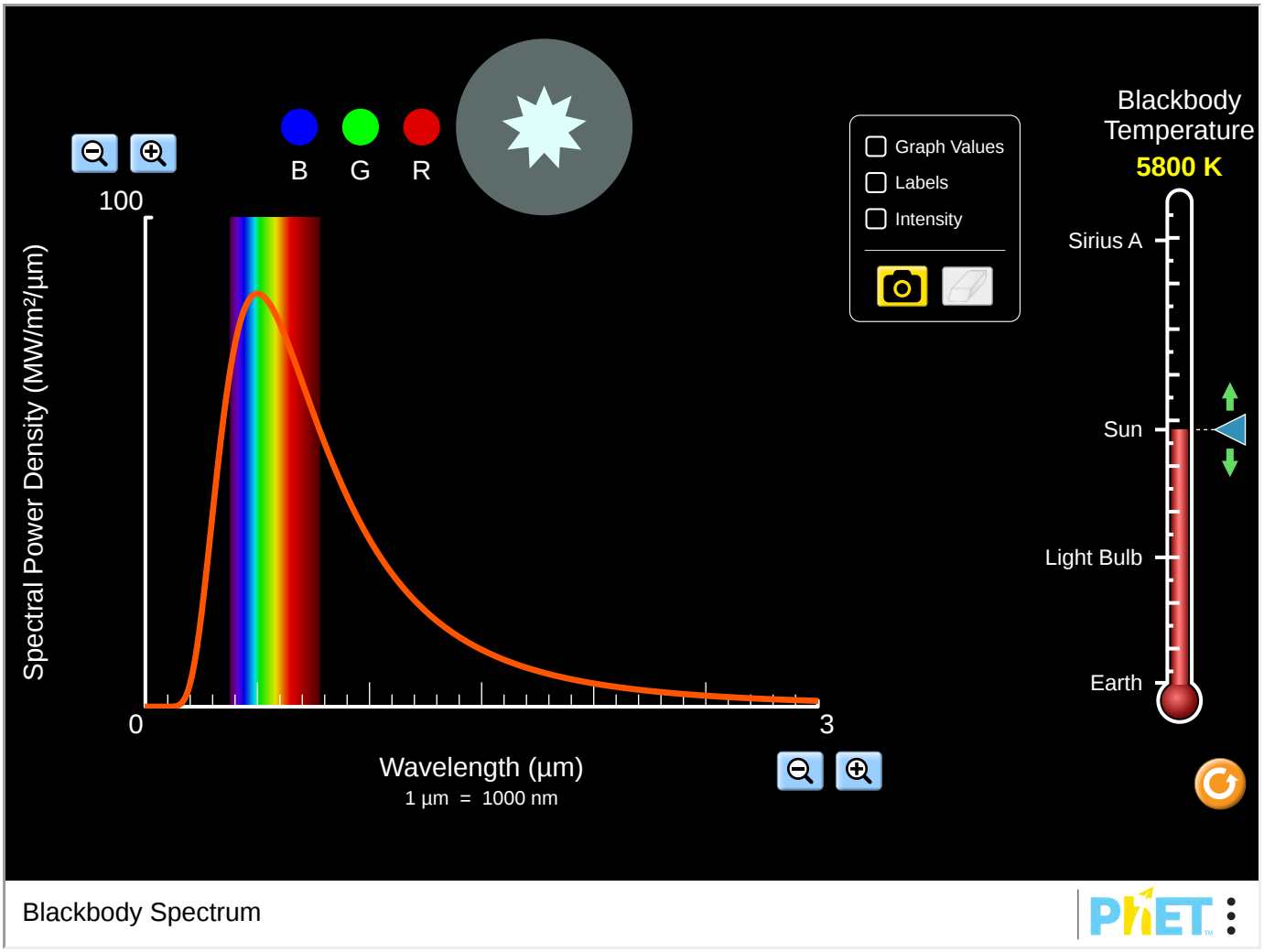


Figure 1.3: PHET Interactive Simulations. University of Colorado, Boulder. https://phet.colorado.edu/en/simulat...ectrum/credits

Play with the slider and magnifying glass icons to view the Earth's emission spectrum (peak at 8.3 μM, spanning 5-16 μM). This overlaps with the CO_2 IR absorption peak (Figure 2) centered at 667 cm^{-1} (15 μM) with a wavelength range span of about 500–850 cm^{-1} (12-20 μM). The sun's spectrum has little intensity at 10-15 μM, so it contributes nothing to CO_2 absorbance at those wavelengths. It's light just passes through the atmosphere until it strikes Earth.

Since the start of the Industrial Revolution, humans have been releasing ever-increasing amounts of CO_2 into the atmosphere from burning fossil fuels, methane from agricultural practices, and natural gas production. As of January 2025, CO_2 levels have reached 427 ppm, while methane has increased to 1900 parts per billion (ppb) or 1.9 ppm.

Interactive graphs showing atmospheric CO_2 and methane over time are shown in Figures **1.4** below.

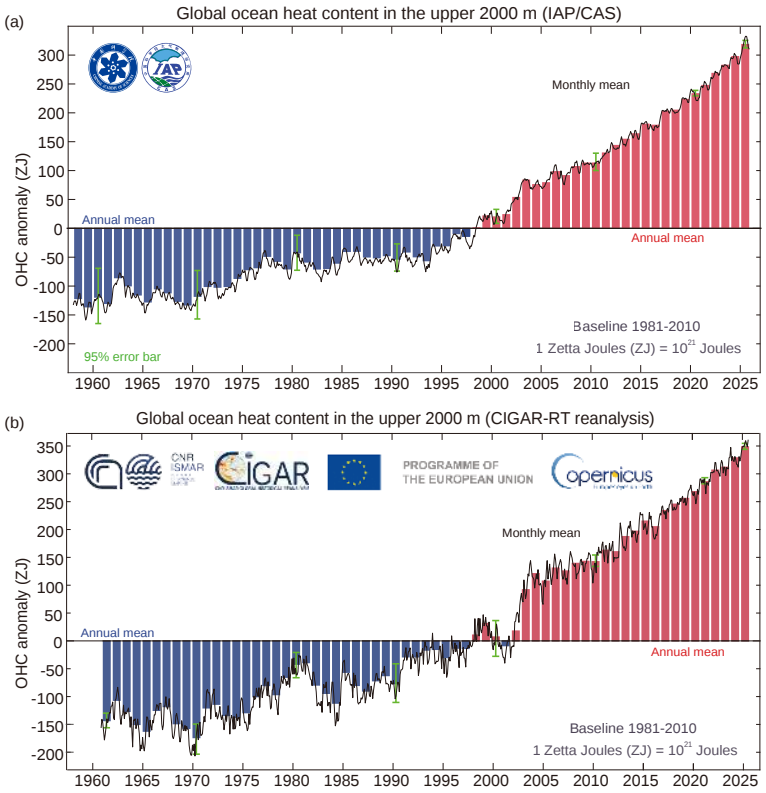
https://geo.libretexts.org/@go/page/34456

Figures **1.4**: Atmospheric CO_2 and methane over the last 800,000 years. Our World in Data.

Increasing atmospheric methane contributes about 20% of the global warming effect of more concentrated CO2, as it has a strong IR absorption spectrum. It has a short atmospheric half-life (about 20 years) compared to CO_2 (hundreds of years). Nitrous oxide (N_2O) is also a powerful greenhouse gas that depletes stratospheric ozone. Our increased use of synthetic fertilizers and manure is the primary anthropogenic source of N_2O. Its emissions are accelerated by poorly drained farmlands.

The net effect is that the Earth is no longer in energy balance. The net contributions of energy input and output are expressed as energy/sec/m^2 of the Earth's surface area. Hence, the units are Joule/s·m^2 = Watts/m^2, where 1 Watt is 1 J/s. From around 2005 to 2019, the average **Earth Energy Imbalance (EEI)** (or budget) was about +460 x 10^{12} W or 460 terawatts (TW) = 4.6 x 10^{14} W. Dividing this by the surface area of the planet (5.1 x 10^{14} m^2) gives an average global value of +0.90 ± 0.15 W/m^2 (or J/(m^2s)). Newer and more refined estimates show it to be +1 W/$m^{2,}$ with most of the excess energy stored in Earth's Oceans, which have a high specific heat capacity and cover 71% of Earth's surface. Most of the remaining excess energy is used to warm land masses and melt ice shields and glaciers. 1 W/m^2 might not seem like a lot, but it is (pardon the pun), astronomically big.

Figures **1.5** below shows the general, continual increase in the ocean heat content (OHC) in zetaJoules (ZJ, 10^{21} J) of the upper 2000 m of the ocean since 1960, with a dramatic acceleration since 2000.



Figures **1.5**: Global upper 2000 m OHC from 1958 through 2025 according to (a) IAP/CAS, (b) CIGAR-RT (from 1961 through 2025), and (c) Copernicus Marine (from 2005 through 2025) (1 ZJ = 10^{21} J). In panels (a) and (b), the black curves represent monthly time series, while the histograms show annual anomalies. Pan, Y., Cheng, L., Abraham, J. *et al.* Ocean Heat Content Sets Another Record in 2025. *Adv. Atmos. Sci.* (2026). https://doi.org/10.1007/s00376-026-5876-0. Creative Commons Attribution 4.0 International License. http://creativecommons.org/licenses/by/4.0/. Here is a link to the Heat Content in the top 700 meters of the ocean - Our World in Data

---

The atomic bomb dropped on Hiroshima released about 1.8 x 10^{13} Joules (some estimates are as high as 9 x 10^{13} Joules) of energy. Assume for the sake of calculation that this energy was released in 1 second over the planet's entire surface (5.1 x 10^{14} m^2). The earth energy imbalance for that one explosion was 0.035 J/m^2·s (0.176 J/m^2·s for the higher estimate). The ratios of the present imbalance (+1 W/m^2) to the distributed bomb's imbalances are 1/0.035 = 28x for the lower energy estimate bomb or 1/0.176 = 5.7 for the higher energy estimate. Hence, the present imbalance, 1 J/m^2s from human-caused climate change, is equivalent to detonating 6-28 Hiroshima-type atomic bombs every second. Other estimates are lower and closer to 600 bombs per day. Regardless, these values should give you a dramatic sense of the imbalance and how unsustainable it is.

Figure **1.6** below represents the Earth's energy budget.

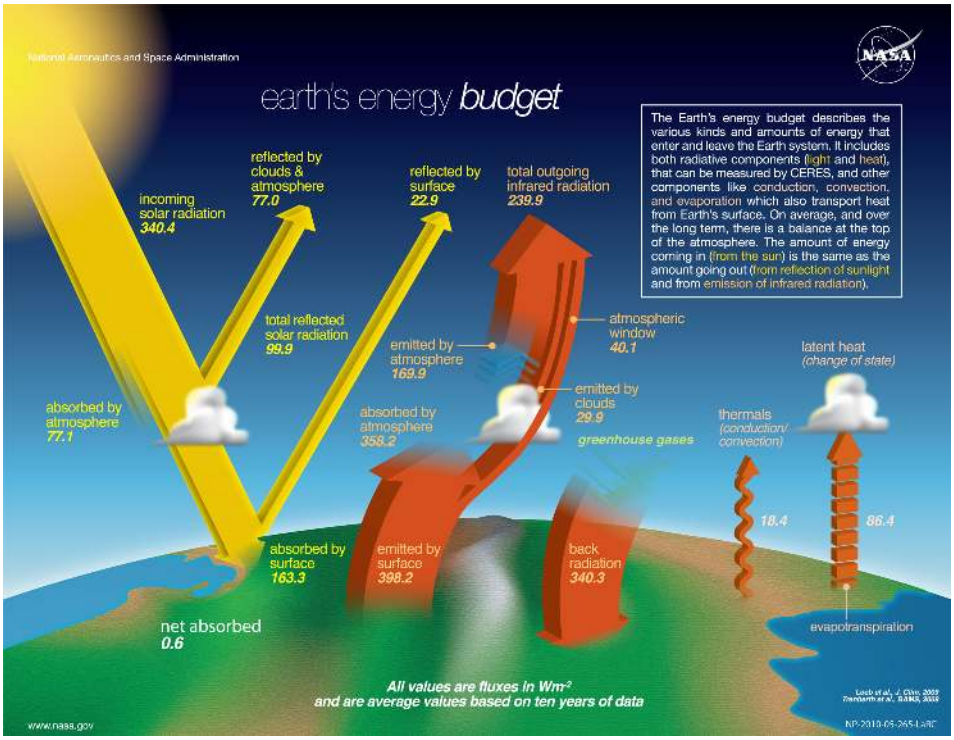


Figure **1.6**: Earth's energy budget, with incoming and outgoing radiation (Values are shown in W/m^2). Satellite instruments (CERES) measure the reflected solar and emitted infrared radiation fluxes. **Year 2021 update**: Net absorbed energy (shown as 0.6) rose to above 1.0 W/m^2 based on independent CERES and ocean heat content measurements. (see Fig. 1 in Loeb et al.(2021), Geoph. Res. Let 48 (13), doi:10.1029/2021GL093047). Public Domain

GLOBAL WARMING POTENTIAL

The **global warming potential (GWP)** calculates the total contribution of all emitted greenhouse gases. It is expressed in units of CO_2 equivalents. It accounts for the contributions of other greenhouse gases, such as CH_4 and nitrous oxide (N_2O), each with unique IR absorption spectra (as shown in Figure 2 above) and atmospheric half-lives. The IPCC uses a 100-year time frame for the calculation of the GWP, which is often abbreviated as GWP100, and uses this formula:

$$\mathbf{CO_2\ equivalent\ kg = CO_2\ kg + (CH_4\ kg \times 28) + (N_2O kg \times 265)} \quad (1.1)$$

- CO_2 has a GWP of 1 by definition since it is the reference. Its time frame in the atmosphere (100s to 1000 years) doesn't matter since it is the reference.
- CH_4 has a GWP of around 27-30 over 100 years, reflecting its higher IR absorbance but lower lifetime (around 12 years).
- N_2O has a GWP of around 265-273 over a 100-year timescale and a lifetime of around 109 years.

Water is also a greenhouse gas, as you can attest on humid days, and its lack in the atmosphere over deserts leads to a large temperature drop at night. It's very different than other greenhouse gases. Its concentration varies enormously (from 40 ppm to 40000 or more) based on humidity and precipitation events, which remove it from the atmosphere. The amount of water in the atmosphere increases with rising global temperatures, leading to more intense precipitation events and further warming in a positive feedback loop. Its concentration in the atmosphere changes significantly on time scales of hours and days, so its atmospheric half-life is short. In contrast, the half-life of CO_2 in the atmosphere is measured in decades to centuries.

The basis for methane's contribution to climate change needs a clearer explanation. Given its IR absorption spectra, it is a very potent greenhouse gas. Many oil companies have indicated a commitment to decreasing methane leakage from pipelines, which would be helpful. Still, these efforts may draw attention away from the fact that CO_2 is the biggest problem. Over 20 years (not 100 as in the GWP calculations above), methane is 80 times as potent as CO_2. Those numbers sound ominous (80X and 20 years, which is not long away)! But you shouldn't compare the two on a kg/kg basis, as the warming from CO_2 could last 1000 years, whereas that from methane lasts only 20 years, after which it disappears. Given its short atmospheric lifetime, the long-term climate effect of methane depends on the rate at which it is added to the atmosphere (megatons/year). Still, for CO_2, it is the net mass added over a longer time, which has a cumulative effect. CO_2 effects continue to increase, but methane effects wane quickly. So you can't easily compare warming over the first 20 years. Consequently, a delay in acting on methane is minimal compared to a delay in acting on CO_2.

Methane contributes to about 30% of net warming, and about 60% of the methane is probably from human activities. As we hit the IPPC Paris target of 1.5 ^{0}C, about 30% of that, or about 0.45 ^{0}C, is from methane; hence, 0.27 ^{0}C comes from human sources. Decreasing human sources of methane will help. But we can't use our efforts to remove methane to avoid or slow down the push for net-zero CO2 emissions.

CLIMATE CHANGES OVER THE LAST MILLION YEARS

THE SKEPTIC'S CORNER: CLIMATE CHANGE MISINFORMATION

Climate has always changed. Our present period is no different, so action is unnecessary.

Indeed, the Earth has been subject to cycles of glaciation and deglaciation for hundreds of thousands of years. Luckily, we can determine atmospheric CO_2 levels dating back hundreds of thousands of years by measuring the entrapped CO2 in ice cores from Antarctica and Greenland. In addition, we've been able to infer temperatures over this time frame using proxies (tree rings, fossils, and more, as described in section 31.2). Figure **1.7** shows how atmospheric CO_2 and temperature have varied over the last 800000 years using Antarctic ice core data.

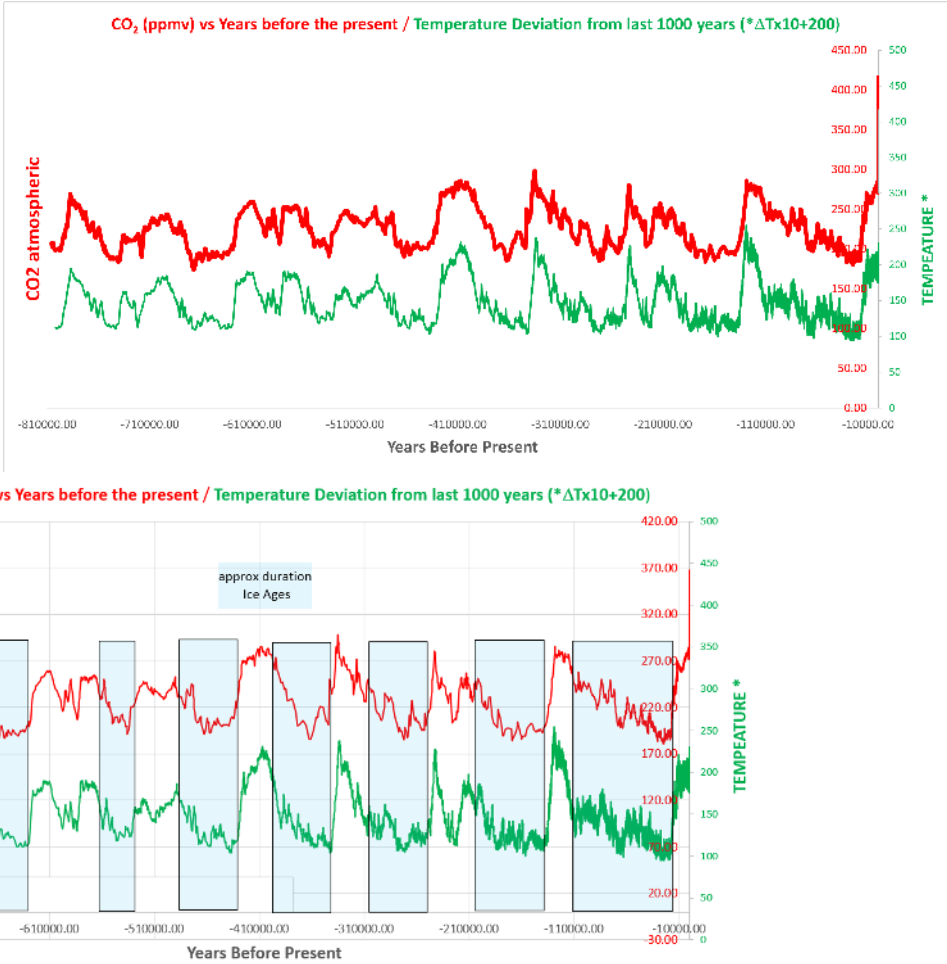


Figure **1.7**: Atmospheric CO2 concentrations (ppm, red) and temperature deviations from the past 1000 years (green) using ice core data and temperature proxies. The bottom figure shows the same graph with the duration of the repeated ice ages shown in light blue. Antarctic Ice Cores Revised 800K YrCO2 Data. Bereiter, B.; Eggleston, S.; Schmitt, J.; Nehrbass-Ahles, C.; Stocker, T.F.; Fischer, H.; Kipfstuhl, S.; Chappellaz, J. http://ncdc.noaa.gov/paleo/study/17975

Several key features of the graph should be apparent:

- Both atmospheric CO_2 and temperature change (ΔT) are periodic. So yes, it is true that "climate changes," as climate change skeptics argue.
- Both CO_2 and ΔT change in synchrony. An obvious question is: what changes first? Does ΔT drive CO_2 changes or vice versa? More on that in a bit.
- **The CO_2 levels in more recent times (on the right-hand side of the graph) have soared to levels not seen in the last 800,000 years**! CO_2 emissions from the burning of fossil fuels cause this change.

Figure **1.7** below zooms in to show both $CO_{2\ atm}$ and temperature values (look at changes, not actual values) since 1000 CE. It also includes annotations on relevant climate and historical events.

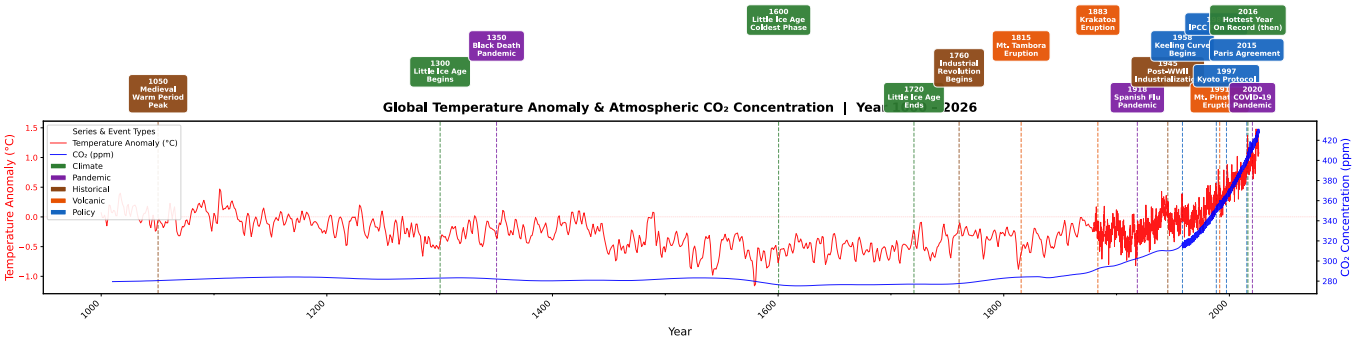
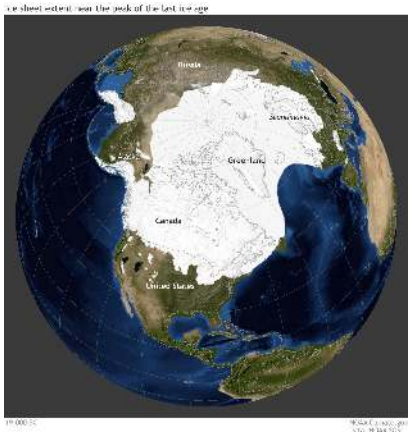


Figure 1.7: $CO_{2\ atm}$ (blue) and temperature values (red, look at changes, not actual values) since 1000 CE. Note that they generally proceed in lock step. Data and data sources from the 2 Degrees Institute.

Over those 800K years, the Earth has experienced cycles of glaciation/deglaciation, including recurring ice ages. Figure (\PageIndex{8}\) below shows a depiction of the last ice age, which peaked 21,000 years ago (left). At that time, the ice cap over New York City was about 1 mile high (right) as CO_2 was 185 ppm!



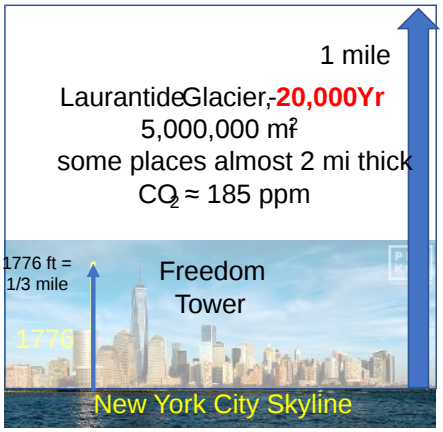


Figure 1.8: The Laurentide glacier during the last ice age (left) and its peak height over present-day Manhattan. https://www.climate.gov/news-feature...oming-sunlight

By 5000 BCE, the glacier had retreated to more modern levels, leaving ice over the Arctic Ocean and Greenland. CO_2 levels were then around 260 ppm. A change of just 100 ppm in CO_2 was sufficient to melt the Northern Hemisphere glaciers. The image above is not "Northern Hemisphere-Centric," since the great glaciers were confined to the Northern Hemisphere during the ice ages. That's because glaciers grow over land, and most of the land on the planet is in the Northern Hemisphere. (Our climate studies won't include when one continent - Pangea- existed.) The video below shows an animation of the Northern Hemisphere ice shield from 19,000 BCE to now, with a projected future assuming little action to reduce CO_2 emissions. Pay special attention to the graphs, which also show sea level changes.

https://geo.libretexts.org/@go/page/34456



Best estimates by Tierney et al now show that during the last ice age, the average global temperature was 6 degrees Celsius (11 F) cooler than today, which in the 20th century is 14 C (57 F). The Arctic, however, was much colder (about 14 C or 25 F). The group also came up with an estimate of **climate sensitivity**, the increase in temperature with increasing CO_2. That value is a **rise of 3.4 °C (6.1 °F) for a doubling in CO_2**. In 1896, Arrhenius, recognizing that CO_2 was a greenhouse gas, calculated that doubling atmospheric CO_2 would cause a rise of 4-5 °C. No one can say we haven't known!

A new value for climate sensitivity, giving a **rise of 4.8 °C (8.6 °F) for a doubling of CO_2,** was determined by Hansen et al (2023) using more precise data about temperatures and CO_2 concentrations derived from isotopic analyses of ice core samples. If this value holds, the environment needed for human life and our present society is seriously jeopardized unless we take immediate measures to stop emissions and cool the planet. In addition, the rate of increase in global and ocean temperatures has accelerated after 2010, and the likely culprit is a decrease in toxic SO_2 aerosols released by ocean vessels in the North Pacific and Atlantic Oceans, and in China, from the reduction of dirty coal-burning facilities. Aerosols reflect incident solar light and increase cloud formation, both of which help cool the planet. Paradoxically, reducing anthropogenic aerosols, while great for cardiovascular and pulmonary health, will accelerate global warming. India would be much warmer now if not for the high aerosol concentrations from smog that cover many of its large cities and countryside.

WHAT THE SCIENCE SHOWS

Climate, CO_2, and temperature have always changed over geological time, but our present rise in anthropogenic CO_2 in such a brief time is unprecedented. This has led to CO_2 levels far exceeding those during the warmer interglacial periods when Northern Hemisphere glaciers retreated.

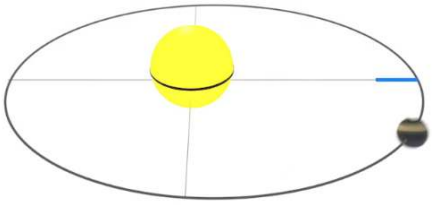
THE ICE AGES, CO_2, AND TEMPERATURE

THE SKEPTIC'S CORNER: CLIMATE CHANGE MISINFORMATION

It's not CO_2 levels that are causing the observed increases in temperature. CO_2 levels are rising as temperatures increase, so we don't have to worry about them. It's a natural process requiring no action to reduce fossil fuel use. Why reduce it if it doesn't cause global warming?

Data and models show that the global increase in temperature is mainly driven by rising CO_2 levels (and not rising temperatures driving rising CO_2). That begs the question as to what starts the process of deglaciation. It turns out that cyclic increases in solar irradiance that increase temperatures, especially in the Northern Hemisphere, start deglaciation. A prime factor is the changes in the orbital dynamics of the Earth around the Sun. As you know, the orientation of the Earth's rotation axis remains generally fixed and pointed in the same orientation as the Earth rotates around the sun. This fixed orientation leads to Earth's annual spring, summer, fall, and winter cycles. In winter, the Northern Hemisphere is pointed away from the sun, leading to decreased solar irradiance per square meter and causing winter there. When the Earth is on the opposite side of the sun, the axis points in the same direction but tilts towards the sun, leading to summer in the northern hemisphere. However, the Earth's orbital dynamics do change cyclically over long periods. These long-term changes in the Earth's orbital shape (eccentricity), tilt (obliquity), and wobble (precession) are called the Milankovitch Cycle and are illustrated in Figure 1.8. These cycles cause small temperature increases that start deglaciation. **Click on each image below** to download and view short videos illustrating these orbital changes.

Change in eccentricity (orbital shape) - (100,000 yr cycle)



Change in obliquity (tilt) (41,000 yr cycle)



Axle precession (wobble) (26,000 yr cycle)



Figure 1.8: The Milankovitch cycle showing changes in the Earth's orbital dynamics with respect to the sun. https://climate.nasa.gov/news/2948/m...arths-climate/

Based on these cycles, Milankovitch calculated that recurring ice ages should occur approximately every 41000 years. Ice ages occurred at this interval, from about 3 million years ago (MYA) to 1 million years ago (MYA). About 800,000 years ago (mid-Pleistocene), they lengthened to about 100,000 years, corresponding to the Earth's eccentricity cycle. The increased cycle duration led to longer-lasting glaciers that moved further south into the Northern Hemisphere. This shift can't be accounted for solely by Earth's orbital eccentricity, since the change in solar irradiance wouldn't have been sufficient to cause it.

CORRECTION - 3/23/26: One likely explanation for the increase in time between ice ages during this **Mid-Pleistocene Transition (MPT)** was proposed by John A. Clark et al. It goes like this. Before extensive glaciation occurred, the outer surface of the earth was exposed to significant weathering. This converted the outer rock layer in the Northern Hemisphere into broken rock, dirt, and dust, collectively called **regolith**. When ice sheets initially formed on this, the ice more readily slid over it (lower frictional resistance), leading to faster ice-shield spread and thinner ice shields that more easily melted during deglaciation. The formation/melting of the ice shields was mostly affected (forced) by the obliquity of Earth's axis, which changed over a 40,000-year cycle.

Over time, the soft regolith was eroded and transported by the glaciers as they extended. This left bare rock. Subsequent cycles of glaciation formed ice shields that moved more slowly and thus became thicker. These required longer melting times, supporting a shift to a 100 Kyr cycle. The glaciers then grew over 2 or more obliquity cycles. Evidence supporting this includes the absence of ancient regolith and the exposure of bedrock in Canada and Scandinavia. Punctuating these rhythmic orbital and ice-age cycles are other events, such as large volcanic eruptions and asteroid impacts, that can produce minor to major climate changes and resulting mass extinctions.



March, 2026. New ice core data from Antarctica offers another explanation for the 40Kyr-to-100Kyr transition during the Mid-Pleistocene and supports the role of the oceans in storing and releasing heat. These findings increase our understanding of our present climate change as well. Marks-Peterson et al. analyzed ice-core data from the Allan Hills Blue Ice Area (BIA) that formed over a continuous 3-million-year period. (These types of analyses will be discussed in subsequent chapter sections.) They could directly measure CO_2 and methane in individual ice core layers and determine the age of each vertical layer using ^{40}Ar dating. An old, long ice core is difficult to analyze because ice pressure fuses layers, making measurements more challenging. Given this compression, in this analysis, *an entire glaciation cycle would be compressed into a single layer.*

The data covered a different time sampling than the 800,000-year continuous ice core record (from EPICA Dome C and others) shown in Figure 4 above, which shows CO_2 changing from about 180 ppm during glacial maxima to ~280 ppm during interglacial periods, a net change of ~80-100 ppm. The paper examined whether the long-term baseline (a center with periodic increases and decreases) for CO_2 and CH_4 changed over 3 million years, but with less time resolution due to compression as described above.

The analysis showed no significant variation in average CO_2 across the Mid-Pleistocene transition, as CO_2 remained consistently low. The same finding was obtained for the **Pliocene-Pleistocene Transition** (~2.6 MYa) when CO_2 was about 250 ppm. CO_2 declined by only about 20 ppm (from roughly 250 ppm to 230 ppm) across the entire Pleistocene. Methane did not change. Yet average temperatures dropped more than 2 ^0C globally and 3.5 ^0C in the Antarctic. So, relative stability in CO_2 occurred from the start of Northern Hemisphere glaciation (around 2.6 MYA at the start of the Pleistocene) and the Mid-Pleistocene transition. Hence, CO_2 changes during these times can't solely contribute to changes in glaciation cycles from 40KYr to 100KYr..

During these times, the extent of the Northern Hemisphere ice sheets increased dramatically. Hence, other factors contribute to cooling during these transitions. (Reminder: the Pleistocene Epoch,2.6 million–11,700 years ago, is the period of the ice ages, while the Holocene (11,700 years ago–present) is the current warm period, although many think we are in a new Epoch called the Anthropocene, representing human-driven environmental changes.) The pre-Industrial Revolution average CO_2 level of around 280 falls within the Pleistocene average range determined in the paper. Our present value of over 420 is disastrously high and without precedent over 3 million.

The authors suggest that over time frames of millions of years (not the recurrent glaciation cycles over the last 800 MYr, which were driven by orbital and regolith changes), other factors, such as changes in the ocean circulation, increases in ice sheet reflection (albedo), feedback caused by plants, and additional geological

changes. CO_2 remains tightly coupled to temperature on orbital timescales (the glacial cycles), but the long-term cooling trend appears to have been driven by other mechanisms. The data is consistent with the regolith explanation offered above for the 40KYr to 100KYr change in glaciation cycles.

Figure **1.9** shows how a combination of tilt angle, precession axis, and orbital shape at around 200 KYA (narrow rectangle across all the graphs) combined to lead to low glacial ice volume (bottom graph).

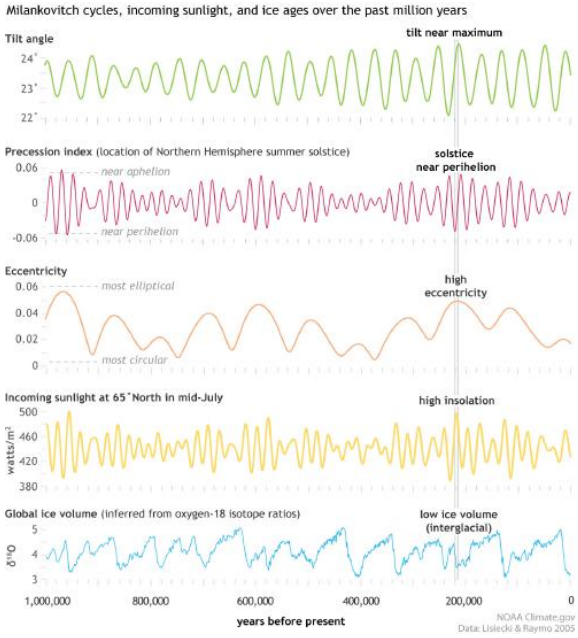


Figure **1.9**: Milankovitch cycle contribution to ice volume over the past 1M years

If orbital changes (or **forcing**) trigger deglaciation, what is the role of increasing levels of the greenhouse gas CO_2, which covary with temperature (see Figure 3)? Temperature increases derived from orbital and hence solar "forcing" seem to precede CO_2 increases for short periods (perhaps 100 - 200 years). After that, CO_2 accounts for almost all of the global temperature increase during deglaciation, with CO_2 and temperature rising together. A global increase of about 0.3 °C due to the Milankovitch cycle leads to greater Northern Hemisphere irradiance. This causes some localized melting of the Northern ice shield, leading to higher ocean temperatures in the Northern Hemisphere. These increases slow a major ocean current, the **Atlantic Meridional Overturning Circulation (AMOC)**, inhibiting the burial and return of cold water in tropical and southern oceans. This, in turn, led to a warming in the south, accompanied by the release of large amounts of CO2 stored in the oceans (see Carbon Cycle in 31.3). The release of this greenhouse gas was then responsible for most of the warming that led to massive degradation. This "interhemispheric see-saw" heat transfer from northern to southern waters is key. For most of the warming during glacial melting, CO_2 and temperature change synchronously.

Recent Updates: April 16, 2026

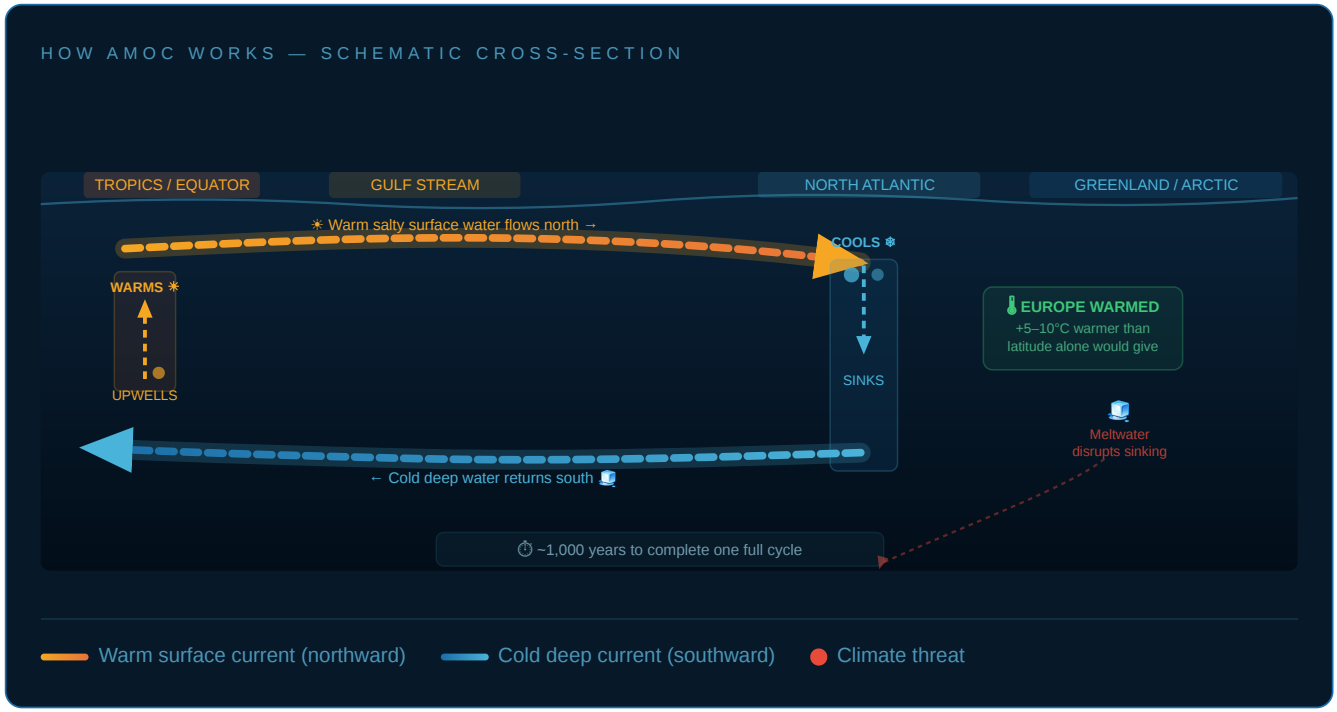
The graphic information and explanation of the AMOC in Figure **1.10** below were made using Claude AI.

https://geo.libretexts.org/@go/page/34456

OCEAN SCIENCE EXPLAINER

The AMOC — Atlantic's Conveyor Belt

A giant loop of ocean currents that regulates climate across the entire North Atlantic — and is showing signs of strain.



Figures 1.10 The AMOC. Anthropic. (2025). *Claude* (Claude Sonnet 4.6) [Large language model]. Retrieved May 2, 2025, from https://claude.ai.



April 15, 2026

Unfortunately, a recent report shows the AMOC has a 50% chance of weakening over this century. Here is the abstract and reference to the paper:

"Climate models show considerable discrepancies in their future projections around the Atlantic, mainly due to uncertainties in the fate of the Atlantic Meridional Overturning Circulation (AMOC). Climate models suggest a 32 ± 37% reduction in AMOC strength by 2100 (90% probability, Shared Socioeconomic Pathways 2-4.5 scenario). [The newer, most refined model] gives an estimate of the AMOC slowdown of 51 ± 8% (90% probability), i.e., a weakening ~ 60% stronger than suggested by the multimodel mean. This more substantial AMOC weakening has key implications for future adaptation strategies. Valentin Portmann *et al.*, Observational constraints project a ~50% weakening of the AMOC by the end of this century. *Sci. Adv.* **12**, eadx4298 (2026).DOI:10.1126/sciadv.adx4298

Here are some consequences of a slowing of the AMOC:

- a cooler, stormier climate, drier summers, and wetter winters in Europe, counteracting some of the warming in that area;
- the accumulation of warm water on the eastern North American coast, causing higher sea level rise compared to other regions (as warm water has a greater volume);
- major disruption of tropical rains, causing flooding and droughts in different regions, including the Amazon and tropical Africa;
- a strong decline in ecosystem mass over the North Atlantic, affecting the size and location of fish;
- a dangerous positive feedback loop of less CO_2 deposited and sequestered in the ocean, increasing atmospheric CO_2;
- changes in the jet stream with stronger westerly winds in mid-latitudes and an extension of the jet stream over the North Atlantic, having significant effects on weather and climate;
- In a more positive effect, the Arctic ice cap would likely expand.

Interpreting climate data is difficult. For example, it was found, by measuring 15N/14N ratios, that gases like N_2 and, by extension, CO_2 could rapidly diffuse through the compacting snow (firn, comprising the top 50-100 meters of the ice cap) until they became trapped in the solid ice beneath it. This would lead to "newer" CO_2 in older ice samples, and the conclusion that temperature changes preceded changes in CO_2. The data are corrected to address the "apparent" time shift.

The CO_2 trapped in bubbles in Antarctic ice core samples reflects global CO_2 levels, given atmospheric circulation. However, the temperatures measured from the same core samples (see Chapter 31.2) represent **local** (Antarctic) temperatures. Ice core samples from Greenland and ocean sediment samples from around the world determine temperatures at different locations over time. All of this data is required to model the climate. Combined, they lead us to our present interpretation of the linkage of CO_2 and temperature rise over time.

WHAT THE SCIENCE SHOWS

Increased solar irradiance on Earth, resulting from cyclic changes in the Earth's orbit, leads to short, small temperature increases in the Northern Hemisphere. These increases lead to the release of the greenhouse gas CO_2 from the oceans, causing synchronous global warming and subsequent deglaciation.

So when skeptics say that temperature increases precede CO_2 increases, you can acknowledge they did, but that the bulk of the warming is attributed to increasing CO_2 released from ocean stores, leading to synchronous temperature increases and deglaciation. Using chemical terms, small temperature increases from orbital forcing catalyzed the release of large amounts of dissolved CO_2 from the ocean. Chapter 31.3 will explore the carbon cycle in more detail and examine how it affects CO_2 levels.

Recent Updates: April 10, 2026

THE SKEPTIC'S CORNER: YES, CO_2 HAS INCREASED, BUT ITS EFFECTS HAVE PLATEAUED, SO NO WORRIES ABOUT ADDITIONAL FOSSIL FUEL EMISSIONS!

This is the argument of a preeminent physicist with expertise in spectroscopy but not in climate science. He states that the absorption of emitted infrared light by CO_2 (atm) has peaked because its concentration is high enough to saturate the absorption (0% transmittance), so extra CO_2 would have no effect. If so, we can continue burning fossil fuels without worrying about their effects on global warming. Climate scientists have refuted this idea using three main arguments.

1. Spectral line widening prevents saturation

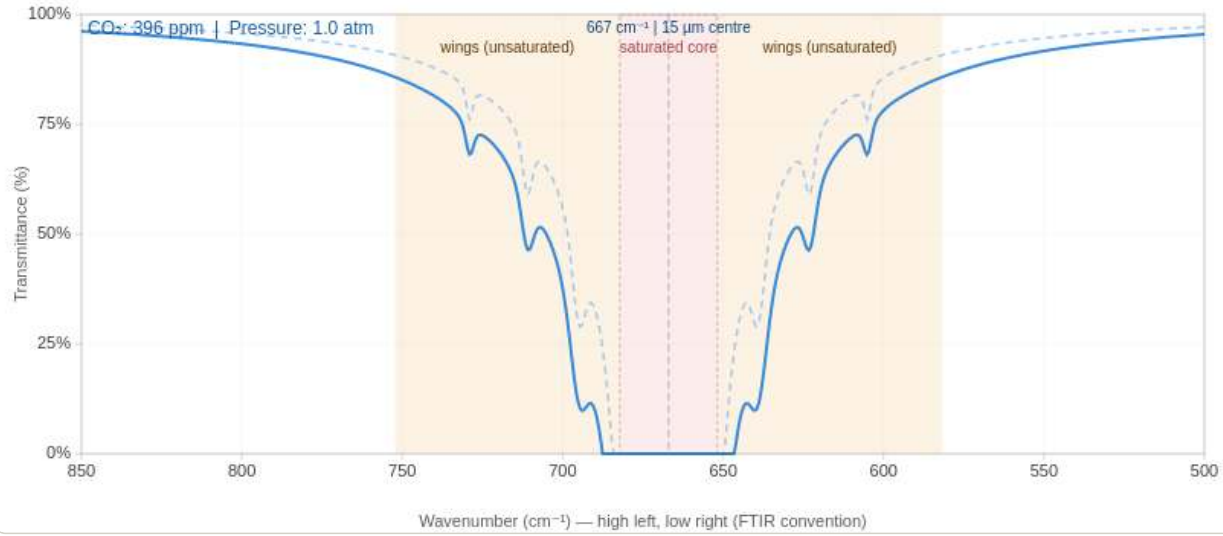
Beer's Law states that $A_{667\ cm^{-1}\ or\ 15\ \mu M} = \varepsilon bc$, where c is the concentration. If there is sufficient CO_2 to absorb all the IR light at 15 μM, the signal saturates, and additional CO_2 won't absorb any more IR light. It would escape into space, with no additional warming of the planet. However, the main absorbance band at 15 μM is wide and becomes wider with increasing CO_2, so additional CO_2 can still absorb and trap IR at the wavelengths, or "wings," surrounding the main 15 μM peak. This is illustrated in Figures **1.11** below.

CO_2 Infrared Absorption Band Broadening

Transmittance spectrum around the dominant 15 μm (667 cm^{-1}) greenhouse band. Adjust sliders to see band widening as CO_2 concentration increases.

CO_2 concentration — 396 ppm

Atmospheric pressure — 1.0 atm



Current CO_2 transmittance — Pre-industrial (280 ppm) — Saturated core — Active wing zone

How to read this diagram

Figure 11: IR transmission spectra of CO_2 with increasing CO_2. Drag the sliders to see the band broaden in real time. The dashed blue line shows the pre-industrial baseline (280 ppm) for comparison. *Claude* (Claude Sonnet 4.6) [Large language model]. Retrieved May 2, 2025, from https://claude.ai.

The main peak becomes broader due to collisions with molecules (most notably O_2 and N_2). At higher pressure (lower altitude, as in the troposphere), there are more collisions per second, and the wings are wider as the energy levels for the absorption are perturbed. You can see this by dragging the pressure slider — lower pressure (higher altitude) narrows the band. Another factor leading to broadening is the Doppler effect. If a photon and CO_2 are moving in different directions during absorption, the photon's frequency changes slightly, leading to band broadening. You likely associate the Doppler effect with a shifting frequency of a siren moving away from you.

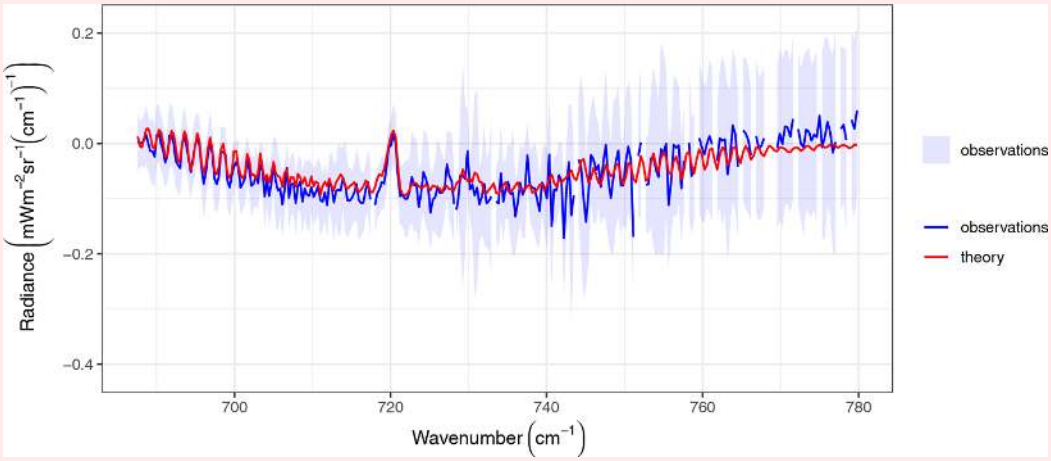
It is well known that doubling the concentration of CO_2 does not double the temperature. This assumes a linear relationship between the two. Rather, a doubling of CO_2 produces a net increase but far less than a doubling of the temperature change, so the relationship is logarithmic in CO_2, not linear. This suggests some but not complete saturation of the CO_2 infrared absorption. We've explored **climate sensitivity**, the increase in temperature with increasing CO_2, earlier in this section, and showed that a doubling of CO_2 gives an increase of 3.4 °C (6.1 °F) or possibly even higher. Climate sensitivity is included in all climate models, so any saturation effect is already accounted for.

2. CO_2 is distributed in the upper troposphere and stratosphere

CO_2 is not just located close to the ground where it is emitted. In the upper troposphere and stratosphere, its concentration is lower and much less "saturated," and infrared light is still absorbed. Moreover, at these heights, less heat is radiated back into space as colder objects radiate less.

3. Direct satellite data show a decrease in IR radiation from the atmosphere with increasing CO_2

This is clearly the "smoking gun" to refute the saturation argument. Figures **1.12** below shows the annual mean radiance differences from the Earth due to CO_2 increases. The data are from the Atmospheric Infrared Sounder (AIRS) satellite (blue line) and are compared with theory (red line) during 2003–2012.



Figures **1.12**: Annual mean radiance differences (in $\mathrm{mW\,m^{-2}\,sr^{-1}\,(cm^{-1})^{-1}}$) due to CO_2 increase from the AIRS observations (blue line) and from theory (red line) and standard deviations for the AIRS observations (blue shading), illustrating the direct impact of CO_2 increase on the spectral radiances during the 2003–2012 period. João Teixeira, R. Chris Wilson, and Heidar Th. Thrastarson. Atmospheric Chemistry and Physics. 24, 6375–6383, 2024. https://doi.org/10.5194/acp-24-6375-2024. Creative Commons Attribution 4.0 License.

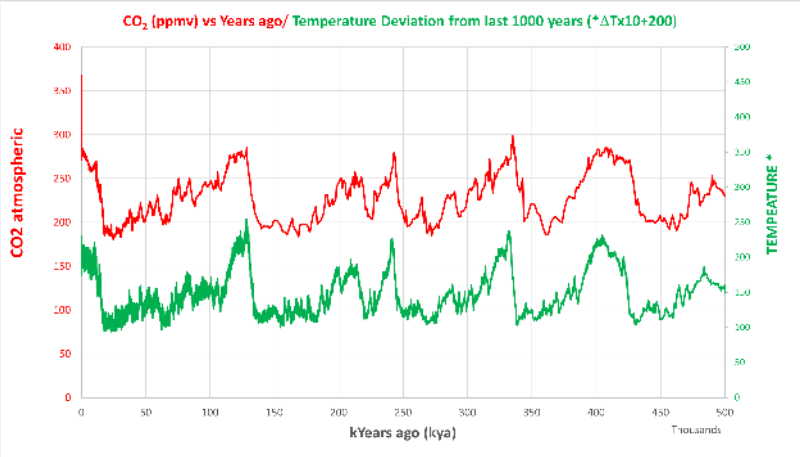
Here is the significance of these observations taken directly from the paper: "This figure is focused on the 680-to-780 $\mathrm{cm^{-1}}$ spectral range, which represents the R branch of the 15 µm CO_2 band and is a spectral region where the CO_2 signal is particularly significant. In this spectral region, enhanced absorption in the troposphere, where temperature decreases with height, reduces outgoing "infrared" radiation (y-axis values are negative). From a broader climate perspective, the reduction in outgoing radiation is behind the increase in global surface temperature that is necessary for the overall climate system to re-establish energy balance at the top of the atmosphere, and as such it is a critical component of global warming. During this period, the measured monthly mean CO_2 mole fraction at Mauna Loa increased on average by approximately 2 ppm $\mathrm{yr^{-1}}$".

The main proponent of the saturation argument is leading the present US administration's efforts to refute the overwhelming scientific consensus on the main cause of present climate change: CO_2 emitted from burning fossil fuels.

We refute another of his arguments, that increasing CO_2 is good for the planet since it is merely plant food, in another section.

TERMINATION OF THE ICE AGES

How did the ice ages terminate? Contributions from orbital forcing derived from the Milankovitch cycle also play a role. Another factor seems to be dust derived from regolith, produced by glacier movement, as mentioned above. How can that hypothesis be tested? Using proxies for dust, namely iron and long-chain n-alkanes (derived from plant waxes) that have been deposited in sediments. First, look at a graph of CO_2 and temperature changes and superimpose those on iron and long-chain fatty acid levels, as shown in Figure **1.13**.



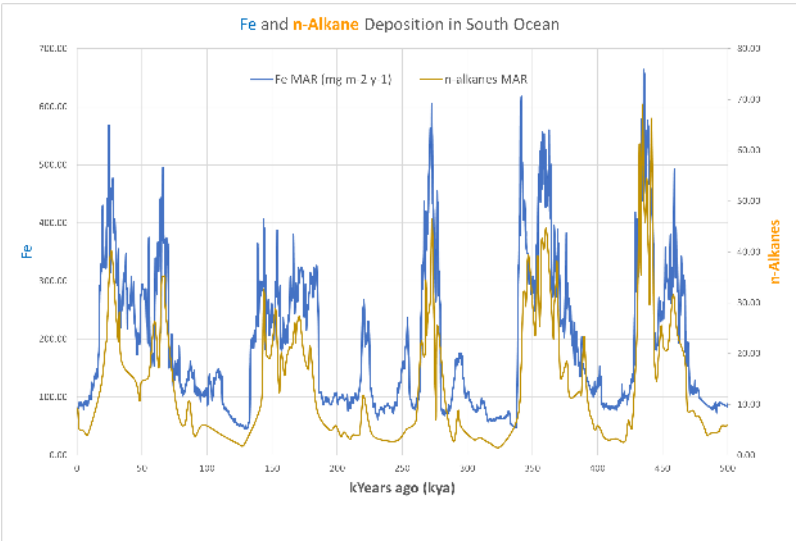


Figure **1.13**: Fe and n-alkane deposition compared to CO_2 and temperatures in the Southern Ocean over the last 500,000 years. Note that the x-axis shows time in kYA going to the right. (so the past is towards the right).

A close examination of the two vertically aligned graphs from around 120 K to 130 KYA shows that iron and n-alkane depositions are at a minimum while CO_2 and temperature are peaking! What explains this negative correlation? It depends on the intimate connection of the biosphere with the nonbiological world (an arbitrary distinction).

Iron and n-alkanes are circulated and delivered in dust. The long-chain alkanes, highly abundant in waxes and enriched in odd-carbon-number chains, were presumably derived from leaf waxes, which prevent water loss from plants, especially at higher temperatures. Dust deposits were first observed in geological time during the transition from the warmer Pliocene (5.3 to 2.6 MYA) to the Pleistocene (2.6 MYA to 11.7 KYA; see Figure 8 below). During the warmer Pliocene, the difference between global and atmospheric temperatures was lower, and with this smaller temperature gradient, winds capable of globally transporting dust would be diminished. Also, the warmer Pliocene (5.3 to 2.6 MYA) would have had more rain, which would have removed dust from the global circulation.

As temperatures cooled in the Pleistocene (2.6 MYA to 11.7KYA), cycles of glaciation would produce more dust-containing regolith (rocks, soil, and dust) at the southern ends of the ice shield, which would be dispersed by stronger global winds driven by higher temperature gradients and less rainfall. Dust contains carbon (for example, long-chain fatty acids) and, perhaps more importantly, iron, which is needed for oceanic phytoplankton growth. Without Fe, the uptake of CO_2 by phytoplankton (primary production) would not occur, leading to increased CO_2 in the atmosphere. Stronger regional atmospheric winds would lead to increased nutrient upwelling and deep-ocean CO_2 release. The CO_2 would enter the atmosphere more readily in the absence of dust deposition of iron.

In summary:

- High CO_2 and high temperature (lower global temperature gradients, more rain) are associated with lower dust levels, as indicated by proxies Fe and n-alkanes. Low dust levels lead to lower deposition of Fe and n-alkanes in the ocean, which decreases phytoplankton primary production and the fixation of CO_2 into biomass. This leads to increased CO_2 movement from the ocean to the atmosphere, increasing temperature. This is an example of a positive feedback loop (higher temperatures leading to higher temperatures).
- Low CO_2 and low temperature (higher global temperature gradients, stronger winds, less rain) are associated with high dust deposition of Fe and n-alkanes. This increases phytoplankton primary production and decreases CO_2 flux from the ocean to the atmosphere, forming a negative feedback loop.

https://geo.libretexts.org/@go/page/34456

By the end of a glacial deposition cycle, dust, blown by stronger winds from higher temperature gradients, was increasingly deposited on the ice sheets. In addition to increasing heat absorption by the sheets, it would also decrease their reflectivity (albedo). Both effects would promote ice sheet melting. Also, a cooler planet during the glacial maximum had less precipitation, which, along with lower CO_2, would lead to more plant and tree death, increasing soil erosion and desertification, both effects which would have increased dust production and its deposition on ice sheets. Then, when CO_2 rose to 280 ppm, plant life renewed, and dust levels dropped.

CLIMATE CHANGE FROM 66 MILLION YEARS AGO TO NOW

Antarctic ice core data cover the last 2 million (M) years. Ocean sediment data can go back 66 million years (MYA), just before the dinosaurs died following the massive asteroid impact that formed the Chicxulub crater, buried beneath the Yucatán Peninsula in Mexico. A brief review of geological eras, periods, and epochs is shown below in Figure **1.14**

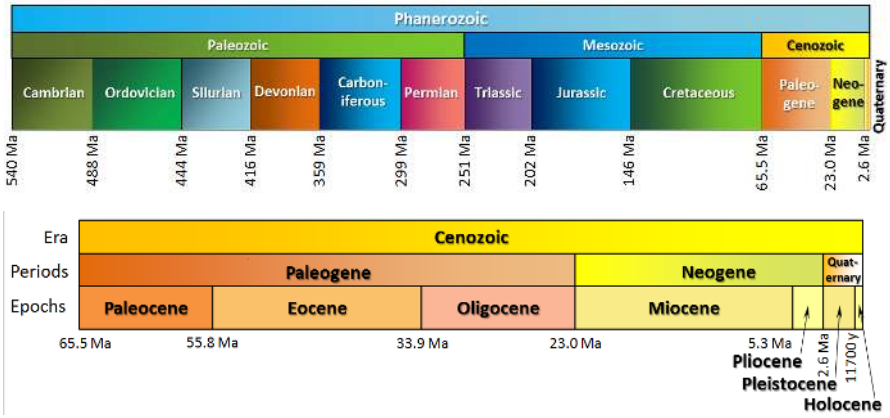


Figure **1.14**: Geological Era, Periods and Epochs

CO_2 levels and associated temperatures derived from ocean sediment cores going back to 66 MYA are shown in Figure **1.10**.

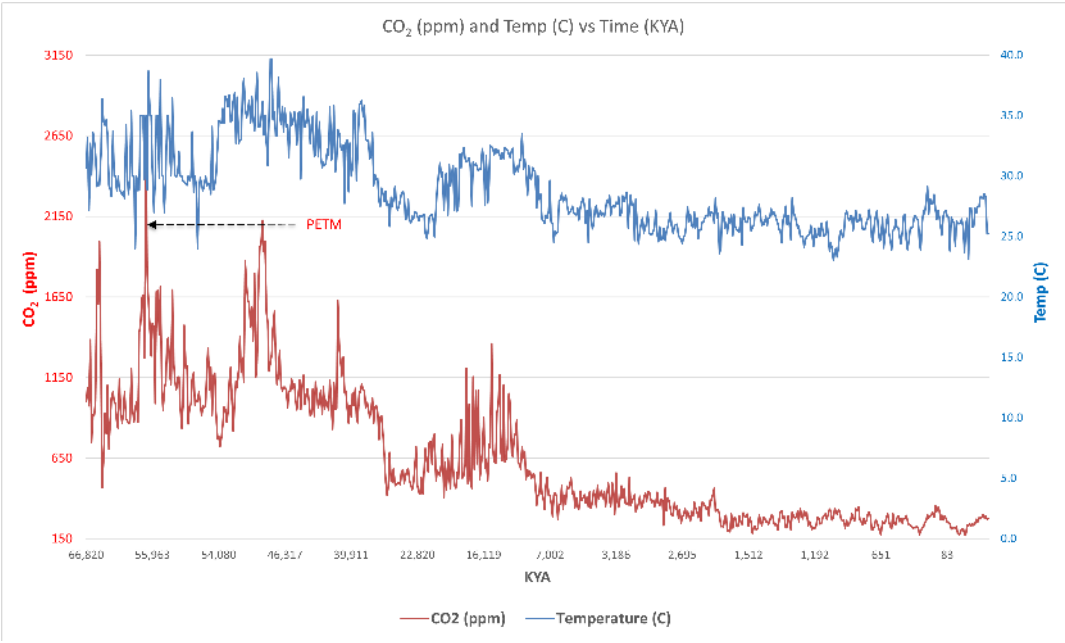


Figure **1.14** CO_2 levels (red) and temperatures (blue) derived from ocean sediment cores going back to 66 MYA = 66,000 KYA . Data from Rae et al. Annual Review of Earth and Planetary Sciences, 49, 2021

Again, note the parallel rise and fall of CO_2 and temperature. Eventually, they fell further in the Pliocene (5.3 to 2.6 MYA) and Pleistocene (2.6 MYA to 11.7KYA) epochs with cyclic glacier/interglacial periods we've discussed above. Northern hemisphere glaciation started in the late Miocene (10 to 6 MYA), and both poles of the planet had glacial sheets.

The time frame shown in Figure 9 encompasses the Cenozoic era (65 MYA when the dinosaurs died to about now). CO_2 levels were much higher than today in the greenhouse Paleocene and Eocene eras, but decreased to about 500 ppm in the Oligocene (34 MYA). An almost stepwise drop in CO_2 and temperature occurred in the **Eocene to Oligocene transition (EOT)**, about 33 MYA. Data shows the development of large ice sheets in Antarctica at that time. Before the EOT (33 MYA), Antarctica was ice-free, as shown in the recreation in Figure **1.15**.

https://geo.libretexts.org/@go/page/34456



Figure **1.15**: Reconstruction of the West Antarctic mid-Cretaceous temperate rainforest. Image credit: J. McKay / Alfred-Wegener-Institut / CC-BY 4.0. https://www.sci.news/othersciences/p...ing-09921.html

Proxy temperature data indicate that the transition was most likely driven by decreased CO_2, with some orbital forcing probably involved. Present models still struggle to explain the EOT (33 MYA) transition, but it is clear that both CO_2 and temperature decreased. Where did the CO_2 go? Most assuredly into the oceans.

To understand that, we have to understand a bit about the carbon cycle, which we will discuss more fully in the next chapter section. Let's briefly discuss the role of atmospheric CO_2 and its interaction with the ocean. The main atmospheric gases, N_2 and O_2, are present at very low concentrations in the ocean because they are nonpolar and generally unreactive. CO_2 is also a nonpolar trace gas, but unlike other nonpolar gases, it can readily react with water to form HCO_3^- and CO_3^{-2}, which are abundant in ocean reserves. Hence, ocean chemistry of CO_2 largely determines atmospheric CO_2 levels. The coupled reactions of CO_2 are shown below.

$$\mathbf{CO_2(\ g,\ atm) \leftrightarrow CO_2(aq,\ ocean)} \tag{1.2}$$

$$\mathbf{CO_2(aq,\ ocean\ ) + H_2O(I,\ ocean\ ) \leftrightarrow H_3O^+(aq) + HCO_3^-(aq)} \tag{1.3}$$

$$\mathbf{H_2O(I) + HCO_3^-(aq) \leftrightarrow H_3O^+(aq) + CO_3^{2-}(aq,\ sparingly\ soluble\ )} \tag{1.4}$$

This chemistry helps determine the ocean's pH. Figure **1.16** shows atmospheric CO_2 and ocean pH levels over the last 66 million years.

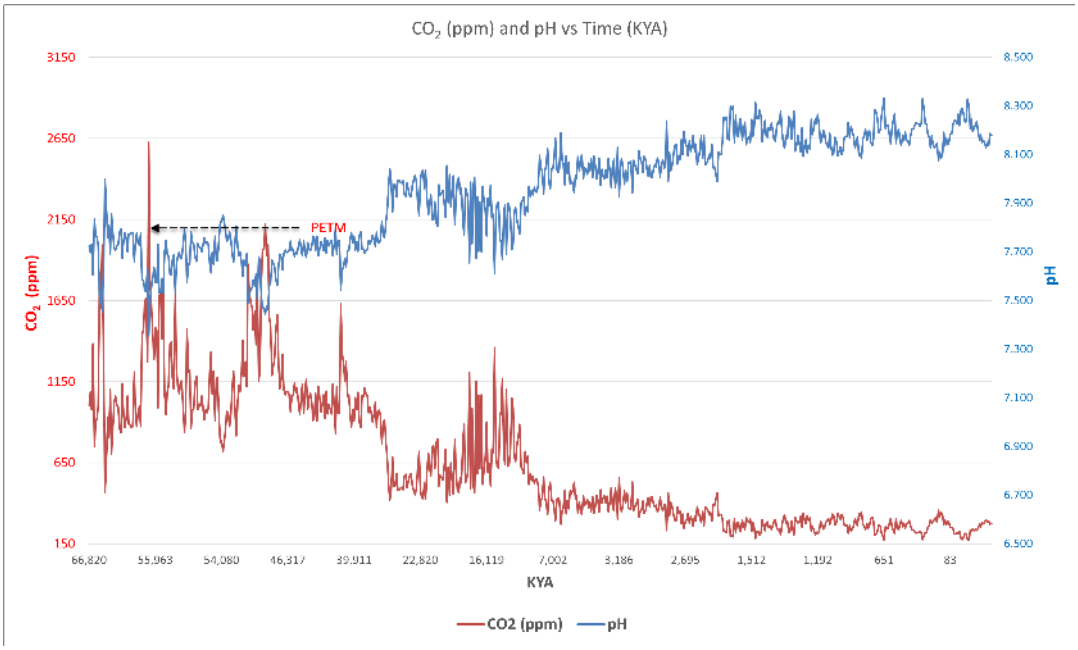


Figure **1.16**: Atmospheric levels of CO_2 and ocean pH over the last 66 million years

Before the EOT at 34 MYA, atmospheric CO_2 levels were higher and ocean pH levels lower (around 7.7). After the EOT (33 MYA), atmospheric CO2 is much lower, and ocean pH is higher (more basic, 7.9, rising to 8.1). What happened to the CO_2 is a bit unclear. Atmospheric CO_2 decreased as it moved into the oceans, but wouldn't that have lowered pH based on the chemical equations presented above? It would have, but it turns out that the ocean alkalinity is determined not just by H_3O^+ produced by the equations above but by the dissolved inorganic carbon ions, HCO_3^- (aq) and CO_3^{2-} (aq), which are conjugate bases. Increased HCO_3^- (aq) and SiO_4^{-2} (aq) from weathering solid carbonates and silicates that entered the oceans would raise ocean pH.

A little review of introductory chemistry helps here.

Let's take bicarbonate, the weak conjugate base of the weak acid carbonic acid. HCO_3^- can act as both an acid and base.

Rx 1: Acts as an acid: HCO_3^- (aq) + H_2O (l) ↔ H_3O^+(aq) + CO_3^{2-} (aq)

$$K_{a2} = \frac{[H_3O^+]\,[CO_3^{2-}]}{[HCO_3^-]} = 4.7 \times 10^{-11} \tag{1.5}$$

Rx 2: Acts as a base: HCO_3^- (aq) + H_2O (l) ↔ H_2CO_3 (aq) + OH^- (aq)

$$K_{b2} = \frac{[H_2CO_3]\,[OH^-]}{[HCO_3^-]} = 2.2 \times 10^{-8} \quad (1.6)$$

The equilibrium constant for the reaction of HCO_3^- as a base is much larger, so bicarbonate is a stronger base than an acid.

Whatever the mechanism of CO_2 drawdown, it led to lower temperatures during the EOT transition. The ocean's increased alkalinity also consumed H_3O^+, increasing ocean pH.

Figure **1.17** summarizes planetary temperatures across geological time.

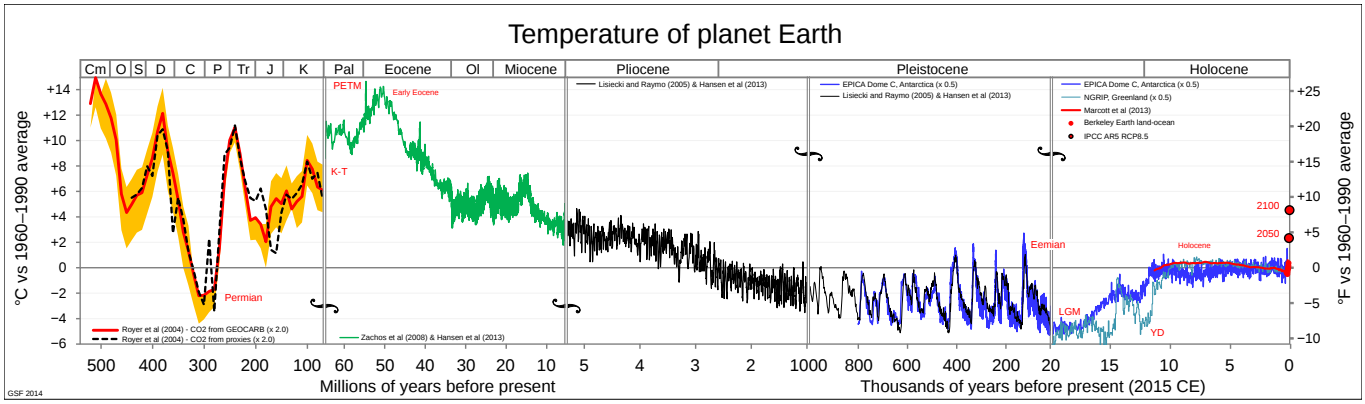


Figure **1.17**: Earth's temperature over 500 million years. https://commons.wikimedia.org/wiki/F...alaeotemps.png. (Excel available). Creative Commons Attribution-Share Alike 3.0 Unported

Several key features should be noted. The last time CO_2 was as high as today (415 ppm) was about 3 million years ago. Repetitive cycles of glaciation/deglaciation are obvious in the Pleistocene (2.6 MYA to 11.7 KYA). Note: This figure has been misinterpreted, leading to misinformation in the popular press and some podcasts, as it shows a general decrease in atmospheric CO_2 levels since the end of the dinosaurs (65 MYA). It shows that our current CO_2 levels most closely resemble those of 3-4 million years ago. At that time, Earth's temperature was likely 3 °C above what it is today, and the seas were 25 meters higher than they are today. In addition, the steep slope of the present rise is unprecedented in the year's historical record.

At around 56 MYA, a temperature spike of about 5^0 - 9 ^{0}F (or even more) on an already warmer planet occurred over about a 100 K-year timeframe. This is known as the **Paleocene/Eocene thermal maximum (PETM)**. It is the closest example to the current rate of CO_2 injection into the atmosphere, so it gives us a basis for what we may see with our current CO_2 spike. The poles warmed to nearly 70 ^{0}F, and alligators and palm trees were found there. The warming also led to the spread of tropical rainforests from the equator, allowing the evolution and proliferation of new plant species, including flowering plants and an incredible biodiversity of insects, birds, and animals that relied on them. Flowering plants produce fruits, which helped drive the evolution of mammals and the first true primates, including the tiny Teilhardina magnoliana. It may have resembled the picture in Figures **1.18** below. (https://en.wikipedia.org/wiki/Teilhardina). Big eyes and hands would help them find fruit in tropical forests.



Figures **1.18**: Teilhardina magnoliana

The temperature increase was caused by a dramatic spike in CO_2 from deep-sea volcanoes and vents, which also led to a dramatic drop in ocean pH as measured by the loss of deep-sea $CaCO_3$ (chalk). Methane hydrates were also released. These environmental and biosphere changes are visually evident in geological deep-sea sediment records as shown in Figure **1.19**.

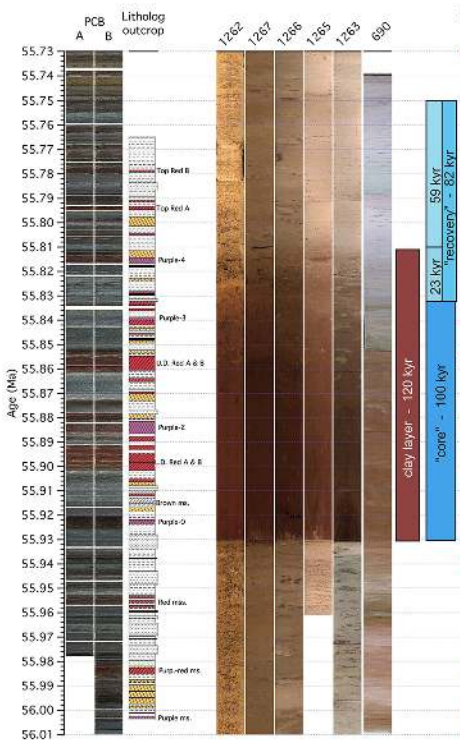


Figure **1.19**: Overview of the Paleocene–Eocene Thermal Maximum (PETM, 55.5 MYA) data from deep-sea records and the terrestrial Polecat Bench (PCB) drill core against age. Westerhold et al. Clim. Past, 14, 303–319, 2018. https://doi.org/10.5194/cp-14-303-2018. Creative Commons Attribution 3.0 License

Sediment cores were taken at various sites (1262, 1267, 1266, 1265, 1263, and 690), aligned from left to right according to water depth, from deep to shallow. Note that 55.93 million years ago, at the start of the PETM, there was a sharp transition from light brown/gray, enriched in chalk, to dark brown, enriched in clay. Ocean acidification dissolved the chalk. It took over 100,000 years to recover.

This very short time frame is called the **Paleocene/Eocene thermal maximum (PETM**,55.5 MYA), which shows very quick spikes (on the geological time scale) can and do occur. Approximately 1.5 petagrams (10^{15}) of CO_2 were released annually during the PETM. We are now releasing about 25 petagrams per year. Our current rate of warming is much higher than during the PETM (55.5 MYA). The best candidates for the source of CO_2 responsible for the PETM are volcanoes, the oceans, and permafrost. Methane hydrates (a solid form of methane found in low-temperature, high-pressure waters) might also be another factor.

The PETM and time after allowed for the optimal evolution of primates. That time might be called the Age of the Primates (analogous to the Age of the Dinosaurs). Figure 13 shows that the arrival of the Oligocene was accompanied by much lower temperatures resulting from CO_2 drawdown. This decimated primate habitats, except in tropical rainforests. Primates disappeared completely from North America but thrived in Africa. Tectonic forces generated the African Rift Valley, characterized by diverse geology and a less homogeneous, more fractured landscape, which again posed new challenges but also provided new habitats for the evolution of primates and the eventual appearance of Homo Sapiens.

Update from December 3, 2023, Science

In December 2023, a refinement of CO_2, temperature, and sea-level-rise data since the demise of the dinosaurs 65 million years ago was published. (The geological interval from 66 million years ago to now is called the Cenozoic Era and consists of 3 periods: the Paleogene until 23 MYA, the Neogene until 2.6 MYA, and the Quaternary.) A group, the Cenozoic Carbon Dioxide Proxy Integration Project (CenCO2PIP) Consortium, reviewed and reevaluated all "proxy" measurements used to determine past climate conditions (we will discuss proxies using isotope ratios in ice cores and sediments as proxies for actual CO_2, temperature, and sea level changes in the next few sections). Figure **1.20** below shows the revised data, representing our best. For this work, pay close attention to graphs A (CO_2), B (relative temperature changes), and C (sea level changes). Note that CO_2 levels in 2022 were last seen 14 million years ago!

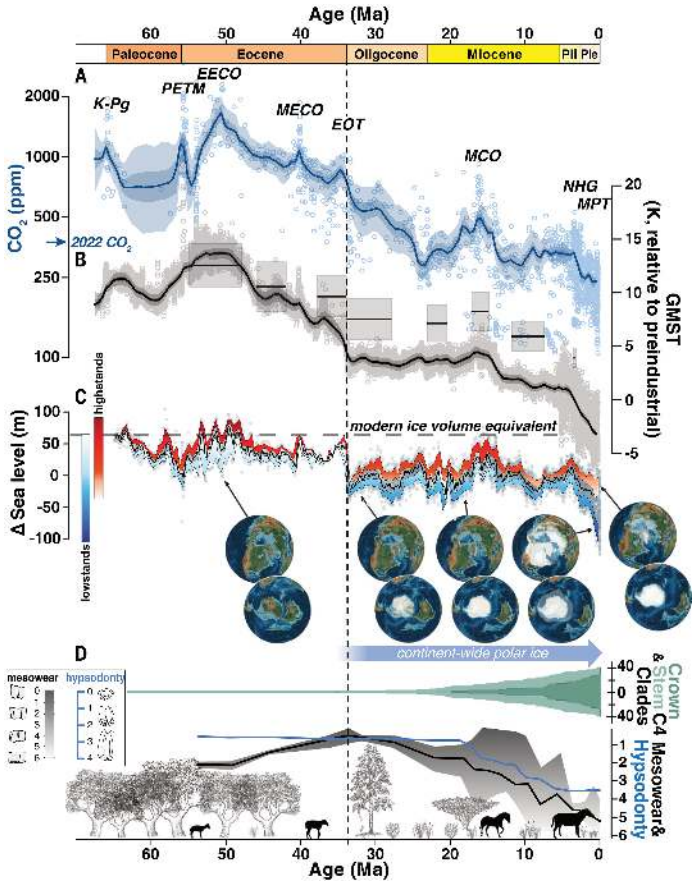


Figure 1.20: Category 1 paleo-CO_2 record compared to global climate signals. From The Cenozoic CO_2 Proxy Integration Project (CenCO_2PIP) Consortium, Toward a Cenozoic history of atmospheric CO_2.*Science***382**, eadi5177(2023). DOI:10.1126/science.adi5177. Reprinted with permission from AAAS.

The legend below is directly taken from the Science article. The vertical dashed line indicates the onset of continent-wide glaciation in Antarctica.

(**A**) Atmospheric CO_2 estimates (symbols) and 500-kyr mean statistical reconstructions (median and 50 and 95% credible intervals: dark and light-blue shading, respectively). Major climate events are highlighted: K-PG, Cretaceous/Paleogene boundary; PETM, Paleocene Eocene Thermal Maximum; EECO, Early Eocene Climatic Optimum; MECO, Middle Eocene Climatic Optimum; EOT, Eocene/Oligocene Transition; MCO, Miocene Climatic Optimum; NHG, onset of Northern Hemisphere Glaciation; and MPT, Mid-Pleistocene Transition. The 2022 annual average atmospheric CO_2 of 419 ppm is indicated for reference.

(**B**) Global mean surface temperatures estimated from benthic $\delta^{18}O$ data following Westerhold *et al*. (solid line, individual proxy estimates as symbols, and statistically reconstructed 500-kyr mean values shown as the continuous curve, with 50 and 95% credible intervals) and from surface temperature proxies (gray boxes).

(**C**) Sea level after with gray dots displaying raw data; the solid black line reflects median sea level in a 1-Myr running window. High- and lowstands are defined within a running 400-kyr window, with lower and upper bounds of highstands defined by the 75th and 95th percentiles and lower and upper bounds of lowstands defined by the 5th and 25th percentiles in each window. Globes depict select paleogeographic reconstructions and the growing presence of ice sheets in polar latitudes.

(**D**) Crown ages show that C_4 clades, with CCMs adapted to low CO_2, initially diversified in the early Miocene, and then rapidly radiated in the late Miocene. Flora transition from dominantly forested and woodland to open grassland habitats based on fossil phytolith abundance data. North American equids typify hoofed animal adaptations to new diet and environment, including increasing tooth mesowear (black line; note the inverted scale), hypsodonty (blue line), and body size.

The results reconfirm the strong correlation across geologic time of CO_2 and temperature, but there are some time intervals when they were out of synchrony. One example is from 37 to 34 MYA, around the Eocene to Oligocene transition (EOT), described above. In Figure 15, CO_2 didn't change much as the Earth cooled prior to the EOT. In contrast, CO_2 levels dropped sharply in the Oligocene as temperatures remained flat. The start of the Oligocene also saw a large drop (55 m) in sea levels, coincident with the EOT, the fall in temperatures, and the rise in glaciation. The authors state that some of the divergences in CO2 and temperatures are likely not directly related to CO_2 but to other variables, such as changes in "paleogeography" arising from continental drift, plate tectonics, etc., that might have altered ocean currents, as well as changes in the reflectivity of sunlight. In addition, the proxies used for those times might have been affected by unaccounted-for changes in seawater composition and pH.

This extensive data presented an opportunity of calculate the climate sensitivity (how much temperature changes with a doubling of CO_2) as we discussed above. The value calculated by Tierney was about 3.4 °C (6.1 °F), although Hansen's recent estimate is higher. This particular value is the equilibrium climate sensitivity (ECS), which includes relatively fast feedbacks like cloud cover and sea ice that act over 100s of years. The value calculated in the new study is not as fine-grained (coarser) at resolutions of 1000s of years, so instead they calculate a much longer-term climate sensitivity called the Earth Systems Sensitivity (ESS) that includes long-term (geological time) events such as changes in continent-wide ice sheets. The value of ESS is between 5°C (9°F) to 8°C (14.4°F), much higher than the ECS widely accepted for our present time. A doubling of CO_2 without some mechanism for drawdown, if sustained over geological time, would transform the world of

the distant future. It would be similar to conditions during the Paleocene/Eocene thermal maximum (PETM), when the poles warmed to near 70 0F, allowing alligators and palm trees to occur there.

This chapter is divided into two sections. Read Chapter 01B, "Back to the Present and Future of Climate Change," to see where we are and where we are headed!

SUMMARY

(Summary written by Claude, Anthropic)

This chapter introduces the fundamental science behind climate change, focusing on how human activities have altered the Earth's energy balance and disrupted long-established climate patterns. Key points include:

- **Historical Foundations and Urgency:**
  - Early studies by Eunice Foote and John Tyndall laid the groundwork for understanding the greenhouse effect.
  - Modern climate models (developed since the 1980s) and recent observations confirm that anthropogenic CO_2 emissions are driving rapid global warming, necessitating immediate and aggressive action.
- **The Greenhouse Effect and Energy Imbalance:**
  - Earth's climate is maintained by a balance between incoming solar radiation and outgoing infrared radiation.
  - Greenhouse gases such as CO_2, methane (CH_4), and nitrous oxide (N_2O) absorb infrared radiation, effectively insulating the planet.
  - Pre-industrial CO_2 levels (~280 ppm) have risen to 427 ppm as of January 2025, upsetting this balance and storing excess energy primarily in the oceans.
  - The current energy imbalance is significant—equivalent to detonating several Hiroshima-type atomic bombs every second—illustrating the unsustainability of current trends.
- **Global Warming Potential (GWP):**
  - GWP is a metric used to compare the warming effects of different greenhouse gases in CO_2-equivalents over a 100-year period.
  - Although CH_4 is more potent on a per-mass basis over short time frames, CO_2 remains the principal concern due to its long atmospheric lifetime and cumulative impact.
- **Climate Variability Over Geological Time:**
  - Ice core data reveal that while CO_2 and temperature have fluctuated naturally over the past 800,000 years, the recent rapid rise in CO_2 levels is unprecedented.
  - The chapter discusses glacial-interglacial cycles, highlighting how relatively small changes in CO_2 (100 ppm) historically corresponded with major shifts in global climate.
- **Orbital Forcing and Feedback Mechanisms:**
  - The Milankovitch cycles (changes in Earth's eccentricity, obliquity, and precession) initiate small temperature increases that trigger deglaciation.
  - These temperature rises lead to the release of CO_2 from the oceans, amplifying warming through positive feedback loops.
  - Dust feedbacks are also explored, showing how variations in dust deposition can either enhance or mitigate warming by influencing phytoplankton growth and planetary albedo.
- **Long-Term Climate Change and Carbon Cycle Interactions:**
  - The chapter reviews data spanning from 66 million years ago to the present, illustrating how CO_2 levels and global temperatures have paralleled each other over geological time.
  - Major events such as the Paleocene–Eocene Thermal Maximum (PETM) are discussed, providing context for the rapid changes occurring today.
  - The interactions between atmospheric CO_2 and ocean chemistry are detailed through chemical equilibria, explaining shifts in ocean pH and alkalinity that accompany changes in CO_2 concentrations.
- **Implications for Future Climate:**
  - Updated data indicate that equilibrium climate sensitivity (ECS) and the longer-term Earth Systems Sensitivity (ESS) may be higher than previously estimated, suggesting that a doubling of CO_2 could eventually raise global temperatures by 5–8 °C.
  - The chapter concludes by emphasizing the critical need to address CO_2 emissions to avoid future climate scenarios that could jeopardize human habitability and ecosystem stability.

Overall, this chapter provides a comprehensive framework that combines historical context, physical principles, and biochemical processes to explain current climate change. It lays the groundwork for understanding how climate dynamics are interconnected with global biogeochemical cycles, setting the stage for further exploration of climate mitigation and adaptation strategies in subsequent sections.

1: The Basics of Climate Change is shared under a CC BY-NC-SA 4.0 license and was authored, remixed, and/or curated by LibreTexts.

2: BACK TO THE PRESENT AND FUTURE OF CLIMATE CHANGE

Search Fundamentals of Biochemistry

LEARNING GOALS

(Learning goals written by Claude, Anthropic)

By the end of this chapter, students should be able to:

Anthropogenic Warming and Its Causes

- Explain why orbital mechanics, volcanic activity, solar variability, land-use change, and aerosols cannot account for warming since 1880, identify fossil fuel combustion as the sole factor matching the observed temperature record, and interpret the seasonal zig-zag in the Keeling Curve in terms of Northern Hemisphere plant photosynthesis.
- Describe the Little Ice Ages (~1450–1850) and the 536 AD climate collapse as natural climate anomalies caused by volcanic aerosols, AMOC disruption, and reduced solar irradiance — and explain why these events, despite their devastating human consequences, do not support the argument that present warming is natural and harmless.
- Use total solar irradiance data from 1610 to the present to explain why solar variability cannot account for warming since 1910, and explain why high CO_2 levels have effectively eliminated the possibility of the next glacial cycle.

Climate Justice and Global Emissions

- Compare national CO_2 emissions on both a total and per capita basis, identify which nations bear the greatest historical responsibility for cumulative emissions since the Industrial Revolution, and articulate the ethical case for wealthy high-emitting nations supporting climate adaptation in vulnerable low-emitting nations.
- Explain the aerosol paradox: why decreasing SO_2 emissions — beneficial for cardiovascular, pulmonary, and cancer health — paradoxically accelerates warming by reducing solar reflection and cloud formation, and connect this to the post-2015 acceleration in Earth's Energy Imbalance.

Future Projections and Societal Choices

- Define Representative Concentration Pathways (RCPs) and Shared Socioeconomic Pathways (SSPs), describe the key assumptions of SSP1 through SSP5, and predict associated CO_2 equivalent concentrations and temperature increases by 2100 for each scenario.
- Explain the implications of Hansen et al.'s (2023) revised climate sensitivity of 4.8°C per CO_2 doubling for the feasibility of the 1.5°C and 2°C IPCC targets, and identify the political, institutional, and economic barriers to the rapid action required.
- Explain why Earth's Energy Imbalance (EEI) is a critical metric for tracking climate change, describe its trend from ~0.6 W/m² in 2000 to a projected ~1.36 W/m² in the 2020s, and connect this trend to the reduced aerosol cooling from ship fuel regulations and Chinese coal plant reductions.

BACK TO THE RECENT PAST AND PRESENT

Let's return to more recent human history and the anthropogenic forcing of our climate. Figure **2.1** shows atmospheric CO_2 levels since 1000. Zoom in on the steep rise in CO_2 that started around 1760 with the Industrial Revolution

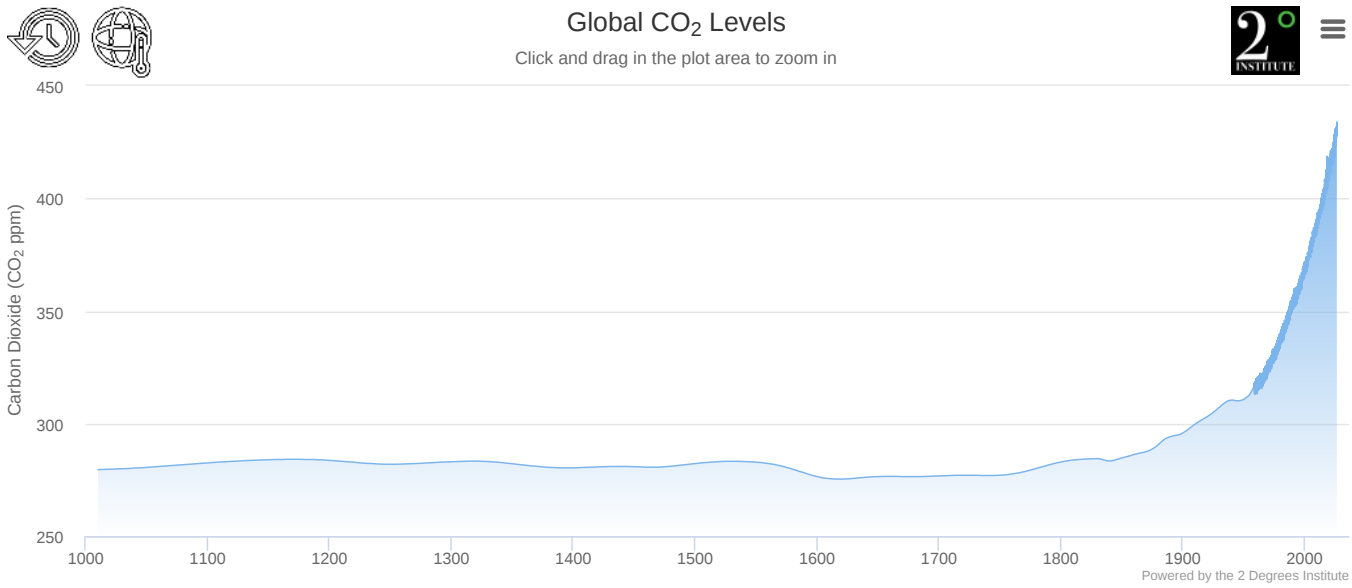


Figure **2.1**: An interactive graph of atmospheric CO_2 over more recent times.

Zoom in on the steep rise in CO_2 that started around 1760 with the Industrial Revolution.Figure **2.1**: Interactive graph of atmospheric CO_2 vs time over the last 1000 years. Historical CO_2 record from the Law Dome DE08, DE08-2, and DSS ice cores. Credits: D.M. Etheridge, L.P. Steele, R.L. Langenfelds, R.J. Francey and the Division of Atmospheric Research, CSIRO, Aspendale, Victoria, Australia. 2 Degrees Institute. https://www.2degreesinstitute.org/. Also, https://www.co2levels.org/

Orbital mechanics **cannot** explain the planet's warming over the brief (geological) period since the Industrial Revolution. Neither can volcanic activity, changes in solar activity, changes in land use (for example, deforestation that slows photosynthesis and CO_2 removal from the atmosphere), or even aerosols released by burning fossil fuels (which would decrease global temperature by increasing the reflection of sunlight). Click on Figure **2.2** to see an animated explanation of which factors best explain the global temperature increase since 1880. The results are clear: It's us!

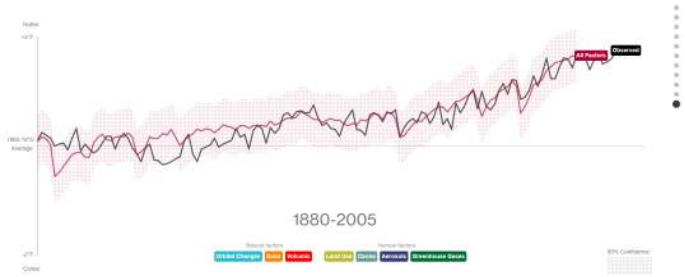


Figure **2.2**: Factors contributing to global warming based on NASA data and NASA's Goddard Institute for Space Studies (GISS) climate models.

Unfortunately, other greenhouse gases have also risen since 1975, as shown in Figure **2.3**.

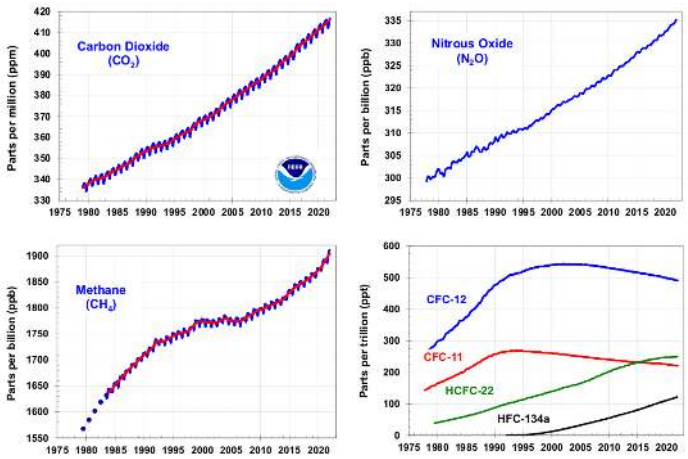


Figure **2.3**: Rise in greenhouse gases since 1975. https://www.co2.Earth/annual-ghg-index-aggi

Take special note of the zig-zag nature of the CO_2 curve. The curve dips slightly in the summer, when plants in the Northern Hemisphere actively remove CO_2. Increasing methane now accounts for up to 20% of the warming observed. Figure **2.17** shows an interactive graph of a very worrisome rise of atmospheric methane with time.

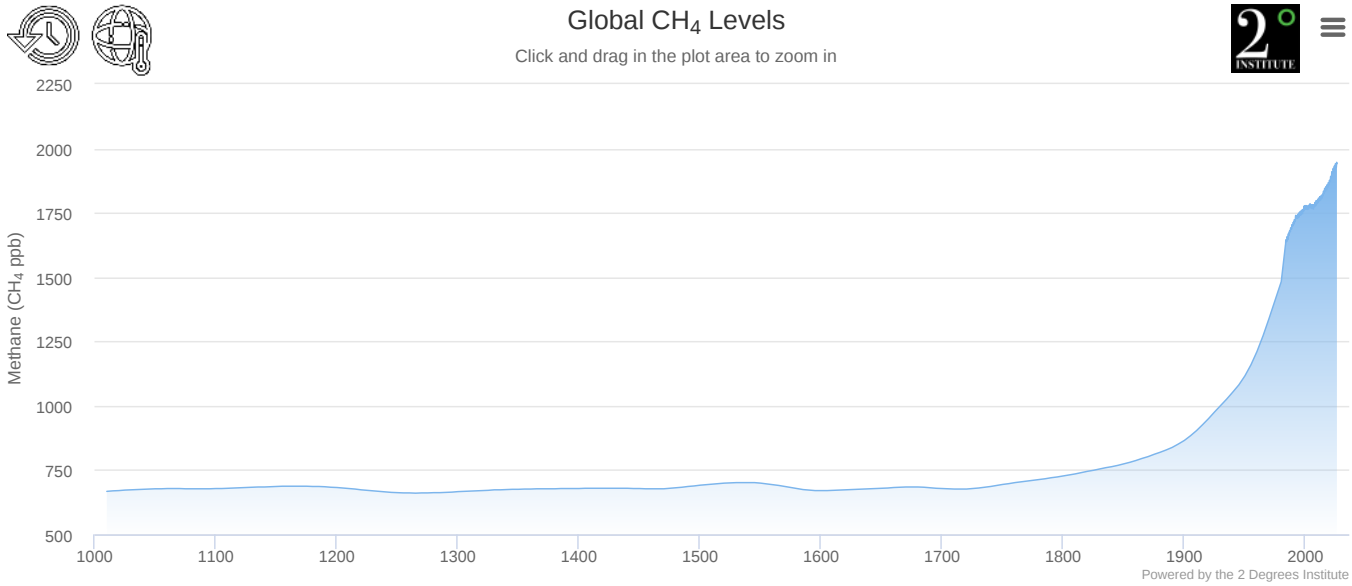


Figure **2.17**: Interactive graph of atmospheric CH_4 vs time over the last 1000 years. 2 Degrees Institute. https://www.2degreesinstitute.org/

Present-day warming is unequivocally caused by humans burning fossil fuels.

PAST CLIMATE ANOMALIES

THE SKEPTIC'S CORNER: CLIMATE CHANGE MISINFORMATION

In recorded human history, there have been other periods of climate change, so we shouldn't worry about the present! Look at the Little Ice Ages!

Several dramatic but short-lived (in geological time) climate changes have punctuated recorded human history. Let's look at two, mostly to equip you to address climate skeptics. They also show the sensitivity of our climate to subtle changes.

The Little Ice Ages

Actual and proxy temperature records show a mild period in Europe from around 950-1100, followed by colder weather, especially from 1450 to 1850. The latter period is called the "Little Ice Ages," although no significant expansion of the Northern Hemisphere ice shield occurred. It was especially cold worldwide in 1816 when much of the world experienced a "year without summer." The effect in 1816 had a clear cause: the eruption of Mount Tambora in Indonesia on April 10, 1815.

In addition to this identifiable influence in 1816, a cool period was reported in the northern hemisphere from about 1800 to 1820, which began earlier than the Tambora eruption. Also, a low period of the sun's irradiance, the Dalton Minimum, occurs from 1790 to 1860. Proxies for solar activity in the 1600s also show small drops in solar irradiance, as discussed below. The dip in global average temperatures following the Medieval Warm Period is shown in Figure **2.4**.

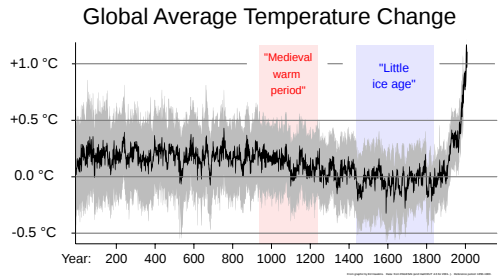


Figure **2.4**: Dip in global average temperatures following the Medieval warm period, By RCraig09 - Own work, CC BY-SA 4.0, https://commons.wikimedia.org/w/inde...curid=87832845

Modern climate change has been captured in literature and art. One example is a painting showing "Ice Fairs" on the Thames in London, shown in Figure **2.5**.



Figure **2.5**:https://commons.wikimedia.org/wiki/F...enell.jpgdfdfd

Many factors probably contributed to the Little Ice Ages, including a drop in solar irradiance. A newer explanation has also been proposed. Marine records show that the water near Greenland and the Nordic seas was warmer, caused by a strengthening of the Atlantic Meridional Overturning Circulation (AMOC). This would have caused the loss of Arctic ice in the late 1300s and 1400s, cooling the water and diluting its salinity since ice, when it crystallized with a tetrahedral hydrogen-bonded coordination of water, excludes salt. This would have collapsed the AMOC and its heat transfer to the northern waters, leading to rapid and prolonged cooling. An analogous strengthening of the AMOC was observed between 1960 and 1980, which was attributed to a long-duration high-pressure system over Greenland. A similar event might have occurred to kick-start the Little Ice Age. Tree rings indicate higher solar irradiance before the Little Ice Age, which may be associated with the initial strengthening of the AMOC.

The Little Ice Ages also affected China and may have contributed to crop failure in 1644, when the Ming Dynasty fell. An Arctic hurricane in 1588 helped destroy the Spanish Armada. The Great Fire in London in 1666 was preceded by a very dry summer that followed an exceptionally cold winter. Food production was severely disrupted, which might have led to significant social change in Europe and elsewhere as the Plague shattered societal and cultural norms.

The 1816 eruption of Mount Tambora in present-day Indonesia greatly exacerbated the effects of cooling. The ash and SO_2 aerosols block solar irradiance. Droughts, floods, cholera epidemics, famine, and migration from Europe to the US and East to West partly arose from this event.

One of the worst times to be alive: 536

Historians report that in 536 AD, parts of Europe, the Middle East, and Asia experienced 24 hours of darkness for up to 18 months. Summer temperatures plummeted. Famines occurred for a few years after. It snowed in China in the summer. The worst effects were in the Northern Hemisphere, but they were worldwide. It was probably the most pronounced cooling in the last 2000 years. To make matters worse, a pandemic erupted around 541, spreading from southern Asia to northern Europe. It had a huge effect on the Byzantine Empire and is known as the Justinian (bubonic) Plague after the Byzantine emperor. Crop failures, trade expansion, and an influx of rodents driven by the cold temperatures could have led to and exacerbated the plague.

This second and more severe example of cooling was shorter-lived on a geological time scale. Temperatures fell in the summer by about 1.5-2.5^{0}C. A "smoking gun" has been linked to this cooling: a volcanic explosion in Iceland. In addition, another eruption occurred in 540, which lowered the temperature by 1.5-2.50C, and another in 547. The combined effects of climate change and the plague led to a significant economic decline in Europe. Signs of airborne lead in the ice in 640, arising from silver mining, suggest a recovery of economic growth. You should ask yourself how the modern world copes with such an occurrence.

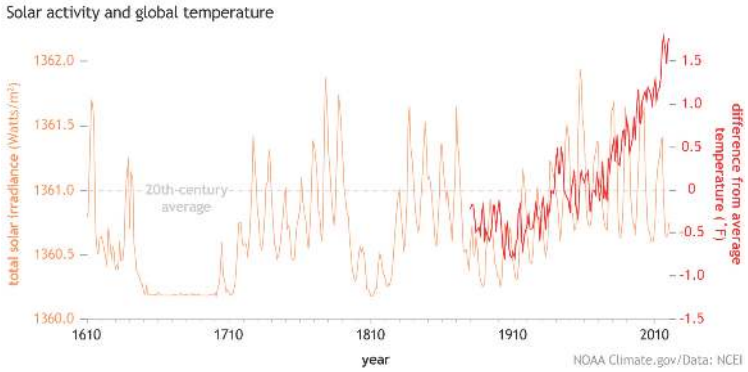
WHAT THE SCIENCE SHOWS

The Little Ice Ages and the climate changes preceding and after the Justinian plague had multiple causes, including volcanic eruptions, small changes in solar irradiance, and changes in the North Atlantic ocean currents and associated weather patterns. These short-term climate changes had disastrous effects on people's lives and the economic health of societies. Predicted future warming arising from CO_2 emitted from fossil fuel use (and other greenhouse gas causes) would bring far worse immediate and potentially irreversible consequences. As people who know the causes of climate change, we must act with due diligence and speed to avert the worst climate future.

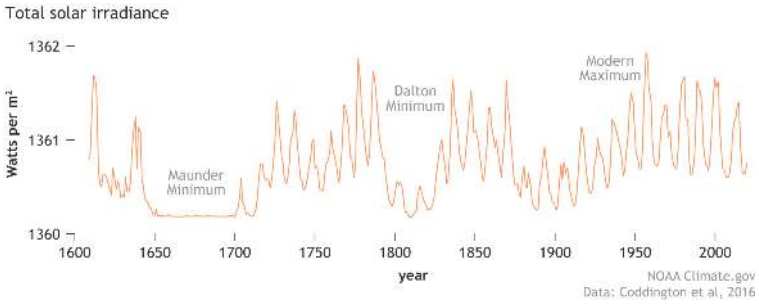
THE SKEPTIC'S CORNER: CLIMATE CHANGE MISINFORMATION

It's not CO_2 levels that cause any observed increases in temperature. The sun's activity is changing. It always has and always will. There's nothing we can do about it.

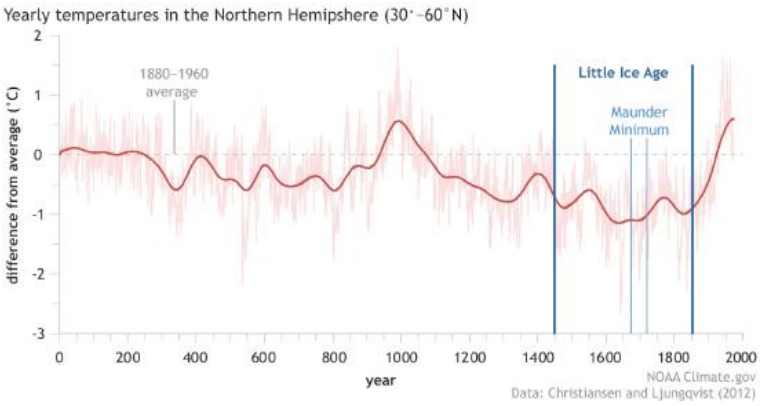
We have discussed how the orbital forcing of the climate kick-started each of the recurring ice ages in the Pleistocene. Some effects of the change in solar activity independent of the sun's orbit have been noted above. Specifically, we have shown that it cannot account for present warming. We present a series of graphs from the NOAA (National Oceanic and Atmospheric Administration) in the collective Figure **2.6** below to show the actual change in solar activity over recent times. Comments are shown at the bottom of each graph.



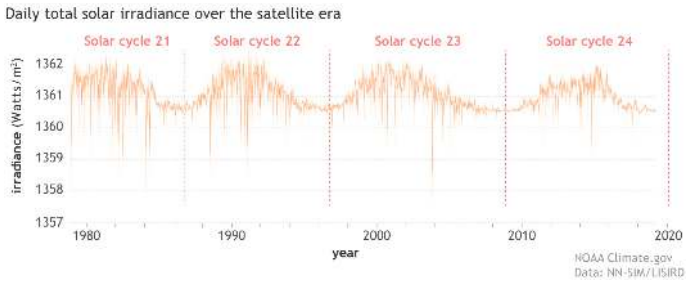
(Above) The maximum % spread between the lowest and highest is very small. Such a small change shouldn't have such dramatic effects on climate unless sustained, as it was from around 1630-1700. Hence, this decline in solar activity likely contributed to the Little Ice Age. The regular rise and fall (spikes) are associated with the 11-year sunspot cycle activity. Note that the rise in average temperature since 1910 (shown in red) cannot be accounted for by a change in solar activity



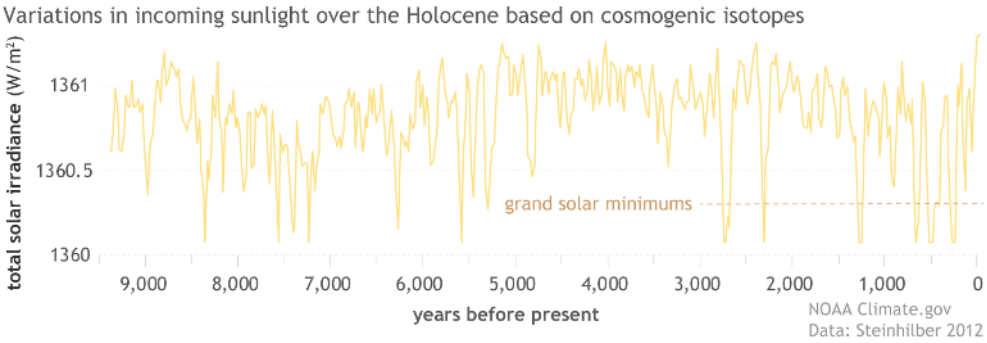
The above graph shows that the irradiance decreased by about 0.06% (although other values have been reported as high as 0.22%) during the Maunder Minimum, which occurred in the Little Ice Age. The average decrease in terrestrial temperatures was 1.0-2 ^{0}C.



The graph above shows yearly average temperatures in the Northern Hemisphere. The dark red line shows the average change. Note that the averages are lower during the Little Ice Age, with the lowest values and the lowest spike temperatures near and in the Maunder Minimum.



(Above) The graph shows the 11-year repeat of sunspot activity and resulting solar irradiance. Although activity dropped in 2020, it was the **second-warmest year** on record since 1880.



This graph does not show the effects of orbital climate forcing. Rather, it shows that solar activity did not change significantly for the 10,000 years before 0 CE.

Figures **2.6**: Solar activity changes in recent geologic time.

This would be true if not for the massive amount of CO_2, approximately 1.5 trillion tons, injected into the atmosphere since the Industrial Revolution from using fossil fuels. Not all of that is still in the atmosphere, but enough to raise CO_2 to levels not seen for 3 million years. Based on the relationship between CO_2 and temperature across the ice ages, science can predict when conditions might exist to initiate and propagate the next ice age. The data arising from these models, illustrated in Figure **2.7**, show how much incoming solar radiation (insolation) must arrive at the Earth (watts/m^2) to trigger the next ice age.

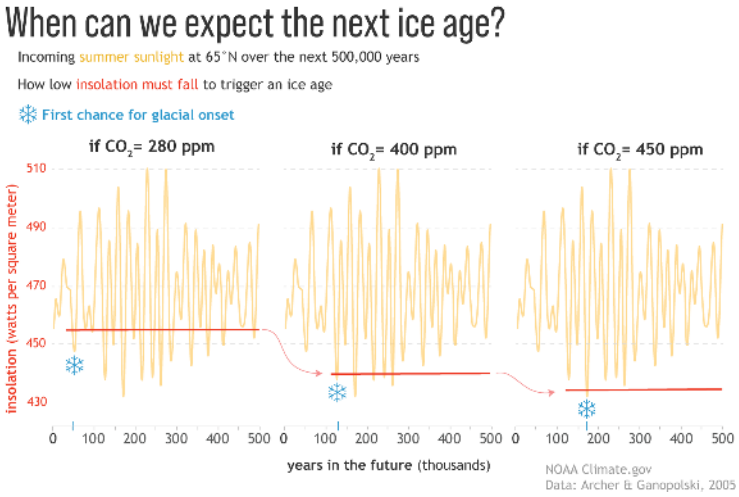


Figure **2.7**: Incoming solar radiation required to trigger the next ice age.

As shown on the left side of the figure, if CO_2 were 280 ppm (typical of peaks in past interglacial periods), it would take repetitive insolation drops below the threshold of about 455 watts/m^2 (red line) to start glaciation. As of November 2022, we are at 415 ppm and rising. If it rises to 450 ppm, as it assuredly will in the absence of carbon capture, it would require much less insolation since the greenhouse effect of the higher CO_2 would warm the atmosphere. The right graph shows there is little chance of another ice age in the absence of large and sustained volcanic activity or an asteroid impact that would block solar radiation.

WHAT SCIENCE SAYS

Changes in solar irradiance (not changes in Earth's orbital dynamics) **cannot** account for warming since the Industrial Revolution. They have contributed to short-term (geological time-scale) cooling during the Little Ice Ages.

Summary of Climate Change Causes and Effects Since 900 AC

Figure **2.8** summarizes possible contributions to temperature change over the last 1000 years. Note again that our current warming can be attributed solely to greenhouse gases (GHGs). One panel shows changes in land use. This has caused a decline in temperature since 1800. That effect is caused by deforestation and other land-cover changes, which lead to greater reflection of incident solar radiation back into space. This effect is greater in winter if the altered land is snow-covered. Deforestation would also decrease CO_2 capture (photosynthesis) by plants, raising the temperature. That component has been added to the GHG panel.

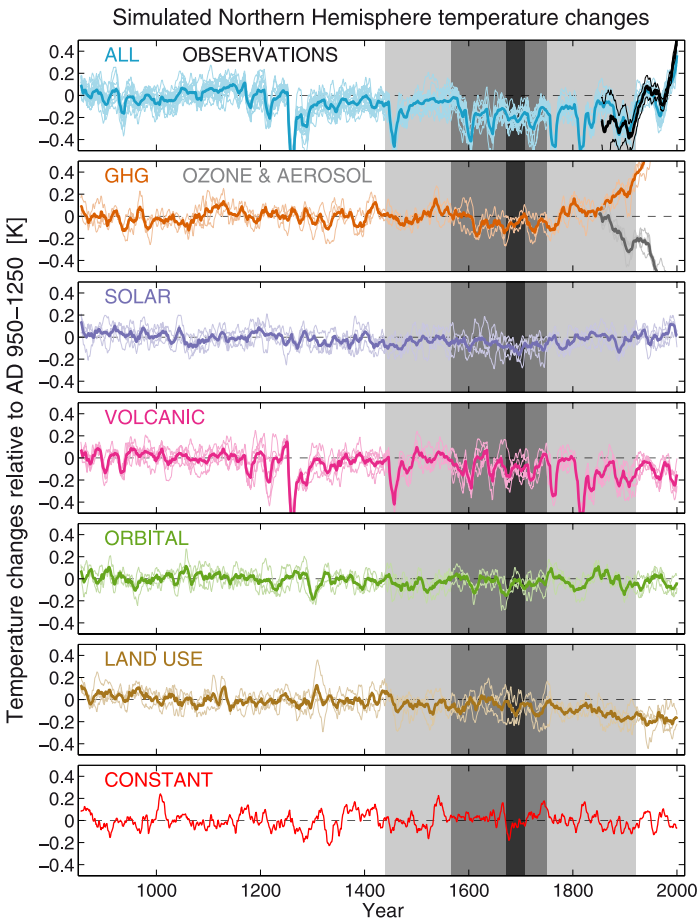


Figure **2.8**: Simulated northern hemisphere temperature changes, smoothed with an 11-year running mean, relative to AD 950–1250. Owens et al. J. Space Weather Space Clim. 2017, 7, https://doi.org/10.1051/swsc/2017034. Creative Commons Attribution License (http://creativecommons.org/licenses/by/4.0).

The black line in the top panel shows the observed instrumental northern hemisphere temperature variations with their associated uncertainties (Morice et al., 2012), which match the simulations well. The bottom panel shows a simulation with no changes to the radiative forcings. This quantifies the magnitude of natural internal variability in the simulations without changes in forcings. Note periodic but short-term dips in temperature due to volcanic activity. Warming since the Industrial Revolution is due to emissions from burning fossil fuels.

CLIMATE JUSTICE: THE EMITTERS AND THE AFFECTED

THE SKEPTIC'S CORNER: CLIMATE CHANGE MISINFORMATION

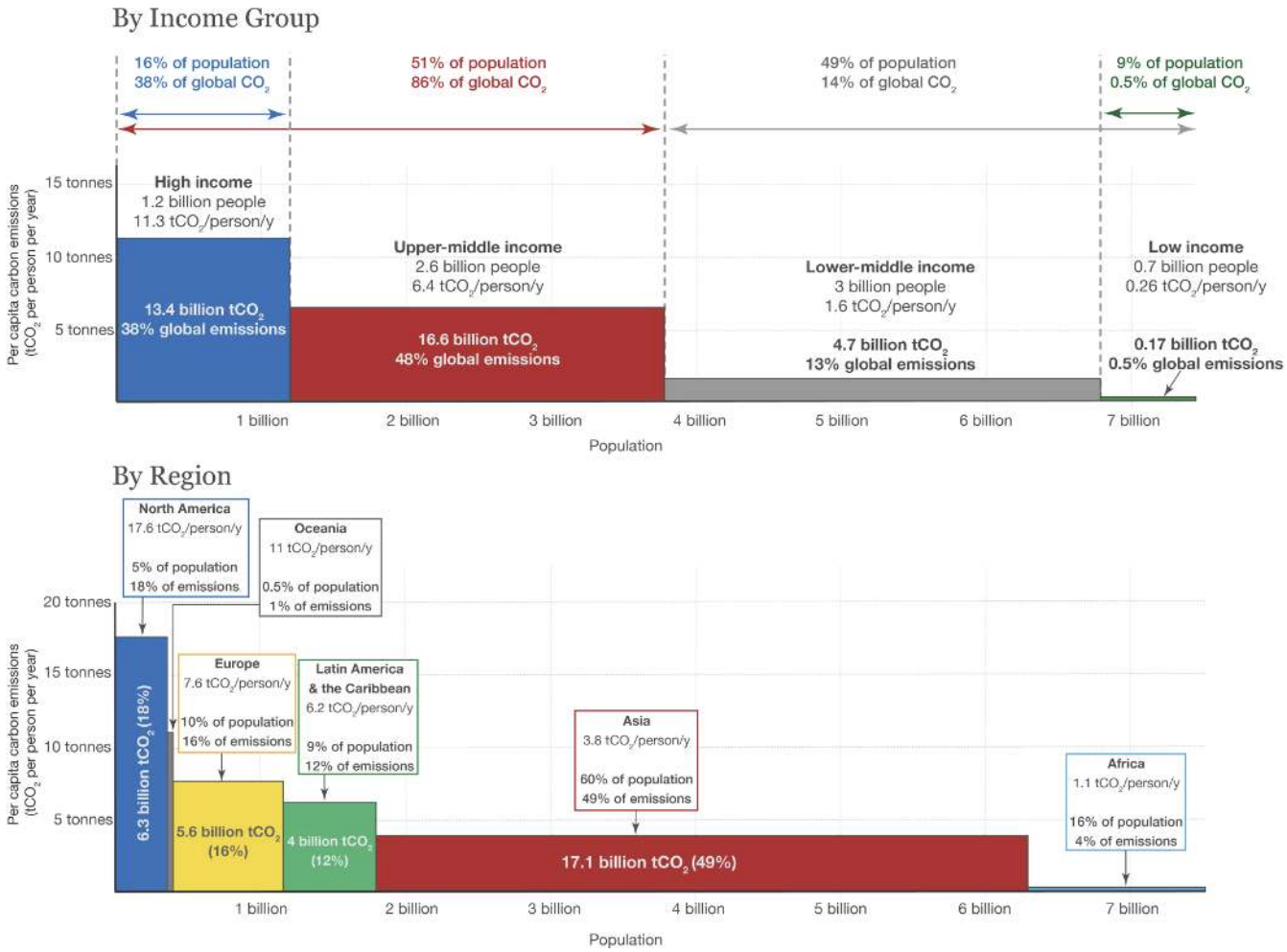
Why should we make changes to reduce fossil fuel emissions when China is the biggest emitter of CO_2?

We present a series of graphs in Figure **2.9** below, taken from CO_2 Emissions - Our World in Data, to show which countries have emitted the most CO_2 in the past and now. In a just world, those countries that have emitted the most should move swiftly and forcefully not only to reduce emissions but also to support other countries' transitions to clean fuels and to help them with climate change mitigation and adaptation. We don't wish to demonize the fossil fuel industry and those who work in it. The use of fossil fuels, which are high energy, high density, and cheap fuel (because of historically massive subsidies) has lifted millions if not billions out of poverty over time. We had no alternative to fossil fuels until recently. Most did not realize how significantly fossil fuel use would affect our present and future climate, human health, and the entire biosphere. Yet, we can't just stop using fossil fuels without inflicting great economic pain on those who can least afford it. To help those currently suffering and those who will suffer most in the future, and to help ourselves, our children, and our grandchildren, we must move away from using fossil fuels as soon as possible through a planned drawdown of their use.

Above: The dip in total world emissions in 2020 was due to the COVID-19 pandemic. Unfortunately, the rise has resumed. China is now the biggest net emitter, but the US and EU emissions are dropping. India is on the rise, and if it follows a similar economic path as China, which it needs to lift many out of poverty, it will come with a huge cost in CO_2 emissions unless it can jumpstart their conversion to clean fuels. The world needs to help.

Above: Although China is the largest net emitter, **the US and Australia are the biggest emitters per person**, although that is dropping.

The US still leads the world in total CO_2 emitted since the Industrial Revolution. We also have the greatest GDP. In 2022, Pakistan suffered tragic flooding exacerbated by climate change. Up to a third of the country was underwater. In a just world, the biggest emitters would aid the rest of the world.



Above: Inequality is evident in this graph as the wealthiest people (high and upper-middle income) collectively contribute 86% of CO_2 emissions

Figure **2.9**: CO_2 emissions by country and income since the industrial revolution. Our World in Data. Creative Commons BY license.

WHAT SCIENCE SAYS

Since the beginning of the Industrial Revolution, the United States has emitted the most CO_2 per capita. China is not even close.

FUTURE PROJECTIONS

We know the science and the consequences if we choose not to act or act in ways insufficient to meet the challenges of climate change. It is one of the most difficult challenges we have faced as a species. It requires sacrifice and united action for the common good. The benefits of our choice are mostly in the future and for future generations.

The Intergovernmental Panel on Climate Change (IPCC), composed of leading climate scientists and experts, has defined several **Representative Concentration Pathways (RCPs)** leading to different emissions and climate futures. Where we end up depends on economic, social, and political choices. The IPCC initially designated four pathways, RCP 2.6, 4.5, 6, and 8.5, with higher numbers associated with higher temperatures and CO_2 levels. Each assumes a starting value and estimated emissions (which depend on technology, politics, economics, etc). RCP 8.5 assumes extra radiative forces (heat energy/(m^2s)) by 2100 equal to 8.5 J/(s m^2) or 8.5 watts/m^2. This worst-case scenario assumes business as usual with no interventions to reduce our emissions, a totally unlikely scenario given present actions (including the rapid rise of clean energy). The RCP 2.6 scenario assumes that the peak radiative forcing would be 3 watts/m^2, declining through strong governmental and economic actions to 2.5 by 2030-2040. Table **2.1** below shows the four RCP scenarios with projected ending CO_2 equivalents (which include other greenhouse gases) and temperature increases.

RCP (W/m^2)	Timeframe	$CO_{2\ atm}$ equivalents (ppm)	Temp increase (°C/°F)	Description
8.5	in 2100	1370	4.9/8.8	rising
6.0	after 2100	850	3/5.4	stabilizing without overshoot
4.5	after 2100	650	2.4/4.3	stabilizing without overshoot
2.6	decline from 3 before 2100	490	1.5/2.7	peak and decline

Table **2.1** below shows the four RCP scenarios with projected ending CO_2 equivalents

Translating the projected CO_2 equivalents in the atmosphere into associated temperature increases requires a high-quality estimate of climate sensitivity (temperature rise per unit CO_2 increase). Figure **2.10** shows the likely temperature increase for the four scenarios.

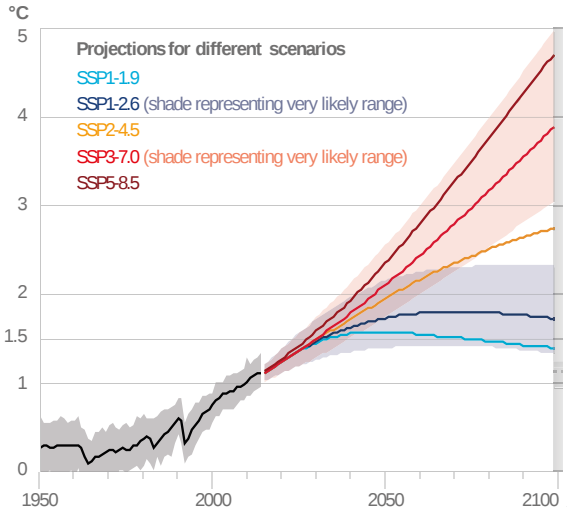


Figure **2.10**: Projected temperature rises for 4 RCP scenarios. Pörtneret al. *Climate Change 2022: Impacts, Adaptation, and Vulnerability.* Contribution of Working Group II to the Sixth Assessment Report of the Intergovernmental Panel on Climate Change. doi:10.1017/9781009325844.001.

The scenarios in Figure 10 are labeled SSP#-##, where the second number ## corresponds to the RCP number. The IPCC 6th report, issued in 2021, changed from using RCP scenarios to Shared Socioeconomic Pathways (SSPs), based on possible social and economic developments that would pose different challenges to reducing future temperature increases and, hence, different strategies for mitigation and adaptation. The SSP scenarios are consistent with the RCP scenarios but use a more enhanced socio-economic and political framework for their construction. The mitigation strategies are based on the RCP forcing levels. The SSP scenarios are described below. They start with SSP1, which leads to a world that has adapted well and moved away from fossil fuels, and end with SSP5, which assumes continued and high reliance on fossil fuels.

2023 - NEW CLIMATE SENSITIVITY CALCULATIONS

We mentioned in 31.1A that a new value for climate sensitivity, which gave rise to a **rise of 4.8 °C (8.6 °F) for a doubling of CO_2** was determined by Hansen et al. (2023). This value has startling implications. If this new value holds, the IPCC/UN call to keep warming to 1.5°C above the pre-industrial revolution average is now **impossible**. We are already there or will be there in a few years. Likely, we will not make the changes required to keep warming below 2°C before 2050. The reasons for our inaction are politicians who continue to support the fossil fuel industry and who block significant legislation to act now, religious institutions and leaders who don't make climate action a sacred duty, and the fossil fuel industry that continues to expand fossil fuel exploration and mislead the public as to the causes of climate change and action to address it. Those who say we can't afford to act never mention the much greater cost of inaction!

SSP1: **Sustainability – Taking the Green Road (Low challenges to mitigation and adaptation)**
The world is gradually but pervasively shifting toward a more sustainable path, emphasizing more inclusive development that respects perceived environmental boundaries. Management of the global commons slowly improves, educational and health investments accelerate the demographic transition, and the emphasis on economic growth shifts toward a broader emphasis on human well-being. Driven by an increasing commitment to achieving development goals, inequality is reduced across and within countries. Consumption is oriented toward low material growth and lower resource and energy intensity.

SSP2: **Middle of the Road (Medium challenges to mitigation and adaptation)**
The world follows a path where social, economic, and technological trends do not shift markedly from historical patterns. Development and income growth proceed unevenly, with some countries making relatively good progress while others fall short of expectations. Global and national institutions work toward but make slow progress in achieving sustainable development goals. Environmental systems experience degradation, although there are some improvements, and overall, the intensity of resource and energy use declines. Global population growth is moderate and levels off in the second half of the century. Income inequality persists or improves slowly, and challenges to reducing vulnerability to societal and environmental changes remain.

SSP3: **Regional Rivalry – A Rocky Road (High challenges to mitigation and adaptation)**
A resurgent nationalism, concerns about competitiveness and security, and regional conflicts push countries to increasingly focus on domestic or, at most, regional issues. Policies shift over time, becoming increasingly oriented toward national and regional security issues. Countries focus on achieving energy and food security goals within their own regions at the expense of broader-based development. Investments in education and technological development decline. Economic development is slow, consumption is material-intensive, and inequalities persist or worsen over time. Population growth is low in industrialized countries and high in developing countries. A low international priority for addressing environmental concerns results in severe environmental degradation in some regions.

SSP4: **Inequality – A Road Divided (Low challenges to mitigation, high challenges to adaptation)**
Highly unequal investments in human capital, combined with widening disparities in economic opportunity and political power, lead to greater inequality and stratification across and within countries. Over time, a gap widens between an internationally connected society contributing to the global economy's knowledge- and capital-intensive sectors and a fragmented collection of lower-income, poorly educated societies working in a labor-intensive, low-tech economy. Social cohesion degrades, and conflict and unrest become increasingly common. Technology development is high in the high-tech economy and sectors. The globally connected energy sector is diversifying through investments in carbon-intensive fuels such as coal and unconventional oil, as well as low-carbon energy sources. Environmental policies focus on local issues in middle and high-income areas.

SSP5: **Fossil-fueled Development – Taking the Highway (High challenges to mitigation, low challenges to adaptation)**
This world places increasing faith in competitive markets, innovation, and participatory societies to produce rapid technological progress and develop human capital as the path to sustainable development. Global markets are increasingly integrated. There are also significant investments in health, education, and institutions to enhance human and social capital. At the same time, the push for economic and social development is coupled with the exploitation of abundant fossil fuel resources and the adoption of resource and energy-intensive lifestyles worldwide. All these factors lead to rapid global economic growth as the global population peaks and then declines in the 21st century. Local environmental problems, such as air pollution, are successfully managed. There is faith in effectively managing social and ecological systems, including, if necessary, geo-engineering.

The projected increases in emitted CO_2 (Gigatons/yr) and other greenhouse gases over the next 80 years for each SSP scenario are shown in Figure **2.11**. The second number in the SSP label is the RCP scenario number, based on radiative forcing, as listed in Table 1 above.

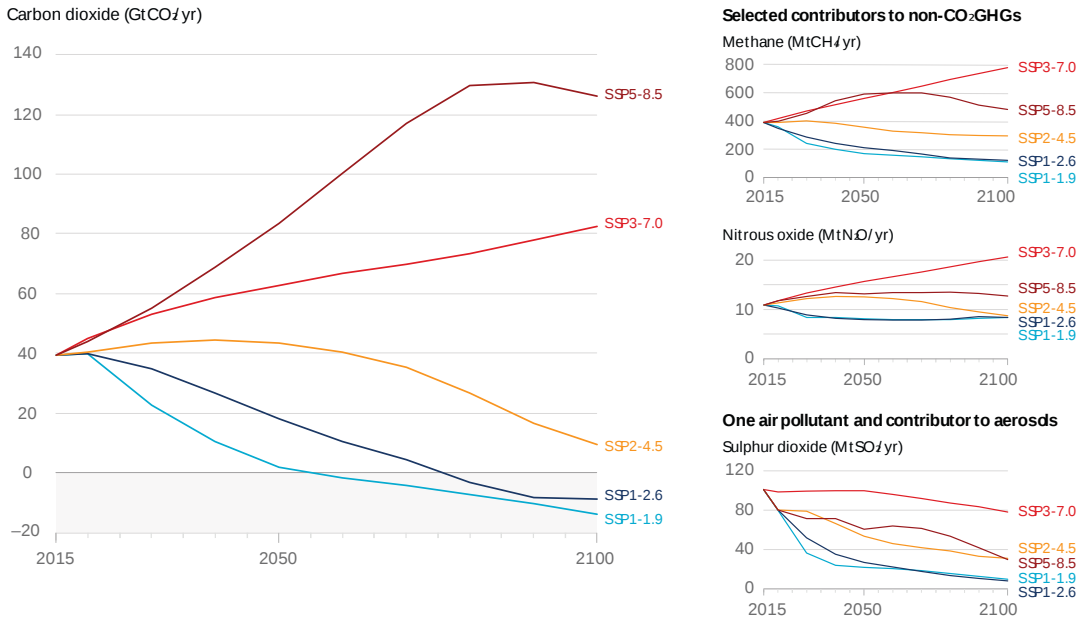


Figure **2.11**: Projected increases in greenhouse gases under different SSP (RCP) scenarios. Masson-Delmotte et al. Climate Change 2021: The Physical Science Basis. Contribution of Working Group I to the Sixth Assessment Report of the Intergovernmental Panel on Climate Change. Cambridge University Press, Cambridge, United Kingdom and New York, NY, USA, pp. 3−32, doi:10.1017/9781009157896.001.

Note the welcome decline in SO_2, which causes acid rain and aerosols. This shows that under all SSP scenarios, we are moving to clean up our air (in this case, reducing SO_2 from burning sulfur-enriched coal or capturing SO_2 before it enters the atmosphere). Paradoxically and unfortunately, decreasing aerosols leads to higher temperatures because incident solar irradiance is less reflected.

Our final figure, Figure **2.12**, shows how each greenhouse gas and SO_2 are projected to change in 2081-2100, compared to 1850-1900 levels, for each SSP scenario.

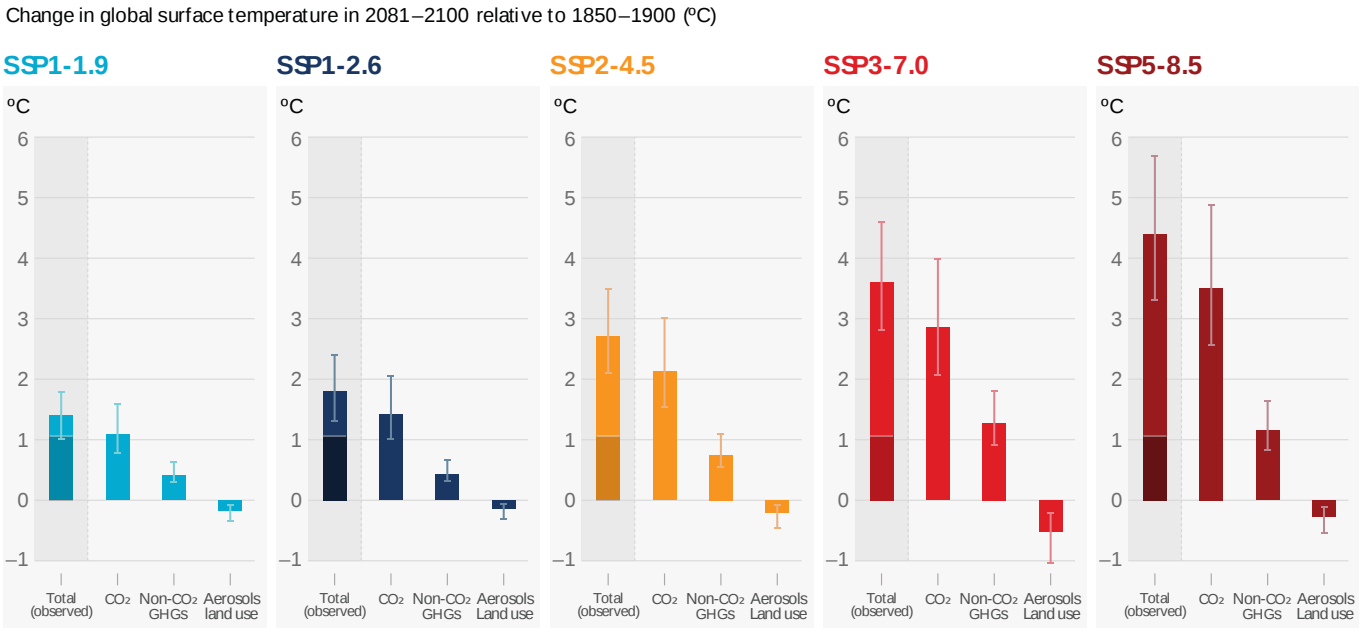


Figure **2.12**: Projected changes in greenhouse gases and SO_2 in 2081-2100 compared to 1850-1900 levels for different SSP scenarios. Masson-Delmotte et al, ibid.

We discussed in Chapter 32.1: A that Earth's Energy Imbalance (EEI) rose from about +0.6 Watts/m2 in 2000 to +0.9 W/m2 from 2005 to 2019, and to +1.0 W/m2 in 2021. The trend is, unfortunately, upward, as shown in Figure **2.13**.

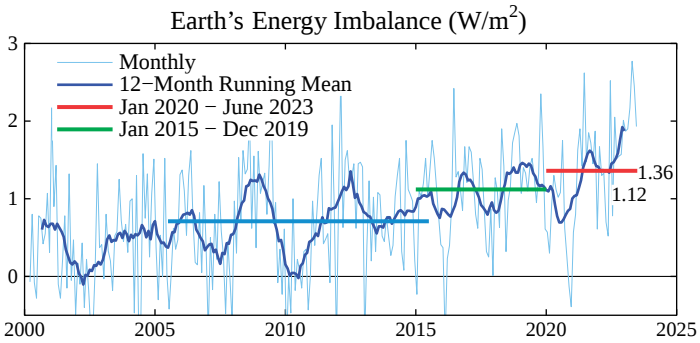


Figure **2.13**: Earth's Energy Imbalance since 2000. 12-month running-mean of Earth's energy imbalance from CERES satellite data normalized to 0.71W/m2 mean for July 2005–June 2015 (blue bar). James E Hansen, Makiko Sato, Leon Simons, Larissa S Nazarenko, Isabelle Sangha, Pushker Kharecha, James C Zachos, Karina von Schuckmann, Norman G Loeb, Matthew B Osman, Qinjian Jin, George Tselioudis, Eunbi Jeong, Andrew Lacis, Reto Ruedy, Gary Russell, Junji Cao, Jing Li, Global warming in the pipeline, *Oxford Open Climate Change*, Volume 3, Issue 1, 2023, kgad008, https://doi.org/10.1093/oxfclm/kgad008. Creative Commons Attribution License (https://creativecommons.org/licenses/by/4.0/)

The projected value of 1.36 (red bar) for the 2020s bodes poorly for our ability to reverse the effects of climate change. The large change that began around 2015 likely stems from decreased atmospheric sulfate emissions (required by legislation) from ships in the northern Atlantic and Pacific oceans and from coal burning in China. These decreases in atmospheric aerosols, which cause cardiovascular, pulmonary, and cancer diseases, paradoxically increase global warming. Sulfate aerosols reflect solar radiation. They also form clouds, which do the same. Both cool the planet. Aerosols that contribute to some of the worst pollution in the world in cities in South Asia have helped keep temperatures from rising to dangerous levels.

? THE SULFUR CYCLE AND DIMETHYLSULFIDE - ON EARTH

See below for more information.

Link

We have discussed the carbon and nitrogen cycles. The sulfur cycle also plays a role in the Earth's climate. As described above, sulfur aerosols (such as those produced by SO_2) can locally lower atmospheric temperatures by reflecting incoming solar radiation. Of course, they also harm the environment and human health by contributing to the formation of acid rain. Reduced sulfur-containing compounds, such as H_2S (hydrogen sulfide), **$(CH_3)_2S$ (dimethyl sulfide)**, and **DMSP (dimethylsulfoniopropionate)**, are also part of the cycle. A simplified version of the sulfur cycle is shown in the Figure **2.14** below.

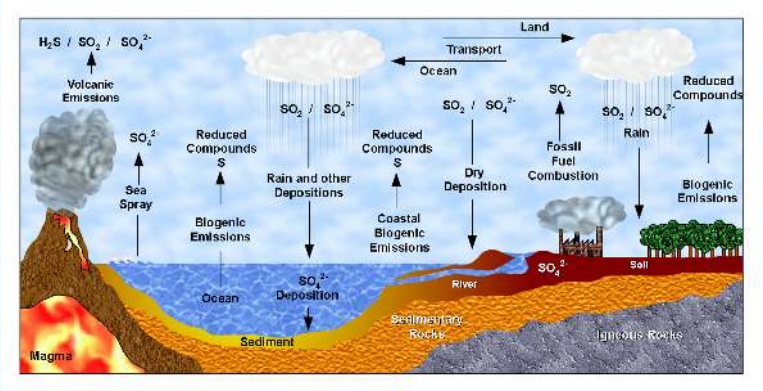


Figure **2.14**: The sulfur cycle. Elmer Robinson and Robert C. Robbins. Bantle, CC0, via Wikimedia Commons. https://commons.wikimedia.org/wiki/F...o_Enxofre).png. Creative Commons CC0 1.0 Universal Public Domain Dedication

DMS is released into the atmosphere by ocean phytoplankton, other microorganisms, and some plants. These can form aerosols that help cool the climate and transfer sulfur to the land. The structures of DMS and DMSP, along with the enzymes involved in their formation, are shown below in Figure **2.15**.

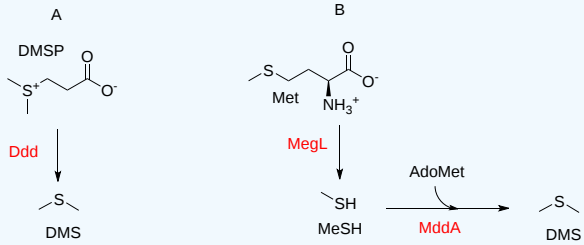


Figure **2.13**: **Formation of Methylsulfide.** After Carrión, O., Curson, A., Kumaresan, D. *et al*. A novel pathway producing dimethylsulphide in bacteria is widespread in soil environments. *Nat Commun* **6**, 6579 (2015). https://doi.org/10.1038/ncomms7579.

Panel A shows the DMSP cleavage pathway, catalyzed by DMSP lyase enzymes (Ddd) found in some bacteria. Panel B shows the pathway in *Pseudomonas deceptionensis* M1^T. Methionine (Met) is converted to MeSH using Met gamma lyase enzyme (MegL) in *P. deceptionensis* M1^T. MeSH is methylated to DMS by the enzyme MddA (a membrane protein methanethiol S-methyltransferase) using Ado-Met as the methyl donor.

DMSP can be synthesized from methionine via a variety of pathways, as shown in Figure **2.16**.

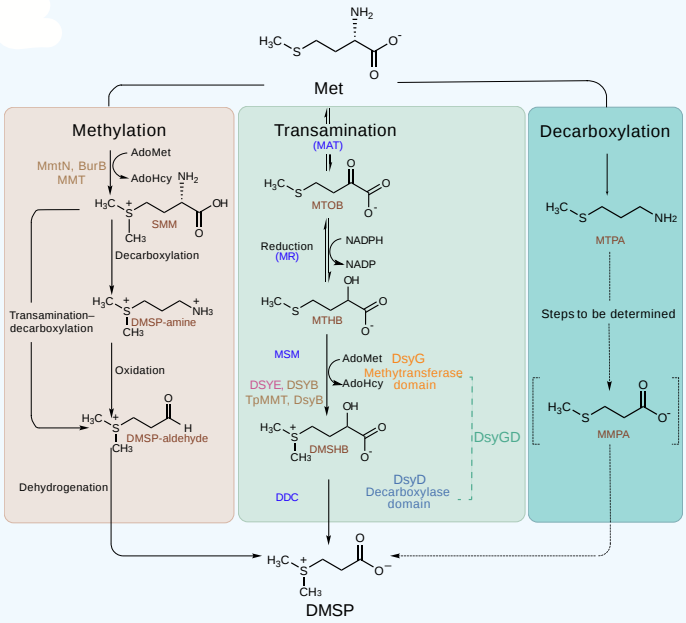


Figure **2.16**: **DMSP biosynthesis genes, enzymes, and pathways.** Wang, J., Curson, A.R.J., Zhou, S. *et al.* Alternative dimethylsulfoniopropionate biosynthesis enzymes in diverse and abundant microorganisms. *Nat Microbiol* **9**, 1979–1992 (2024). https://doi.org/10.1038/s41564-024-01715-9. Creative Commons Attribution 4.0 International License. http://creativecommons.org/licenses/by/4.0/.

The 'methylation' pathway in some higher plants with the methionine (Met) *S*-methyltransferase (MMT) and bacteria containing MmtN or another methyltransferase (BurB) (left); the 'transamination' pathway in algae, bacteria, and corals with DSYB/DsyB, DsyGD/DsyG, DSYE and/or TpMMT (middle); and the 'decarboxylation' pathway in *Crypthecodinium cohnii* (right). The pathways are named after their first reaction step (in larger font). AdoMet, *S*-adenosylmethionine; AdoHcy, *S*-adenosylhomocysteine; NADP, nicotine adenine dinucleotide phosphate; MAT, methionine aminotransferase; MR, MTOB reductase; MSM, MTHB *S*-methyltransferase; DDC, DMSHB decarboxylase; SMM, *S*-methylmethionine; MTOB, 4-methylthio-2-oxybutyrate; MTHB, 4-methylthio-2-hydroxybutyrate; DMSHB, 4-dimethylsulfonio-2-hydroxybutyrate; MTPA, 3-methylthiopropylamine; MMPA, 3-methylmercaptopropionate.

DMSP is not a minor microbial product. Petagrams (10^{15}) are made in surface water and more in other ocean regions. Intracellular DMSP (often at millimolar concentrations) is an osmolyte that helps cells cope with the osmotic stress of living in saltwater. It also provides carbon and sulfur to marine organisms. DMS is released into the atmosphere and cycles diurnally, giving the oceans their characteristic smell. It and DMSP are signaling molecules in fish and whales.

These last two chapters clearly show that humans have been engaged in large-scale geoengineering of the planet and its biosphere. We must develop new methods and technologies to lower the Earth's temperature. One might be the large-scale production of salt aerosols over the oceans, which would reflect incident sunlight and increase cloud formation.

This chapter shows how our climate fate will depend on our individual and collective choices as societies.

SUMMARY

(Summary written by Claude, Anthropic)

This chapter returns from deep geological time to examine the causes and trajectory of present-day warming, the lessons of historical climate anomalies, the global inequity of emissions, and the range of possible climate futures depending on societal choices.

Anthropogenic warming is unequivocal. Atmospheric CO_2 has risen steeply since the Industrial Revolution (~1760), from ~280 ppm to 427 ppm in 2025. NASA climate models clearly show that orbital dynamics, volcanic activity, solar variability, land-use change, and aerosols cannot account for observed warming since 1880; greenhouse gases from fossil fuel combustion are the sole factor that matches the observed temperature record. The seasonal oscillation visible in the CO_2 Keeling Curve reflects drawdown by Northern Hemisphere plant photosynthesis each summer. Methane, now at 1,900 ppb, accounts for approximately 20% of current warming.

Historical climate anomalies. Two notable natural climate disruptions are examined not to equate them with current warming, but to illustrate climate sensitivity and equip students to address skeptics. The Little Ice Ages (~1450–1850) were caused by a combination of reduced solar irradiance (the Maunder Minimum, ~0.06% decrease), volcanic aerosols, and likely a collapse of the AMOC triggered by Arctic ice melt and salinity dilution. Their effects included crop failures, plagues, the destruction of the Spanish Armada, and social upheaval across Europe and China. The climate collapse of 536 AD — the most severe cooling of the last 2,000 years, causing 18 months of darkness in parts of Europe, Asia, and the Middle East — was caused by a massive Icelandic volcanic eruption, compounded by further eruptions in 540 and 547, and was followed by the Justinian bubonic plague. Both events produced ~1.5–2.5°C of cooling with devastating consequences — far smaller in magnitude than projected future warming, yet catastrophic for affected populations.

Solar activity cannot explain present warming. Total solar irradiance data from 1610 to the present show that although the Maunder Minimum (~1630–1700) coincided with Little Ice Age cooling, solar activity has not increased in a manner that could explain warming since 1910. The 11-year sunspot cycle produces negligible net temperature change. In 2020, solar activity was near a cycle minimum, yet global temperatures were the second-warmest on record since 1880. Furthermore, present CO_2 levels (~427 ppm and rising toward 450 ppm) have raised the solar insolation threshold required to trigger glaciation to the point where the next ice age is effectively precluded without a massive sustained volcanic or asteroid-impact event.

Climate justice. Since the Industrial Revolution, the United States has emitted the most cumulative CO_2 per capita of any major nation — far exceeding China. Although China is now the largest annual net emitter, its per capita emissions remain lower than the US. The wealthiest income groups (high and upper-middle income) collectively account for 86% of global CO_2 emissions, yet the most severe climate impacts fall disproportionately on low-income, low-emission nations. Pakistan's catastrophic 2022 flooding — when a third of the country was submerged — exemplifies this inequity. A just response to climate change requires wealthy high-emitting nations to both rapidly reduce their own emissions and actively support lower-income nations in climate adaptation and clean energy transition.

Future projections. The IPCC defines five Shared Socioeconomic Pathways (SSP1–SSP5), ranging from aggressive decarbonization and international cooperation (SSP1, ~1.5°C warming) to continued high fossil fuel dependence (SSP5, ~4.9°C warming) by 2100. These correspond to Representative Concentration Pathways (RCPs) characterized by their radiative forcing in W/m² by 2100. Hansen et al.'s (2023) revised climate sensitivity of 4.8°C per CO_2 doubling — higher than the IPCC's commonly used 3.4°C — implies that the 1.5°C target is already out of reach and the 2°C target is in serious jeopardy without immediate, drastic action.

A critical paradox complicates near-term projections: reducing SO_2 aerosol emissions — mandated by clean air legislation and clearly beneficial for cardiovascular, pulmonary, and cancer health — simultaneously removes a cooling shield. Reduced sulfate aerosols from maritime shipping regulations and Chinese coal plants are the likely explanation for the acceleration of Earth's Energy Imbalance (EEI) after ~2015, from ~0.9 W/m² to a projected ~1.36 W/m² in the 2020s. Aerosols reflect solar radiation and seed cloud formation; their removal therefore accelerates warming. This means that improving air quality and reducing CO_2 emissions must proceed together, as eliminating aerosols without eliminating the underlying CO_2 forcing will worsen warming in the near term.

The chapter closes with the recognition that humanity has already been conducting large-scale, unintentional geoengineering of Earth's climate system. Intentional interventions — such as marine cloud brightening through salt aerosol production — are now being seriously considered as complements to the essential primary strategy: rapid, planned elimination of fossil fuel use.

2: Back to the Present and Future of Climate Change is shared under a CC BY-NC-SA 4.0 license and was authored, remixed, and/or curated by LibreTexts.

3: USE OF ISOTOPE ANALYSIS IN MEASURING CLIMATE CHANGE

Search Fundamentals of Biochemistry

LEARNING GOALS

(Learning goals written by Claude, Anthropic)

By the end of this chapter, students should be able to:

Proxies, Ocean Microorganisms, and Climate Archives

- Distinguish between direct measurements and proxy measurements of past CO_2 and temperature, describe at least four proxy types (tree rings, coral bands, pollen, foraminifera shells), and explain why combining multiple proxies from thousands of global sites produces more reliable reconstructions than any single proxy alone.
- Distinguish between zooplankton and phytoplankton, explain why foraminifera shells — but not dinoflagellate remains — are preserved in ocean sediments and useful for paleoclimate reconstruction, and describe how benthic versus planktonic foraminifera record different climate signals (global ice volume vs. local surface temperature).

Radioactive Isotope Dating

- Explain how ^{14}C is produced in the atmosphere, incorporated into living organisms, and used to date samples up to ~55,000 years old, identify the key assumptions and calibration requirements of the method, and explain how fossil fuel combustion and nuclear weapons testing have altered atmospheric ^{14}C levels.
- Identify at least three other radioactive isotope systems used for longer-range dating ($^{40}K/^{40}Ar$, $^{26}Al/^{10}Be$, $^{238}U/^{206}Pb$) and explain the underlying principle — that the ratio of parent to daughter isotope changes predictably with time after a system closes.

Stable Isotopes and $\delta^{18}O$ in Ice Cores

- Define $\delta^{18}O$, explain how it is calculated relative to V-SMOW, and interpret positive and negative values in terms of ^{18}O enrichment or depletion relative to the standard.
- Explain isotope fractionation — why $H_2{}^{16}O$ evaporates preferentially over $H_2{}^{18}O$ — and describe how Rayleigh distillation produces progressively more negative $\delta^{18}O$ values in precipitation moving toward the poles, making polar ice strongly depleted in ^{18}O ($\delta^{18}O \approx -30$ to $-55‰$).

$\delta^{18}O$ in Ocean Sediment Cores and Paleotemperature

- Explain the two reinforcing reasons foraminifera shells become enriched in ^{18}O during cold/glacial periods — thermodynamic enrichment of ^{18}O in calcite at lower temperatures, and enrichment of $H_2{}^{18}O$ in seawater as $H_2{}^{16}O$ is locked in ice sheets — and express the combined effect in simplified form.
- Describe the Kim and O'Neil fractionation equation relating temperature to the calcite-water fractionation factor α, explain how it is used to derive paleotemperature from $\delta^{18}O$ measurements, and identify the factors beyond temperature (salinity, pH, shell size, biological effects) that complicate interpretation and require species-specific empirical calibration.

This chapter will explore how to reconstruct CO_2 and temperature values across millions of years. It is truly a remarkable, if not awe-inspiring, achievement that shows the intellectual rigor and endurance scientists employ to obtain, interpret, and model data. The graphs of CO_2 vs. temperature across such a vast swath of time shown in the previous chapter section were obtained from analyses of oxygen and carbon isotopes in chemical species from ice and ocean-floor sediments. Interpreting the isotope data requires understanding the link between individual and linked chemical and biochemical reactions. So, we have to deeply dive into isotopes and their use.

WHY STUDY ISOTOPE EFFECTS

- Isotopes and their effects are critical to understanding the structure and activity of biochemical reactions and to climate science.
- Isotope partitioning into water and biomolecules involves both equilibrium and nonequilibrium reactions and processes, similar to linked biochemical reactions and pathways.
- The study and application of isotope effects can integrate and expand learning from previous science courses.

In more global terms

- We must assess the quality and robustness of our data and models to support our understanding of biochemistry and climate change.
- Scientific and ethical rigor are essential for pursuing knowledge, explanations, and solutions in biochemistry and climate change. It is necessary to trust our experts and believe in their findings.

ABSOLUTE AND PROXY MEASUREMENTS FOR CO_2 AND TEMPERATURE

It's simple to see how CO_2 levels over the last 800,000 years have been determined from ice cores, since ancient air is trapped in bubbles in them. The bubbles can be liberated by melting/shattering and analyzed. However, how can we infer temperature changes or actual temperature from ice core samples and both CO_2 and temperature from ocean sediment cores? Scientists use "proxies" to determine temperature, as modern thermometers and temperature scales were invented only recently (in the early and mid-1700s by Fahrenheit and Celsius). These proxies include tree rings, growth bands in coral, pollens found in core samples, and calcite shells from marine organisms found in lake and ocean sediments. The organisms include certain types of algae, phytoplankton like dinoflagellates and diatoms, and foraminifera (single-celled protozoans with shells).

From a more chemical perspective, analyses of the isotopic composition of ice, using the $^{18}O/^{16}O$ ratio in water, and of marine sediments, using the ratio of $^{18}O/^{16}O$ and $^{13}C/^{12}C$ in carbonate-containing shells, have proved critical in determining temperatures back millions of years. Even molecules in leaf waxes (as discussed in Chapter 31.1) can be used. Isotope analyses of diatoms (with silicate shells) in lake sediments are also useful.

The analysis of proxies is quite complicated, as many factors contribute to the measurements derived from proxy use. Take tree rings as an example. The width of a given ring depends not only on temperature but also on precipitation. Each proxy must be calibrated using alternative data, such as tree-ring data. Proxy data from ice cores extends back a few million years, while marine sediment data extends back as far as 100 million years. Isotope analysis in rocks formed from marine or land sediments can go back billions of years. Recently collected proxy data (tree rings) can be compared with actual temperature measurements from the same period. The calibration relationships can then be used for past samples. Alternatively, proxy data can be taken across many different places and temperatures to develop calibration constants, an approach useful for pollen analysis. To calibrate past data, organisms could also be cultured under different temperatures, nutrient conditions, and CO_2 levels. Statistically, it is best to combine multiple proxies to reconstruct past temperatures. Proxy data sets are available for over 10,000 sites worldwide. Figure **3.1** below links to sites compiled by Carbon Brief, where databases with information about each study are available.

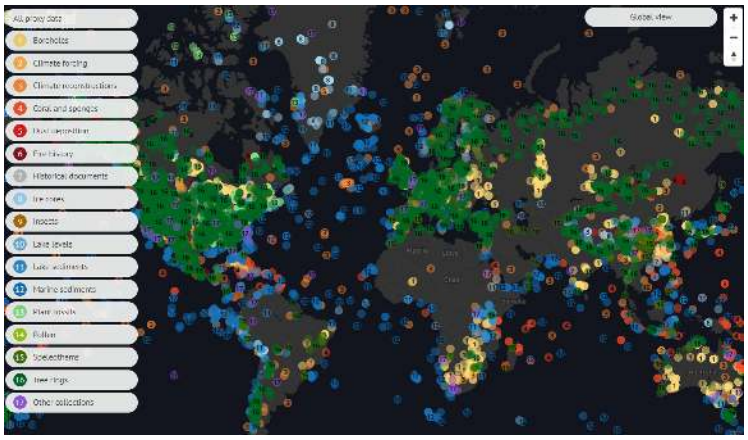


Figure **3.1**: Map of over 10,000 proxy data studies and sites. Robert McSweeney, Zeke Hausfather, and Tom Prater. https://interactive.carbonbrief.org/...-distant-past/

Most people might care little about climate change millions of years ago. The value of understanding climate change in the past is, in part, to build confidence in the data, methods of analysis, and climate models to better understand the relationship between CO_2 and temperature. Some, particularly the PAGES 2k Consortium, focus on the last 2000 years of the Common Era. Figure **3.2** shows global mean temperatures obtained from proxy data (yrs 0 - 2000) and direct observations (through the use of thermometer and satellite measurements) since around 1850.

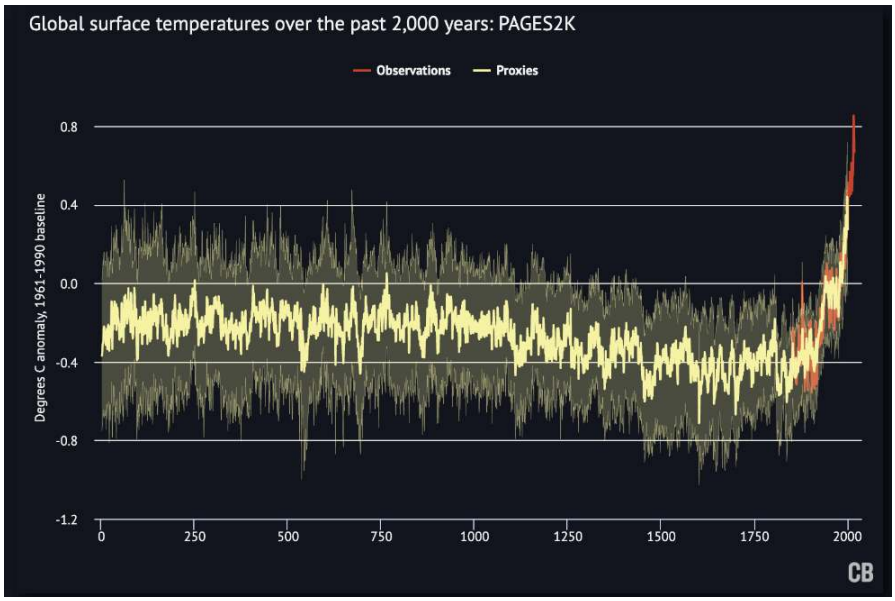


Figure 3.2: Global mean surface temperature reconstruction (yellow line) and uncertainties (yellow range) for the years 0-2000 period from the PAGES 2k Consortium along with observations from Cowtan and Way from 1850-2017. Data available in the NOAA Paleoclimate Archive.

Note the overlap of proxy measurements and direct observations of temperatures since around 1850.

OCEAN MICROORGANISMS

Biochemistry students come from many backgrounds, but not all have a strong background in biology. Let's look at a few relevant topics in this chapter to help with that and to develop a sense of wonder about the microorganisms that inhabit the oceans and play such a key part in the biosphere. These descriptions are probably new for those with a "chemistry-centric" focus.

Plankton

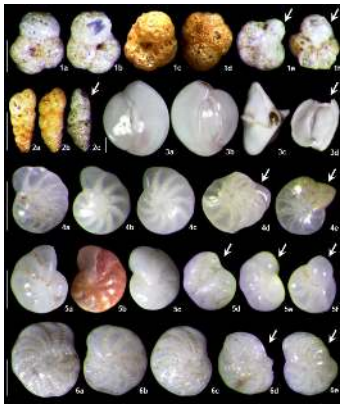
The word plankton derives from a Greek word meaning drifter or wanderer. There are two main types. One is **zooplankton,** which are not plants but rather microscopic animals and protozoans. They are heterotrophs that don't synthesize their food. Most have calcite shells. The other is **phytoplankton,** autotrophic organisms that use photosynthesis to produce food. Hence, they are carbon "capturers", key players in the carbon cycle in maintaining atmospheric CO_2 and producing O_2. The phytoplankton broadly includes algae (protists), cyanobacteria (also known as blue-green algae), and dinoflagellates, which also fit into other groups. Here are some examples. Also, remember that protists are eukaryotic organisms, not animals, plants, or fungi.

Table 3.1 below lists types and examples of plankton.

Type of plankton	Examples
Zooplankton (heterotrophs)	Benthic foraminiferans, which live mostly on the sea bottom and in sediment, capture carbon indirectly in the carbon cycle through carbonate in their shells. Planktonic foraminifera, which live near the surface but are found buried in ocean sediments after their death Dinoflagellates that don't photosynthesize are small animals, including tiny fish and crustaceans such as krill and jellyfish. Radiolarians, single-cell protozoans that have calcium silicate shells
Phytoplankton (autotrophs, primary producers)	Diatoms Photosynthesizing dinoflagellates Blue-green algae, which are prokaryotic bacteria Green algae, photosynthetic eukaryotic protists. Some foraminifera that live near the surface water and can photosynthesize

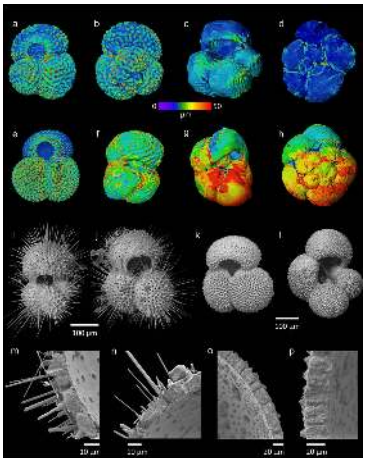
Zooplankton

Existing shells in marine sediments from foraminifera have been critical for dating studies and for determining CO2 levels and temperatures over millions of years. Two major types are benthic foraminifera (which live at the sea bottom and in sediment) and a smaller group of planktonic foraminifera, which live near the surface. They are heterotrophs, but when they ingest small autotrophic phytoplankton, some can retain and sequester their chloroplasts, which can continue photosynthesis for a while. Figures **3.3 – 5** below show examples of zooplankton that have been important in climate studies.



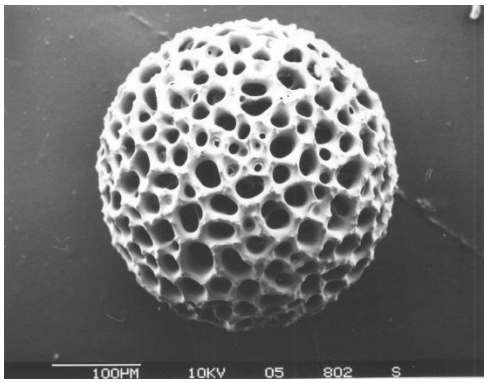
Figures **3.3 above: Benthic foraminifera:**

Live mostly at the sea bottom and in sediment); capture carbon indirectly through the carbon cycle by incorporating CO_3^{2-} into their shells. Living benthic foraminifera in the Bohai Sea, showing normal specimens and abnormal individuals (indicated by arrows).



Figures **3.4 above: Planktonic foraminifera**

They live near the surface but are buried in ocean sediments after death. (**a**–**h**) Nano-CT scan of planktonic foraminifera specimens with a color map of test thickness, warm colors indicating areas of relatively thicker shell; (**a**,**b**) *Globigerinoides ruber* (*Tara*), (**c**) *Globigerina bulloides* (*Tara*), (**d**) *Neogloboquadrina dutertrei* (*Tara*), (**e**) *G. ruber* (*Challenger*), (**f**) *Trilobatus trilobus* (*Challenger*), (**g**) *N. acostaensis* (*Challenger*), (**h**) *N. dutertrei* (*Challenger*); (**i**–**p**) SEM images of selected planktonic foraminifera specimens; (**i**) *T. trilobus* (*Tara*), (**j**) *G. ruber* (*Tara*), (**k**) *G. ruber* (*Challenger*), (**l**) *G. bulloides* (*Challenger*), (**m**,**n**) *G. ruber* test cracked to reveal wall texture (*Tara*), (**o**,**p**) *G. ruber* test cracked to reveal wall texture (*Challenger*).



Figures **3.5 Above: Radiolaria .**single-cell protists that secrete silica

Figures **3.3 – 5**: Examples of zooplankton. Benthic foraminifera: https://commons.wikimedia.org/wiki/F...raminifera.p; Planktonic foraminifera: Creative Commons Attribution 4.0 International License. Fox, L., Stukins, S., Hill, T. *et al*. Quantifying the Effect of Anthropogenic Climate Change on Calcifying Plankton. *Sci Rep* **10**, 1620 (2020). https://doi.org/10.1038/s41598-020-58501-w. http://creativecommons.org/licenses/by/4.0/.; Radilaria: https://commons.wikimedia.org/wiki/F...ria-sp2_hg.jpg

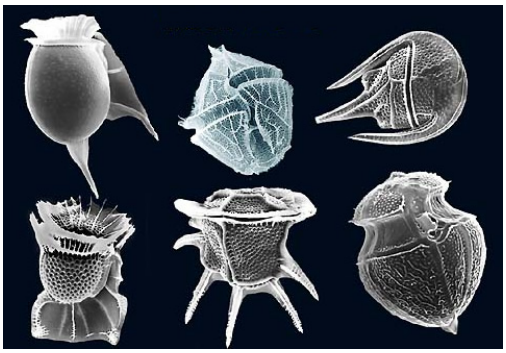
Phytoplankton

Phytoplankton are microscopic plants that use photosynthesis, capture CO_2, and produce O_2. Hence, they are primary autotrophs. We will consider three types: diatoms, photosynthetic dinoflagellates, and coccolithophores. Diatoms and photosynthetic dinoflagellates are the major ones and are prey for the zooplankton. They are described in Figures **3.6 – 8** below.



Figures **3.6 Above: diatoms**

Single-celled eukaryotic algae are surrounded by a silica shell (test). These can reach 1 mm in diameter and take various shapes. Some can form multicellular chains. They engage in high-efficiency photosynthesis, resulting in carbohydrate synthesis. They are found in coastal and cold-water habitats that are rich in nutrients.



Figures **3.7 Above: photosynthetic dinoflagellates**

Algae with a single shell. They are smaller than diatoms. Most have two flagella for motion. They have a cellulose shell, which degrades upon death. Hence, they don't have shells that enter the sediment. Some are nonphotosynthetic and are considered zooplankton.



Figures **3.8 Above: coccolithophores**

Coccolithus pelagicus is covered with a $CaCO_3$ shell, a coccosphere. These are very small single-cell algae that form interlinked calcium carbonate circulate plates that cover the surface.

Figures **3.6 – 8**: Some phytoplankton. Diatoms: https://commons.wikimedia.org/wiki/C...le:Diatom2.jpg; photosynthetic dinoflagellates: https://commons.wikimedia.org/wiki/F...lagellates.jpg; coccolithophores: https://commons.wikimedia.org/wiki/F..._pelagicus.jpg

Along the coast in summer, nutrient-rich upwelling can lead to the explosive growth of dinoflagellates, turning the water red-gold (often called a red tide). Some species in these blooms produce neurotoxins such as saxitoxin (an inhibitor of sodium channels), which can produce paralytic shellfish poisoning if shellfish from the bloom area are eaten, and brevetoxin (which stimulates voltage-gated sodium channels in nerve and muscle).

Ice cores from Antarctica and Greenland can extend to over 3.4 km (2.1 miles) in depth and yield direct information on CO_2 and indirect temperature measurements. Until recently, continuous ice core records covered 130,000 years in Greenland and 800,000 years in Antarctica. Remarkably, a single continuous ice core 2,800 meters (1.74 miles) long that extends to the bedrock in Antarctica, dating back 1.2 million years, is now available. Analysis of this core might reveal the cause of the extension of the glacial cycle from 40,000 to 100,000 years, starting around 1 million years ago. Data spanning 2 million years is available from discontinuous cores. Concentrations of trapped CO_2 as a function of time and the temperature of each layer in these cores can be determined. Figure **3.9** shows a section of an ice core from the West Antarctic Ice Sheet Divide (WAIS Divide).



Figure **3.9**: *The dark band in this ice core from the West Antarctic Ice Sheet Divide (WAIS Divide) is a layer of volcanic ash that settled on the ice sheet approximately 21,000 years ago. Credit: Heidi Roop, NSFhttps://icecores.org/about-ice-cores*

The remains of plankton shells described above are found in sea sediment cores. Analyses of shells, especially those of foraminifera, have provided climate data dating back tens of millions of years. For ice and ocean sediment cores, isotope analyses have been the key to obtaining CO_2 and temperature data.

ISOTOPE ANALYSES

To analyze ice and ocean sediment cores, three things are needed: the age of the layer, a direct or indirect measure of atmospheric CO_2 at the time the layer was deposited, and an indirect measure of the temperature at the time of deposition. As shown in the figure above, ice core samples have rings, similar to trees, that can be used to count backward in time. The rings get harder to distinguish the further back you go. Figure 3 above shows a visible dark band deposited by volcanoes 21,000 years ago. Ultimately, isotopic analyses of H_2O and CO_2 in ice

samples and of carbonates in minerals from deposited microfossils in ocean samples are critical in determining past CO_2 and temperature values.

Most readers are familiar with ^{14}C radiocarbon dating and ^{13}C-NMR. Metabolic pathways have been elucidated using ^{2}H (deuterium), ^{3}H (tritium), ^{13}C, and ^{14}C to label specific atoms in substrates and follow their flow into products. These same isotopes have been used in kinetic experiments to determine enzyme reaction mechanisms. In this section, we will explore isotopes in some detail.

Use of unstable radioactive isotopes

^{14}C radiocarbon dating is limited in climate analyses due to its short half-life ($t_{1/2}$ = 5730 years). In contrast to most isotopes made in stellar nucleosynthesis or by the radioactive decay of a precursor radioactive element to an isotope of another element, ^{14}C is made continually in the atmosphere when high-energy neutrons (n) from solar radiation react with atmospheric nitrogen (N). The neutron kicks out a proton to form ^{14}C, as shown in the nuclear reaction below.

$$n + {}^{14}_{7}\mathrm{N} \rightarrow {}^{14}_{6}\mathrm{C} + p \tag{3.1}$$

^{14}C becomes oxidized to form $^{14}CO_2$, which can enter the carbon cycle and the organic carbon pool through uptake by photosynthetic organisms and organisms that consume them. It can also form inorganic bicarbonate and carbonate ions, which could enter shells.

All living things take in ^{14}C until their death, after which ^{14}C decays through converting a neutron to a proton, a beta particle (electron), and an antineutrino, forming stable ^{14}N. Hence, ^{14}C in dead organisms or their remains decays with a $t_{1/2}$ of 5730 years, in a process unaffected by temperature or pressure. ^{14}C dating can be used on samples dating back about 55,000 years, a timespan representing 9.6 half-lives. Only 0.13% of the original ^{14}C would be left. Data from this method provides the organism's age at death.

Carbon-14 dating assumes that the amount of carbon-14 in the environment is constant. However, the burning of fossil fuels and detonation of nuclear weapons have altered its amount (see box below). Changes in solar activity and the resulting changes in high-energy neutrons also affect the amount of carbon-14. Also, given the relatively short time frame of ^{14}C dating, differences in CO_2 based on its sequestration and circulation in the oceans are factors. Oceans cover 61% of the Northern Hemisphere compared to 81% of the Southern Hemisphere. Books on calibration factors can be used to control these effects. The calibrations are based on data from tree rings, lake and ocean sediments, corals, and stalagmites, which date back 55,000 years.

NUCLEAR WEAPONS, FOSSIL FUELS, AND ^{14}C DATING

In the 1950s up to 1962, nuclear weapons were tested in the air, doubling the amount of ^{14}C in the air. Organisms and the ocean have taken up this ^{14}C spike. Also, since then, the amount of CO_2 from burning fossil fuels has increased dramatically. This source does not contain ^{14}C because it derives from fossils that have long since decayed. The effects canceled each other in 2021. Since 2021, more CO_2 from fossil fuels has been added, so the net effect is now lower levels of ^{14}C, equivalent to preindustrial time. It will continue to lessen until well after we stop using fossil fuels. By 2050, the levels might be equivalent to those in the Middle Ages. This, and the human-made halt to the next ice age glaciation cycle, are yet another warning about our effects on the entire biosphere.

The decay of other "unstable" radioactive isotopes is used for dating samples and determining the age of burial:

- ^{39}Ar, an extremely rare isotope ($t_{1/2}$ =269 yr), has been used to date ice cores from the Tibetan Plateau over the last 1,300 years.
- ^{40}K ($t_{1/2}$ = 1.25 billion yr) decays to ^{40}Ar (stable), so their ratios can be used to determine how much time has passed since magma solidified into rock, based on diffusion rates of the resulting stable ^{40}Ar.
- The $^{26}Al/^{10}Be$ ratio in buried samples is used in dating analyses. The two isotopes are rare and are produced in a fixed ratio (6.75/1) when formed in surface quartz by solar radiation (much as ^{14}C is produced). When buried through geological processes, there is no further production of the isotope, but fortunately (for those who measure the age of burial), they decay with different half-lives ($t_{1/2}$ = 717,000 yr for ^{26}Al and $t_{1/2}$ = 1.39 million yr for ^{10}Be)
- The ratios of $^{21}Ne/^{26}Al$ and $^{21}Ne/^{10}Be$ can be used. ^{21}Ne is a stable isotope, and these ratios are independent of the $^{26}Al/^{10}Be$ rate.
- Uranium isotopes are widely used to measure age on a long-term time scale. ^{238}U ($t_{1/2}$ =4.45 billion yr) is converted to ^{206}Pb (stable) and ^{235}U ($t_{1/2}$ =704 million yr) to ^{207}Pb (stable) by parallel decay routes, which allow for multiple types of dating measurement.

Use of stable isotopes

Most of the data and graphs of CO_2 and temperature vs time (years ago) presented in Chapter 31.1 were determined using stable isotopes that do not decay. Much of the data is based on the ratio of the stable isotope pairs of oxygen ($^{18}O/^{16}O$) or carbon ($^{13}C/^{12}C$) in buried ice or ocean sediment cores. These isotopes have also been used to infer temperatures or temperature changes when targets were buried in ice cores or ocean sediments. Temperatures at the time of water deposition in ice layers are often inferred from $^{18}O/^{16}O$ ratios in the layers.

ICE CORE $^{18}O/^{16}O$ ANALYSES

The oceans are vast and generally homogeneous reservoirs that can provide clues to long-term climate change. Short-term climate change would have limited effects on the oceans. The $^{18}O/^{16}O$ ratios in Greenland and Antarctic ice cores have enabled dating and temperature reconstruction back 800K years, and possibly even longer, since the ratio is determined by the $^{18}O/^{16}O$ in the liquid oceans at the time of ice formation.

The natural abundances of ^{18}O (0.205 %) and ^{16}O (99.757 %) give a ratio of the two isotopes of 0.0021, which is so small that the exact ratio is inconvenient for routine use. Rather, a comparison of the ratios in a target sample vs a universal reference, the **$\delta^{18}O$ value**, is determined using a mass spectrometer. The $\delta^{18}O$ value is calculated using the following equation:

$$\delta^{18}O = \left[\frac{\left(\frac{^{18}}{^{16}}O\right)_{\text{sample}}}{\left(\frac{^{18}}{^{16}}O\right)_{\text{reference}}} - 1 \right] * 1000 \qquad (3.2)$$

Similar δ values are determined for D/H ratios ($\delta^{2}H$) and for $^{13}C/^{12}C$ ($\delta^{13}C$)

- The reference for $\delta^{18}O$ calculations is the Standard Mean Ocean Water (SMOW or V-SNOW)
- The $\delta^{2}D$ reference value is also based on SMOW or V-SNOW
- The standard for the analogous $\delta^{13}C$ value is the Cretaceous Peedee Belemnite (an extinct order of squid-like cephalopods with an internal cone skeleton) sample from the Peedee Belemnite (PDB) formation in South Carolina, USA. This standard is no longer available, so an alternative, NBS 19, a carbonate material, is used in a new V-PDB (Vienna-PDB) scale.

Table **3.4** shows the ratio of the isotope abundancies in nature and in the references.

Element ratio	Ratio of natural abundance	Reference ratio
$^{18}O/^{16}O$	0.205/99.757 = 0.00205	0.0020052 (SMOW or V-SMOW)
$^{13}C/^{12}C$	1.1/98.9 =0.0111	0.011238 (PDB or V-PDB)
$^{2}H/^{1}H$ (D/H)	0.0156/99.9844 = 0.000156	0.00015576

Note that the ratios of the standards, and likewise of the samples, are small. Also note that in the equation for $\delta^{18}O$, the bracketed term is multiplied by 1000.If multiplied by 100, the value for $\delta^{18}O$ would be a percentage. Instead, it's multiplied by 1000 to convert it to **per mill** (per mil or ‰) or parts per thousand (just like percent is parts per 100). Hence 1‰ is 1 part per 1000 or 0.1%.

Equations can be just collections of letters with little intuitive meaning, or the user can deconstruct them to make intuitive sense. To help readers understand this equation, which most have likely never encountered, given its importance in climate studies, let's look at three sets of conditions. If ...

- ^{18}O is enriched in the sample compared to the reference, then $(^{18}O/^{16}O)_{sample}/(^{18}O/^{16}O)_{reference}$ is >1, so subtracting 1 makes the bracketed term +, along with $\delta^{18}O$;
- ^{18}O in the sample is equal to that in the reference, then $(^{18}O/^{16}O)_{sample}/(^{18}O/^{16}O)_{reference}$ =1, so the bracketed term = 0, and $\delta^{18}O = 0$;
- ^{18}O in depleted in the sample compared to the reference, then $(^{18}O/^{16}O)_{sample}/(^{18}O/^{16}O)_{reference}$ <1, so the bracketed term is -, along with $\delta^{18}O$.

A sample with a higher $^{18}O/^{16}O$ ratio (enriched in the heavier isotope) than the SMOW reference will have a positive (+) δ value. If the $^{18}O/^{16}O$ ratio of the substance is lower (depleted in the heavier isotope) than the SMOW reference, the δ value will be negative (-). The δvalues of SMOW (O and H isotopes) and PDB (C isotopes) are zero as they are compared to themselves.

Now let's examine ice and ocean $\delta^{18}O$ values and see how delta values are used as proxies for temperature or changes in temperature at deposition.

The ice shields form from snow that forms from water evaporated from the oceans. Water can have multiple isotopic compositions, but based on the % abundances, the most likely ones are $H_2{}^{16}O$ and $H_2{}^{18}O$. The lighter $H_2{}^{16}O$ evaporates more readily from the mid-latitudes of the oceans, and when it reaches the poles, it condenses to form snow and eventually ice enriched in $H_2{}^{16}O$. Urey showed that the vapor pressure of $H_2{}^{18}O$ is about 1% less than that of $H_2{}^{16}O$ between 46.35°C and 11.25°C.

In addition, the $H_2{}^{18}O$ that evaporates at lower latitudes is more likely to condense and be removed in rain, leaving the southern oceans enriched in $H_2{}^{18}O$. This effect is quite significant: water, in the form of ice, in Greenland and Antarctica has about 5% less $H_2{}^{18}O$ than water at 20 ^{0}C from midlatitudes, making the $\delta^{18}O$ of water a proxy for temperature **but even better as a measure of ice volume and from that sea levels**.

Now consider the Ice Ages, when oceans were enriched in $H_2{}^{18}O$. During glacial melting of $H_2{}^{16}O$-enriched ice, with meltwater flowing into the oceans, $H_2{}^{18}O$ would get diluted with $H_2{}^{16}O$. At the same time, sea salinity would decrease because ice forms without ocean salts.

These differences in $H_2{}^{18}O/H_2{}^{16}O$ values in ice core samples are converted to $\delta^{18}O$ values, which can be positive or negative, as shown in Figure **3.10**.

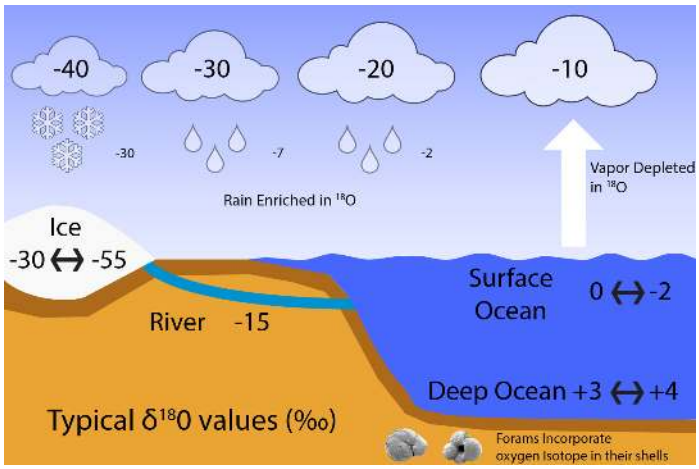


Figure **3.10**: Typical $\delta^{18}O$ values (in permil). Andreas Schmittner. https://eng.libretexts.org/Bookshelv...A_Paleoclimate

Surface ocean water has $\delta^{18}O$ values of around zero. Due to fractionation during evaporation, less heavy isotopes are incorporated into the air, which leads to negative delta values of around -10 ‰ for the evaporated water vapor. Condensation prefers the heavy isotopes, as described above. In this example, the first precipitation thus has a $\delta^{18}O$ value of about -2 ‰,(more positive than the first vapor). The remaining water vapor will be further depleted in ^{18}O relative to ^{16}O, and its $\delta^{18}O$ value will become more negative (-20 ‰). Any subsequent precipitation event further depletes ^{18}O. This process, known as **Rayleigh distillation**, results in very low $\delta^{18}O$ values of less than -30 ‰ for snow falling onto ice sheets. Thus, ice has a very negative $\delta^{18}O$ of between -30 and -55 ‰. Deep ocean values today are about +3 to +4 ‰. During the last glacial maximum, as more water was locked up in ice sheets, the remaining ocean water became heavier in $\delta^{18}O$ by about 2 ‰. Foraminifera build their calcium carbonate ($CaCO_3$) shells using the surrounding seawater. Thus, they incorporate the oxygen-isotopic composition of the water into their shells, which are then preserved in sediments and can be measured in the lab. Bralower and David Bice. https://www.e-education.psu.edu/earth103/node/5. Creative Commons Attribution-NonCommercial-ShareAlike 4.0 International License(link is external).

In summary, Greenland and Antarctic ice is enriched in ^{16}O during cold conditions since $H_2{}^{16}O$ preferentially evaporates, condenses, and freezes into ice at the poles. In addition, as we will see below, deep-sea Foraminifera shells contain more ^{18}O in shells since water is enriched with $H_2{}^{18}O$ in cold conditions, since less evaporates. Hence, $\delta^{18}O$ becomes more positive.

The interactive graph below shows how Rayleigh Distillation drives changes in $\delta^{18}O$ in polar ice as a function of temperature at the tropics and at different latitudes. Move the sliders to see the calculated $\delta^{18}O$ values.

PART 2 OF 7 — OXYGEN ISOTOPE FRACTIONATION & ICE CORE PROXIES

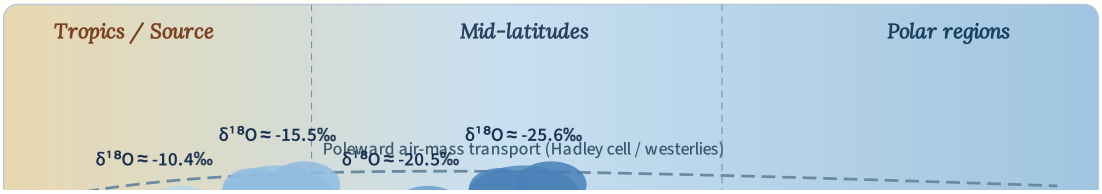
Rainout & Poleward Transport: Rayleigh Distillation

As ^{16}O-enriched vapor moves from the tropics toward the poles, it cools and condenses. Each precipitation event preferentially removes $H_2{}^{18}O$ from the remaining vapor (because it condenses more readily). By the time air masses reach polar regions, the residual moisture is extremely depleted in ^{18}O.

This progressive depletion follows **Rayleigh distillation**: with each condensation step, the vapor becomes lighter — more negative in $\delta^{18}O$. Adjust the sliders below to see how source temperature and number of rainout events determine how depleted polar precipitation becomes.

Source temperature (tropics): 28°C

Number of rainout steps: 4



Anthropic. (2025). *Claude* (Claude Sonnet 4.6) [Large language model]. Retrieved May 2, 2025, from https://claude.ai

OCEAN SEDIMENT CORE $^{18}O/^{16}O$ ANALYSES

In the last section, we looked at $\delta^{18}O$ values in ice core layers and their use as proxies for land and ocean temperatures and, more fundamentally, as indicators of ice volume, affecting sea levels and ocean salinity. It's amazing what we can surmise about past climate based on the fact that $H_2{}^{16}O$ evaporates more readily than $H_2{}^{18}O$, and that $H_2{}^{18}O$ that did evaporate condenses at low and mid-latitudes more readily than $H_2{}^{16}O$. These two factors lead to the enrichment of $H_2{}^{16}O$ in polar ice and $H_2{}^{18}O$ in low and mid-latitude ocean water. Remember that evaporation and condensation are physical reactions involving a state change.

Yet ice cores extend only so far back in geological time. To go back further, scientists analyze shells buried in ocean sediments. More specifically, they analyze the $^{18}O/^{16}O$ isotopic ratio in calcium carbonate (calcite, $CaCO_3$) from the buried shells of organisms such as foraminifera. (Calcite is a stable anhydrous form of $CaCO_3$, but it can form different calcite phases under high pressure.) Now, we are dealing with a new atom, C, in the carbonates. Hence, the interpretation of $\delta^{18}O$ in buried carbonate is influenced by more factors than in solid or liquid water. It must include these factors

- the chemical reactions of inorganic carbonate formation (precipitation) and dissolution (compared to the physical reactions of water evaporation and condensation)

- the biological formation of $CaCO_3$ in shells
- an understanding of the carbon cycle
- the temperature at which the $CaCO_3$ was deposited
- the salinity at deposition, as the formation of $CaCO_3$ from its ions, and the overall ionic strength of the medium in which $CaCO_3$ formed, would influence the thermodynamics and kinetics of how the separate ions approach each other to form the solid
- equilibrium and kinetic controls of the precipitation reactions.

We will see below that Foraminifera shells in ocean core samples contain more ^{18}O in cold conditions because $H_2{}^{18}O$ iis enriched in those conditions. Hence, $\delta^{18}O$ becomes more positive.

To truly understand biochemistry, we must include both biological and chemical aspects. Biochemistry requires synthesizing knowledge from many disciplines, including introductory chemistry (where precipitation reactions were likely first covered) and analytical chemistry (which delves more deeply into them). Hence, we don't apologize for bringing back your previous knowledge of precipitation reactions. At the same time, our description of the use of $\delta^{18}O$ values in buried ocean sediments is very simplified.

We must consider two reactions to understand $\delta^{18}O$ values in calcite Foraminifera shells. The first describes how ^{18}O gets into CO_3^{2-} in the first place. The second describes the seemingly simple reactions to form $CaCO_3$ from its ions.

ENRICHMENT OF $CACO_3$ WITH ^{18}O

The reaction below best describes the incorporation or **fractionation** of ^{18}O from $H_2{}^{18}O$ into calcite shells.

$$\text{Fractionation Reaction: } (1/3)\ CaC^{16}O_3 + H_2{}^{18}O \rightarrow (1/3)\ CaC^{18}O_3 + H_2{}^{16}O$$

In this reaction, the most abundant source of ^{18}O is $H_2{}^{18}O$. Figure **3.11** shows a simplified reaction mechanism.

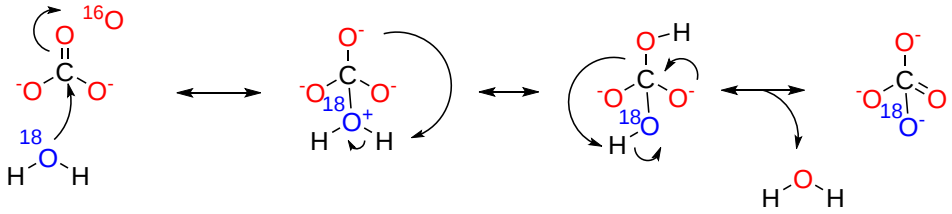


Figure **3.11**: Incorporation of ^{18}O into carbonate from $H_2{}^{18}O$

More broadly, there would be an exchange of isotopes in the entire **dissolved inorganic pool (DIC)** = $CO_2(aq)$ + H_2CO_3 + HCO_3^- (bicarbonate) + CO_3^{2-} (carbonate) with H_2O.

FORMATION OF $CACO_3$

Two reactions in general describe calcite formation and its growth:

$$Ca^{2+}(aq) + CO_3^{2-}(aq) \leftrightarrow CaCO_3 \tag{3.3}$$

and

$$Ca^{2+}(aq) + HCO_3^-(aq) \leftrightarrow CaCO_3 + H^+ \tag{3.4}$$

These show that the uptake of ^{18}O into $CaCO_3$ should also take HCO_3^- into account

In an environmentally controlled laboratory setting, reaction 3 above can be considered to be at equilibrium and defined by a Ksp value, as you learned in introductory chemistry courses, in which reaction is written as the dissociation of the two ions from the solid.

Chapter 4.12 discussed the relationships between K_{eq}, ΔG^0, ΔH^0, DS^0, and temperature. There is an inverse relationship between K_{eq} and temperature.

$$\begin{aligned} \Delta G^0 &= \Delta H^0 - T\Delta S^0 = -RT\ln K_{eq} \\ \ln K_{eq} &= -\frac{\Delta H^0 - T\Delta S^0}{RT} \\ \ln K_{eq} &= -\frac{\Delta H^0}{RT} + \frac{\Delta S^0}{R} \end{aligned} \tag{3.5}$$

Assuming that the formation of $CaCO_3$ is in equilibrium, you would expect that $CaCO_3$ would be enriched in ^{18}O and have a $+\delta^{18}O$ value. Let's see why.

Urey showed that, under equilibrium conditions, calcite is slightly enriched in $C^{18}O_3^{2-}$ probably because the heavier carbonate has a lower vibrational energy, which favors its stability and the formation of the solid. In addition, the incorporation of ^{18}O is even more pronounced in

colder water, which, as we have seen, has a +$\delta^{18}O$ value (given the greater propensity of $H_2{}^{16}O$ to evaporate).

Hence, in cold periods with large ice shields, $\delta^{18}O$ values from shells of foraminifera living in the illuminated upper ocean (planktic foraminifera, which engage in photosynthesis) and deep-sea benthic foraminifera are more positive. When ice shield melts, the $\delta^{18}O$ values of water become more negative, and so do the values of $\delta^{18}O$ values of the foraminifera.

- As planktic forams live in the upper ocean (0–200 m), their $\delta^{18}O$ values are determined by surface ocean temperature and the seawater $\delta^{18}O$. Planktic foraminifera $\delta^{18}O$ values are proxies for local temperatures because they are in a more dynamic, less-mixed environment and are more affected by evaporation and precipitation.
- In contrast, benthic forams live on the sea floor at great depth, where the ocean temperature is relatively constant (~1–4°C). The $\delta^{18}O$ values of their carbonate shells serve as proxies for global ice volume. As an example, when ice shields are large in periods of glaciation, the $\delta^{18}O$ of the whole ocean increases, due to sequestration of more $H_2{}^{16}O$ in ice. At the last glacial maximum, sea levels were about 120–130 meters lower than today (about 3% of the total ocean volume). Benthic foraminifera give a global temperature estimate as deep waters are more homogeneous.

Yet the formation of $CaCO_3$ in shells in many cases is **not** in equilibrium and is in part determined by the concentration of the reactants, the rate of diffusion of ions into and out of the growing calcite shell, which would also depend on salinity (affecting electrostatic attractions of the ions to the growing crystal), the pH (which affects the ratio of CO_3^{2-} and HCO_3^-) and biological effects (from the mechanism by which shells are formed which at some point may involve HCO_3^- transporters). It also depends on the transfer of carbonate within the dissolved inorganic carbon pool (DIC). The reaction is in equilibrium in some species of foraminifera but not others.

The term **fractionation** is often used in the isotope and climate literature (as we saw with Ralyleigh fractionation of $H_2{}^{16}O$ in polar ice). Using water as an example, fractionation describes the ratio of heavy to light O isotopes as they partition between the liquid, solid, and gas phases. The fractionation factor determines the $\delta^{18}O$ value of water. Likewise, a fractionation process determines the partitioning of ^{18}O from water into CO_3^{2-} and $CaCO_3$during calcite precipitation. The **fractionation factor α** is the ratio of the isotopes' changes in a physical (e.g., a phase transition) or chemical process. It is the factor by which the abundance ratio of two isotopes will change during a chemical reaction or a physical process.

In controlled studies of calcite ($CaCO_3$) formation from HCO_3^-, the $CaCO_3$ exhibits different oxygen isotope concentrations depending on the initial concentrations of reactants. The size of a shell can also affect the $\delta^{18}O$ of additionally deposited $CaCO_3$. These ideas support the notion that isotopic fractionation in $CaCO_3$ occurs through both equilibrium and kinetic processes.

Hence, $\delta^{18}O$ of shells depends on two environmental signals:

- temperature at the time of shell formation and
- seawater $\delta^{18}O$ (which depends of global ice volume).

This makes the interpretation of $\delta^{18}O$ values in ocean cores more challenging. Theoretical **"paleotemperature" equations** have been developed to relate temperature T to $\delta^{18}O$ in calcite under equilibrium conditions.

One recent calibration equation for the formation of calcite from HCO_3^- (obtained by bubbling the reaction mixture with N_2 at various temperatures) was derived by Kim and O'Neil in 1997. The equation was derived from carefully controlled laboratory studies that apply under equilibrium conditions and is shown below. The Kim and O'Neil equation shows the relationship between the fractionation factor alpha (α) of $^{18}0/^{16}0$ between inorganically precipitated $CaCO_3$ (calcite) and H_2O as a function of temperature is shown below.

$$1000 \ln \alpha (\text{Calcite- } H_2O) = 18.03 \left(10^3 T^{-1}\right) - 32.42 \tag{3.6}$$

Alpha is the fractionation factor, and T is in Kelvin. Note: An update of this equation to conform to IUPAC conventions gives 10^3 ln α = 18.04 x 1000 / T - 32.18)

The oxygen isotope fractionation factor alpha between two substances, A and B, is defined as

$$\alpha = \left(^{18}O/^{16}O\right)_A / \left(^{18}O/^{16}O\right)_B \tag{3.7}$$

The left-hand side of the equation (1000xlnα) is used for convenience, and its relationship to $\delta^{18}O$ values (which are expressed per %o) is analogous to the use of pKa = -log[K_A] instead of K_A.

An alternative form of the Kim and O'Neil equation is expressed in quadratic form.

$$T(^\circ C) = 16.1 - 4.64 \cdot \left(\delta^{18}O_{calcite} - \delta^{18}O_{water}\right) + 0.09 \cdot \left(\delta^{18}O_{calcite} - \delta^{18}O_{water}\right)^2 \tag{3.8}$$

A controlled equilibrium study using cultured foraminifera B. marginata of different sizes at different temperatures yielded an experimental equation to compare several theoretical equations. Figure 3.12 shows graphs of the empirically determined equation (non-red lines) vs the theoretical Kim and O'Neil equation (red line).

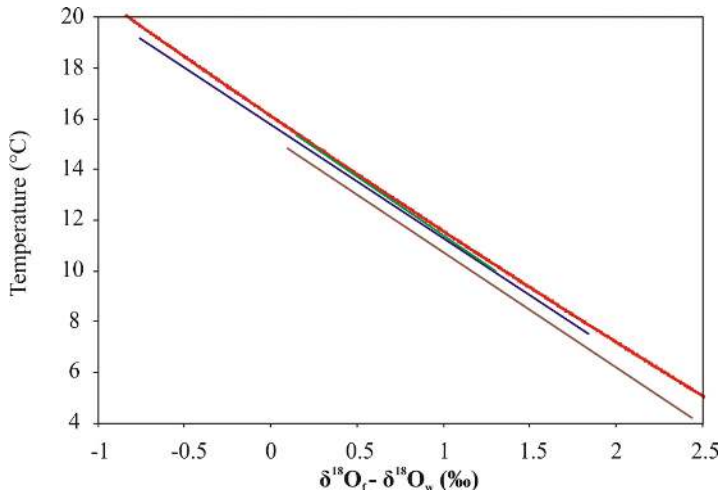


Figure 3.12: Comparison of experimental calibration equation with the theoretical equation for equilibrium calcite of Kim and O'Neil (1997). Barras, Christine & Duplessy, J.-C & Geslin, Emmanuelle & Michel, Elisabeth & Jorissen, Frans. (2010). Calibration of $\delta^{18}O$ of cultured benthic foraminiferal calcite as a function of temperature. Biogeosciences. 7. 1349-1356. 10.5194/bg-7-1349-2010. CC Attribution 3.0 License

The brown, blue, and green lines represent the calibration equations for cultured B. marginata from the < 150, 150–200, and 200–250 µm size fractions, respectively. The red line represents the quadratic equation derived from the Kim and O'Neil (1997) relationship.

A quick inspection of the empirical equation for different sizes of B. marginata shows the same relationships between T and $\delta^{18}O$ values as shown in Table 3.5 below. (The f and w in the equation represents forams (calcite) and water, respectively)

	Size fraction	Temperature range	T (°C) = b + a * ($\delta^{18}O_f$-$\delta^{18}O_w$)		R^2
			a	b	
Equation (1)	≤150 µm	4.1-14.7°C	– 4.54 (± 0.14)	15.25 (± 0.17)	0.97
Equation (2)	150-200 µm	7.9-19.3°C	– 4.49 (± 0.13)	15.73 (± 0.14)	0.98
Equation (3)	200-250 µm	10.1-14.7°C	– 4.61 (± 0.37)	16.00 (± 0.33)	0.93
Equation (4)	>250 µm	10.1-14.7°C	– 5.31 (± 0.23)	16.93 (± 0.23)	0.99

Table 3.5: Best fit linear plot of temperature T vs. ($\delta^{18}O_f$ - $\delta^{18}O_w$) for foraminifera B. marginata vs. size, where the subscript f is foraminifera, and w is water.

We take this "deep dive" into how oxygen isotopes in ice and deposited shells in ocean core samples give you a basic understanding of how creative and rigorous scientists have been in reconstructing past climates. To reiterate, during a glacial period, foraminifera shells become enriched in ^{18}O for *two* reasons:

- cold water fractionates more strongly, giving shells more enriched in ^{18}O
- ^{16}O is preferentially locked in ice sheets, making sedimented shells enriched in ^{18}O

In a simplified form, this can be expressed as:

$$\Delta\delta^{18}O_{foram} = \Delta\delta^{18}O_{temperature} + \Delta\delta^{18}O_{ice\ volume} \quad (3.9)$$

These effects are separated through a combined analysis of deep- and surface-water samples.

The interactive calculator below provides insights into the controls on Foram Shell $\delta^{18}O$. Use the sliders to calculate the foraminifera calcification temperature and explore how temperature and ice-volume effects contribute to the measured $\delta^{18}O$ signal. The calculator was produced using Claude AI.

p>

FORAMINIFERA $\Delta^{18}O$ — INTERACTIVE CALCULATOR

What Controls Foram Shell $\delta^{18}O$?

Foraminifera shells incorporate oxygen from seawater as they grow, but the $\delta^{18}O$ of the shell depends on *two independent factors*: the temperature of the water at calcification, and the $\delta^{18}O$ of the seawater itself (which rises during glacial periods as ^{16}O gets locked in ice sheets).

$$T\,(°C) = 16.9 - 4.0 \times (\delta^{18}O_{calcite} - \delta^{18}O_{seawater})$$

Shackleton (1974). $\delta^{18}O_{calcite}$ vs. VPDB; $\delta^{18}O_{seawater}$ vs. VSMOW. Rearranged: $\delta^{18}O_{calcite} = \delta^{18}O_{sw} + (16.9 - T) / 4.0$

The two-component problem: A measured change in foram $\delta^{18}O$ reflects *both* a temperature change *and* an ice-volume change in the seawater. Separating them requires an independent temperature proxy — typically Mg/Ca ratios in the same shells.

Anthropic. (2025). *Claude* (Claude Sonnet 4.6) [Large language model]. Retrieved May 2, 2025, from https://claude.ai

? CA AND MG EFFECTS IN FORAMINIFERAL SHELL MEASUREMENTS

Click for more details

Answer

The Mg/Ca ratio in foram shells is a **temperature-only** proxy — magnesium substitutes for calcium in the calcite lattice more readily at higher temperatures. There is one big difference: the Mg/Ca ratio is **not sensitive to seawater $\delta^{18}O$ or ice volume**, so it gives you temperature independently of the isotope signal.

If you measure both Mg/Ca and $\delta^{18}O$ on the same foram shells, you can use Mg/Ca to determine the calcification temperature, then use that to calculate what $\delta^{18}O$ the shell *should* have from temperature alone. The difference arises from ocean water $\delta^{18}O$, which reflects global ice volume.

We take this opportunity to reshow the graph that reconstructs changes in planetary temperatures over the last 66+ million years (Figure **3.13**). Data between 66 MYA and 100,000 years ago (note the change in scale on the x-axis to fit a large time range in a single graph) were obtained, partly from δ18O values in deep-sea sediments. In contrast, data from around 100,000 YA to the advent of modern temperature recordings were mostly obtained from $\delta^{18}O$ measurements of ice core samples from Antarctica and Greenland. Of course, other temperature proxies, as described above, were also important.

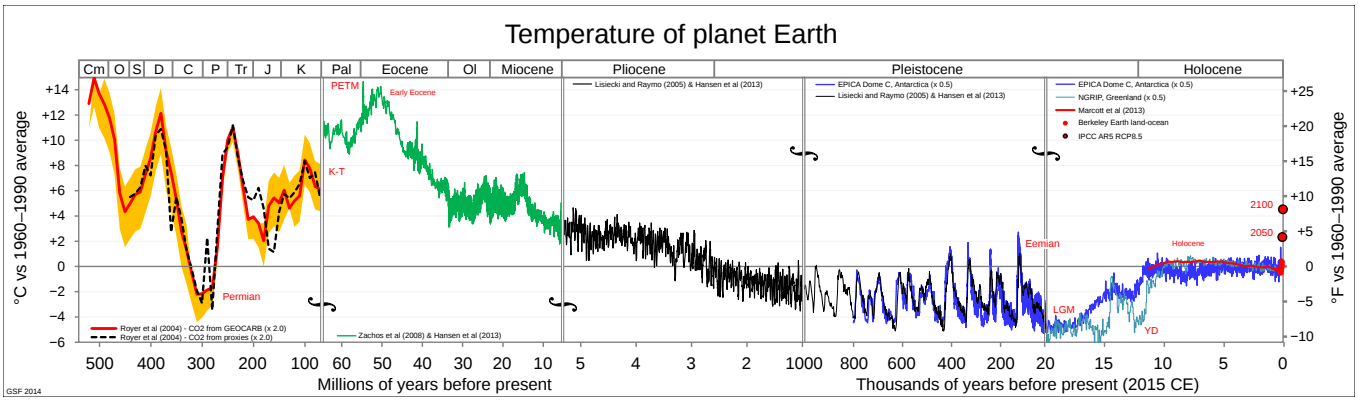


Figure **3.13**: https://commons.wikimedia.org/wiki/F...alaeotemps.png. (Excel available). Creative Commons Attribution-Share Alike 3.0 Unported

These detailed but hopefully understandable explanations of the relationship of temperature with $\delta^{18}O$ in foraminifera shells from ocean sediment cores were presented for reasons expressed at the beginning of Chapter 31.2:

- Isotopes and their effects are critical to understanding the structure and activity of biological systems and to climate science.
- Isotope partitioning into water and biomolecules involves both equilibrium and nonequilibrium reactions and processes, similar to linked biochemical reactions and pathways.
- The study and application of isotope effects can integrate and expand learning from previous science courses.

Astute readers will notice that we concentrated on $\delta^{18}O$ values (in water and carbonates) and barely mentioned $\delta^{13}C$ values for carbonate precipitations. We will discuss that in the next chapter as we consider the carbon cycle.

SUMMARY

(Summary written by Claude, Anthropic)

This chapter delves into the sophisticated methods used to reconstruct past atmospheric CO_2 levels and global temperatures over millions of years using isotope analyses. It highlights how scientists extract and interpret data from ice cores and ocean sediment cores—key records that have preserved information in the form of isotope ratios of oxygen ($\delta^{18}O$) and carbon ($\delta^{13}C$). The chapter emphasizes the following points:

- **Isotope Fundamentals and Their Significance:**
  The study begins by outlining why isotope effects are crucial not only for understanding biochemical structures and reactions but also for decoding Earth's climate history. The partitioning of isotopes into water and biomolecules involves both equilibrium and non-equilibrium processes that mirror many biochemical pathways.
- **Proxies for Past Climate Reconstruction:**
  Since direct measurements of temperature and CO_2 are available only from recent centuries, scientists rely on "proxies" such as tree rings, coral growth bands, and the shells of marine organisms (e.g., foraminifera, diatoms). These proxies, calibrated against modern observations, allow researchers to infer past temperature variations and atmospheric CO_2 levels extending back millions to billions of years.
- **Isotope Analyses in Ice and Sediment Cores:**
  The chapter explains how isotopic ratios—especially $^{18}O/^{16}O$—in ice cores from Antarctica and Greenland serve as indicators of past temperature changes and ice volumes, while similar analyses of carbonate shells in marine sediments provide complementary data on ocean temperatures and global climate trends.
- **Chemical Reactions and Fractionation Processes:**
  Detailed discussions focus on how isotopic fractionation occurs during the evaporation and condensation of water and the precipitation

of calcium carbonate ($CaCO_3$) in foraminifera shells. The theoretical framework, including the Kim and O'Neil calibration equations, illustrates how temperature influences isotope partitioning and thus the $\delta^{18}O$ values measured in climate proxies.

- **Interdisciplinary Integration:**
  Finally, the chapter underscores the importance of integrating knowledge from chemistry, biology, and geology. By linking the study of isotope effects in biochemical systems to their application in climate science, students gain a comprehensive understanding of how ancient climate records are constructed, validated, and used to inform models of future climate change.

Overall, this chapter provides junior and senior biochemistry majors with both the theoretical background and practical applications of isotope analysis in reconstructing Earth's climatic history, demonstrating how rigorous scientific methods underpin our understanding of global climate dynamics.

3: Use of Isotope Analysis in Measuring Climate Change is shared under a CC BY-NC-SA 4.0 license and was authored, remixed, and/or curated by LibreTexts.

4: CLIMATE CHANGE - THE CARBON CYCLE AND CARBON CHEMISTRY

Search Fundamentals of Biochemistry

LEARNING GOALS

(Learning goals written by Claude, Anthropic)

By the end of this chapter, students should be able to:

Stocks, Fluxes, and Mass Balance in the Carbon Cycle

- Define carbon stocks (GtC) and fluxes (GtC/yr), perform dimensional analysis to interconvert GtC, Gt CO_2, and ppm, and apply the Law of Mass Conservation to the global carbon budget to show that anthropogenic fossil fuel emissions (+9.6 GtC/yr) are now the single largest flux in the carbon cycle.
- Interpret carbon budget diagrams showing EFOS, ELUC, SLAND, SOCEAN, and GATM, explain why the cumulative +275 GtC from fossil fuel emissions since 1850 translates to a ~129 ppm rise in atmospheric CO_2, and use Le Châtelier's Principle to predict how decreasing atmospheric CO_2 would affect oceanic uptake rates.
- Describe how simple Vcell-based carbon cycle models are constructed from stock reserves and apparent rate constants (J = kapp[stock]), explain what assumptions simplify such models, and interpret why their outputs closely match IPCC SSP1-2.6 projections despite those simplifications.
- Explain the ExxonMobil disinformation case: describe what their internal models accurately predicted, what their executives publicly claimed, and why this is a defining example of deliberate scientific misinformation with global consequences.

Ocean Carbon Chemistry and $\delta^{13}C$ as a Climate Proxy

- Write the coupled equilibrium reactions linking atmospheric CO_2 to dissolved CO_2, carbonic acid, bicarbonate, and carbonate in the ocean, explain how these reactions buffer ocean pH, and describe how rock weathering and ocean uptake regulate long-term atmospheric CO_2.
- Explain the kinetic isotope effect for ^{13}C — why its lower zero-point energy raises the activation energy for bond formation/cleavage — and use this to predict why RuBisCO discriminates against $^{13}CO_2$, why plants and organic matter have more negative $\delta^{13}C$ values than atmospheric CO_2, and why C3 plants ($\delta^{13}C \approx -25$ to $-30‰$) differ from C4 plants ($\delta^{13}C \approx -10$ to $-15‰$).
- Interpret positive and negative $\delta^{13}C$ excursions in ocean sediment carbonate records — explaining how high primary productivity and organic carbon burial produce positive excursions while mass extinctions and massive carbon injection produce negative ones — and apply this framework to the Lomagundi-Jatuli event, the PETM, the Permian-Triassic boundary, and the K-Pg boundary.
- Use $\delta^{13}C$ data from ice cores to explain two specific historical events: the ~7–10 ppm CO_2 drop and positive $\delta^{13}C$ excursion in 1500–1650 CE following the Great Dying of Indigenous peoples (reforestation of ~56 million hectares), and the decreasing $\delta^{13}C$ since the Industrial Revolution as definitive evidence that rising CO_2 is from biogenic fossil fuel combustion.

The Methane Cycle and •OH as Atmospheric Scrubber

- Describe the global methane budget — identifying major sources (wetlands, agriculture, fossil fuels, landfills) and their characteristic $\delta^{13}CCH_4$ values — and explain how $\delta^{13}C$ isotope source attribution showed that ~85% of post-2007 methane growth came from microbial rather than fossil fuel sources, representing a dangerous positive climate feedback.
- Explain the photochemical production of •OH from ozone photolysis and water vapor, write the rate-limiting H-abstraction reaction that initiates CH_4 oxidation ($CH_4 + {\bullet}OH \rightarrow {\bullet}CH_3 + H_2O$), explain why this gives atmospheric methane a half-life of 9–10 years, and connect •OH depletion to extended methane atmospheric lifetime as an additional positive warming feedback.

THE CARBON CYCLE

In the last chapter section, we used oxygen isotopes in ice and ocean sediment cores going back millions of years to address the history and mechanisms of climate change. We focused on $^{18}O/^{16}O$ ratios in H_2O and calcite ($CaCO_3$) shells and on the corresponding $\delta^{18}O$ values in ice and sediment cores to determine CO_2 and temperature over climatic history. Now it's time to talk about the other key atom, **C**, the ratio of $^{13}C/^{12}C$ and corresponding $\delta^{13}C$ values, not only in $CaCO_3$ but also in CO_2 and the organic molecules it transforms into through photosynthesis and the heterotrophic organisms that consume them. ^{13}C partitions not only into inorganic carbon but also into organic molecules throughout life. Hence, we need a more detailed understanding of the **carbon cycle**.

The carbon cycle is likely discussed in introductory chapters in biology textbooks, but probably never in chemistry texts. It is fundamental to understanding climate, its control and change, and human processes that alter it. Figure **4.1** shows one representation of the carbon cycle. Calculated amounts of carbon found in the **lithosphere** (the solid part of the Earth), the **atmosphere** (specifically the lower part, the troposphere), and the **hydrosphere** are shown. (The **cryosphere**, the ice found in Greenland and Antarctica, is not shown. The **biosphere** includes part of these "spheres" that harbor life. Since life has been found 10 km down in the crust, we'll refer to the entire region shown in the diagrams as the biosphere. Alternatively, carbon can be found in four key reservoirs: atmospheric, terrestrial, oceanic, and buried sediments

Figure **4.1** presents carbon stores in petagrams (10^{15} g) or gigatons of carbon (GtC), where 1 petagram equals 1 billion metric tons (approximately 1.1 billion US tons).

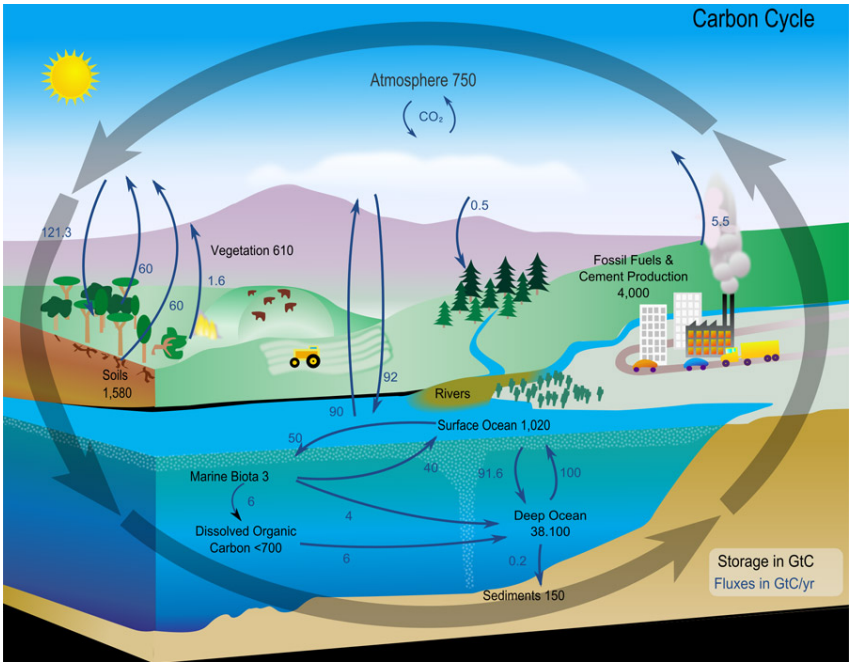


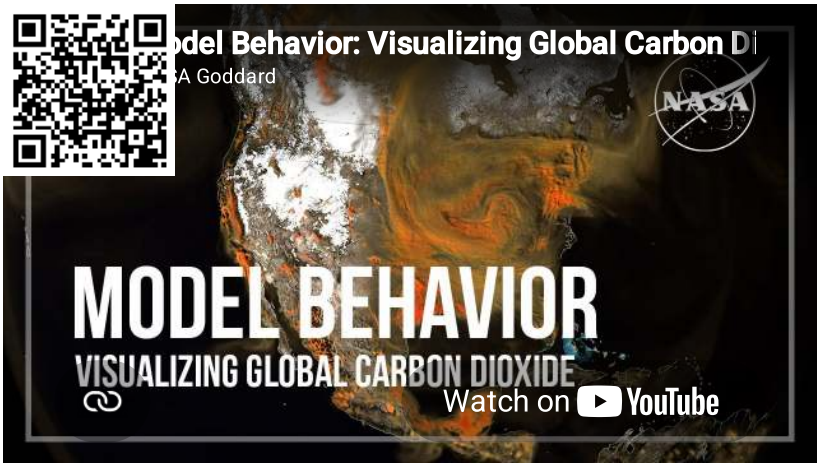
Figure **4.1**: The carbon cycle. https://commons.wikimedia.org/wiki/F...te_diagram.svg

In addition to the total amount of carbon stored in each region (GtC), the net changes in carbon per year as it moves into and out of reserves (GtC/yr) are shown in blue arrows with attached numbers.

Carbon exchanges in the cycle occur at different time scales. Geologically, "fast" exchange, on a time scale of up to 1000s of years, occurs among the oceans, atmosphere, and land. In contrast, a slow exchange (over hundreds of thousands to millions of years) occurs in deep soils, deep ocean sediments, and rocks. We will mostly consider exchanges among the atmosphere, land, and oceans.

CO_2 in the terrestrial biosphere is removed by photosynthesis and returned by respiration by autotrophs like plants and heterotrophs like microbes that consume soil carbon and plant remains. CO_2 in the atmosphere is also removed by ocean autotrophs, such as ocean phytoplankton, and by partitioning into dissolved inorganic carbon (DIC) species such as HCO_3^- and CO_3^{2-}.

Before we probe some relevant reactions within the carbon cycle and analyze them quantitatively, let's get a visual impression of how CO_2 flows into and through the atmosphere (in 2020) with this stunning, high-resolution video model from NASA. Listen to the narration to visualize the sources of significant emissions (power plants, forest fires) and the changes in emissions driven by human activity across day/night cycles.



Now let's look at the factors driving our rising CO_2 levels and global warming. To do that, we must put numbers on the cycle to quantify it.

QUANTIFYING THE CARBON CYCLE

In Chapter 31.1, we used parts per million (ppm) to express the amount of CO_2 in the atmosphere. Table **4.1** below shows how to translate the percentage (parts per 100) for each component gas in the atmosphere (with which you are familiar) into ppm.

Gas	% (parts per 100) in atm	parts per million
N_2	78.09	780,900
O_2	20.94	209,400
Ar	0.93	9300
CO_2	0.0415	415

Table **4.1**: Unit conversion - % to ppm

Climate scientists use ppm instead of concentration (in molecules/m^3) because they want to know the relative percent increase over time, which is independent of temperature or pressure. In contrast, concentration depends on T and P, as you will remember from the ideal gas law, PV=nRT or n/V=P/RT, which you studied in introductory chemistry.

It is important to use dimensional analysis to interconvert units as well. Table **4.2** below shows conversion factors to switch between GtC, Gt CO_2, and ppm.

Convert from	to	conversion factor
GtC (Gigatons of carbon)	ppm CO_2	divide by 2.124
GtC (Gigatons of carbon)	PgC (Petgrams of carbon)	multiply by 1
Gt CO_2 (Gigatons of carbon)	GtC (Gigatons of C)	divide by 3.664 = 44.01/12.01)
GtC (Gigatons of carbon)	MtC	multiply by 10000

Table **4.2**: Unit conversion - GtC and Gt CO_2

To be more technical, atmospheric CO_2 concentrations are expressed as the mol fraction of CO_2 in dry air. The ppm for CO_2 is µmol CO_2 per mole of dry air.

We need to assign numbers to the components of the carbon cycle to analyze them quantitatively. Otherwise, we can't know what is happening, nor can we predict the future with any certainty. For many, stoichiometry and reaction kinetics are probably the least-liked parts of chemistry, but they are critical for understanding climate change. We have to apply them globally. Two key terms are important:

Stocks or reserves: How much carbon (mass in Gigatons or petagrams) is stored in given locations in the biosphere? This allows us to understand, for example, what % of all carbon stocks are in the ocean. Stocks are usually reported in gigatons of carbon (GtC), not carbon dioxide, because many stocks (such as fossil fuels) consist mostly of C and H, not oxygen. As in stoichiometry calculations in introductory chemistry courses, GtC in the atmosphere can be converted to gigatons of CO_2 using dimensional analysis.

Fluxes (rates): How much carbon is transferred from one reserve to another per year (Gigatons/yr). Climate scientists apply the Law of Mass Conservation, which you learned in introductory chemistry, to the biosphere.

Figure **4.2** shows the reserves/stock (GtC) for reserves and **decadal (2012-2021) average** fluxes (large and small arrows, GtC/yr) for individual or aggregated stocks.

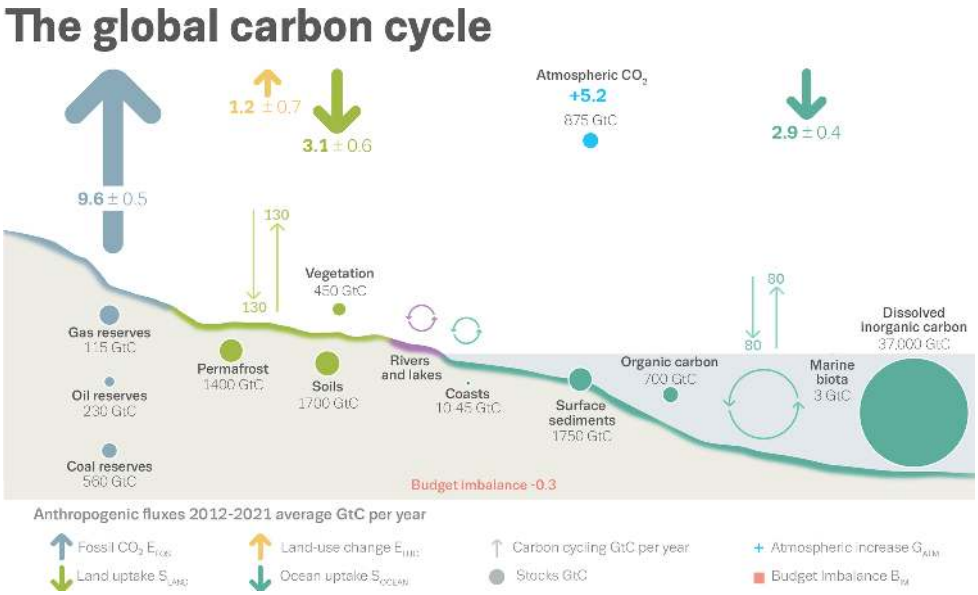


Figure **4.2**: Schematic representation of the overall perturbation of the global carbon cycle caused by anthropogenic activities **averaged globally for the decade 2012–2021**. E represents emission and S "sink". Earth Syst. Sci. Data, 14, 4811–4900, 2022. https://doi.org/10.5194/essd-14-4811-2022. © Author(s) 2022. This work is distributed under the Creative Commons Attribution 4.0 License.

The abbreviations used are E_{FOS} (emissions, fossil fuels), E_{LUC} (emissions land use changes - principally deforestation), S_{LAND} (terrestrial CO_2 sink), S_{OCEAN} (ocean CO_2 sink), G_{ATM} (Growth Rate CO_2 atm), B_{IM} (carbon budget imbalance). Uncertainties are also shown, except for the atmospheric CO_2 growth rate, which is known precisely through modern measurements. (It's also the easiest to measure). Human-caused (anthropogenic) changes occur on top of the carbon cycle.

The upward arrows indicate release into the atmosphere, and the downward arrows indicate absorption in the oceans and land. The thickness of the arrows gives a relative measure of the size of the emission or absorption. The thickest arrow and highest value (9.6 GtC/yr) is for the anthropogenic emission of carbon from our

use of fossil fuels. Think about that! **Humans are presently the most significant contributors to the carbon cycle**. Before the Industrial Revolution, human contributions were minimal.

IT'S WORSE THAN THAT!

Figure 2 above shows that, on average, 9.6 GtC/yr was released from fossil fuel use between 2012 and 2021. The actual flux of anthropogenic carbon released **in 2021 was 9.9 GtC**, equivalent to 36.4 Gt CO2.

If you add the up arrows and subtract the down ones from that sum, you get +4.8 GtC/yr. This represents the net average increase in GtC in atmospheric CO_2 per year for 2012-2021. That is close to the accurately and precisely known value of +5.2 GtC/yr increase from the CO_2 we pour into the atmosphere from burning fossil fuels. Hence, the figure above is unbalanced (about 0.3 GtC too low - the BIM carbon budget imbalance). Still, given the difficulty in calculating these values, it is remarkably close to "mass balance," as you learned in introductory chemistry classes. In general, before the Industrial Revolution, the sum of the fluxes that added CO_2 to the atmosphere was equal to the sum of the fluxes that removed it. That is, the system was in a **steady state.** That is no longer the case.

Figure **4.3** shows a breakdown of the factors contributing to annual (left) and cumulative (right) fluxes of carbon (GtC/yr), a metric for CO_2 flux, over time since 1850.

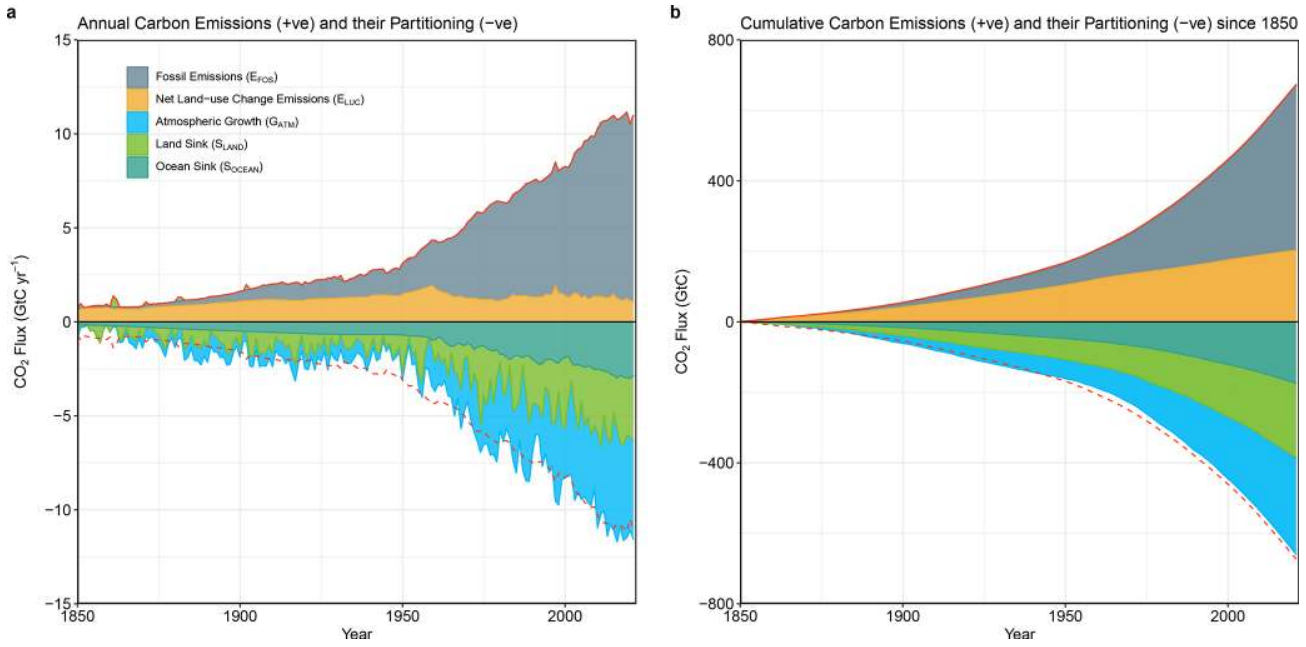


Figure **4.3**: Combined components of the global carbon budget as a function of time for fossil CO_2 emissions (E_{FOS}, including a small sink from cement carbonation; grey) and emissions from land-use change (E_{LUC}; brown), as well as their partitioning among the atmosphere (G_{ATM}; cyan), ocean (S_{OCEAN}; blue), and land (S_{LAND}; green). Panel **(a)** shows annual estimates of each flux (GtC yr^{-1}, and panel **(b)** shows the cumulative flux (the sum of all prior annual fluxes) since the year 1850. Again, the graph shows GtC not Gt CO_2. . © Author(s), ibid

You might ask why the atmospheric growth in CO_2 (shown in green) is negative. We'll answer that question below.

Lastly, let's consider the cumulative changes in GtC released and absorbed since 1850 (before the US Civil War and before the large CO_2 release in modern times). Those data are shown in a bar graph in panel A of Figure **4.4**. The bar graph in the right panel shows the mean decadal averages shown in Figure 2 above.

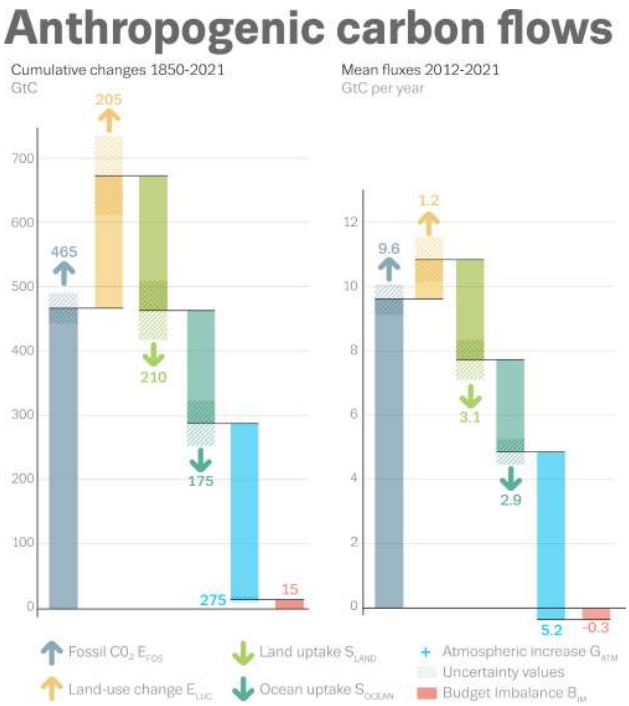


Figure **4.4**: Total cumulative changes in GtC released and absorbed since 1850 (panel A) and mean decadal fluxes (panel B). E_{FOS} (emissions, fossil fuels), E_{LUC} (emissions land use changes - mostly deforestation), S_{LAND} (terrestrial CO_2 sink), S_{OCEAN} (ocean CO_2 sink), G_{ATM} (Growth Rate CO_2 atm), B_{IM} (carbon budget imbalance). © Author(s), ibid

The positive emission and negative absorption contributions are easily seen in the bar graph. The blue bar represents the net carbon emission from fossil fuels and fills the gap to complete the mass balance, as discussed above. It also explains the negative blue region in Figure 3. Keep in mind that the blue net flux from fossil fuels is positive.

The cumulative contributions from fossil fuel emissions required to close the gap and fulfill mass balance are +275 GtC, which, when multiplied by the conversion factor (1ppm/2.124 GtC), translates into a 129.5 ppm increase in atmospheric CO2 over that time. This is very close to independent measurements of a rise of 129.3 ppm (14.7-284.7) over that time.

The data from Figure **4.4** has been entered in the first four columns of Table **4.3** below.

Source	Subtype	Stock reserves (GtC)	J (Fluxes) GtC/yr (avg 2012/2021) + emission - absorption	$J=k_{app}[stock]$
Atmosphere	-	875		
Buried Fossil Fuels	Coal	560	+9.6	J=+9.6=k[905] (905 is the sum of stocks) k=0.0106
	Oil	230		
	Gas	115		
Terrestrial	Permafrost	1,400	+1.2 (Land use Δ) -3.1 (Land uptake)	J_{use}=+1.2=k_{use}[3550]; k_{use}=0.000338 J_{up}=-3.1=k_{up}[875]; k_{up}=0.00354
	Soil	1,700		
	Vegetation	450		
Oceans	Coasts	10-45	-2.9	J=-2.9=k[875] k=0.00331
	Ocean Surface Sediments	1,750		
	Organic carbon	700		
	Marine Biota	3		
	Dissolve Inorganic Carbon (DIC)	37,000		

We can use this data to develop a crude computational model predicting future CO_2 emissions using Vcell, the program we used to produce time-course (concentration vs time) graphs for both simple and coupled signal transduction reaction pathways.

Vcell can be used to calculate fluxes (J) in reaction pathways, where J is the change in concentration of a species with time, given the initial concentration or amount of a reactant and the rate constants affecting its production or removal. If we use the amount of carbon (GtC) in each reservoir in the biosphere and crust as a relative measure of "concentration" and the known fluxes (GtC/yr) for the transfer of carbon to and from the atmosphere as given in Table 3, we could calculate an "apparent rate constant for each flux using this equation:

$J_{stock} = k_{app}$[stock] (where stock is given in GtC).

$$J_{stock} = k_{app}[\text{ stock in GtC}] \quad (4.1)$$

These "apparent" rate constants are needed to run the Vcell simulation that can reproduce the actual fluxes shown in Figures 2 and 4. The simulation can be run over time

A simple four-term model based on Figures 2 and 4 is shown below. Run the simulation and see how atmospheric CO_2 changes with time. This model is offered only to show how climate models are made and used. The graphs are valid and sound given the input parameters, but the outputs are based on many assumptions that greatly simplify the model. For example, it assumes no new fossil fuel input from new drilling or mining.

A SIMPLE INTERACTIVE EXERCISE

Alter the sliders on the model to change the rates of removal of $CO_{2\ atm}$ through land uptake and ocean uptake. Also, change the rate of CO_2 input from land use changes and burning fossil fuels. Try to "flatten" the curve earlier and to decrease $CO_{2\ atm}$ faster.

You can also download the spreadsheet and plot the individual contributions to CO2 atm.

This simulation shows $CO_{2\ atm}$ levels peaking at about 982 GtC in 51 years (2073), from its average decadal (2011-2021) value of 875. That is an increase of 107 GtC from now (50 ppm CO_2 rise from the present 414 to 463 ppm). Over 50 years, this gives an average annual rise of 2.14 GtC/yr or about 1 ppm CO_2/yr. A comparison of the predicted atmospheric CO_2 (ppm) levels through 2100 for the IPCC SSP1-2.6 scenario (**blue**) and simple Vcell model (**red**) is shown in Figure **4.5**.

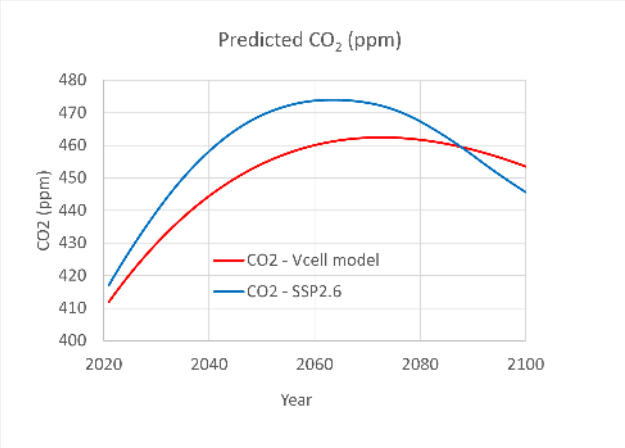


Figure **4.5**: Predicted atmospheric CO_2 (ppm) for SSP1-2.6 scenario (**blue**) and simple Vcell model (**red**)

SSP1-2.6 data - History: Meinshausen et al. GMD 2017 (https://doi.org/10.5194/gmd-10-2057-2017); Future: Meinshausen et al., GMD, 2020 (https://doi.org/10.5194/gmd-2019-222). https://climateanalytics.org/media/g...-3571-2020.pdf. https://gmd.copernicus.org/articles/13/3571/2020/

However imperfect the Vcell model is (incorrect assumptions, lack of complexity and feedback mechanisms, etc), the results shown above are very close to the projected increases in carbon dioxide in ppm described in IPCC reports for the SSP1-2.6 socioeconomic pathways, shown in the right panel (dark blue line) of Figure **4.6**. This pathway predicts a rise of approximately 1.8^0 C in average global temperatures.

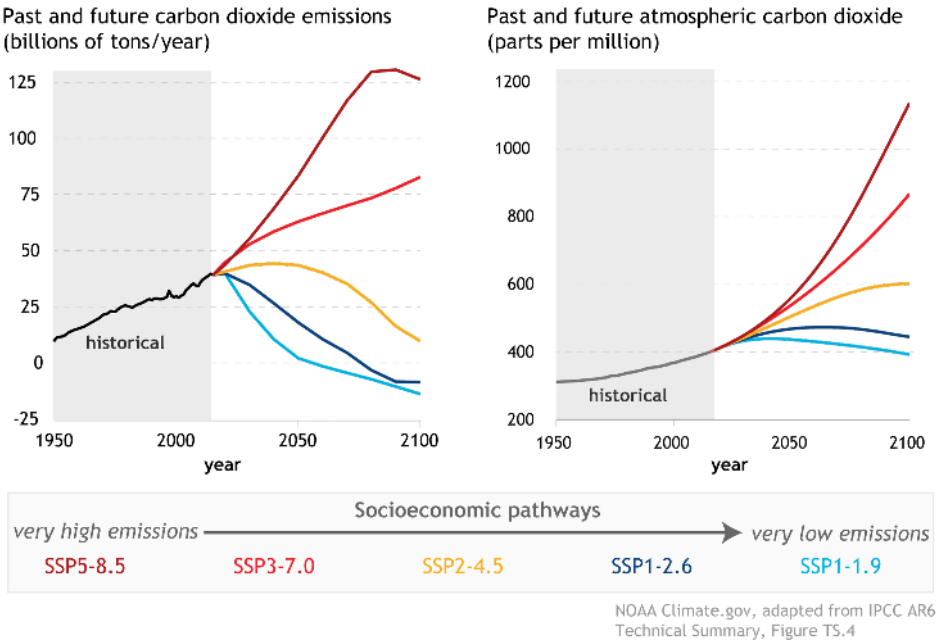


Figure **4.6**: IPCC, 2021: Summary for Policymakers. In: Climate Change 2021: The Physical Science Basis. Contribution of Working Group I to the Sixth Assessment Report of the Intergovernmental Panel on Climate Change [Masson-Delmotte, V., P. Zhai, A. Pirani, S.L. Connors, C. Péan, S. Berger, N. Caud, Y. Chen, L. Goldfarb, M.I. Gomis, M. Huang, K. Leitzell, E. Lonnoy, J.B.R. Matthews, T.K. Maycock, T. Waterfield, O. Yelekçi, R. Yu, and B. Zhou (eds.)].

Again, remember that the model is based on a ten-year average of CO_2 emissions. Think of all the other assumptions in this model (other than the stock reserves and fluxes) that would give higher or lower values of future CO_2 levels. One major one is that flux values are all held constant to allow calculations of the apparent rate constants for Vcell use. The model depletes much of the fossil fuel reserves. In addition, CO_2 emissions in 2021 were 9.9 GtC/yr and are going up!

In addition, a change in one parameter can affect the others. For example, the net uptake of atmospheric CO_2 by the land and oceans increased from 1960 to 2010, which makes sense given that higher atmospheric CO_2 levels are forcing greater uptake (think Le Châtelier's Principle). Since the Industrial Revolution, the oceans have absorbed nearly 40% of the CO_2 emitted by burning fossil fuels. If the uptake rate decreases (i.e., if we start to saturate oceanic uptake), CO_2 accumulation in the atmosphere will accelerate. Data also suggest that if we successfully decrease CO_2 in the atmosphere, the oceans would respond by decreasing their uptake, slowing the rate of temperature reduction.

An interesting example relating atmospheric and ocean CO_2 occurred from 1990 to 2000, when it was shown that the sea acted as a weaker sink. This occurred because of a decreasing gradient (the Δ or"effective concentration differences") between atmospheric CO_2 and ocean CO_2, which decreased the ocean's ability to act as a sink for CO_2. You can decrease the Δ in two ways:

- decreasing the rate of CO_2 entry into the atmosphere from fossil fuel use. There was, indeed, a temporary slowdown in this decade.
- by temporarily making the ocean a better sink. This happened in 1991 after the eruption of Mt. Pinatubo, which led to decreased air and ocean temperatures. CO_2 is a nonpolar gas with higher solubility in water at lower temperatures (think about soda). This was a short-term, minor effect compared to the reduced rate of fossil fuel emissions.

More complex models with additional terms for CO_2 emissions and absorption can be developed. One is shown in Figure **4.7**. This model adds CO_2 release from the soil through microorganisms and plant respiration (CHO to $CO_{2\ atm}$). Another term has been added for release by the oceans.

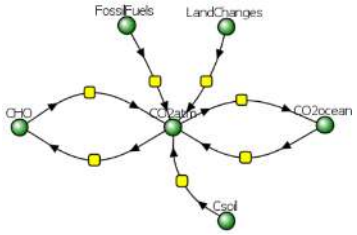


Figure **4.7**: More complicated Vcell climate model.

Fortunately, we don't have to rely on these simple models to predict future trends in temperature and CO_2. A complex dynamic model simulator in accordance with many different climate models is available at your fingertips. Developed at MIT and Climate Interactive, and available in any web browser, the EN-ROADS program allows users to adjust sliders for key inputs and view forecasted future temperatures and CO_2 levels. In line with RCP and IPCC SSP pathways that link future emissions to socio-economic policies (discussed in Chapter 31.1), the program allows users to adjust variables such as carbon pricing and incentives to transition to clean energy across the transportation, building, and energy supply sectors. Access the program directly from this page by clicking the Close icon in the program window in Figure **4.8** below.

https://geo.libretexts.org/@go/page/34459

Figure 4.8: EN-ROADS global climate simulator

Here is also an external link to the En-Roads global climate simulator (Developed by Climate Interactive, the **MIT Sloan Sustainability Initiative**, and **Ventana Systems**).

A SIMPLE INTERACTIVE EXERICSE

Move the interactive sliders to see how they affect greenhouse gas emissions and global temperatures. Here is a link to a one-page tutorial on how to use them.

COP28 Meeting in Dubai, UAE: December 2023 Agreements

At this climate meeting in Dubai, delegates agreed to "the need for deep, rapid and sustained reductions in greenhouse gas emissions in line with 1.5 °C pathways and called on Parties to contribute to the following global efforts, in a nationally determined manner, taking into account the Paris Agreement and their different national circumstances, pathways and approaches". These included:

(a) Tripling renewable energy capacity globally and doubling the global average annual rate of energy efficiency improvements by 2030;
(b) Accelerating efforts towards the phase-down of unabated coal power;
(c) Accelerating efforts globally towards net-zero emission energy systems, utilizing zero- and low-carbon fuels well before or by around mid-century;
(d) Transitioning away from fossil fuels in energy systems in a just, orderly, and equitable manner, accelerating action in this critical decade to achieve net zero by 2050 in keeping with the science;
(e) Accelerating zero- and low-emission technologies, including, inter alia, renewables, nuclear, abatement and removal technologies such as carbon capture and utilization and storage, particularly in hard-to-abate sectors, and low-carbon hydrogen production;
(f) Accelerating and substantially reducing non-carbon-dioxide emissions globally, including in particular methane emissions, by 2030;
(g) Accelerating the reduction of emissions from road transport on a range of pathways, including through the development of infrastructure and rapid deployment of zero- and low-emission vehicles;
(h) As soon as possible, phase out inefficient fossil fuel subsidies that do not address energy poverty or just transition.

A SIMPLE INTERACTIVE EXERCISE

Here is a link to an EN-ROADS climate model that shows the effects of the actions recommended at COP28. Explore the model by moving sliders and returning them to the preset positions. These models show that aggressive action in all sectors contributing to climate change would bring down projected temperature increases to 1.7 ^{0}C (3 ^{0}F), still above the 1.5 ^{0}C limit. Of course, this assumes that the world has the political will to carry them out.

COP28 was held in a "petrostate" whose main source of revenue is fossil fuels (30% of its GDP comes from them). At the start of the meeting, it was unclear if any strides could be made to reduce fossil fuel production and use. The fossil fuel industry has been (and likely still is) a main source of misinformation on climate change. One example is documented below.

THE SKEPTIC'S CORNER: CLIMATE CHANGE MISINFORMATION

We should all be skeptical of models, especially ones that predict changes 80 or more years into the future. We gain confidence in a model if it accurately fits data from the past and the future. We mentioned in Chapter 31.1 that oil company scientists knew of the likely climatic effects of fossil fuel emissions, but the company executives did not act on their models. Their models were startlingly accurate, as shown in Figure 4.9 below, which shows their predictions for both CO_2 levels and the associated increases in temperature caused by them.

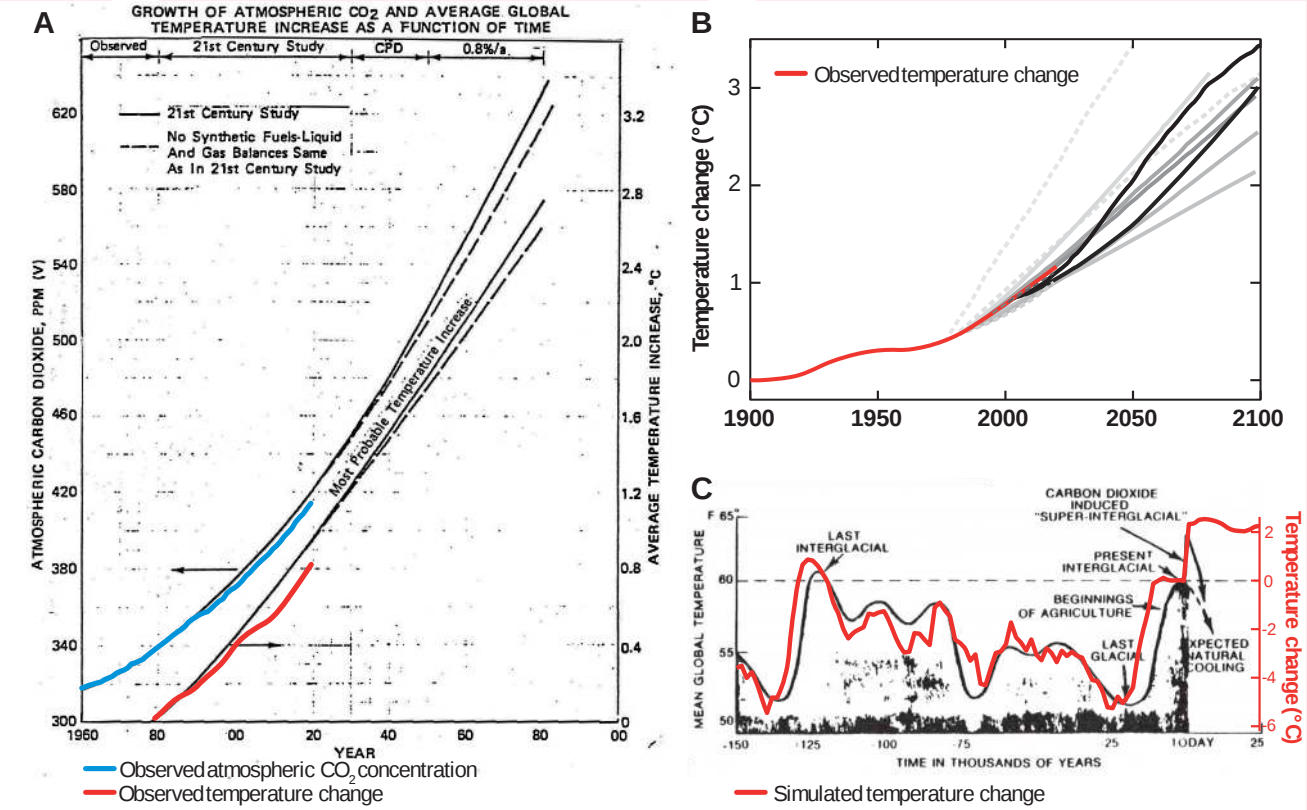


Figure **4.9**: Historically observed temperature change (red) and atmospheric carbon dioxide concentration (blue) over time, compared against global warming projections reported by ExxonMobil scientists. Supran, G., Rahmstorf, S., and Oreskes, N. Assessing ExxonMobil's global warming projections. Science (2023). https://www.science.org/doi/abs/10.1...cience.abk0063. Reprinted with permission from AAAS. Not for reuse.

Panel (A) shows "Proprietary" 1982 Exxon-modeled projections.

Panel (B) summarizes projections in seven internal company memos and five peer-reviewed publications between 1977 and 2003 (gray lines).

Panel (C) shows a 1977 internally reported graph of the global warming "effect of CO_2 on an interglacial scale." (A) and (B) display averaged historical temperature observations. In contrast, the historical temperature record in (C) is a smoothed Earth system model simulation of the last 150,000 years.

As these graphs clearly show, oil companies have known for over 40 years, since the late 1970s, of the climatic effects of CO_2 emissions. They could even predict the temperatures since the last ice age. In the 70s, solar and wind energy were much more expensive to produce and use than they are now. Still, if we had subsidized their development back then, as we have done for decades for the fossil fuel industry, our current climate situation would be much less precarious.

"Company executives chose to publicly denigrate climate models, insist there was no scientific consensus on anthropogenic climate change, and claim the science was highly uncertain when their own scientists were telling them the opposite" (ref). They also propagated the myth that the global climate was actually cooling. This is a powerful and unsettling example of disinformation with enormous consequences.

For more information on subsidies, visit the link below.

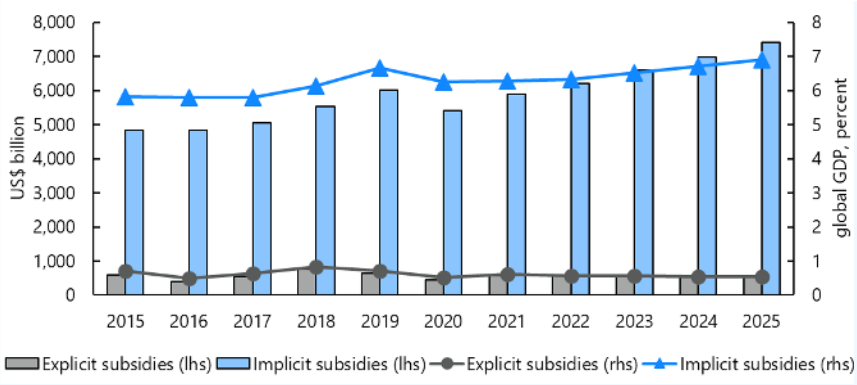
? FOSSIL FUEL SUBSIDIES

Click below.

Answer

The figure below shows worldwide fossil fuel subsidies in US$ billion and as a percentage of global GDP from 2015 to 2025.

https://geo.libretexts.org/@go/page/34459



Worldwide subsidies in US $billion and in % global GDP. The bar graphs are for US$biillons, and the circles and triangles are for % global GDP. IMF. https://www.imf.org/en/Publications/W...bsidies-466004

The subsidies are broken down into explicit subsidies (tax breaks or direct payments to help fossil fuel companies cover their uncompensated costs) and implicit subsidies (undercharging for the environmental costs of fossil fuel use that oil companies don't pay). These latter "hidden" costs are passed down to countries, states, and individuals. In 2020, global subsidies totaled $5.9 trillion, or 6.8% of global GDP. The explicit subsidies given to fossil fuel companies, about 8% of the total, amounted to $472 billion just in 2020!

The figure below shows just explicit subsidies (data from the IEA and graphs from Our World in Data).

Explicit subsidies make fossil fuels cheaper, which certainly helps people with limited resources. In 2022, the world increased explicit subsidies to help defray increased consumer energy costs arising from the war in Ukraine. Explicit subsidies hide the true cost of fuel and energy.

The fossil fuel industry is mature and has benefited from explicit subsidies (dating back to 1916, with the Intangible Drilling Costs subsidy for drilling and well-preparation expenses). Back then, subsidies were needed to promote this industry, which helped many out of poverty and provided cheap energy for

economic development and people's welfare. We didn't know the actual cost to biosphere health and a stable climate. Clean energy is not a mature industry and needs subsidies to grow. The IEA *Government Energy Spending Tracker* documents governmental spending on all types of energy, including clean energy and short-term support, to help industry and people pay energy costs. The IEA shows that from 2020 to 2023, governments worldwide spent about $1.34 trillion on clean energy investment, exceeding subsidies for fossil fuels (which are necessary to grow the clean energy sector). Short-term energy affordability measures aim to help shield consumers and industries facing soaring energy prices. Likewise, they have spent $900 billion (over and above existing dollars) to assist consumers with higher energy costs.

Now that we have seen the big picture, let's look at how carbon moves through various pools of carbon-containing molecules. We have discussed photosynthesis in detail in Chapter 20, so we will focus more on dissolved inorganic carbon (DIC), including species such as HCO_3^- and CO_3^{2-}. Another view of the carbon cycle that includes the weathering of rocks to produce silicates and bicarbonates, along with the formation of shells in the ocean from HCO_3^-, CO_3^{2-}, and silicates, is shown in Figure **4.10**.

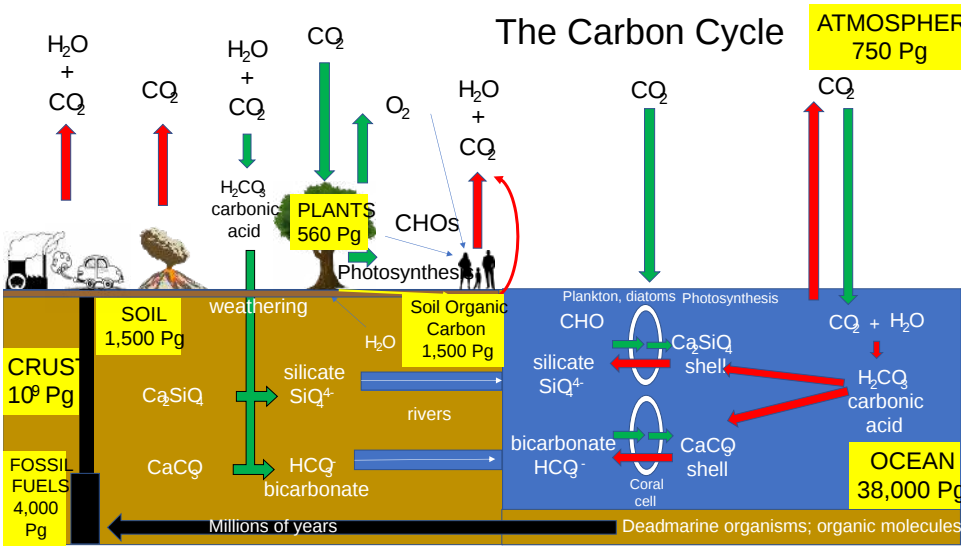


Figure **4.10**: Another view of the carbon cycle

Let's focus on the oceans first. The reversible movement of CO_2 from the atmosphere to the oceans, $CO_{2\ atm} \leftrightarrow CO_{2\ ocean}$, depends on the difference in the partial pressures of CO_2 (ΔpCO_2) in the atmosphere and surface waters. The reaction is also driven to the right by the removal of CO_2 (aq), which forms carbonic acid (H_2CO_3), which then reacts to form bicarbonate (HCO_3^-) and carbonate (CO_3^{2-}). These coupled reactions chemically buffer ocean water, thus regulating ocean pCO_2 and pH.

pCO_2 is not homogeneous in ocean surface waters and varies with current and temperature conditions. CO_2 can be more readily released from upwellings of nutrient-rich and warm waters, especially in the tropics. In cold Northern waters and the Southern Ocean, where water sinks, it is taken up from the atmosphere (again, CO_2 is more soluble in cold water).

As we discussed in Chapter 31.1, ocean chemistry of CO_2 largely determines atmospheric CO_2 levels. The coupled reactions of CO_2 in the oceans are shown below.

$$\mathbf{CO_2(\ g,\ atm) \leftrightarrow CO_2(aq,\ ocean)} \tag{4.2}$$

$$\mathbf{CO_2(aq,\ ocean\ ) + H_2O(I,\ ocean\ ) \leftrightarrow H_3O^+(aq) + HCO_3^-(aq)} \tag{4.3}$$

$$\mathbf{H_2O(I) + HCO_3^-(aq) \leftrightarrow H_3O^+(aq) + CO_3^{2-}(aq,\ sparingly\ soluble\ )} \tag{4.4}$$

These reactions should be familiar to all chemistry students and were presented previously in Chapter 31.1 and in Chapter 2. A significant source of oceanic bicarbonate is the weathering of rocks such as limestone and marble, both of which are forms of $CaCO_3$. The relevant reactions are shown below.

$$\begin{aligned} &\mathbf{CaCO_3(\ s) + H_2O \leftrightarrow Ca^{2+}(aq) + CO_3^{2-}(aq)} \\ &\mathbf{CO_3^{2-}(aq) + H_2O \leftrightarrow HCO_3^-(aq) + OH^-(aq)} \end{aligned} \tag{4.5}$$

CO_2 is nonpolar and not very soluble in water. Either is CO_3^{2-} in the presence of divalent cations like Ca^{2+}. However, HCO_3^- is and can be considered a "soluble" form of carbon. This soluble form from terrestrial weathering enters rivers and eventually reaches the ocean. It is also the form of carbonate that is transferred into cells by anion transporters for eventual shell formation. HCO_3^- is also a chief regulator of both blood and ocean pH. Weathering is slow compared to anthropogenic CO_2 emissions from fossil fuel use, but it is nevertheless a key player in the carbon cycle and in regulating ocean pH.

The same weathering reactions on silicate rocks lead to the transfer of silicate ions into rivers and the ocean, where diatoms use them to form $CaSiO_4$ shells. As oceans absorb more CO_2, they become more acidic, mimicking the effects of "weathering" on the shells of living organisms, potentially leading to their death. Silicon is directly underneath carbon in the periodic table, so the simplified reaction is analogous to those we see with CO_2 and its inorganic ions.

$$\mathbf{H_4SiO_4 = SiO_2 + 2H_2O} \tag{4.6}$$

H_4SiO_4 is silicic acid.

$^{13}C/^{12}C$ RATIOS IN ICE CORE AND OCEAN SEDIMENTS

We can now explore how carbon isotopes can be used for more than radio-^{14}C dating, which is quite limited in climate studies. However, ^{13}C, a stable isotope of carbon, is extremely useful because C-^{13}C bond dynamics are influenced by it. Reaction rates are affected by the presence of ^{13}C when C-C bonds are made or cleaved. This isotope effect leads to different $^{13}C/^{12}C$ ratios in reactants and products, resulting in different $\delta^{13}C$ values.

Isotopes have a long history in the study of biochemical reactions. The k_{cat} and k_{cat}/K_M values for enzyme-catalyzed reactions can be affected if the rate-limiting step involves cleavage or the creation of a C-^{13}C, C-D (deuterium), or C-T (tritium) bond. Substrates labeled with the isotopes have similar transition state energies for the formation/cleavage of a bond involving an isotope. Still, the ground state vibrational energy for the isotope-substituted atom is proportionately lower, as illustrated in Figure **4.11**.

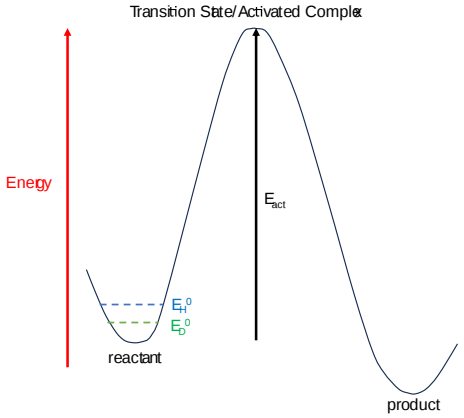


Figure **4.11**: Kinetic Isotope Effects.

This primary **kinetic isotope effect** leads to a higher activation energy for bond formation or cleavage involving the isotope. For C-D and C-T bond cleavages that are rate-limiting, the rates are 7X and 16X slower than the cleavage of a C-H bond, respectively. Cleavage or formation of bonds to heavy isotopes of carbon, oxygen, nitrogen, sulfur, and bromine has much smaller isotope effects (ranging from 1.02 to 1.10). The difference in the magnitude of the kinetic isotope effect is directly related to the percentage change in mass. Large effects are observed when hydrogen is replaced with deuterium because the mass difference is very large (mass is doubled).

Hence, the kinetic isotope effect is at play in carbon fixation in photosynthesis. This is evidenced by the observation that $^{13}C/^{12}C$ ratios are lower in plants than in the atmosphere, showing that $^{12}CO_2$ is preferentially "fixed" in the ribulose bisphosphate carboxylase/oxygenase reaction in plants and other photosynthetic organisms. Also, $^{12}CO_2$, a lighter molecule, diffuses more rapidly through the stomata, which are regulated pores in leaves that facilitate the passage of CO_2, O_2, and H_2O.

Chapter 31.2 discussed using $\delta^{18}O$ values in ice and ocean core sediments to measure past CO_2 and temperatures.

$$\delta^{18}O = \left[\frac{\left(\frac{^{18}O}{^{16}O}\right)_{\text{sample}}}{\left(\frac{^{18}O}{^{16}O}\right)_{\text{reference}}} - 1 \right] * 1000$$

$\delta^{18}O$ values for ice core water samples were easier to interpret than $\delta^{18}O$ values for $CaCO_3$ samples since the deposition of ice is a simple physical process compared to the complexity of the deposition of $CaCO_3$ in ocean sediments, which depends on chemical reactions and nonequilibrium processes (as described in Chapter 31).

Climate scientists can determine and use $\boldsymbol{\delta^{13}C}$ values as well. An analogous equation for it is shown below.

$$\delta^{13}C = \left[\frac{\left(\frac{^{13}C}{^{12}C}\right)_{\text{sample}}}{\left(\frac{^{13}C}{^{12}C}\right)_{\text{reference}}} - 1 \right] * 1000$$

Compared to using $\delta^{18}O$ in carbonate samples, using $\delta^{13}C$ is also more difficult. The shells of ocean sediment foraminifera were made from dissolved inorganic carbon (DIC) in the ocean at the time, so their $\delta^{13}C$ values reflect that. However, shell formation is not a simple equilibrium process, since biological shells form rapidly; hence, kinetic effects in carbonate and, by extension, isotope fractionation are important. In addition, the biochemistry of shell formation is complicated.

In the open ocean, planktic foraminifera are perhaps the most important marine organisms that form shells, given that they produce and export about 2.9 Gt $CaCO_3$/yr into the sea. Their shells form in a process involving many metastable calcite phases. It starts with a soft template that contains Mg^{2+} and Na^+ ions, which play a key role in crystallization. Growth occurs by successive additions of "chambers" to the shell. An F-actin mesh that forms microtubular structures leads to the formation of protective envelopes during chamber formation. The layered templates sequester and help control shell mineralization, separate bulk seawater, and favor an intracellular vs. extracellular process for biomineralization. Seawater containing minerals becomes vacuolized in a process that excludes a competing cation, Mg^{2+}, for some foraminifera. In addition, both Ca^{2+} and HCO_3^- transporters are required. This combination forms an environment low in Mg^{2+} and supersaturated in Ca^{2+} and CO_3^{2-} for calcite formation. The kinetic fractionation of ^{13}C isotopes into shells is also different from that for ^{18}O isotopes since the "pool" of oxygen in the oceans is much greater than that of carbon. Likewise, the $\delta^{13}C$ is more location-dependent than the $\delta^{18}O$.

Buried organic matter can also be studied. The $\delta^{13}C$ value for buried organic matter depends on primary land and ocean productivity. As mentioned above, autotrophs preferentially take up $^{12}CO_2$. Heterotrophs that eat them also become enriched in ^{12}C. Hence, organisms have negative $\delta^{13}C$ values, typically around −25‰, which depend on the pathways of incorporation and metabolism. Methane in oceanic hydrates can be either biogenic, produced by methanogens at

low temperatures, or thermogenic, produced during high-temperature reactions. Biogenic methane has a $\delta^{13}C$ of around -60‰, while thermogenic methane has a value of around −40‰. Terrestrial plants have different δ^{13} values. $\delta^{13}C$ in C_4 plants range from -16 to −10‰ while for C_3 plants they range from −33 to −24‰.

Correction: 5/2/26)

Changes in $\delta^{13}C$ in ocean sediments and ice cores are used in climate studies (just as are $\delta^{18}O$ values in ice cores and deposited shells in ocean sediments). The following explanation of changes in $\delta^{13}C$ values may help those with a chemistry-centric view of biochemistry who struggle with mass balance across the whole biosphere.

Photosynthesis strongly favors $^{12}CO_2$ over $^{13}CO_2$ in both land plants and marine phytoplankton, as described above. Hence, living organic matter is depleted in ^{13}C relative to the **inorganic** carbon reservoir. When photosynthesis (primary production) is high, the organic material on death is buried in sediments before entering the inorganic pool. Hence ^{12}C is effectively removed from the ocean's dissolved inorganic carbon (DIC) pool. The residual DIC becomes increasingly enriched in ^{13}C, and carbonate minerals (including the calcite shells of foraminifera) precipitated from the DIC pools are correspondingly higher (more positive $\delta^{13}C$ values). This rise is called a **positive $\delta^{13}C$ excursion**, and it signals periods **when life was productive and carbon burial was robust**.

During mass extinction events, when both terrestrial and marine primary production drop precipitously, organic carbon burial slows dramatically. ^{12}C that would otherwise have been sequestered in sediments instead accumulates in the ocean-atmosphere carbon pool, driving DIC, and carbonate $\delta^{13}C$ toward more negative values. This is called a **negative $\delta^{13}C$ excursion** and is a characteristicsignature in the sedimentary recordat **major extinction events,** such as the Permian–Triassic and Cretaceous–Paleogene boundaries.

What is tricky to understand is the difference between sedimentary carbonate $\delta^{13}C$ values and ice-core $\delta^{13}C$ values in sequestered CO_2. These are related yet distinct.

- Ocean core carbonate $\delta^{13}C$ reflects past ocean DIC reservoirs and is the primary source of positive and negative **$\delta^{13}C$ excursions** over geological time frames of millions of years.
- Ice-core $\delta^{13}C$ of trapped CO_2 directly reflects past atmospheric composition, but extends back only ~800,000 years, so it can't capture mass extinctions.

EXAMPLES OF CLIMATIC EVENTS ACCOMPANIED BY CHANGES IN $\Delta^{13}C$.

Negative excursions

Extrinction events are best seen in **negative $\delta^{13}C$ excursion**in ocean sediments, although one, the PETM (below) is particularly clear in the sedimentary record. The most dramatic negative excursions are associated with mass extinctions and rapid disruptions of the carbon cycle.

- The **Permian–Triassic boundary** (~252 Ma) records a drop of 3–8‰ in marine carbonate sections worldwide — one of the largest and most abrupt negative excursions in the Phanerozoic, coinciding with the largest mass extinction in Earth history and likely reflecting a catastrophic collapse of marine productivity combined with massive volcanic CO_2 injection from the Siberian Traps.
- The **Cretaceous–Paleogene boundary** (~66 Ma) shows a sharp negative excursion of 2–3‰ in both planktonic foram carbonates in ocean sediment cores and in bulk carbonate from terrestrial and marine sections, reflecting the productivity collapse following the Chicxulub impact.
- The **Paleocene–Eocene Thermal Maximum** (PETM, ~56 Ma) is characterized by a negative carbon isotope excursion of 3–5‰ recorded globally in marine sediments, soil carbonates, and terrestrial organic matter — caused by a massive injection of isotopically light carbon into the ocean-atmosphere system, the source of which is still debated (methane hydrates, volcanic carbon, or a combination).

Positive excursions

- The **Lomagundi–Jatuli event** (~2.2–2.1 GYa) is the largest known positive $\delta^{13}C$ excursion in Earth history — carbonate rocks from this period record values of +8 to +12‰, far above the typical marine carbonate value of ~0‰, suggesting a huge burial of organic carbon possibly in the Great Oxidation Event (when atmospheric O_2 dramatically increased from near zero to 0.1-2%).
- The **Neoproterozoic** (1,000 MYA to 541 MYA) time frame is the final era of the Precambrian. During this time, Earth faced t extreme climate changes (Snowball Earth), supercontinent fragmentation, and the rise of complex, multicellular life. This era had many large positive excursions (with a few interspersed negative ones). The early **Cambrian** also records a large positive excursion coinciding with the diversification of animal life and increased burial of organic carbon.

MORE RECENT CHANGES IN $\Delta^{13}C$

1500-1650 CE

We examined $\delta^{18}O$ values during the Little Ice Ages in Chapter 31.2. What about $\delta^{13}C$ values? CO_2 and $\delta^{13}C$ values from 1000 to 1900 are shown in Figure **4.12**.

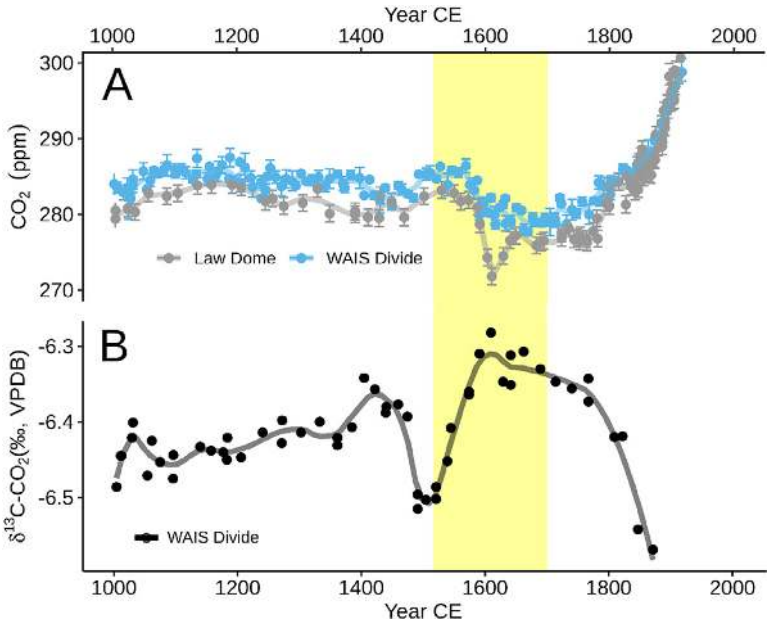


Figure **4.12**: CO_2 and $\delta^{13}C$ values from 1000 to 1900. Koch et al. Quaternary Science Reviews, 207, 2019, 13-36. https://doi.org/10.1016/j.quascirev.2018.12.004. CC BY license (http://creativecommons.org/licenses/by/4.0/).

Panel (A) shows the CO2 concentrations recorded in two Antarctic ice cores: Law Dome (grey, MacFarling Meure et al., 2006) and West Antarctic Ice Sheet (WAIS) Divide (blue, Ahn et al., 2012).

Panel (B) shows the carbon isotopic ratios recorded in CO2 from the WAIS Divide ice core (black, Bauska et al., 2015), showing an increased terrestrial carbon uptake over the 16th century (B). The yellow box spans the major indigenous depopulation event (1520 - 1700 CE). Loess smoothed lines for visual aid.

Koch et al have strong evidence to suggest that the cooling after 1510 (area in the yellow box in the above figure) was associated with a dip in CO_2 caused by the reforestation of Indigenous peoples' land in Meso and South America after epidemics of European disease killed upwards of 90% (around 55 million) of the indigenous peoples. The open and agricultural land reverted to forests. The diseases included smallpox, measles, influenza, the bubonic plague, malaria, diphtheria, typhus, and cholera. Domesticated farm animals introduced from Europe to the Americas were responsible for most of the disease. Along with the deaths of so many people came a concomitant return of cleared and agricultural lands (about 56 million hectares, or 212,000 mi^2) to forest and plant growth. This may have led to a 7-10 ppm drop in CO_2 in the late 1500s and early 1600s, peaking in 1601 (middle of the yellow box). This decrease in temperature was associated with a small rise (small positive excursion) in the $\delta^{13}C$ values, as $^{12}CO_2$ was preferentially removed from the atmosphere. Global surface air temperatures decreased by around 0.15 ºC. This "Great Dying" of Indigenous peoples shows the power of humankind to globally alter the climate in calamitous ways, even before the use of fossil fuels. The decrease in $\delta^{13}C$ values before 1500 was unexplained.

1800 to the present

$\delta^{13}C$ values can also be used to show that the increase in CO_2 since the industrial revolution is due to the burning of fossil fuels, which is of biogenic origin and hence has more negative $\delta^{13}C$ values. Figure **4.13** shows atmospheric CO_2 levels in ppm plotted along with $\delta^{13}C$ values. There is a perfect correlation between the rise in atmospheric CO_2 from the Industrial Revolution onward and the decrease in $\delta^{13}C$ values.

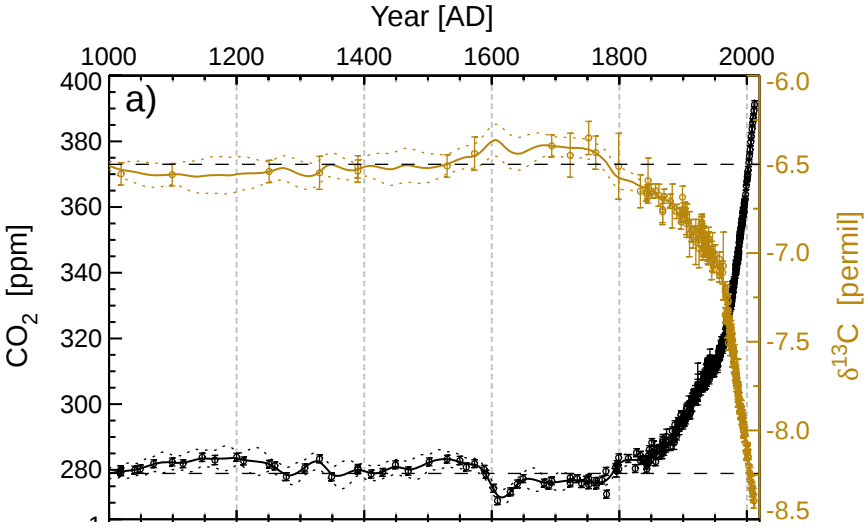


Figure 4.13: CO_2 concentration (black circles) and the $\delta^{13}C$ (brown circles) from 1000 to 2010. Rubino et al. Journal of Geophysical Research: Atmospheres. https://doi.org/10.1002/jgrd.50668. With permission (Copyright Clearance Center). another link: https://www.researchgate.net/figure/...fig1_393188182

Figure 4.14 below summarizes theδ13C values in four carbon reservoirs (atmosphere, terrestrial, ocean, and buried sediments).

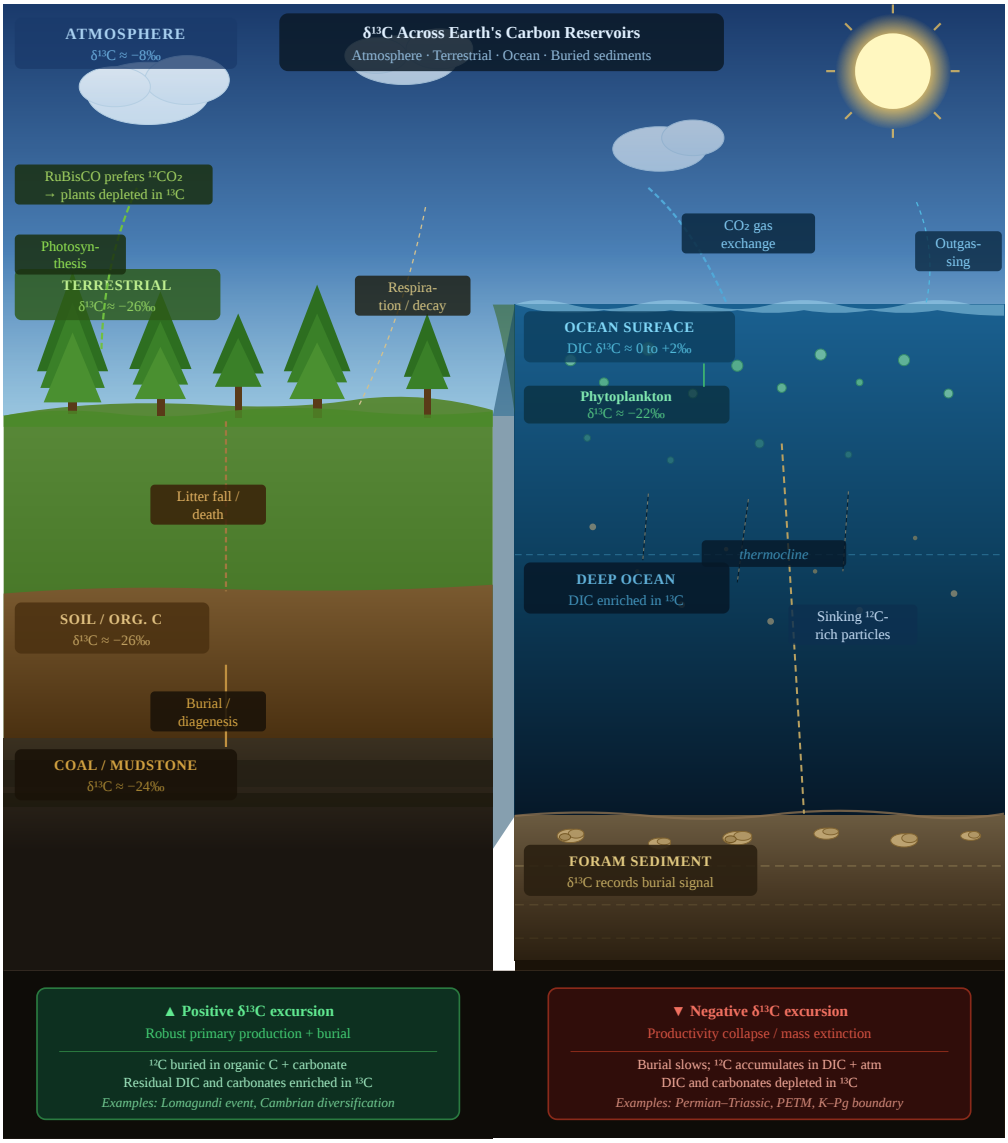


Figure 4.14: δ13C values in four carbon reservoirs (atmosphere, terrestrial, ocean, and buried sediments). Anthropic. (2025). *Claude* (Claude Sonnet 4.6) [Large language model]. Retrieved May 2, 2025, from https://claude.ai

THE METHANE CYCLE

CH_4 is mentioned only indirectly above as it contributes to CO_2 "equivalent" emissions. As mentioned in Chapter 32.01a, methane is a much more potent greenhouse gas, with a global warming potential (GWP) 30x that of CO_2 in the first 20 years of its release. It has a much shorter lifetime in the atmosphere due to chemical reactions that destroy it, so a given amount of released methane contributes to warming only over decades. However, of the total warming observed over the last 100 years, if CO_2 has contributed 1 unit of warming, CH_4 has contributed 0.6 units. Its concentration has increased 2.6x since the Industrial Revolution, and its rise is accelerating. Hence, we must move to limit the rise in anthropogenic CH_4, mainly from fossil fuel production (leakage during production, transport, and storage) and agricultural practices. Figure 4.15 below shows sources and sinks for CH_4, with orange showing anthropogenic contributions, green natural ones, and hatched a combination. 2/3 of the release is anthropogenic.

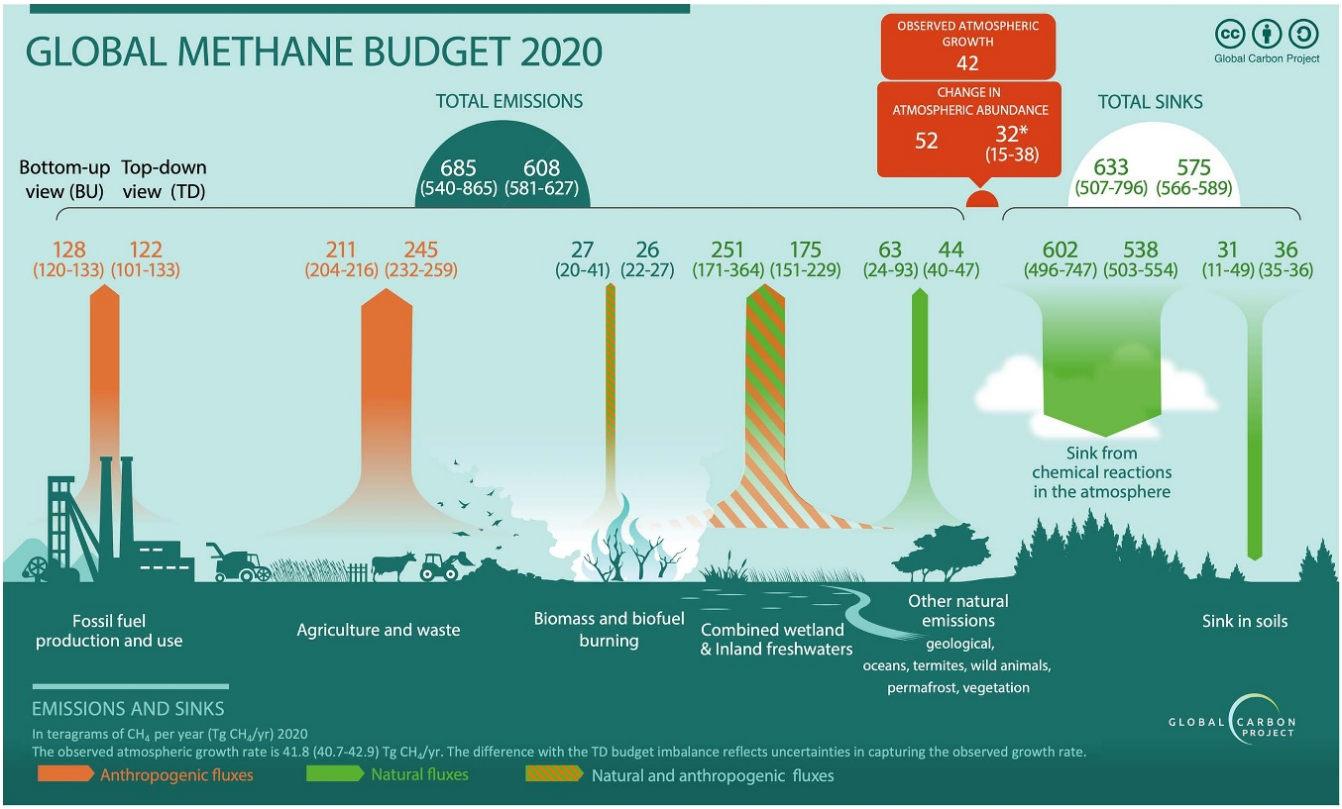


Figure **4.15**: The global methane budget (Tg CH_4 yr^{-1}) for the year 2020 based on top-down methods for natural sources and sinks (green), anthropogenic sources (orange), and mixed natural and anthropogenic sources (hatched orange-green for 'Biomass and biofuel burning' and 'Combined wetland & inland freshwaters'). R B Jackson et al 2024 Environ. Res. Lett. 19 101002. **DOI** 10.1088/1748-9326/ad6463. Creative Commons Attribution 4.0 license.

There was a sharp spike in atmospheric methane in 2020 and 2021, but the source was unclear. $\delta^{13}C_{CH4}$ measurement (which gives a measure of $^{13}C/^{12}C$ ratio of CH_4) for samples from around the world over time significantly decreased in those years. This suggests that the likely source of increased emissions was microbes from wetlands, waste storage, and livestock, characterized by $\delta^{13}C_{CH4}$= –62‰. Burning of biomass and biofuel is characterized by $\delta^{13}C_{CH4}$ values of –24‰, while fossil fuel CH_4 emissions are about –45‰.

Figure **4.16** below shows the result of computer simulations (solid, dashed, and dotted lines) that attempt to partition the increases in $CH_{4\ atm}$ into contributions from fossil fuels (FF) and microbes (MICR). The actual values are shown as green diamonds. OH represents the hydroxyl radical, which helps scrub the atmosphere of methane; we will ignore this for this discussion. The top part shows the increase in CH_4 concentrations. In 2008, the slope increased, then again in 2014, and yet again in 2021. (The bottom part of the graph shows that the overall $\delta^{13}C_{CH4}$ becomes increasingly negative starting around 2008 in ways that paralleled the increases in $CH_{4\ atm}$.

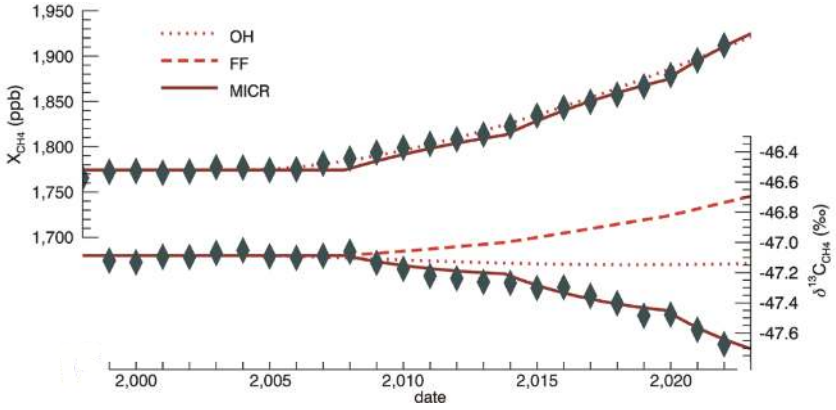


Figure **4.16**: (A) Modeled response of CH_4 mole fraction and $\delta^{13}C_{CH4}$ due to different CH_4 growth drivers. Fossil-fuel emissions (FF), microbial emissions (MICR), hydroxide (OH). Modified from S.E. Michel, X. Lan, J. Miller, P. Tans, J.R. Clark, H. Schaefer, P. Sperlich, G. Brailsford, S. Morimoto, H. Moossen, J. Li, Rapid shift in methane carbon isotopes suggests microbial emissions drove record high atmospheric methane growth in 2020–2022, Proc. Natl. Acad. Sci. U.S.A. 121 (44) . e2411212121, https://doi.org/10.1073/pnas.2411212121 (2024). Creative Commons Attribution License 4.0 (CC BY).

The decrease in $\delta^{13}C_{CH4}$ best be accounted for by increasing microbial emissions, but if emission increases were only from MICR, the observed $\delta^{13}C_{CH4}$ would be even more negative. To make the decrease less negative, the best-fit model required increases in FF emission. Further increases in both (but mostly MICR) occurred in 2014. The final increase in 2021 and 2022 was from only MICR. Hence, it is likely that 85% of CH_4 growth from 2007 to 2020 was due to increased microbial emissions. This is very worrisome, as it implies that global warming and climate change drive greater microbial methane production, amplifying greenhouse warming in a positive and deleterious feedback loop. What's worse, it is happening now! Here is a link to the NOAA site on atmospheric CH_4 levels.



A paper published in February 2026 showed that the sharper rise in atmospheric methane in the period 2020-2023 was likely caused by reductions in the atmosphere's scrubber for CH_4, the hydroxyl free radical ($OH^{\cdot}$), along with increasing emissions of biological methane. (P. Ciais *et al.*, Why methane surged in the atmosphere during the early 2020s. *Science* **391**, eadx8262(2026). DOI:10.1126/science.adx8262.)

Carbon Tracker is a website that tracks methane emissions detected by satellites. In the upper-left corner, click **Show Filters,** then check only CH4 to track emissions. Expand the map to see individual contributors to emissions.

There are no "chemical" scrubbers for emitted CO_2 in the atmosphere. Fortunately, there is for CH_4, which accounts for the much shorter lifetime of atmospheric methane. The scrubber is the atmospheric hydroxyl radical, •OH, which is formed photochemically continuously during daylight hours. Its formation during daylight hours is shown in Figure **4.17** below.

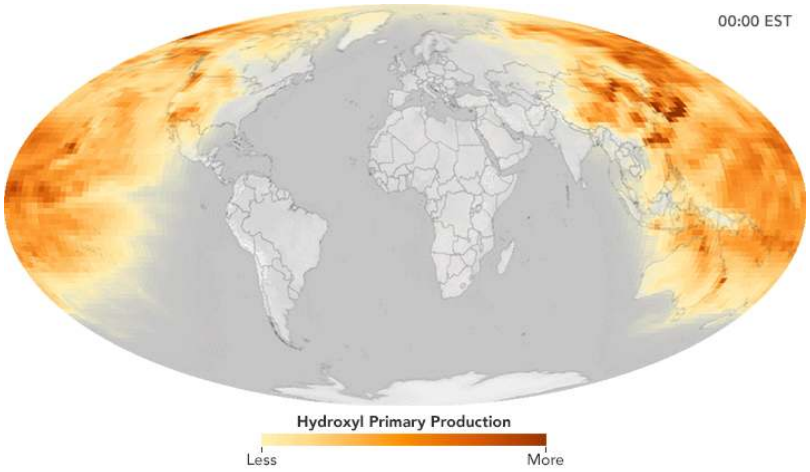


Figure **4.17**: The hydroxyl free radical concentration in the atmosphere. Detergent-like Molecule Recycles Itself in the Atmosphere. https://science.nasa.gov/earth/earth...sphere-144358/

You can see the hydroxyl radical is formed in daylight hours, suggesting a photocatalytic cycle. It is produced by this reaction of ozone:

$O_3 + h\nu\ (\lambda < 320\ nm) \rightarrow O(^1D) + O_2$, where $O(^1D)$ is single oxygen, more reactive than triplet oxidation as we discussed in 12.3: The Chemistry and Biochemistry of Dioxygen

Then the singlet O reacts with water vapor:

$$O(^1D) + H_2O \rightarrow 2\ \bullet OH$$

The free radical then abstracts, in a rate-limiting step, a hydrogen atom from CH_4 to form the methyl free radical, $\bullet CH_3$.

$$CH_4 + \bullet OH \rightarrow \bullet CH_3 + H_2O$$

This reaction is slow, giving methane a half-life of 9-10 years in the atmosphere. The $\bullet CH_3$ reacts in a series of steps to form CO_2.

The net photoreaction of the carbon in CH_4 is:

$$CH_4 + 2O_2 \rightarrow CO_2 + 2\ H_2O$$

? SEE THE REST OF THE STEPS

Click below.

Answer

A series of other radical propagating and terminating reactions with O_2 and nitric oxide in the air then occur on a faster time scale:

$$\bullet CH_3 + O_2 \rightarrow CH_3OO\bullet \text{ (methylperoxy radical)}$$

$$CH_3OO\bullet + NO \rightarrow CH_3O\bullet + NO_2$$

$$CH_3O\bullet + O_2 \rightarrow HCHO \text{ (formaldehyde)} + HO_2$$

$$HCHO + h\nu \rightarrow H\bullet + HCO\bullet$$

$$HCO\bullet + O_2 \rightarrow CO + HO_2$$

$$CO + \bullet OH \rightarrow CO_2 + H\bullet$$

$$H\bullet + O_2 \rightarrow HO_2$$

$$HO_2 + NO \rightarrow \bullet OH + NO_2$$

SUMMARY

(Summary written by Claude, Anthropic)

This chapter develops a quantitative understanding of the global carbon cycle — its major reservoirs, the fluxes connecting them, and the chemical and isotopic tools used to track carbon movement through the biosphere — building the foundation needed to understand both past climate change and future projections.

Stocks, fluxes, and mass balance. Carbon exists in four major reservoirs: the atmosphere (~875 GtC), the terrestrial biosphere (~3,550 GtC, including permafrost, soil, and vegetation), the oceans (~39,500 GtC, dominated by dissolved inorganic carbon), and buried fossil fuels (~905 GtC). Carbon fluxes — transfers between reservoirs in GtC/yr — operate on fast timescales (ocean/atmosphere/land exchange, up to thousands of years) and slow timescales (deep sediment and rock cycling, millions of years). Before the Industrial Revolution, these fluxes were approximately balanced. Since then, fossil fuel combustion (~9.6 GtC/yr averaged over 2012–2021, rising to 9.9 GtC/yr in 2021), combined with land-use change (~1.2 GtC/yr), has overwhelmed natural sinks — land uptake (~3.1 GtC/yr) and ocean uptake (~2.9 GtC/yr) — leaving a net atmospheric accumulation of ~5.2 GtC/yr. The cumulative fossil fuel contribution since 1850 (~275 GtC) translates to a ~129 ppm rise in atmospheric CO_2, matching independent measurements precisely. Humans are now the dominant force in the global carbon cycle.

Climate modeling. Simple kinetic models of the carbon cycle — treating each reservoir's stock as a concentration and each flux as proportional to stock size via an apparent rate constant — can reproduce observed CO_2 trends and project future concentrations. Despite many simplifying assumptions, a four-term VCell model predicts atmospheric CO_2 peaking near 982 GtC (~463 ppm) around 2073 under current emissions trajectories, closely tracking the IPCC SSP1-2.6 scenario. More sophisticated models, such as the EN-ROADS simulator developed at MIT and Climate Interactive, incorporate socioeconomic pathways, policy levers, and feedback mechanisms. ExxonMobil's internal climate models from 1977–2003 — kept from the public while executives promoted disinformation — accurately predicted both CO_2 levels and temperature increases to the present day, demonstrating that the science was settled decades ago and that delay was a deliberate choice.

Ocean carbon chemistry. CO_2 partitions between the atmosphere and ocean according to the partial pressure difference (ΔpCO_2), and is drawn into solution by its conversion to carbonic acid, bicarbonate (HCO_3^-), and carbonate (CO_3^{2-}). These coupled equilibria buffer ocean pH and regulate atmospheric CO_2 levels. Rock weathering — of limestone, marble, and silicate rocks — delivers additional HCO_3^- and silicate ions to the ocean, supporting shell formation by foraminifera and diatoms respectively. As ocean CO_2 uptake increases with rising atmospheric concentrations (consistent with Le Châtelier's principle), ocean acidification threatens these calcifying organisms. If oceanic uptake saturates, atmospheric CO_2 accumulation will accelerate.

Carbon isotopes and $\delta^{13}C$. Stable carbon isotope ratios ($^{13}C/^{12}C$) expressed as $\delta^{13}C$ values provide powerful tools for tracking carbon through the biosphere. Kinetic isotope effects — arising from the lower ground-state vibrational energy of bonds to heavier isotopes — cause photosynthesis to preferentially fix $^{12}CO_2$, making organic matter and fossil fuels depleted in ^{13}C ($\delta^{13}C \approx -25‰$ for C3 plants; $\approx -60‰$ for biogenic methane). In ocean sediment records, high primary productivity and organic carbon burial remove ^{12}C from the dissolved inorganic carbon (DIC) pool, enriching it in ^{13}C and producing positive $\delta^{13}C$ excursions in carbonate shells — as seen during the Lomagundi–Jatuli event (~2.2–2.1 GYa, +8 to +12‰) and the Neoproterozoic. Conversely, mass extinctions, volcanic CO_2 injection, or rapid release of isotopically light carbon drive negative $\delta^{13}C$ excursions — seen at the Permian–Triassic boundary (−3 to −8‰), the Cretaceous–Paleogene boundary (−2 to −3‰), and the PETM (−3 to −5‰). In ice cores, the decline in atmospheric $\delta^{13}C$ since 1800 — perfectly correlated with rising CO_2 — provides independent confirmation that the source is fossil fuel combustion. A smaller positive $\delta^{13}C$ excursion in the late 1500s to early 1600s reflects the reforestation of ~56 million hectares of Indigenous land in the Americas following the Great Dying (1520–1700 CE), which killed an estimated 55 million people through European diseases and caused a measurable ~7–10 ppm dip in atmospheric CO_2 and ~0.15°C of global cooling.

The methane cycle. Atmospheric methane has increased 2.6-fold since the Industrial Revolution and contributes approximately 0.6 units of warming for every 1 unit from CO_2 over the past 100 years. Roughly two-thirds of present methane emissions are anthropogenic, from fossil fuel production and leakage, livestock, and waste. $\delta^{13}C_CH4$ analysis — exploiting the distinct isotopic signatures of microbial ($\approx -62‰$), fossil fuel ($\approx -45‰$), and biomass combustion ($\approx -24‰$) sources — reveals that ~85% of methane growth from 2007 to 2020 came from microbial sources, primarily wetlands and livestock, with the 2020–2022 spike driven almost entirely by microbial emissions. This is deeply alarming because it implies a positive feedback loop: global warming stimulates microbial methane production, which drives further warming. The atmosphere does possess a chemical scrubber for methane — the hydroxyl radical (•OH), produced photochemically from ozone and water vapor — which abstracts a hydrogen atom from CH_4 in the rate-limiting step, giving methane an atmospheric half-life of ~9–10 years and ultimately converting it to CO_2. No equivalent scrubber exists for CO_2, explaining the profound difference in their atmospheric lifetimes and long-term climate impacts.

4: Climate Change - The Carbon Cycle and Carbon Chemistry is shared under a CC BY-NC-SA 4.0 license and was authored, remixed, and/or curated by LibreTexts.

5: BIOFUELS A - CORN AND SUGAR CANE ETHANOL

LEARNING GOALS

(Learning goals written by Claude, Anthropic)

By the end of this chapter, students should be able to:

Ethanol Production: Feedstocks and Fermentation

- Compare the energy densities of ethanol, octane, hydrogen, and biodiesel using standard combustion enthalpies (kJ/g), explain why bioethanol releases ~63% of the energy of gasoline per gram, and write the three coupled equations that describe why bioethanol is theoretically carbon-neutral while identifying what those equations omit.
- Describe the four generations of bioethanol feedstocks, explain the key enzymatic steps converting corn starch to glucose — including α-amylase (endoglucosidase, retention of configuration), β-amylase (exoglucosidase, inversion of configuration), and glucoamylase (cleaves both α(1,4) and α(1,6) bonds) — and connect the retention vs. inversion mechanisms to SN2-like versus double-displacement mechanisms at the anomeric carbon.
- Describe the structure of the invertase (SInv) homooctamer from *S. cerevisiae* — explaining how identical subunits form two types of dimers (closed AB/CD with hydrophobic active-site floor; open EF/GH with an additional Asp-Lys salt bridge) — and explain the double-displacement retention mechanism by which Asp22 forms a glycosyl-enzyme intermediate and Glu203 acts as general acid/base to hydrolyze sucrose to glucose and fructose.

Life Cycle Analysis: Is Bioethanol Better Than Fossil Fuels?

- Define life cycle analysis (LCA), carbon intensity (CO_2 equiv per unit of activity), and global warming potential (GWP_{100}), write the GWP_{100} equation incorporating CH_4 (GWP ≈ 28) and N_2O (GWP ≈ 265), and explain why N_2O emissions from nitrogen fertilizers are a major hidden cost of bioethanol production.
- Interpret the Lark et al. corn ethanol LCA — including how the Renewable Fuel Standards increased corn cultivation by 2.8 Mha, fertilizer use by 3–8%, and N_2O emissions, producing a carbon intensity ≥24% higher than gasoline — and explain why studies that ignore land-use change emissions systematically underestimate corn ethanol's true carbon intensity.
- Use dimensional analysis to convert the sugar cane LCA result from kg CO_2 equiv per ton of sugar cane at the farm gate (53.6 kg/ton) to kg CO_2 equiv per liter of ethanol, add the plant-gate contribution (0.60 kg/L), and apply an energy-content correction factor (33.6/21.2 MJ) to compare sugar cane bioethanol (~0.95 kg CO_2 equiv per gasoline-equivalent liter) to gasoline (~2.3 kg CO_2 equiv/L).

Biofuels vs. Solar: The Opportunity Cost Argument

- Quantify the land-use opportunity cost of biofuels by comparing the energy yield per hectare of corn bioethanol (~22,000 km of EV driving) to solar panels (~3 million km), explain why 1.5 million hectares of solar would meet all US driving needs versus the 25 million hectares of corn now used for bioethanol covering only 10% of driving fuel, and articulate why this comparison represents a fundamental policy choice rather than merely a technical one.
- Identify at least three additional negative environmental impacts of sugarcane bioethanol beyond climate change — including freshwater and marine eutrophication, particulate matter formation, and terrestrial acidification — and explain why a complete LCA must account for all of these, not only CO_2 equivalent emissions.

INTRODUCTION

The world has a great need for energy. We have invested vast sums of money in finding and using fossil fuels. At first glance, fossil fuels appear to be an ideal energy source since they are highly reduced, easily stored, energy-dense, and abundant. Yet we now know the immense cost of their use: pollution that shortens lives and climate change. We have dramatically increased our bioethanol production from corn and sugar cane to reduce our reliance on fossil fuels for transportation. Ethanol is partially oxidized as it has one oxygen atom in the two-carbon molecule. Hence, the energy released per gram is about 63% (by mass) and 70% (by volume) of that of gasoline. The energy values for various fuels are shown in Table **5.1** below, where ΔH_c° is the standard enthalpy of combustion.

Table 5.1: Energy values for a variety of fuelsData source: https://www.engineeringtoolbox.com/s...nt-d_1987.html

Name	Formula	State	$-\Delta H_c°$ *kJ/mol*	$-\Delta H_c°$ *kJ/g or MJ/kg*	$-\Delta H_c°$ *kcal/kg*
Ammonia	NH_3	gas	383	22.48	5369
Butane	C_4H_{10}	gas	2878	49.50	11823
Carbon (graphite)	C	cry	394	32.81	7836
Carbon monoxide	CO	gas	283	10.10	2413
Ethanol	C_2H_6O	liq	1367	29.67	7086
Hydrogen	H_2	gas	286	141.58	33817
Methane	CH_4	gas	891	55.51	13259
Methanol	CH_4O	liq	726	22.65	5410
Naphthalene	$C_{10}H_8$	cry	5157	40.23	9609
Octane	C_8H_{18}	liq	5470	47.87	11434
Propane	C_3H_8	gas	2220	50.33	12021
wood (red oak)				14.8	3540
coal (lignite)				15	3590
coal (anthracite)				27	4060
methyl stearate (biodiesel)	$(CH_3(CH_2)_{16}(CO)CH_3$			40	9560

Nevertheless, ethanol is readily made and is a valuable biofuel. A glance at the table suggests that H_2 would be the best possible fuel, given its highest energy release per gram and its lack of carbon. It can't be produced at the needed scale and isn't easy to store and transport. The critical infrastructure for its widespread use is lacking. Yet these factors could be solved. We'll explore biohydrogen in a separate chapter.

In theory, bioethanol is carbon-neutral, since each carbon in the ethanol is derived from atmospheric CO_2 during photosynthesis. The combustion of ethanol returns CO_2 to the atmosphere in a net-zero-emission fashion, as shown in the reactions below.

Eq 1: $\mathbf{6CO_2}$ (g) + $6H_2O$ (l) → $C_6H_{12}O_6$ (s) + $6O_2$ (photosynthesis)

Eq 2: $C_6H_{12}O_6$ (s) → $2\ CH_3CH_2OH$ (l) + $\mathbf{2CO_2}$ (g) (anaerobic ethanol biosynthesis)

Eq 3: $2CH_3CH_2OH$ (l) + $6O_2$ → $\mathbf{4CO_2}$ (g) + $6H_2O$ (g) (combustion of ethanol)

Six CO_2s in, six out! It seems simple, but it's not since we have to manufacture bioethanol, which is energy and land-intensive. We'll explain more later. First, let's explore how ethanol is synthesized for its two major uses: drinking and use as a biofuel.

ETHANOL PRODUCTION OVERVIEW

The scale of worldwide ethanol production is quite staggering. Let's first consider the production of ethanol by yeast for alcoholic beverages. About 100 billion US gallons/yr (BGY) of beer, 7 BGY of wine, and 6 BGY of spirits are produced yearly. Assuming beer, wine, and spirits are about 5%, 12%, and 40% ethanol by volume, respectively, the volume of actual ethanol/year made by yeast in these alcoholic beverages is about 5 BGY (beer), 0.85 BGY (wine), and 2.4 BGY (spirits). This amounts to about 8.3 billion gallons of ethanol produced by these microorganisms. Compare this to fuel ethanol production each year, shown in Figure 5.1.

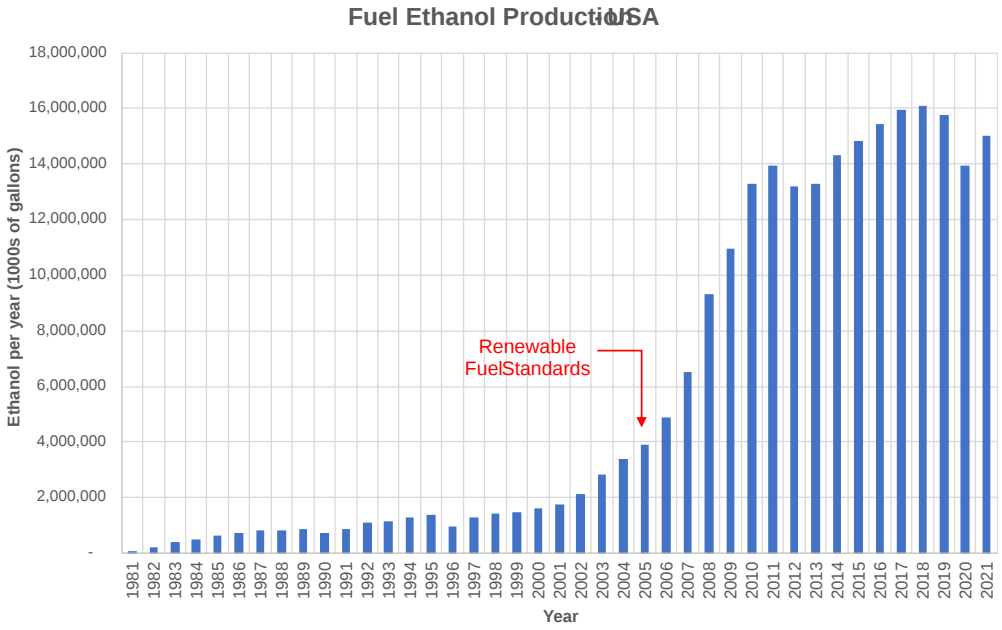


Figure **5.1**: US Fuel Ethanol Production. Data from **U.S. Bioenergy Statistics**

Note that the y-axis is in units of 1000s gallons of ethanol. Peak US production was in 2018, when 16 billion gallons were produced, about 1/10 of the gasoline used yearly in the US. The year the Renewable Fuel Standards (RFS) were introduced in the USA (2005) is also shown. This dip in 2020 is attributed to the COVID-19 pandemic.

The US and Brazil produce about 85% of fuel ethanol, as shown below in Figure **5.2**.

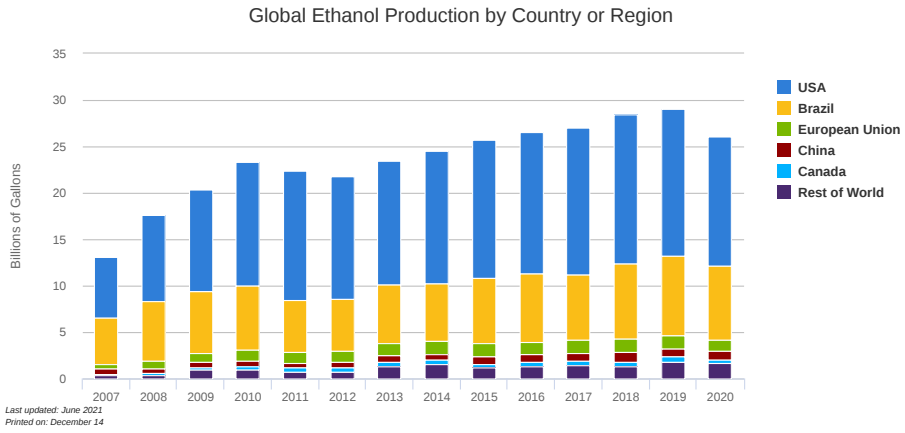


Figure **5.2**: Fuel ethanol production (billions of gallons or BG) around the world per year. https://afdc.energy.gov/data/10331

Almost all US ethanol is made from corn, while Brazil's primary source is sugar cane.

Now, the world produces 3x more ethanol for driving than for drinking. These statistics show that the world can quickly respond when it meets our needs.

AN OVERVIEW OF ETHANOL BIOSYNTHESIS

Whether ethanol is made for the beverage or biofuel industries, yeast plays a major role, as we explored in Chapter 14.2: Fates of Pyruvate under Anaerobic Conditions- Fermentation. Yeast contains all the enzymes necessary to convert glucose (6C), made from various "feedstocks", to pyruvate (3C) through the glycolytic pathway. This is followed by the conversion of pyruvate to ethanol via two key yeast enzymes. First, pyruvate is decarboxylated to acetaldehyde by **pyruvate decarboxylase**, which uses TPP as a cofactor. Acetaldehyde is then reduced to ethanol by **ethanol dehydrogenase**, using NADH as a substrate/cofactor, regenerating NAD+ and allowing glycolysis to continue. Figure **5.3** shows these combined anaerobic reactions, known as fermentation.

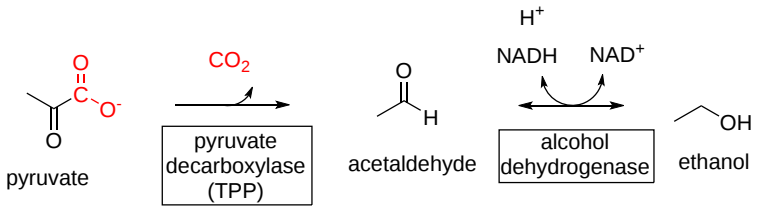


Figure **5.3**: Summary of Ethanol Fermentation in Yeast

Yeast is a facultative (not obligate) anaerobe that can produce energy by glycolysis and ethanol fermentation without oxygen. Of course, in the presence of oxygen, the pyruvate made from glycolysis in yeast is preferentially converted to acetyl-CoA, which enters the citric acid cycle and oxidative phosphorylation pathways to maximize ATP production. Yeast is abundant, so all that is needed is a significant source of glucose.

An abundant source of glucose for bioethanol production is plants that contain starch (for example, corn) or abundant simple sugars (for example, sucrose in sugar cane). Starch, an α(1,4) glucose polymer with α(1,6) branches, can be readily broken down in an industrial setting with amylases into glucose. A significant problem with this "first" generation source of glucose is that food crops (corn and, to a lesser degree, sugar cane) are used for biofuel rather than food. "Second" generation sources of glucose are crop and wood waste products that contain cellulose, a β-(1,4) glucose polymer, and lignin. A significant problem with cellulose is the high chemical stability of the β-(1,4) glycosidic bond. Fungi and bacteria are sources of β-glycosidases to liberate free glucose from cellulose. "Third" generation sources of glucose use algae, which do not displace cropland for bioethanol production. A "fourth" generation source of glucose uses genetically engineered organisms that could become future sources of bioethanol. Figure **5.4** summarizes the different generations of feedstock sources for bioethanol production.

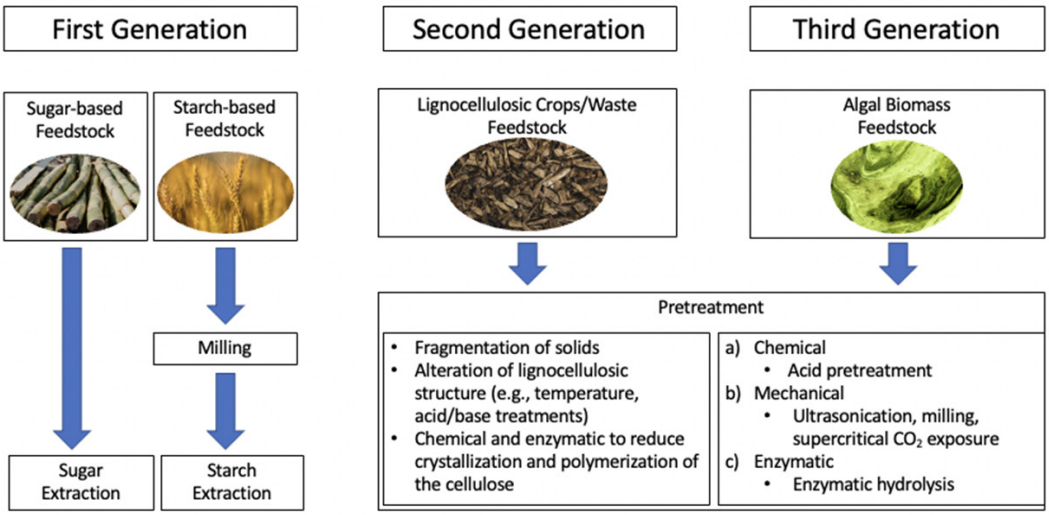


Figure **5.4**: Generation feedstock sources for bioethanol production. Tse, T.J.; Wiens, D.J.; Reaney, M.J.T. *Fermentation* **2021**, *7*, 268. https://doi.org/10.3390/fermentation7040268. Creative Commons Attribution (CC BY) license (**https://creativecommons.org/licenses/by/4.0/**).

We will discuss first-generation sources, such as corn and sugarcane, which are used to produce most of the world's bioethanol in this chapter section and the other two in subsequent sections.

CORN BIOETHANOL

Corn is a significant source of starch, an α(1,4) polymer of glucose with α(1,6) branches. Hence, glucosidases are used to hydrolyze starch to glucose. First, the dry corn is ground in a mill, breaking the corn kernel's outer coat and increasing access to the starch. Heated water is added to form a mash or slurry. Cooking at temperatures above 85 °C helps hydrolyze some glycosidic bonds and reduces the slurry's viscosity. During liquefaction, the pH is adjusted to approximately 6.0. Different **α-amylases** (endoglycosidases) are added, which cleave the α (1,4) glycosidic bonds to produce shorter dextrins (containing branched glucose units not cleaved by α-amylases), and α (1,4) linked glucose oligosaccharides of lengths from 2 glucose units (called maltose) up to 7-8. **β-amylase**, an exoamylase, is also used, which successively cleaves maltose units, Glc α (1,4)Glc, from the nonreducing ends of the chains

Alpha-amylases

A mixed-rendered structure of the human pancreatic alpha-amylase is shown below in Figure 5.5.

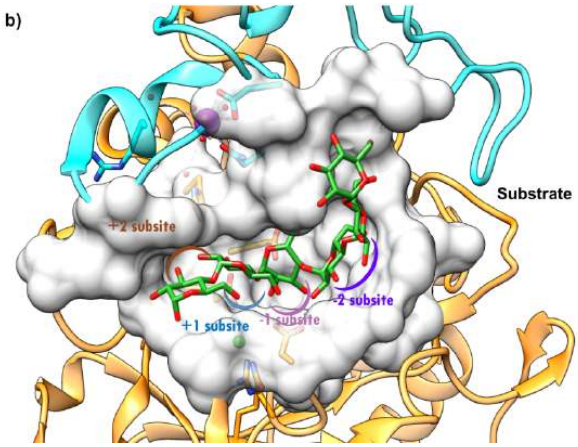
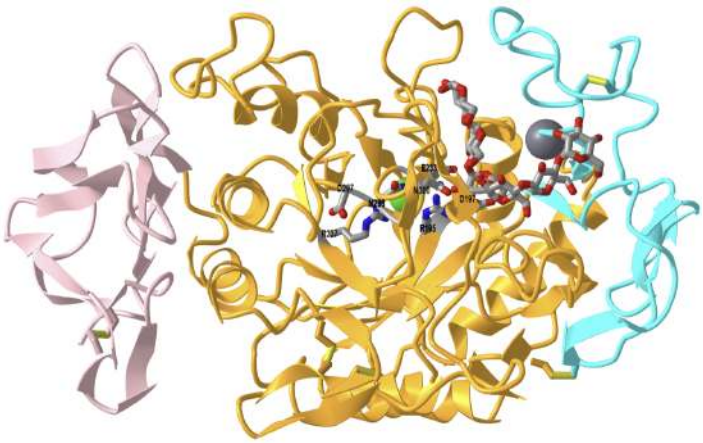


Figure 5.5: Surface representation of the active site of HPA (5TD4) *https://pdb101.rcsb.org/global-healt...ha-glucosidase*. CC-BY-4.0 license. Attribution: David S. Goodsell and the RCSB PDB.

The surface view highlights the deep C-shaped groove into which the substrate, in this case, octaose, is bound. Consistent with protease substrate numbering, the starch substrate is numbered -2, -1, +1, and +2, with cleavage occurring between the -1 and +1 bound alpha-glucose residues. The protein has three domains (orange, blue, and pink). This particular structure contained an active-site mutant (Asp300Asn, D300N). The enzyme has bound calcium and chloride ions. Ca^{2+} maintains the necessary structure, while Cl^-, bound in the C domain, is an allosteric activator.

The octaose binding site is between the A and B domains. Asp197, Glu233, and Asp300 are critical catalytic residues, with Asp 197 acting as a nucleophile to produce a glycosylated intermediate hydrolyzed in the next step. Asp197 and Glu233 act as general acids/bases. We will explore similar mechanisms for the action of beta-amylase (below) and cellulase (in the next chapter section).

Figure 5.6 shows an interactive iCn3D model of starch binding sites on the Human pancreatic alpha-amylase D300N variant complexed with an octaose substrate (5TD4)



NCBI iCn3D Figure 5.6: Starch binding sites on the Human pancreatic alpha-amylase D300N variant complexed with an octaose substrate (5TD4). (Copyright; author via source). Click the image for a popup or use this external link: https://structure.ncbi.nlm.nih.gov/i...W29jf4yAc1JEq9

The domains in the enzyme are color-coded, as in Figure 4. Key active site residues for binding and catalysis are shown as sticks and labeled.

Beta amylase

β-amylase (also called β-1,4-maltosidase) is a key enzyme in the **saccharification** process, in which starch and cellulose are broken down into monosaccharides. β-amylase is abundant in crops (wheat, barley, soybeans, etc.), other higher plants, bacilli, and fungi. It is used in the production of beer and caramel (malt syrup). As an exo-glycosidase, it cleaves Glc α(1,4) Glc (maltose) units from the nonreducing end of starch. It is called β-amylase since the hydrolysis proceeds with the inversion of configuration at the reducing end of the freed maltose. It

can't cleave at α-1,6 branches, so if used alone, this enzyme produces free maltose and large β-limit dextrins. When fruits ripen, the enzyme cleaves starch into the sweet disaccharide maltose. It is also used in seed germination.

MALTING

Plants have to sprout, which requires energy and free sugars. Maltose is produced on activation of β-amylase during seed germination and sprouting. Although maltose is less sweet than sucrose and fructose, it is used in hard candies because it withstands the heat required in candy production. Malting of grains is accomplished by adding water to sprout them, which leads to the formation of maltose and other sugars. This is followed by drying, after which the malted grains are used as sweeteners in the food industry. Malted grains are used to produce beer, whisky, some baked goods, and other drinks. Barley is the most commonly malted cereal grain.

Huge amounts of amylases are needed for corn ethanol production, and they must withstand the conditions necessary for the industrial production of ethanol. Much effort has been devoted to finding and characterizing microbial β-amylases. We'll describe one, AmyBa, from *B. aryabhattai*. Figure **5.7** shows sequence similarities among various bacterial β-amylases.

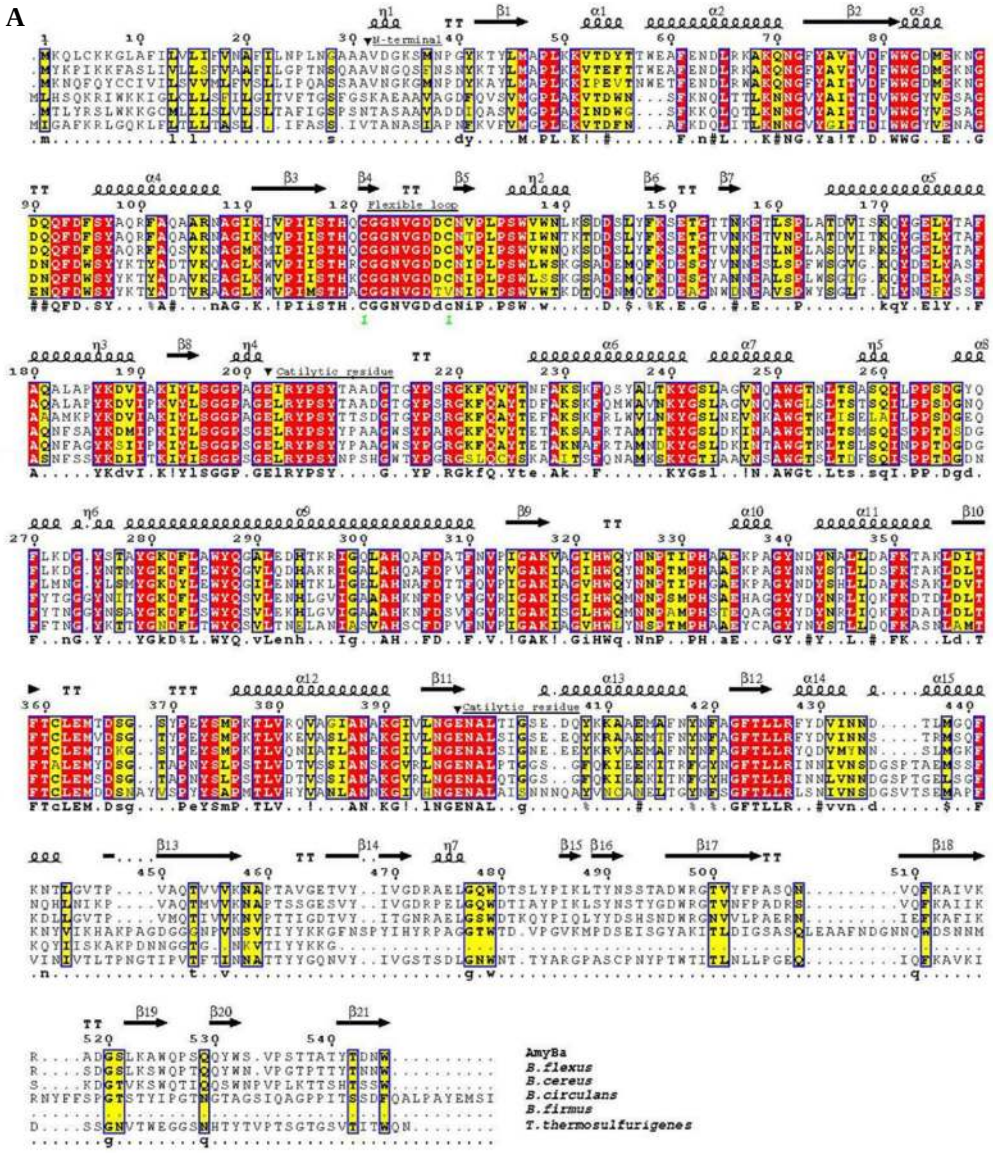


Figure **5.7**: Sequence and structure analysis of AmyBa. . Duan, X., Zhu, Q., Zhang, X. *et al.* Expression, biochemical, and structural characterization of high-specific-activity β-amylase from *Bacillus aryabhattai* GEL-09 for application in starch hydrolysis. *Microb Cell Fact* **20**, 182 (2021). https://doi.org/10.1186/s12934-021-01649-5. Creative Commons Attribution 4.0 International License. Creative Commons Attribution 4.0 International License. http://creativecommons.org/licenses/by/4.0/.

Panel A shows multiple sequence alignments of β-amylases. The strictly conserved residues are displayed on a red background, and the highly conserved residues are shown on a yellow background. The secondary structure elements are shown for *B. cereus* β-amylase (PDB ID: 5BCA). The signal-peptide-cleavage site and two catalytic residues (E) are indicated by black triangles (black inverted triangles). Conservation of the flexible loop motif (HXCGGNVGD) is noted. β-amylase accession numbers are as follows: *B. aryabhattai* (WP_033580731.1), *B. cereus* (P36924.2), *B. flexus* (RIV10038.1), *B. firmus* (P96513.1), *B. circulans* (P06547.1), *T. thermosulfurigenes* (P19584.1).

A comparison of the structures of *B. aryabhattai* β-amylase with soybean β-amylases is shown in Figure 5.8.

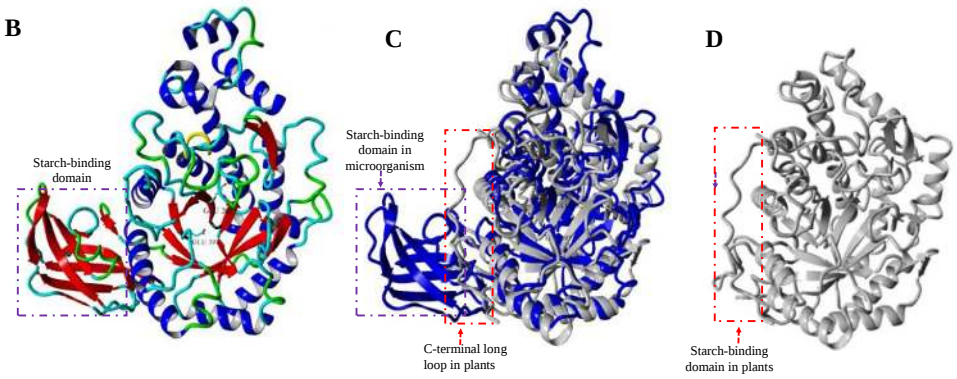
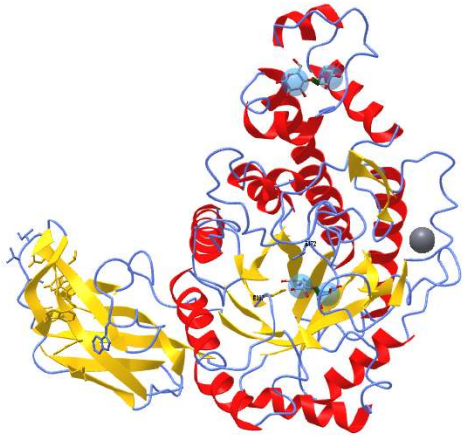


Figure 5.8 **B** Three-dimensional molecular model of *B. aryabhattai* β-amylase (AmyBa). **C** Superimposition of AmyBa (Blue) and soybean β-amylases (PDB ID: 1Q6C) (gray) and **D** (PDB ID: 1Q6C) (gray). The C-terminal SBD in microbial β-amylases (box, purple) and the C-terminal loop in plants (box, red). Duan, X, et al., ibid.

The AmyBa has an additional starch-binding domain at the carboxy terminus (Panel B) compared to soybean β-amylases (Panel D).

Since no structures of (AmyBa are publicly available, we present Figure 5.9, which shows an interactive iCn3D model of beta-amylase from Bacillus cereus var. mycoides in complex with maltose (1J0Z)



NCBI iCn3D Figure 5.9: Beta-amylase from Bacillus cereus var. mycoides in complex with maltose (1J0Z). (Copyright; author via source). Click the image for a popup or use this external link: https://structure.ncbi.nlm.nih.gov/i...S2aWbL3z3jPnW8

Like alpha-amylase, β-amylase has an N-terminal catalytic domain with a beta-barrel, a connecting second domain, and a third C-terminal domain, composed primarily of antiparallel β-sheets. Two key catalytic side chains, Glu 172 and Glu 367, are in the beta-barrel.

In Chapter 20.6, we discussed starch synthesis (not its hydrolysis) in detail. We showed that the reaction, which uses an NDP-sugar as a glycan donor, could proceed either with retention or inversion of the anomeric carbon of the donor NDP-sugar. This is illustrated for the reaction of a C1 α-NDP donor monosaccharide with a monosaccharide acceptor to produce the α(1,4) link with retention of configuration or the β(1,4) link with inversion as shown in Figure 5.10 below.

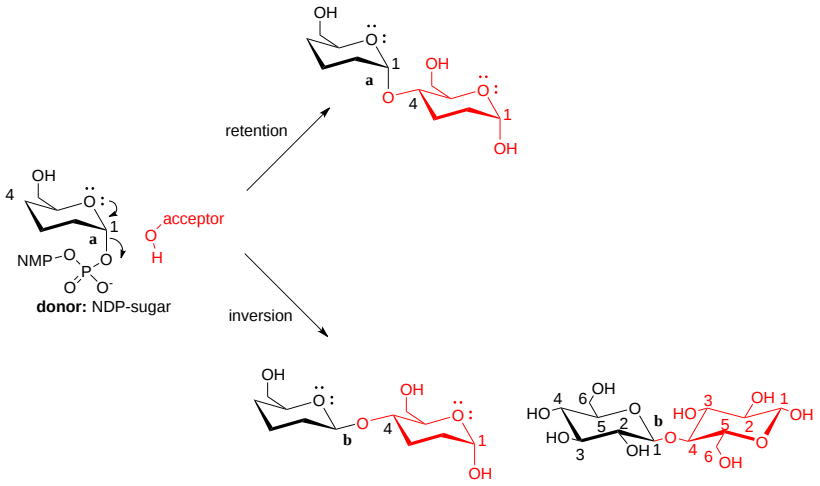


Figure 5.10: Reaction of a donor NDP-monosaccharide and an acceptor monosaccharide with retention or inversion of configuration at the anomeric carbon of the donor

The same stereochemical outcomes are possible for the hydrolysis of acetal bonds by glycosyl hydrolases. Alpha-amylases cleave the α (1,4) glycosidic bonds to produce shorter dextrins (containing branched glucose units not cleaved by alpha-amylases), and α (1,4) linked glucose oligosaccharides of lengths from 2 glucose units (maltose) up to 7-8. This reaction, hence, proceeds with the retention of configuration. In contrast, beta-amylases cleave starch to produce maltose with an inversion of configuration at the anomeric-reducing end of the maltose. We explore the chemistry of retention and inversion further in the next section on cellulase, which cleaves the β(1,4) acetal link in cellulose. In general, reactions that proceed with inversion react via an S_N2 mechanism, similar to the nucleophilic attack on alkyl halides. For the glycosyl transferases that proceed with inversion, the attacking nucleophile on the acceptor is made more nucleophilic by general base catalysis by a deprotonated glutamic or aspartic acid.

Figure 5.11 shows the results of *in-silico* docking studies of a small glycan, maltotetraose, to AmyBa.

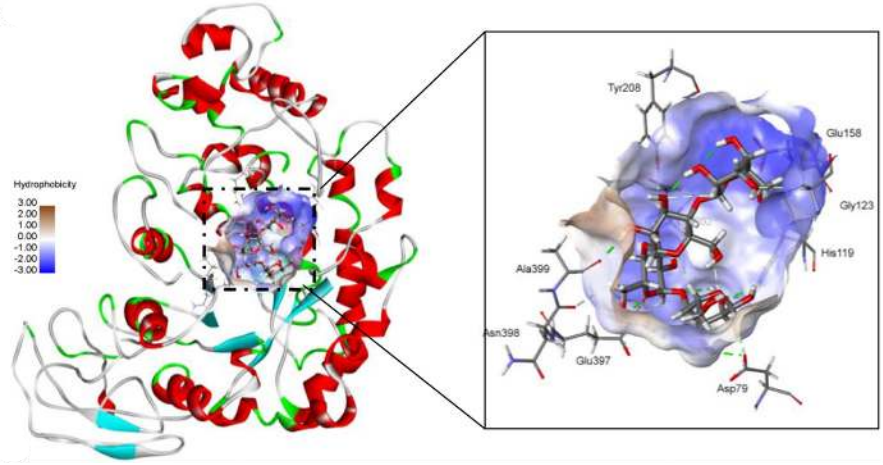


Figure 5.11: Molecular docking of AmyBa with maltotetraose. The overall structure and substrate binding pocket analysis of AmyBa are shown.

AmyBa displayed very high amylase activity compared to other microbial β-amylases, and its enzymatic activity was much closer to that of sweet potato β-amylase. Molecular dynamics and docking programs can be used to calculate binding energies for substrates. The binding energy and enzymatic activities of bacteria and sweet potato β-amylase were highly correlated, suggesting that the extensive interactions between AmyBa and maltotetraose help drive catalysis by using the energy released upon binding to lower the reaction's activation energy.

SACCHARIFICATION

To enter glycolysis and fermentation, maltose must be converted to the monosaccharide glucose. The conversion of a polysaccharide to its monomers is called saccharification. To complete the conversion of starch to glucose, another enzyme, glucoamylase (also called amyloglucosidase and γ-amylase), is added. As an exoglucosidase, it cleaves both α (1,4) in amylose, amylopectin, and maltose and α

(1,6) branches to form free glucose. It is a member of the glycoside hydrolase family 15 in fungi, glycoside hydrolase family 31 of human maltase-glucoamylase, and glycoside hydrolase family 97 of bacterial forms.

FERMENTATION

Glucose ($C_6H_{12}O_6$) can now enter the glycolytic pathway and continue to ethanol after conversion of pyruvate to acetaldehyde by pyruvate decarboxylase and final conversion of acetaldehyde to ethanol by alcohol dehydrogenase:

$$C_6H_{12}O_6\,(s) \rightarrow 2\,CH_3CH_2OH\,(l) + \mathbf{2CO_2}\,(g)\ \text{(anaerobic ethanol biosynthesis)}$$

The yeast Saccharomyces cerevisiae catalyzes this entire pathway.

The final fermentation process yields a 12-15% ethanol solution, which is distilled to form a 95% ethanol/5% water azeotrope. The water is removed by adding zeolites (molecular sieves), which adsorb water but not ethanol.

LIFE CYCLE ANALYSIS OF BIOETHANOL: IS IT BETTER THAN FOSSIL FUELS?

We reiterate the promise of bioethanol to address global warming and climate change by presenting again the chemical equations that suggest that its use as a fuel is carbon neutral:

$$\mathbf{6CO_2}\,(g) + 6H_2O\,(l) \rightarrow C_6H_{12}O_6\,(s) + 6O_2\ \text{(photosynthesis)}$$

$$C_6H_{12}O_6\,(s) \rightarrow 2\,CH_3CH_2OH\,(l) + \mathbf{2CO_2}\,(g)\ \text{(anaerobic ethanol biosynthesis)}$$

$$2CH_3CH_2OH\,(l) + 6O_2 \rightarrow \mathbf{4CO_2}\,(g) + 6H_2O\,(g)\ \text{(combustion of ethanol)}$$

If only these three equations for the production and use of corn bioethanol were the only factors influencing **net** CO_2 emission from bioethanol burning, there would be no controversy about its use. Yet the actual CO_2 emissions depend on many more factors hidden from view by these simple equations. A **life cycle analysis (LCA)** is needed to determine corn ethanol's environmental impact (in this case, net CO_2 emissions) across all phases of its life, from cradle to grave, including corn planting and bioethanol use for transportation.

All models must be tested. It's easiest to start with the simplest model. If the data fit the model, great, you're done. If not, new, more expansive models must be developed and tested. Those who vociferously support bioethanol often cite the simple stoichiometry in the three equations to claim that bioethanol is carbon neutral. Most would want a detailed life cycle analysis (LCA) before jumping to an immediate conclusion.

LCAs are very challenging, and data on a global scale is required. Some global-scale measurements have significant uncertainties and are, at best, estimates. A recent study looked at the impact of a specific event, the adoption of the **US Renewable Fuel Standards (RFS)** that regulate biofuels in the US (which produces about half of all the world's biofuels), on CO_2 emissions from the significant increase in corn plant and corn ethanol that followed the adoption of the standard. Using LCA based on a series of economic and environmental metrics, the model shows that bioethanol is not a panacea for CO_2 emissions and may be more detrimental than using fossil fuels in vehicles.

The study calculated changes in corn ethanol's **carbon intensity** after the standards were adopted. Scientists have used other events that led to immediate changes (e.g., 9/11) and 1-2-year changes (e.g., the COVID-19 pandemic) to examine environmental parameters such as CO_2 emissions.

Carbon intensity measures how much CO_2 or CO_2 equivalents are emitted per unit of activity. The unit activity can be kWh of electricity generated, megajoules of energy (MJ) produced by fuel, amount of oil produced, bushels of a particular food produced, or dollars generated (GDP). Ideally, policies should be implemented to decrease carbon intensity. The use of green energy derived from solar and wind lowers carbon intensity. **Energy intensity**, the total energy production per GDP, is a similar metric.

Figure **5.12** shows carbon intensity per GDP per country over the last 30 years (data from Our World in Data).

Figure 5.12: Consumption-based carbon intensity from 1990 to 2018. Our World in Data.

The world is generally moving toward more efficient energy production, but our energy consumption is still dramatically increasing.

The LCA model showed that the renewable fuel standards (RFS) policy led to these interrelated outcomes. It:

- increased corn prices by 30% and the prices of other crops by 20%
- increased US corn cultivation by 2.8 Mha (8.7%) and total cropland by 2.1 Mha (2.4%) in the years following policy enactment (2008 to 2016). (1 hectare is an area of a square with 100 meters sides, equivalent to 10,000 m^2
- increased annual nationwide fertilizer use by 3 to 8%
- increased water quality degradation by 3 to 5%
- increased emissions from domestic land use changes

According to the study, these combined produced a carbon intensity of corn ethanol that was "no less than gasoline and likely at least 24% higher. "

The changes in the metric are visually described in Figure 5.13.

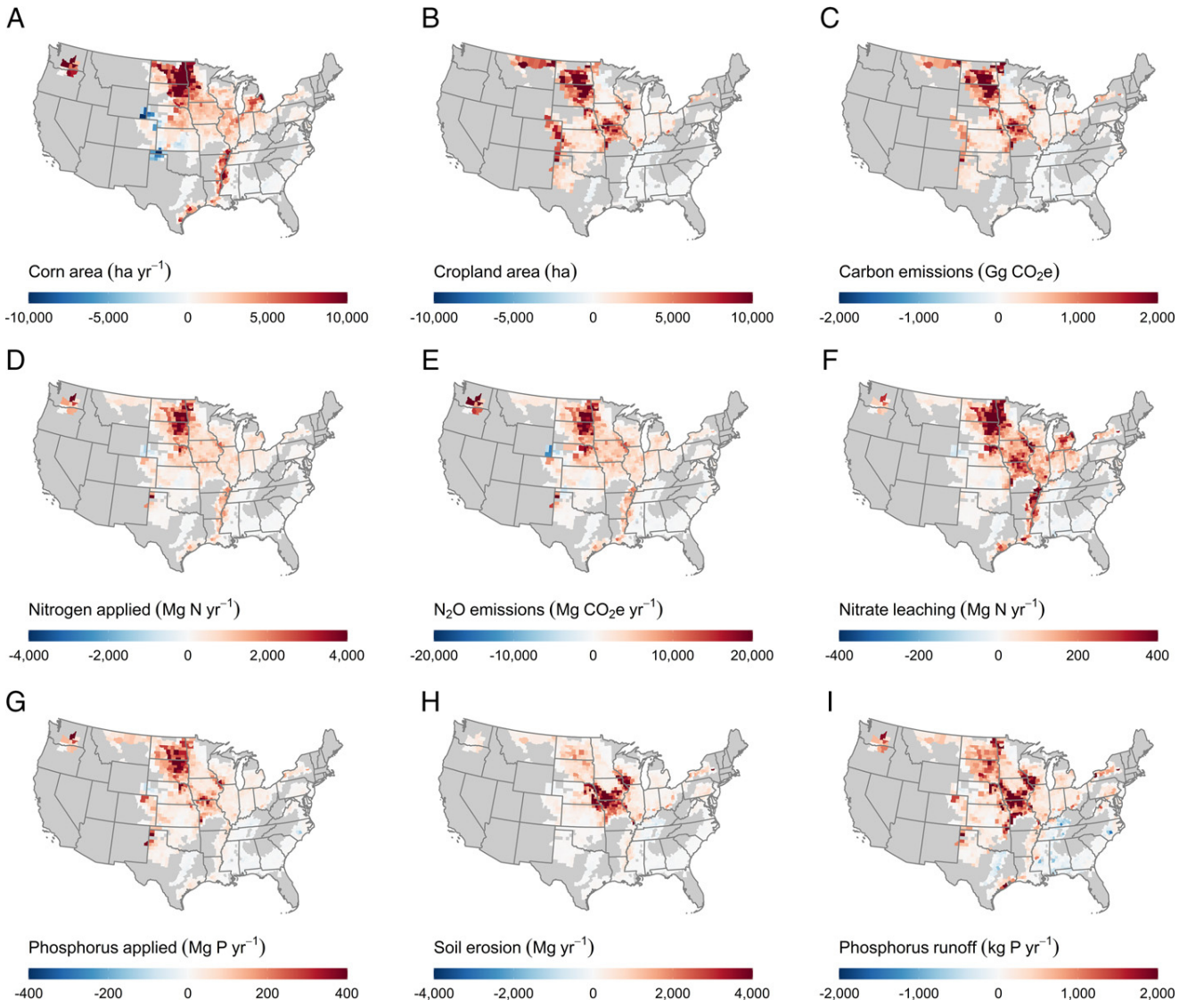


Figure **5.13**: *Changes due to the RFS. (A) Corn planted area. (B) Cropland area. (C) Carbon emissions. (D) Nitrogen applications. (E) Nitrous oxide emissions. (F) Nitrate leaching. (G) Phosphorus applications. (H) Soil erosion. (I) Phosphorus runoff. Positive numbers indicate an increase due to the RFS. Field-level results were aggregated at the county level for enumeration and visualization.* Tyler J. Lark et al. PNAS. 119, 2022 (https://doi.org/10.1073/pnas.2101084119) Creative Commons Attribution License 4.0 (CC BY).

Land use changes include farming land that was retired or designated for conservation programs. Tilling additional land releases carbon stored in the soil. Increased farming significantly increased fertilizer production, leading to N_2O emissions. In addition, more of the existing cropland was planted with corn. These findings contrast with a USDA **study** showing that corn ethanol has a 39% lower carbon intensity than gasoline, which was attributed to carbon capture from newly planted crops. However, that study did not account for emissions from land use changes.

LCA can identify production processes that lead to the greatest negative consequences, which, for the sake of this chapter, are greenhouse gas emissions. For example, the LCA for corn ethanol might improve if the CO_2 released during anaerobic ethanol biosynthesis could be captured. Outcomes would also change if renewable energy sources were used for stages of production that currently use fossil fuels. These studies also don't account for the hazardous pollutants released during bioethanol production.

This rigorous LCA did not address the moral question of using land that could feed people to produce bioethanol for our ever-bigger vehicles. In addition, opponents of solar energy installations argue that they require so much land that they would displace agricultural uses. What is missing from their argument is the vast amount of land used now for corn ethanol. Farmers planted 90 million acres of corn in 2022 in the US, about 90% of the size of the entire state of California. 44% of that corn went to biofuels, and only 12% went to human

consumption. In addition, approximately 44% was used to feed animals for human consumption, an inefficient and unsustainable use of cropland and resources.

Figure 5.13a below shows how little corn is grown in the USA for human consumption.

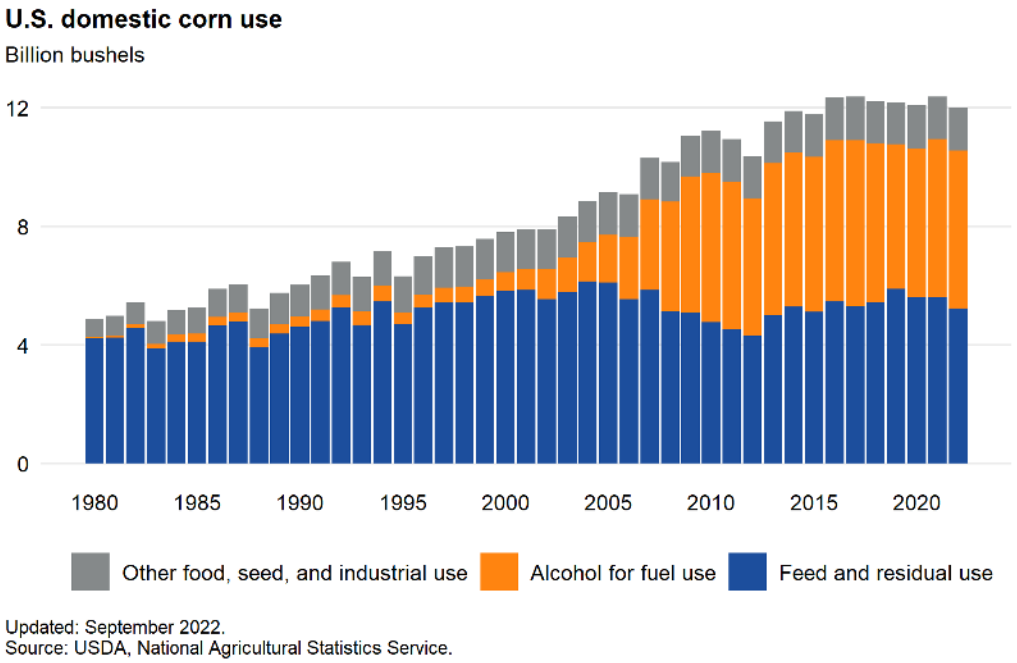


Figure 5.13a: Corn and Other Feed Grains - Feed Grains Sector at a Glance. Updated 1/5/2025.

Hannah Ritchie at Our World in Data (the source of many interactive graphs in this chapter) has eloquently and persuasively argued for using solar power to charge electric vehicles rather than corn bioethanol. Here are some conclusions she draws:

- 20 m^2 of solar panels produce 1 MWh of electricity per year. This implies that the 25 million hectares of land now used for corn bioethanol (which covers just 10% of our driving fuel) could be covered with solar cells and produce 12,500 TWh. That is about 3 times the USA's annual electricity consumption in 2023.
- Considering just transportation, the main use of biofuels, 1 hectare of solar panels, would allow electric vehicles to travel 3 million km (1.87 million miles). In contrast, 1 hectare of corn for bioethanol will enable cars to travel 22,000 km (13,700 miles).
- People drive approximately 5 trillion km (3.1 trillion miles) annually in the USA. 1.5 million hectares of solar panels would fulfill that energy need (just 6% of the 25 million hectares of land used to produce corn bioethanol, which powers just 10% of our driving needs.

Using agricultural land for crops and solar panels would be a win for all.

PRODUCTION OF SUCROSE AND BIOETHANOL FROM SUGARCANE

Like corn, sugar cane, a tropical, perennial grass, is used (mainly in Brazil) to produce ethanol. Sugar cane is a C4 plant with a high ability to fix carbon. It is a **perennial** that does not need replanting each year, making it a better feedstock than corn for bioethanol production. In 2020, sugar cane was by far the most-produced crop or livestock product in the world (1.87 billion metric tons), followed by corn (1.16 billion metric tons). The production by country for both corn and sugar cane is shown in Figure 5.14.

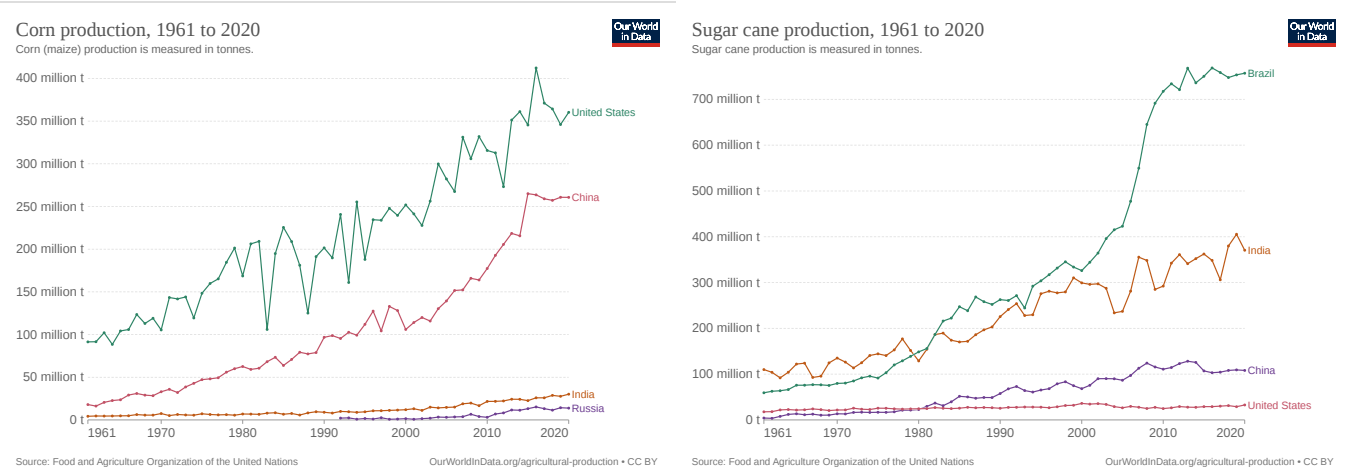


Figure **5.14**: Corn and sugar cane production by country. Graphs from Our World in Data. https://ourworldindata.org/agricultural-production#

It might surprise you that sugar cane production is so high compared to grain crops that provide nutrition (not just "sweet" calories), but given our addiction to sweet foods, it shouldn't.

Sugar cane is often harvested manually in developing countries. It is then cut, milled, and mixed with water to extract the soluble sucrose (table sugar). Figure **5.15** shows the sugar cane components during extraction.

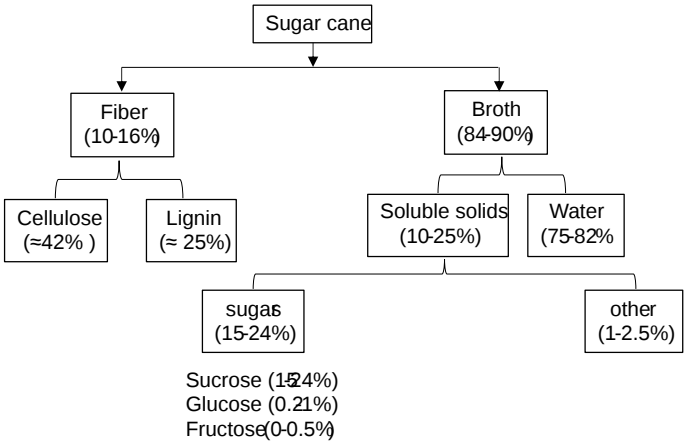


Figure **5.15**: Components of Sugar Cane (after Larissa Canilha et al. J Biomed Biotechnol. 2012; 2012: 989572. doi: 10.1155/2012/989572

Sucrose is a nonreducing disaccharide (O-α-D-glucopyranosyl-(1,2)-β-D-fructofuranoside). Its structure is shown in Figure **5.16**.

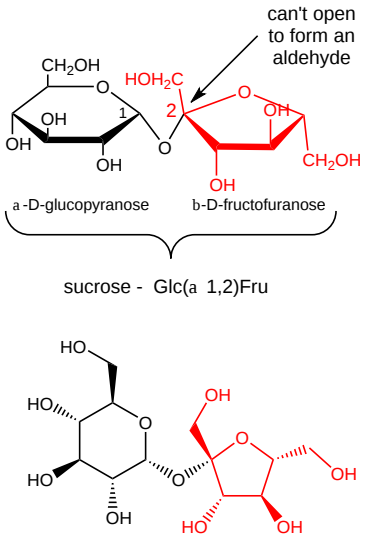


Figure **5.16**: Structure of fructose

SUCROSE, CARAMEL AND MOLASSES

Sucrose decomposes at 186 °C (367 °F), rather than melting (a feared event for organic chemistry students who wish to record melting temperatures in the lab), to form caramel. Molasses is a viscous liquid product derived from refining sugar cane or sugar beets. It is used as a sweetener for its taste and is also a component of brown sugar. On a sweetness scale, if sucrose is assigned a value of 100, fructose is 140, high fructose corn syrup is 120-160, and glucose is 70-80.

In bioethanol production, sucrose is hydrolyzed by the enzyme **invertase** into monomeric glucose and fructose. Invertases are activated during the milling and liquefaction of sugarcane, so if sucrose is the desired commercial product, an additional clarification step (heating to 115°C and treating with lime and sulfuric acid) is necessary to prevent hydrolytic cleavage of sucrose.

BIOETHANOL PRODUCTION FROM SUGAR CANE SUCROSE

Bioethanol can be made from either the fibrous lignocellulose remains of the sugar cane, called **bagasse,** or from water-soluble sucrose. We will describe the production of cellulosic ethanol from field crop stalks, called stover, and leaves, straw, wood chips, and sawdust (all "waste" biomass) in Chapter 31.5. The same principles apply to bioethanol production from **bagasse (**the solid residue left after sugar cane juice extraction). Note that bagasse is often burned to provide energy for sugar cane processing.

Sugar cane, sugar beets, and sweet sorghum, a C4 plant similar to sugar cane, are also used to produce bioethanol. Sweet sorghum is a very efficient plant for producing biomass through photosynthesis. It grows in temperate and tropical climates, has a short growing period, and is resistant to drought and cold. Its stalks contain free sugars and lignocellulose.

This chapter will focus on bioethanol production from sugar cane sucrose. Again, this is accomplished using yeast (Saccharomyces cerevisiae), which contains the enzyme **invertase 2** (**beta-fructofuranosidase 2 or Saccharase**), which converts sucrose into fructose and glucose, which can enter the glycolytic and fermentation pathways.

Invertase, shown in 1842 to invert the stereochemistry of sugars, was first isolated from yeast in 1860. It has a secreted, glycosylated, homooctameric form and an intracellular form, both of which are products of the same gene. It's a member of Family 32 of the glycoside hydrolases. The structure of the Saccharomyces invertase (SInv) octamer is shown in Figure **5.17** below.

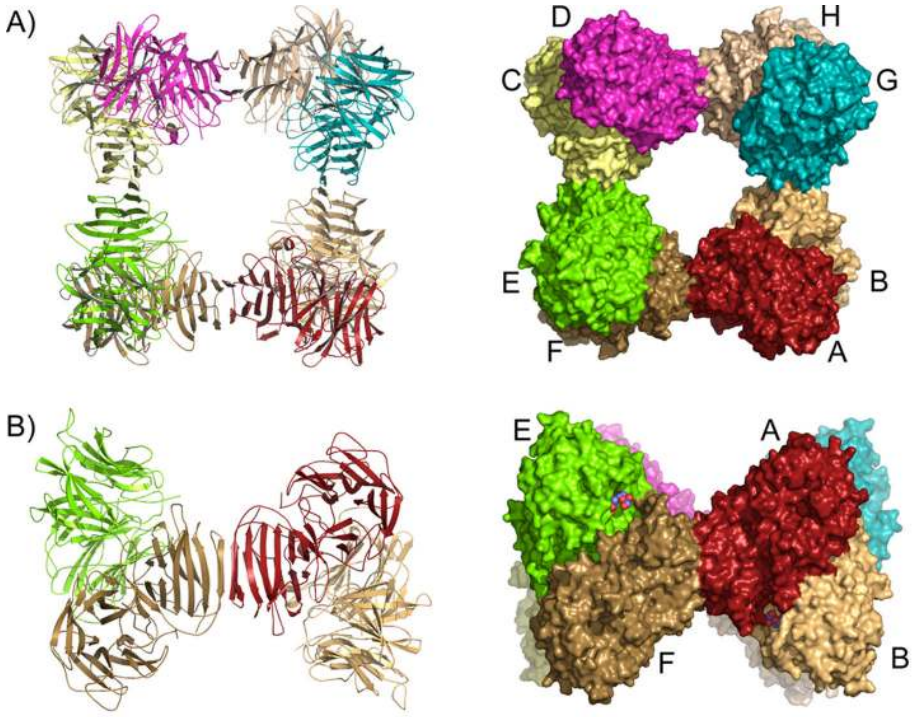


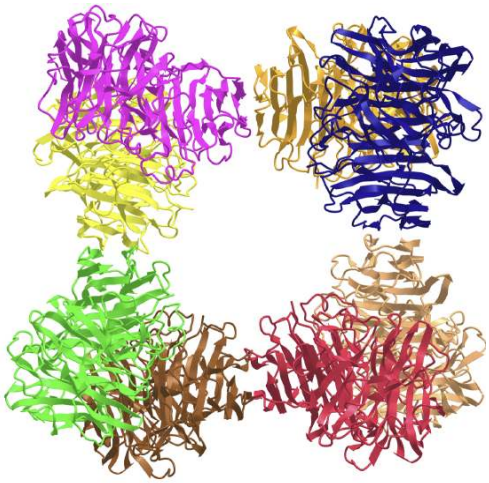
Figure 5.17: Structure of octameric SInv. M.Angela Sainz-Polo et al. JBC, 288, 9755-9766 (2013). DOI:https://doi.org/10.1074/jbc.M112.446435. Creative Commons Attribution (CC BY 4.0)

Panel a shows views of the SInv octamer in ribbon (*left*) and solvent-accessible surface (*right*) representations, with each subunit colored differently.

Panel *b shows that t*he octamer is rotated 90°, illustrating that it can be best described as a tetramer of two different kinds of dimers, AB/CD and EF/HG, which are compared by superimposing subunit F on subunit B in *c*

Even though all eight subunits in the octamer are identical (58.5K, 512 aa), the quaternary structure of the 8-mer can best be viewed as a tetramer of dimers (i.e., 4 dimers pack to form two packed tetramers giving the octamer). The AB and CD dimers pack in a "closed form" with a narrow active-site pocket, allowing a glycan of 3-4 monomers. The EF and GH dimers pack in an "open form" with a wide active site pocket for longer glycans. Of course, our main interest here is in the binding of sucrose.

Figure 5.18 shows an interactive iCn3D model of Saccharomyces cerevisiae invertase (4EQV)



NCBI iCn3D Figure 5.18: Saccharomyces cerevisiae invertase (4EQV). (Copyright; author via source).
Click the image for a popup or use this external link: https://structure.ncbi.nlm.nih.gov/i...ysQW8YSrvPkus9

The color coding of the subunits is the same as shown in the right top image of Panel A, Figure 16 above.

The GH32 enzymes, including invertase, have a catalytic domain consisting of a 5-bladed β-propeller. Each blade has four antiparallel beta-strands. The blades surround an active site enriched in carboxyl side chains.

The "closed" active site of the AB and CD dimers is flanked by Phe 388 and Phe 296, which provide hydrophobic interactions. The "open" form active site of the EF and GH dimers also has a salt bridge between Asp 45 and Lys 385. These are shown in Figure **5.19**, along with a bound **1-kestose**, which is a trisaccharide"sucrose analog" found in vegetables. It consists of a β-D-fructofuranose connected to β-D-fructofuranosyl and α-D-glucopyranosyl residue at the 1- and 2-positions.

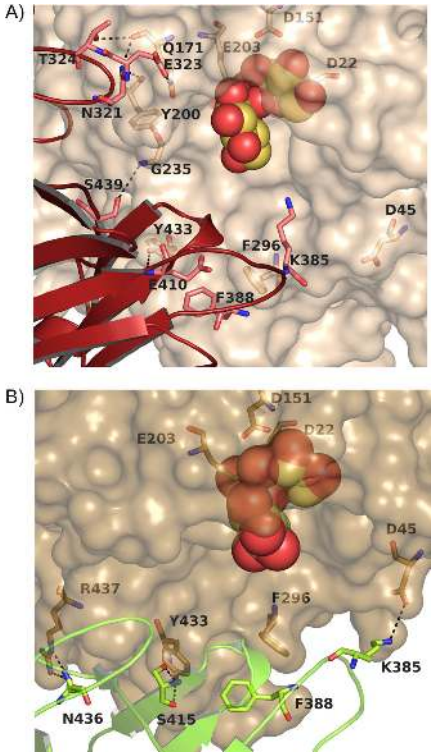


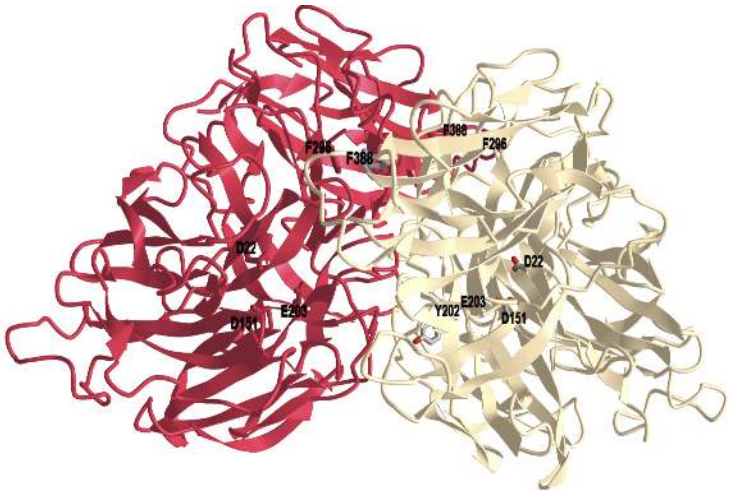
Figure **5.19**: Dimer interface at the active site. The octameric SInv active site interfaces are detailed, keeping the same color pattern as above with one subunit being shown in ribbon representation for clarity. Angela Sainz-Polo et al. JBC, 288, 9755-9766 (2013). DOI:https://doi.org/10.1074/jbc.M112.446435. Creative Commons Attribution (CC BY 4.0)

Panel A shows that the AB/CD dimers have tight interactions between the catalytic and β-sandwich domains. Hydrophobic interactions are observed at the base of the catalytic pocket, mediated by Phe-388 and Phe-296.

Panel *b*, by contrast, shows that the EF/GH dimers interact only through their β-sandwich domains. In addition, the catalytic pocket contains a new salt bridge between Asp-45 and Lys-385 from the β-sandwich domain, which lines the cavity. A putative 1-kestose molecule is shown in a spherical representation.

The hydrolysis of sucrose by invertase proceeds with the retention of configuration at the anomeric carbon. An active site, Aspartate 22, acts as a nucleophile to form a glycosylated intermediate (fructose-Asp). This is followed by the hydrolysis of the intermediate. An active site, Glutamate 203, acts as a general acid/base. Fructose could also be transferred to another glycan via a transglycosylation reaction. The hydrophobic side chains Phe-388 and Phe-296 line the base of the active site pocket.

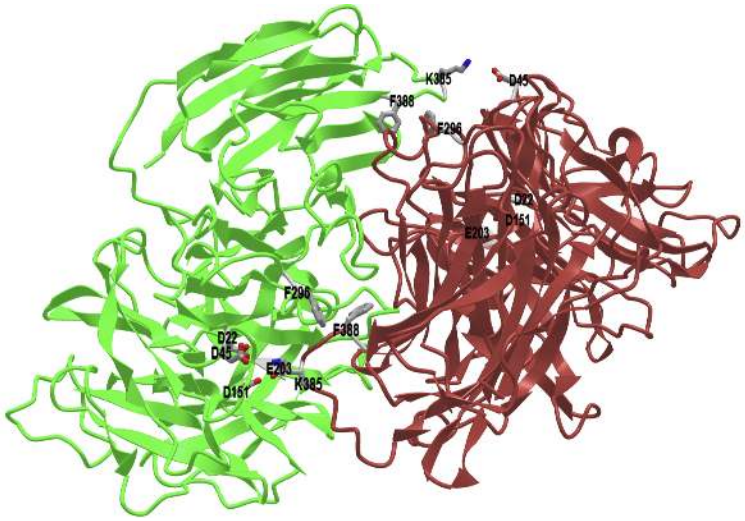
Figure **5.20** shows an interactive iCn3D model of the **AB dimer** of Saccharomyces cerevisiae invertase with key active site residues (4EQV)



NCBI iCn3D Figure 5.20: **AB dimer** of Saccharomyces cerevisiae invertase with key active site residues (4EQV). (Copyright; author via source).

Click the image for a popup or use this external link: https://structure.ncbi.nlm.nih.gov/i...hX9FbxLLip1f97

Figure 5.21 shows an interactive iCn3D model of the **EF dimer** of Saccharomyces cerevisiae invertase with key active site residues (4EQV). It has an additional salt bridge between Asp-45 and Lys-385.



NCBI iCn3D Figure 5.21: **EF dimer** of Saccharomyces cerevisiae invertase with key active site residues (4EQV). (Copyright; author via source).

Click the image for a popup or use this external link: https://structure.ncbi.nlm.nih.gov/i...Dh33BtT5c8GXK6

LIFE CYCLE ANALYSIS OF SUGAR CANE ETHANOL

Does the production of bioethanol from sugar cane lead to lower net CO_2 emissions than bioethanol produced from corn? The answer depends on whether sucrose (first generation) or lignocellulose (second generation) from bagasse is used as the feedstock.

A recent LCA has been performed for the first-generation (sucrose feedstock) production of bioethanol from sugarcane in Ecuador. This sugar-based feedstock has a lower production cost. It requires just grinding and the addition of yeast for fermentation; it does not require a saccharification step.

Figure 5.22 shows the various stages and processes used to perform LCA on the bioethanol production from sugar cane sucrose. It's presented to show the complexity of such analyses, so look at the details only if you are especially interested.

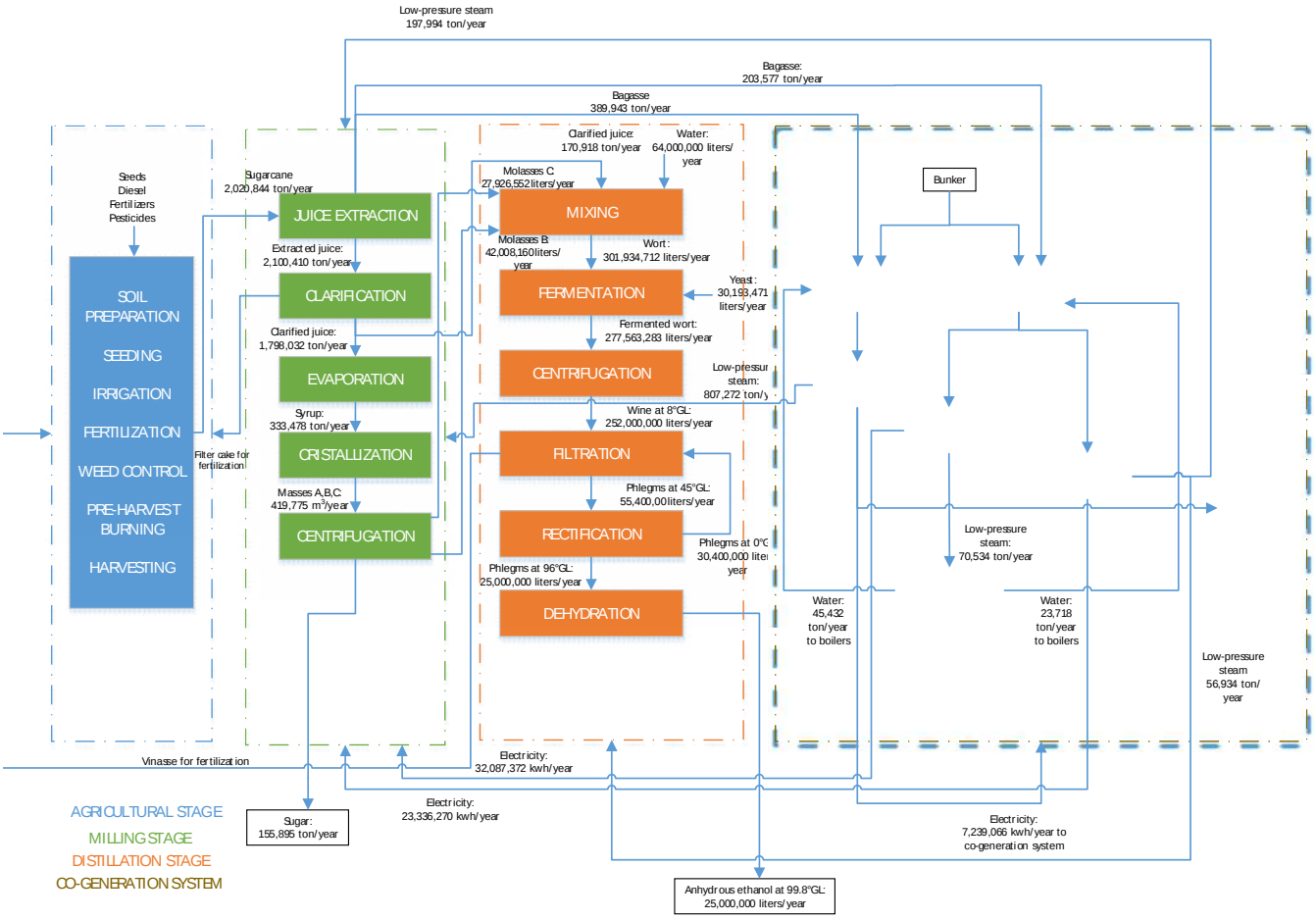


Figure 5.22: Anhydrous ethanol life cycle system boundaries and main product flow quantification for 2018. Arcentales-Bastidas, D.; Silva, C.; Ramirez, A.D. The Environmental Profile of Ethanol Derived from Sugarcane in Ecuador: A Life Cycle Assessment Including the Effect of Cogeneration of Electricity in a Sugar Industrial Complex. *Energies* **2022**, *15*, 5421. https://doi.org/10.3390/en15155421. Creative Commons Attribution (CC BY) license (**https://creativecommons.org/licenses/by/4.0/**)

The study analyzed four stages, agricultural, milling, distillation, and electricity generation (presumably by burning the byproduct bagasse), for impacts. They defined two functional units:

- 1 ton of sugarcane "at the farm gate" for the agricultural stage;
- 1 L of ethanol "at the plant (factory) gate".

The key results of the study are as follows:

- The **global warming potential (GWP)** impact at the "farm gate" was 53.6 kg of carbon dioxide equivalent (kg CO_2 equiv) per ton of sugarcane produced. This arises mainly from N_2O (34%), a potent greenhouse gas emitted during the process, and from diesel fuel used in agricultural machinery (24%).
- The GWP for 1 L of ethanol produced at the plant gate was 0.60 kg CO_2 equiv, with the distillation phase accounting for the largest share.

Before proceeding further, let's explain the key term, **global warming potential (GWP)**, which is widely used in LCA. It accounts for the contributions of other greenhouse gases, such as methane (CH_4) and nitrous oxide (N_2O), each with unique IR absorption spectra and atmospheric half-lives. The IPCC uses a 100-year time frame for the calculation of the GWP and uses this formula:

CO_2 Equivalent kg = CO_2 kg + (CH_4 kg x 28) + (N_2O kg x 265)

$$\mathbf{CO_2\ equivalent\ kg = CO_2\ kg + (CH_4\ kg \times 28) + (N_2O\ \mathit{kg} \times 265)} \quad (5.1)$$

- CO_2 has a GWP of 1 by definition since it is the reference. Its time frame in the atmosphere (100s to 1000 years) doesn't matter since it is the reference.
- CH_4 has a GWP of around 27-30 over 100 years, reflecting its higher IR absorbance but lower lifetime (around 12 years).

- N_2O has a GWP of around 265-273 over a 100-year timescale and a lifetime of around 109 years.

The equation can be amended to account for other greenhouse gases emitted from manufacturing and refrigerant use. These include Freon-12 (Dichlorodifluoromethane) (CFC-12), with a lifetime of 100 years and a GWP100 of 10,200, and SF6 (used in the electricity industry to keep networks running safely and reliably), with a lifetime of 3200 years and a GWP00 of 23,500!

NITROUS OXIDE - A POTENT GREENHOUSE GAS, BUT NOT A LAUGHING MATTER

N_2O (laughing gas) is an overlooked source of greenhouse gases, accounting for about 7% of the warming effect of long-lived, high-GWP gases. Agricultural practices lead to about 65% of its total emissions. It is a component of the soil and atmosphere nitrogen cycle. In soil, its concentration depends on soil microbes that engage in nitrification and denitrification processes. These depend on the amount of fixed nitrogen, oxygen levels, and metabolically available carbon sources. The nitrification reaction, which occurs in aerated, moist soils, involves the oxidation of $NH_3 \leftrightarrow NH_4^+$ to NO_2 and NO_3^-, with some N_2O produced. The primary source of N_2O occurs under anaerobic conditions. These general reactions are shown below.

- Nitrification (aerobic, oxidation): $N_2 \rightarrow (NH_3 \leftrightarrow NH_4^+) \rightarrow NO_2 \rightarrow NO_3^-$
- Denitrification (anaerobic, reduction): $NO_3^- \rightarrow NO_2^- \rightarrow NO \rightarrow N_2O \rightarrow N_2$

In anaerobic environments, NO serves as an electron acceptor during microbial respiration. N_2O is produced when excess nitrogen is available (beyond the needs of plants and microorganisms), so excessive use of fertilizers and manure increases its production. Nitrifying and denitrifying bacteria are most active in producing N_2O in environments with abundant N relative to assimilatory demands by other microorganisms or plants (Firestone and Davidson, 1989), as is often the case following soil amendment with fertilizers, manure, or crop residues. Physical soil processing (such as tillage) also affects N2O emissions by introducing crop residues into the soil, altering soil particle size and surface area, and altering soil porosity. These affect soil substrate/product availability and the rates of aqueous and gas diffusion.

Let's use dimensional analysis from introductory chemistry to convert the GWP from the farm gate/agricultural stage (53.6 kg CO_2 equiv/ton of sugar cane) to kg CO_2 equiv/1L of ethanol (EtOH) so we can add it to the GWP from the plant gate, which is expressed in kg CO_2 equiv/L ethanol produced. The dimensional conversion is shown in Table **5.2** below.

53.6 kg CO_2 equiv	1 ton SC	1 L Juice	=	0.1 kg CO_2 equiv
1 ton SC	800 L juice	0.7 L EtOH		1 L EtOH produced

Table **5.2**: Conversion of 53.6 Kg CO_2 equiv/ton of sugar cane from the farm gate (left-hand column) to 0.1 Kg CO_2 equiv/1L of ethanol (EtOH).

Now, add this to the reported 0.60 kg CO_2 equiv/1 L of ethanol from the plant (factor) gate, and you will get a total of **0.7 kg CO_2 equiv/1 L** of ethanol produced from sugar cane. This compares with a reported value of **2.3 kg CO_2 equiv**/1 L of gasoline produced, so, based on this study, sugar cane-derived bioethanol is significantly better, as its manufacturing emits less CO_2 equiv than gasoline manufacturing.

But remember that ethanol is partially oxidized and produces less energy per unit of mass on combustion. Burning 1 L of gasoline releases 33.6 MJ of energy, while 21.2 MJ is released on burning ethanol, so we should multiply the 0.7 kg CO2 equiv /1 L of ethanol by 33.6/21.2 = 1.6 to give a normalized **carbon intensity = 0.95.** This uses the equivalent amount of ethanol (1.6 L) to give the same energy as 1 L of gasoline. Still, burning sugar to produce bioethanol is better than burning gasoline on a CO_2-equivalent basis.

The promise of bioethanol is based on the notion that 1 C atom is used to produce it and 1 C atom is released during its combustion, as illustrated in the equations we saw above (and presented again below).

Eq 1: $6CO_2$ (g) + $6H_2O$ (l) → $C_6H_{12}O_6$ (s) + $6O_2$ (photosynthesis)

Eq 2: $C_6H_{12}O_6$ (s) → 2 CH_3CH_2OH (l) + $2CO_2$ (g) (anaerobic ethanol biosynthesis)

Eq 3: $2CH_3CH_2OH$ (l) + $6O_2$ → $4CO_2$ (g) + $6H_2O$ (g) (combustion of ethanol)

Now add to this series of net-zero CO_2 reactions the release of CO_2 from the manufacture of bioethanol, and you can see that the notion of net 0 for biofuels is misleading. Based on the analyses above, burning bioethanol from sugar cane produces significantly less CO_2 equiv than gasoline, but it's nowhere near net 0. Biofuel use can play a big role in reducing emissions when it replaces gasoline, but it must be coupled with other ways to reduce emissions (such as solar and wind) to achieve the magnitude of reductions we need. It also appears the jury is still out on the environmental benefits of corn bioethanol.

The LCA analysis described above assesses the global warming potential of using sugarcane sucrose for bioethanol production. However, bioethanol production from sugar cane juice has other negative impacts, as listed below in Table **5.4**.

Table 5.4: Impact categories included in the LCA

Impact Category	Characterization Factor	Reference Unit
Climate change	Climate change—GWP100	kg CO2eq.
Freshwater eutrophication	Freshwater eutrophication potential—FEP	kg Peq.
Marine eutrophication	Marine eutrophication potential—MEP	kg Neq.
Abiotic depletion	Metal depletion—MDP	kg Feeq.
Photooxidant formation	Photochemical oxidant formation potential—POFP	kg NMVOCeq.
Particulate matter emissions	Particulate matter formation potential—PMFP	kg PM10eq.
Terrestrial acidification	Terrestrial acidification potential—TAP100	kg SO2eq.

BIOFUELS OR SOLAR?

The case for devoting so much land to biofuel production is weak, as outlined above. Even if it is marginally better in net emissions compared to using fossil fuels, that does not account for what economists call opportunity cost, the cost of things not done or considered in the decision to use biofuels to address climate change. What benefits are we missing when choosing one options, biofuels, versus another (solar for example).

The world is clearly accelerating its investment in biofuels, as indicated in Figure 5.23 below.

Figure 5.23: Biofuel energy production since 1990. Hannah Ritchie and Pablo Rosado (2026) - “Putting solar panels on land used for biofuels would produce enough electricity for all cars and trucks to go electric”. Published online at OurWorld. inData.org. Retrieved from: 'https://archive.ourworldindata.org/2...-vehicles.html' [Online Resource] (archived on January 23, 2026

This graph includes both ethanol and biodiesel (from oil crops such as soybeans and palm oil, discussed in a future section) generated not only from corn (the US) but also from sugarcane (Brazil, also discussed in a future section). What if the same equivalent land use presently devoted to biofuel crop production were used for solar panel installation? Presently, about 32 million hectares (about 124K square miles, the land area of Poland) are used to produce biofuels (1400 TWh, which power 4% of our transport). If they were instead covered with solar panels, 23 times as much electrical energy (32,000 TWh/yr) could be produced each year (Ritchie and Rosado, ibid.). This area of solar cells would not be installed in one place but would be distributed around the world and could, in part, be colocated on land used for agriculture. The emerging field of agrivoltaics does exactly that.

Ritchie and Rosado note that only 1% of the sun's energy is used to produce biomass, and that even more is effectively lost when that biomass is turned into fuel. In contrast, modern photocells convert around 22% of the sun's energy directly into electrical energy. That could help decarbonize the transport industry as we move from internal combustion engines to electric vehicles.

SUMMARY

(Summary written by Claude, Anthropic)

This chapter examines the biochemistry, industrial processes, and environmental impact of first-generation bioethanol production from corn and sugar cane — the dominant biofuels globally — within the broader context of climate change mitigation.

Energy context. Ethanol contains one oxygen atom in a two-carbon molecule, making it partially oxidized and consequently less energy-dense than gasoline: it releases ~29.7 kJ/g versus ~47.9 kJ/g for octane, delivering about 63% of gasoline's energy by mass and 70% by volume. The US produced 16 billion gallons of fuel ethanol at peak production in 2018 — about one-tenth of annual US gasoline consumption — with the US and Brazil together accounting for ~85% of global fuel ethanol. The theoretical case for bioethanol rests on three coupled reactions: photosynthesis fixes atmospheric CO_2 into glucose, fermentation converts glucose to ethanol plus CO_2, and combustion returns CO_2 to the atmosphere. This stoichiometric argument suggests net-zero carbon emissions, but a full life cycle analysis reveals a far more complex picture.

Corn starch hydrolysis: enzyme biochemistry. Corn starch — an α(1,4) glucose polymer with α(1,6) branches — must be hydrolyzed to free glucose before fermentation. This requires three enzyme types working in sequence. α-Amylase (endoglucosidase) cleaves internal α(1,4) bonds to produce short dextrins and maltooligosaccharides, proceeding with retention of anomeric configuration via a covalent glycosyl-enzyme intermediate; Asp197 acts as the nucleophile and Glu233 as the general acid/base, with Ca^{2+} maintaining structure and Cl^- acting as an allosteric activator. β-Amylase (exoglucosidase) cleaves successive maltose units from non-reducing ends with inversion of anomeric configuration — an SN2-like mechanism using two glutamate residues — but cannot cleave α(1,6) branch points, leaving large β-limit dextrins. Glucoamylase (γ-amylase) completes saccharification by cleaving both α(1,4) and α(1,6) bonds to release free glucose. Industrial microbial β-amylases, such as AmyBa from *Bacillus aryabhattai*, offer high specific activity and an additional C-terminal starch-binding domain; molecular docking studies show that binding energy correlates strongly with enzymatic activity, supporting an induced-fit mechanism.

Sugar cane and invertase biochemistry. Sugar cane — a C4 perennial grass and the world's most-produced crop (1.87 billion metric tons in 2020) — is primarily used in Brazil for bioethanol. Its sucrose (a non-reducing α(1,2)-linked glucose-fructose disaccharide) is hydrolyzed by invertase (β-fructofuranosidase) with retention of configuration. *S. cerevisiae* invertase is an octamer best described as a tetramer of dimers: the AB/CD dimers adopt a "closed" active-site configuration stabilized by hydrophobic Phe-388 and Phe-296 interactions, while the EF/GH dimers adopt an "open" configuration with an additional Asp45–Lys385 salt bridge. The catalytic mechanism involves Asp22 as a nucleophile forming a fructose-enzyme intermediate, and Glu203 as a general acid/base. Sugar cane has significant advantages over corn: it requires no saccharification step (sucrose is directly fermentable), does not need annual replanting, and has higher photosynthetic efficiency through C4 metabolism.

Life cycle analysis of corn ethanol. The Lark et al. (2022) study used the adoption of the US Renewable Fuel Standards (2005) as a natural experiment to assess the full environmental impact of expanding corn ethanol production. The results were sobering: the policy increased corn cultivation by 2.8 million hectares, raised fertilizer use by 3–8%, increased N_2O emissions (a GWP_{100} of 265), degraded water quality by 3–5%, and released soil carbon through land-use change. The combined carbon intensity of corn ethanol was found to be "no less than gasoline and likely at least 24% higher." These findings directly contradict a USDA study claiming 39% lower carbon intensity — the discrepancy arising from the USDA study's failure to account for land-use change emissions. The moral question of using food cropland for fuel (44% of US corn goes to biofuels; only 12% to direct human consumption) adds further weight to the critique.

Life cycle analysis of sugar cane ethanol. An Ecuadorian LCA of sugar cane sucrose-based bioethanol found a farm-gate GWP of 53.6 kg CO_2 equiv/ton of sugarcane, dominated by N_2O emissions (34%) from fertilizer use and diesel combustion (24%). Converting to comparable units (0.1 kg CO_2 equiv/L ethanol from the farm gate plus 0.60 kg CO_2 equiv/L from the plant gate = 0.70 kg CO_2 equiv/L) and normalizing for the lower energy density of ethanol (×1.6 to match gasoline's energy output) gives a carbon intensity of ~0.95 kg CO_2 equiv/L-gasoline-equivalent — substantially lower than gasoline's 2.3 kg CO_2 equiv/L. Sugar cane ethanol is therefore significantly better than gasoline on a lifecycle basis, but far from carbon-neutral. N_2O — produced by nitrifying bacteria under aerobic conditions and denitrifying bacteria under anaerobic conditions whenever excess fixed nitrogen is present — is a major and often underappreciated contributor to the GWP of any nitrogen-fertilizer-intensive crop.

Biofuels versus solar: the opportunity cost. The most powerful challenge to large-scale biofuel expansion comes from land-use efficiency comparisons. Approximately 32 million hectares currently devoted to biofuel crops produce ~1,400 TWh/year of energy, powering ~4% of global transport. If covered with modern photovoltaic panels (~22% efficiency vs. ~1% for biomass), the same land area would generate ~32,000 TWh/year — 23 times more energy. Per hectare, solar enables electric vehicles to travel ~3 million km versus ~22,000 km from corn ethanol. Hannah Ritchie's analysis concludes that 1.5 million hectares of solar panels — just 6% of current US corn bioethanol land — could power all US passenger driving. The concept of opportunity cost is central: every hectare devoted to biofuels is a hectare unavailable for vastly more efficient solar energy production, food crops, or carbon-sequestering natural ecosystems. Biofuels can play a transitional role in reducing emissions compared to fossil fuels in hard-to-electrify sectors, but the emerging consensus is that solar electrification of transportation is far superior to bioethanol as a climate mitigation strategy.

5: Biofuels A - Corn and Sugar Cane Ethanol is shared under a CC BY-NC-SA 4.0 license and was authored, remixed, and/or curated by LibreTexts.

6: BIOFUELS B - CELLULOSIC ETHANOL

LEARNING GOALS

(Learning goals written by Claude, Anthropic)

By the end of this chapter, students should be able to:

Cellulose Structure and Stability

- Explain the three reinforcing reasons cellulose resists enzymatic hydrolysis — the intrinsic stability of the β(1,4) glycosidic bond ($t_{1/2} \approx 5$ million years uncatalyzed), crystalline packing of cellulose Iα and Iβ polymorphs stabilized by intralayer hydrogen bonds and interlayer hydrophobic planes from axial C–H atoms, and encasement by lignin in the secondary cell wall — and contrast this with the much greater reactivity of starch's α(1,4) bonds.
- Describe the composition and organization of the primary and secondary plant cell walls — including the roles of cellulose microfibrils (40–60%), hemicellulose (20–40%), pectin, and lignin — and explain why most bioethanol-relevant cellulose comes from the secondary cell wall of woody plants and switchgrass.

Lignin Structure and Degradation

- Describe how the three monolignols (p-coumaryl, coniferyl, sinapyl alcohols) are derived from phenylalanine via cinnamic acid, and explain how peroxidase-catalyzed phenoxide radical formation drives oxidative coupling to produce the heterogeneous, covalently cross-linked lignin polymer.
- Describe the four-copper active site of fungal laccase from *Trametes versicolor* (T1, T2, T3α, T3β), explain how four sequential single-electron transfers oxidize lignin aromatic substrates with O_2 as the terminal electron acceptor producing water, and identify the key substrate-binding residues (His-458, Asp-206, Asn-264, Phe-265) and why thermochemical pretreatment is required before enzymatic delignification can be effective.

Cellulase Biochemistry and the Processive Cycle

- Distinguish the inversion mechanism (single SN2-like water attack, two carboxylate general acid/base catalysts) from the retention mechanism (double-displacement via a glycosyl-enzyme intermediate) of glycoside hydrolases, predict the stereochemical outcome at the anomeric carbon for each, and identify which mechanism TrCel7A uses with Glu217 as nucleophile and Glu212/Asp214 as acid/base catalysts.
- Describe the modular architecture of TrCel7A — catalytic domain (CD) with a 50 Å substrate tunnel, glycosylated linker, and C-terminal carbohydrate-binding module (CBM) — and explain how each component contributes to the processive cycle of cellulose chain threading, hydrolysis, cellobiose expulsion, and eventual desorption.
- Explain how the triplet tyrosines (Y5, Y31, Y32) of the CBM bind to the hydrophobic face of crystalline cellulose through π-stacking and van der Waals interactions, how N- and O-glycosylation of the linker enhances cellulose binding, and why nonproductive adsorption of the same CBM surface to lignin reduces effective cellulase concentration available for catalysis.

INTRODUCTION

In the last section, we explored how ethanol can be made from corn starch, an α(1,4) polymer of glucose with α(1,6) branches. Its production, however, comes at a cost. Recent life-cycle studies have shown that, compared to fossil fuels, corn ethanol releases as much, if not more, CO_2. In addition, is it ethically justifiable to remove so much land from food production to produce bioethanol that, at present, is worse than fossil fuels from a climatic perspective?

To address these issues, significant work has been done to produce ethanol from cellulose, a β(1,4) polymer of glucose, the most abundant biomolecule on Earth. Cellulose from trees, switchgrass, and "waste biomass" are prime sources for bioethanol production. Waste biomass includes stover (field crop stalks and leaves), straw, wood chips, and sawdust. About 113 gallons of ethanol can be made from one ton of corn stover, close to the 124 gallons produced from corn.

Nature routinely breaks down cellulose using cellulases, enzymes found in bacteria, fungi, protozoans, plants, and some animals. Ruminants and even termites obtain cellulases from microbes living within their guts. The fungal-mediated decay of dead trees requires microbial cellulase,s but think how slow that process is. This stems partly from the very strong β(1,4) glycosidic link connecting glucose monomers in the polymer, which, in the absence of a catalyst and at neutral pH, has an estimated half-life of 5 million years. Fossilized plants have been found to have intact cellulose and chitin, a β(1,4) polymer of N-acetylglucosamine. The β(1,4) glycosidic link in cellulose is orders of magnitude more stable than the phosphodiester bond of nucleic acids and the amide link of proteins. They are, however, readily cleaved by

glycosidases such as cellulases, which can increase the k_{cat}/K_M over the uncatalyzed rate by up to 10^{17} fold, even in the absence of active site metal ions to facilitate hydrolysis (reference).

Another reason for the slow decay of dead trees is the complex structure of the cell wall, particularly the presence of another tree polymer, lignin. Lignin stabilizes the cell wall and creates substantial barriers to cellulose's access to additional glycosidases.

A final reason for cellulose's extreme stability is the "quaternary" structure of the β(1,4)-linked cellulose strands, which consist of densely packed, intertwined strands that limit solvent (in this case, water) accessibility necessary for hydrolysis. In addition, some exposed surface planes of the packed cellulose strands are hydrophobic. This might seem startling, given the polymer's polar nature. Let's review it now since our goal is to present climate change from a biochemical perspective! Some of this material has been presented in previous chapters, but we will reuse it here so this chapter section can stand alone.

A REVIEW: THE PLANT CELL WALL

(See Chapter 7.3 for more details.) There are about 35 types of plant cells, and each may have a different cell wall depending on the local needs of that cell. Cells synthesize a thin cell wall that extends and stays thin as the cell grows. Figure **6.1** shows the primary cell wall of plants. The primary cell wall contains cellulose microfibrils (no surprise) and two other polymers, pectin and hemicellulose. The middle lamella, which consists of pectins, is somewhat analogous to the extracellular matrix.

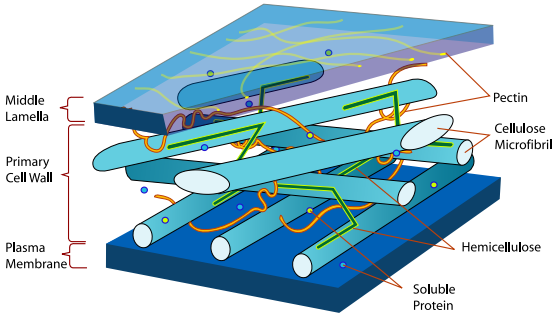


Figure **6.1**: Primary cell wall of plants. https://commons.wikimedia.org/wiki/F...diagram-en.svg

After cell growth, the cell often synthesizes a secondary cell wall, thicker than the primary wall, for greater rigidity. Since the enzymatic machinery for its synthesis is in the cytoplasm and the cell membrane, it is deposited between the cell membrane and the primary cell wall, as shown in the animated image in Figure **6.2**.

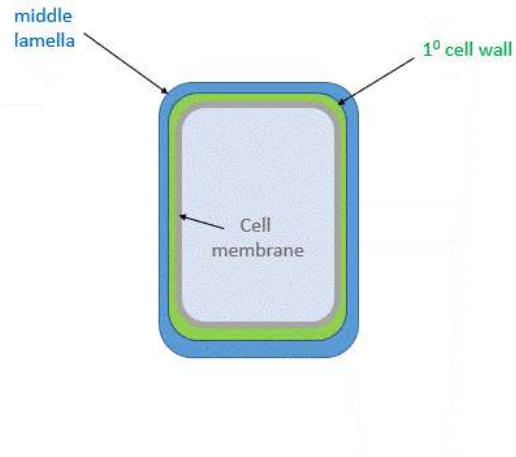


Figure **6.2**: Primary and secondary cell wall of plants

Figure **6.3** shows a structural representation of the primary and secondary cell walls.

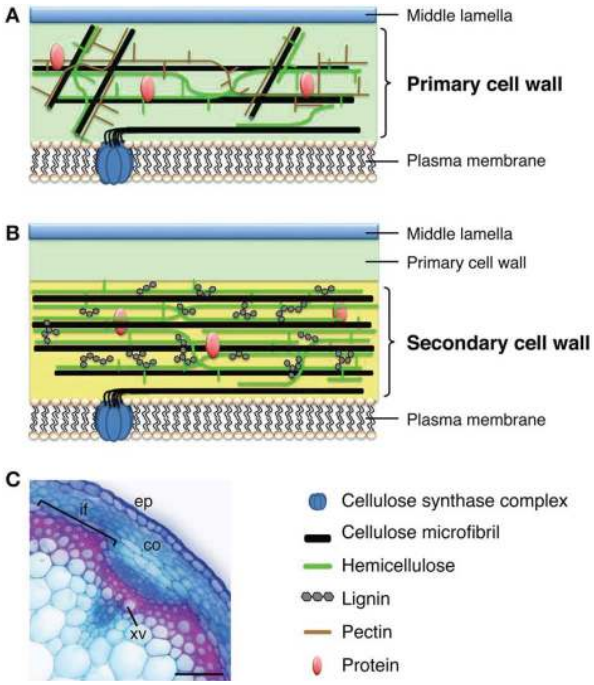


Figure **6.3**: structural representation of both the primary and secondary cell walls of plants. Nakano Yoshimi et al. Frontiers in Plant Science (6), 288 (2015) https://www.frontiersin.org/article/...015.00288/full. Creative Commons AttributionLicense (CC BY).

The middle lamella, which contains pectins, **lignins,** and some proteins, helps "glue together" the primary cell walls of surrounding plants.

Primary Cell Wall:

The main component of the primary plant wall is the homopolymer cellulose (40% -60% mass) in which the glucose monomers are linked β(1→4)-linked into strands that collect into microfibrils through hydrogen bond interactions. Two other groups of polymers, **hemicellulose** and **pectin,** make up the plant cell wall.

Hemicellulose can make up 20-40% of the mass. These polymers have β(1,4) backbones of glucose, mannose, or xylose (called xyloglucans, xylans, mannans, galactomannans, glucomannans, and galactoglucomannans along with some β(1,3 and 1,4)-glucans. The most abundant hemicellulose in higher plants is the xyloglucans, which have a cellulose backbone linked at O6 to α-D-xylose. **Pectin** consists of linked galacturonic acids forming homogalacturonans, rhamnogalacturonans, and rhamnogalacturonans II (RGII) [12] [13]. Homogalacturonans (α1→4) linked D-GalA make up more than 50% of the pectin. Figure **6.4** shows some structures. They are generally branched, shorter than cellulose chains, and can often crystallize.

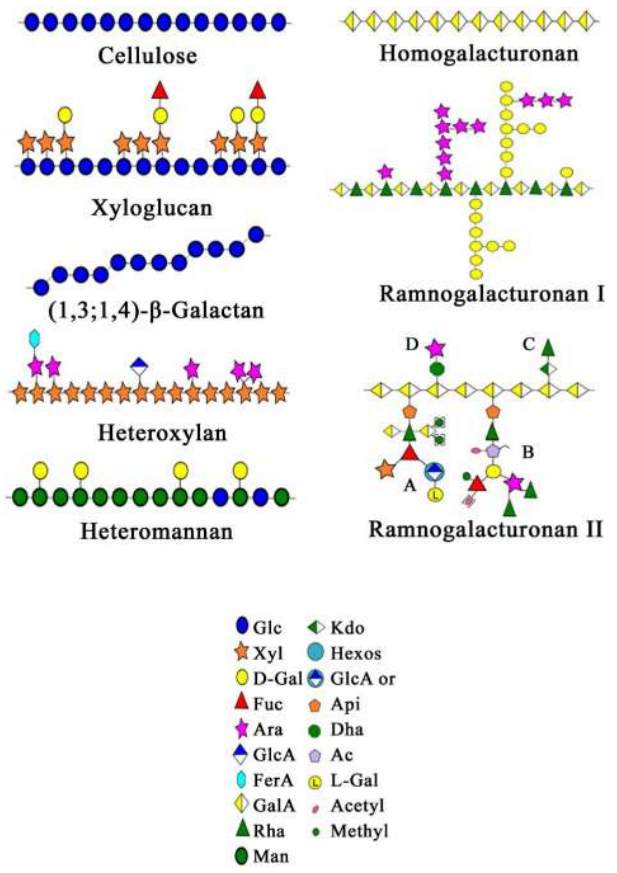


Figure 6.4: Variant of the cell wall components of a plant. Costa and Plazanet. Advances in Biological Chemistry 06(03):70-105. DOI: 10.4236/abc.2016.63008. License CC BY 4.0

Secondary Cell Wall

The structure of the secondary cell wall depends on the cell's function and environment. It contains cellulose fibers, hemicellulose, and a new polymer, **lignin**. It is abundant in xylem vessels and fiber cells of woody plants. It gives the plant extra stability and new functions, including the transport of fluids through channels. The proportion of cellulose in the secondary cell wall is higher than in the primary cell wall, and it is less hydrated than in the primary cell wall. Given the relative volume of the secondary and primary cell walls inferred from Fig. 2, most of the tree-derived cellulose for bioethanol production comes from the secondary cell wall. Switch grasses, a perennial plant, are also valuable sources of cellulose (**32–45% wt**) and hemicellulose (21–31% wt), but they also contain significant amounts of lignin (12–28% wt). In summary, the secondary cell wall, formed after the cell stops growing, accounts for most of the carbohydrate biomass of plants.

Glycosidases, mostly α- and β-amylases, are needed to convert corn-derived starch into glucose for fermentation and ethanol production. Likewise, cellulases are required to degrade cellulose into glucose for the production of cellulosic ethanol. However, it is a much more complex process since most cellulose is in the secondary cell wall. The lignin barrier in the walls protects cellulose from accessibility to cellulases, even after chemical and thermal pre-processing. In addition, xylans, which can make up 30% of the mass of the secondary cell wall, also inhibit cellulose degradation.

A thermochemical process can convert cellulose to the synthetic gases CO and H_2, which can be used as reactants to form ethanol. We'll discuss the biochemical process that uses pretreatment and enzymatic hydrolysis to produce cellulosic ethanol. Lignin can be recovered and used to provide energy for the industrial-scale synthesis of cellulosic ethanol.

Let's explore the barriers lignin poses and how they can be surmounted to facilitate access to cellulose and the liberation of glucose for cellulosic ethanol production.

LIGNIN STRUCTURE AND REACTIVITY

Lignins, which can make up to 25% of the biomass weight of secondary walls, are made from phenylalanine derivatives but more directly from cinnamic acid. This is made from hydroxylated phenylalanine and converted through other steps to hydroxycinnamic alcohols called

monolignols, as shown in Figure **6.5**. Three typical monomers, p-coumaryl, coniferyl, and sinapyl alcohols, can polymerize into lignins, with their units in the polymer (P) named hydroxyphenyl, guaiacyl, and syringly, respectively.

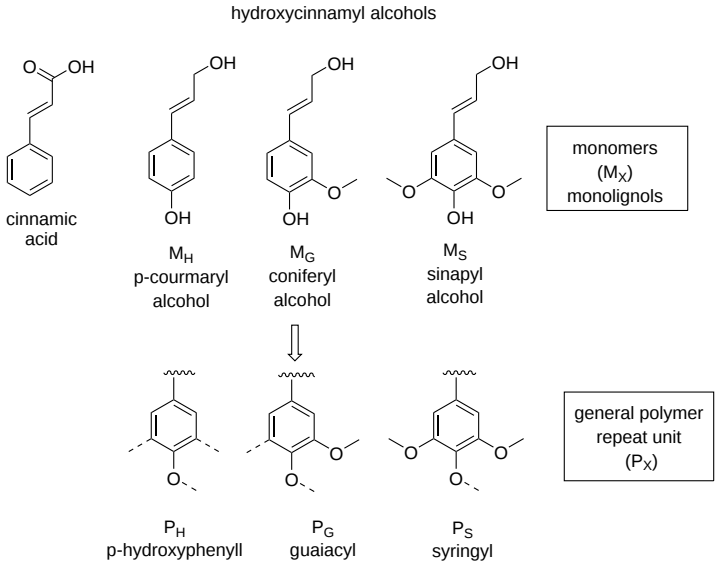


Figure **6.5**: Monolignols and their polymers

Lignols are activated phenolic compounds that form phenoxide free radicals (catalyzed by peroxidase enzymes), which can attack a second lignol to form covalent dimers. Reaction mechanisms for dimerizing the M_S sinapyl alcohol-free radical are shown in Figure **6.6**.

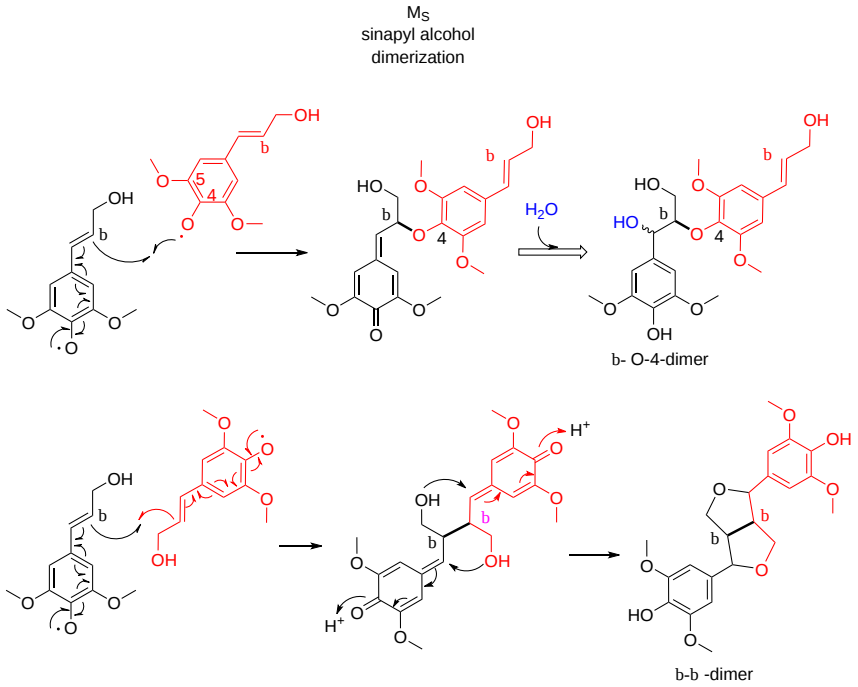


Figure **6.6**: Dimers of lignols

Now, imagine this polymerization continuing, forming more phenolic free radicals and coupling at multiple sites to form a large covalent lignin polymer. Figure **6.7** shows one example of a larger lignin.

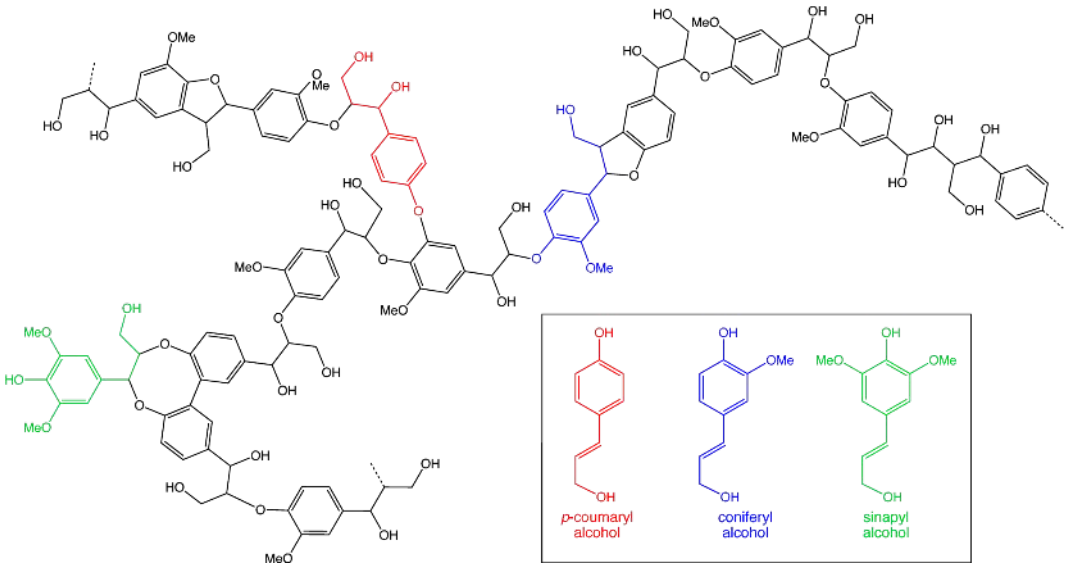


Figure **6.7**: A larger lignin. https://commons.wikimedia.org/wiki/C...ile:Lignin.png . By Smokefoot - Own work, CC BY-SA 3.0, https://commons.wikimedia.org/w/index.php?curid=16022799

Lignin strengthens the cell wall and further stabilizes the already unreactive cellulose fibers. Let's look at a specific example - using corn stover (CS) as a cellulose source. This process includes chemical pretreatment of the biomass source and the addition of a bacterial strain, *Pandoraea* sp. B-6 (B-6) isolated from long, narrow strips of bamboo (slips). Bamboo is a type of woody grass that grows rapidly. These bacteria produce two extracellular lignin-degrading enzymes, manganese peroxidase (MnP) and laccase (Lac). Laccase (Lac) is a multi-copper oxidase that uses O_2 to oxidize the syringyl, guaiacyl, and *p*-hydroxyphenyl monomers in lignins. MnP has similar properties. These and other enzymes can lead to the depolymerization of lignin and the degradation of lignin-derived aromatic compounds

The addition of the B-6 bacteria (a source of MnP and Lac) to milled corn stover (CS) did not increase the rate of lignin degradation unless the corn stover was preincubated with a tetrahydrofuran-water (THF–H_2O) solution with 0.5 wt% sulfuric acid and heated to 150 oC. This led to the erosion of the corn stover, allowing access to the bacterial enzyme. The untreated and pre-treated CS surface, along with a diagram showing access of Lac and MnP to the lignin, is shown in Figure **6.8**.

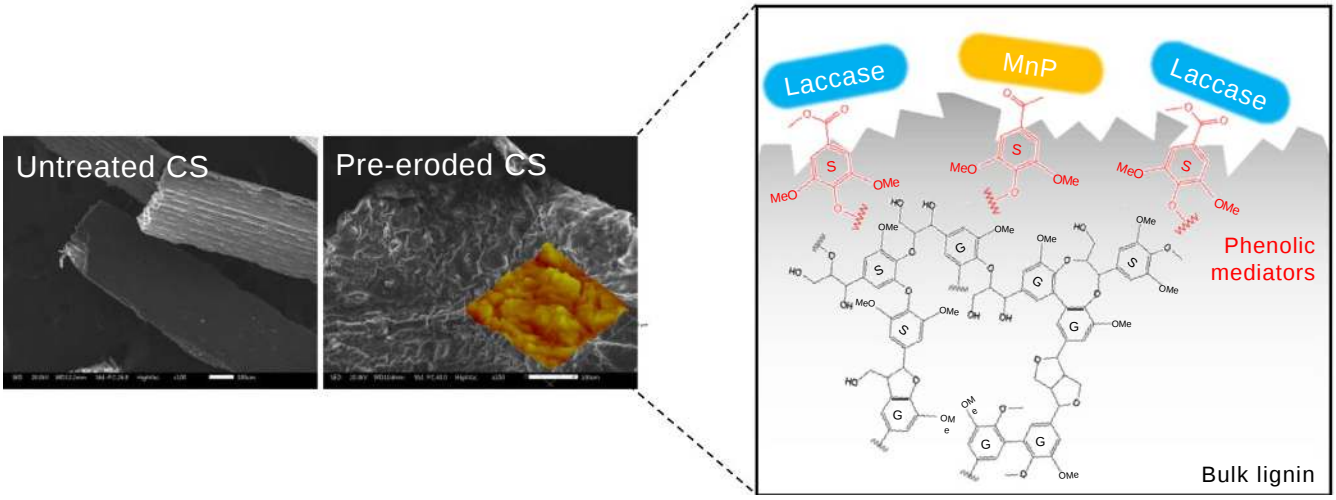


Figure **6.8**: Untreated and pre-treated CS surface and Lac and MnP interaction with lignins. Zhuo, S., Yan, X., Liu, D. *et al.* Use of bacteria for improving the lignocellulose biorefinery process: the importance of pre-erosion. *Biotechnol Biofuels* **11**, 146 (2018). https://doi.org/10.1186/s13068-018-1...068-018-1146-4. Creative Commons Attribution 4.0 International License (http://creativecommons.org/licenses/by/4.0/)

In addition to restricting cellulase's access to cellulose, it can also nonspecifically adsorb to lignin and its pretreated forms. The lignin derivatives exhibit a more hydrophobic surface, which promotes cellulase interactions. Some plant laccases are involved in lignin biosynthesis, but in bacteria and fungi, they are likely involved in degradation.

Of course, fungi, which are prime degraders of dead biomass in forests, are also sources of enzymes for lignin degradation. For example, species of white rot fungi produce manganese peroxidase (MnP), lignin peroxidase (LiP), versatile peroxidase (VP), and laccase (Lac). They form reactive lignin-derived aromatic free radicals (similar to those produced in lignin synthesis), leading to the breaking of ether bonds, aromatic ring cleavage, and the removal of methoxy groups from the substrate, a process called delignification. Pretreatment of the biomass increases the yields of available cellulose. Fungi, however, grow slowly, and the delignification rate is still low. In addition, they have hydrolytic enzymes that reduce cellulose yield. That is why bacterial sources like B6 are sought for delignification.

As this is a biochemistry textbook, let's explore the structure and function of fungal laccase. The enzyme can bind many hydroxylated and methoxy-aromatic compounds as substrates, so its active site must be adaptable and likely dynamic. The laccase (TvL) from the fungus Trametes versicolor has been used for structural analyses, in-silico docking experiments, and molecular dynamics simulations.

The enzyme contains four copper ions at a T1 Cu site and a trinuclear Cu cluster (T2 Cu, T3α Cu, and T3β Cu) at a T2/T3 site. As the mechanism involves free radical intermediates with O_2 as both oxidant and substrate, 4 electrons are transferred in single-electron steps to the T1 Cu, then to the other three coppers, and finally to O_2, forming 2 water molecules as products. The amino acid side chain ligands ligating four copper ions are shown for white rot fungi laccase from Trametes Versicolor in Figure **6.9**.

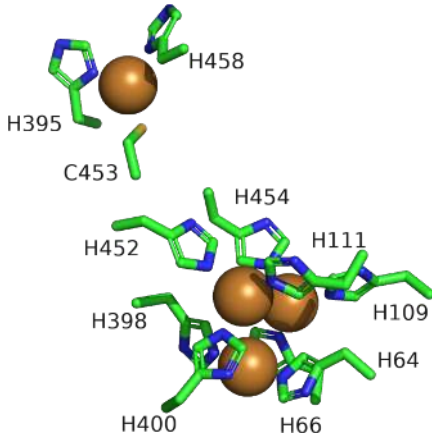
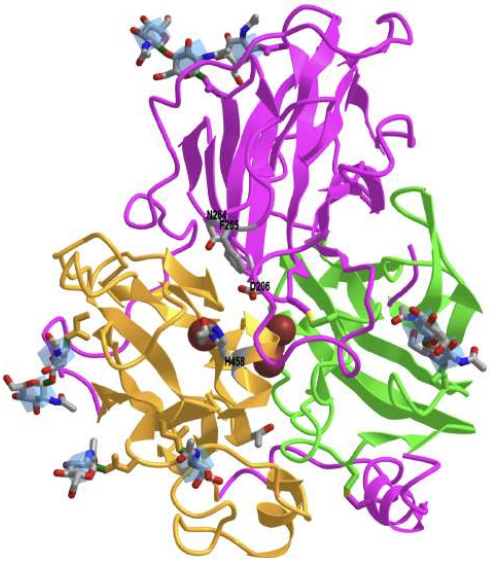


Figure **6.9**: T1 Cu (top left) and the trinuclear Cu cluster (T2, T3α and T3β) and their ligands for Trametes Versicolor laccase (TvL, pdb: 1GYC)

Fungal laccases are extracellular proteins with about 550 amino acids arranged in three cupredoxin-like, beta-barrel domains. The T1 Cu is close to the surface and is found in domain 3, while the other copper ions are buried at the interface between domains 1 and 3. Figure **6.10** shows an interactive iCn3D model of Laccase from the Fungus *Trametes Versicolor* (1GYC)



NCBI iCn3D Figure **6.10**: Laccase from the Fungus Trametes Versicolor (1GYC). (Copyright; author via source).
Click the image for a popup or use this external link: https://structure.ncbi.nlm.nih.gov/i...cSYir86P9nxSW6

Domain 1 is green, domain 2 magenta, and domain 3, which contains the single T1 Cu, is orange. The protein is glycosylated, as shown in the blue glycan cube cartoons representing N-acetylglucosamine. Key substrate binding and catalytic side chains are shown in sticks and labeled; Asp 206 is a critical residue involved in substrate binding.

The binding interactions of TvL with various aromatic substrates are shown schematically in Figure **6.11**.

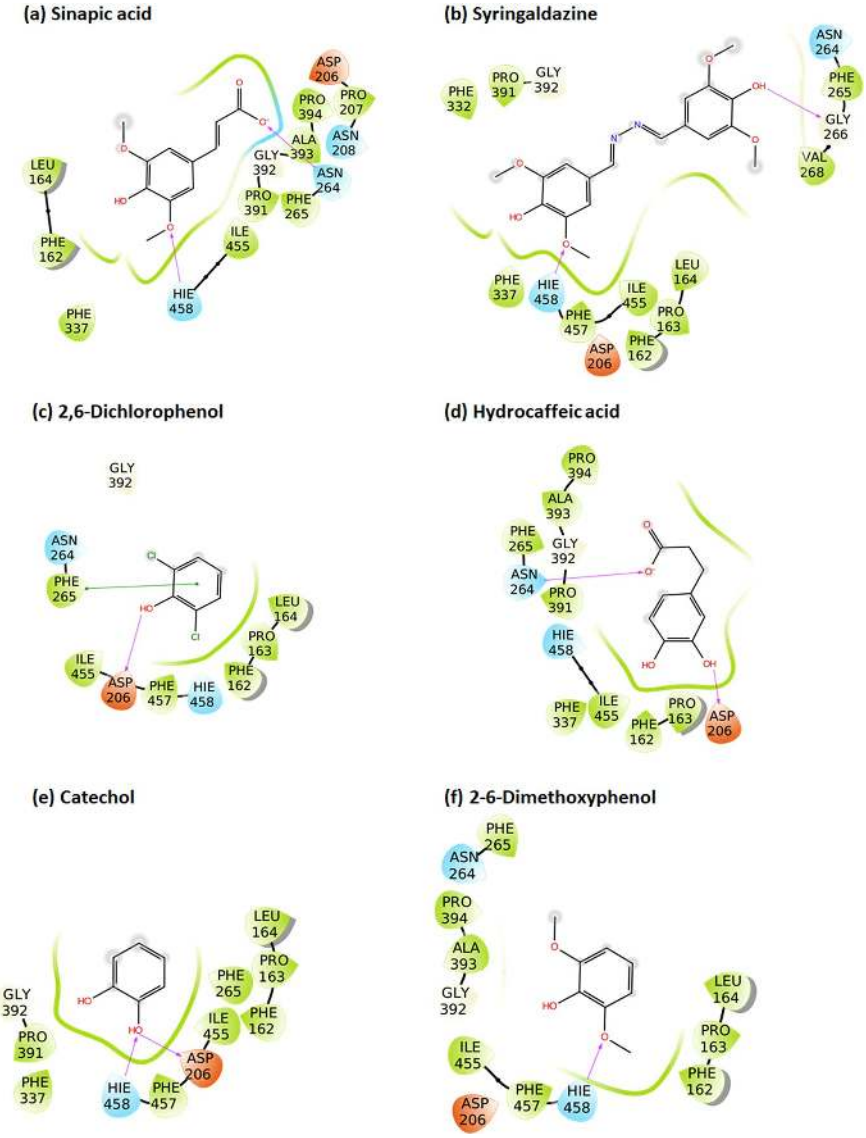


Figure **6.11**: Binding modes of representative compounds for TvL. Mehra, R., Muschiol, J., Meyer, A.S. *et al.* A structural-chemical explanation of fungal laccase activity. *Sci Rep* **8**, 17285 (2018). https://doi.org/10.1038/s41598-018-35633-8. Creative Commons Attribution 4.0 International License. http://creativecommons.org/licenses/by/4.0/

Most substrates interact with the highly conserved His-458 (blue color, ligand for the Ti Cu)and Asp-206 (orange color) residues and form hydrogen bonds, salt bridges, or π-π stacking interactions. Asn-264 (blue) and Phe-265 (green) form important hydrogen bonding and π-π stacking interactions with substrates. The green color highlights nonpolar side chains. Ligands bind near the Ti Cu in domain 3 to initiate electron transfer. The active site of TvL must be dynamic to bind the various-sized ligands shown above. Molecular dynamics simulations, shown in Figure **6.12**, support this.

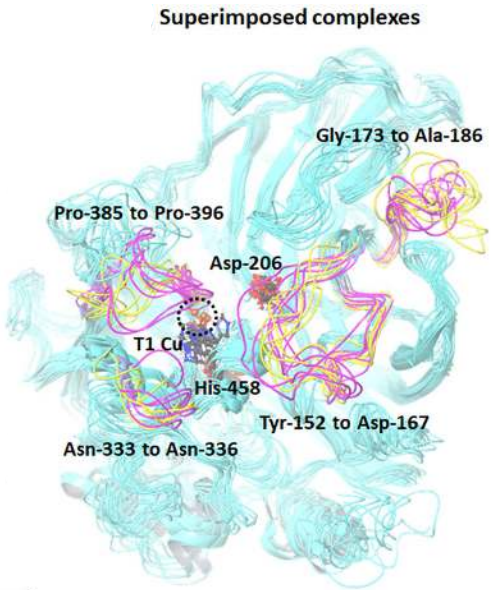


Figure 6.12: Display of molecular dynamics simulations showing the loop regions of TvL (magenta colored) and another laccase, CuL (yellow colored), and high levels of fluctuations. Mehra, R., ibid.

BREAKING DOWN CELLULOSE

We just explained how the lignin barrier could be degraded to allow cellulase to access cellulose. As we described above, this also poses a difficult challenge given the stability and inaccessibility of the glucosidic bonds in cellulose. The inaccessibility of "naked" cellulose fibers stems partly from the tight binding of cellulose strands into crystal lattices. Multiple crystal forms of cellulose, called polymorphs, can form. Plant cellulose has two predominant polymorphs, cellulose Iβ and Iα. Their structures are shown below in Figure **6.13**.

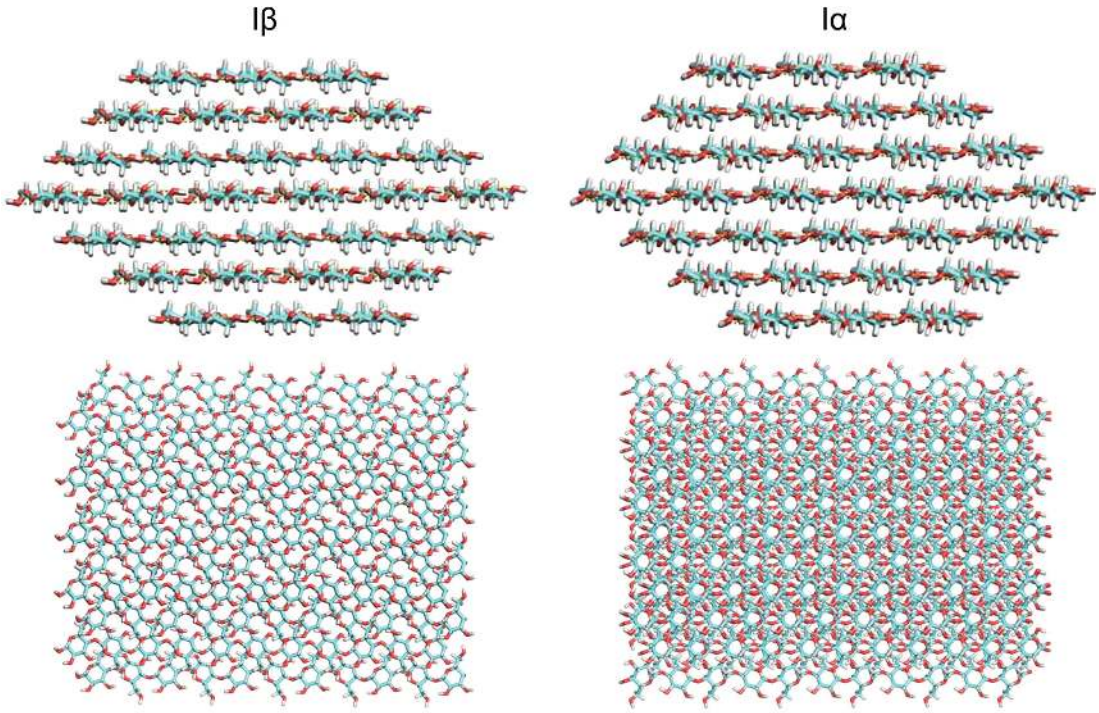


Figure **6.13**: Natural and synthetic cellulose polymorphs. Christina M. Payne et al. *Chem. Rev.* 2015, 115, 3, 1308–1448 (2015), https://doi.org/10.1021/cr500351c. Open access through a Creative Commons public use license.

They both form hydrogen bonds within a layer, with the main differences resulting from interlayer stacking. There are no hydrogen bonds between layers. You might find that surprising at first glance, but remember that all the OH groups in the lowest-energy chair form of

glucose are equatorial, which allows intralayer hydrogen bonding. The interactions between layers predominantly arise from van der Waals interactions, specifically induced dipole-induced dipole interactions. The hydrophobic planes, arising from axial H atoms projecting above and above each planar layer of the cellulose fibers, can be readily seen in Figure **6.14**.

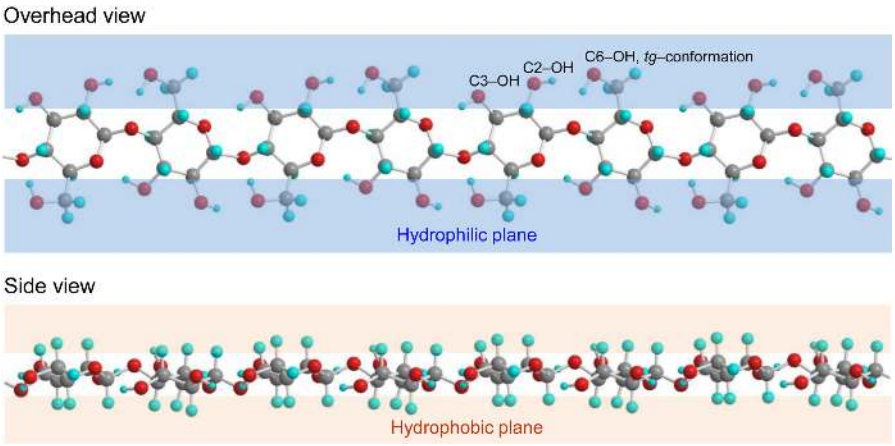


Figure **6.14**: Hydrophobic planes arising from axial H atoms projecting above and above each planar layer of the cellulose fibers. Akira Isogai et al. Progress in Polymer Science, 86 (2018), https://doi.org/10.1016/j.progpolymsci.2018.07.007. Creative Commons license

Now, we can explore the structure of cellulases and how they bind to and cleave cellulose.

Cellulases, which cleave β(1,4) glycosidic bonds in cellulose, are members of a family of enzymes that go by many names, including **glycosidases** or, more recently, **glycoside hydrolases (GH)**. The Carbohydrate Active Enzymes (CAZypedia) has over 128 glycoside hydrolase (GH) family web pages, with enzymes that form hemiacetals during glycosidic bond cleavage. Fungal cellulases that act on cellulose are found in GH families 5, 6, 7, 12, and 45.

There are many types of secreted or cell-surface cellulases, including endoglucanases, exoglucanases (example is cellobiohydrolases (CBHs), and β-glucosidase (BG)). We will focus on **cellobiohydrolases (CBHs)**, the most studied one, which cleaves a 2-glucose unit (cellobiose) from either end of cellulose as it proceeds (processes) along the chain. Fungal and bacterial CBHs can also act on crystalline cellulose. The resulting cellobiose is further cleaved by β-glucosidases. Ruminants and even termites obtain cellulases from microbes living within their guts. The enzyme has a "tunnel" between two surface loops, which interacts with and processively cleaves cellulose.

As mentioned above, fungi are the major degraders of biomass and are critical to the carbon cycle. Some fungi(brown-rot) use the Fenton reaction (Chapter 13.3) to produce the very reactive hydroxyl free radical (·OH), which causes biomass degradation. Filamentous fungi (such as white and soft rot and *T. reesei*) use enzymes. The T. reesei cellulase, cellobiose hydrolase 1, is now called *Tr*Cel7A because it belongs to the GH 7A family.

Cellulase mechanism.

We have previously described the mechanisms of polysaccharide synthesis (Chapter 20.3), so we will discuss the mechanism of the very similar reaction of cellulose degradation by cellulase in less detail. Two general mechanisms are possible: one leading to retention of configuration at the resulting hemiacetal end of cellobiose, and another leading to inversion of configuration. These mechanisms are shown in Figure **6.15** for glucose in alpha-linkage at the anomeric carbon (not the beta-linkage found in cellulose).

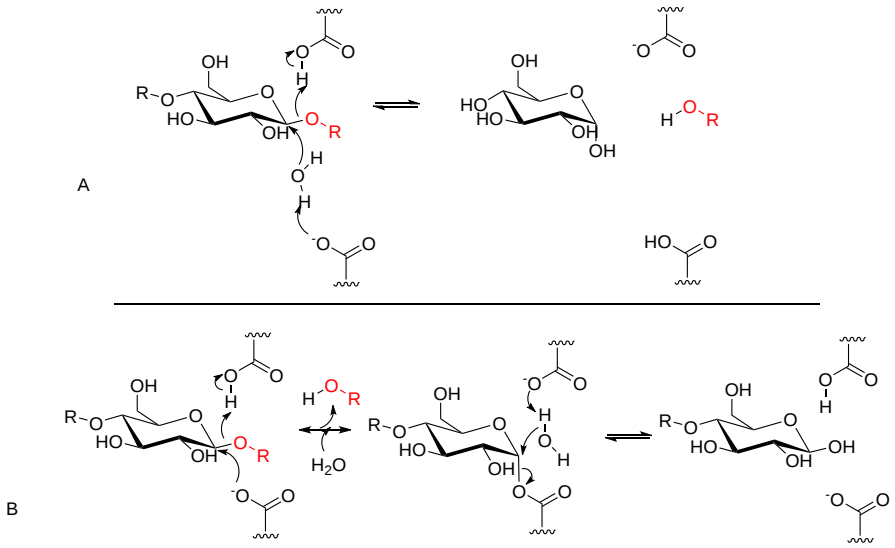


Figure **6.15**: Two Primary Catalytic Mechanisms of GHs. After Payne et al. *Chem. Rev.* 2015, 115, 3, 1308–1448. https://doi.org/10.1021/cr500351c.

Scheme (A) shows the reaction that inverts the configuration. Water acts as a nucleophile in an S_N2 reaction, with catalytic assistance by two proximal carboxylic acid side chains acting as general acids and bases. This results in an inversion of the stereochemistry at the anomeric carbon.

Scheme (B) proceeds with the retention of configuration as two different nucleophilic attacks occur. First, an active site carboxylate forms a covalent acetal intermediate with the anomeric carbon. The carboxylate, hence, acts as a nucleophilic catalyst. Water, acting as a nucleophile, then attacks to form the hemiacetal with the expulsion of the carboxylate leaving group. As discussed in Chapter 20.3 (section on glycosyl transferases), other variants of these mechanisms would include an S_N1 reaction or one with an oxocarbenium-like transition state.

The CBH1 (family 7) has a long tunnel for binding cellulose. The CBH1 (*Tr*Cel7A) cellulose catalytic site spans at least nine glucose monomers (n-7, n-6,...,n-1,n+1, n+2) with cleavage typically of a cellobiose from the reducing end (between n-1 and n+1). The structure of the *Tr*Cel7A glycoside hydrolase (cellobiose hydrolase) with a small bound cellulose is shown in Figure **6.16**.

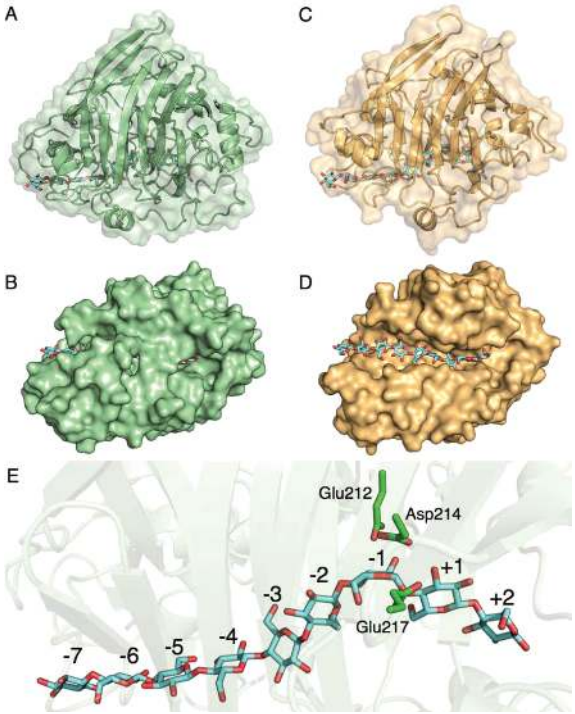


Figure **6.16**: Crystal structure of the first GH7 CBH and EG. Payne et al. *Chem. Rev.* 2015, 115, 3, 1308–1448. https://doi.org/10.1021/cr500351c Open access through Creative Commons public use license.

The ligand from the *Tr*Cel7A Michaelis complex (PDB code 4C4C (441)) is shown in all panels. (A) CBH *Tr*Cel7A CD (PDB code 1CEL (172)) view from the side, exhibiting the β sandwich structure characteristic of GH7 enzymes. *Tr*Cel7A was the first GH7 structure solved and is the best-characterized member of the GH7 family. (B) *Tr*Cel7A view from the bottom showing the more closed substrate binding "tunnel". (C) EG *F. oxysporum* Cel7B (PDB code 1OVW (174)) view from side. (D) *Fo*Cel7B view from the bottom showing the more open binding "groove". (E) *Tr*Cel7A Michaelis complex (PDB code 4C4C (441)) shows the standard numbering of the substrate binding sites (catalytic residues shown in green for reference). A cellulose chain enters from the −7 site. Hydrolysis occurs between the −1 and +1 sites. The +1/+2 sites are termed the "product sites".

Active site carboxylates (E212, D214, and E217) are shown near the -1/+1 cleavage site in Figure **6.17**. Glu 217 is covalently attached to the -1 glucose, supporting the retaining mechanism illustrated in Fig 15 above.

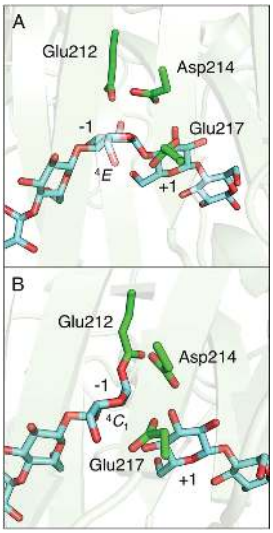


Figure **6.17**: Michaelis complex and glycosyl-enzyme intermediate of *Tr*Cel7A. Payne et al. ibid.

Panel (A) shows the *Tr*Cel7A Michaelis complex (PDB code 4C4C (441)).

Panel (B) shows a *Tr*Cel7A glycosyl-enzyme intermediate (PDB code 4C4D (441)) with a covalent bond between the nucleophile and the broken cellooligomer chain. There is an approximate 30° rotation of the E217 nucleophile during glycosylation.

Figure **6.18** shows a more detailed view of the first step (glycosylation f Glu 217) for the *Hypocrea jecorina* GH Family 7 cellobiohydrolase Cel7A

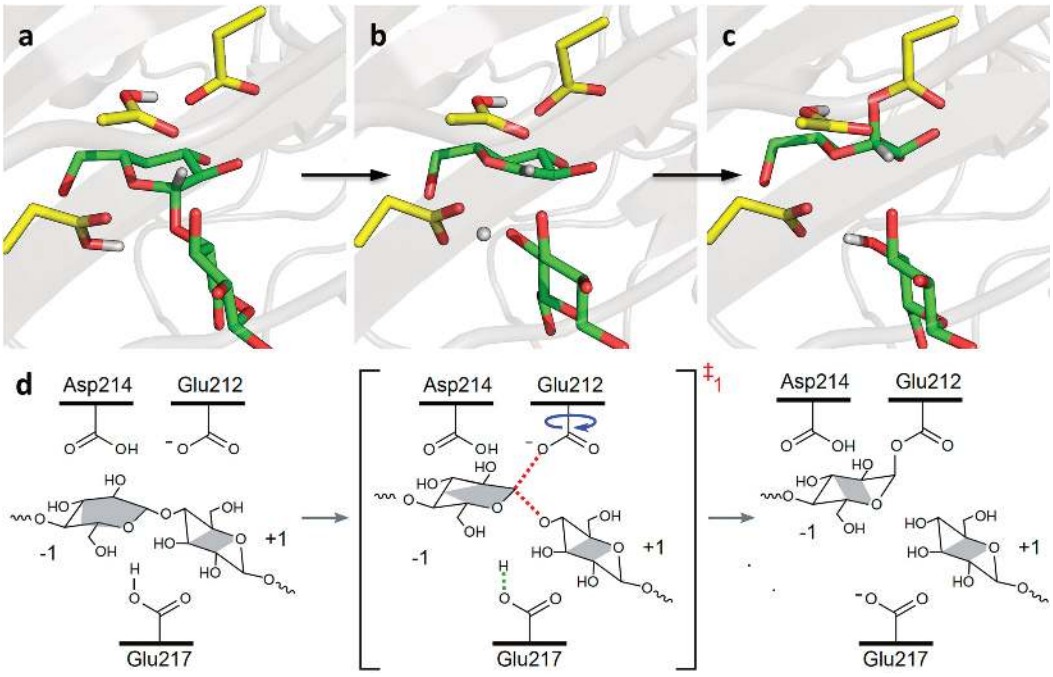


Figure **6.18**: Figure 2. Glycosylation step for *Hypocrea jecorina* GH Family 7 cellobiohydrolase Cel7A. Knott, Brandon C. et al. - J. Am. Chem. Soc.329 (2013) https://doi.org/10.1021/ja410291u. Open access article published under an ACS AuthorChoice License

Panel (a) shows a snapshot of the reactant's conformation from a representative AS trajectory (with the substrate in green and catalytic residues in yellow) for the glycosylation step. The proton resides on Glu217.

Panel (b) shows a representative snapshot of the transition state. The −1 glucopyranose ring now adopts a different conformation.

Panel (c) shows the product of the glycosylation reaction.

Panel (d) shows a schematic view of the overall glycosylation reaction with the collective variables identified by LM colored at the transition state. The best three-component RC identified by LM includes the forming/breaking bonds involving the anomeric carbon, the breaking bond between Glu217 and its proton, and the orientation of the nucleophile Glu212.

Figure **6.19** shows the corresponding deglycosylation (of Glu 217) step.

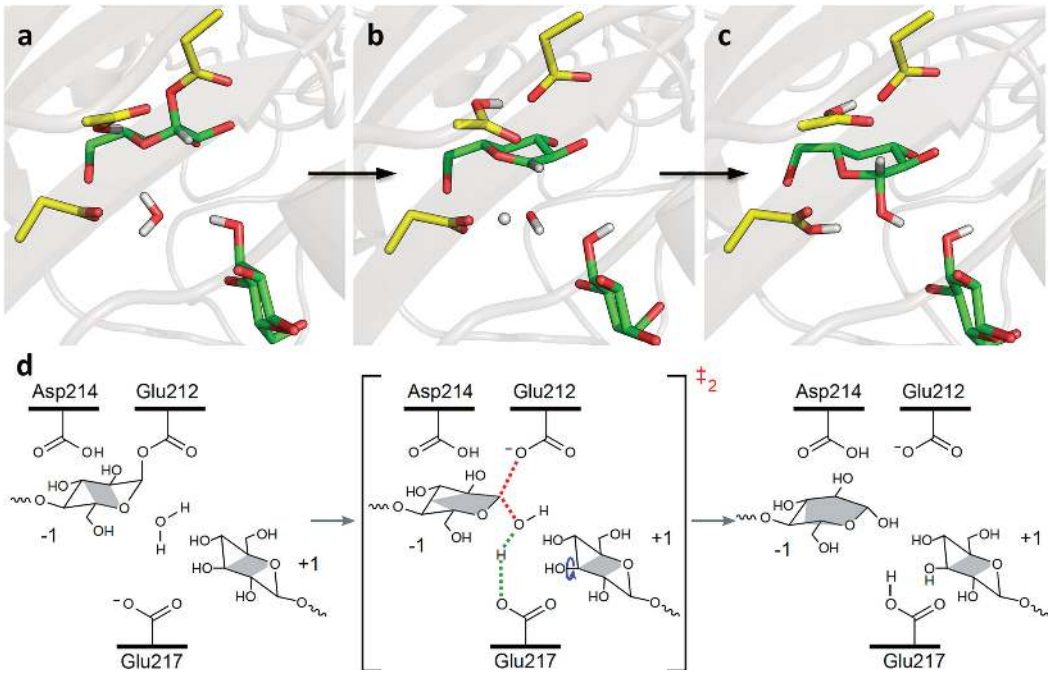


Figure **6.19**: Figure 4. Deglycosylation step results. Knott, Brandon C. et al, ibid

Panel (a) shows a snapshot of the reactant conformation from a representative AS trajectory (with the substrate in green and catalytic residues in yellow) for the deglycosylation step. The covalent glycosyl–enzyme bond is intact, and the cellobiose product is in primed GEI mode.

Panel (b) shows a representative snapshot of the transition state. Note the distorted conformation of the −1 sugar as the nucleophilic water molecule is ripped apart.

Panel (c) shows a snapshot of the product in which the glycosyl-enzyme bond has been broken, and the catalytic residues have been regenerated.

Panel (d) shows a schematic view of the overall deglycosylation reaction with the collective variables identified by LM colored at the transition state. The best three-component RC identified by LM includes the forming/breaking bonds involving the anomeric carbon, the forming/breaking bonds involving the transferring proton, and the orientation of the C3 hydroxyl of the +1 sugar.

BINDING OF CELLULASE TO CELLULOSE FIBERS AND LIGNIN

Many glycoside hydrolases contain distinct carbohydrate-binding domains/modules (CBD/CBM) and catalytic domains (CD). For example, TrCel7A can be cleaved by the protease papain into a 56K domain with catalytic activity on small substrates but not large cellulose ones and a smaller 10K (C-terminal) domain that itself is glycosylated and which binds to the hydrophobic surface of cellulose crystals.

In addition, many GHs have **linkers** connecting the catalytic domain (CD) and the carbohydrate module (CBM), which add different functions to the enzymes. The linkers vary in size and amino acid sequence. Linkers in fungi tend to be long and N- and O-glycosylated, affecting binding/catalysis. The linkers can also be intrinsically disordered, which adds dynamic complexity to their effects.

The cellulose-binding site on cellulase has been determined by solution NMR using a synthetic 36-amino-acid protein fragment from the C-terminal domain of *Trichoderma reesei* Cel7A (the "carbohydrate binding module or CBM"). The amino acids involved in cellohexaose (6-mer) binding were determined by perturbation of the 2D NMR structure on binding cellohexaose. As mentioned above, cellulase also binds lignin, decreasing its catalytic efficiency towards cellulose. Results of NMR binding studies of the *Tr*Cel7A carbohydrate-binding module with cellohexaose and lignins from Japanese cedar (C-MWL) and *Eucalyptus globulus* (E-MWL) are shown in Figure 6.20.

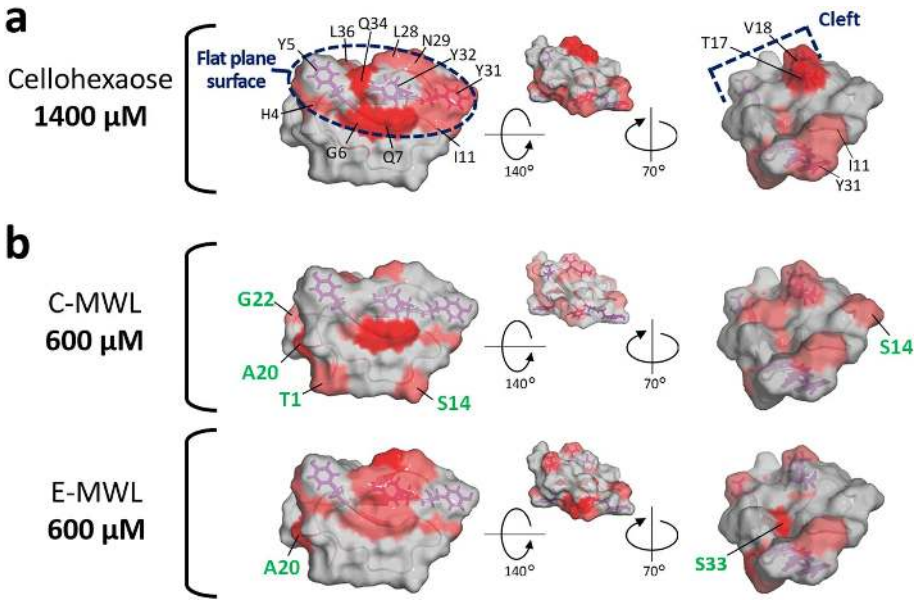


Figure 6.20: Comparison of interaction property between cellohexaose and MWLs. Tokunaga, Y., Nagata, T., Suetomi, T. *et al.* NMR Analysis on Molecular Interaction of Lignin with Amino Acid Residues of Carbohydrate-Binding Module from *Trichoderma reesei* Cel7A. *Sci Rep* **9**, 1977 (2019). https://doi.org/10.1038/s41598-018-38410-9. Creative Commons Attribution 4.0 International License. http://creativecommons.org/licenses/by/4.0/.

Panel (**a**) shows cellohexaose bound to the flat plane surface and cleft. A triplet tyrosine (Y5, Y31, Y32) and H4, G6, Q7, I11, L28, N29, Q34, L36 define the flat plane surface**.**

Panel (**b**) shows both MWLs bound to multiple binding sites, some of which are included in the flat plane surface and cleft, even in low titrant concentrations. These non-specific binding sites are labeled green.

Figure 6.21 shows an interactive iCn3D model of the C-terminal cellulose-binding module of cellobiohydrolase I from Trichoderma reesei (2CBH).

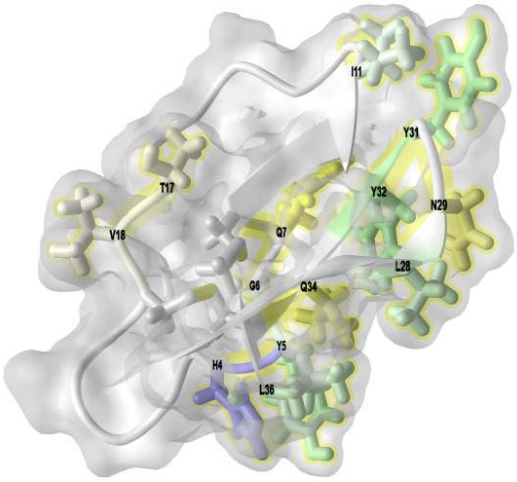


Figure 6.21: C-terminal cellulose-binding module of cellobiohydrolase I from Trichoderma reesei (2CBH). (Copyright; author via source). Click the image for a popup or use this external link: https://structure.ncbi.nlm.nih.gov/i...Yva8BVMQCGdUZ7

This synthetic carbohydrate-binding module (CBM) from the C-terminal domain of cellobiohydrolase I consists of 36 residues. NMR was used to determine the structure of the CBM. 2D NMR was used to determine the amino acids interacting with cellulose. The interacting side chains are shown as sticks underneath the molecular surface (gray). The side chains are colored by hydrophobicity, with green (most hydrophobic) and yellow (somewhat hydrophobic). The numbering system refers to the 36-amino acid synthetic peptide, not the native protein. This model clearly shows that this domain binds to the hydrophobic face of the cellulose microcrystal.

The *Tr*Cel7A CBM has glycosylated serine and threonine side chains that affect binding. The interaction of the CBM with the nonpolar cellulose surface is shown in Figure 6.22.

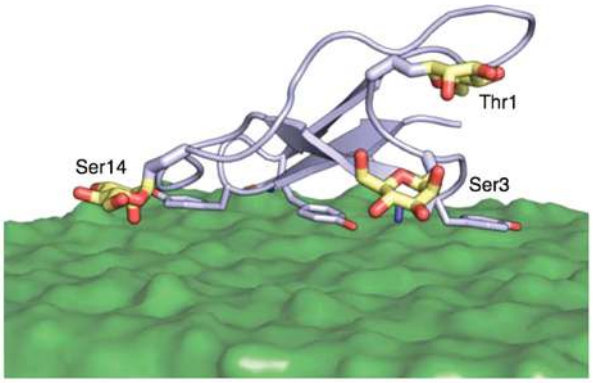


Figure 6.22: Glycosylated *Tr*Cel7A CBM on the hydrophobic surface of cellulose. Payne et al., ibid.

Note that the aromatic groups of the triplet tyrosines, Y5, Y31, and Y32 (not labeled), are coplanar with the cellulose surface.

As mentioned above, linkers that connect the C-terminal carbohydrate-binding module (CBM) to the catalytic domain (CD) can vary in length and sequence and are also N- and O-glycosylated. Figure 6.23 shows the interactions of the glycosylated linkers with the cellulose fibers.

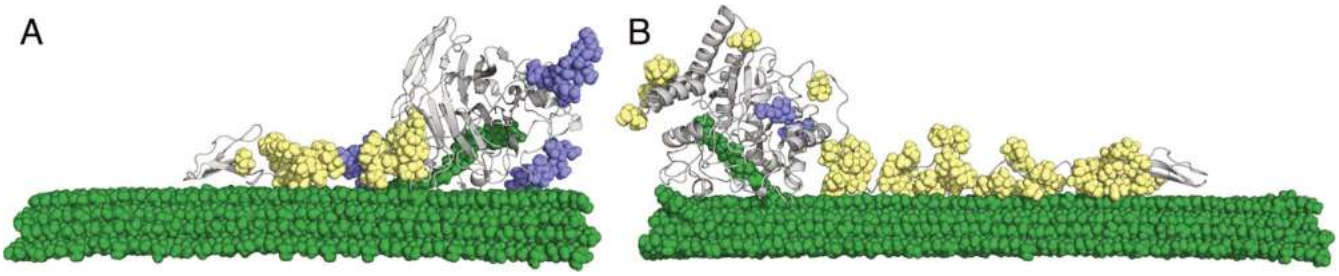


Figure **6.23**: Molecular snapshots of *Tr*Cel7A and *Tr*Cel6A wherein the linker binds to the cellulose surface from microsecond-long MD simulations. Payne et al., ibid.

These computational predictions of cellulose linkers enhancing CBM binding to the cellulose surface were corroborated experimentally via binding isotherm measurements. *N*-glycosylation and *O*-glycosylation are shown in blue and yellow. The glycans attached to the enzyme significantly enhance cellulase binding to cellulose fibers. Payne et al. *Chem. Rev.* 2015, 115, 3, 1308–1448. https://doi.org/10.1021/cr500351c Open access through Creative Commons public use license

A pictorial view of the hydrolytic cleavage of cellobiose from cellulose fibers is shown in Figure **6.24**.

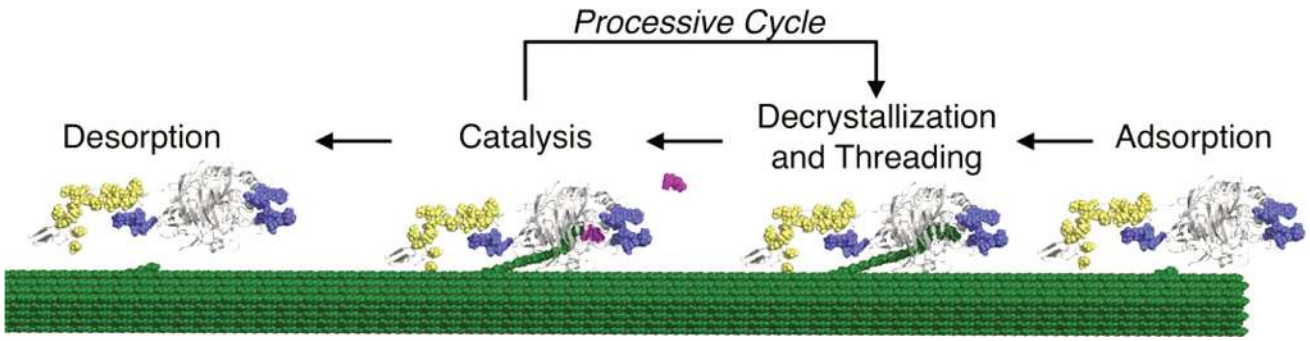


Figure **6.24**: Complete processive cycle of a GH7 CBH. *Tr*Cel7A is shown with its CD, linker, and CBM in gray "cartoon" representation. Payne et al., ibid.

N-glycosylation and *O*-glycosylation are shown in blue and yellow, respectively. The cellulose surface is green, and the released cellobiose product magenta. Following the CBM and CD adsorption to the substrate and initial chain threading, *Tr*Cel7A processively cleaves cellobiose from a cellulose chain end. The "Processive Cycle" includes chain processivity, hydrolysis, and product expulsion. This processive cycle repeatedly occurs until the enzyme desorbs from the cellulose surface.

Figure **6.25** shows an interactive iCn3D model of cellulose bound to cellobiohydrolase I from Trichoderma reesei (7CEL)

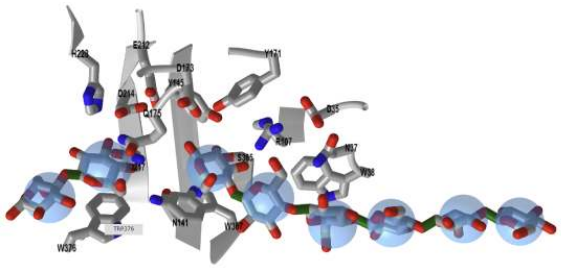


Figure **6.25**: Cellulose bound to cellobiohydrolase I from Trichoderma reesei (7CEL). (Copyright; author via source). Click the image for a popup or use this external link: https://structure.ncbi.nlm.nih.gov/i...hfJFWg6hmJAxg7

SUMMARY

(Summary written by Claude, Anthropic)

This chapter examines the biochemical barriers to cellulosic ethanol production — the conversion of lignocellulosic biomass from agricultural waste, wood, and dedicated energy crops into fermentable glucose — and the enzyme systems nature has evolved to overcome them.

Why cellulose is so resistant. Cellulose is the most abundant biomolecule on Earth and an attractive bioethanol feedstock precisely because it is not a food crop. It is a β(1,4)-linked glucose homopolymer whose glycosidic bonds have an estimated uncatalyzed hydrolysis half-life of 5 million years — far more stable than the α(1,4) bonds of starch, the phosphodiester bonds of DNA, or the amide bonds of proteins. This extraordinary stability arises from three reinforcing factors: the intrinsic chemical stability of the β-acetal bond; the crystalline packing of cellulose chains into two polymorphs (Iα and Iβ) stabilized by intralayer hydrogen bonds and interlayer hydrophobic interactions from axial

C–H planes (limiting water access); and the encasing of cellulose within the secondary plant cell wall by hemicellulose (β(1,4)-backbones of xylose, mannose, or glucose, comprising 20–40% of wall mass) and lignin. About 113 gallons of ethanol can be produced per ton of corn stover — close to the 124 gallons from corn grain — making waste biomass a compelling feedstock if the enzymatic barriers can be overcome. Cellulases can increase the hydrolysis rate by up to 10^{17}-fold over the uncatalyzed reaction without metal cofactors, making them among the most catalytically powerful enzymes known.

The lignin barrier. Lignin — up to 25% of secondary wall biomass — is synthesized from three monolignols (p-coumaryl, coniferyl, and sinapyl alcohols) derived from phenylalanine via cinnamic acid. Peroxidase enzymes generate phenoxide free radicals that couple at multiple sites to form a highly branched, heterogeneous polymer. Lignin stabilizes the cell wall, physically blocks cellulase from accessing cellulose, and also nonspecifically adsorbs cellulase through hydrophobic interactions, reducing its effective concentration available for productive hydrolysis. Thermochemical pretreatment (e.g., THF–H_2O with 0.5% H_2SO_4 at 150°C) partially erodes the biomass surface, enabling subsequent enzymatic delignification. Bacteria such as *Pandoraea* sp. B-6 and white-rot fungi produce two key delignifying enzymes: laccase and manganese peroxidase. Fungal laccase from *Trametes versicolor* (TvL) contains four copper ions organized as a T1 Cu site (near the surface in domain 3, where substrates bind) and a trinuclear T2/T3 cluster (buried at the domain 1/3 interface, where O_2 is reduced to water). Four single-electron transfers — mediated by His-458, Asp-206, Asn-264, and Phe-265 as key substrate-interaction residues — generate lignin-derived aromatic free radicals that drive ether bond cleavage, ring opening, and demethoxylation (delignification). The active site is dynamic, as confirmed by molecular dynamics simulations, accommodating a wide variety of aromatic substrates.

Cellulase mechanism and structure. Cellobiohydrolases (CBHs) are the most important cellulases industrially; *Trichoderma reesei* Cel7A (TrCel7A, GH family 7) is the best-characterized. It processively cleaves cellobiose (a glucose dimer) from the reducing end of a cellulose chain as it threads through a ~50 Å tunnel formed by two surface loops. The reaction proceeds by retention of anomeric configuration through a double-displacement mechanism: Glu217 acts as a nucleophile to form a covalent glycosyl-enzyme intermediate, then water attacks with general acid/base assistance from Glu212 and Asp214 to regenerate the enzyme. This contrasts with inverting glycosidases, which proceed via a single SN2-like water attack. The catalytic cycle involves initial distortion of the −1 glucopyranose ring at the transition state, followed by expulsion of cellobiose from the +1/+2 product sites.

Domain architecture and cellulose binding. TrCel7A has a modular structure: a large catalytic domain (CD) connected via a long, N- and O-glycosylated linker to a small C-terminal carbohydrate-binding module (CBM). The 36-residue CBM binds specifically to the hydrophobic face of crystalline cellulose through a flat surface defined by a triplet of tyrosine residues (Y5, Y31, Y32) that stack coplanarly against the cellulose surface via π-stacking and van der Waals interactions, supported by additional contacts from H4, G6, L28, N29, Q34, and L36. Glycosylation of the linker — both N- and O-linked sugars — significantly enhances CBM binding to cellulose fibers, as confirmed by molecular dynamics simulations and binding isotherms. The processive catalytic cycle consists of CBM and CD adsorption to the cellulose surface, initial chain threading, repeated hydrolysis and product (cellobiose) expulsion, and eventual desorption. A critical complication is that the same CBM surface that binds cellulose also binds lignin nonproductively, reducing catalytic efficiency — a key target for protein engineering to improve cellulosic ethanol yields.

6: Biofuels B - Cellulosic Ethanol is shared under a CC BY-NC-SA 4.0 license and was authored, remixed, and/or curated by LibreTexts.

8: BIODIESEL, SYNGAS AND BIOAVIATION FUELS

Search Fundamentals of Biochemistry

LEARNING GOALS

(Learning goals written by Claude, Anthropic)

By the end of this chapter, students should be able to:

Biodiesel and Triacylglycerol Feedstocks

- Compare diesel and gasoline in carbon chain length, energy content (36.9 vs. 33.7 MJ/L), and combustion mechanism, describe the four generations of biodiesel feedstocks with their key trade-offs, and write the transesterification reaction converting triacylglycerols to fatty acid methyl esters and glycerol.
- Describe the anabolic pathway for triacylglycerol synthesis in microalgae — identifying ACCase (committed step), FAS, FAT, GPAT, LPAAT, PAP, and DGAT as key enzymatic targets — and explain why each represents a site for genetic engineering to increase lipid yield for third- and fourth-generation biodiesel.

Syngas: Production, Chemistry, and Uses

- Write the simplified reactions for incomplete combustion of biomass to syngas (CO + H_2), the water-gas shift reaction, and its reverse, explain how each adjusts the H_2/CO ratio, and compare the ratios produced by steam reforming (~3), biomass gasification (~0.6–1), and electrocatalytic CO_2 reduction (0–2) against the optimal ratio for Fischer-Tropsch synthesis (~2).
- Explain electrocatalytic CO_2 reduction (ECR) — how electrons from water oxidation at an anode reduce CO_2 at a heterogeneous catalyst cathode — interpret standard reduction potentials for CO_2 → formate, CO, methanol, ethanol, and methane, and explain why renewable electricity is essential for this process to be climate-beneficial.
- Compare the carbide, enol, and CO-insertion mechanisms of Fischer-Tropsch synthesis — identifying the rate-limiting step and role of the metal catalyst surface in each — and explain why iron catalysts are preferred over cobalt for biomass-derived syngas due to lower H_2/CO ratios and better water-gas shift activity.

Chemical Synthesis of Food

- Explain why fats are the most tractable macronutrient to produce by chemical synthesis, compare the GHG emissions of chemically synthesized fats (<0.8 g CO_2 equiv/kcal) versus conventional palm oil (>1.5 g CO_2 equiv/kcal), and describe the environmental consequences of palm oil agriculture that make chemical synthesis an attractive alternative.

Sustainable Aviation Fuel: Life Cycle Analysis and Policy

- Describe the molecular composition of Jet A-1 fuel (C8–C16 alkanes, cycloalkanes, aromatics) and explain how Fischer-Tropsch synthesis from lignocellulosic feedstocks produces molecules in this range for sustainable aviation fuel (SAF).
- Define carbon price ($/t CO_2e), use the SAF cost table to show that a carbon price of $175/t CO_2e — equal to the estimated social cost of carbon — makes miscanthus-based SAF cost-competitive with conventional jet fuel, and interpret the miscanthus LCA showing that 23.2 Mha of marginal cropland could supply up to 76% of projected US aviation fuel needs at ~$4.1/gal with a $50/t CO_2e carbon price.

Note: A significant portion of the chemistry described below is centered more on organic chemistry than on biochemistry. It is presented as part of a comprehensive discussion of alternative fuels.

Diesel fuel was used in 1900 in an engine designed by Rudolf Diesel. The fuel was peanut oil. That might have worked fine in 1900, but a century later, the demands for diesel fuel are met not by peanut oil, a legume, but by oil. Gasoline (petrol) consists of molecules containing 5-12 carbons, compared to diesel, which contains 12-20. Both are obtained through fractional distillation of oil (petroleum). Diesel has a higher boiling and melting point and releases more energy per liter (36.9 vs. 33.7 MJ) than gasoline. Regular gasoline contains about 17% n-alkanes, 32% branched alkanes, 5% cycloalkanes, 2% alkenes (olefins), and 30% aromatics. High octane gas can contain around n- and branched alkanes, with the rest from alkenes. Diesel fuel contains about 75% saturated hydrocarbons and 25% aromatics, including alkylbenzenes and naphthalenes. In a diesel engine, ignition occurs in the fuel-air mixture through compression, without a spark. They use glow plugs, which provide heat but not spark.

BIODIESEL

Oils (triacylglycerol) produced from biomass can be converted to diesel fuel. In the following sections, we will discuss the synthesis of gases and liquid fuels from nonpetroleum sources, such as biomass, by producing the synthetic gases H2 and CO (collectively called syngas) and condensing them into liquid fuels via the Fischer-Tropsch reaction. This section will focus on using fats to produce biodiesel. Triacylglycerols for biodiesel production can come from plants, animals, algae, and even food industry waste oils. Because biodiesel fuel is composed of carbon-based molecules (often fatty acid esters) with high melting and boiling points, it is often blended with regular diesel (for example, a 20% **b**lend called **B**20). Still, it can be used at 100% (B100). Biodiesel enriched in unsaturated fatty acids has lower melting points and is less prone to problems in cold weather.

As with bioethanol production from lignocellulosic food stocks, biodiesel production has evolved through multiple generations, as shown in Figure 8.1 below.

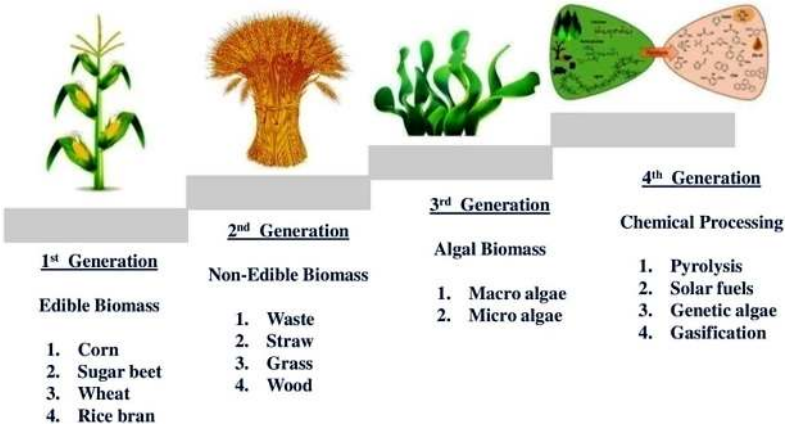


Figure 8.1: Palani Vignesh et al., Oil Gas Sci. Technol. – Rev. IFP Energies nouvelles, 76 (2021) 6. DOI: https://doi.org/10.2516/ogst/2020088. Creative Commons Attribution License (https://creativecommons.org/licenses/by/4.0)

Table 8.1 below shows each biodiesel generation's advantages and disadvantages.

Biodiesel generation	Advantages	Disadvantages
1st generation biodiesel	1. Low emission of greenhouse gas. 2. Easy and low-cost technology for conversion.	1. Yield is inadequate to meet the demand. 2. Causes food shortages. 3. High land footprint.
2nd generation biodiesel	1. Using food waste as a feedstock. 2. Use of non-agricultural land to grow a limited amount of crops.	1. Costly pre-treatment. 2. Sophisticated technology is used to transform biomass into fuel.
3rd generation biodiesel	1. Simple to grow algae. 2. No competition for the use of food crops; wastewater and seawater can be used.	1. More resource usage for algae cultivation. 2. Low lipid level or biomass accumulation in algae.
4th generation biodiesel	1. High biomass and production yield. 2. More capability to eliminate CO_2.	1. The cost of the bio-reactor is higher. 2. At the early stage of research, a high investment is needed.

Table 8.1: Advantages and disadvantages of various biodiesel generations. Palani Vignesh et al., ibid

Triacylglycerol feedstocks for biodiesel are often converted to methyl or ethyl esters through an alcoholysis or transesterification reaction, as shown in Figure 8.2 below.

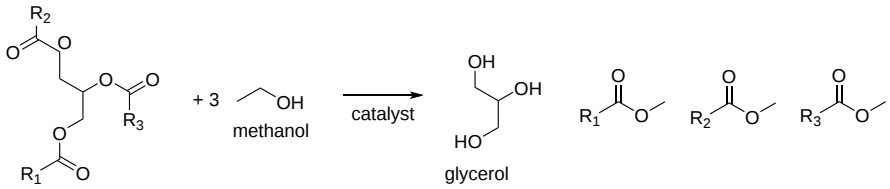


Figure 8.2: Methanolysis/transesterification of triacylglycerol to produce methyl-fatty acid ester for biofuels

This reaction is simply a base-catalyzed cleavage of the ester bonds in the triacylglycerol. Alternatively, vegetable oil can be hydrogenated at high pressure and temperature to produce a variant called "renewable diesel".

Figure 8.3 below shows feedstocks and processing for first-generation biodiesel production.

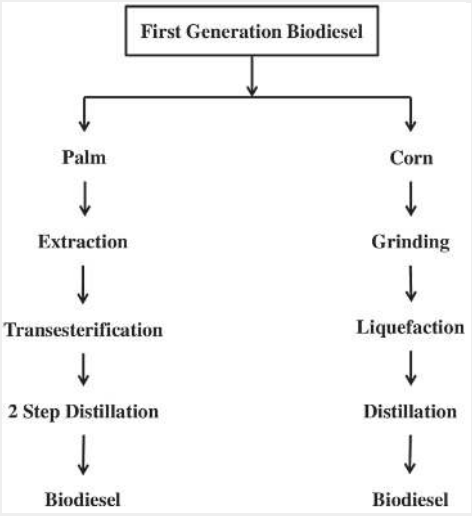
Feedstock: Processing Method	1st Gen Processing
Waste cooking oil: esterification/transesterification Food crops: extraction/transesterification Organic oils: hydrolysis, distillation Animal fat: hydrolysis, fermentation Bioethanol/butanol: chemical synthesis	

Figure 8.3: Feedstocks and processing for first-generation biodiesel production. Palani Vignesh et al., ibid

Figure 8.4 below shows feedstocks and processing for second-generation biodiesel production

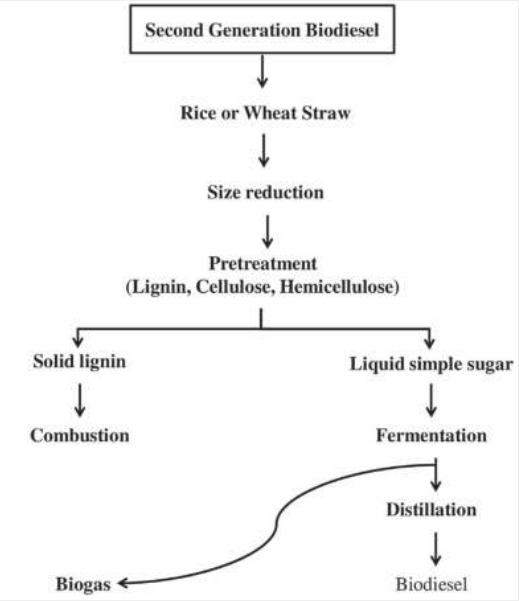
Feedstock: Processing Method	2nd Gen Processing
Cellulose: advanced fermentation Hemicellulose: hydrolysis Lignin: gasification Tannins: biological synthesis Vegetable oil/animal fats: hydrogenation	

Figure 8.4 below shows feedstocks and processing for second-generation biodiesel production. Palani Vignesh et al., ibid

Finally, Figure 8.5 below shows the processing steps for 3rd and 4th generation biodiesel from algae.

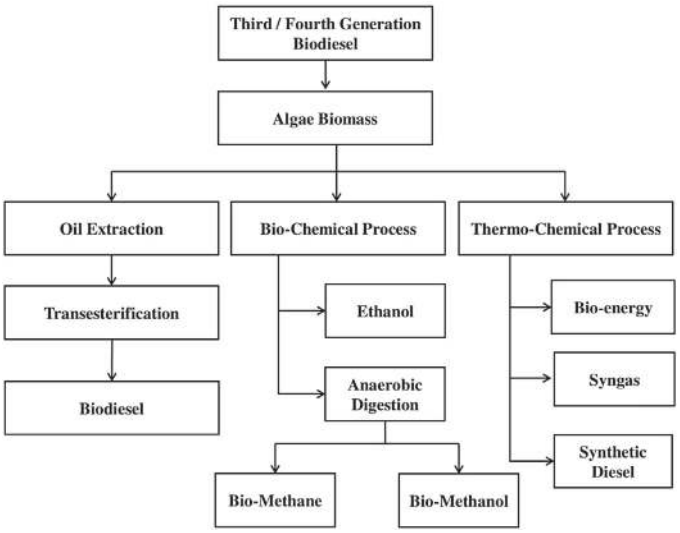


Figure 8.5: Processing steps for 3rd and 4th generation biodiesel from algae. Palani Vignesh et al., ibid

Let's consider 3rd and 4th-generation biodiesel production using algae. First, algae can be used to produce a range of products for biofuels and chemical feedstocks. These are reviewed in Figure 8.6 below.

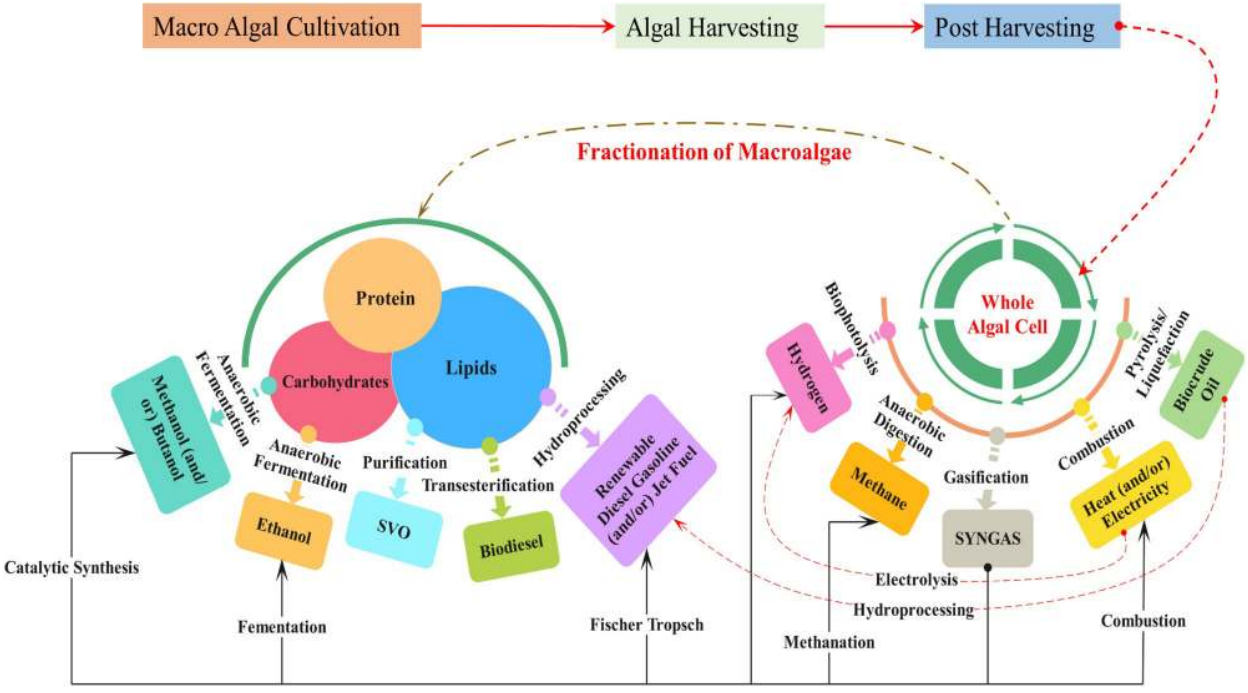


Figure 8.6: Macroalgal biofuel refinery; Godvin Sharmila V et al., Bioengineered. 2021 Dec;12(2):9216-9238. doi: 10.1080/21655979.2021.1996019. PMID: 34709971; PMCID: PMC8809944. Creative Commons Attribution License (http://creativecommons.org/licenses/by/4.0/)

To maximize biodiesel production from algae (3rd and 4th generation), steps in the anabolic pathways for fatty acid and triacylglycerol synthesis could be genetically modified. Below is an overview of triacylglycerol synthesis in microalgae in Figure 8.7.

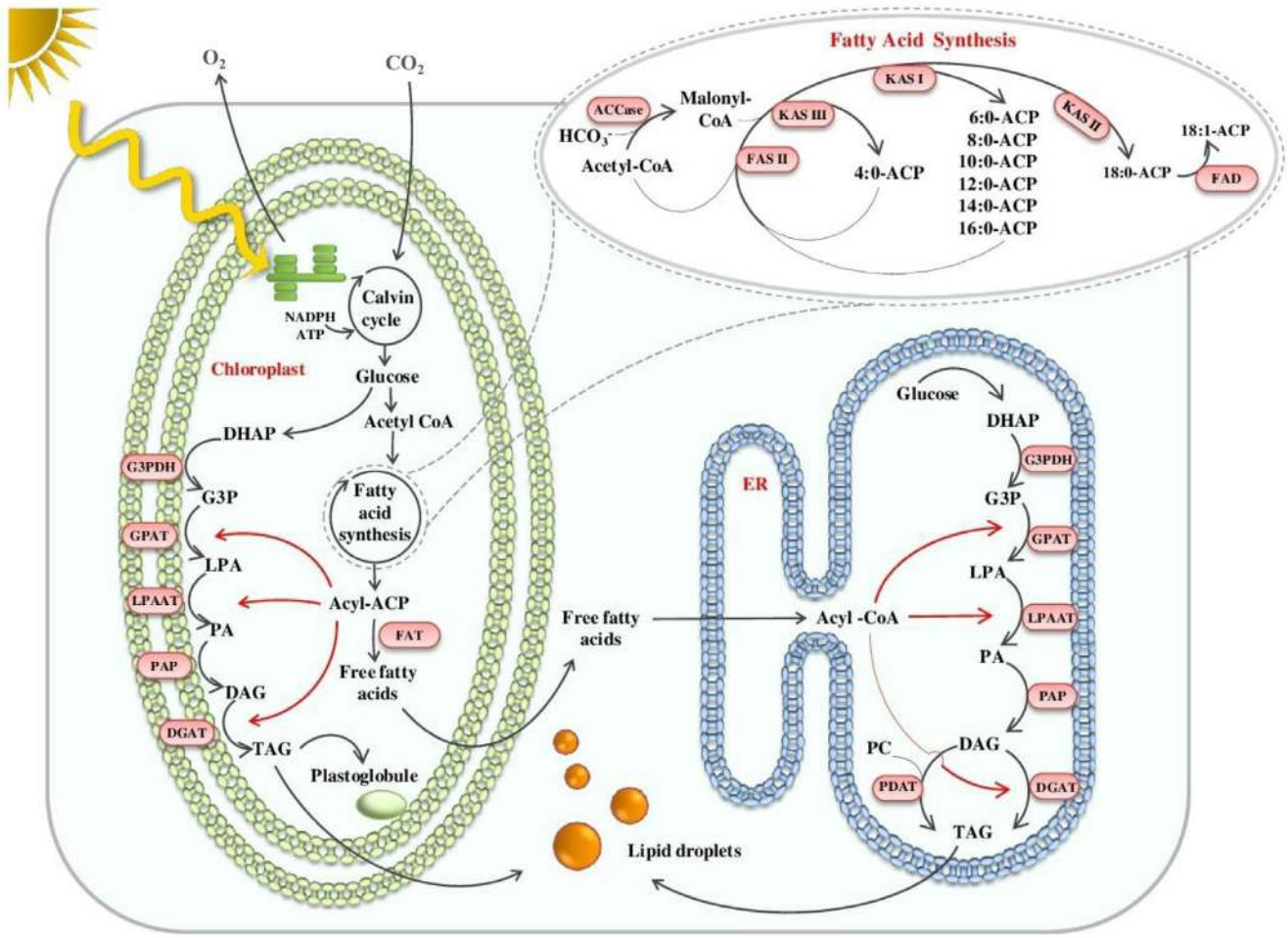


Figure 8.7: Schematic illustration of TAG synthesis in microalgae. NADPH; Nicotinamide adenine dinucleotide phosphate; ATP, Adenosine Triphosphate; DHAP, dihydroxyacetone phosphate; G3P/G3pDH, Glyceraldehyde 3-phosphate / G3P dehydrogenase; GPAT, Glycerol 3-phosphate acyltransferase; PA/LPA/LPAAT/PAP, Phosphatidic acid/Lyso-PA/LPA acyltransferase/PA phosphatase; DAG/DGAT, di-Acylglycerol/ DAG acyltransferase; FAT, Fatty acyl-ACP thioesterase; ACP, Acyl-carrier protein; ER, Endoplasmic reticulum; PC, Phosphatidylcholine; PDAT, Phospholipid: DGAT; ACCase, Acetyl-CoA carboxylase; FAS, Fatty acid synthase; KAS, 3-ketoacyl-ACP synthase; FAD, Flavin adenine dinucleotide. Sharma PK, et al. *Front. Mar. Sci.* 5:382, 2018. doi: 10.3389/fmars.2018.00382. Creative Commons Attribution License (CC BY).

Each step in the combined pathways is a site for optimization, as shown in Figure 8.8 below.

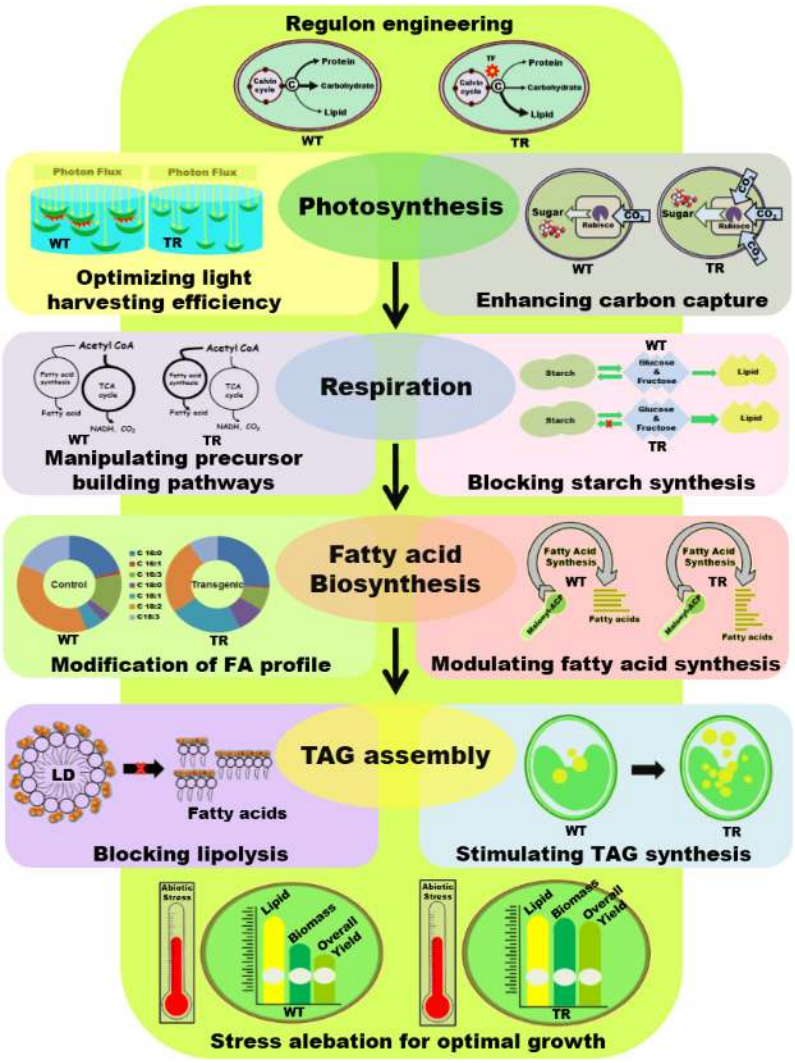


Figure 8.8: Schematic illustration of different genetic engineering strategies applied in microalgae for biodiesel application. WT, Wild type cells; TR, Transgenic cells; TF, Transcription factor; TCA, Tricarboxylic acid cycle; NADH, Nicotinamide adenine dinucleotide; FA, Fatty acid; LD, Lipid droplet. Sharma PK, et al., ibid

Life-cycle analyses of third-generation biodiesel production indicate they would lead to a net decrease in CO2 emissions, but most appear incomplete.

SYNTHETIC GAS (SYNGAS)

What if biomass could produce "gasoline-like" fuel as an alternative to using fossil fuels to power our vehicles and as feedstock for chemical production? We have already discussed the production of bioethanol from 1st-generation (plant starch), 2nd-generation (lignocellulosic), and 3rd-generation (algal) feedstocks. Bioethanol is routinely added to gasoline at up to 15%. It is also found in E85 (or flex fuel), a gasoline blend containing 50% to 80% ethanol.

Instead of producing ethanol from glucose fermentation, wood could be partially burned to produce **"synthetic gases"** (CO and H2), called syngas. These gases could be further burned in vehicles to power them or converted via chemical processes (e.g., the Fischer-Tropsch reaction) into liquid organic fuels.

Indeed, when fossil fuels were lacking, wood was used to create syngas to power vehicles. During World War II, up to a million cars in Europe were powered by wood gas. A bus powered by wood gas (syngas) generated by a gasifier on a trailer is shown in Figure 8.9 below.



Figure 8.9: Bus power by wood gas c. 1943 in Leeds, England. By Ministry of Information Photo Division Photographer, Smith Norman? - http://media.iwm.org.uk/iwm/mediaLib.../large.jpgThis is photograph D 15675 from the collections of the Imperial War Museums. Public Domain, https://commons.wikimedia.org/w/inde...curid=24364067

The syngas emitted was cleaned to remove tars and soot/ash particles by passing through charcoal before entering the vehicle through a tube. Tar with polycyclic aromatic hydrocarbons and methane could be reduced if wood or coal were first converted to char by **pyrolysis** (heating to high temperatures in the relative absence of air) before use.

The gases, derived from the incomplete combustion of wood, contain CO and H_2 in varying proportions depending on the burning temperature and the source (wood or coal). A general and very simplified reaction for the incomplete combustion reaction is:

$$\text{Carbon feedstock} + \text{air} \rightarrow CO + H_2 + CH_4 + CO_2 + H_2O + N_2 \tag{8.1}$$

Of course, the reaction is not clean, and many organic side products are produced.

The relative ratios of CO and H_2 produced can be changed by the addition of water in a second reaction called the **water gas shift (WGS) reaction** (as water shifts the ratio of CO to H_2):

$$CO + H_2O \leftrightarrow CO_2 + H_2 \quad (\Delta H = -41.2 \text{ kJ/mol.}) \tag{8.2}$$

If run in reverse (rWGS) and at high temperatures, the water-shift reaction could be used to capture carbon. The H_2 could come from the electrolysis of water

$$2H_2O(I) \rightarrow 2H_2(g) + O_2(g) \quad (\Delta H = 286 \text{ kJ/mol}) \tag{8.3}$$

The electrocatalytic reduction of CO_2 and H_2O to produce syngas is shown in 8.10.

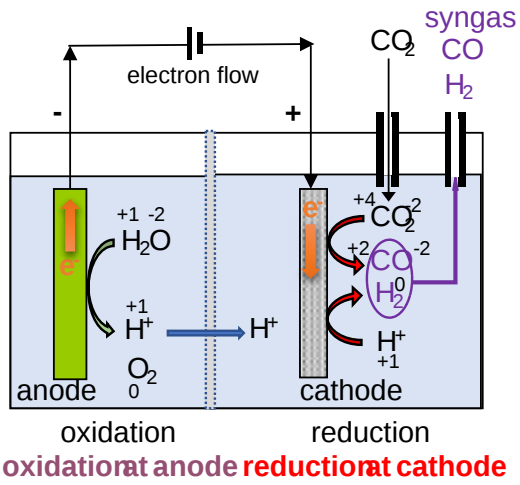


Figure 8.10: Syngas Generation by electrocatalytic reduction of CO_2 and H_2O. (after Kang Cheng et al. Advances in Catalysis, 60 (2017). https://doi.org/10.1016/bs.acat.2017.09.003

The diagram shows the oxidation numbers of each element. The cathode acts as a catalyst for the reaction. Since the reaction requires a power source, this process is greener if the electricity is generated from renewable sources (wind/solar).

ELECTROCATALYTIC REDUCTION OF CO_2 FOR SMALL MOLECULE FUEL AND CHEMICAL FEEDSTOCKS

Electrocatalytic CO_2 reduction (ECR) offers the potential to capture CO_2 before it is emitted into the atmosphere and convert it into small alkanes, alcohols, and acids for fuels (e.g., methanol and ethanol) and for chemical synthesis (e.g., CO and formate). Again, this would require a clean source of electricity to power these endergonic reactions. Table 8.2 below shows the standard reduction potentials for a variety of half-reactions that could be coupled to form the main ECR products.

Products	Acid		Base	
	Equation	*E*(V)	Equation	*E*(V)
Hydrogen	$2H^+ + 2e^- \rightarrow H_2$	0.000	$2H_2O + 2e^- \rightarrow H_2 + 2OH^-$	−0.828
Carbon monoxide	$CO_2 + 2H^+ + 2e^- \rightarrow CO + H_2O$	−0.104	$CO_2 + H_2O + 2e^- \rightarrow CO + 2OH^-$	−0.932
Methane	$CO_2 + 8H^+ + 8e^- \rightarrow CH_4 + 2H_2O$	0.169	$CO_2 + 6H_2O + 8e^- \rightarrow CH_4 + 8OH^-$	−0.659
Methanol	$CO_2 + 6H^+ + 6e^- \rightarrow CH_3OH + H_2O$	0.016	$CO_2 + 5H_2O + 6e^- \rightarrow CH_3OH + 6OH^-$	−0.812
Formic acid/formate	$CO_2 + 2H^+ + 2e^- \rightarrow HCOOH$	−0.171	$CO_2 + H_2O + 2e^- \rightarrow HCOO^- + OH^-$	−0.639
Ethylene	$2CO_2 + 12H^+ + 12e^- \rightarrow C_2H_4 + 4H_2O$	0.085	$2CO_2 + 8H_2O + 12e^- \rightarrow C_2H_4 + 12OH^-$	−0.743
Ethane	$2CO_2 + 14H^+ + 14e^- \rightarrow C_2H_6 + 4H_2O$	0.144	$2CO_2 + 10H_2O + 14e^- \rightarrow C_2H_6 + 14OH^-$	−0.685
Ethanol	$2CO_2 + 12H^+ + 12e^- \rightarrow CH_3CH_2OH + 3H_2O$	0.084	$2CO_2 + 9H_2O + 12e^- \rightarrow CH_3CH_2OH + 12OH^-$	−0.744
Acetic acid/acetate	$2CO_2 + 8H^+ + 8e^- \rightarrow CH_3COOH + 2H_2O$	0.098	$2CO_2 + 5H_2O + 8e^- \rightarrow CH_3COO^- + 7OH^-$	−0.653
n-Propanol	$3CO_2 + 18H^+ + 18e^- \rightarrow CH_3CH_2CH_2OH + 5H_2O$	0.095	$3CO_2 + 13H_2O + 18e^- \rightarrow CH_3CH_2CH_2OH + 18OH^-$	−0.733

Table 8.2: Lei Fan et al. Science Advances. 21 Feb 2020, Vol 6, DOI: 10.1126/sciadv.aay3111. Creative Commons Attribution-NonCommercial License 4.0 (CC BY-NC).

The reactions are complex and require CO_2 to adsorb onto the cathode's electrocatalytic surface. Here is a possible reaction pathway for the conversion of CO_2 to methane:

$$CO_2 \rightarrow *COOH \rightarrow *CO \rightarrow *CHO \rightarrow *CH_2O \rightarrow *CH_3O \rightarrow CH_4 + *O \rightarrow CH_4 + *OH \rightarrow CH_4 + H_2O \quad (8.4)$$

The catalysts employed are heterogeneous (i.e., not in solution) and typically organometallic transition-metal complexes. Possible reaction pathways to produce small CO_2 electrochemical reduction products are shown in Figure 8.11 below.

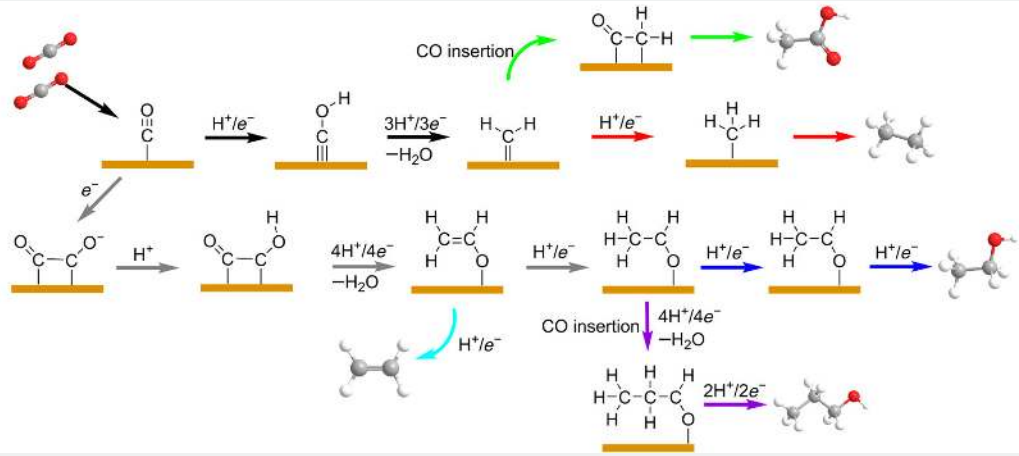


Figure 8.11: Possible reaction pathways to produce small CO_2 electrochemical reduction products. Lei Fan et al., ibid

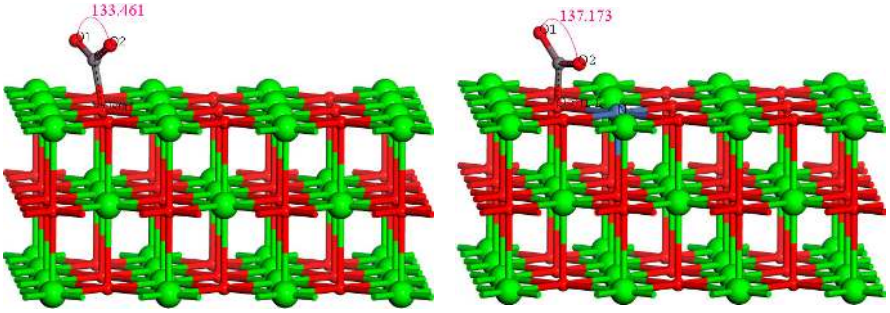
This technology is still in development, and it will require the development of more robust catalysts and cells before it becomes commercially viable.

The synthesis of syngas (typically described as a mixture of CO, CO_2, and H_2) is widespread, used in various processes, and used to make many products, including hydrocarbons for fuel and oxygen-containing derivatives such as methanol and ethanol. CO and H_2 produce alkanes and alkenes in the Fischer-Tropsch reaction (described below).

$$CO + 2H_2 \rightarrow (CH_2) + H_2O \quad \Delta H = -165\ kJ/mol \quad (8.5)$$

where CH_2 is a methylene repeat in longer-chain alkanes.

The CO_2 produced in syngas can be somewhat selectively removed by adsorption onto a CaO catalyst, as shown in Figure 8.12 below.



(a) (b)

Figure 8.12: Adsorption configurations of CO_2 on the surfaces of CaO-based catalysts at 650 °C: (**a**) CO_2 adsorption on CaO (100) surface; (**b**) CO_2 adsorption on 10 wt% % Ni/CaO (100) surface. Green, red, gray, and purple balls represent Ca, O, C, and Ni atoms. Zhao, B. et al. *Catalysts* **2019**, *9*, 757. https://doi.org/10.3390/catal9090757. Creative Commons Attribution (CC BY) license (**http://creativecommons.org/licenses/by/4.0/**)

CO, CH4, and H2 adsorption energies are so small that they have little effect on CO_2 adsorption.

At present, the easiest way to make syngas is to react natural gas (methane) and steam under very high temperatures (up to 1000 °C) over a Ni catalyst (a process called steam reforming). This results in a high H_2/CO ratio of about 3. It can be done with liquified natural gas using Ni-ZrO_2-CeO_2-La_2O_3 catalyst. This process inherently would do little to decrease CO_2 emissions. A **gasification** method converts coal, lignocellulosic biomass, and waste to syngas, with an H_2/CO ratio of <1 for coal and about 0.6-1 for biomass. The electrocatalytic method described above has an H_2/CO ratio of 0-2, depending on the nature of the cathodic catalyst. Syngas can also be produced by partial oxidation of methane. For the subsequent reactions (Fisher-Tropsch), the optimal H_2/CO is about 2. In the gasification of lignocellulosic

biomass, the water-gas shift (WGS) reaction is used to increase the H_2/CO ratio. This requires lots of water and also produces CO_2. The water shift reaction use catalysts such as Co–Mo–Al_2O_3, Fe_2O_3–Cr_2O_3, and Cu–ZnO–Al_2O_3) for coal gasification.

Syngas can be used to make small-molecule energy and chemical feedstocks, such as ethanol (as well as liquid alkanes and alkenes). Given the many types of products, it is often essential to selectively produce and purify them for commercial use. One method for ethanol production is shown in Figure **8.13** below.

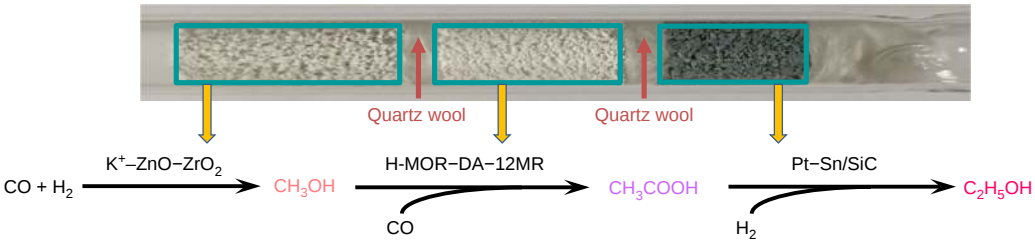


Figure 8.13: Conversion of syngas to ethanol proceeds through a tandem mechanism via methanol and acetic acid intermediates using a variety of sequentially positioned catalysts. Kang, J., He, S., Zhou, W. *et al.* Single-pass transformation of syngas into ethanol with high selectivity by triple tandem catalysis. *Nat Commun* **11**, 827 (2020). https://doi.org/10.1038/s41467-020-14672-8. Creative Commons Attribution 4.0 International License. http://creativecommons.org/licenses/by/4.0/.

H-MOR is a zeolite, a microporous, crystalline structure made of aluminosilicate.

Bioethanol can also be converted to CO and H_2 via steam reforming, as shown in the equation below.

$$\mathbf{C_2H_5OH + H_2O(+\ heat\ ) \rightarrow 2CO + 4H_2} \tag{8.6}$$

Even with the ability to capture CO_2 from syngas synthesis, a central concern is whether syngas and syngas-derived fuels are associated with lower net CO_2 emissions. A life cycle analysis would be necessary to determine this.

FISCHER-TROPSCH SYNTHESIS (FTS) OF FUELS

Fischer was head of the Kaiser-Wilhelm Institute for Coal Research in Germany at the start of World War I. Germany had abundant coal but needed oil for the war, so its efforts were redirected toward that end. Fischer and Tropsch developed the water shift reaction discussed above. They deployed new cobalt catalysts to produce oil, ultimately covering 25% of car fuel and 10% of German military fuel needs in World War II. Large amounts were also made in South Africa during the Apartheid regime.

The Fischer–Tropsch synthesis (FTS) is a polymerization-like reaction that is used to convert gas-to-liquids (GTL), coal-to-liquids (CTL), or biomass-to-liquids (BTL) fuels. It starts with syngas (H_2 and CO) produced from the gasification of coal/biomass or from steam reforming/partial oxidation of natural gas, with the H_2/CO ratio determined by the water-shift reaction. If coal or biomass is used, a cleanup of residual products with heteroatoms and metal ions is necessary. The clean syngas is then passed into a reactor containing the catalyst required for FTS of fuels. These reaction systems are summarized in Figure **8.14**.

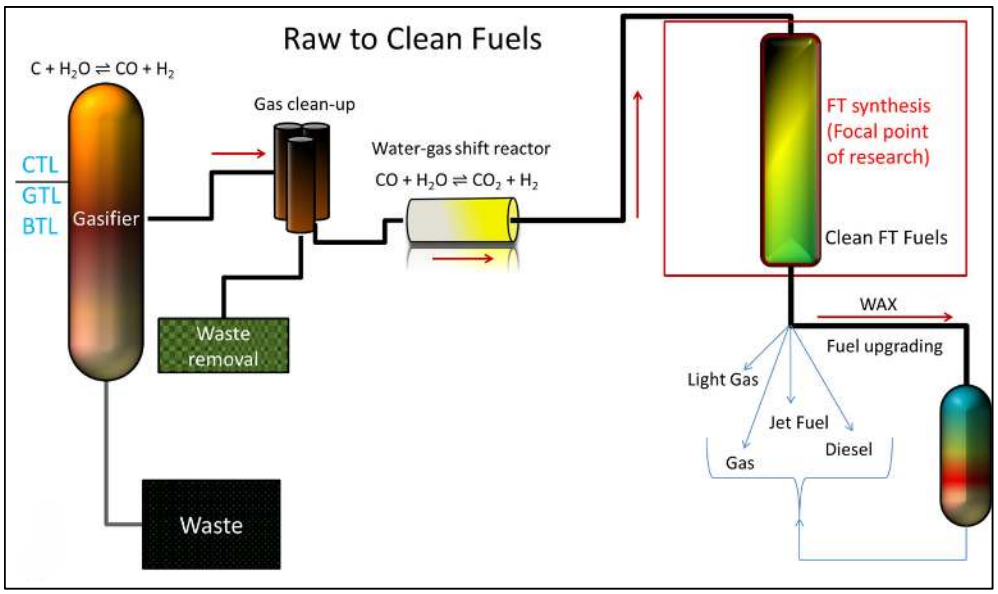


Figure 8.14: A simplified diagram of the Coal-to-Liquids (CTL), Gas-to-Liquids (GTL), and Biomass-to-Liquids (BTL) processes. Shafer, W.D.; Gnanamani, M.K.; Graham, U.M.; Yang, J.; Masuku, C.M.; Jacobs, G.; Davis, B.H. Fischer–Tropsch: Product Selectivity–The Fingerprint of Synthetic Fuels. *Catalysts* **2019**, *9*, 259. https://doi.org/10.3390/catal9030259. Creative Commons Attribution (CC BY) license (**http://creativecommons.org/licenses/by/4.0/**).

The FTS reaction is conducted at moderate temperatures and pressure to produce fuels (diesel and jet), lubricants, waxes, and chemical feedstocks. The main representative reactions are given by:

N-alkane production:

$$(2n+1)H_2(g) + nCO(g) \rightarrow C_nH_{2n+2} + nH_2O \tag{8.7}$$

Alkene production:

$$(2n)H_2(g) + nCO(g) \rightarrow C_nH_{2n} + nH_2O \tag{8.8}$$

The products can range from 1 carbon (CH4) to over 70, depending on the catalyst, T, P, and the H2/CO ratio. The FTS is a polymerization reaction that begins when the gas adsorbs onto the catalytic surface. It is followed by multiple cycles of free radical initiation, propagation, termination, desorption, and reabsorption.

Since this book focuses on structure/function and reaction mechanisms, we would be remiss not to include at least a simplified mechanism for these complex reactions. Several mechanisms have been proposed. Since iron was/is used in the catalyst, and since iron can form iron carbides, Fisher proposed a carbide mechanism. A second enol mechanism has also been proposed. Both are shown in Figure 8.15 below.

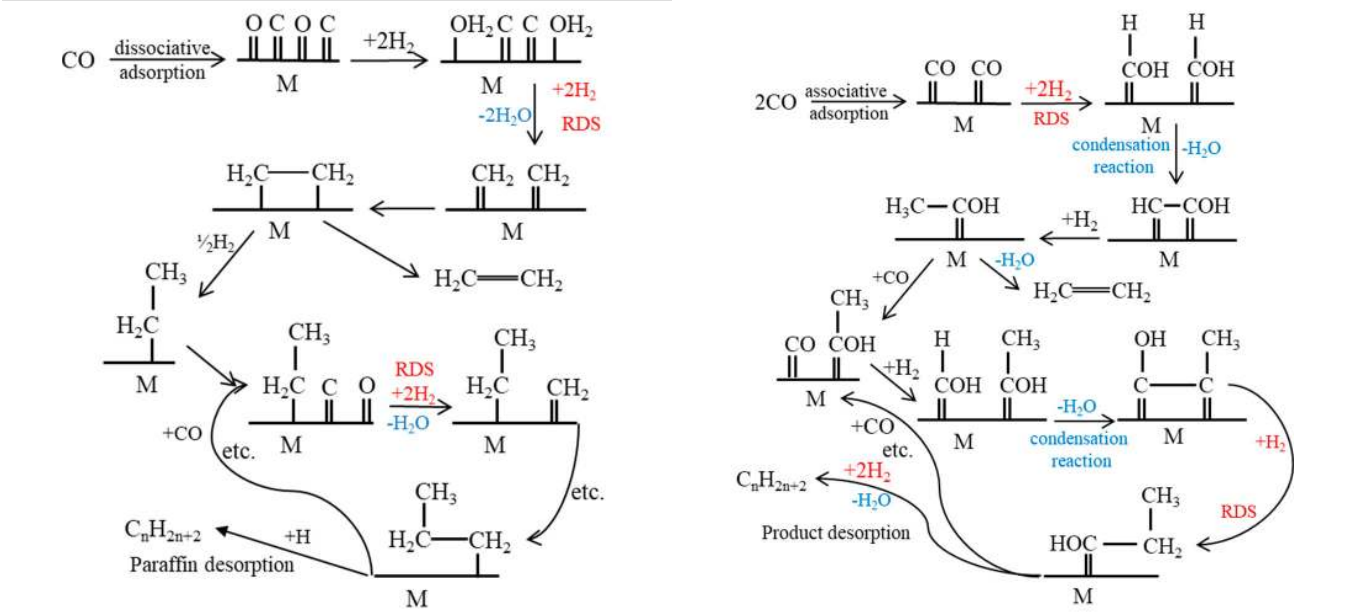


Figure **8.15**: Proposed mechanisms for the Fischer-Tropsch reaction. Left: A proposed FTS route based on the carbide mechanism; Right: A proposed FTS route based on the enol mechanism. M is the metal surface.

In the carbide mechanism, CO adsorbs on the metal catalyst and dissociates into C and O atoms that cover the surface. These are hydrogenated to form H_2O and CH_2 (methylene), and H_2 adds as the reaction proceeds, as shown.

In the enol mechanism, CO adsorbs without dissociation into atoms. It reacts on the surface to surface-bound H atoms (that arise from the dissociation of adsorbed H_2) to form hydroxymethylene (M-CHOH). This enol condenses with adjacent hydroxymethylenes. The rate-determining step is the hydrogenation of adsorbed CO.

Another proposed mechanism, CO insertion, is shown in Figure **8.16**

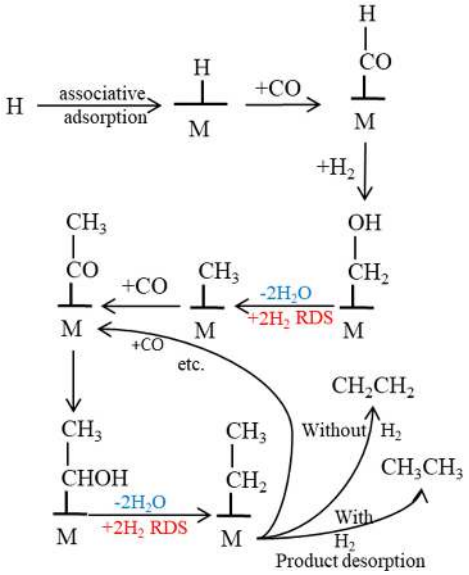


Figure **8.16**: A proposed FTS route based on the CO insertion mechanism.

In this model, CO inserts into a bond from a hydrogen atom to a metal on the catalyst. The rate-limiting step is the hydrogenation of CO to the CH_2 methylene group. The assumed monomer in this mechanism is simply CO, which inserts into metal-carbon bonds.

Generally, the FTS reaction catalyst has either cobalt or iron ions. The metal catalyst can also be doped with potassium and copper ions and bind silica and alumina. Iron is abundant and cheap and better promotes the water-gas-shift reaction, so it is best for FTS of fuels from coal and biomass since syngas derived from them has a lower H_2/CO ratio.

https://geo.libretexts.org/@go/page/34463

CHEMICAL SYNTHESIS OF FOOD

Suppose fuels can be synthesized from nonpetroleum sources and agricultural waste. Why not use the reactions described above (such as syngas production, the Fischer-Tropsch process, and electrochemical reduction) to make food, not just fuel? The agricultural sector accounts for about 25% of total greenhouse gas emissions, so it is ripe (no pun intended) for novel ways to produce foodstuffs (think of them as feedstocks for human consumption).

It should be obvious from the chemistry that the simplest type of food produced by these reactions is fats, rather than the more synthetic and stereochemically complex proteins and carbohydrates. Presently, the world relies on palm oil derived from palm trees as a fat source in crackers, cookies, breads, and other food products. Typical palm oil production has been associated with large-scale deforestation of rainforests and their associated impacts on climate and biodiversity. Americans consume about 8 kg (17.6 lbs) of palm oil products yearly, including cosmetics, cleaning products, and waxes. Figure 8.17 below shows the scale of palm oil production in the world, which might come as a surprise since we more frequently encounter soybean, sunflower, rapeseed (source of canola oil), and olive oils in our stores.

Figure 8.17: Vegetable Oil Product in the World. Our World in Data. https://ourworldindata.org/palm-oil

The general chemical pathways used to synthesize proteins, fats, and carbohydrates are illustrated in Figure 8.18 below. The fat synthesis pathways relevant to this discussion are represented in the central part of the figure.

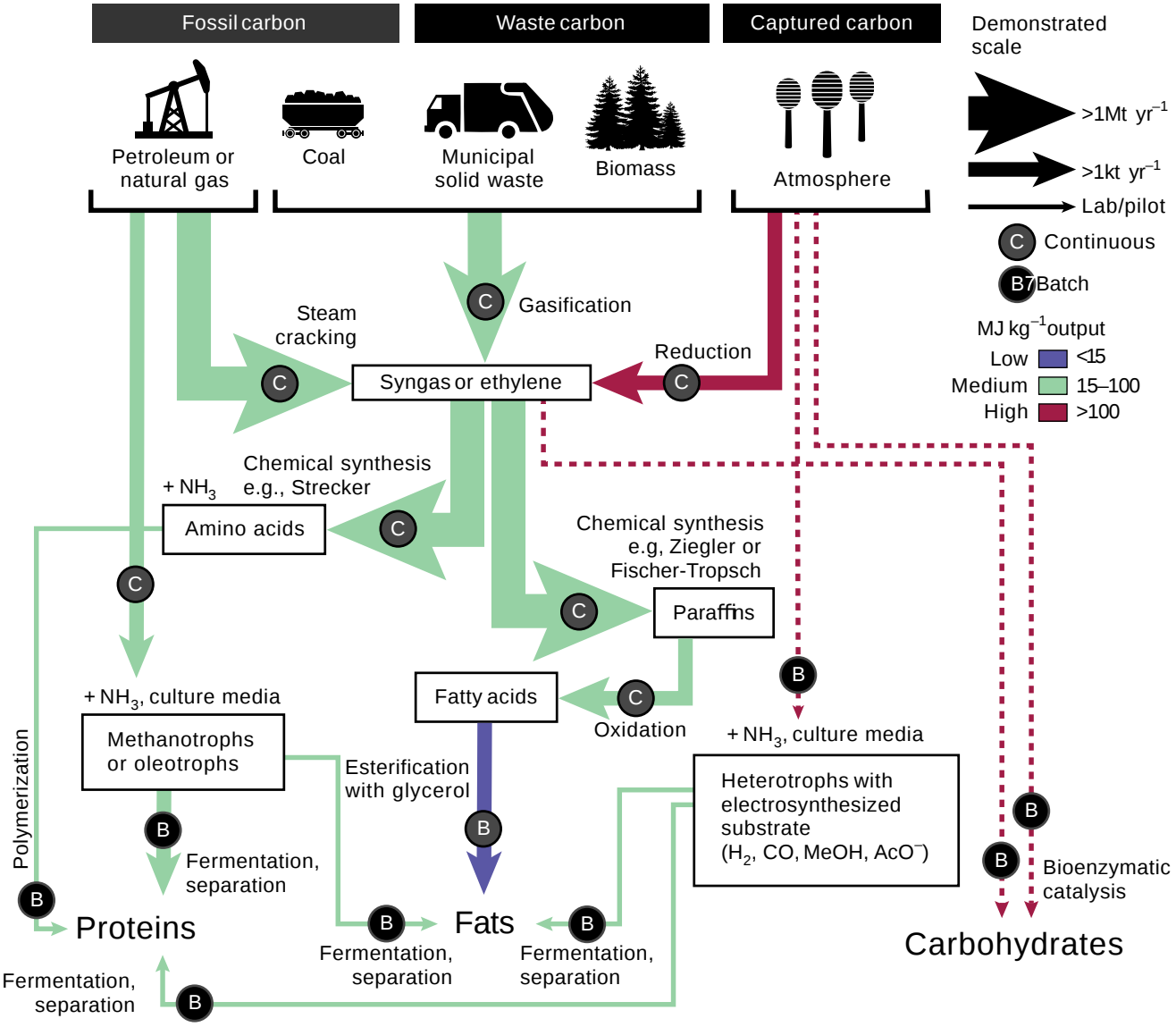


Figure 8.18: **Schematic of potential pathways to synthesize food without agriculture.** Davis, S.J., Alexander, K., Moreno-Cruz, J. *et al.* Food without agriculture. *Nat Sustain* (2023). https://doi.org/10.1038/s41893-023-01241-2. Creative Commons Attribution 4.0 International License. http://creativecommons.org/licenses/by/4.0/.

Proteins, fats, and carbohydrates can be synthesized from various carbon feedstocks through chemical and biological pathways (arrows). The weight and color of the arrows indicate the scale at which the different processes have been demonstrated and the energy required per mass unit output, respectively. Dashed lines indicate where energy requirements remain highly uncertain. Circular labels on each arrow further indicate whether the process is typically continuous (C) or batched (B). NH_3 is ammonia, H_2 is hydrogen gas, MeOH is methanol, and AcO^- is acetate (agriculturally produced carbon feedstocks are omitted).

It is estimated that chemical synthesis of fats could yield <0.8 g CO_2 equiv/kcal, compared with>1.5 g CO_2 equiv/kcal for the current biological synthesis and processing of palm oil in Brazil or Indonesia. This advantage would increase if the CO_2 for the chemical synthesis could be captured from the atmosphere, yielding net-zero emissions.

Figure 8.19 shows both land use and energy emissions of $CO_{2\ equiv}$/kcal for agriculturally produced fats (panel a) versus equivalents for chemical-synthesized fats.

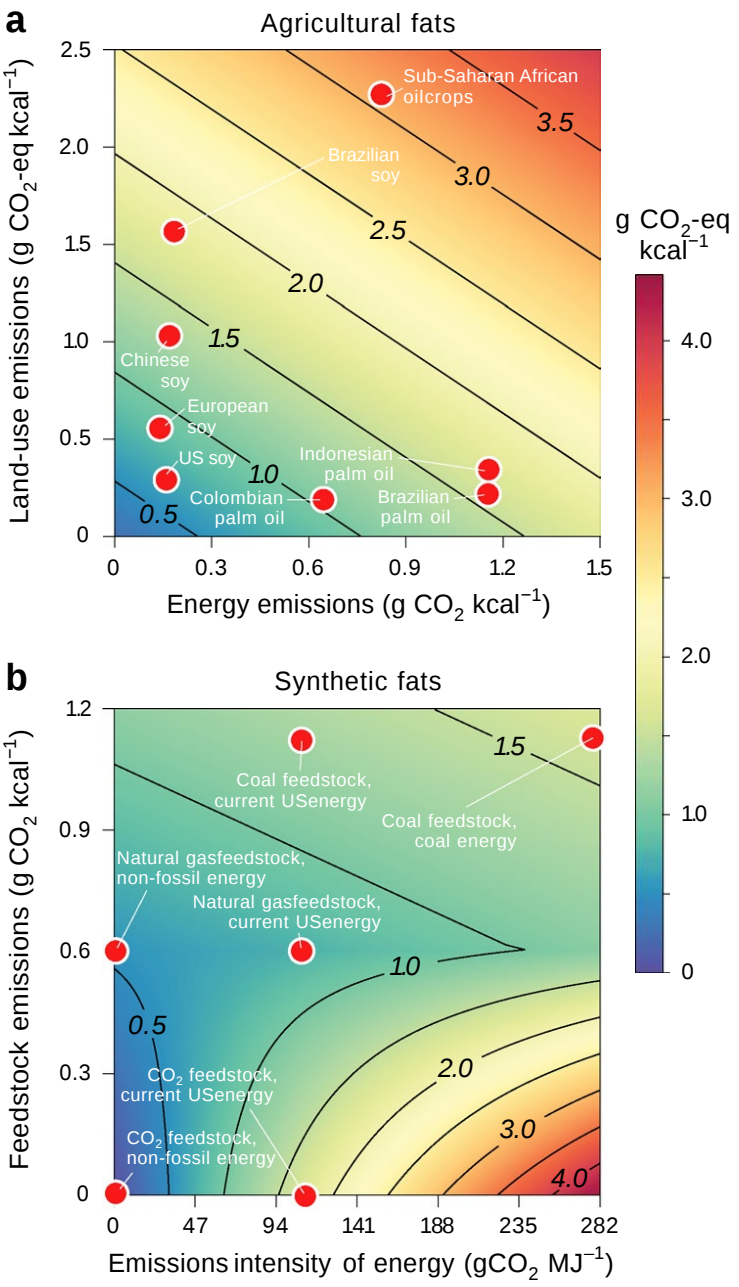


Figure 8.19: **Comparison of emissions per calorie of edible fats.** Davis, S.J et al., ibid.

Panels a and **b** use shading and contours to show grams of CO_2-equivalent GHG emissions per kilocalorie of edible fat produced by conventional agriculture (Panel **a**) and chemical synthesis (Panel **b**). Agricultural emissions are shown as the sum of land-use emissions (*y*-axis) and energy-related emissions (*x*-axis), and emissions from synthesis are shown as a function of feedstock emissions intensity (*y*-axis) and energy emissions intensity. Red circles denote specific estimates based on literature and assumed values. Feedstock emissions include process-related conversion of feedstock to CO2—for example, during the extraction of natural gas, the gasification of coal, and the eventual human respiration of fossil feedstock.

BIOAVIATION FUEL

Now we can turn our attention to the production and analysis of bioaviation fuel, which is more similar to kerosene and diesel than to ethanol in its composition. As we saw for bioethanol production, the feedstocks can be 1st, 2nd, and 3rd generation, as shown in Table **8.3** below.

https://geo.libretexts.org/@go/page/34463

First-generation (1-G)	Second-generation (2-G)	Third-generation (3-G)	Fourth-generation (4-G)
• Oil-seed crops: camelina, oil palm, rapeseed, soybean, sunflower, salicornia • Sugar and starchy crops: corn, wheat, sugarcane, sugar beets	• Oil-seed energy crops: jatropha, castor bean • Grass energy crops: switchgrass, miscanthus, Napier grass • Wood energy crops: poplar, willow, eucalyptus • Agricultural and forestry residues: corn stover, sugarcane bagasse, wood harvesting/processing residues • Food and municipal waste: used cooking oil, animal fats, biogenic fraction of municipal solid waste	• Algae: microalgae	• Genetically modified organisms • Non-biological feedstocks: CO2, renewable electricity, water

Table 8.3: Feedstocks for bio-aviation fuel production. Doliente SS, Narayan A, Tapia JFD, Samsatli NJ, Zhao Y and Samsatli S (2020) Bio-aviation Fuel: A Comprehensive Review and Analysis of the Supply Chain Components. *Front. Energy Res.* 8:110. doi: 10.3389/fenrg.2020.00110. Creative Commons Attribution License (CC BY).

A typical jet aviation fuel (Jet A-1) contains n- and branched-alkanes (often called paraffins) and some alkenes (often called olefins) with 8-16 carbon atoms, cycloalkanes, and aromatics. A comparison of the components of Jet-A1 with a typical bioaviation fuel, Bio-Jet, is shown in Figure 8.20 below.

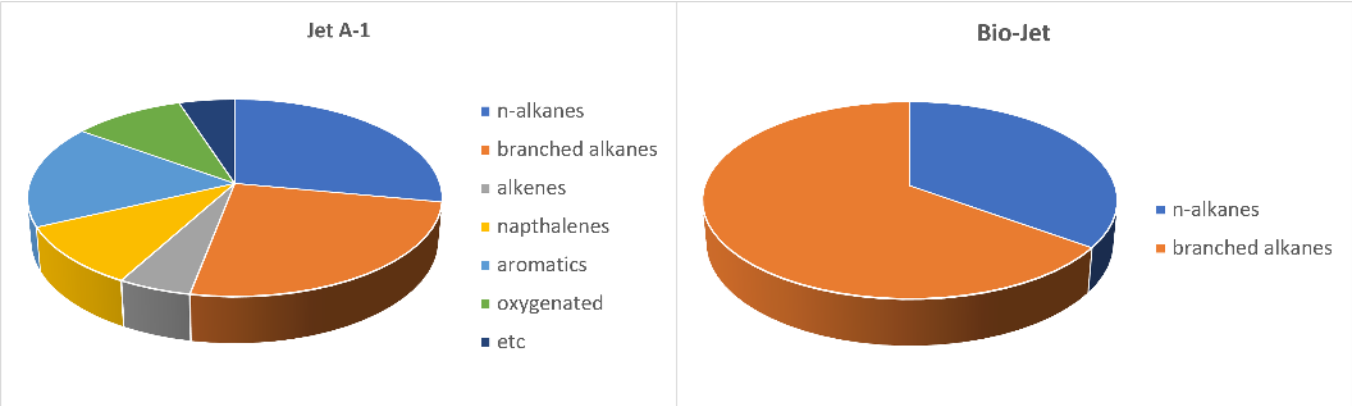


Figure 8.20: Molecular-class compositions of (a) Jet A-1 and (b) bio-jet identified by the relative signal area percentage analysis of GC–MS. After Cheon Hyeon Cho, Hee Sun Han, Chae Hoon Sohn, and Jeong Sik Han. *ACS Omega* **2021** *6* (40), 26646-26658. DOI: 10.1021/acsomega.1c04002.

Bioaviation fuel can be made from feedstocks containing triacylglycerols or from readily available feedstocks shown in Table 2 above, to produce syngas for use in the Fischer-Tropsch reaction. We've already discussed those reactions above. Instead, let's focus on whether bioaviation fuel, better termed sustainable aviation fuels (SAF), is good for our climate. This presupposes that battery-powered planes and jets are not scalable to our current environmental needs.

LIFE CYCLE ANALYSIS - JET FUEL FROM GRASSES

As expected, the US is the largest user of aviation fuel and accounts for 25% of aviation CO_2 emissions, as much as all the greenhouse gases emitted from fuel use in Spain. It is estimated that the US will need approximately 30 billion gallons per year (BGY) of jet fuel in 2040. A bio-jet fuel industry based on cellulose as a feedstock could theoretically produce that amount. If the industry costs are estimated at $123 billion, then the cost of jet fuel would be $4.30/gal. About 60% of the costs would arise from biomass conversion to sustainable aviation fuel (SAF), which we described above. Those costs include the building of the biorefineries. Their cost would be spread over the plants' lifetimes. The fuel would be derived from syngas from the Fisher-Tropsch reaction, a reasonably mature technology. The costs would be much lower (closer to $1/gal) if infrastructure costs were excluded. These total costs are comparable to the price paid for regular jet fuel (around $2.2/gal in 2021). Consumer costs would not go up 2-fold since fuels are only part of the cost paid by passengers (15-25%)

Consumers' current prices for fossil fuels are well below their actual costs. The present price/gal does not include the external costs of using fossil fuels. These include climate change impacts on infrastructure, agriculture, industry, and other sectors, as well as on human health (primarily through negative health consequences and diseases exacerbated by fossil fuel pollution). We all ultimately pay for these hidden costs resulting from a failed market for pricing fossil fuels. On top of this, the fossil fuel industry has been massively subsidized for decades.

2026 IRAN WAR

The 2026 war in Iran has produced the largest energy shock in history. It is presently (May 2026) being felt more outside the US. The availability of aviation fuel has been seriously compromised. 20% percent of oil passes through the Strait of Hormuz. Most oil refining to produce jet fuel occurs in Asia, which imports most of its oil from the Middle East. Kuwait and Bahrain are leading producers of jet fuel, which also passes through the Strait. Jet fuel has doubled in cost. This latest energy crisis is likely to catalyze the shift away from fossil fuels toward locally produced clean energy.

Different prices have been placed on carbon emissions from fossil fuels to resolve this issue in the market. The carbon price is based on the number of tons of CO_2 equivalent emitted ($US/ton CO_2e). If a reasonable carbon price is applied, bio-jet fuels produced from lignocellulosic feedstocks via the Fischer-Tropsch reaction would be theoretically competitive with conventional jet fuels derived from fossil fuels. The extra added cost for sustainable aviation fuel (SAF) compared to traditional aviation fuel at different prices placed on carbon is shown in Table **8.4** below, assuming an average cost of $2.20/gal for traditional aviation fuel.

Price on carbon ($US/t CO2e)	SAF - Traditional Aviation Fuel ($/gal)
0	+$1.90/gal
$50	+$0.60/gal
$175	$0

If the cost of traditional jet fuel rose to $3/gal, as it did in the US in March 2022, SAF and conventional jet fuel would cost the same if a carbon price of $100/t CO2e were applied to both. The actual "social" cost of carbon has been calculated (9/22) to be $175/ton CO_2e.

Factors other than carbon costs should be included in these analyses. These include the issue of sustainable land use for SAF feedstocks. A recent analysis shows that it would be possible to produce 30 billion gall/yr of cellulosic SAF by planting 23.2 Mha (Million hectares, about the size of the state of Wyoming) of marginal agricultural lands (about one-third of croplands and 2/3 noncrop lands) in the Midwest with miscanthus, with a net cost of $4.1/gal and assuming a carbon price of a $50/ t CO2e. Miscanthus is a rapidly growing, tall perennial grass with a high yield that grows in moderate climates. The life-cycle analysis included interactions among the atmospheric, land-surface, ecosystem, and economic systems. Miscanthus gigantheus is shown below in Figure **8.21**.

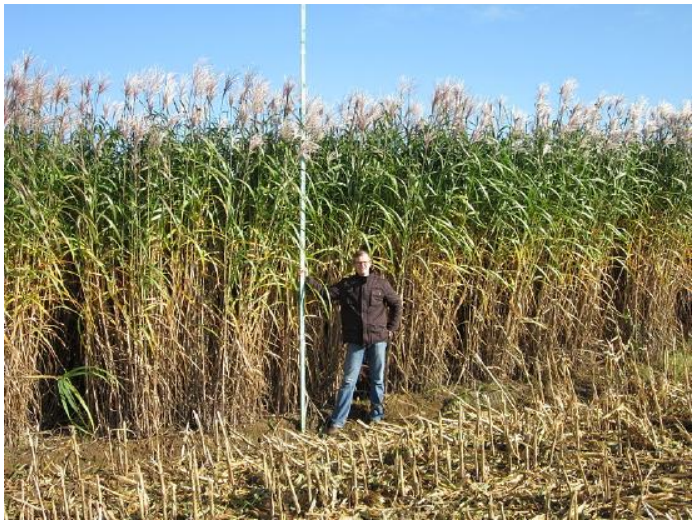


Figure **8.21**:Miscanthus gigantheus. https://commons.wikimedia.org/wiki/F...us_Bestand.JPG. Creative Commons Attribution-Share Alike 3.0 Unported

Figure **8.22** shows some data from the study. Four scenarios are presented, each represented by a bar graph.

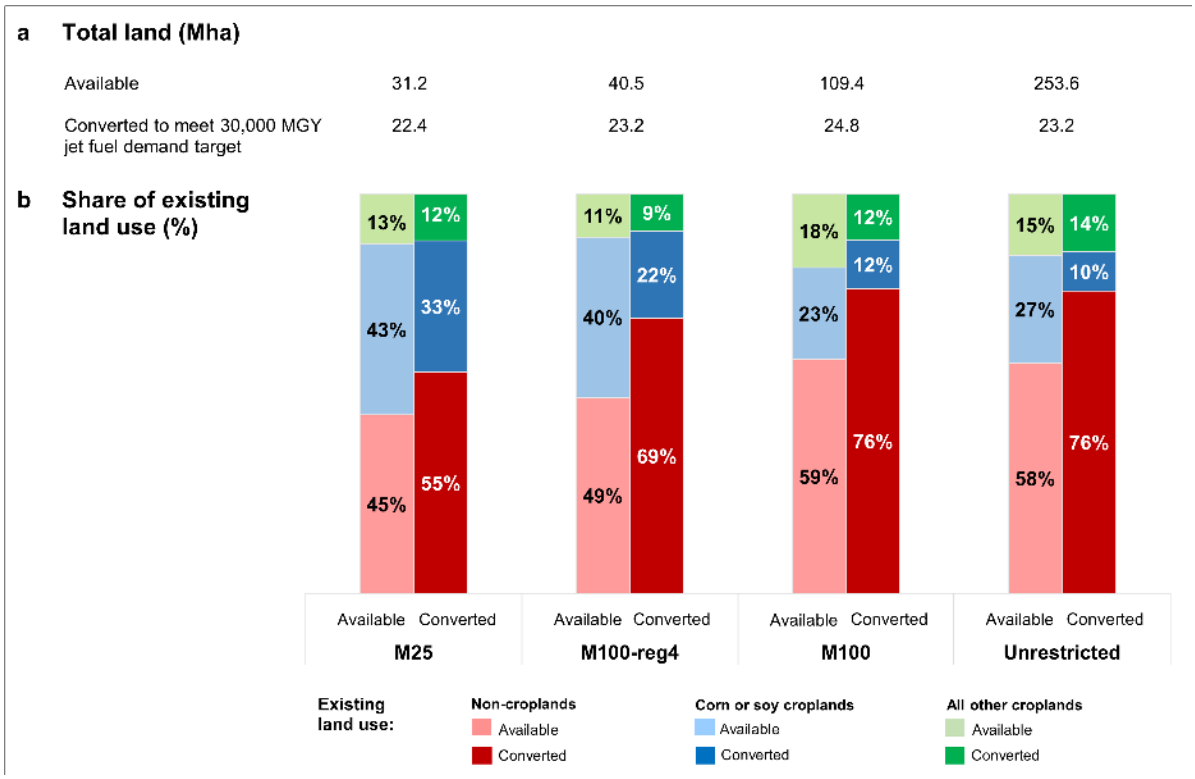


Figure 8.22: Land availability and conversion by existing use. Excel data and graph from https://dataverse.harvard.edu/datase...910/DVN/VBFLI2. CC0 1.0 Public Domain.

Four scenarios (left to right) produced 30 MG/yr of SAF using a carbon price of $50/t CO2e.

- M25: only 25% of the marginally useful land was used
- M100-reg4: marginal land bases with the lowest hydrological and climatic risks
- M100: all of the marginally included land was made available
- Unrestricted

Panel (a) shows that in each case, about 23.2 Mha of land was converted to growing miscanthus from the available land. Pane (b) shows stacked bars showing the percentages of each land type available and converted for each scenario. The last scenario shows that demand can be met with the lowest % conversion of marginal land to corn/soybeans and other crops. It would appear that the marginal croplands converted to SAF production would be the same lands diverted to bioethanol production. Nevertheless, it would appear that up to 76% of projected aviation fuel needs could be met by planting marginal cropland and noncrop land for cellulosic SAF production. The study found that using available lands in the Plains was not feasible.

SUMMARY

(Summary written by Claude, Anthropic)

This chapter examines three advanced routes to replacing fossil fuels in transportation: biodiesel from triacylglycerols, liquid fuels from syngas via Fischer-Tropsch synthesis, and sustainable aviation fuel (SAF) — connecting chemistry and biochemistry to climate policy and life cycle analysis.

Biodiesel. Diesel fuel (C12–C20 hydrocarbons, 75% saturated, 25% aromatic) releases more energy per liter (36.9 MJ) than gasoline (33.7 MJ) and ignites by compression rather than spark. Biodiesel is produced by transesterification (methanolysis) of triacylglycerols — a base-catalyzed alcoholysis that replaces the glycerol backbone with methanol to produce fatty acid methyl esters (FAME) and free glycerol. First-generation biodiesel from edible crops (palm oil, soybean, rapeseed) is constrained by food competition and land use. Second-generation biodiesel from non-edible waste oils reduces this conflict. Third-generation biodiesel from microalgae avoids cropland competition entirely and can use wastewater or seawater for cultivation; fourth-generation approaches use genetically engineered organisms or non-biological CO_2 feedstocks. To maximize triacylglycerol yields in microalgae, genetic engineering targets the fatty acid synthesis pathway at multiple nodes: acetyl-CoA carboxylase (ACCase, the committed step), fatty acid synthase (FAS), fatty acyl-ACP thioesterase (FAT), and the Kennedy pathway enzymes GPAT, LPAAT, PAP, and DGAT that assemble triacylglycerols in the endoplasmic reticulum.

Syngas: production and uses. Syngas — a mixture of CO and H_2 — has powered vehicles since World War II, when up to one million European cars ran on wood gas from vehicle-mounted gasifiers. It is produced by incomplete combustion of wood or coal, steam reforming of natural gas (H_2/CO ~3, using Ni catalyst at up to 1000°C), or gasification of coal/biomass (H_2/CO ~0.6–1). The water-gas shift reaction (CO + H_2O → CO_2 + H_2) adjusts the H_2/CO ratio upward; its reverse (rWGS) at high temperatures can be used for CO_2 capture. Electrocatalytic CO_2 reduction (ECR) — using electrons from water oxidation at an anode to reduce CO_2 at a biocathode — offers a potentially carbon-neutral route to syngas, methanol, formate, ethanol, and methane, provided the electricity is renewable. Standard reduction potentials for these half-reactions range from ~−0.1 to −0.5 V vs. SHE, with multi-electron products requiring progressively more reductive conditions. CO_2 can be selectively removed from syngas by adsorption onto CaO-based catalysts, leaving CO, CH_4, and H_2 largely unaffected due to their much lower adsorption energies. Syngas can be converted to ethanol via a tandem catalytic process through methanol and acetate intermediates using sequentially positioned catalysts including zeolites (H-MOR).

Fischer-Tropsch synthesis. The FTS reaction — developed in Germany to produce oil from coal during World War II — converts syngas to liquid alkanes and alkenes through a polymerization-like surface reaction with chain lengths from C1 to >C70 depending on catalyst, temperature, pressure, and H_2/CO ratio. The optimal H_2/CO ratio is ~2, achieved from biomass gasification using the water-gas shift reaction. Three mechanistic proposals exist: the carbide mechanism (CO dissociates to surface C and O, then is hydrogenated to CH_2 methylene units); the enol mechanism (CO adsorbs intact, reacts with surface H to form hydroxymethylene, which condenses with adjacent species); and the CO insertion mechanism (CO inserts into metal-carbon bonds, with CH_2 as the rate-limiting product). Iron catalysts are preferred for biomass- and coal-derived syngas (lower H_2/CO, active in water-gas shift) while cobalt catalysts are preferred for natural gas-derived syngas. Both are doped with K and Cu to improve selectivity and stabilized on silica/alumina supports.

Chemical synthesis of food. Agriculture accounts for ~25% of global GHG emissions, and palm oil — the world's most produced vegetable oil — is associated with large-scale tropical deforestation. Chemical synthesis of fats from CO_2, syngas, methanol, or acetate offers an alternative with a GHG footprint of <0.8 g CO_2 equiv/kcal versus >1.5 g CO_2 equiv/kcal for palm oil, with net-zero potential if atmospheric CO_2 is used as feedstock. Fats are the most tractable food macronutrient to synthesize chemically because they lack the stereochemical complexity of carbohydrates and proteins; chemical pathways to fatty acids and triacylglycerols from small-molecule feedstocks are well established, in contrast to the enzymatic stereoselectivity required for amino acid or sugar synthesis.

Sustainable aviation fuel. Aviation accounts for significant global CO_2 emissions; the US alone contributes 25% of aviation emissions. Meeting projected US demand of ~30 billion gallons per year (BGY) by 2040 with cellulosic SAF is theoretically feasible: a study modeling miscanthus cultivation on 23.2 Mha of marginal agricultural land in the US Midwest found that up to 76% of projected aviation fuel needs could be met at ~$4.1/gal assuming a carbon price of $50/t CO_2e. Bio-jet fuel composition (C8–C16 n-alkanes, branched alkanes, cycloalkanes, and some aromatics) is matched to conventional Jet A-1 specifications through Fischer-Tropsch synthesis from lignocellulosic syngas. At current unsubsidized market prices, SAF costs ~$1.90/gal more than conventional jet fuel; this gap closes to zero at a carbon price of $175/t CO_2e — precisely the estimated social cost of carbon. The current fossil fuel market fails to price in the external costs of climate change, infrastructure damage, agricultural disruption, and health impacts, effectively subsidizing conventional fuel at the expense of the public. The 2026 conflict disrupting Strait of Hormuz oil flows — which carry ~20% of global oil — has sharply accelerated interest in domestically produced SAF as an energy security imperative as well as a climate

8: Biodiesel, Syngas and Bioaviation fuels is shared under a CC BY-NC-SA 4.0 license and was authored, remixed, and/or curated by LibreTexts.

9: BIOHYDROGEN - AN INTRODUCTION

Search Fundamentals of Biochemistry

LEARNING GOALS)

(Learning goals written by Claude, Anthropic)

By the end of this chapter, students should be able to:

Hydrogen as a Fuel and Indirect Greenhouse Gas

- Compare the energy density of H_2 (141.58 kJ/g) to ethanol, octane, and methane using combustion enthalpy data, explain why H_2 is theoretically the ideal fuel, and describe the "color" classification system identifying which colors involve net CO_2 emissions and what fraction of current global H_2 derives from fossil fuels.
- Explain why H_2 is an indirect greenhouse gas — describing its reaction with •OH (H_2 + •OH → H_2O + H•), how this reduces •OH availability for methane oxidation thereby extending CH_4 atmospheric lifetime, and how H• initiates free-radical chains producing tropospheric ozone — and connect this to the need to minimize H_2 leakage during production and transport.
- Assign oxidation numbers to H in H_2, H^+, and H_2O, write the two *E. coli* reactions (formate dehydrogenase and hydrogenase) that produce H_2 from formate, and connect H_2 redox chemistry to the analogous electron transport chain and photosynthetic water oxidation frameworks.

Biological H_2 Production: Biophotolysis and Fermentation

- Distinguish direct biophotolysis (PSII → ferredoxin → hydrogenase → H_2, electrons from water) from indirect biophotolysis (glucose → pyruvate → PFOR → ferredoxin → hydrogenase → H_2, electrons from fermentation), explain why indirect photolysis is conducted anaerobically, and describe how sulfur deprivation reduces PSII O_2 evolution to enable sustained H_2 production in *Chlamydomonas reinhardtii*.
- Describe the structure of PFOR (267 kDa homodimer, three [Fe_4S_4] clusters per monomer, TPP cofactor), explain its role in oxidative decarboxylation of pyruvate to produce reduced ferredoxin for H_2 generation, and contrast with pyruvate:formate lyase (PFL1) as an alternative anaerobic fermentation route.
- Distinguish photofermentation (organic acid oxidation → nitrogenase → H_2, one photosystem, anaerobic) from dark fermentation (heterotrophic anaerobic biomass degradation → hydrogenase → H_2), write representative acidogenic, acetogenic, and methanogenic reactions identifying which produce and which consume H_2, and explain why nitrogenase produces H_2 at only 4 ATP/H_2 in the absence of N_2 versus 16 ATP/H_2 during N_2 fixation.

Electrochemical Production and Critical Evaluation of H_2

- Describe microbial electrolytic cells (MECs) — explaining how microbial oxidation of organic substrates at the anode generates electrons that reduce H^+ to H_2 at the cathode, enhanced by applied external voltage — and distinguish these from photoelectrochemical cells (PECs) that use light-sensitive semiconductor electrodes.
- Articulate the thermodynamic and economic arguments against large-scale H_2 as an energy carrier — including ~70% energy loss during electrolysis, steel pipeline incompatibility, leakage risks, liquid storage cost (~50% of combustion energy), and the scale problem (producing current industrial H_2 from renewables would require the entire US grid) — and explain why direct electrification of vehicles and heat pumps is more efficient than using renewables to produce H_2 as an intermediary.

HYDROGEN AS A FUEL

Hydrogen gas would be ideal if it could be produced at scale, easily transported and stored, or produced at local sites on demand (all of these are long shots as described at the end of this chapter). The reaction for the "burning" of hydrogen shows that the only greenhouse gas emitted is H_2O.

$$2H_2(g) + O_2(g) \rightarrow 2H_2O(g) \tag{9.1}$$

H_2O comes and goes in our atmosphere on short timescales and does not continually build up, as does CO_2 from burning fossil fuels. The standard heat of combustion (in kJ/g or kcal/kg) for H_2 is far higher than any other fuel, as shown in Table **9.1** below, making it an ideal fuel.

Name	Formula	State	$-\Delta H_c°$ *kJ/mol*	$-\Delta H_c°$ *kJ/g or MJ/kg*	$-\Delta H_c°$ *kcal/kg*
Ammonia	NH_3	gas	383	22.48	5369
Butane	C_4H_{10}	gas	2878	49.50	11823
Carbon (graphite)	C	cry	394	32.81	7836
Ethanol	C_2H_6O	liq	1367	29.67	7086
Hydrogen	**H_2**	**gas**	**286**	**141.58**	**33817**
Methane	CH_4	gas	891	55.51	13259
methyl stearate (biodiesel)	$(CH_3(CH_2)_{16}(CO)CH_3$	liq	1764	40	9560
Naphthalene	$C_{10}H_8$	cry	5157	40.23	9609
Octane	C_8H_{18}	liq	5470	47.87	11434
Propane	C_3H_8	gas	2220	50.33	12021
wood (red oak)	-	solid	-	14.8	3540
coal (lignite)	-	solid	-	15	3590
coal (anthracite)	-	solid		27	4060

Table **9.1**: Energy values for various fuels. Data source: https://www.engineeringtoolbox.com/s...nt-d_1987.html

We won't discuss large-scale H_2 storage or transport, two fundamental and likely intractable engineering problems. Instead, we will focus on producing "biohydrogen." Of course, the prefix "bio" can mean many things, including the production of H_2 in syngas using cellulose as a feedstock, the electrolysis of water powered by solar/wind energy, and its production by hydrogenases, enzymes found in some microbes.

The fuel industry uses different colors to describe hydrogen based on how it is produced. They are shown in Table **9.2**.

Color	Method of production
Green	electrolysis of H_2O using solar/wind to generate electricity (expensive at present)
Blue	steam reforming of natural gas (CH_4) with the other product, CO_2 captured and stored (CCS)
Grey	steam reforming of natural gas (CH_4) without CO_2 capture and storage
Black (coal/oil)	gasification to form syngas
Pink (purple/red)	electrolysis powered by nuclear energy, which does not emit CO_2; heat emitted produces steam for blue/gray H_2 production
Turquoise	methane pyrolysis (heat in the absence of O_2) to form H_2 and C
Yellow	electrolysis using solar power without conversion to electricity as the power source.
White	underground H_2 released through fracking

Table **9.2**: Different "colors" of hydrogen based on production methods

Of course, H_2 in syngas can be produced from biomass, as described in Chapter 32.8, but it is unclear if a hydrogen color has been assigned to it.

At present, the important feedstocks for H_2 production worldwide are natural gas (48%), oil (30%), coal (18%), and electrolysis (4%)—mostly fossil fuels.

METHODS OF PRODUCTION

H_2 production is also classified based on the chemical processes used to produce it. These processes include

1. **Biological** (use of live bacteria and algae cells)
2. **Thermochemical**: (gas and liquid fuel reforming, coal and biomass gasification),
3. **Electrochemical (electrolytic)**: (photothermal, photoelectrolytic, and photobiological)

We will organize this chapter section using these three processes. We will start with Biological (1), followed by Electrochemical/Electrolytic (3), and end with Thermochemical (2). They are summarized in Figure **9.1**.

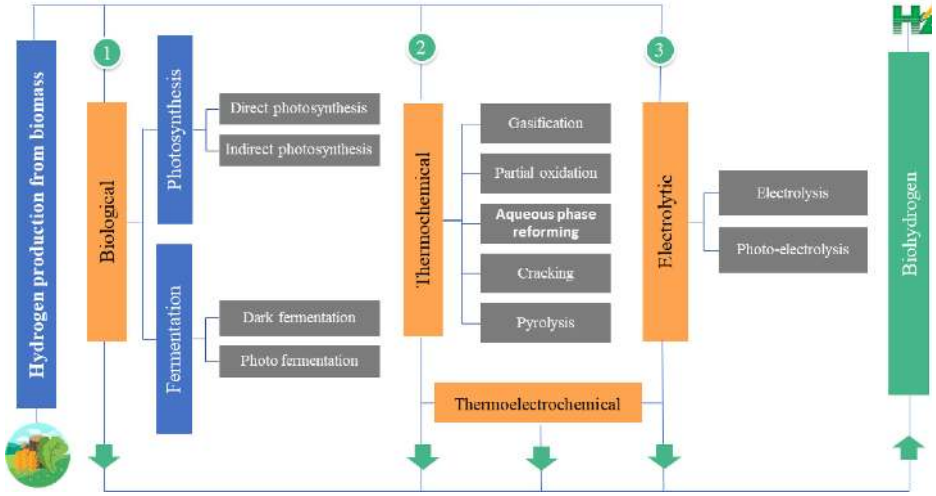


Figure 9.1: The main pathways for H_2 production based on biomass. M.G. Eloffy et al., Chemical Engineering Journal Advances, 12 (2022). https://doi.org/10.1016/j.ceja.2022.100410. Creative Commons license

Biomass can serve as feedstock for all these methods, and the resulting product can be called biohydrogen. Of course, as discussed in the previous chapter, nonbiological feedstocks are also the predominant sources used in thermochemical and electrochemical methods.

$2H^+ \leftrightarrow H_2$: AN OVERVIEW

We will discuss the production of H_2 as an energy source for society. For industry use, it can be used in fuel cells to power spacecraft and cars, as shown in the reaction below.

$$\begin{aligned} O_2 + 4H^+ + 4e^- &\longrightarrow 2H_2O \\ H_2 &\longrightarrow 4H^+ + 4e^- \end{aligned} \qquad (9.2)$$

In the next section, we will discuss the **hydrogenases** that produce and use H_2 in microbes. This chapter will treat them very generally. However, we need to review the topic.

Use of H_2 as a *source* of electrons for reduction reactions.

Each hydrogen in H_2 has an oxidation number of 0. Each can be oxidized to H^+ (oxidation number +1), with the 2 electrons transferred to a substrate/cofactor or to a series of substrates with successively higher standard reduction potentials (better oxidizing agents), forming reduced products.

$$H_2 + (\text{substrate})_{OX} \rightarrow 2H^+ + (\text{product})_{RED}$$

This general reaction is analogous to the mitochondrial electron transport chain, in which electrons are passed from a source (NADH) to oxidized acceptor molecules. The general reaction below shows each redox pair in the electron transport chain.

$$NADH/NAD^+ \rightarrow FAD/FADH_2 \rightarrow UQ/UQH2 \rightarrow \text{Cyto } C_{OX}/\text{Cyto } C_{RED} \rightarrow O_2/H_2O$$

Some organisms have evolved to produce energy by oxidizing H_2. This reaction is analogous to how photosynthetic organisms obtain energy through water oxidation. In photosystem II, the oxygen-evolving complex oxidizes oxygen in H_2O (oxidation number -2) to O_2 (oxidation number—0). Some redox pairs, starting with H_2O/O_2, are shown below for photosystem II.

$$H_2O/O_2 \rightarrow P680/P680^* \rightarrow (\text{Plastoquione})_{OX}/(\text{Plastoquione})_{RED}$$

The first reaction is endergonic and requires photons as an energy source photons.

Use of H^+ as a *sink* for electrons for oxidation reactions that produce H_2.

H^+ has an oxidation number of +1. Hence, it can be reduced to H_2 (oxidation number 0) as it gains electrons from substrates/cofactors that are oxidized. This general reaction is shown below.

$2H^+ + (\text{substrate/cofactor})RED \rightarrow H_2 + (\text{substrate/cofactor})OX$

Many microorganisms can produce H_2 through variants of photosynthesis or fermentation, both of which provide the two electrons needed. E. coli has four hydrogenases (Hyd 1, 2, 3, and 4). It forms H_2 through two reactions catalyzed by:

- formate (HCO_2^-) dehydrogenase (FDH): $2HCO_2^- \rightleftharpoons 2CO_2 + 2H^+ + 2e^-$
- hydrogenase (H_2ase): $2H^+ + 2e^- \rightarrow H_2$

The C in formate has an oxidation number of +2 and is oxidized to CO_2, in which the C has an oxidation number of +4.

NOTHING IS SIMPLE: H_2 IS AN INDIRECT GREENHOUSE GAS.

H_2 is not a greenhouse gas as it doesn't have any bond vibrations that produce transient dipoles and, hence, does not absorb in the infrared region of the spectrum. Yet it can affect atmospheric methane levels, a potent greenhouse gas, and ozone, leading to warming. It's not the emissions from H_2 combustion, but rather the leakage of H_2 gas transported to and stored in the atmosphere that is problematic.

Most of the H_2 that enters the atmosphere diffuses into the soil and is taken up by bacteria. The rest react with hydroxyl radicals (·OH) in the atmosphere, as shown in the reaction below.

$$H_2 + \cdot OH \rightarrow H_2O + H\cdot \text{ (atomic hydrogen)}$$

The reaction of ·OH with H_2 decreases the availability of hydroxyl radicals to react with the very potent greenhouse gas methane (CH_4). That reaction is shown below.

$$CH_4 + \cdot OH \rightarrow \cdot CH_3 + H_2O$$

The methyl radical $\cdot CH_3$ reacts rapidly with oxygen to form the methylperoxy radical ($CH_3O_2\cdot$). This eventually forms formaldehyde, a water-soluble molecule that precipitation removes from the atmosphere. Hence, the reaction of H_2 with ·OH increases the atmospheric half-life of CH_4.

·OH is a key molecule in the troposphere and is considered a methane "sink" that leads to the drawdown of methane. We discussed the extreme reactivity of ·OH in Chapter sections 12.3 and 12.4. It's so reactive that its half-life is in the order of seconds. It is also present at very low concentrations of less than 1 part per trillion.

·OH is produced from ozone, O_3, by the following reactions:

$$O_3 + h\nu\ (UV) \rightarrow O_2 + \cdot O$$

$$\cdot O + H_2O \rightarrow 2\ \cdot OH$$

The first reaction is photolysis, and experiments during a solar eclipse have shown that the production of atmospheric ·OH stops!

Dr. Paul Crutzen, Nobel Prize winner in Chemistry, described ·OH as the "detergent of the atmosphere" since it can react with and oxidize many deleterious trace gases in the troposphere, making them more water-soluble and removing them from the atmosphere. A main reaction of ·OH is carbon monoxide (CO). It also reacts with volatile organic compounds (VOCs) and NOx ($NO + NO_2$), which are precursors of tropospheric ozone, a health hazard. Even though dioxygen, which comprises 20% of the atmosphere, is also an excellent oxidizing agent, it reacts slowly kinetically.

Very few gases are not oxidized by ·OH. The refrigerant gases chlorofluorocarbons are and would enter the stratosphere if they didn't react with ·OH. In the stratosphere, they react with stratospheric ozone, reducing its protective effect against harmful UV radiation. It does react with hydrochlorofluorocarbons (HCFCs).

Figure 9.2 below summarizes the adverse climatic effects of the oxidation of H_2 in the atmosphere.

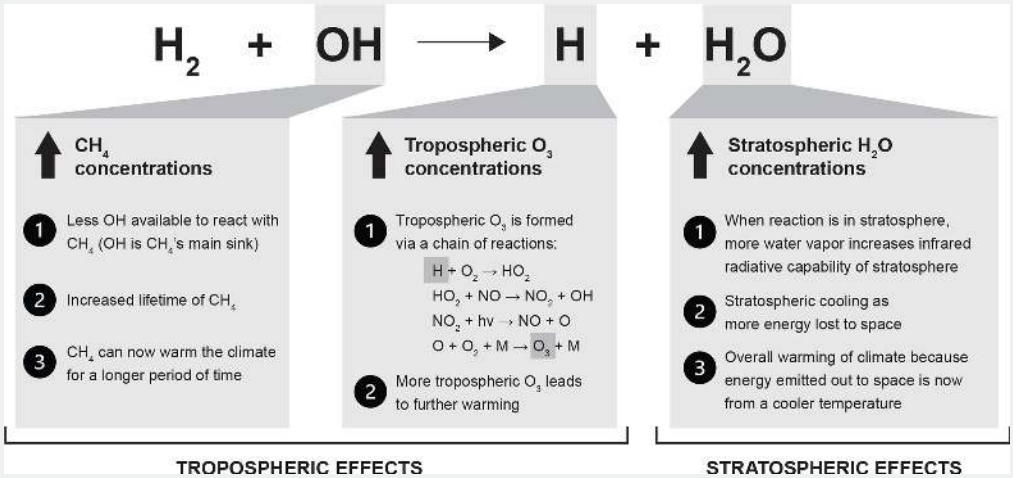


Figure 9.2: Effects of hydrogen oxidation on atmospheric greenhouse gas concentrations and warming. I. Ocko and Steven P. Hamburg, Atmos. Chem. Phys., 22, 9349–9368, 2022. https://doi.org/10.5194/acp-22-9349-2022. Creative Commons Attribution 4.0

License.

The central panel notes that H· (atomic hydrogen) can initiate a free-radical reaction to produce tropospheric ozone (O_3). This pollutant is a greenhouse gas and causes serious health consequences.

The message is this: Care must be taken to minimize methane and H_2 leakage during production and use as fuels.

BIOHYDROGEN FROM MICROALGAE

We will focus most of our attention on the Biological (1) and Electrolytic (3) processes for producing biohydrogen from microalgae. The Biological processes (1) require hydrogenases for H_2 production within cells. The Electrolytic (3) processes use microalgae as a feedstock to provide substrates that other microbes can ferment. These can be combined to increase production. Figure **9.3** below summarizes the Biological (1) and Electrolytic (3) metabolic processes that can be used for microalgae H_2 production.

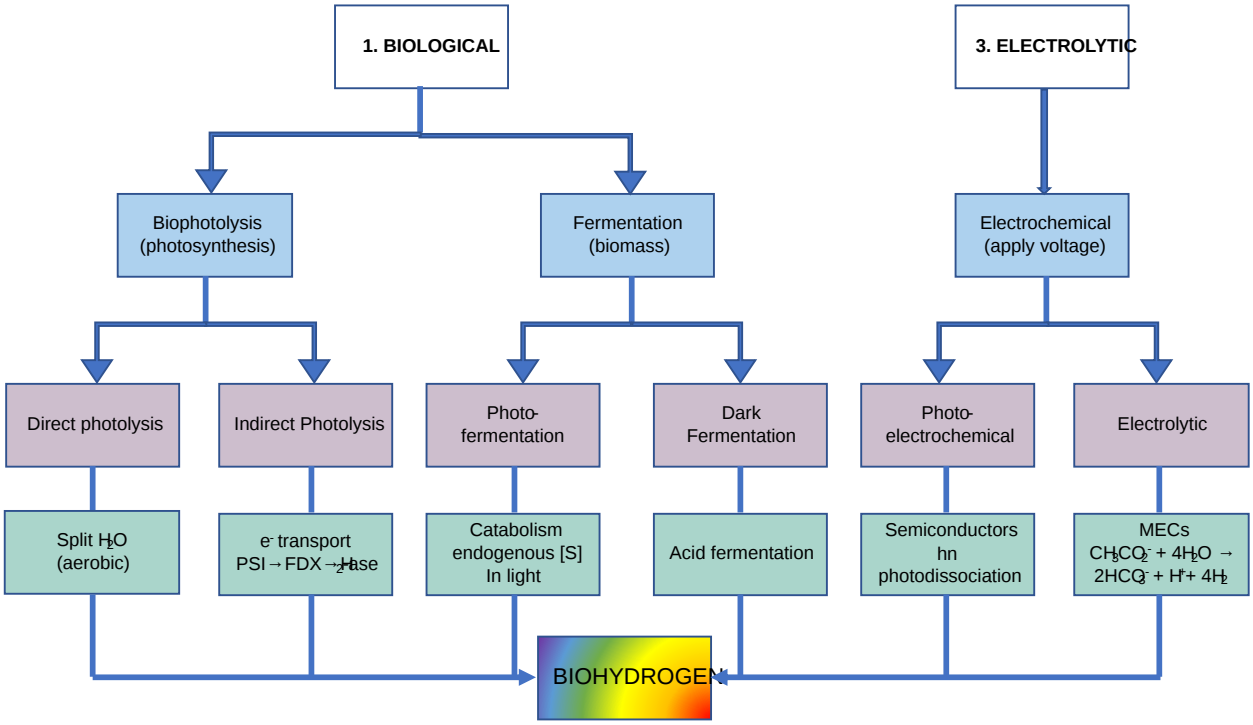


Figure **9.3**: Metabolic pathways of biohydrogen production by micro-algal biomass. modified from Ahmed SF et al. *Front. Energy Res.* 9:753878. doi: 10.3389/fenrg.2021.753878. Creative Commons Attribution License (CC BY).

These are mainly classified into three categories: i) the photobiological process through which biohydrogen is produced *via* direct and indirect photolysis in the microalgae, ii) fermentation, and iii) the electrochemical process that comprises photoelectrochemical and electrolytic.

BIOLOGICAL (1) - BIOPHOTOLYSIS (PHOTOSYNTHESIS)

This consists of two processes: Direct and Indirect Photolysis (photosynthesis). Both use light to drive the ultimate reduction of $2H^+$ to H_2 using hydrogenase or nitrogenase. We will explore the details in the next chapter section. The biophotolysis process is divided into indirect (using electrons from substrates) and direct (using electrons from water). These processes are simplified in Figure **9.4**.

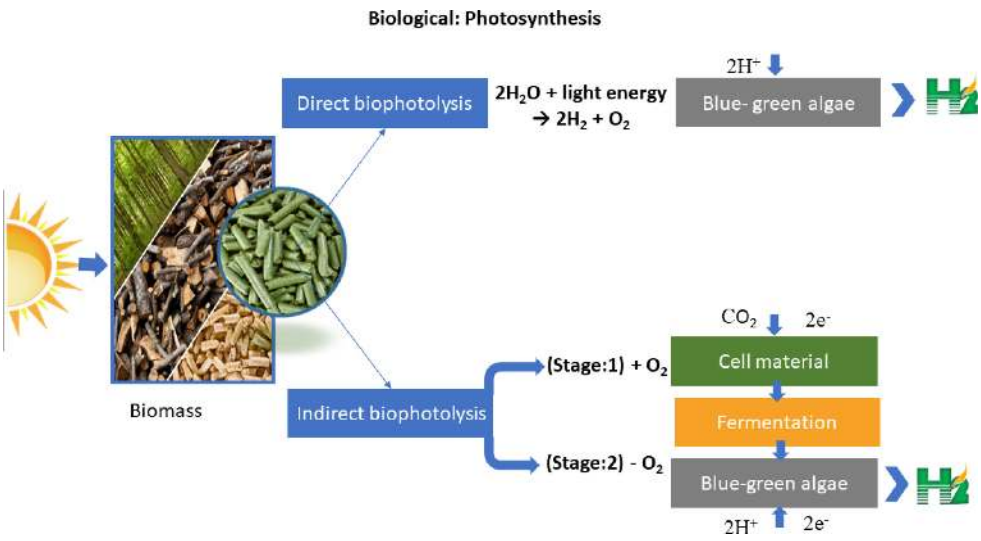


Figure 9.4: Schematic diagram for biological (biophotolysis) process. M.G. Eloffy et al.

Direct Biophotolysis (photosynthesis)

In direct biophotolysis (photosynthesis), water molecules are oxidized in Photosystem II, which contains the Oxygen Evolving Complex (OEC). This endergonic process is driven by light. The electrons lost from water are passed through Cytochrome b_6f and Photosystem I to ferredoxin, then $NADP^+$, which gets reduced to NADPH (as discussed in Chapter 20). These reactions are illustrated in Figure 9.5.

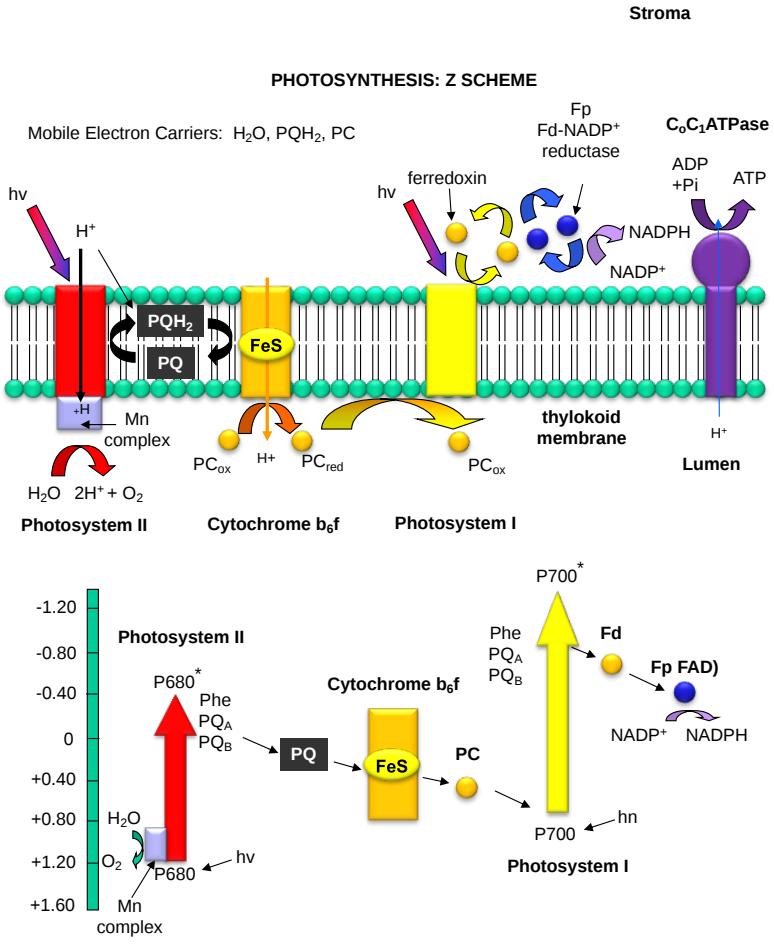


Figure 9.5: Light reaction of photosynthesis and associated standard reduction potentials

In direct photolysis, electrons are passed directly from reduced ferredoxin to $2H^+$ in a reaction catalyzed by a hydrogenase, as shown in Figure **9.6** below.

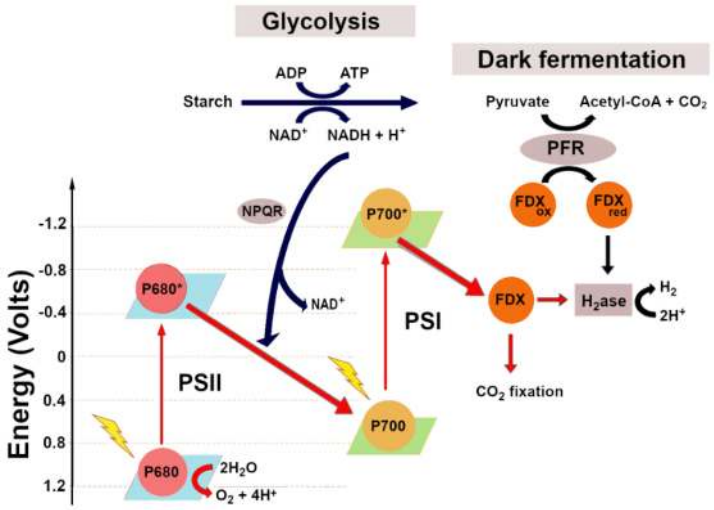


Figure **9.6**: Metabolic hydrogen production pathways used by *Chlamydomonas reinhartii*.FDX: ferredoxin; H_2ase: hydrogenase; NPQR: NADPH−plastoquinone oxidoreductase; PFR: pyruvate:ferredoxin oxidoreductase; PSI: photosystem I; PSII: photosystem II. Touloupakis, E.; Faraloni, C.; Silva Benavides, A.M.; Torzillo, G. Recent Achievements in Microalgal Photobiological Hydrogen Production. *Energies* **2021**, *14*, 7170. https://doi.org/10.3390/en14217170. Creative Commons Attribution (CC BY) license (**https://creativecommons.org/licenses/by/4.0/**).

The overall reaction is simplified in the equation below.

$$2H_2O + \text{Light} \rightarrow 2H_2 + O_2 \tag{9.3}$$

One problem with direct photolysis is that O2 can damage hydrogenases. Again, we will discuss the biochemistry of hydrogenases in great detail in the next chapter section.

Indirect Biophotolysis

This process bypasses the damaging effects of O_2 on hydrogenase by being carried out in the absence of O_2, using fermentation to provide electrons for the hydrogenase reduction of $2H^+$ to H_2. Photosynthesis is required to make the carbohydrates necessary for fermentation. Glucose can then be oxidized anaerobically (in the dark to avoid O_2 formation from photosynthesis) to form pyruvate through the glycolytic pathway. Pyruvate can then be oxidatively decarboxylated via **pyruvate:ferredoxin oxioreductase (PFR)** as ferredoxin is reduced. It then passes its electrons on through hydrogenase to produce H_2. The pathway is illustrated in the top/right parts of the above figure, and the reaction diagram in Figure **9.7** below.

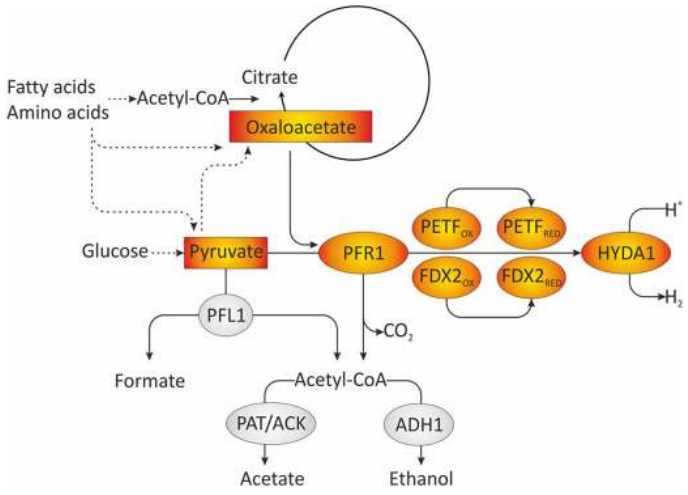


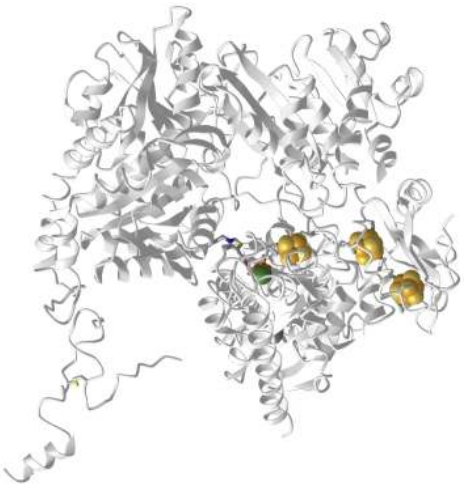
Figure **9.7**: **Model of fermentative pathways involved in dark anaerobic H_2 production in *C. reinhardtii*.** Proteins are shown as ovals. Photosynthetic ferredoxin (PETF). Jens Noth et al., Journal of Biological Chemistry, 288

(2013). https://doi.org/10.1074/jbc.M112.429985. Creative Commons license.

Glucose and some amino acids can be converted into pyruvate, a substrate for PFR1 in the single-cell algae *C. reinhardtii*. PFR1 converts pyruvate to acetyl-CoA and CO_2, with the electrons being used to reduce ferredoxin. The reduced FDX2 passes electrons through hydrogenase (HYDA1) to form H_2.

Another enzyme used to continue fermentation, **pyruvate:formate lyase (PFL1),** converts pyruvate to formate and acetyl-CoA, which can be metabolized further to acetate and ethanol. A shift to pyruvate oxidation via PFR1 occurs when PFL1 is mutated or under long-term anoxic conditions.

The key enzyme, pyruvate:ferredoxin oxioreductase(PFR), uses thiamine pyrophosphate (TPP) as a cofactor for the oxidative decarboxylation of the α-keto acid pyruvate, as expected. Figure **9.8** shows an interactive iCn3D model of the pyruvate ferredoxin oxidoreductase (PFOR) from Desulfocurvibacter africanus in anaerobic conditions (7PLM).



NCBI iCn3D Figure **9.8**: Pyruvate ferredoxin oxidoreductase (PFOR) from Desulfocurvibacter africanus in anaerobic conditions (7PLM). (Copyright; author via source). Click the image for a popup or use this external link: https://structure.ncbi.nlm.nih.gov/i...XRFMoVhaoRbW86

PFOR, abbreviated here, is a 267 kDa homodimer containing three [Fe_4S_4] clusters (spacefill) per monomer. Only one monomer is shown, and TPP is shown in sticks.

Again, indirect photolysis occurs in the absence of O_2. Light illumination leads to only transient H_2 synthesis. If sulfur is limited in the growth media of the algae, more sustained H_2 production occurs, as the lack of sulfur reduces PSII activity. Hence, H_2 production can be maximized by depleting sulfur and minimizing O_2, even in light. In the absence of O_2, hydrogenase gene expression increases. Nutrient depletion also leads to the production of formate and acetyl-CoA via the enzyme pyruvate:formate lyase (PFL1). This is predominant in *Chlamydomonas* cells in the dark.

The green microalgae *C. reinhardtii* make most of its H_2 (approximately 90%) using direct photolysis. Commercially, H_2 production by indirect photolysis is carried out in a separate, sealed bioreactor to avoid O_2. Indirect photolysis is shown in the above figures.

The reactions to this process are as follows :

$$\begin{aligned} 12H_2O + 6CO_2 + h\nu &\rightarrow C_6H_{12}O_6 + 6O_2 \\ C_6H_{12}O_6 + 12H_2O + h\nu &\rightarrow 12H_2 + 6CO_2 \end{aligned} \tag{9.4}$$

BIOLGOCIAL (1) - FERMENTATION

We have just discussed fermentation processes **within living microalgae cells**. Now, let's consider fermentation processes using **nonliving biomass feedstocks** supplied to microbes to produce H_2. This offers a significant way to make biohydrogen. A schematic diagram for Biological (1) fermentation is shown below in Figure **9.9**:

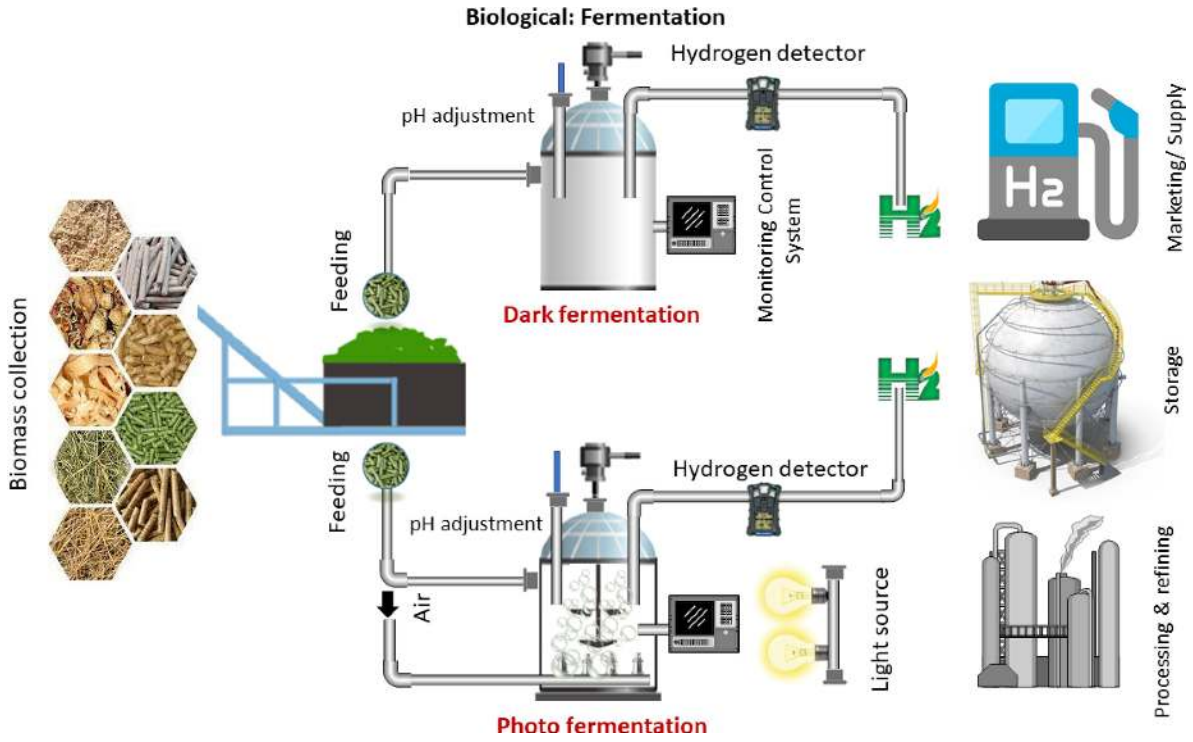


Figure 9.9: Schematic diagram for biological (fermentation) process. M.G. Eloffy et al.

Fermentation involves the decomposition of organic biomass to produce CO_2 and H_2. The fermentation process can be separated into photofermentation (light fermentation) and dark fermentation.

Photofermentation

Some photosynthetic bacteria and microalgae use Photofermentation to produce H_2 from organic acids like acetic, butyric, lactic, and succinic acids. Oxidation of the acids produces CO_2 along with protons and electrons for H_2 production. Electrons are transferred through photosystem I and, eventually, to nitrogenase. It is a fermentation process because it is anoxic.

Some photosynthetic bacteria, such as purple nonsulfur bacteria, a facultative anoxygenic phototroph, and some microalgae, can produce H_2 using a simplified system with only one photosystem and the enzyme nitrogenase. The photosystem cannot generate an oxidizing agent strong enough to oxidize H_2O, but under anaerobic conditions, it can oxidize organic acids and even H2S to provide electrons for H_2 production. These reactions are shown below in Figure 9.10.

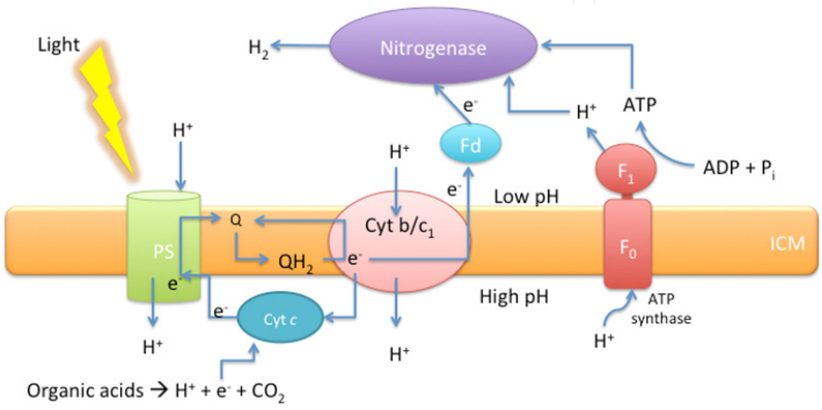


Figure 9.10: Photofermentative hydrogen production in PNSB.

Deo, D., Ozgur, E., Eroglu, I., Gunduz, U., & Yucel, M. (2012). Photofermentative Hydrogen Production in Outdoor Conditions. Hydrogen Energy - Challenges and Perspectives. doi: 10.5772/50390. Creative Commons Attribution 3.0 License,

We studied nitrogenase in Chapter x.xx. The net reaction for the fixation of nitrogen is shown below.

$$N_2 + 8H^+ + 8e^- + 16ATP \rightarrow 2NH_3 + H_2 + 16ADP + 16Pi \quad (9.5)$$

In this reaction, N_2 is reduced as the N atoms go from a 0 oxidation state to +3 in NH_3. The needed electrons are generated from organic acids, fed into the system, and eventually transferred to ferredoxin, which transfers them to protons. The ratio of N_2 to H_2 produced is 1:1, at the expense of 16ATPs per H_2 produced.

The ATP produced by the collapse of the proton gradient through F_oF_1ATPase powers the reaction.

In the absence of N_2, the net reaction becomes

$$2H^+ + 2e^- + 4ATP \rightarrow H_2 + 4ADP + 4Pi \quad (9.6)$$

The electrons are still fed into nitrogenase, but in the absence of the substrate N_2, they are used to reduce $2H^+$ to H_2. Note that only 4 ATPs are required per H_2 produced, a significant energy gain.

ATP produced during photosynthesis would be used for anabolic biosynthesis, contributing to biomass, so extra ATP is needed to support H_2 synthesis beyond that needed for growth. As anabolism is a reductive process (compared to oxidative catabolism), adequate sources of electrons for reduction are required. Multiple pathways need electrons, including CO_2 fixation, N_2 fixation (with associated H_2 production), and the production of organic acids such as polyhydroxybutyrate. The bacteria use photosynthesis and the Calvin cycle under photoautotrophic conditions to fix CO_2. When external energy supplies from organic acids are present, the bacteria can become photoheterotrophic. Under these conditions, the Calvin cycle maintains redox balance.

Dark Fermentation

We indirectly studied dark fermentation in our discussion of hydrogenases in microalgae above. Hydrogenases are induced in dark conditions, and this pathway involves heterotrophic fermentation (anaerobic) in some bacteria and microalgae. Many microbial species are used. Industrial wastewater enriched in organic material can be used as a feedstock.

Feedstock materials are hydrolyzed and subjected to fermentation, during which H_2 can be produced. For example, pyruvate produced by glycolytic fermentation can be oxidatively decarboxylated to acetyl-CoA and CO_2 by pyruvate:ferredoxin oxidoreductase, with electrons passed to ferredoxin and, via hydrogenase, to H_2 (as we described above). H_2 is involved in steps after fermentation, including acetogenesis and methanogenesis. These processes are illustrated in Figure 9.11 below.

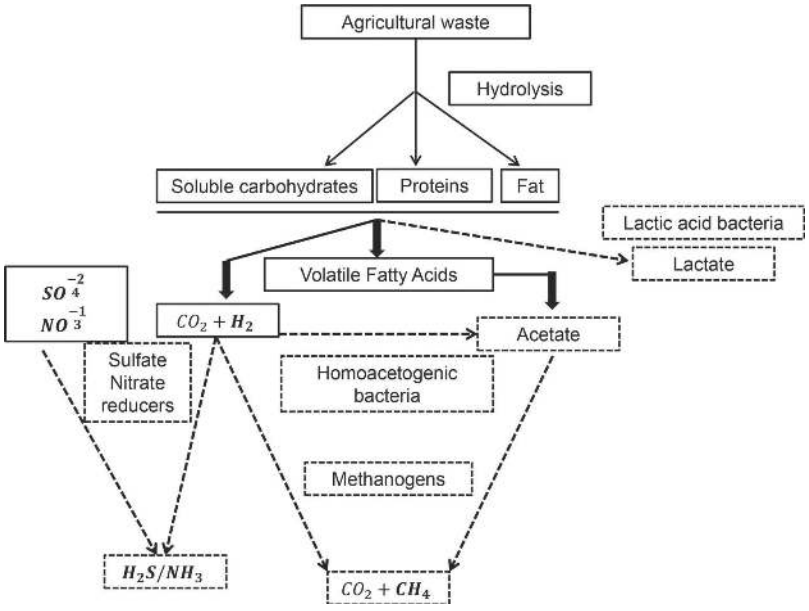


Figure 9.11: The steps involved in anaerobic digestion [9]. Rosa, P. R. F., & Silva, E. L. (2017). Review of Continuous Fermentative Hydrogen-Producing Bioreactors from Complex Wastewater. Frontiers in Bioenergy and Biofuels. doi: 10.5772/65548. Creative Commons Attribution 3.0 License

Examples of acidogenic (formation of short carboxylic/fatty acid), acetogenic (formation of acetic acid), and methanogenic (formation of methane) reactions that produce (and a few that consume) H_2 are shown in Table 9.3 below.

Acidogenic reactions
$C_6H_{12}O_6 + 2H_2O \rightarrow 2CH_3COOH + 2CO_2 + 4H_2$
$C_6H_{12}O_6 + 2H_2O \rightarrow CH_3CH_2CH_2COOH + 2CO_2 + 2H_2$
Acetogenic reactions
$CO_2 + 4H_2 \rightarrow CH_3CO_2H + 2H_2O$
$CH_3CHOHCO_2H + H2O \rightarrow CH_3CO_2H + CO_2 + 2H_2$
$CH_3CH_2OH + H2O \rightarrow CH_3CO_2H + 2H_2$
$CH_3CH_2CO_2H + 2H_2O \rightarrow CH_3CO_2H + CO_2 + 3H_2$
$CH_3(CH_2)_2CO_2H + 2H_2O \rightarrow 2CH_3CO_2H + 2H_2$
Methanogenic reactions
$4H_2 + CO_2 \rightarrow CH_4 + 2H_2O$
$CH_3CO_2H \rightarrow CH_4 + CO_2$
$2CH_3(CH_2)_2CO_2H + 2H_2O + CO_2 \rightarrow 4CH_3CO_2H + CH_4$

Table **9.3**: Example of acidogenic, acetogenic, and methanogenic reactions in dark fermentation. Adapted from Rosa, P. R. F., & Silva, E. L., ibid.

We have described a few of the enzymes involved in acidogenic reactions above. Figure **9.12** summarizes the steps in acidogenesis.

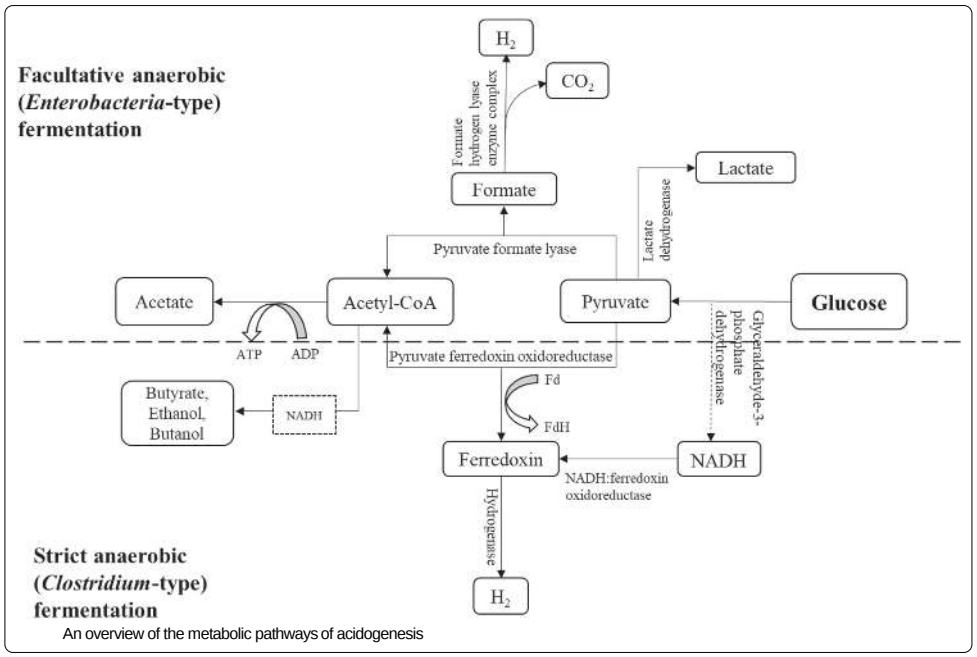
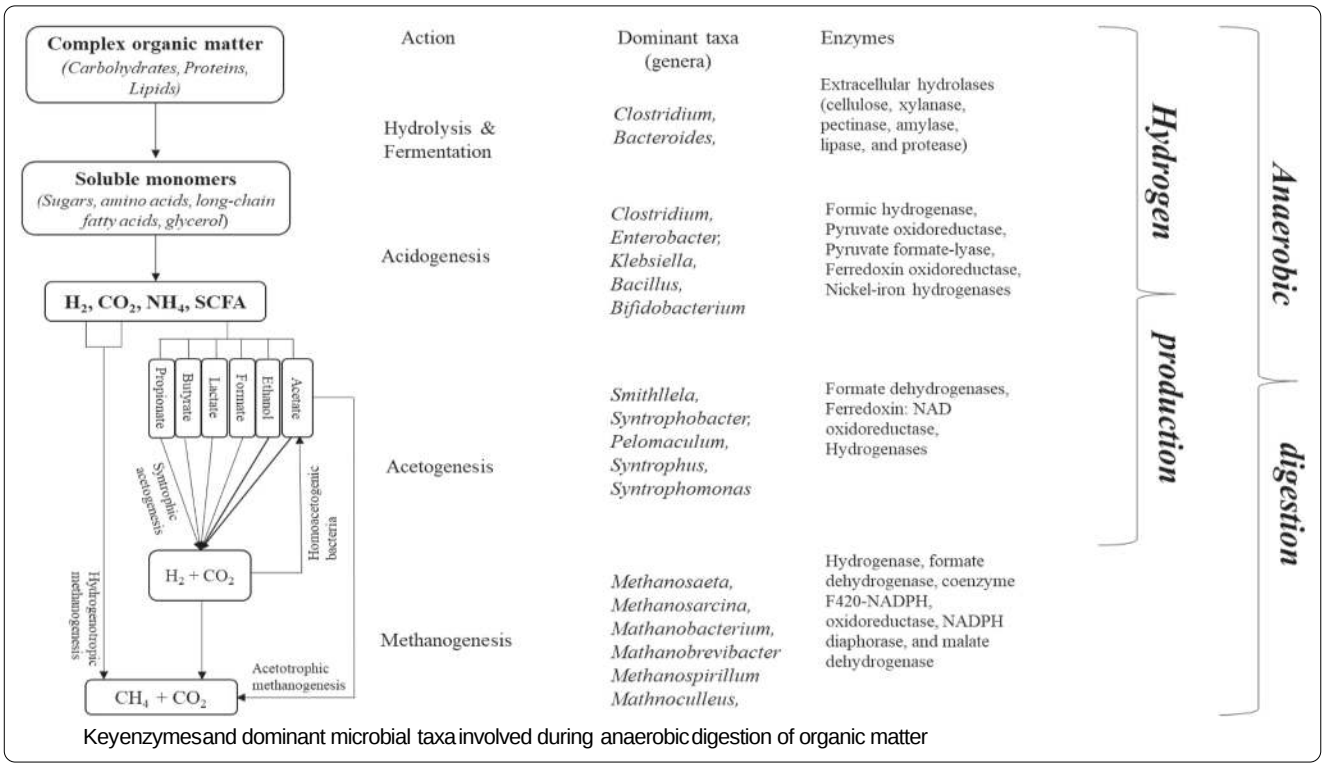


Figure **9.12**: An overview of the metabolic pathways of acidogenesis. Dzulkarnain, E.L.N., Audu, J.O., Wan Dagang, W.R.Z. *et al.* Microbiomes of biohydrogen production from dark fermentation of industrial wastes: current trends, advanced tools, and future outlook. *Bioresour. Bioprocess.* **9**, 16 (2022). https://doi.org/10.1186/s40643-022-00504-8. http://creativecommons.org/licenses/by/4.0/.

Figure **9.13** below shows a more complex list and summary of dark fermentation reactions.



Keyenzymesand dominant microbial taxa involved during anaerobic digestion of organic matter

Figure **9.13**: Key enzymes and dominant microbial taxa involved during anaerobic digestion of organic matter. Dzulkarnain, E.L.N.et al. Ibid.

ELECTROCHEMICAL/ELECTROLYTIC (3)

Two primary electrochemical/electrolytic methods for H_2 production are photoelectrochemical and electrolytic, as shown below in Figure **9.14**.

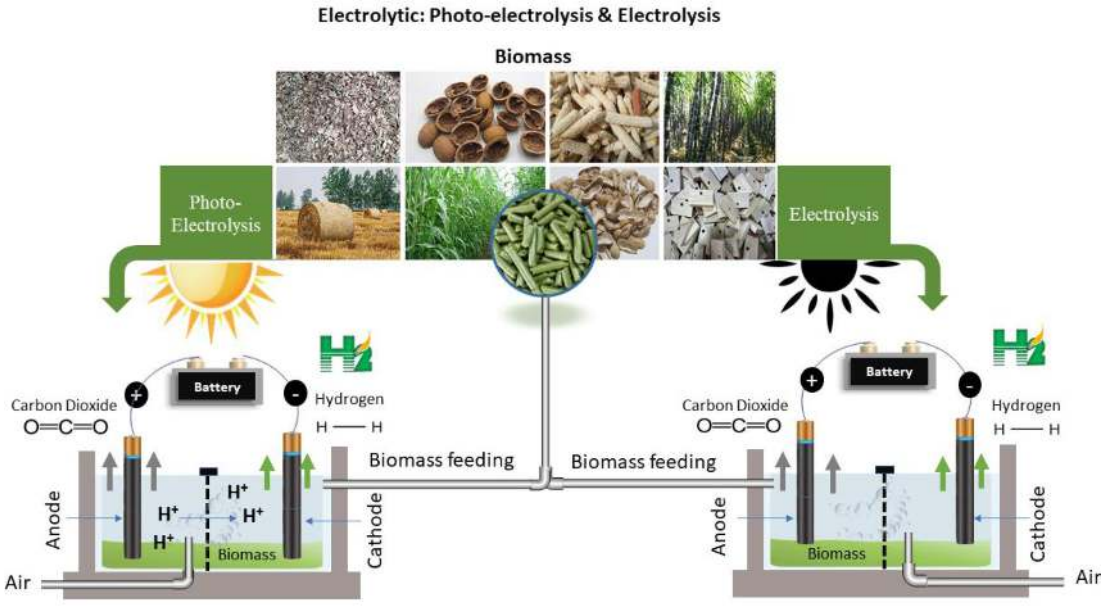


Figure **9.14**: Schematic diagram for the electrochemical process. M.G. Eloffy et al.

Electrolysis

https://geo.libretexts.org/@go/page/34464

In a microbial electrolytic cell (MEC), microalgae/cyanobacteria use industrially and metabolically processed feedstocks to oxidize organic substrates (e.g., acetic acid) to CO_2. The released electrons move from the anode (where oxidation occurs) to the cathode, where H+ is reduced to H_2. An external voltage increases the flow of electrons to the cathode, facilitating the process. This increases H2 production beyond that from just microbial fermentation in the electrolytic cell. Cyanobacteria and a mix of green microalgae and bacteria that can use dark fermentation (i.e., combining the processes described above) are used.

Photoelectrochemical

Microbial photoelectrochemical cells (PEC) use light-sensitive semiconductor electrodes for water electrolysis. A membrane separates the two electrodes, allowing protons to be reduced to form H_2.

2. THERMOCHEMICAL FROM BIOMASS

We have already explored thermochemical methods to produce syngas (H_2 and CO) and to further use it in the Fischer-Tropsch reaction to make small and large molecules for chemical feedstocks and fuels. We also discussed electrochemical methods for producing syngas and other small organic molecules, such as formate and ethanol, from CO_2. Figure **9.15** shows a schematic diagram for thermochemical (gasification) processes to produce H_2.

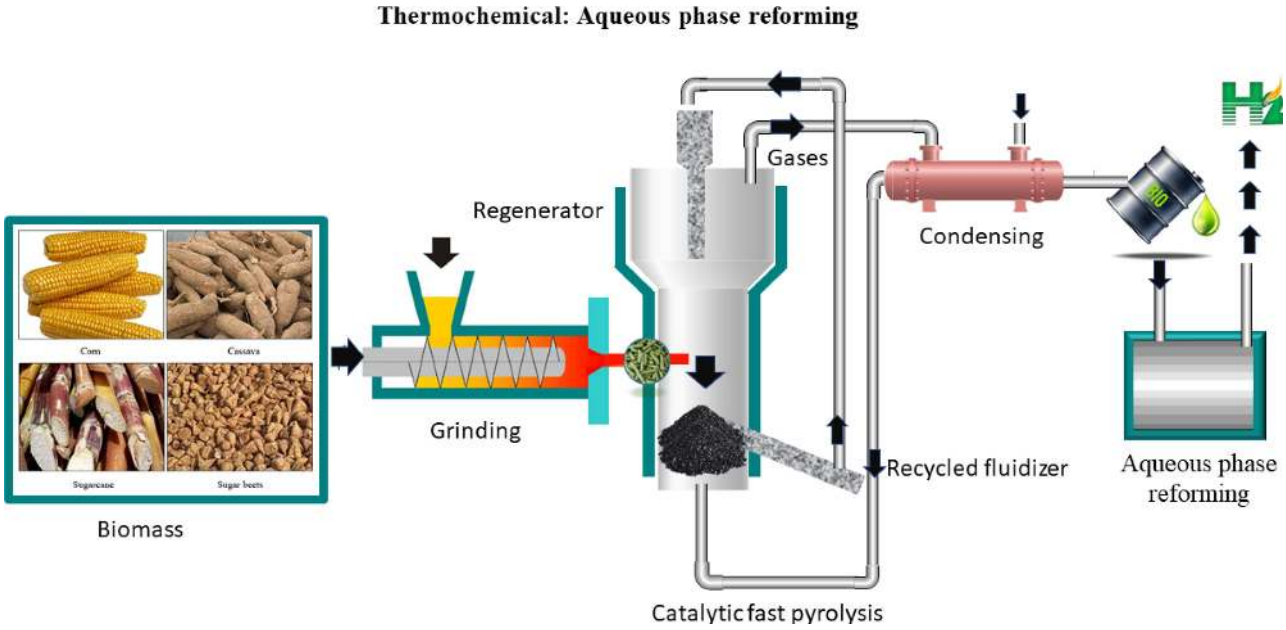


Figure **9.15**: Schematic diagram for thermochemical (aqueous phase reforming) process. M.G. Eloffy et al.

CLEAN H_2: THE REALITY AND THE HYPE

On the surface, ocean water has an almost limitless supply of hydrogen. The problem is that it is locked up as stable water, which is also a stable byproduct of the oxidation of carbon-containing molecules by O_2. Now, we wish to make clean H_2 to power our energy needs. As alluded to above, even if we had enough H_2 produced by electrolyzers (for example), it can't be easily stored or transported. It takes steel pipes to transport natural gas, but they can't be used for H_2, which makes them brittle. As the smallest possible gas, it's also the leakiest. A new and very expensive underground infrastructure would be needed. Using current technology to drill deep geothermal wells would be much easier, safer, cleaner, and cost-effective. Making H_2 locally has the same problems. Producing a highly combustible product like pinkH_2 locally at a nuclear plant is dangerous, not even accounting for the huge expense of building nuclear power plants. H_2 can be stored in a liquid state at 20K, which requires about half the energy it would produce on combustion. Hydrogen generation and storage must be practical, scalable, and economical. That's not possible now or soon enough to combat the present warming.

From a thermodynamic and economic perspective, using H_2 to reduce CO_2 (g) produced as a byproduct of cement production or burning fossil fuels and form methanol and higher alcohols, only to burn it again to power vehicles and planes, seems ludicrous. The

same applies to blue hydrogen. In both situations, we are trying to defy entropy in capturing and using a diluted, very stable molecule, CO_2, and reusing it to make energy-dense, thermodynamically unstable hydrogen-containing fuels.

Approximately 100 M tons of H_2 are currently used as chemical feedstocks, mostly to produce NH_3 for fertilizers. Another is to further oxidize fuel stocks to improve their fuel quality. Less than 0.1% of present H_2 production is used directly as an energy source. Most of the H_2 produced comes from fossil fuels such as methane, a greenhouse gas that contributes about 2% to warming. Making the presently manufactured 100 M tons of clean H_2 from renewables using electrolyzers would take all the electricity produced from fossil fuels, nuclear, and renewable sources combined from the entire US grid! Logically, it makes sense to use renewables directly as a power source, not first to make H_2 and then use it as a power source. Only 30% of the energy used to power the electrolyzer is captured during water splitting. Why not use clean electrical energy to directly power electric heat pumps and vehicles, which are much more efficient? We need electrons and electrical energy, not further combustion of fossil fuels, to produce H2, to power our future.

For more information on the problems with H_2 as an energy source, listen to the Volt Podcast Taming the Hydrogen Hype, in which David Roberts, the host, interviews Joe Romm. The Volt Podcast is a superlative source of information on what is needed for our energy transition away from fossil fuels.

SUMMARY

(Summary written by Claude, Anthropic)

This chapter evaluates hydrogen as a potential clean fuel — examining its thermodynamic advantages, the biological and electrochemical pathways for its production, and a sobering assessment of the practical and thermodynamic limitations that constrain its role in the energy transition.

Hydrogen's promise and limitations as a fuel. With a combustion enthalpy of 141.58 kJ/g — far exceeding methane (55.51 kJ/g), octane (47.87 kJ/g), and ethanol (29.67 kJ/g) — and producing only water upon combustion, hydrogen is theoretically the ideal fuel. The fossil fuel industry classifies hydrogen by production method (green: electrolysis from renewables; blue: steam reforming with carbon capture; grey: steam reforming without capture; black: coal gasification; pink: nuclear electrolysis; turquoise: methane pyrolysis). Currently, 96% of global H_2 production derives from fossil fuels; only 4% from electrolysis. Critically, H_2 is not a direct greenhouse gas (it lacks IR-absorbing bond dipoles) but is an indirect one: atmospheric H_2 reacts with the hydroxyl radical (•OH) — the "detergent of the atmosphere" produced photochemically from ozone and water vapor — competing with •OH's reaction with methane and thereby extending CH_4's atmospheric lifetime. Atomic hydrogen (H•) produced in this reaction also initiates free radical chains that generate tropospheric ozone, a health hazard and greenhouse gas. These indirect warming effects mean H_2 leakage during production, storage, and transport must be minimized.

Hydrogen redox chemistry. H_2 (oxidation state 0) can act as either a reductant (donating 2 electrons to reduce substrates) or as the product of H^+ reduction (gaining 2 electrons). *E. coli* produces H_2 through a coupled two-enzyme system: formate dehydrogenase oxidizes formate (C oxidation state +2) to CO_2 (+4), generating H^+ and electrons, and hydrogenase reduces $2H^+$ to H_2 using those electrons. This electron flow parallels the mitochondrial electron transport chain, with ferredoxin serving an analogous role to the ubiquinone pool.

Direct biophotolysis. In *Chlamydomonas reinhardtii* and other green microalgae, direct biophotolysis routes electrons from water oxidation at PSII through cytochrome b6f, PSI, and ferredoxin directly to hydrogenase rather than to $NADP^+$, producing H_2 as the terminal product. The overall reaction is $2H_2O \rightarrow 2H_2 + O_2$. The major limitation is that O_2 produced by PSII irreversibly damages [Fe-Fe] hydrogenases. Sulfur deprivation selectively suppresses PSII activity, reducing O_2 evolution and enabling sustained H_2 production under illumination. Approximately 90% of *C. reinhardtii* H_2 production occurs via this direct photolytic route.

Indirect biophotolysis. Under anaerobic conditions in the dark, glucose from prior photosynthesis is oxidized through glycolysis to pyruvate, which is then oxidatively decarboxylated by pyruvate:ferredoxin oxidoreductase (PFOR) — a 267 kDa homodimer with three $[Fe_4S_4]$ clusters per monomer using TPP as cofactor — to acetyl-CoA and CO_2, with electrons transferred to ferredoxin. Reduced ferredoxin then donates electrons via hydrogenase to H^+, producing H_2. This pathway avoids O_2 exposure of hydrogenase. An alternative route via pyruvate:formate lyase (PFL1) produces formate and acetyl-CoA under prolonged dark anoxia.

Photofermentation. Purple non-sulfur bacteria (PNSB) and some microalgae produce H_2 from organic acids (acetate, butyrate, lactate, succinate) using a single photosystem under strict anaerobic conditions. Electrons from organic acid oxidation flow through the photosystem to ferredoxin and then to nitrogenase — which normally reduces N_2 to NH_3 (consuming 16 ATP per H_2 produced as a byproduct) but, in the absence of N_2, can dedicate all electron flow to H_2 production at a significantly reduced cost of 4 ATP per H_2. The photosystem cannot oxidize water but can oxidize H_2S or organic acids as electron donors.

Dark fermentation. Heterotrophic anaerobic bacteria and microalgae produce H_2 from organic biomass feedstocks — including industrial wastewater — through a four-stage sequence: hydrolysis of complex polymers, acidogenesis (producing short-chain fatty acids and H_2), acetogenesis (producing acetic acid and H_2), and methanogenesis (producing CH_4 consuming H_2). Representative acidogenic reactions

include glucose → 2 acetate + $2CO_2$ + $4H_2$, and acetogenic reactions include lactate + H_2O → acetate + CO_2 + $2H_2$. Methanogenic archaea consume H_2 ($4H_2 + CO_2 \rightarrow CH_4 + 2H_2O$), representing a competing pathway that diverts electrons from H_2 toward CH_4.

Electrochemical and thermochemical production. Microbial electrolytic cells (MECs) combine microbial oxidation of organic substrates at the anode with proton reduction to H_2 at the cathode, enhanced by an applied external voltage. Photoelectrochemical cells (PECs) use light-sensitive semiconductor electrodes to drive water splitting directly. Thermochemical gasification of biomass produces syngas, whose H_2/CO ratio is adjusted by the water-gas shift reaction for downstream applications.

The honest assessment of hydrogen as an energy carrier. Despite its theoretical appeal, the chapter closes with a critical evaluation that punctures much of the hydrogen hype. Electrolysis captures only ~30% of input electricity in H_2; using renewables directly for electrification is far more efficient. H_2 embrittles steel pipelines, requiring entirely new and enormously expensive infrastructure. Liquid H_2 storage at 20K requires energy equivalent to ~50% of H_2's combustion value. Producing the current 100 million metric tons per year of industrial H_2 from renewables would consume the entire US electricity grid. The thermodynamic absurdity of capturing dilute, stable CO_2 and using it to make energy-dense H_2 fuels, only to combust them again, is explicit. H_2's legitimate near-term role is as a chemical feedstock — primarily for NH_3 fertilizer synthesis (the Haber-Bosch process) and for fuel upgrading — not as an energy carrier to power transportation or heating. Direct electrification via electric vehicles and heat pumps is the rational path for most energy applications, making genuine clean hydrogen a complement to, not a substitute for, a renewable electricity grid.

9: Biohydrogen - An Introduction is shared under a CC BY-NC-SA 4.0 license and was authored, remixed, and/or curated by LibreTexts.

10: BIOHYDROGEN - HYDROGENASES

Search Fundamentals of Biochemistry

LEARNING GOALS

(Learning goals written by Claude, Anthropic)

By the end of this chapter, students should be able to:

Hydrogenase Classification and [NiFe] Hydrogenases

- Classify hydrogenases into three major types ([NiFe], [FeFe], [Fe]), describe the primary physiological function of each (H_2 oxidation, H_2 production at kcat ~10,000 s^{-1}, hydride transfer), and identify the four [NiFe] subgroups (Groups 1–4) with representative physiological roles.
- Describe the subunit architecture of the membrane-bound [NiFe] MBH — large periplasmic subunit (NiFe active site), small subunit ([4Fe-3S] cluster chain anchoring to membrane), cytochrome b (quinone electron transfer) — and explain the electron flow from H_2 oxidation into the bacterial respiratory chain, connecting this to Complex II of mitochondrial electron transport.
- Explain electron bifurcation as a thermodynamic strategy — how simultaneous exergonic electron transfer to NAD^+ ($E_0' = -280$ mV) subsidizes endergonic electron transfer to ferredoxin ($E_0' = -500$ mV) — and describe the pentameric NiFe-HydABCSL from *A. mobile*, identifying FMN as the bifurcation point and tracing electron flow from H_2 oxidation through FeS clusters to cofactors.

[FeFe] Hydrogenases: Structure, Mechanism, and O_2 Protection

- Describe the H-cluster active site of [FeFe]-hydrogenases — [4Fe-4S] cubane linked via Cys-503 to [$2Fe_2S$] subcluster with CO/CN ligands and azadithiolate (-SCH_2-NH-CH_2S-) bridge — identify the distal Fe (Fed) as the H_2 binding/production site, and explain how the hydrophobic active-site environment restricts O_2 access.
- Trace the catalytic cycle for H_2 evolution through the states Hox → Hred → $HredH^+$ → $HsredH^+$ → Hhyd → $HhydH^+$ → Hox[H_2], identifying the oxidation states of [4Fe-4S] and [2Fe] subclusters at each step, the role of the azadithiolate nitrogen as a proton relay, and the final H_2 release from Fed.
- Describe the bifurcating [FeFe] HydABC from *Thermotoga maritima* as a heterododecamer, identify FMN as the bifurcation site coupling NADH oxidation to simultaneous ferredoxin reduction (endergonic) and H^+ reduction to H_2 (exergonic), and explain the structural homology of HydA/B/C to Complex I subunits Nqo3/1/2 and its evolutionary implications.
- Describe four O_2 protection strategies in [FeFe]-hydrogenases — irreversible inactivation (no protection), CO binding forming reversible Hox-CO, sulfide binding forming Hinact via Htrans, and cysteine ligation forming Hinact by conformational change — and explain why engineering O_2 tolerance is a key challenge for biotechnological H_2 production.

INTRODUCTION

In the last section, we described different ways to produce H_2 and the colors ascribed to them based on the environmental impacts. Many look to produce and use H_2 to provide energy without releasing CO_2. As shown in the reaction below, H_2 can be used in fuel cells to power spacecraft and cars.

$$\begin{aligned} O_2 + 4H^+ + 4e^- &\longrightarrow 2H_2O \\ H_2 &\longrightarrow 4H^+ + 4e^- \end{aligned} \qquad (10.1)$$

H_2-powered cars, considered a zero-emission fuel, are already available. These fully electric cars use fuel cells that oxidize H_2 to generate electrical energy.

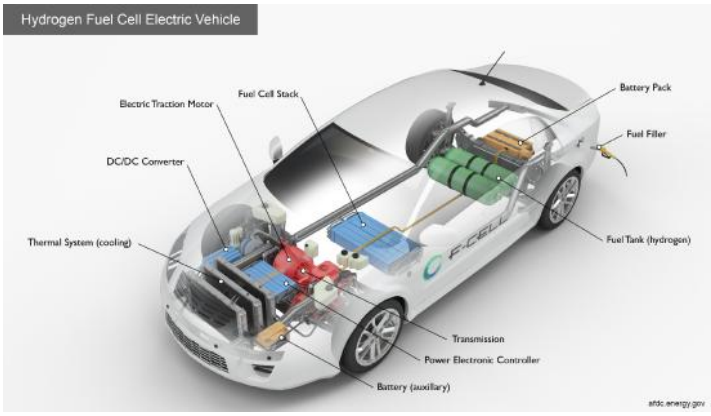


Figure **10.1**: https://afdc.energy.gov/vehicles/how...tric-cars-work

Given the scale required, most H_2 is produced by steam reforming of natural gas and water electrolysis. From a biochemical perspective, cells have evolved to make H_2 and use H_2 as an energy source. Direct microbial production of H_2 is unlikely to meet society's energy needs. The 2023 International Energy Agency (IEA) report, "Hydrogen patents for a clean energy future", doesn't mention direct microbial production. However, much can be learned by studying how **hydrogenases (H_2ases, Hyd)**, enzymes that make or use H_2, work. (Don't confuse hydrogenases with dehydrogenases that directly use NAD^+/NADH and FAD/$FADH_2$) for redox reactions. Transition-metal active-site mimetics can serve as potential catalysts for more industrial-scale production of H_2.

Although the reversible formation of H_2 involves the most elemental particles in chemistry, protons (H^+) and electrons (e^-), the biological reactions that produce and consume H_2 are complex. Before we proceed, let's see how these reactions are similar to other biochemical reactions and pathways we have already discussed.

Use of H_2 as a *source* of electrons for reduction reactions.

Each hydrogen in H_2 has an oxidation number of 0. Each can be oxidized to H^+ (oxidation number +1) with the 2 electrons transferred to a substrate/cofactor or a series of sequential substrates with higher and higher standard reduction potentials (better oxidizing agents), forming reduced products.

$$H_2 + (\text{substrate})_{OX} \rightarrow 2H^+ + (\text{product})_{RED}$$

This general reaction is analogous to the mitochondrial electron transport chain, in which electrons are passed from a source (NADH) to oxidized acceptor molecules. The general reaction below shows each redox pair in the electron transport chain.

$$NADH/NAD^+ \rightarrow FAD/FADH_2 \rightarrow UQ/UQH2 \rightarrow \text{Cyto } C_{OX}/\text{Cyto } C_{RED} \rightarrow O_2/H_2O$$

Some organisms have evolved to produce energy by oxidizing H_2, which is analogous to the photosynthetic oxidation of water. In photosystem II, the oxygen-evolving complex oxidizes oxygen in H_2O (oxidation number -2) as it forms O_2 (oxidation number 0). Some redox pairs, starting with H_2O/O_2, are shown below for photosystem II.

$$H_2O/O_2 \rightarrow P680/P680^* \rightarrow (\text{Plastoquione})_{OX}/(\text{Plastoquione})_{RED}$$

The first reaction is endergonic and requires photons as an energy source.

Use of H^+ as a *sink* for electrons for oxidation reactions that produce H_2.

H^+ has an oxidation number of +1. Hence, it can be reduced to H_2 (oxidation number 0) as it gains electrons from substrates/cofactors that are oxidized. This general reaction is shown below.

$$2H^+ + (\text{substrate/cofactor})RED \rightarrow H_2 + (\text{substrate/cofactor})OX$$

Many microorganisms can produce H_2 through variants of photosynthesis or fermentation, both of which provide the two electrons needed. E. coli has four hydrogenases (Hyd 1, 2, 3, and 4). It forms H_2 through two reactions catalyzed by:

- formate (HCO_2^-) dehydrogenase (FDH): $2HCO_2^- \rightleftharpoons 2CO_2 + 2H^+ + 2e^-$
- hydrogenase (H_2ase): $2H^+ + 2e^- \rightarrow H_2$

The C in formate has an oxidation number of +2 and is oxidized to CO_2, in which the C has an oxidation number of +4.

The formate hydrogenlyase (FHL) complex contains both the formate dehydrogenase (FDH) and a hydrogenase (H_2ase) and reversibly interconverts HCO_2^- and H_2. The *E. coli* FHL-1 complex, which makes H_2 using fermentation, is shown below in Figure **10.2**. The complex can be immobilized on a Macro-mesoporous inverse opal (IO) indium tin oxide (ITO) electrode (IO-IPO) or ITO nanoparticles (NP), which can relay electrons.

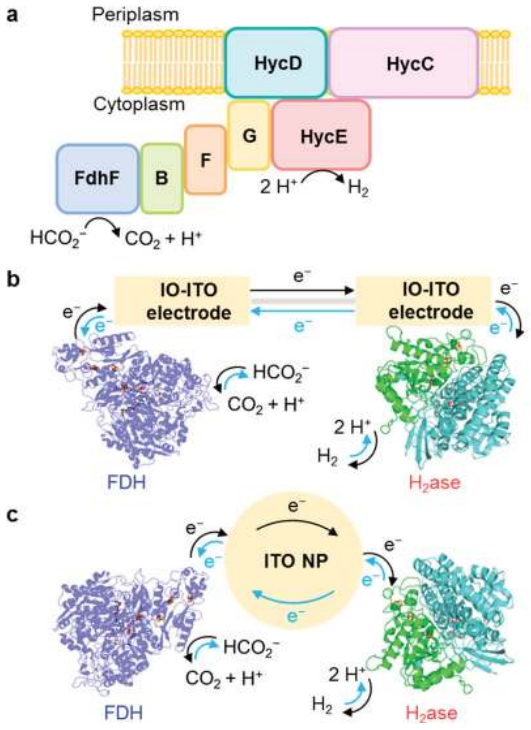


Figure **10.2**: Katarzyna P. Sokol et al. J. *Am. Chem. Soc.* 2019, 141, 44, 17498–17502. https://doi.org/10.1021/jacs.9b09575. **CC-BY license**

Panel (a) shows the biological *E. coli* FHL-1 complex. FdhF, [Mo]-FDH; B/F/G, Fe–S cluster-containing proteins; HycE, [NiFe]-H_2ase; HycD/C, membrane proteins. (17)

Panel (b) shows a IO-ITO|FDH||IO-ITO|H_2ase cell: IO-ITO|FDH wired to IO-ITO|H_2ase electrode.

Panel (c) shows a FDH–ITO–H_2ase nanoparticle (NP) system with enzymes immobilized onto ITO NP in solution. Species size not drawn to scale.

All you need to synthesize H_2 are 2 protons and 2 electrons (potentially derived from photosynthesis). Let's take a deeper look at the hydrogenase that catalyzes H_2 production.

HYDROGENASES (H_2ASES)

Hydrogenases catalyze the reversible conversion of $2H^+ \rightarrow H_2$. A hydrogenase database, HydDB, a web tool for hydrogenase classification and sequence analysis, shows their high diversity and metabolic roles. There are three classes of hydrogenases: the **Ni-Fe** (most abundant, primarily for H_2 conversion to $2H^+$), the **Fe-Fe** (highest k_{cat} for H_2 production), and the **single Fe** hydrogenases, as shown in Table **10.2** below. We won't discuss the single Fe hydrogenases.

CLASSES AND SUBCLASSES OF HYDROGENASES

[NiFe] Group 1: Respiratory H_2-uptake [NiFe]-hydrogenases		
1a	Periplasmic	Electron input for sulfate, metal, and organohalide respiration. [NiFeSe] variants.
1b	Prototypical	Electron input for sulfate, fumarate, metal, and nitrate respiration.
1c	Hyb-type	Electron input for fumarate, nitrat,e and sulfate respiration. Physiologically reversible.
1d	Oxygen-tolerant	Electron input for aerobic respiration and oxygen-tolerant anaerobic respiration.
1e	Isp-type	Electron input primarily for sulfur respiration. Physiologically reversible.
1f	Oxygen-protecting	Unresolved role. May liberate electrons to reduce reactive oxygen species.
1g	Crenarchaeota-type	Electron input primarily for sulfur respiration.
1h	Actinobacteria-type	Electron input for aerobic respiration. Scavenges electrons from atmospheric H_2.
1i	Coriobacteria-type (putative)	Undetermined role. May liberate electrons for anaerobic respiration.
1j	Archaeoglobin-type	Electron input for sulfate respiration$^{\pi}$.
1k	Methanophenazine-reducing	Electron input for methanogenic heterodisulfide respiration.
[NiFe] Group 2: Alternative and sensory uptake [NiFe]-hydrogenases		
2a	Cyanobacteria-type	Electron input for aerobic respiration. Recycles H_2 produced by other cellular processes.
2b	Histidine kinase-linked	H_2 sensing. Activates a two-component system controlling hydrogenase expression.
2c	Diguanylate cyclase-linked (putative)	Undetermined role. May sense H_2 and regulate processes through cyclic di-GMP production.
2d	Aquificae-type	Unresolved role. May generate reductant for carbon fixation or have a regulatory role.
2e	Metallosphaera-type (putative)	Undetermined role. May liberate electrons primarily for aerobic respiration.
[NiFe] Group 3: Cofactor-coupled bidirectional [NiFe]-hydrogenases		
3a	F_{420}-coupled	Couples oxidation of H_2 to the reduction of F_{420} during methanogenesis. Physiologically reversible. [NiFeSe] variants.
3b	NADP-coupled	Couples oxidation of NADPH to the evolution of H_2. Physiologically reversible. May have sulfhydrogenase activity.
3c	Heterodisulfide reductase-linked	Bifurcates electrons from H_2 to heterodisulfide and Fd_{ox} in methanogens. [NiFeSe] variants.
3d	NAD-coupled	Interconverts electrons between H_2 and NAD depending on cellular redox state.

https://geo.libretexts.org/@go/page/34465

[NiFe] Group 4: Respiratory H_2-evolving [NiFe]-hydrogenases		
4a	Formate hydrogenlyase	Couples formate oxidation to fermentative H_2 evolution. May be H^+-translocating.
4b	Formate-respiring	Respires formate or carbon monoxide using H^+ as an electron acceptor. Na^+-translocating via Mrp.
4c	Carbon monoxide-respiring	Respires carbon monoxide using H^+ as an electron acceptor. H^+-translocating.
4d	Ferredoxin-coupled, Mrp-linked	Couples Fd_{red} oxidation to H^+ reduction. Na^+-translocating via Mrp complex.
4e	Ferredoxin-coupled, Ech-type	Couples Fd_{red} oxidation to H^+ reduction. Physiologically reversible via H^+/Na^+ translocation.
4f	Formate-coupled (putative)	Undetermined role. May couple formate oxidation to H_2 evolution and H^+ translocation.
4g	Ferredoxin-coupled (putative)	Undetermined role. May couple Fd_{red} oxidation to proton reduction and H^+/Na^+ translocation.
4h	Ferredoxin-coupled, Eha-type	Couples Fd_{red} oxidation to H^+ reduction in anaplerotic processes. H^+/Na^+-translocating.
4i	Ferredoxin-coupled, Ehb-type	Couples Fd_{red} oxidation to H^+ reduction in anabolic processes. H^+/Na^+-translocating.
[FeFe] Hydrogenases		
A1	Prototypical	Couples ferredoxin oxidation to fermentative or photobiological H_2 evolution.
A2	Glutamate synthase-linked (putative)	Undetermined role. May couple H_2 oxidation to NAD reduction, generating reductant for glutamate synthase.
A3	Bifurcating	Reversibly bifurcates electrons from H_2 to NAD and Fd_{ox} in anaerobic bacteria.
A4	Formate dehydrogenase-linked	Couples formate oxidation to H_2 evolution. Some bifurcate electrons from H_2 to ferredoxin and NADP.
B	Colonic-type (putative)	Undetermined role. May couple Fd_{red} oxidation to fermentative H_2 evolution.
C1	Histidine kinase-linked (putative)	Undetermined role. May sense H_2 and regulate processes via histidine kinases.
C2	Chemotactic (putative)	Undetermined role. May sense H_2 and regulate processes via methyl-accepting chemotaxis proteins.
C3	Phosphatase-linked (putative)	Undetermined role. May sense H_2 and regulate processes via serine/threonine phosphatases.
[Fe] Hydrogenases		
All	Methenyl-H_4MPT dehydrogenase	Reversibly couples H_2 oxidation to 5,10-methenyltetrahydromethanopterin reduction.

Dan Søndergaard et al., *Scientific Reports* **volume 6**, Article number: 34212 (2016). Creative Commons Attribution 4.0 International License. http://creativecommons.org/licenses/by/4.0/.

The three main types have different main functions *in general*. The Ni-Fe, Fe-Fe, and Fe H_2ases generally oxidize H_2, produce H_2, and promote H^- (hydride) transfer, respectively, as shown in Figure **10.3** below.

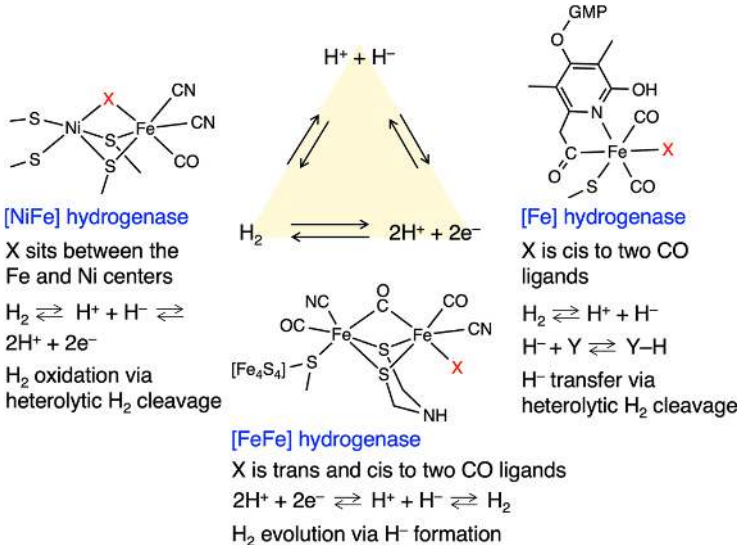


Figure **10.3**: The active site structures of [NiFe] H_2ases that mainly catalyze H_2 oxidation reactions, [FeFe] H_2ases that mainly catalyze H_2 evolution reactions, and [Fe] H_2ases that catalyze H−transfer to the substrate via heterolytic H_2 cleavage. X, possible H_2 active sites; Y, methenyltetrahydromethanopterin; GMP, guanosine monophosphate. Seiji Ogo et al., Science Advances.(2020). DOI: 10.1126/sciadv.aaz81. Creative Commons Attribution-NonCommercial License 4.0 (CC BY-NC).

Much effort has been devoted to developing transition-state analogs of the active site to act as catalysts for H_2 production in fuel cells. Transition-metal catalysts that mimic the structures and activities of the three hydrogenases have been developed. Figure **10.4** shows three specific ones below.

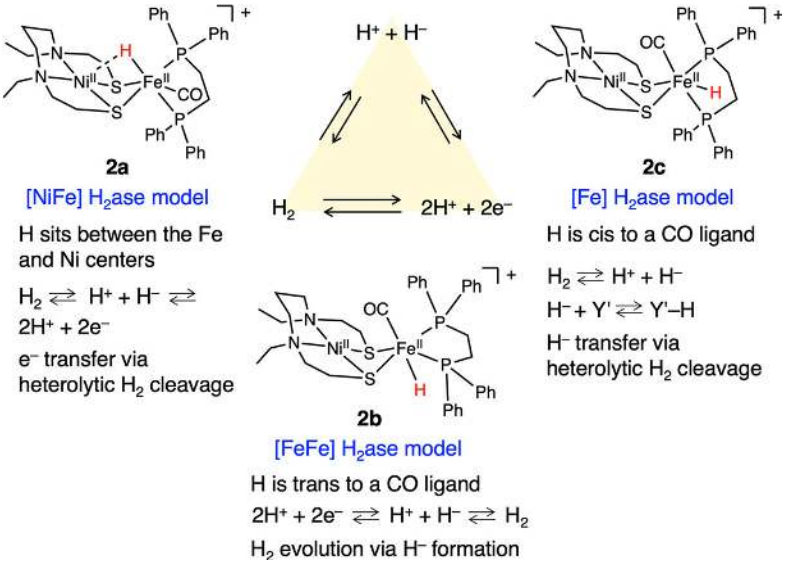


Figure **10.4**: The differing reactivity of the three isomers. Y′, methylene blue $[MB]^+$.Seiji Ogo et al., ibid.

The ligand containing P and PH is bis(diphenylphosphino)ethane.

First, we will explore the Ni-Fe hydrogenases.

NI-FE H_2ASES (HYD):

We'll discuss two examples of Ni-Fe H_2ases

Group 1a periplasmic (membrane-bound) hydrogenases - MBH

These are used in fuel cells and H_2-producing devices because they can adhere to surfaces and serve as useful, heterogeneous (not in solution) catalysts. O_2 also damages some. The enzyme consists of a large periplasmic subunit and a small subunit that anchors the protein to the bacterial plasma membrane. This enzyme oxidizes H_2: $H_2 \rightarrow 2H^+ + 2e^-$. The electrons enter the bacterial respiratory chain through quinones. The transmembrane part of the small subunit binds cytochrome b, which is involved in electron transfer with the quinones, as we saw in Complex II of mitochondrial electron transport. Some soil bacteria (like *Ralstonia eutropha*) can use H_2 as their sole energy source. The orientation of a NiFe MBH within a bacterial cell is shown in Figure **10.5** below.

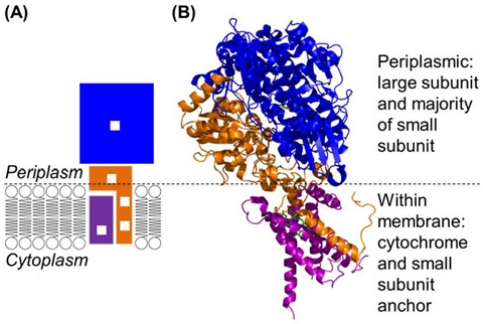


Figure **10.5**: The orientation of a NiFe MBH within a bacterial cell. Lindsey A. Flanagan* and Alison Parkin. Biochem Soc Trans. 2016 Feb 15; 44(1): 315–328 (2016). doi: 10.1042/BST20150201 Creative Commons Attribution License 3.0.

Panel (**A**) shows a cartoon depiction of a NiFe MBH's location within the cytoplasmic membrane. White boxes represent the redox-active metal centers, and blue, orange, and purple blocks indicate the large, small, and cytochrome subunits, respectively.

Panel (**B**) shows how the *E. coli* hydrogenase-1 large (blue ribbon), small (orange ribbon), and cytochrome (purple ribbon) subunits can interact.

Figure **10.6** shows an interactive iCn3D model of the O_2-Tolerant Membrane-Bound Hydrogenase 1 from Escherichia coli in Complex with Its Cognate Cytochrome b (4GD3). The same color coding is used for the subunits as in the above figures.

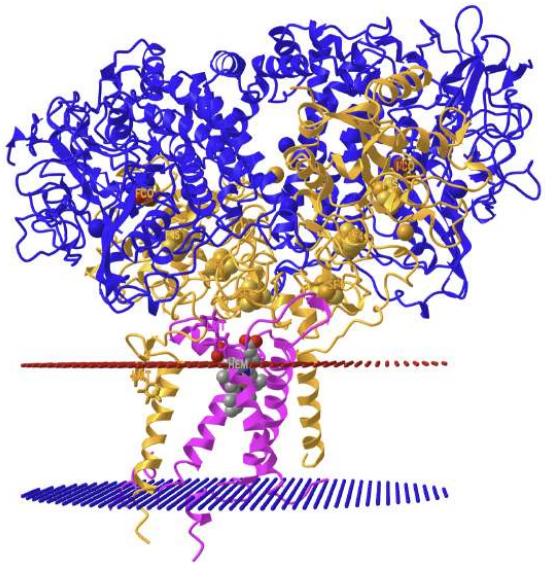


Figure **10.6**: O_2-Tolerant Membrane-Bound Hydrogenase 1 from Escherichia coli in Complex with Its Cognate Cytochrome b (4GD3). (Copyright; author via source). Click the image for a popup or use this external link: https://structure.ncbi.nlm.nih.gov/i...9p4CSQRDPM8nL7

The large and small chains of hydrogenase are shown in blue and orange, respectively, while cytochrome b is shown in magenta. Cofactors and key metals are shown in spacefill. F4S is the Fe4-S3 cluster, SF4 is the iron-sulfur cluster, HEM is hemoglobin, FCO is carbon monoxide-(dicyano) Fe, and Ni is nickel.

The biological (functional) unit consists of two heterodimers. At low O_2 levels, a single dimer can reactivate the other dimer upon exposure to O_2. The enzyme is present at its highest concentration during anaerobic fermentation. Remember that E. coli is a facultative anaerobe that

can shift its metabolic pathways to fit conditions. Perhaps its primary role is to reduce O2 to water and protect enzymes sensitive to it. Cytochrome b may mostly anchor the dimeric H2ase in the membrane.

A bifurcating Ni-Fe H_2ase

These enzymes are more complicated. They oxidize H_2 and direct the two electrons through a complex pathway that bifurcates the flow to different substrates/cofactors. They move an electron to a low-potential (i.e., not a strong oxidizing agent) high-energy species, which is reduced in an endergonic process. The other electron simultaneously moves to a high-potential (i.e., a strong oxidizing agent), low-energy species, which is also reduced in an exergonic process. The overall electron transfer is thermodynamically favorable. An example might prove helpful. NADH ($E^{0'}$ = -280 mV, higher potential) can reduce the protein ferredoxin ($E^{0'}$ = -500 mV, lower potential), which can then pass its electrons in other reactions, including the formation of H_2, CH_4, and NH_3. ATP is not required.

BIFURCATING ENZYMES - WE'VE SEEN ONE BEFORE!

Four classes of bifurcating enzymes that use FAD/$FADH_2$ or FMN/$FMNH_2$ are known. They are optimal because they can participate in either 1 or 2-electron transfers. We will see an example of a Fe-Fe H_2ase further below.

In electron transport, we encountered an electron bifurcating complex in the Q-cycle of Complex III. Reduced ubiquinone (UQH2, or ubiquinol) is oxidized, and the two lost electrons are bifurcated to cytochrome C in a high-potential pathway and to UQ to reform UQH_2, as shown in Figure **10.7** below.

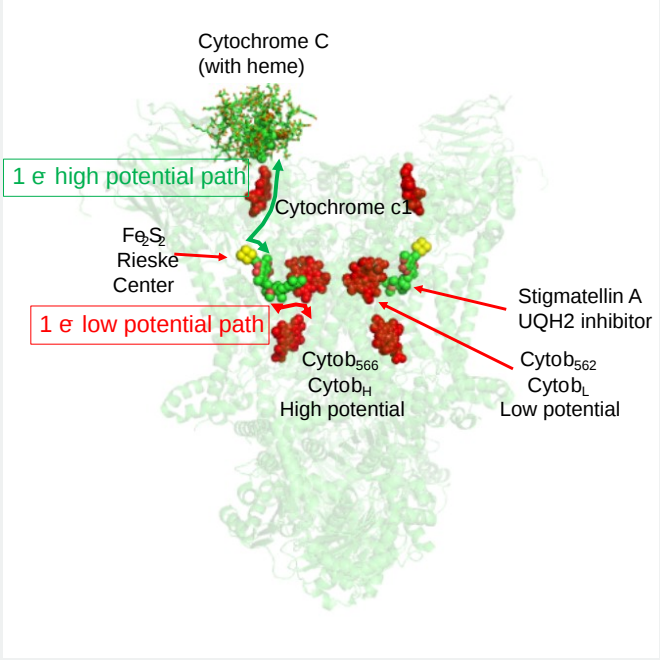
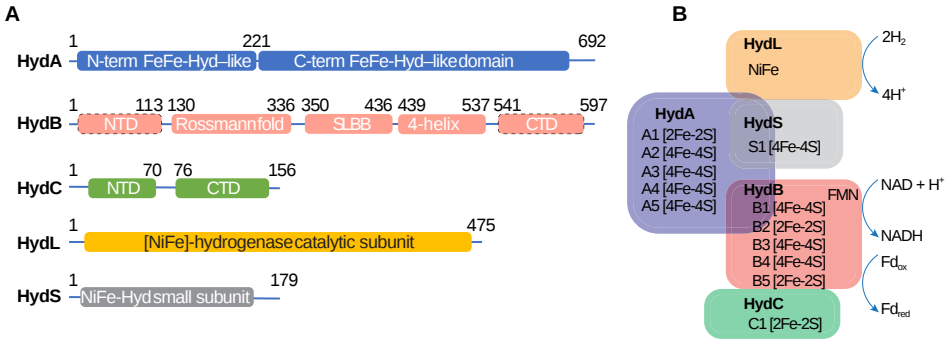


Figure **10.7**: Electron bifurcation in Complex III

One example of a bifurcating Ni-Fe H_2ase is the NiFe-HydABCSL protein from the bacteria *A. mobile*. The general structure of the pentameric form of the functional decamer is shown in Figure **10.8** below.



https://geo.libretexts.org/@go/page/34465

Figure **10.8**: Structure of the *A. mobile* NiFe-HydABCSL pentamer. XIANG FENG et al. ***SCIENCE ADVANCES.*** 2022. DOI: 10.1126/sciadv.abm7546. Creative Commons Attribution License 4.0 (CC BY). https://creativecommons.org/licenses/by/4.0/

The five subunits are called HydA (Hyd = hydrogenase), HydB, HydC, HydL (large subunit), and HydS (small subunit). Pane (**A**) shows the domain structure of the five subunits. The NiFe-HydB NTD and CTDs are partially flexible, as indicated by dashed outlines. Panel (**B**) shows the subunit organization of the NiFe-Hyd complex and their associated cofactors.

NiFe-HydABCSL hydrogenase can reversibly oxidize H_2 with 2 electrons, reducing ferredoxin in an endergonic process and NAD in an exergonic process. FMN is surrounded by a FeS cluster and appears to be the bifurcation point. The reaction is as follows:

- The HydL oxidizes H_2 with two electrons passing through the FeS centers in HydA to HybB.
- The electrons are passed to FMN, where the bound NAD gets reduced.

Figure **10.9** jdkfjdkjfdkjff

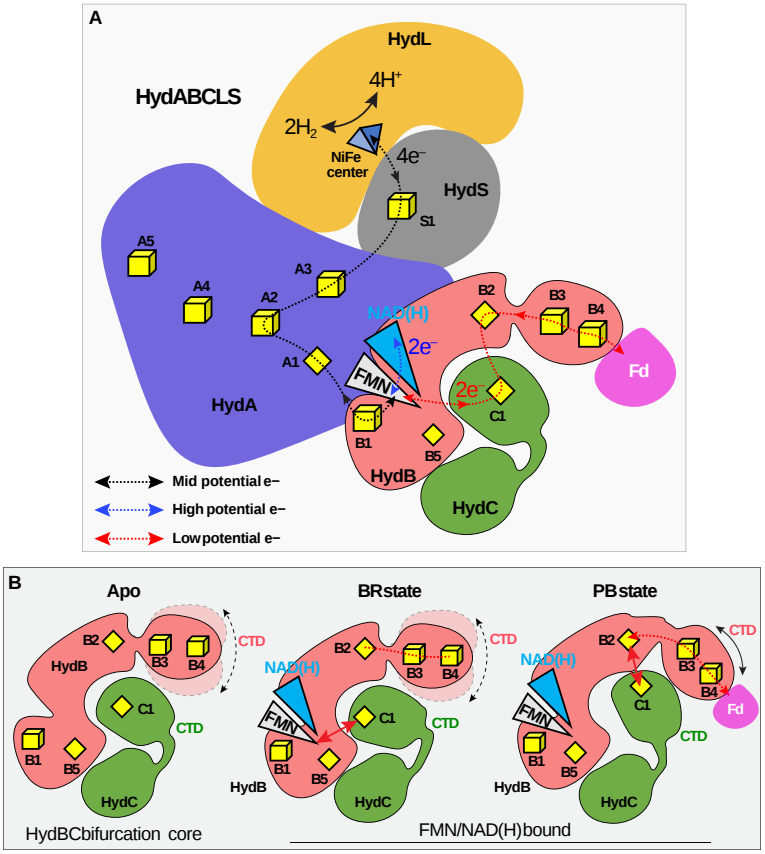


Figure **10.9**: Proposed mechanism of electron bifurcation/confurcation in *A. mobile* NiFe-HydABCSL.

(**A**) Overall electron transfer pathway, highlighting the three branches of the electron transfer path. The mid-potential path is a black dashed line, the exergonic path is a blue dashed line, and the endergonic path is a red dashed line. (**B**) Conformational changes in the HydBC bifurcation core from the electron bifurcation state (BR state) to the electron transduction state (PB state).

Figure **10.10** shows an interactive iCn3D model of the electron bifurcating Ni-Fe hydrogenase complex HydABCSL in FMN/NAD(H) bound state **7T30**

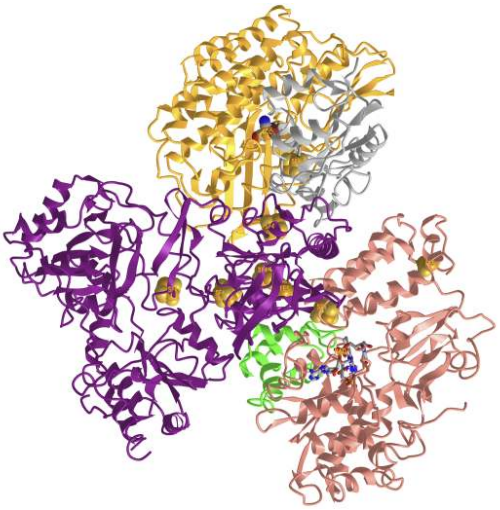


Figure **10.10**: Electron bifurcating Ni-Fe hydrogenase complex HydABCSL in FMN-NAD(H) bound state (**7T30)**. (Copyright; author via source). Click the image for a popup or use this external link: https://structure.ncbi.nlm.nih.gov/i...G9nKGwqvuuh6G7

Figure **10.11** shows an interactive iCn3D model of the cofactors in the electron bifurcating Ni-Fe hydrogenase complex HydABCSL in FMN/NAD(H) bound state **7T30**

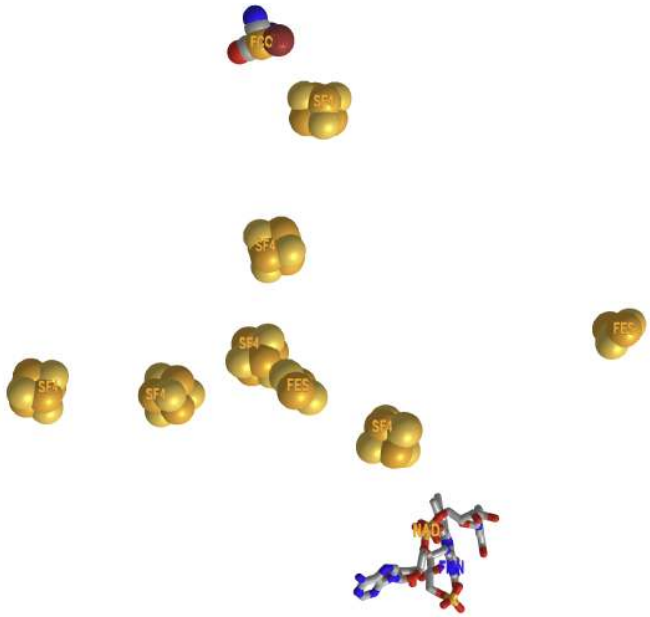


Figure **10.11**: Cofactors in the electron bifurcating Ni-Fe hydrogenase complex HydABCSL in FMN-NAD(H) bound state (**7T30)**. (Copyright; author via source). Click the image for a popup, or use this external link: https://structure.ncbi.nlm.nih.gov/i...hHuzaWUDYCMnAA.

Zoom in on the Ni-Fe catalytic site. The ligands that form coordinate covalent bonds to the Fe are called FCC, or carbon monoxide-(dicyano)-Fe, Figure **10.12** below. There are also bridging sulfurs between Fe and Ni.

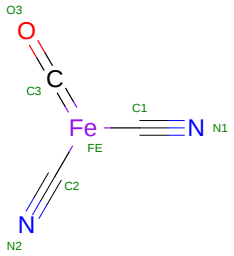


Figure **10.12**: Carbonmonoxo-dicyano-Fe and is shown in detail in

FE-FE HYDROGENASES

These enzymes catalyze various reactions as illustrated in Figure **10.13** below.

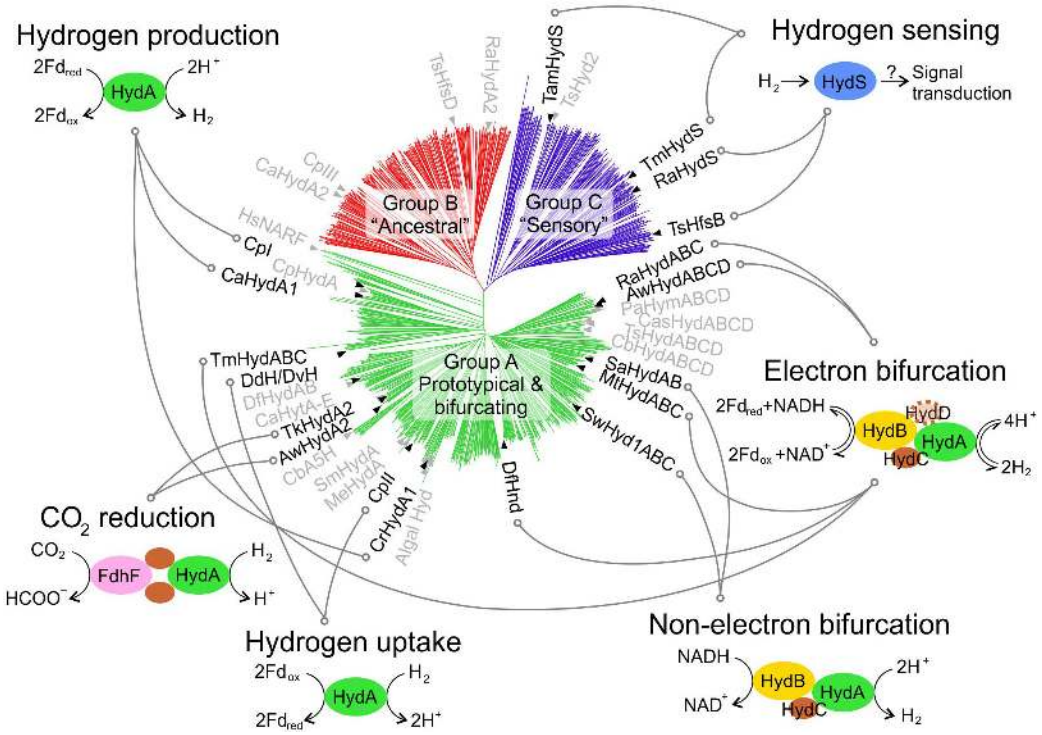


Figure **10.13**: [FeFe]-hydrogenases phylogeny and known functions. Morra S. Front Microbiol. 2022 Mar 2;13:853626. doi: 10.3389/fmicb.2022.853626. PMID: 35308355; PMCID: PMC8924675. Creative Commons Attribution License (CC BY)

As previously proposed, a phylogenetic tree shows the evolutionary relationships among [FeFe]-hydrogenase sequences from public databases. Enzymes experimentally characterized are indicated on the tree to show their relative position. The proposed physiological function of each enzyme is also presented where known. Hyd, hydrogenase subunit; FdhF, formate dehydrogenase subunit; $Fd_{rex/ox}$, reduced/oxidized ferredoxin; $NADH/NAD^+$, reduced/oxidized nicotinamide adenine dinucleotide. They are found in prokaryotic and eukaryotic microorganisms but not in Archaea.

These are the most active for H_2 production with a k_{cat} around 10,000 s^{-1}. They contain a Fe_2S_2 cluster with CO and CN ligands forming bonds to the iron, with the iron ions bridged by a $-SCH_2-NH-CH_2S-$ (aza-dithiolate). A cysteine links the Fe2S2 to a Fe_4S_4 cluster. These two are called the **H-cluster (or $[Fe]_H$**. Within this class are a soluble, monomeric cytoplasmic form, a heterodimeric periplasmic form, and a soluble, monomeric chloroplastic form. This one has a ferredoxin, connecting it to the electron transport chain in photosynthesis. Some in this group, using both NADH and ferredoxin, are called bifurcating types, as they send two electrons from a donor in two different directions. More on this later.

They contain multiple FeS clusters. The H-cluster consists of a Fe_2S_2 cluster linked to a Fe_4S_4 (cubane-like) cluster via a cysteine. The Fe_2S_2 group has CO and CN ligands, with the two Fe ions of the Fe_2S_2 unit coordinated by an azadithiolato ligand, as shown below in Figure **10.14**.

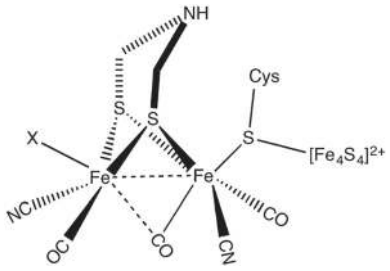


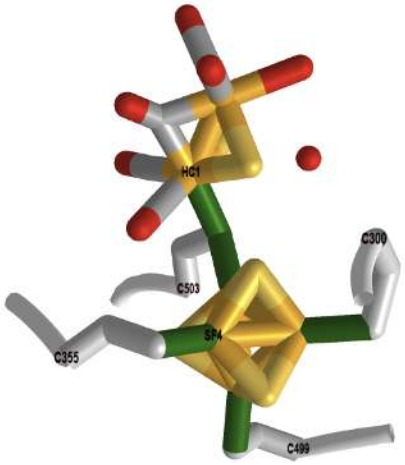
Figure **10.14**: Chemical structure of the H-cluster, which is the active site of the [FeFe] hydrogenase enzyme. Rakesh C. Puthenkalathil et al., Phys. Chem. Chem. Phys., 2020, 22, 10447. https://pubs.rsc.org/fa/content/arti.../cp/c9cp06770a. This article is licensed under a Creative Commons Attribution 3.0 Unported License

The Fe in the [2Fe2S] cluster is linked to the [4Fe-4S] cubane and has six ligands, so it is saturated. The other Fe has an extra coordination site denoted by X, which can bind H^+ or H_2. The cluster is buried in a hydrophobic catalytic site, which helps restrict O_2 access.

As we did for the Fe-Ni H_2ases, we will study two examples of Fe-Fe H_2ases.

Fe-Fe hydrogenase (CpI) from Clostridium pasteurianum

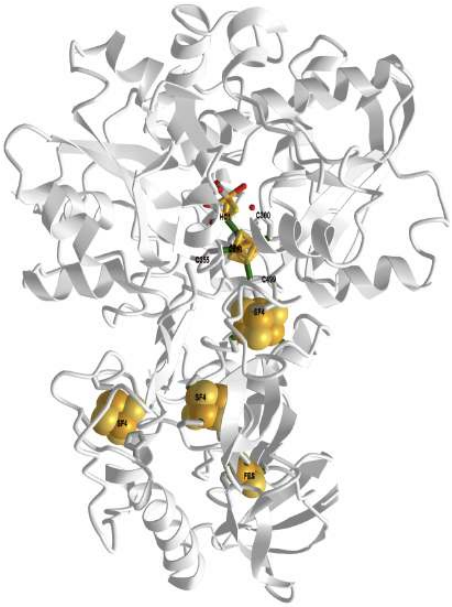
Figure **10.15** shows an interactive iCn3D model of the H-Cluster (HC1) of Fe-Fe hydrogenase (CpI) from Clostridium pasteurianum (1FEH).



NCBI iCn3D Figure **10.15**: H-Cluster (HC1) of Fe-Fe hydrogenase (CpI) from Clostridium pasteurianum (1FEH). (Copyright; author via source). Click the image for a popup or use this external link: https://structure.ncbi.nlm.nih.gov/i...TksW8FGn7crh39

In this model, all CN ligands are shown as CO. The sulfurs are shown in green. Hover over the atoms/ions to identify them. (In iCn3D, choose, **Select, Select on 3D, atom**). The [4Fe-4S] subcluster forms coordinate covalent bonds with four cysteines (300, 355, 499, and 503), with one cysteine (503) forming a bridge to the [2Fe] cluster. The Fe ions in that cluster are surrounded by an octahedral arrangement of ligands. One of the ligands is water (no connecting C atom).

Figure **10.16** shows an interactive iCn3D model of the Fe-Fe hydrogenase (CpI) from Clostridium pasteurianum (1FEH)



NCBI iCn3D Figure **10.16**: Fe-Fe hydrogenase (CpI) from Clostridium pasteurianum (1FEH). (Copyright; author via source). Click the image for a popup or use this external link: https://structure.ncbi.nlm.nih.gov/i...QJsoZ8zbvkpDc7.

As we mentioned above, the net reaction is:

$$2H^+ + (\text{substrate/cofactor})RED \rightarrow H_2 + (\text{substrate/cofactor})OX$$

Many microorganisms can produce H_2 through variants of photosynthesis or fermentation, both of which provide the two electrons needed. E. Coli has four hydrogenases (Hyd 1, 2, 3, and 4). It forms H_2 through two reactions catalyzed by:

- formate (HCO_2^-) dehydrogenase: $2HCO_2^- \rightleftharpoons 2CO_2 + 2H^+ + 2e^-$
- hydrogenase 3: $2H^+ + 2e^- \rightarrow H_2$

Figure **10.17** below shows a reaction scheme for the production of H_2 linked to photosystem I in the chloroplast of microalgae under anaerobic conditions. It starts with the absorption of a photon by P700, which, in the excited state, transfers an electron to a 4Fe4S cluster in ferredoxin. This transfers an electron to the HC-cluster, then to H^+.

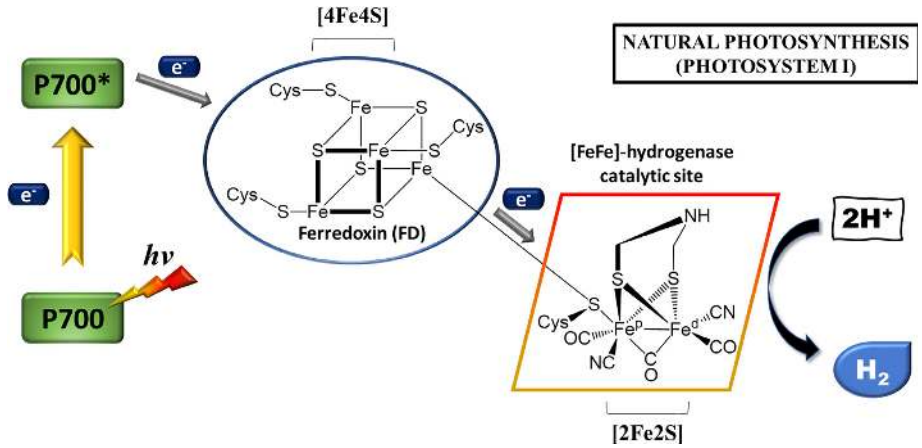


Figure **10.17**: Schematic representation of electron flow from Photosystem I to an [FeFe]-hydrogenase via a ferredoxin redox mediator (Photosystem I). JuanAmaro-Gahete et al., Coordination Chemistry Reviews. 448, December 2021. https://doi.org/10.1016/j.ccr.2021.214172. Creative Commons CC-BY

A possible mechanism for forming H_2 in the H cluster is shown below in Figure **10.18**.

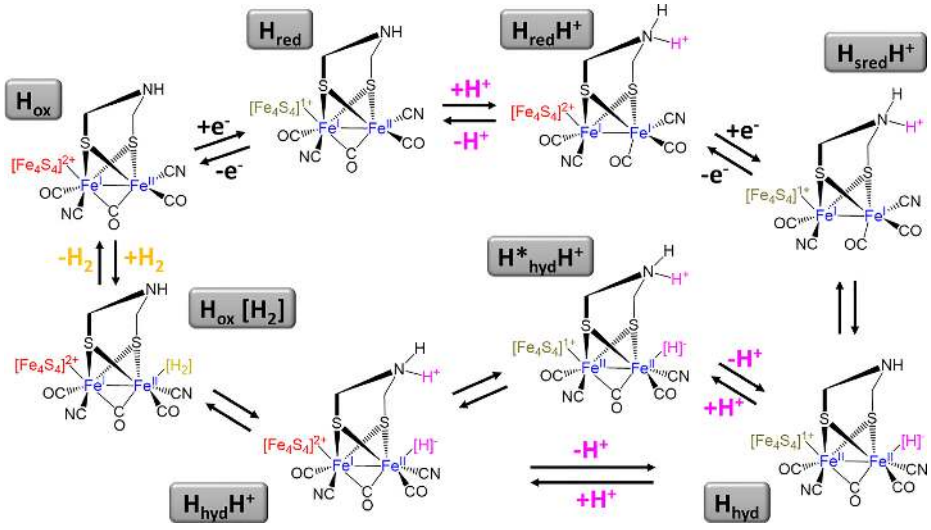


Figure **10.18**: Proposed mechanistic cycle for hydrogen evolution in the H cluster by [FeFe]-hydrogenase adapted from Lubitz et al. JuanAmaro-Gahete et al., ibid

Start at the top left, which shows the rest of the oxidized state. In the enzyme's most oxidized resting system (H_{ox}), the [4Fe4S] cubane is in a 2 + oxidation state while the catalytic subcluster [2Fe] is a mixed-valence Fe^IFe^{II} state. The first one-electron reduction results in the

formation of the H_{red} state, in which the [4Fe4S] subcluster is reduced to the 1+ oxidation state. Protonation of the N of aza-propane-1,3-dithiolate ligand (adt-*N*) triggers an intramolecular charge shift to form $H_{red}H^+$ in which the [4Fe4S] cubane is in the 2 + state and the [2Fe] subsite is reduced to a homovalent Fe^IFe^I state. Subsequent one-electron reduction of the subcluster [4Fe4S] gives rise to the "super-reduced" state $H_{sred}H^+$. In the next step of the catalytic cycle, an intermediate hydride state [H_{hyd}] is formed by an intramolecular proton shift from the adt-*N* to the distal iron F_d. This process is coupled to an electron rearrangement in the [2Fe] subsite, leading to a formal $Fe^{II}Fe^{II}$ oxidation state. The addition of a second proton coupled to another charge shift from the reduced [4Fe4S] to the [2Fe] subsite, either in one or two discrete steps, gives rise to [$H_{hyd}H^+$] that is characterized by a formal Fe^IFe^{II} oxidation state. At this point, there is an equilibrium between the $H_{hyd}H^+$ and $H_{ox}[H_2]$ in which the hydride and the proton are combined into a hydrogen molecule at the distal iron of the system. The catalytic cycle is closed by H_2 release, returning to the initial H_{ox} configuration.

A bifurcating [Fe-Fe] hydrogenase from *Thermotoga maritima* (HydABC)

This enzyme, functionally a heterododecamer, uses NADH as a source of electrons, which passes them to FMN, the bifurcation site, with one electron going to oxidized ferredoxin (Fd_{ox}) and the other to H^+ for reduction to Fd_{RED} and H_2. The enzyme consists of a dimer of trimeric subunits HydA, HydB, and HydC, with each dimer $(HydABC)_2$ interacting with another $(HydABC)_2$ to form a heterododecamer; both halves acting independently. The two trimers (HydABC) in the dimer $(HydABC)_2$ are connected by a [4Fe–4S] cluster. A flexible loop in the B and A chain has a "closed" and "open" bridge conformation, with a nearby Zn^{2+} important in the loop conformation.

Figure **10.19** below shows the HydABC tetramer's cryo-EM structure and the redox cofactors' arrangement.

https://geo.libretexts.org/@go/page/34465

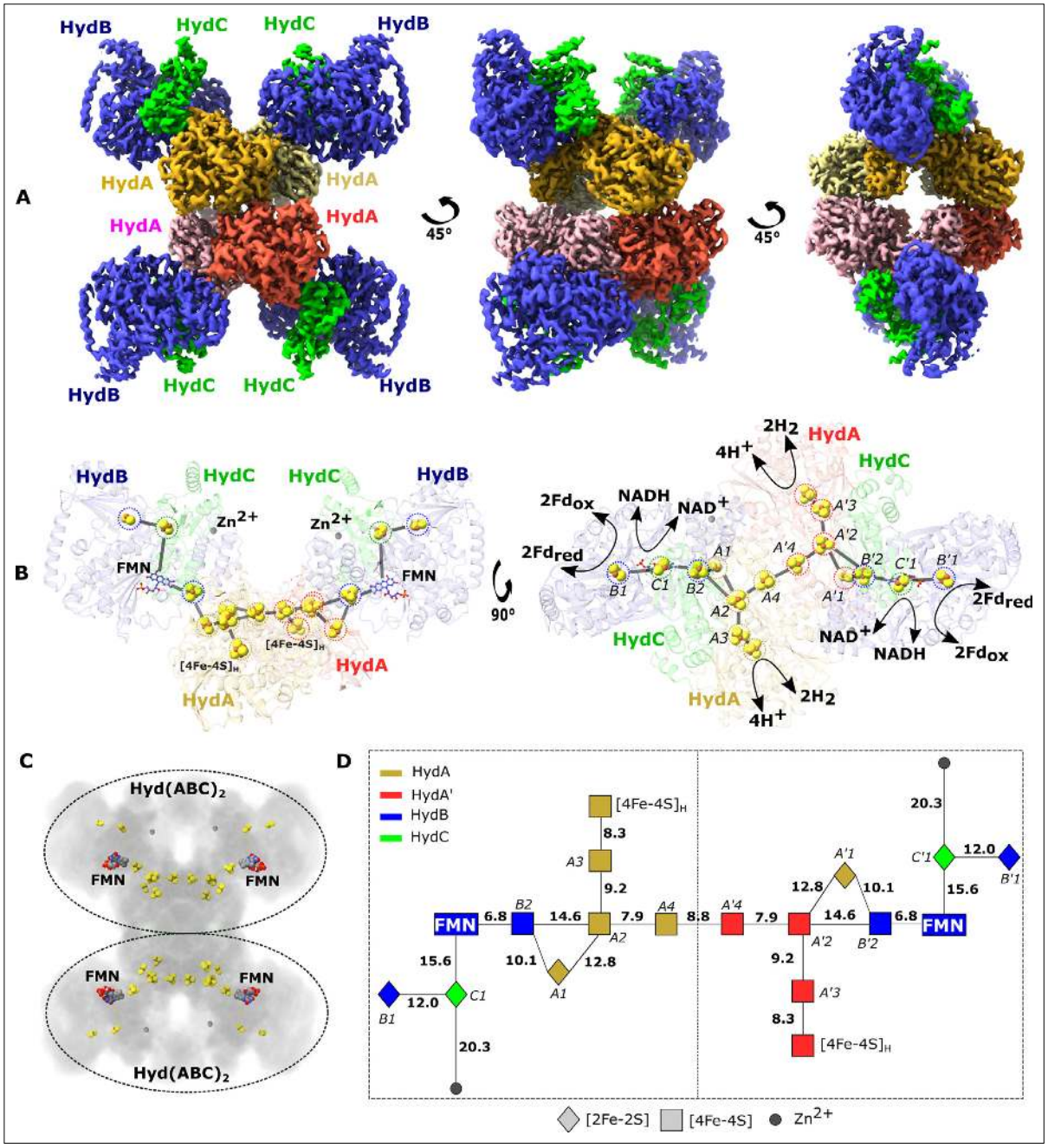


Figure **10.19**: Cryo-EM structure of the HydABC tetramer and arrangement of the redox cofactors. Chris Furlan et al. (2022) eLife 11:e79361. https://doi.org/10.7554/eLife.79361. Creative Commons Attribution License

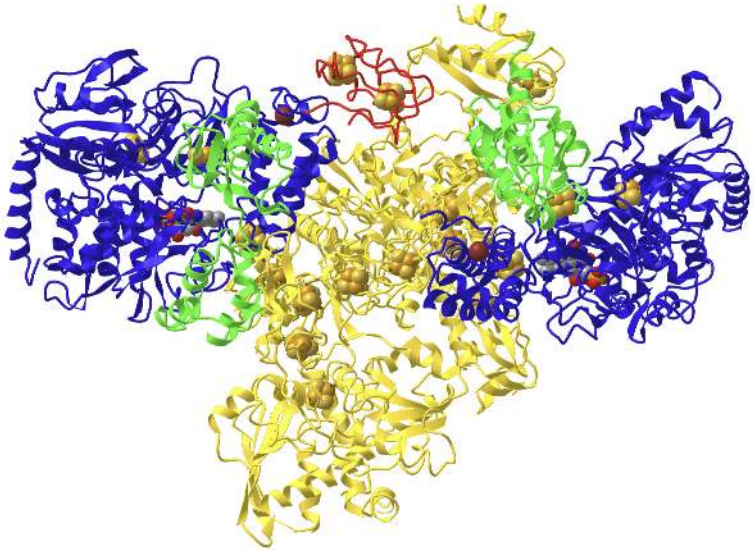
Panel (**A**) shows the unsharpened 2.3 Å map of Hyd(ABC)$_4$ with D2 symmetry enforced, showing a tetramer of HydABC heterotrimers. All four copies of HydB and C are colored blue and green, respectively. The four HydA copies that make up the complex's core are orange, yellow, pink, and red. The top and bottom halves of the complex are constituted by dimers of HydABC protomers (each HydABC unit is a protomer); the two protomers within the same dimer are strongly interacting, while a weaker interaction is present between the top and bottom dimers.

Panel (**B**) shows the HydABC dimer, highlighting the iron-sulfur clusters and flavin mononucleotide (FMN) constituting the electron transfer network.

Panel (**C**) shows the arrangement of redox cofactors within the protein complex, with two independent, identical redox networks (dashed circles); each network comprises iron-sulfur clusters belonging to a Hyd(ABC)$_2$ unit, consisting of two strongly interacting HydABC protomers.

Panel (**D**) shows a schematic of the electron-transfer network for one of the two identical Hyd(ABC)$_2$ units, with edge-to-edge distances (in Å) between the various cofactors. Note that our structure is of apo-HydABC and contains only the [4Fe–4S]$_H$ subcluster of the H-cluster. The $2H^+/H_2$ interconversion reaction in (**B**) illustrates the site at which this reaction occurs, but this will only occur in the fully assembled H-cluster, including [2Fe]$_H$.

Figure **10.20** shows an interactive iCn3D model of the electron-bifurcating [FeFe] hydrogenase from *Thermotoga maritima* (HydABC) (7P5H), using the same colors as the figure above.



NCBI iCn3D Figure **10.20**: electron-bifurcating [FeFe] hydrogenase from *Thermotoga maritima* (HydABC) (**7P5H)**. (Copyright; author via source).

Click the image for a popup, or use this external link: https://structure.ncbi.nlm.nih.gov/i...2hwCUnJ9BgwJi8.

Only the dimer (HydABC)$_2$ is shown. The A (gold), B (blue), and C (green) chains are colored as in the previous figure. The conformationally flexible loop at the C-terminal of a B chain in the closed state is shown in red. The gate also includes the C-terminal part of the A subunit near it.

Figure **10.21** shows the closed-bridge and open-bridge conformations of HydABC (the closed loop was shown in the model above).

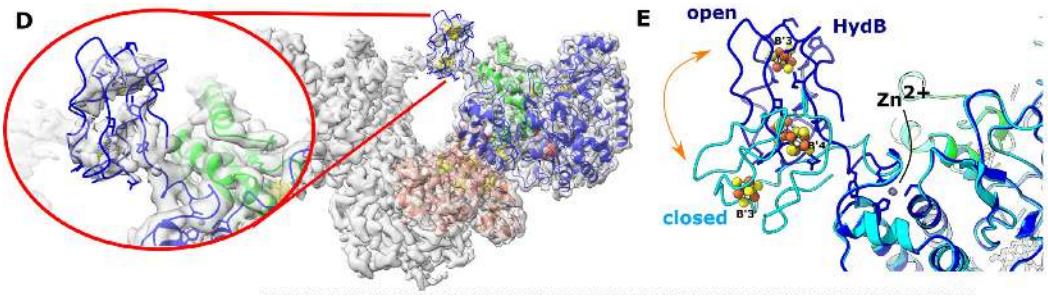


Figure **10.21**: closed-bridge and open-bridge conformations of HydABC from *Thermotoga maritime*.

Panel (**D**) shows the HydB bridge domain in the open position and its fitted model. Panel (**E**) shows a Zn^{2+} hinge region and the two possible conformations of the HydB bridge domain, open (blue) and closed (light blue).

The similarities in cofactor arrangement in the *Thermotoga maritime* Hyd A, B, and C subunits compared to the Nqo1, Nqo2, and Nqo3 subunits in Complex I from *Thermus thermophilus* (discussed in Chapter 19.1) are shown in Figure **10.22** below.

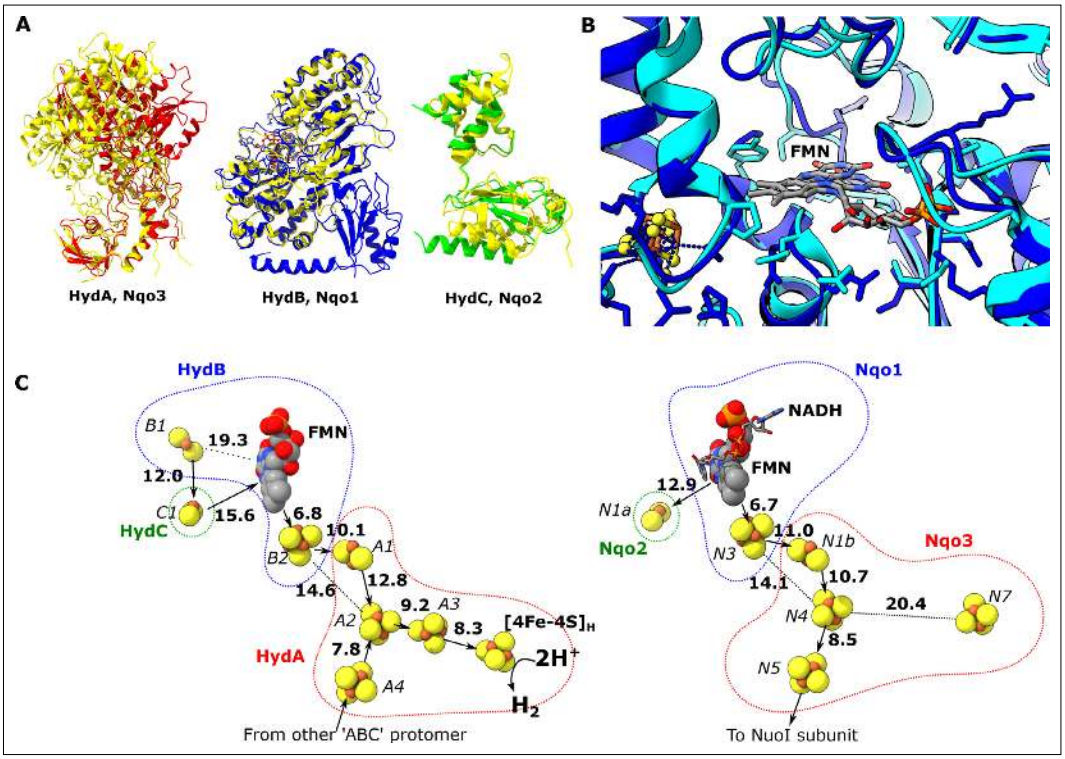


Figure **10.22**: Comparison of the HydA, B and C subunits of the electron bifurcating [FeFe] hydrogenase from *Thermotoga maritima* with the Nqo3, 1 and 2 subunits from respiratory complex I from *Thermus thermophilus*.

Panel (**A**) shows the subunits HydA (red), HydB (blues), and HydC (green) overlaid with, respectively, Nqo3, Nqo1, and Nqo2 (all yellow) of complex I from *T. thermophilus* (Gutiérrez-Fernández et al., 2020, PDB: 6ZIY).

Panel (**B**) compares the NADH-binding site of the Nqo1 subunit of complex I from *T. thermophilus* (light blue) with the flavin mononucleotide (FMN) site in HydB; the high similarity suggests that NADH binds in the proximity of FMN in HydABC, similar to complex I.

Panel (**C**) shows an electron transfer network in HydABC compared to complex I from *T. thermophilus*, with edge-to-edge distances indicated in bold. The red, blue, and green dotted lines indicate the cofactors present in the HydA (Nqo3), HydB (Nqo1), and HydC (Nqo2) subunits, respectively. Note that our structure is of the apo-HydABC and lacks the $[2Fe]_H$ subcluster of the H-cluster. The $2H^+/H_2$ interconversion reaction in (**C**) illustrates the site at which this reaction occurs, but this will only happen in the fully assembled H-cluster, including $[2Fe]_H$.

Here is a link to a video showing the conformational change observed between the 'Bridge closed forward' (7P8N) and 'Open bridge' (7PN2) classes.

In the video, the HydB C-terminal iron-sulfur cluster domain is colored blue, and the HydA C-terminal iron-sulfur cluster domain is colored orange. The zinc ion (gray sphere) and ligating residues (three cysteine ligands and one histidine) are also shown. The location of the HydA C-terminal domain when the bridge is open is unknown, so it is shown transparently in both states for reference.

The geometric separation of catalytic sites and the bifurcation mechanism **prevent** these thermodynamically favored reactions from happening

- H_2 production from ferredoxin oxidation (in the absence of NADH oxidation)
- NAD^+ reduction by H_2 (in the absence of ferredoxin reduction)
- ferredoxin oxidation by NAD^+

OXYGEN SENSITIVITY OF FE-FE H_2ASES

We have noted that Fe-Fe H_2ases can be sensitive to O_2. A possible mechanism involves interacting an Fe ion (Fe_d, the distal Fe) with oxygen, forming damaging free radicals. As CO binds more strongly than O_2 to the iron in hemoglobin, its interaction with the H-center can help protect the H_2ases. Sulfides can also afford protection. These mechanisms are illustrated in Figure **10.23**:

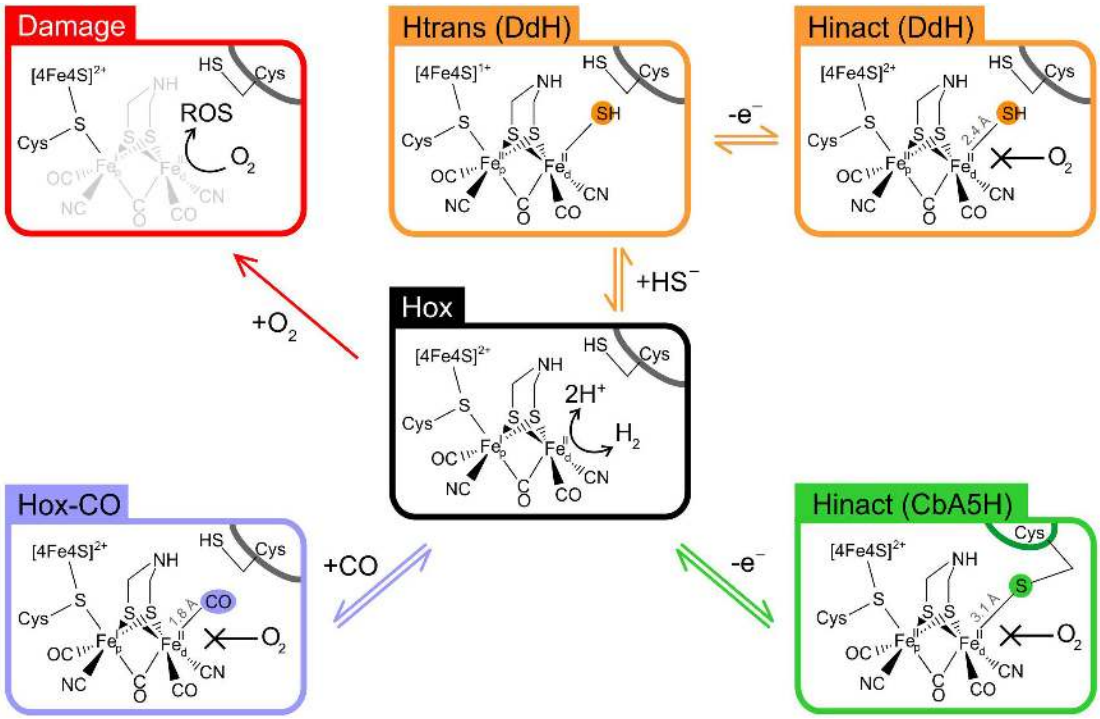


Figure 10.23: Oxygen tolerance strategies in [FeFe]-hydrogenases. Morra S, ibid.

Schematic representation of the H-cluster in the oxidized active state Hox (center). In the absence of any exogenous protectant, numerous [FeFe]-hydrogenases undergo irreversible inactivation due to H-cluster damage with loss of Fe atoms (red pathway); carbon monoxide acts as a protective agent due to its ability to form Hox-CO by binding reversibly to the H-cluster at the same site as O_2 (purple pathway); in DdH, a similar mechanism occurs when sulfide binds to the H-cluster forming Hinact, *via* the Htrans intermediate (orange pathway); in CbA5H, a conformational change in the protein structure allows for a conserved cysteine to directly bind to the H-cluster, forming Hinact (green pathway). Fe_p, proximal iron atom; Fe_d, distal iron atom; Cys, cysteine residue.

SUMMARY

(Summary written by Claude, Anthropic)

This chapter examines the molecular machinery of biological hydrogen metabolism — the hydrogenase enzymes — in detail, connecting their structural biochemistry to the thermodynamics of electron transfer and their relevance to biotechnological H_2 production.

Hydrogenase classification. Three structurally and functionally distinct classes of hydrogenases exist. [NiFe]-hydrogenases are the most widespread and primarily oxidize H_2, passing electrons into respiratory chains. [FeFe]-hydrogenases are the most active for H_2 production, with kcat values around 10,000 s^{-1} — roughly 100-fold faster than [NiFe] enzymes. [Fe]-hydrogenases (single-iron, or Hmd) are found only in methanogens and catalyze hydride transfer to methenyl-tetrahydromethanopterin. Within each class, functional specialization is extensive: the [NiFe] family alone spans four major groups encompassing respiratory uptake enzymes (Group 1), sensory H_2-detecting enzymes (Group 2), cofactor-coupled bidirectional enzymes (Group 3), and respiratory H_2-evolving enzymes including formate hydrogenlyase (Group 4, subgroup 4a, as found in *E. coli*). Synthetic transition-metal complexes that mimic hydrogenase active sites — using ligands such as bis(diphenylphosphino)ethane — are under development as industrial H_2 production catalysts.

Membrane-bound [NiFe] hydrogenase. The prototypical Group 1 [NiFe] MBH, exemplified by *E. coli* hydrogenase 1, is a membrane-anchored heterotrimer. The large periplasmic subunit contains the NiFe active site where H_2 is oxidized ($H_2 \rightarrow 2H^+ + 2e^-$); the small subunit harbors a chain of FeS clusters including an unusual [4Fe-3S] cluster involved in O_2 tolerance; the cytochrome b subunit anchors the complex in the membrane and transfers electrons to the quinone pool, coupling H_2 oxidation to aerobic respiration. The *E. coli* enzyme is most abundant during anaerobic fermentation and is proposed to protect O_2-sensitive enzymes by scavenging O_2 and reducing it to water. Soil bacteria such as *Ralstonia eutropha* use Group 1 hydrogenases as their sole energy source, oxidizing atmospheric H_2.

Electron bifurcation in [NiFe] hydrogenases. The bifurcating NiFe-HydABCSL from *Acetomicrobium mobile* illustrates a sophisticated thermodynamic strategy also seen in mitochondrial Complex III's Q-cycle. This pentameric enzyme simultaneously directs two electrons from H_2 oxidation along two paths: one electron reduces oxidized ferredoxin (Fdox, $E_0' = -500$ mV) in an endergonic step, while the other reduces NAD^+ ($E_0' = -280$ mV) in an exergonic step. FMN, surrounded by FeS clusters in the HydB subunit, is the bifurcation point. The overall reaction is thermodynamically favorable despite the endergonic ferredoxin reduction, because the exergonic NAD^+ reduction subsidizes it — enabling the enzyme to produce reduced ferredoxin (a potent reductant for N_2 fixation, methanogenesis, and other anabolic processes) without consuming ATP.

[FeFe]-hydrogenase active site and mechanism. The [FeFe]-hydrogenases contain the H-cluster, a uniquely complex active site: a [4Fe-4S] cubane cluster connected via a bridging cysteine to a [$2Fe_2S$] subcluster whose two iron atoms are coordinated by CO and CN ligands (unusual in biology) and bridged by an azadithiolate (-SCH_2-NH-CH_2S-) ligand. The distal Fe (Fed) has an open coordination site (X) for H_2 and H^+ binding. The azadithiolate nitrogen serves as a proton relay, shuttling protons between solvent and the Fe active site. The proposed catalytic cycle begins with the oxidized resting state (Hox), where [4Fe-4S] is $2+$ and [2Fe] is mixed-valence Fe(I)Fe(II). Sequential one-electron reductions and protonations cycle through Hred, $HredH^+$, $HsredH^+$, and Hhyd states, with a critical hydride intermediate at Fed in the Hhyd state. A second proton addition forms $HhydH^+$, from which H_2 is released at Fed, regenerating Hox. In microalgal chloroplasts, electrons from PSI-excited P700 flow through ferredoxin to the H-cluster, coupling photosynthetic light reactions directly to H_2 production under anaerobic conditions.

Bifurcating [FeFe] hydrogenase from *Thermotoga maritima*. The HydABC enzyme from *T. maritima* is a heterododecamer — a dimer of tetramers, each tetramer composed of two HydABC heterotrimers — with two independent, identical redox networks. NADH is oxidized at an FMN site in HydB (structurally homologous to the FMN-binding Nqo1 subunit of mitochondrial Complex I), and electrons bifurcate: one to oxidized ferredoxin (endergonic) and one to H^+ to produce H_2 (exergonic). A flexible loop in HydB adopts "closed" and "open" bridge conformations regulated by a nearby Zn^{2+} ion, controlling electron transfer between the two HydABC protomers. The structural homology between HydA/B/C and Complex I subunits Nqo3/1/2 — including conserved FeS cluster arrangements and FMN binding geometry — suggests a deep evolutionary connection between anaerobic H_2 metabolism and the aerobic respiratory chain, with hydrogenases potentially representing ancestors of Complex I.

Oxygen sensitivity and protection. [FeFe]-hydrogenases are generally more O_2-sensitive than [NiFe] enzymes. O_2 reaches the H-cluster through gas channels in the protein and binds at Fed, generating reactive oxygen species that destroy the [$2Fe_2S$] cluster irreversibly. Four protective strategies have been identified: CO binding at Fed forms a stable, reversible Hox-CO inhibited state; sulfide binding in *D. desulfuricans* hydrogenase forms a reversible inactive state (Hinact) via the Htrans intermediate; conformational change in CbA5H allows a conserved cysteine to directly ligate the H-cluster forming Hinact; and some enzymes have no protection and undergo irreversible inactivation. Engineering these protective mechanisms into highly active [FeFe]-hydrogenases is a major goal for biotechnological H_2 production in aerobic environments.

10: Biohydrogen - Hydrogenases is shared under a CC BY-NC-SA 4.0 license and was authored, remixed, and/or curated by LibreTexts.

11: A WARMER WORLD- TEMPERATURE EFFECTS ON CHEMICAL REACTIONS

Search Fundamentals of Biochemistry

LEARNING GOALS

Learning goals written by Claude, Anthropic)

By the end of this chapter, students should be able to:

Thermoregulation and Climate Vulnerability

- Distinguish ectothermy from endothermy and homeothermy from poikilothermy, explain why these are independent descriptors, describe the four mechanisms of heat exchange (radiation, evaporation, convection, conduction), and predict which organisms face greater direct biochemical risk from climate-driven temperature increases.

The Arrhenius Equation and Activation Energy

- State the Arrhenius equation, explain how it derives from the Maxwell-Boltzmann distribution of molecular kinetic energies, derive the two-temperature form, and use it to calculate that Ea ≈ 54 kJ/mol produces a doubling of reaction rate ($Q_{10} \approx 2$) for a 10°C increase near room temperature.
- Explain why a plot of ln k versus 1/T is linear with slope −Ea/R, interpret this relationship to extract activation energies from experimental rate data, and apply it to soil enzyme Ea values (β-glucosidase avg 44.9, cellobiohydrolase 42.0, peroxidase 33.2, phenol oxidase 58.9 kJ/mol) to predict how warming will accelerate lignocellulose decomposition and soil CO_2 release.

The Q_{10} Temperature Coefficient

- Define Q_{10}, write and apply the equation relating Q_{10} to rate constants and temperatures, explain why Q_{10} is not a constant — decreasing as absolute temperature increases — and interpret $Q_{10} > 2$, $= 1$, and < 1 in biological contexts including enzyme denaturation.
- Apply Q_{10} reasoning to soil respiration data (annual $Q_{10} \approx 2.76$, daily average ≈ 2.04, decreasing with temperature), explain why Q_{10} models are adequate for simple reactions but inadequate for complex anaerobic decomposition processes, and identify VCell/COPASI-style systems biology approaches as more appropriate alternatives.

Conformational Dynamics and Enzyme Catalysis

- Explain how temperature affects enzyme-catalyzed reactions through both rate constant changes and conformational flexibility, using RNase A as an example — describing how His 48, located 18 Å from the active site, regulates rate-limiting product release through coupled loop motions, and predicting the consequence of His 48 → Ala mutation on kcat.

Inspiration for the chapter comes from Biochemical Adaptation by Hochachka and Somero.

Organisms adapt to their environment, with temperature among the main drivers. This has occurred over geological time (think of arctic camels 3.4 million years ago!) and space with temperature gradients in terrestrial and aquatic environments. This is evident in the different species that thrive at different mountain heights and ocean depths. Species that can move have advantages in selecting an environment best suited to their thermal needs. Historically, homo sapiens have engaged in seasonal migration, and aquatic species in vertical migrations.

Temperature effects are universal throughout life, and physiological and biochemical adaptations are ubiquitous. Metabolically active life can exist from around -15 ºC to about 121 ºC (thermal saline springs). Unless greenhouse gas emissions decrease significantly from current levels, parts of the world will become increasingly uninhabitable due to high temperatures and rising sea levels. Estimates for climate refugees range from 1 billion people by 2050.

Two similar questions arise. Can organisms adapt to increasing temperatures as the climate changes, and are organisms living close to their maximal survivable temperatures?

Before we study the effects of temperature on chemical/biochemical reactions, let's review the basics of thermoregulation. The following classification of organisms by types of thermoregulation is from BioLibre text.

TYPES OF THERMOREGULATION (ECTOTHERMY VS. ENDOTHERMY)

Thermoregulation in organisms runs along a spectrum from endothermy to ectothermy. Endotherms generate most of their heat through metabolic processes and are colloquially called “warm-blooded.” Ectotherms use external sources of temperature to regulate their body

temperatures. Ectotherms are colloquially called “cold-blooded” even though their body temperatures often stay within the same temperature ranges as warm-blooded animals.

Ectotherm

An ectotherm, from the Greek (ektós) “outside” and (thermós) “hot,” is an organism in which internal physiological sources of heat are of relatively small or quite negligible importance in controlling body temperature. Since ectotherms rely on environmental heat sources, they can operate at economical metabolic rates. Ectotherms usually live in environments with constant temperatures, such as the tropics or the ocean. Ectotherms have developed several behavioral thermoregulation mechanisms, such as basking in the sun to raise body temperature or seeking shade to lower it. The common frog is an ectotherm that regulates its body temperature in response to the external environment.

Endotherms

In contrast to ectotherms, endotherms regulate their body temperature through internal metabolic processes and usually maintain a narrow range of internal temperatures. Heat is usually generated by an animal’s normal metabolism, but under extreme cold or low activity, an endotherm generates additional heat by shivering. Many endotherms have more mitochondria per cell than ectotherms. These mitochondria enable them to generate heat by increasing the rate at which they metabolize fats and sugars. However, endothermic animals must sustain their higher metabolism by eating more food often. For example, a mouse (endotherm) must consume food daily to maintain its high metabolism, while a snake (ectotherm) may only eat once a month because its metabolism is much lower.

Homeothermy vs. Poikilothermy

Two other descriptors are also used. A **poikilotherm** is an organism whose internal temperature varies considerably. It is the opposite of a **homeotherm**, an organism that maintains thermal homeostasis. Poikilotherms’ internal temperature usually varies with the ambient environmental temperature, and many terrestrial ectotherms are poikilothermic. Poikilothermic animals include many species of fish, amphibians, and reptiles, as well as birds and mammals that lower their metabolism and body temperature during hibernation or torpor. Some ectotherms can also be homeotherms. For example, some tropical fish species inhabit coral reefs with such stable ambient temperatures that their internal temperatures remain constant. Figure 11.1 below shows the energy output vs temperature for a homeotherm (mouse) and a poikilotherm (lizard).

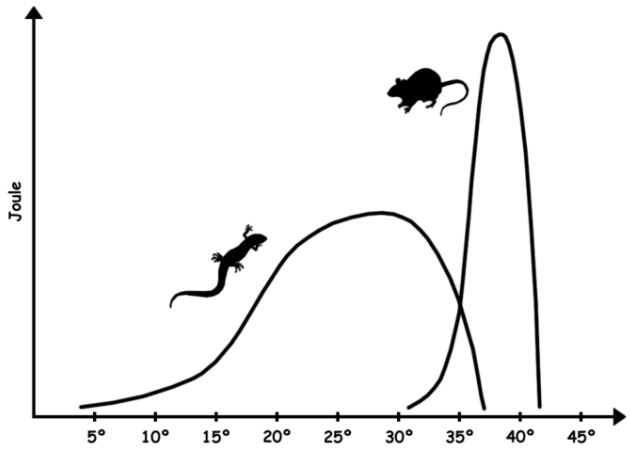


Figure \(\PageIndex{1}\): Homeotherm vs. Poikilotherm: Sustained energy output of an endothermic animal (mammal) and an ectothermic animal (reptile) as a function of core temperature. The mammal is also a homeotherm in this scenario because it maintains its internal body temperature in a very narrow range. The reptile is also a poikilotherm because it can withstand a large range of temperatures.

Another term is **heterothermy**, in which the temperature of a homeotherm can vary across body regions (spatially) and over time (daily or seasonally, as in hibernation). The core of a homeotherm is usually warmer than its extremities, allowing it to cool when needed. Body temperature and metabolic rate decrease during hibernation (or sustained torpor).

Means of Heat Transfer

Heat can be exchanged between an animal and its environment through four mechanisms: radiation, evaporation, convection, and conduction. Radiation is the emission of electromagnetic “heat” waves. Heat radiates from the sun and dry skin in the same manner. When a mammal sweats, evaporation removes heat from the skin's surface. Convection currents of air remove heat from the surface of dry skin as they pass over it. Heat can be conducted from one surface to another through direct contact, as when an animal rests on a warm rock.

Key Points

- Processes such as enzyme production can be modified to adapt to varying body temperatures.
- Endotherms regulate their internal body temperature independently of external temperature fluctuations, while ectotherms rely on the external environment to do so.
- Homeotherms maintain their body temperature within a narrow range, while poikilotherms can tolerate wide variations in internal body temperature, usually due to environmental conditions.
- Heat can be exchanged between the environment and animals via radiation, evaporation, convection, or conduction.

Key Terms

- **ectotherm**: An animal that relies on the external environment to regulate its internal body temperature.
- **endotherm**: An animal that regulates its internal body temperature through metabolic processes.
- **homeotherm**: An animal that maintains a constant internal body temperature, usually within a narrow range of temperatures.
- **poikilotherm**: An animal that varies its internal body temperature within a wide range of temperatures, usually as a result of variation in the environmental temperature.

These terms are diagramed below in Figure **11.2**.

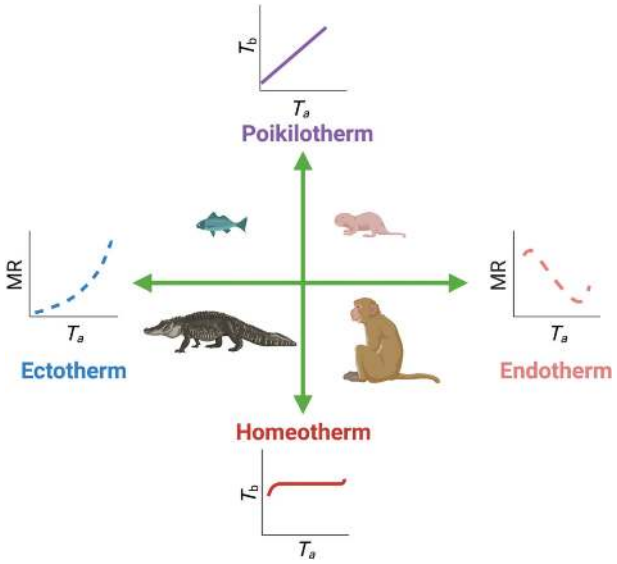


Figure **11.2**: Thermoregulatory Term. Buffenstein et al., Biol. Rev. (2021), doi: 10.1111/brv.12791. Creative Commons Attribution License

We have discussed in the previous chapter sections how temperature can affect macromolecules such as proteins (Chapter 4) and nucleic acids (Chapter 9.1), as well as supramolecular assemblies such as membranes (Chapter 10.3). Temperature effects on small molecules and ions (such as salts in the Hofmeister series and glycerol, Chapter 4.9) in the environment that regulate the function/activity of these larger molecules and assemblies are also important. Hence, we'll review and discuss the effects of temperature on these key molecular species in the next chapter section. First, we'll delve deeper into the general impact of temperature on chemical and biochemical reactions.

TEMPERATURE EFFECTS ON THE RATES OF CHEMICAL REACTIONS

To understand how temperature affects metabolic processes, let's first review its effects on ordinary chemical and biochemical reactions. You may remember the general rule that the rate of a chemical reaction approximately doubles when the temperature increases by 10 °C (10 K). How does that arise? This is generally true in a specific temperature range, as shown below.

The rates of reactions, either endothermic or exothermic, depend on the activation energy (E_a). The activation energy is required to move from a reactant to the transition state, which can then form the product.

The activation energy can be obtained from the Arrhenius equation (that you learned in introductory chemistry), which shows how the rate of an individual chemical reaction depends on temperature.

$$k = Ae^{-E_a/RT} \tag{11.1}$$

where k is the rate constant, E_a is the activation energy, E_a/RT is the average kinetic energy, and A is a constant (the "preexponential" factor).

By taking the natural log (ln) of each side and rearranging the equation, you get a "linearized" equation that is easier for most.

$$\ln k = \ln A - \frac{E_a}{RT} \tag{11.2}$$

A plot of ln k vs 1/T has a slope = E_a/R, from which the activation energy can be calculated.

An alternative form can be derived:

$$\ln \frac{k_2}{k_1} = \frac{E_a}{R}\left(\frac{1}{T_1} - \frac{1}{T_2}\right) \tag{11.3}$$

? A DERIVATION

Here it is!

Derivation

From

$$\ln k_1 = \ln(A) - E_a/RT_1 \tag{11.4}$$

Solve for lnA

$$\ln(A) = \ln(k_1) + E_a/RT_1 \tag{11.5}$$

Substituting into the equation for ln(k_2) gives

$$\ln(k_2) = \ln(k_1) + E_a/RT_1 - E_a/RT_2 \tag{11.6}$$

Rearrange to get

$$\ln(k_2) - \ln(k_1) = E_a/RT_1 - E_a/RT_2 \tag{11.7}$$

Simplify to get the final equation!

$$\ln\left(\frac{k_2}{k_1}\right) = \frac{E_a}{R}\left(\frac{1}{T_1} - \frac{1}{T_2}\right) \tag{11.8}$$

Solving for E_a gives

$$E_a = \frac{R \ln \frac{k_2}{k_1}}{\frac{1}{T_1} - \frac{1}{T_2}} \tag{11.9}$$

Let's use this equation to calculate an E_a that will give a doubling of the reaction rate ($k_2/k_1 = 2$) going from T_1 = 295 K (21.9 ^{0}C, 71.3 ^{o} F) to T_2 = 305 K (21.9 ^{0}C, 89.3 ^{o}F), a 10 ^{o}C temperature rise.

$$\begin{aligned} E_a &= \frac{(8.314)(\ln 2)}{\frac{1}{295} - \frac{1}{305}} \\ &= \frac{\left(8.314 \text{ J mol}^{-1} \text{ K}^{-1}\right)(0.693)}{0.00339 \text{ K}^{-1} - 0.00328 \text{ K}^{-1}} \\ &= \frac{5.76 \text{Jmol}^{-1} \text{ K}^{-1}}{\left(0.00011 \text{ K}^{-1}\right)} \\ &= 52,400 \text{Jmol}^{-1} = 52.4 \text{ kJ mol}^{-1} \end{aligned} \tag{11.10}$$

Hence, if a reaction has an activation energy E_a of about 54 kJ/mol, increasing the temperature from 295 to 305 ^{0}C, (i.e., by 10 ^{0}C), doubles the reaction rate.

Assuming the activation energy is constant, the rate constants increase with temperature because a larger fraction of molecules has the energy ($\geq E_a$) required to react. This is illustrated in Figure **11.3** below.

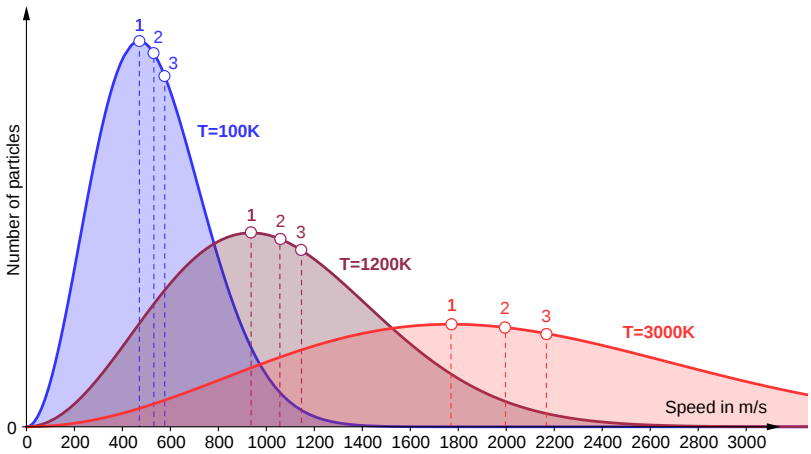


Figure **11.3**: Plot of a Maxwell-Boltzmann distribution of speeds for different temperatures T=100K, T=1200K, T=5000K. Points along the curve show (1) most likely speed, (2) average speed, and (3) thermal speed (velocity that a particle in a system would have if its kinetic energy were equal to the *average* energy of all the particles of the system). https://commons.wikimedia.org/wiki/F...xis-labels.svg. Creative Commons Attribution-Share Alike 4.0 International license.

Let's look at the brown vertical line around 950 m/s. If we take that as the activation energy, very few molecules in the blue distribution have the required kinetic energy $\geq$ Eact to overcome it. At progressively higher temperatures, great fractions (as measured by the area under the curve to the right of the dotted line at 950 m/s) have the required energy; hence, the rates increase with temperature.

When the **temperature change is 10^{o}C**, the ratio of the rate constants (or rates), k_2/k_1 is often called $\mathbf{Q_{10}}$, the **temperature coefficient** (unitless). Q_{10} is not a constant since it depends on the two temperatures that differ by 10 ^{0}C (10 K). Hence, the Q_{10} value for the 10^{0} range from 273-283K differs from the Q_{10} value from 373-383K). For many reactions, Q_{10} is around 2 (doubling the reaction rate) - 3 (tripling the reaction rate) at physiological temperature. Q_{10} =2 for a given E_a only at one set of temperatures that differ by 10 ^{o}C. The variation in Q_{10} values is illustrated in Table **11.1** below for a reaction in which E_a = 44.5 kJ/mol. Q_{10} **decreases** from 2 as the temperatures T_1 and $T_2 = T_1$+10 ^{o}C increase.

T_1 in K (^{o}C)	T_2 (K) (^{o}C)	k_2/k_1 (Q_{10})
273 (- 0.15 ^{o}C)	283 (9.85 ^{o}C)^{o}C	2
373 (99.9 ^{o}C)	383 (110 ^{o}C)	1.45
473 (200 ^{o}C)	483 (210 ^{o}C)	1.26

Table **11.1**: $Q_{10} = k_2/k_1$ values at different temperatures T_1 and T_2 that differ by 10^{o} C.

We will see how this is important in biological settings in a bit. If Q_{10} = 1, the reaction is independent of temperature, and a Q_{10} <1 indicates a reaction that is not functioning. An example might be an enzyme-catalyzed reaction in which the threshold is reached at a higher temperature, $T_2 = T_1 + 10$, at which the enzymes lose an active conformation and start to unfold.

The same equation and the Q_{10}parameters apply to enzyme-catalyzed reactions. The activation energies (E_a) for four enzymes involved in the degradation of lignocellulose in the surface soil and subsoil are shown in Table **11.2** below. The enzymes include two hydrolases, β-glucosidase (BG) and cellobiohydrolase (CB), which cleave cellulose, and two oxidases, peroxidase (PER) and phenol oxidase (POX), which help degrade lignin. The average Ea for these enzymes is about 44.7 kJ/mol, similar to the example in Table 1 above.

Soil	Type	Ea (kJ/mol)			
		BG	CB	PER	POX
Arctic	surface	35.4	39.4	12.7	81.8
Subarctic	surface	36.5	38.6	21.1	45.7
	subsoil	52.2	41.5	22.4	39.4
Temperate 1	surface	40.9	38	64.9	102
	subsoil	49.4	21.2	28	94.8
Temperate 2	surface	31	43.4	25.4	49.5
	subsoil	40.9	39.9	19.8	47.5
Temperate 3	surface	51.5	53.6	28.8	73.2
	subsoil	58.8	46.7	54.2	29
Tropical 1	surface	47.8	50.5	26.5	47.7
	subsoil	56.6	47	47.1	27.1
Tropical 2	surface	39.3	42.5	58.3	82.5
	subsoil	42.8	43.3	22.8	45.5
Avg		44.9	42.0	33.2	58.9

Table **11.2**: Activation Energies (E_a, kJ mol^{-1}) for extracellular soil enzymes involved in the degradation of lignocellulose.Adapted from Steinweg JM et al. (2013) PLOS ONE 8(3): e59943. https://doi.org/10.1371/journal.pone.0059943. Creative Commons CC0 public domain

Q_{10}temperature coefficients are also used to describe biological processes such as respiration, neural signal propagation, and metabolic rates. Many biological processes are affected by temperature, especially in ectotherms, which adjust their body temperatures to their environments, including daily and seasonal temperature shifts. Mammals and birds alter their metabolic rates with temperature, as do hibernating animals.

The Q_{10} **temperature coefficient** is the *factor* by which the reaction rates (k or R) increase (factor of 2, 3, 1.5, etc) for each **10-degree** K or C temperature increase. The following equation gives it:

$$Q_{10} = \left(\frac{k_2}{k_1}\right)^{10°C/(T_2-T_1)} \tag{11.11}$$

It is also called the **van't Hoff's temperature coefficient**. To help understand Q_{10}, let's consider some examples.

- If $T_2 - T_1 = 10^o$, $Q_{10} = k_2/k_1$ for the specified temperature pairs separated by a 10^0 C range (T_1 and T_2=T_1+10). Remember that Q_{10} is not a constant; it depends on the temperature pairs and decreases with increasing temperature.
- If the temperature range is > 10^0 C, the the measured ratio k_2/k_1 is a factor > 1 x Q_{10}
- If the temperature range is < 10^0 C, the the measured ratio k_2/k_1 is a fraction of Q_{10}

This equation can be converted to

$$k_2 = k_1 Q_{10}^{(T_2 - T_1)/10°C} \tag{11.12}$$

where the rate constant k_2 is related to a "base" rate k_1 at a base temperature of T_1. Figure **11.4** below shows an interactive graph of the above equation.

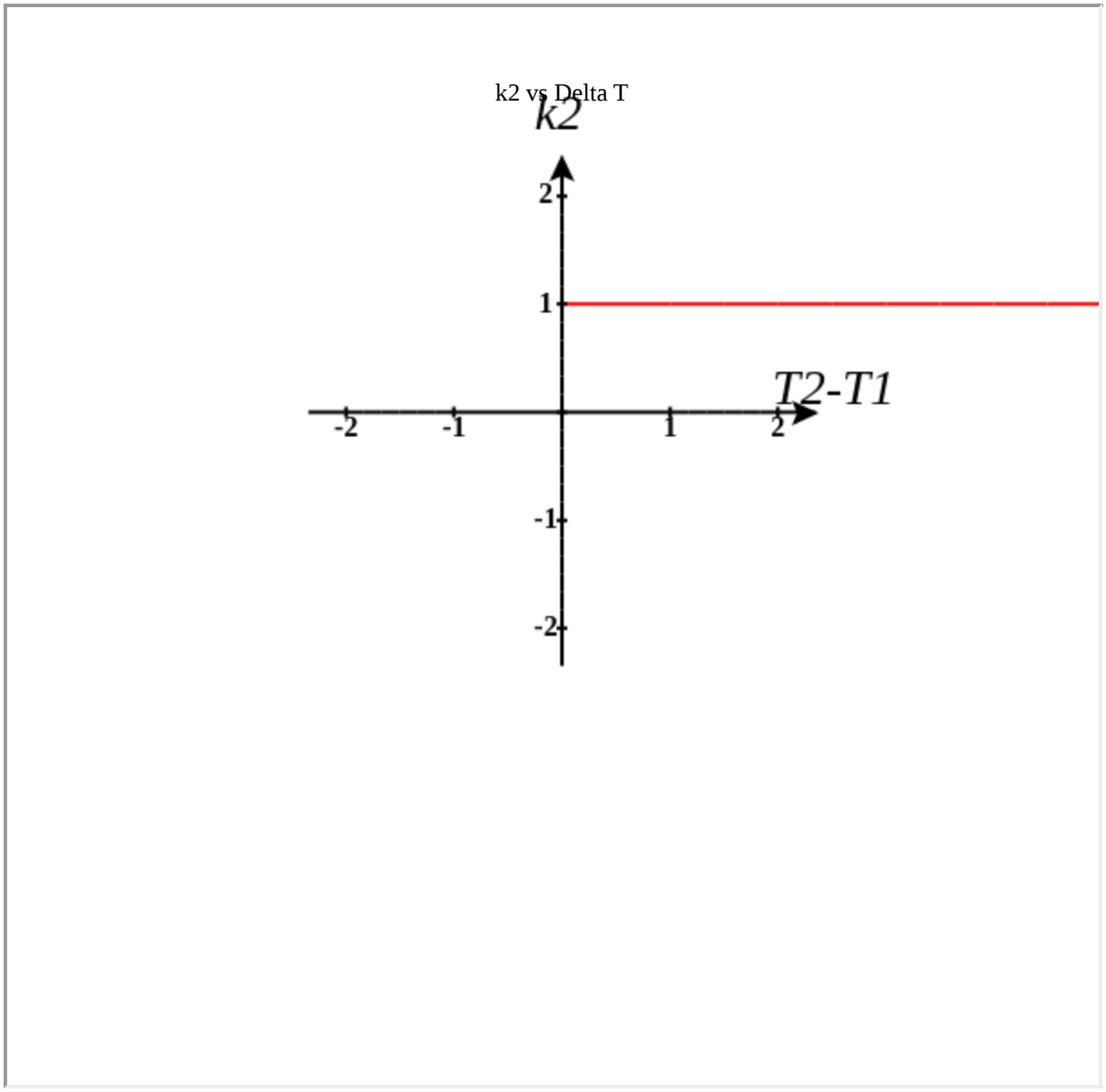


Figure **11.4**: Interactive graph of k_2 (rate 2) vs. delta T at different base rates k_1.

Change the base rate constant, k_1, at a base temperature of T_1 and Q_{10} coefficient to see how they affect k_2.

Note that if Q_{10} =1, then k_2 at T_1 + 10 = k_1 at T_1, so the rate is independent of the temperature.

For most biological systems, the Q_{10} value is ~ 2 to 3 under physiologically relevant conditions. The ratios of the rates (R_2/R_1) for different Q_{10} values are shown in Figure **11.5** below.

https://geo.libretexts.org/@go/page/34466

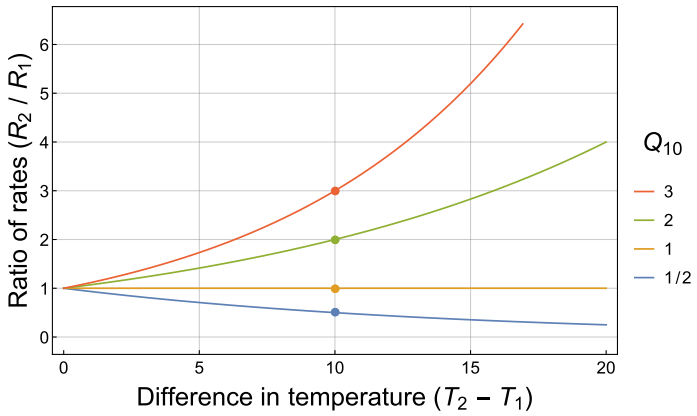


Figure 11.5: Idealized graphs showing the dependence on temperature of the rates of chemical reactions and various biological processes for several different Q10 temperature coefficients. The dots on the graph show how the rate changes with a 10 °C change in temperature. Wikipedia. https://en.wikipedia.org/wiki/Q10_(t...e_coefficient). CC BY-SA 4.0

Again, this hypothetical graph shows the general meaning of Q_{10} values.

The "Q" model has been used to fit complex reaction systems, not just individual reactions. Figure 11.6 below shows the daily mean soil respiration rate as a function of soil temperature. In these graphs, the x-axis is Temperature, not ΔT.

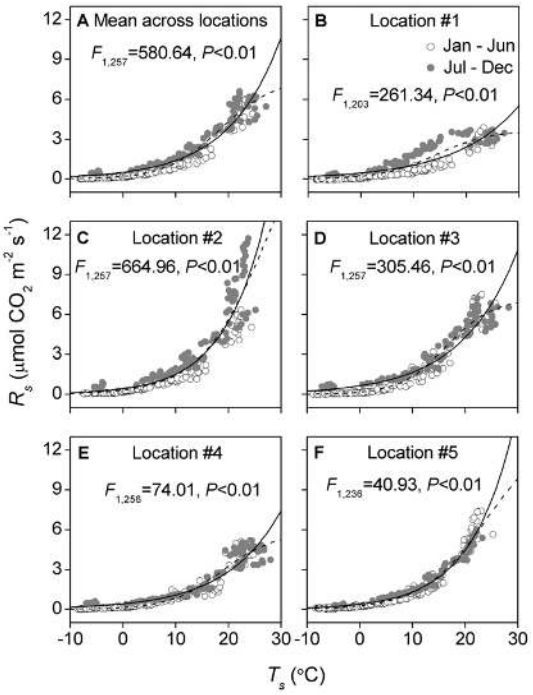


Figure 11.6: Relationships between daily mean soil respiration (R_s) and soil temperature (T_s). Jia X et al., PLoS ONE 8(2): e57858. https://doi.org/10.1371/journal.pone.0057858. Creative Commons Attribution License

The soil temperature, T_s, was measured at a depth of 10 cm. Open circles are from January to June; closed circles are from July to December. The solid lines use a Q_{10} model, in which the observed R_s vs. T_s data are fit with an equation that optimizes the Q_{10} parameter. The dashed lines are fitted using a logistic model we used in Chapter 5.7 to fit ELISA data. R_s is significantly different between the first and second halves of the year.

The soil respiration rate, R_s, at 10 cm depth was strongly affected by temperature, with an annual Q_{10} value of 2.76. Daily estimates of Q_{10} averaged 2.04 and decreased with increasing T_s. A study of seagrass showed that Q10 values are affected by plant tissue age and that Q10 varies significantly with initial temperature and temperature range.

The use of Q_{10} values from the Arrhenius equation assumes that chemical and biochemical processes are exponential functions of temperature. For complex processes such as the decomposition of organic matter, it is better to model the entire system by accounting for the individual enzymes involved. One problem with using Q_{10} values for very complex systems is the choice of the base temperature value

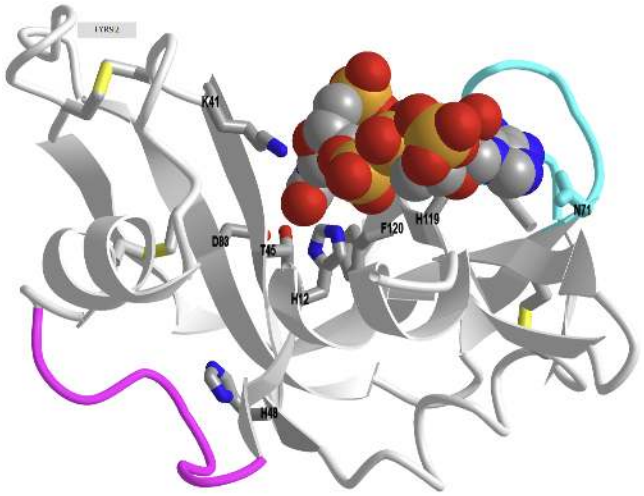
for rate comparisons. The anaerobic decomposition of organic matter is generally a linear function of temperature between 5°C and 30°C, suggesting that a Q10-based model is not ideal. A more complex systems biology approach using programs such as Vcell and COPASI would be preferable and less likely to lead to errors in predicted CH_4 emissions from decomposition.

GETTING BACK TO PROTEINS

Chapter 6.1 explored the mechanisms enzymes use to catalyze chemical reactions. These included general acid/base catalysis, metal ion (electrostatic) catalysis, covalent (nucleophilic) catalysis, and transition state stabilization. Some physical processes included intramolecular catalysis and strain/distortion. The rate-limiting step in enzyme-catalyzed reactions can involve bond breaking in the substrate, product dissociation, and conformational changes required to facilitate binding, catalysis, and dissociation. A rate-limiting conformational change may occur not in the active-site pocket but in nearby loops that modulate the accessibility of the reactant to and the dissociation of the product from the active site. These all may be influenced by temperature, with localized conformational flexibility especially important.

An interesting example of localized conformational changes affecting enzyme activity is RNase A. His 48, 18 Å from the enzyme active site, is involved in the rate-limiting step involving product release.

Figure **11.7** shows an interactive iCn3D model of bovine pancreatic Ribonuclease A in complex with 3'-phosphothymidine (3'-5')-pyrophosphate adenosine 3'-phosphate (1U1B)



NCBI iCn3D Figure **11.7**: Bovine pancreatic Ribonuclease A in complex with 3'-phosphothymidine (3'-5')-pyrophosphate adenosine 3'-phosphate (1U1B). (Copyright; author via source). Click the image for a popup or use this external link: https://structure.ncbi.nlm.nih.gov/i...SnrGYXSVXcLCk6

The substrate is shown in spacefill. The active site side chains and distal His 48 are shown as sticks and labeled. Two flexible loops, Loop 1 (magenta) near His 48 and Loop 4 (cyan) near the active site, are highlighted. During ligand binding, the loops move by a few angstroms, closing the active site and inhibiting product release. Product release is associated with mobile regions, including Loops 1 (20 Å from the active site) and 2. Loop 4, near the active site, is involved in the specificity for purines 5' to the substrate cleavage site. His 48 is conserved in pancreatic RNase A. If mutated to alanine, the k_{cat} decreases by more than 10X, indicating a change in the rate-determining conformational motion. The enzyme is still very active compared to the uncatalyzed reaction. His 48 appears to regulate the rate-limiting coupled motions in the protein.

Figure **11.8** below shows the subtle shift in the conformation of apo-RNase A (magenta, no ligand, 1FS3) to the substrate-bound form (cyan, ligand in sticks, 1U1B). Note the small motion in His 48, shown in the sticks at the bottom of the animated image.



Figure **11.8**: Conformational changes apo-RNase A (magenta, no ligand, 1FS3) on conversion to the substrate-bound form (cyan, ligand in sticks, 1U1B).

We will explore the effects of temperature on protein structure and function further in the next chapter section.

SUMMARY

(Summary written by Claude, Anthropic)

This chapter establishes the physical chemistry and biological context for understanding how temperature — and therefore climate change — affects the rates of chemical and biochemical reactions, providing the quantitative foundation for the two subsequent sections on protein adaptation and ecological consequences.

Thermoregulation and climate vulnerability. Organisms regulate body temperature along a spectrum from endothermy (internal metabolic heat generation, as in mammals and birds) to ectothermy (dependence on external heat sources, as in fish, amphibians, and reptiles). Endotherms maintain narrow internal temperature ranges and require frequent feeding to sustain high metabolic rates; ectotherms operate more economically but track environmental temperatures closely. These strategies are further characterized as homeothermy (narrow internal temperature range) versus poikilothermy (wide tolerance). Critically, ectothermic poikilotherms — including most marine invertebrates, fish, and insects — have internal temperatures that directly follow environmental conditions, making their biochemistry immediately sensitive to climate warming. Two overarching questions motivate the rest of this chapter section: Can organisms adapt to rising temperatures fast enough, and are many species already operating close to their thermal limits?

The Arrhenius equation and activation energy. The rate constant of any chemical reaction depends exponentially on temperature according to the Arrhenius equation: $k = Ae^{-Ea/RT}$. The physical basis is the Maxwell-Boltzmann distribution of molecular kinetic energies: at higher temperatures, a larger fraction of molecules possesses kinetic energy exceeding the activation energy threshold Ea, producing exponentially more frequent productive collisions. A linearized form ($\ln k = \ln A - Ea/RT$) allows activation energies to be extracted from the slope of ln k versus 1/T plots. A two-temperature form of the equation permits direct calculation of how a rate constant changes between any two temperatures given Ea. For a reaction with Ea ≈ 54 kJ/mol, a 10°C temperature increase near room temperature doubles the rate constant — the origin of the familiar "doubling rule."

The Q_{10} temperature coefficient. When the temperature interval is exactly 10°C, the ratio k_2/k_1 is defined as Q_{10}, the temperature coefficient. For most biochemical reactions at physiological temperatures, Q_{10} falls between 2 and 3. A Q_{10} of 1 indicates complete temperature independence; a Q_{10} below 1 signals a process being impaired at the higher temperature — for example, an enzyme losing its active conformation. Crucially, Q_{10} is not a constant: it decreases as absolute temperature increases (demonstrated numerically for Ea = 44.5 kJ/mol across 273–483 K). This means the temperature sensitivity of biochemical processes is greatest at low baseline temperatures — directly relevant to the vulnerability of cold-adapted and polar species to modest warming. Q_{10} reasoning extends beyond individual reactions to complex biological processes including soil respiration (measured annual $Q_{10} \approx 2.76$ in one study, with daily averages of 2.04 declining with increasing temperature), seagrass metabolism, and whole-organism metabolic rates. Activation energies for real extracellular soil enzymes — β-glucosidase (avg Ea 44.9 kJ/mol), cellobiohydrolase (42.0 kJ/mol), peroxidase (33.2 kJ/mol), and phenol oxidase (58.9 kJ/mol) — are consistent with $Q_{10} \approx 2$, confirming that warming will accelerate lignocellulose decomposition and soil CO_2 release in a positive climate feedback. However, for highly complex processes such as anaerobic decomposition (which is linear in temperature from 5–30°C), Q_{10} models are inadequate, and mechanistic systems biology approaches are preferable.

Temperature, conformational dynamics, and enzyme function. Temperature affects enzyme-catalyzed reactions not only by changing rate constants but also by altering protein conformational flexibility, which modulates the rate-limiting step. RNase A provides a detailed example: His 48, located 18 Å from the active site, is involved in the rate-limiting product release step through coupled conformational motions in Loops 1 and 2. Mutation of His 48 to alanine reduces kcat by more than 10-fold, confirming that distal residues regulating protein dynamics can be as important for catalysis as active-site residues. Loop 4, near the active site, controls substrate specificity. These

localized dynamic processes are temperature-sensitive, connecting molecular flexibility directly to the temperature dependence of enzyme activity — a theme developed fully in the following chapter section on thermal adaptation of proteins.

11: A Warmer World- Temperature Effects On Chemical Reactions is shared under a CC BY-NC-SA 4.0 license and was authored, remixed, and/or curated by LibreTexts.

12: A WARMER WORLD- TEMPERATURE EFFECTS ON PROTEINS

Search Fundamentals of Biochemistry

LEARNING GOALS

(Learning goals written by Claude, Anthropic)

By the end of this chapter, students should be able to:

Competing Temperature Effects and Soil Carbon

- Describe how increasing temperature produces competing effects on enzymes — rising kcat and kinact producing a bell-shaped VM curve, rising KM reflecting weaker substrate binding, and declining catalytic power (kcat/kinact) — and explain why organisms near the optimal gray zone are poised near VM but have low catalytic power.
- Explain why soil stores ~1,500 Gt of carbon (more than atmosphere and vegetation combined), how temperature-driven increases in microbial respiration release this stored CO_2, and why no-till farming and high-latitude SOC are particularly vulnerable to warming-driven positive feedback loops.
- Interpret Mount Kilimanjaro altitude-gradient data showing that at a single elevation (2,010 m), simultaneous increases in KM and VM with temperature cancel each other below Scrit (no net rate increase at low substrate concentrations), while intracellular glucose mineralization accelerates at all substrate concentrations — and explain why cold-adapted organisms at 3,020 m show lower Q_{10}KM and Q_{10}VM values and higher Scrit, indicating that thermal adaptation is driven more by the breadth of temperature fluctuation than by mean temperature.

Structural Mechanisms: Ketosteroid Isomerase

- Describe the KSI catalytic mechanism — Asp40 proton abstraction, oxyanion hole stabilization by Tyr16 and Asp/Ser103 — and compare mesoKSI (*P. putida*) and thermoKSI (*M. hassiacum*) in terms of activity at respective optimal temperatures and thermal stability ($\Delta\Delta G° \approx +6.8$ kcal/mol favoring thermoKSI).
- Explain the molecular basis of the D103S stability difference — why buried protonated Asp103 deprotonates upon unfolding (pKa drops from >9 to ~3.7) stabilizing the unfolded state, while Ser103 does not deprotonate on solvent exposure — and connect this to the global survey showing S103 frequency increases with optimal growth temperature across 1,140 KSI sequences.
- Interpret the computational analysis of 2,194 enzyme families showing that thermophiles preferentially harbor Ile-Ile contact pairs, Lys-Glu salt bridges (over Arg-Asp), and Leu/Val → Ile substitutions, and explain the structural rationale for each in terms of conformational flexibility and hydrophobic packing.

Genome-Scale Metabolic Modeling and Thermal Limits

- Describe the enzyme-and-temperature-constrained GEM (etcGEM) of yeast, identify the three temperature-dependent parameters incorporated (kcat, EN denaturation, NGAM), and interpret the model's prediction that below 29°C only kcat limits growth, from 29–35°C both kcat and NGAM limit growth, and above 35°C enzyme denaturation dominates — with squalene epoxidase (ERG1) as the key flux-controlling enzyme at superoptimal temperatures.
- Explain why yeast switches from respiration to fermentation above 37°C in terms of protein concentration limits and ATP yield per protein mass, and connect this metabolic shift to the broader principle that thermal adaptation has systemic consequences beyond individual enzyme kinetics.
- Apply the six questions of Hochachka and Somero to predict organismal vulnerability to climate warming, explain why lethal human temperatures can occur at 29°C at 85% humidity (sweating failure), describe the Antarctic fish synaptic failure case (death at 9°C from acetylcholinesterase dysfunction), and explain why directed evolution demonstrates that organisms can adapt to higher temperatures within limits but cannot transform into thermophilic species.

Inspiration for the chapter comes from Biochemical Adaptation by Hochachka and Somero.

INTRODUCTION

In the previous chapter section, we discussed the generalized effects of temperature on chemical/biochemical reactions. The rate of chemical reactions, including enzyme-catalyzed ones, typically increases 2-3-fold (Q_{10} values) with a 10^0 C increase in temperature over an organism's typical temperature range. Q_{10} values decrease at higher temperature pairs that differ by 10 ^{0}C. A protein enzyme destabilizes at too high a temperature, and Q_{10} values can fall below 1, a sign of potential trouble for an organism subjected to that higher temperature.

As we saw in Chapter 32.11 and will see here, two competing processes affect protein enzymes as temperatures increase. These are increased rates for the catalyzed reaction and increased conformational dynamics, which ultimately lead to denaturation at sufficiently high temperatures. Hence, evolution would presumably select for increased protein stability for organisms adapted to higher temperatures.

For cold-adapted organisms, catalytic rates are expected to decrease. Hence, evolution might lead to higher k_{cat} values for cold-adapted organisms. However, we saw in Chapter 32.11 that the rate-limiting step in enzyme-catalyzed reactions often involves localized conformational changes, which are disfavored at lower temperatures. Hence, evolution would also select enzymes that could maintain flexibility at low temperatures. In Chapter 4.9, we discussed low-temperature protein denaturation. Proteins can be destabilized at low temperatures. In this section, we will study how enzymes can adapt to higher temperatures. We won't discuss how proteins adapt to cold since this topic is less relevant to human-caused climate change.

We will follow the approach used throughout this book - that structure mediates function. We will use a lot of enzyme kinetics since kinetic parameters can tell us much about how the bound substrate goes to a product at high substrate concentrations (k_{cat} or V_M) or low substrate concentrations (k_{cat}/K_M) at different temperatures and for different orthologs of enzymes from species that have adapted to grow at low (psychrophile), medium (mesophile) or high temperatures (thermophiles). We'll next look at the structure of enzymes and the features that allow them to adapt to their optimal growth temperature. Finally, we will look at entire pathways to discern clues as to how they adapt to increased temperatures.

AN OVERVIEW - SOIL ENZYMES

Soil microbes play a key role in the carbon cycle by storing and releasing carbon. Soil temperatures influence the balance between CO_2 uptake and release into the atmosphere.

SOIL ORGANIC CARBON - SOC

The soil is a sink for carbon and stores about 1500 gigatons [Gt] = 1.5 Pt = 1500 Pg), more than the atmosphere and vegetation combined. SOC derives ultimately from photosynthetic organisms. When they die, their carbon is used by heterotrophs for energy and biosynthesis. Carbon can also be returned to the atmosphere by aerobic oxidation by microorganisms, but this requires O_2, which diminishes rapidly with soil depth. Oxygen levels depend on soil porosity, relative amounts of sand and clay, and hydration. Tilling of soil increases O_2 exposure and, hence, the oxidative respiration of SOC, thereby increasing atmospheric CO_2. No-till farming, therefore, can reduce CO_2 emissions into the atmosphere. Inorganic carbon from CO_2 (HCO_3^-, and CO_3^{-2}) binds with cations in the soil (mineralization) or is released into the atmosphere as CO_2.

Carbon input into the soil is mostly determined by photosynthesis, which correlates with root mass and decay, while export is determined by soil microbial respiration (bacteria, fungi, protists). Microorganisms are key in balancing carbon inputs and outputs in soil and are prime determinants of SOC.

SOC is high in northern latitudes since colder temperatures promote lower respiration rates and accumulation of SOC over time. SOC is low in the lush tropics (even given the high photosynthetic rates) because microbial respiration rates are higher at higher temperatures. Deforestation of the lush Amazon Rain Forest will leave soil-poor SOC with little to balance the CO2 released by the decomposition of what's left, as abundant soil microorganisms break it down.

About 21 Gt of the 1500 Gt of SOC consists of microbial mass (12 Gt fungi, 7 Gt bacteria, and 2 Gt from animals). Fungi, hence, are key players in soil metabolism. They are involved in the slow decomposition of organic matter and promote the growth of slow-growing organisms, such as trees. In contrast, bacteria are fast metabolizers abundant in grasslands. Northern soils have higher soil microbial mass than tropical soils, but are less active, allowing for greater SOC stores.

We often think of enzymes working in an aqueous environment in a test tube or a cell (which is very crowded with other molecules). Figure **12.1** below represents the microenvironment of soil enzymes involved in the decomposition of SOC, like cellulose.

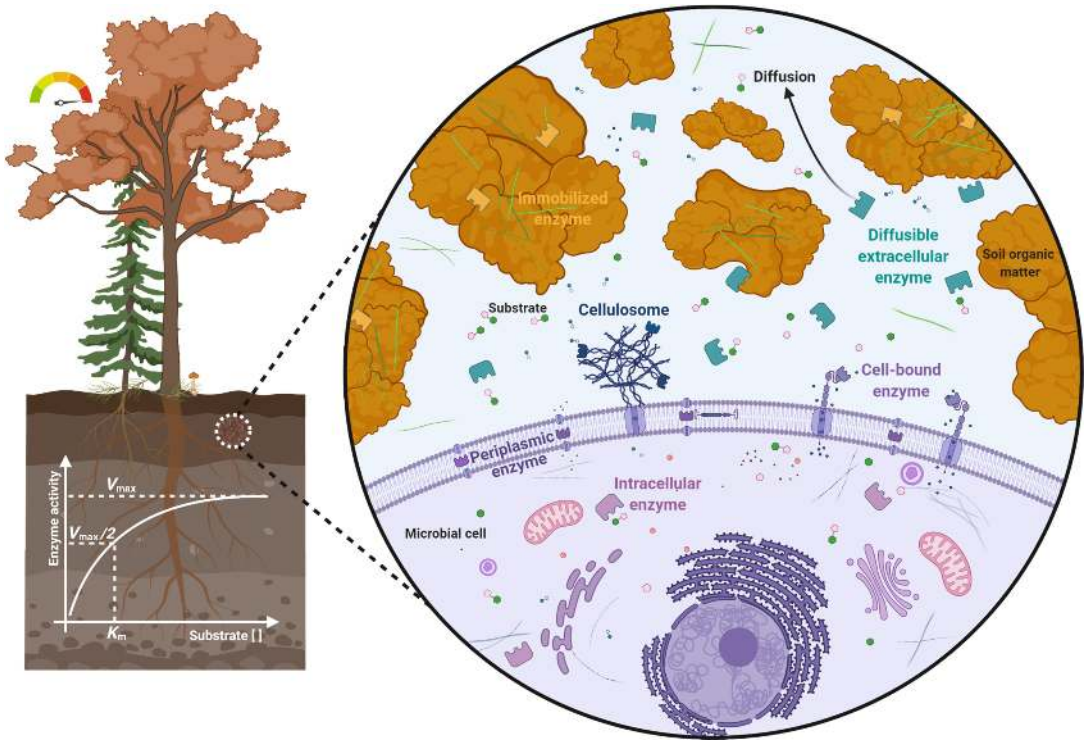


Figure **12.1**: Location of enzymes in soils and their importance for carbon and nutrient cycling. Fanin, N. et al. (2022). Soil enzymes in response to climate warming: Mechanisms and feedbacks. *Functional Ecology*, 36, 1378– 1395. https://doi.org/10.1111/1365-2435.14027. Permission from John Wiley and Sons and Copyright Clearance Center.

Figure **12.2** below gives a review and an overview of the effects of increasing temperature on soil enzymes.

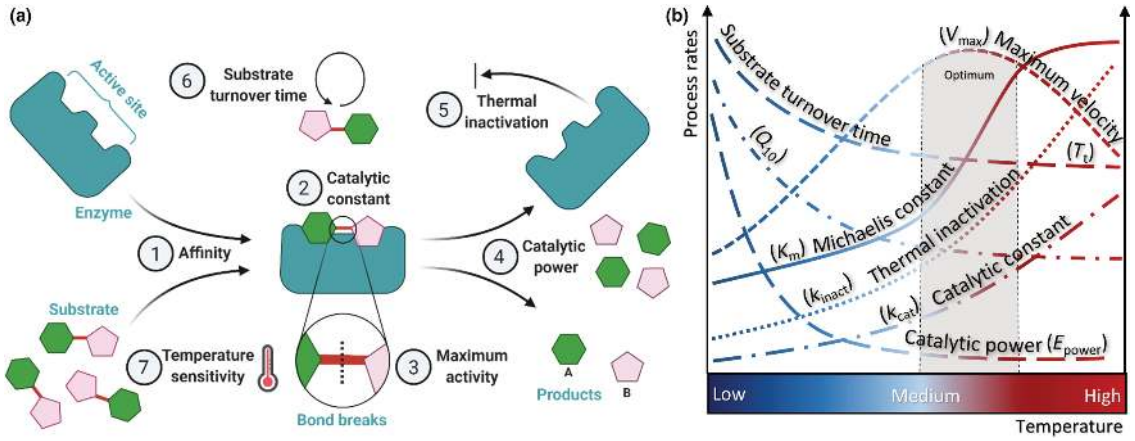


Figure **12.2**: Effects of temperature at the enzyme scale. Fanin, N. et al., ibid. Permission from John Wiley and Sons and Copyright Clearance Center.

Panel (a) shows the many steps involved in enzyme catalysis that can be affected by temperature changes. Step 1 shows the binding of substrates. The K_M (units M) for the enzyme gives a "measure" of the strength of the interaction (but remember that $K_M = K_D$ - the dissociation constant - only under rapid equilibrium conditions). Step 2 reflects k_{cat}, the "net" rate constant for the conversion of bound substrate to product.

Panel (b) shows how key constants change with increasing temperature. The figure shows that k_{cat} increases with temperature, consistent with the Arrhenius equation, and that the temperature coefficient, Q_{10}, decreases (as discussed in Chapter 12.11). (Remember that Q_{10} is the *factor* by which the reaction rate, k or R, changes for each **10-degree** K or C temperature increase). The enzyme's thermal inactivation rate, k_{inact}, also increases with temperature, resulting in a bell-shaped V_M curve. K_m, a measure of the apparent substrate K_D for the enzyme, increases, reflecting weaker binding. The catalytic power, $E_{power} = k_{cat}/k_{inact}$, also decreases with increasing temperature as the

slope of k_{inact} is generally greater than that of k_{cat}. The values on the temperature axis would differ for microbes that grow best at cold temperatures (psychrophiles), moderate temperatures (mesophiles), and high temperatures (thermophiles).

The graphs above show the effects of temperature at the enzyme level. The gray rectangle represents optimal growing conditions, showing that enzymes are poised near V_M for substrate conversion (assuming abundant substrate) but have low catalytic power. Increasing temperatures also affect the microbial community at the level of the individual. These can affect SOC. For example:

- After an increase in SOC decomposition at higher temperatures, subsequent decreases in SOC can occur due to the depletion of available substrates (as enzymes are running at V_M) and changes in carbon use within microbial communities.
- Additional decreases in SOC occur due to increased oxidation and shifts in microbial community composition.
- The levels and types of substrates for enzymes likely change.
- Increased temperatures can lead to greater microbial community mass, which requires more substrate, but in the long term, metabolic shifts might decrease extracellular enzyme activity and microbial biomass.
- Soil conditions also change with increasing temperatures, affecting biomass by altering substrate availability.
- Increased temperature leads to short-term increases in CO_2 emissions due to higher microorganism metabolic rates, explained by the Arrhenius equation. Still, additional effects arise from accompanying changes in the microbial community.

Complex mathematical modeling (as we saw with Vcell, including metabolic and signal transduction pathways) would be needed to understand the effects of warming on SOC stores and their return to the atmosphere as CO_2.

ENZYME PROPERTIES WITH ALTITUDE - MOUNT KILIMANJARO

The loss of SOC due to climate change may be mitigated to some extent as the soil microbial community thermally adapts to lower respiration rates and microbial biomass. As shown in Figure 1, both extracellular and intracellular enzymes must be considered. Extracellular enzymes break down polymers like cellulose into monomers, which are transported into the cell for intracellular respiration and the formation of CO_2 by intracellular enzymes. The extracellular (lytic) and intracellular (oxidative) enzymes might respond differently to higher temperatures. Polymers that are hard to degrade have high activation energies, making soils with higher concentrations of these polymers more sensitive to climate warming (based on the Arrhenius equation).

Changes in the microbial community might include shifts in the fungal/bacterial ratio, which can affect degradation pathways and the rates of enzyme-catalyzed reactions. At higher temperatures, these changes increase conformational flexibility, which can increase k_{cat} and decrease the enzyme's apparent affinity for the substrate, as reflected in higher K_M values. These compensatory effects might leave catalysis unaffected as temperatures increase.

Studies have been conducted on individual degradative enzymes in soil samples from Mount Kilimanjaro. Enzyme kinetic analyses were performed at two different temperatures separated by 10 ^{0}C (10 ^{0}C and 20 ^{0}C), allowing Q_{10} values to be evaluated. The soil samples were collected at different elevations on the mountain to compare the kinetic parameters of enzymes from microbes adapted to those elevations. All organisms in soil from different heights would experience 10 °C, while those at the highest altitudes (3000 m) would encounter 20 ^{0}C only in the summer. The microbes presumably have slightly different optimal growth temperatures and would likely use different adaptive mechanisms at low and high altitudes. Keep in mind that when interpreting the results below, the Q_{10} value determines the sensitivity of a parameter (v_0, K_M, V_M, etc.) to a 10 ^{0}C, increase in the temperature.

Extracellular enzyme activities in soil from one altitude

The activity of three extracellular enzymes in soil samples was studied: β-1,4-glucosidase (degrades cellulose), N-acetylglucosaminidase (degrades chitin from fungi and peptidoglycans from bacteria), and acid phosphatase. The first two enzymes catalyze "recalcitrant" reactions with higher activation energies. Michaelis-Menten plots for the three enzymes in soil samples taken at one height, 2010 meters (m), are shown in Figure **12.3** below. In addition, a plot of glucose conversion to CO_2, an intracellular process, which the authors termed "glucose mineralization" (probably because they trapped CO_2 using OH^- to form HCO_3^-), is also shown.

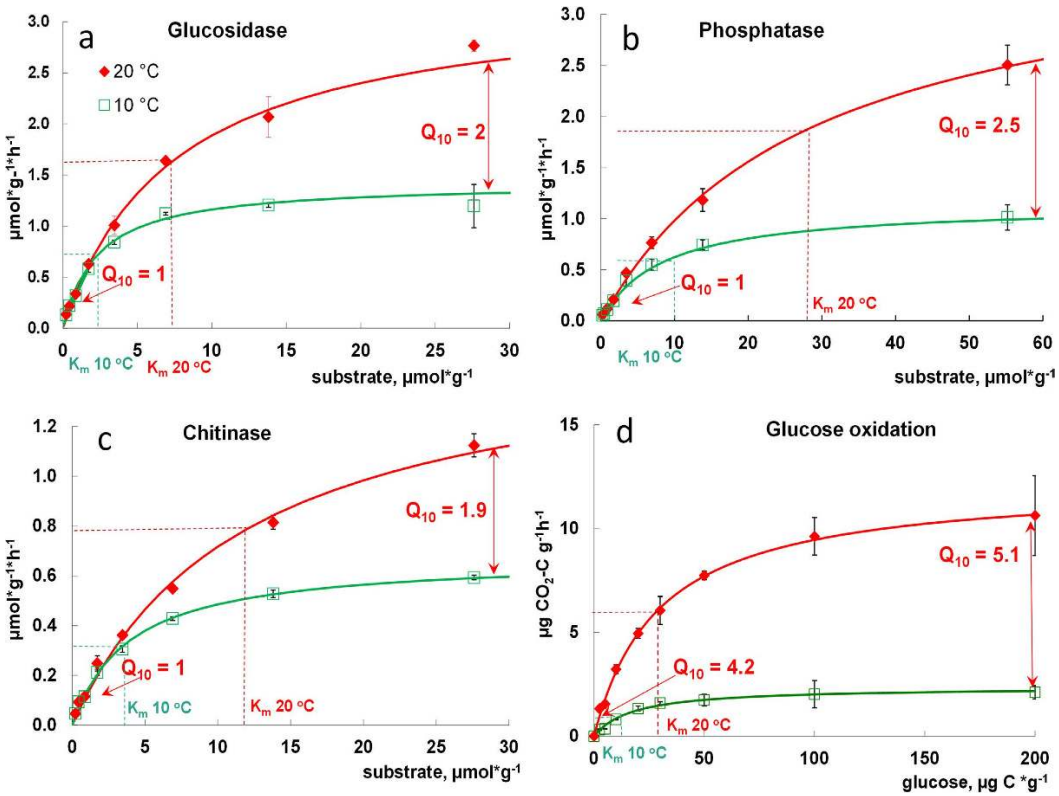


Figure **12.3**: Rates of reactions mediated by hydrolytic enzymes (**a–c**) and rates of glucose oxidation to CO_2 (**d**) as dependent on substrate concentration at 10 and 20 °C for the site located at 2010 m a.s.l. Symbols – experimental data, lines – approximation by Michaelis–Menten kinetics. The **red** lines indicate assays performed at 20^0 C, while the **green** lines are for assays run at 10^0 C. Blagodatskaya, E. *et al.* Temperature sensitivity and enzymatic mechanisms of soil organic matter decomposition along an altitudinal gradient on Mount Kilimanjaro. *Sci Rep* **6**, 22240 (2016). https://doi.org/10.1038/srep22240. Creative Commons Attribution 4.0 International License. http://creativecommons.org/licenses/by/4.0/

The mineralization rate was determined using trace amounts of ^{14}C-labeled glucose, which, if fully oxidized, is converted to $^{14}CO_2$. Given the reaction conditions, the added glucose did not promote microbial proliferation. The authors used a fluorophore (4-methylumbelliferone or MUF)-labeled small substrate analogs for cellulose (MUF-β-D-glucopyranoside), chitin (MUF-N-acetyl-β-D-glucosaminide dehydrate), and acid phosphatase (4-MUF-phosphate). Reactions were carried out in soil samples, and valid initial reaction velocities were determined. The Km values for glucose oxidation (mineralization) are **not** valid K_M values since CO_2 would be produced from the combined actions of the enzymes in glycolysis, pyruvate dehydrogenase, and the citric acid cycle. It could be better called an "operational K_M".

For the three enzymes, the K_M at 20 °C was 25–42% higher than the $V_M = k_{cat}E_{T\,at}$ 20 °C, resulting in $Q_{10}^{KM} > Q_{10}^{VM}$. These compensatory changes canceled any increases in enzyme activity at low substrate concentrations but not at high ones when the enzyme was saturated. Hence, Q10 for the catabolic depolymerization reactions increased with substrate concentration. Note, however, that the rate of intracellular glucose oxidation (mineralization) increased at all substrate concentrations going from 10 to 20 °C, and the canceling effect was not detected, even at low substrate levels. The temperature response of monomer oxidation showed a strongly accelerated reaction rate instead of a canceling effect.

Extracellular Enzyme activities in soils from different altitudes

Next, kinetic analyses were performed on soil samples from 2010 m (warm-adapted microorganisms) and 3020 m (cold-adapted) on the mountain. Plots of Q_{10} (**not** v_0 as in Michaelis-Menten plots) vs. substrate for these studies are presented in Figure **12.4** below to show the temperature adaptation capacities of the enzymes.

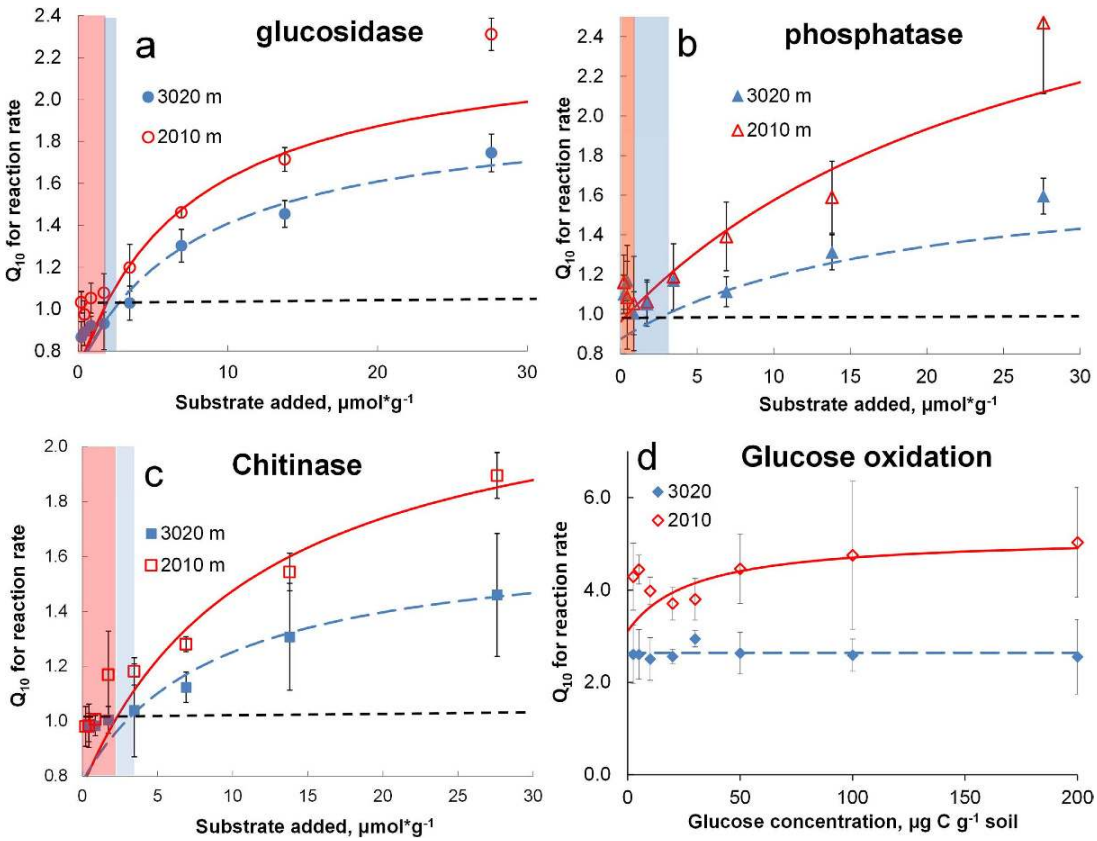


Figure **12.4**: The Q_{10} values for enzymatic activities (**a–c**) and glucose oxidation to CO_2 (**d**) as dependent on substrate concentration at two altitudes. The blue and red rectangles show the concentration range at which no temperature effects occur (i.e $\leq S_{crit}$) with shading colors corresponding to different altitudes. The Q_{10} values derived from experimental data are shown as symbols. The model simulations based on experimentally obtained parameters of Michaelis–Menten kinetics are shown as curves (**a–c**). A non-linear trend was very weakly expressed for glucose oxidation (**d**) at 3020 m elevation. Bars show standard deviations of the means (n = 3). Blagodatskaya, E. *et al. ibid.*

The graphs show that Q10 for polymer degradation increased with increasing substrate concentration. The authors defined a substrate concentration threshold (S_{crit}) below which K_M and V_M values canceled each other out, so no increase in rate was seen with increasing temperature. The width of the rectangles is based on the best-fit dashed **blue** and **red** lines, not the data points. The S_{crit} values were 35–42% larger for the 3020 m (**blue** rectangle) soil samples than at 2010 m (**red** rectangle), even though SOC was lower at that elevation. Q10 values were always lower at $S > S_{crit}$ at higher altitudes. This demonstrates that the enzymes responded less to higher temperatures at higher altitudes (**blue** dots and dashed lower curves). This implies that enzymes at higher latitudes exhibit significant compensatory changes, useful for microorganisms that experience a greater temperature range and larger shifts at these higher altitudes.

Figure **12.5** below shows that the Q values generally decrease over a larger range of altitudes for both enzyme activity (panel A) and glucose oxidation (Panel B).

https://geo.libretexts.org/@go/page/34467

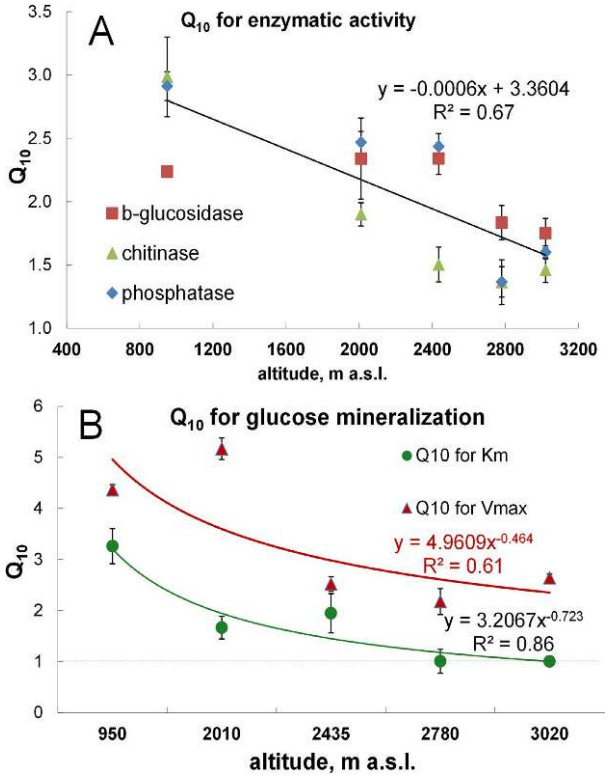


Figure 12.5: The $\mathbf{Q_{10}^{total}}$ values for hydrolytic enzyme activity at saturating substrate concentrations (**A**) and the increase in V_{max} and K_m induced by a temperature increase from 10 to 20 °C for ^{14}C-glucose oxidation (**B**) depending on altitude. Symbols – experimentally derived values for $\mathbf{Q_{10}^{total}}$ (**B**), $\mathbf{Q_{10}^{Vmax}}$ and $\mathbf{Q_{10}^{Km}}$ (**A**). Lines are the trend lines obtained by the best fitting of power (**A**) and linear functions (**B**) at P values < 0.05, bars show standard deviations of the means (n = 3). Blagodatskaya, E. *et al. ibid.*

Panel B shows how Q_{10} values for K_M apparent (**green**) and V_M (**red**) for intracellular glucose oxidation/mineralization both decreased with increasing altitude. Again, consider these K_M and V_M values to be operationally defined and apply them not to an individual enzyme but, in a less rigorous way, to all the enzymes involved in the intracellular oxidation of glucose to CO_2. Investigators could determine these values only by fitting the CO_2 vs [glucose] kinetic data to the Michaelis-Menten equation. All altitudes < 2435 m showed Q_{10} K_M values > 1.9, indicating that the apparent collective K_M values were sensitive to temperature increase. This implies the "collective" set of enzymes responsible for intracellular glucose oxidation was more conformationally flexible, and higher temperatures caused significant increases in apparent K_M values. However, at high altitudes, the Q_{10} values for the apparent K_M were about 1, suggesting no temperature effects on the generic structure and apparent K_M values for the enzymes. The high-altitude enzymes were effectively temperature-stable with respect to K_M values. V_M values were more sensitive to increasing temperatures at all altitudes, but little change was observed between 2435 and 3020 m. This again shows that the enzymes for microorganisms from high altitudes were more strongly adapted to temperature changes, especially at lower substrate concentrations.

The next part can be a bit confusing. The K_M for a given enzyme increases with increasing temperature, as shown in Figure 2. This suggests that the apparent affinity of the given enzyme for substrates decreases, which makes intuitive sense. Figure 12.6 shows that the Q_{10} for K_M (i.e., the sensitivity of K_M to a temperature increase of 10^0 C) decreaseswith increasing elevation for each enzyme studied.

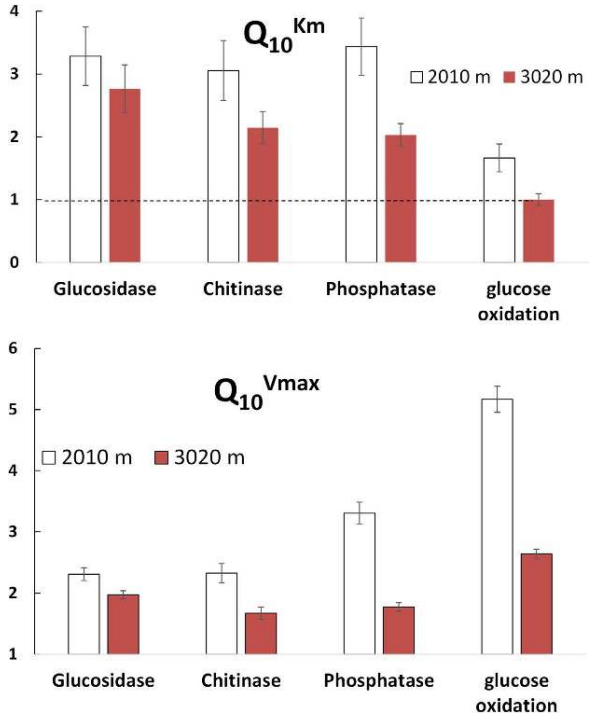


Figure **12.6**: The values of $\mathbf{Q_{10}^{Km}}$ (**a**) and $\mathbf{Q_{10}^{Vmax}}$ (**b**) for hydrolytic reactions and for reactions of glucose oxidation at low and high altitudes. Bars show standard deviations of the means (n = 3).

The figure shows that both Q_{10}^{Km} and Q_{10}^{Vmax} were lower at high altitudes. Hence, the enzymes in organisms from higher altitudes did not respond as strongly to temperature changes. This again suggests that larger compensatory changes are found in enzymes at high latitudes, allowing them to better adapt to the greater temperature range they would experience.

These data suggest that thermal adaptations in the intracellular enzyme are driven more by the wide range of temperatures organisms experience than by the mean temperature. Compensatory and canceling changes in K_M and V_M at low substrate concentration led to a higher S_{crit} in cold-adapted organisms.

STRUCTURAL MECHANISMS FOR ENZYME TEMPERATURE ADAPTATION

Structure determines function. A detailed understanding of how proteins, and more directly enzymes, adapt to temperature changes must come from detailed structural analyses that can be correlated to functions such as enzyme catalytic activity. Two approaches have been used to study the structural bases of enzyme temperature adaptation. One involves the structural analysis of a single enzyme in organisms adapted to different temperatures. The other involves large computational analyses of protein structure databases. We'll discuss both. First, let's explore orthologs (i.e., proteins from the same gene in different species) of a single enzyme, **ketosteroid isomerase (KSI),** from mesophilic (grown at moderate temperatures) and thermophilic (grown at warm temperatures) bacteria.

Figure **12.7** below shows structural and functional features that document KSIs temperature adaptation through changes in activity and stability. Let's step through each panel in order.

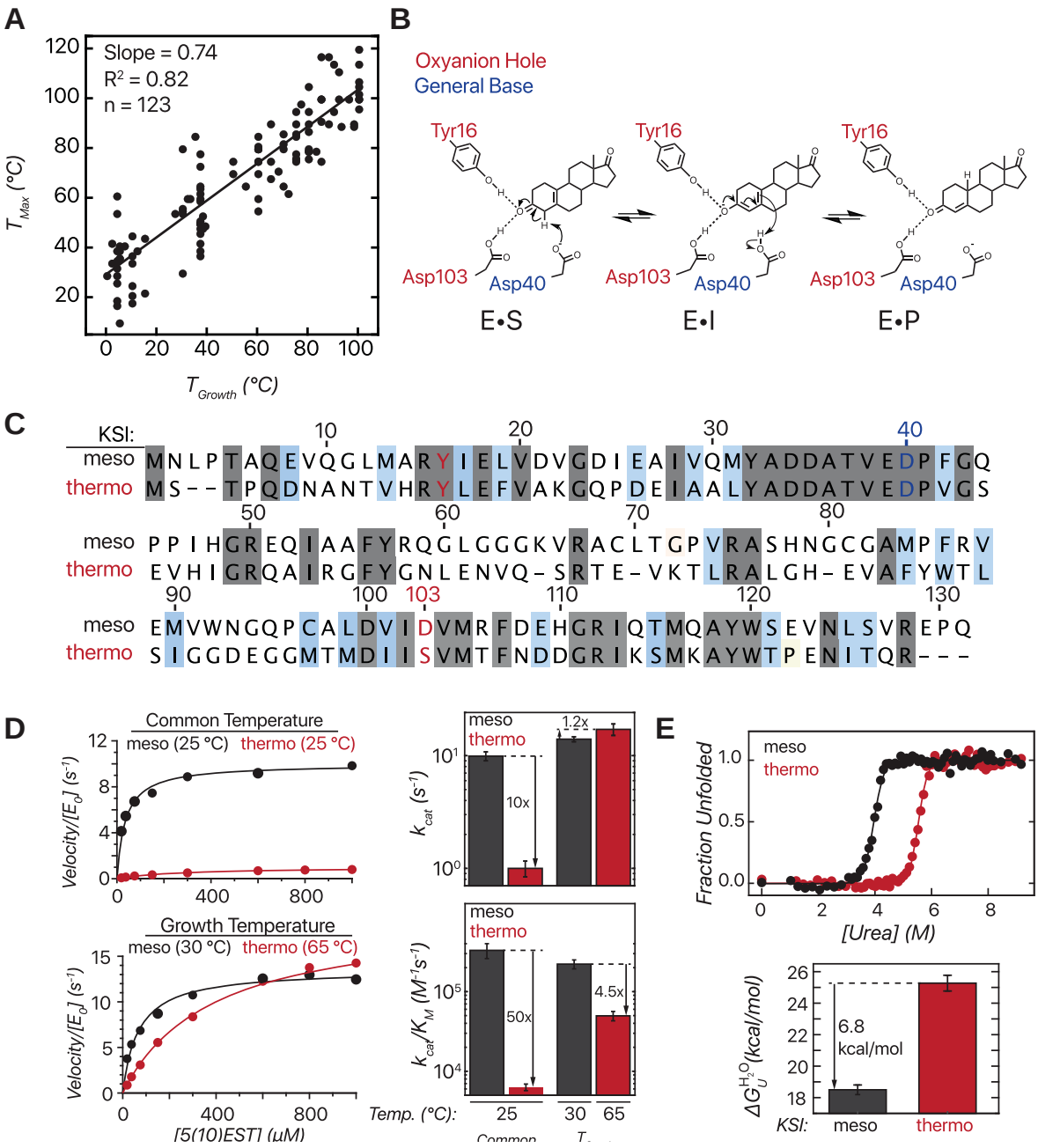


Figure **12.7**: Enzyme temperature adaptation through changes in activity and stability. Pinney et al., Science, 371. (2021). DOI: 10.1126/science.aay2784. Reprinted with permission of the American Association for the Advancement of Science and Copyright Clearance Center.

Panel (**A**) shows that as an organism's optimal growth temperature increases, the optimal temperature for selected enzyme activity also increases. Each dot represents a different species, and the enzymes are broadly chosen across all enzyme commission classes (i.e., the dots do not represent just KSI). There is a strong linear correlation.

Starting with Panel (**B**), we look at KSIs. Panel B shows the mechanism of isomerization of the steroid substrate, 5(10)-estren-3,17-dione [5(10)EST] by KSI. KSI has one of the highest k_{cat} values of enzymes. The reaction changes the position of the C=C double bonds and proceeds through an enolate/oxyanion intermediate (EI) formed after the abstraction of a proton by Asp 40. The transition state, which would have a developing negative charge on the O atom, is stabilized by proximal Tyr 16 and Asp 103 in a developing oxyanion hole.

Panel (**C**) shows the KSI sequences from *P. putida* (a mesoKSI) and *M. hassiacum* (thermoKSI). The sequences are 33% identical, but some key residues (gray) are identical. Similar ones are shown in blue. The thermophilic KSI (thermKSI) has Ser 103 instead of the often conserved Asp 103 in mesophilic organisms (mesoKSI). D103 and S103 are shown in red.

Now let's look at **Panel (D),** which shows activity (v_0/E_0) vs substrate [5(10)EST], for the meso- and thermophilic enzymes. At a nominal temperature (25 ^oC, top left panel), the thermoKSI shows little activity. At their optimal growth temperatures (30^0 C for the mesoKSI and 65 ^0C for thermoKSI, bottom left), the thermoKSI has both a higher $V_M = k_{cat}E_0$, and K_M at 65^0 C. The higher K_M is consistent with the idea that K_m values are usually higher at higher temperatures. The derived k_{cat} and k_{cat}/K_M values are shown in the adjacent histogram. Remember that k_{cat} measures the number of bound substrate molecules converted to product per second (at saturating substrate concentrations). The parameter k_{cat}/K_M is a measure of the effective biomolecular rate constant for product formation at low substrate concentrations ([S] $<<K_M$).

From an evolutionary perspective, early ancestral enzymes probably arose in warmer environments. When the Earth cooled, enzymes had to "solve" the problem, as is evident from the Arrhenius equation (the rate of reaction decreases with decreasing temperature). Hence, evolution would lead to structural changes facilitating higher kcat values, lower K_M values, or both at lower temperatures. We've seen in the examples above that K_M decreases with decreasing temperatures, so evolutionary pressures would more likely lead to increased k_{cat} values. This is consistent with localized changes in protein dynamics as modulators of k_{cat}. The evolutionary pressure to maintain stability would be low since proteins become more stable at lower temperatures.

Now, how thermally stable are the meso- and thermKSI? Urea denaturation experiments were used to determine the $\Delta G^{0\ H2O}{}_U$ for enzyme unfolding, as described in Chapter 4.12. Panel (**E**) shows urea denaturation curves for mesoKSI (black) and thermoKSI (red) monitored by changes in internal tryptophan fluorescence (top) and stabilities extrapolated to 0 M urea ($\Delta G^{H2O}{}_U$) (bottom). The denaturation curve for thermoKSI is significantly shifted to the right. The calculated values for $\Delta G^{0\ H2O}$ unfolding are +18.5 kcal/mol (mesoKSI)and about +25.3 (thermoKSI), a +6.8 kcal/mol difference. These values would be -18.5 kcal/mol (mesoKSI) and about -25.3 (thermoKSI) for the reverse folding reaction (unfolded ↔ folded transition).

Figure **12.8** shows an interactive iCn3D models of the bacterial ketosteroid isomerase from the mesophilic bacteria Pseudomonas Putida (left) and from the thermophilic bacteria Mycobacterium hassiacum (right).

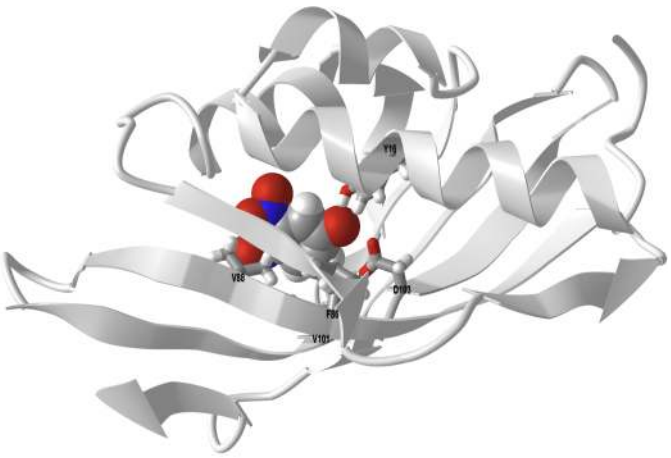


Figure **12.8*a***: Mesophilic Ketosteroid Isomerase D40N mutant (monomer) from Pseudomonas Putida (pKSI) bound to 3,4-dinitrophenol (**6C17**). (Copyright; author via source). Click the image for a popup or use this external link: https://structure.ncbi.nlm.nih.gov/i...kH877KZKPxWsGA

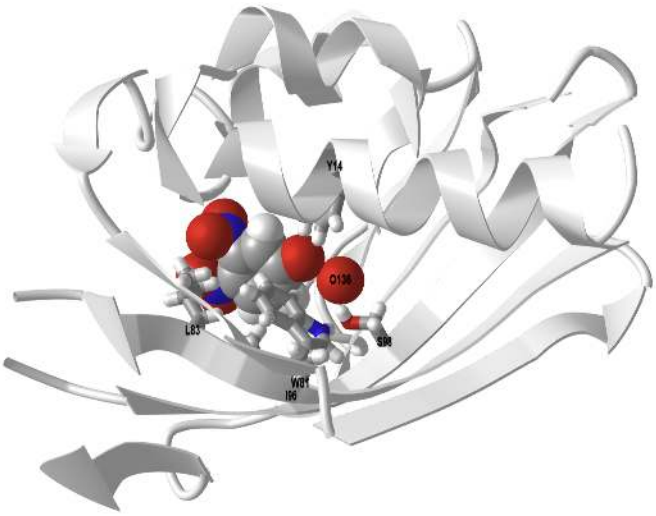


Figure **12.8*b***: Thermophilic Ketosteroid Isomerase D38N mutant (monomer) from Mycobacterium hassiacum (mhKSI) bound to 3,4-dinitrophenol (**6P44**). (Copyright; author via source). Click the image for a popup or use this external link: https://structure.ncbi.nlm.nih.gov/i...YbGw5zr2dRpnK8

Both structures contain a bound 3,4-dinitrophenol, a stable oxyanion, and a transition-state analog. The corresponding active site side chains are shown in colored sticks. Just one monomer of the dimer is shown for each protein for clarity. The key active-site residues F86, V88, V101, and **D103** in mesoKSI are replaced by W86, L88, I101, and **S103** in thermoKSI (all very conservative except for D103S). A water molecule forms a bridging hydrogen bond to the phenolate oxyanion from S103.

Figure **12.9** below shows the key change in Asp 103 (see the mechanism in Fig. 7B) in mesoKSI to Ser 103 + H_2O in thermoKSI

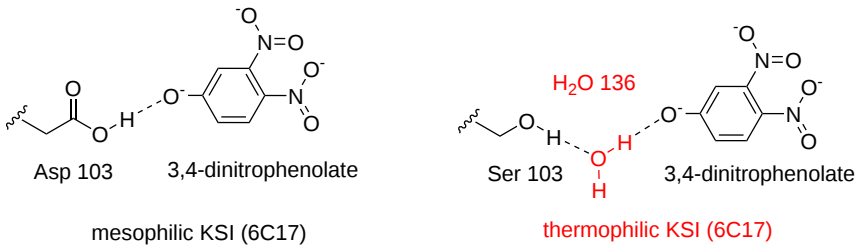


Figure **12.9**: Change from Asp 103 in mesoKSI to Ser 103 + H_2O in thermoKSI

Asp 103 is initially protonated with a pKa is >9, much higher than in an aqueous solution (3.7). The hydrogen bond from the mesoKSI D103 to the phenolate is stronger than the bridging one from Ser 103 in the thermoKSI. This arises from the increased polarity of the OH on a carboxylic acid (Asp) compared to an alcohol (Ser). In addition, the hydrogen bond distance from the bound water to the phenolate is longer than from Asp 103. Hence, the Asp 103 in the thermoKSI improves enzymatic stability. In contrast, thermoKSI is less active at lower temperatures but more stable at higher temperatures. The role of Ser 103 in stabilizing the folded state is shown in Figure **12.10** below

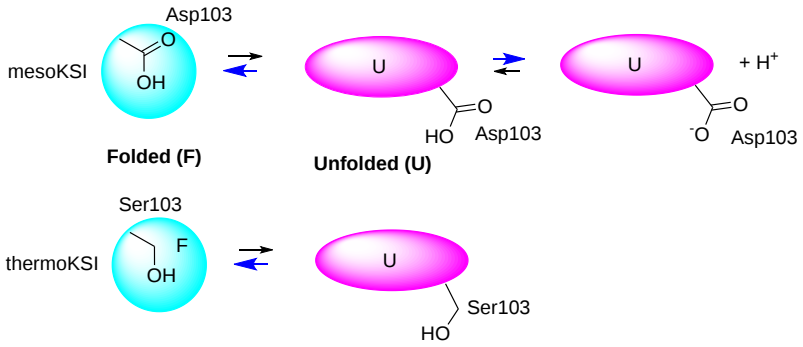


Figure **12.10**: Roles of Asp 103 and Ser 103 in the folding to unfolding transition of KSI

When mesoKSI unfolds, Asp 103, which is protonated and solvent-inaccessible in the native state, becomes solvent-exposed upon denaturation. Its pka drops, which leads to its deprotonation. This extra deprotonation step stabilizes the unfolded state (pulling the reaction to the right), making thermoKSI less thermally stable. In contrast, Ser 103, on solvent exposure, does not deprotonate, so the unfolded state is not additionally stabilized. Hence, Ser 103 leads to greater stability of the folded thermoKSI. The D103/S103 change is found in many KSI from many bacteria.

Here are some additional findings:

- The structures of mesoKSI and thermoKSI are highly similar, even though they have only 33% sequence identity. Figure **12.11** shows the conformational changes in the monomeric ketosteroid isomerase (KSI) going from the mesophilic enzyme (6C17, cyan) to the thermophilic one (6P44, magenta).

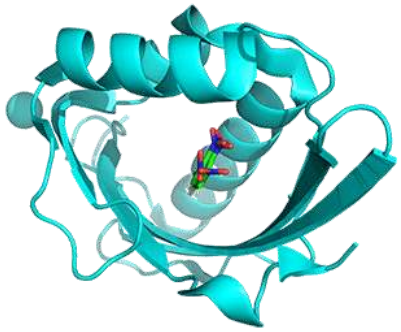


Figure **12.11**: Conformational changes in the monomeric KSI going from the mesophilic enzyme (6C17, cyan) to the thermophilic one (6P44, magenta) enzyme

- The F86W change in the thermoKSI stabilizes the conformation of S103, thereby enhancing its stabilization of the oxyanion in the oxyanion hole and enabling high-temperature activity.

- Other KSI orthologs and mutants exhibit higher enzyme activity when they harbor D103.
- Changing key residues at 86, 88, and 101 in mesoKSI to those found in the thermoKSI additionally increased the stability of the mesoKSI
- Analysis of 1140 KSIs showed that the fraction containing D103 decreases with increasing growth temperature, and the fraction containing S103 increases.

It appears that KSI's thermal adaptation occurs primarily through a single amino acid change (D103S). The change reduces k_{cat} for the mesoKSI 10x at low temperatures but greatly increases stability at high temperatures.

This switch and compensatory changes in activity and stability suggest that protonated Glu and Asp side chains involved in activity might be replaced with other amino acids that confer greater stability but reduce activity. A conserved and protonated active site Glu is found in glycosidases from high-temperature orthologs. Likewise, a protonated Asp side chain is found in thioredoxin. As a control, a change from a protonated Glu in triosephosphate isomerase, distal to the active site, to a Gln has no effect on catalysis and was not observed in thermophiles. It should be noted that not all stabilizing mutations decrease activity, as many examples show. 67 protonated Asp and Glu side chains were identified in the PDB, 14 of which were replaced in high-temperature orthologs.

Conservation of chaining pairs of amino acids between mesophilic and thermophilic organisms.

Are there other broadly found changes in amino acids (in addition to Asp/Glu) at each position in a mesophilic protein and its thermophilic ortholog? Computational analysis in 2194 enzyme families in 5582 bacterial species (for a total of 17 million amino acid pairs) was performed to explore this question. Half of all families had an amino acid at a given position, and this correlated with growth temperature, yielding almost 160,000 key positions. The results of this study are broadly outlined in Figure **12.12** below.

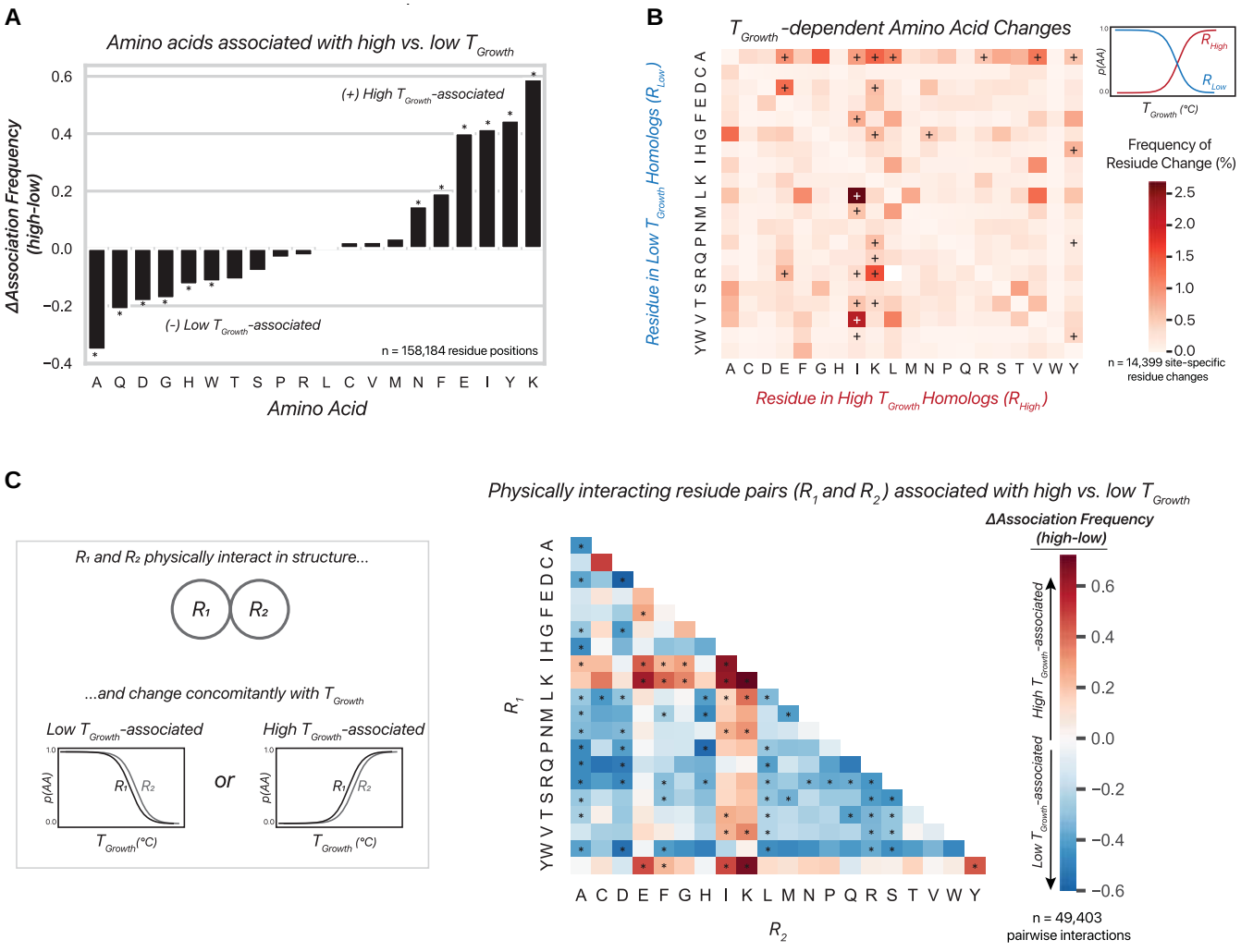


Figure **12.12**: Examination of temperature-associated residues and their interactions. Pinney et al., ibid. Reprinted with permission of the American Association for the Advancement of Science and Copyright Clearance Center.

Let's explain each part of this complex figure.

Panel (**A**) - Preferences in the types of amino acids associated with high or low-temperature growth: Panel (**A**) shows the difference in frequency of association of given amino acids with high to low temperatures. Some amino acids were associated with low-temperature growth. These include alanine (A), glutamine (Q), and aspartate (D), as in KSI. Others were associated with high-temperature growth (E, I, Y, and K). F

Panel (**B**) - Identities and frequencies of site-specific residue changes across temperature growth conditions: Now let's see how a specific acid changes in going from mesophilic (low T) to thermophilic (high T), which shows key temperature-dependent amino acid changes. Panel (**B**) shows the frequency of observed site-specific changes in temperature-associated residues. The "+" indicates that the frequency of a change (such as Leu to Ile) is significant in comparison to the opposite change (Ile to Leu). Indeed, the darkest square is for a Leu (at low temperatures) to Ile (at high temperatures). Other darker squares indicate that these changes occur as temperature increases from low- to high-temperature-adapted bacteria: V → I, R → L, and D → E. The specific one found for KSI, D → S, does not stand out, most likely because of the diverse enzyme types included in the analysis.

Panel (**C**) - Identities and frequencies of physically interacting temperature-associated residue pairs (in a single protein): If one amino acid changes in going from a low to a high-temperature ortholog, it is likely that the original and changed amino acids physically contact different nearby amino acids in their respective protein. Panel (**C**) shows the difference in frequency of association with high vs. low-temperature growth bacterial enzymes for "all possible physically interacting pairs of residues (made up of residues R_1 and R_2) that change concomitantly with *the* growth temperature". The darker blue squares show interacting residue pairs found more often in low-growth temperature enzymes, while the darker maroon squares show contacting pairs in high-growth temperature proteins. The asterisk shows that pairs are statistically significant.

One of the darkest maroon squares (high-temperature enzymes) shows an Ile-Ile interaction pair. The vertical column above Ile (high growth) in Panel B shows that changes to Ile in high-temperature enzymes occur frequently from 6 different amino acids found in low-temperature enzymes. Ile might be favored over Val to maximize buried hydrophobic surface area. Also, compared to Leu, it has greater conformational flexibility and can better fill empty spaces in protein interiors.

A Lys to Glu (K to E) interaction is strongly associated with high-temperature enzymes. In contrast, an Arg-to-Asp (R to D) interaction is strongly associated with low-temperature enzymes. This implies that increasing the number of salt bridges (ion-ion interactions) does not make a protein more thermally adaptable. Lys salt bridges would have greater conformational flexibility than those using Arg. The same applies to Glu compared to Asp. Lys also has the largest hydrophobic surface area, which could enhance hydrophobic packing. Since Arg has hydrogen bond donors that require more adjacent hydrogen bond acceptors, the use of Arg might depend more on adjacent amino acids than on a binary pair.

In summary, these results are more nuanced than previous explanations for high-temperature stability:

- increasing branched chain residues like Ile, Leu, and Val in the packed hydrophobic core. Indeed, as seen in Panel B, the most frequent amino acid change observed is from Leu/Val in low-temperature growth orthologs to Ile in high-temperature growth orthologs. These are all branched-chain amino acids. They occur 2-3x more frequently than the reverse: Ile in low-temperature growth to Leu/Val in high-temperature growth. Panel C shows that Ile preferentially interacts with another Ile in a high-temperature-adapted enzyme. Hence, stability is not improved merely by substituting any hydrophobic side chain.
- increasing the number of salt bridges (ion-ion interactions) and hydrogen-bonding interactions between charged side chains. There are more charged side chains and salt bridges in thermophilic proteins. However, the above data show a clear preference for Lys in thermophilic proteins, as changes from Arg to Lys are common in that group, as shown in Panel B. Likewise, Asp to Glu changes from low to high temperature-adapted proteins are 3 times more likely than the reverse. In addition, Panel C shows that interactions between Lys and Glu are most strongly associated with high-temperature-adapted proteins, while Arg and Asp interactions are most often found in low-temperature-adapted proteins.

ALLOSTERISM AND THERMAL CHANGES

As mentioned, increasing temperature can cause local effects in a protein instead of large global changes that lead to denaturation at high temperatures. Changes occurring in the active site can affect k_{cat}, K_M, and k_{cat}/K_M. Allosteric effects also occur. The protein imidazole glycerol phosphate synthase (HisFH) is a heterodimer with two active sites, so it is considered a bienzyme. The H subunit is a glutaminase, which cleaves glutamine into glutamic acid and ammonia, which can diffuse through a channel to the active site of the F subunit, the cyclase. The enzyme's active form occurs only when both substrates are bound, resulting in long-range allosteric activation. In particular, the oxyanion hole in the H subunit forms in the activated state, stabilizing the tetrahedral transition intermediate in the hydrolysis of glutamine.

Figure **12.13** shows an interactive iCn3D models of the heterodimeric imidazole glycerol phosphate synthase complex (7AC8)

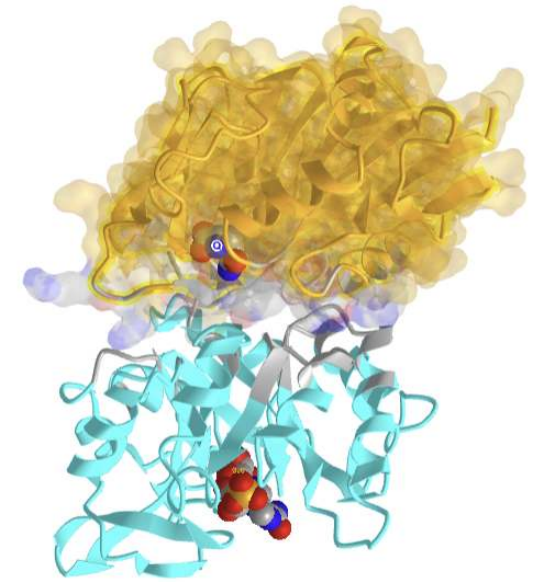


Figure **12.13**: (Copyright; author via source). Heterodimeric imidazole glycerol phosphate synthase complex (7AC8). Click the image for a popup or use this external link: https://structure.ncbi.nlm.nih.gov/i...S5MbiiA9bDvDQ8.

The HisH (glutaminase) subunit is shown in orange with a molecular surface and the bound substrate (spacefill) glutamine. The HisF subunit is shown in cyan, bound to a substrate.

An allosteric effector molecule can bind in the active site of His F and induce long-range conformational changes in this HisH active site, increasing its activity 5000x. The structures involved are shown in Figure **12.14** below.

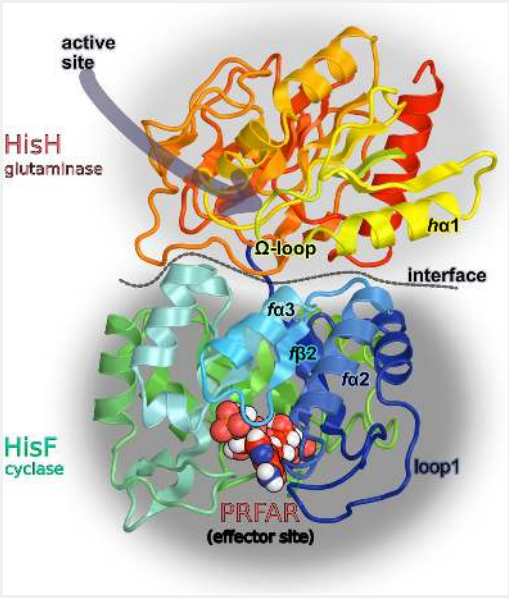


Figure **12.14**: Imidazole glycerol phosphate synthase (IGPS) from the thermophile *Thermotoga maritima* (*T. maritime*). Maschietto, F., Morzan, U.N., Tofoleanu, F. *et al.* Turning up the heat mimics allosteric signaling in imidazole-glycerol phosphate synthase. *Nat Commun* **14**, 2239 (2023). https://doi.org/10.1038/s41467-023-37956-1. Creative Commons Attribution 4.0 International License. http://creativecommons.org/licenses/by/4.0/.

The HisF and HisH subunits are colored in green-to-blue and red-to-yellow gradients, respectively, and separated by a dotted line that marks the interface between HisF and HisH. The labels (*f*α2, *f*α3, *f*β2, loop1, *h*α1, Ω-loop) indicate secondary structure elements directly involved in allosteric regulation.

Molecular dynamics and NMR studies have shown that increases in temperature lead to conformational changes resembling those observed upon binding of the allosteric effector at room temperature. As the temperature of the apoenzyme (no substrates or effects bound) increases from 30 °C to 50 °C, the dynamics and structure increasingly resemble the state induced by the effector. Increasing

temperatures from climate change are likely to cause subtle conformational and dynamic changes in all proteins, with some of these changes having negative consequences.

THERMAL DETERMINANTS OF YEAST METABOLISM

With this basic background, we can attempt to understand the thermal determinants for entire metabolic pathways. This has been attempted in the yeast *Saccharomyces cerevisiae*, a eukaryotic organism that grows optimally around 30 °C, exhibits extremely limited growth at 40 °C, and shows no growth and death at 42 °C.

Mathematical modeling of all metabolic pathways in a cell is a daunting task. Accurate concentrations, rate constants, and dissociation constants are needed for all reactions. **Genome-scale metabolic models** (GEM) use a multitude of constants that are experimentally or computationally determined. There are usually significant uncertainties in the model's parameters. Bayesian statistics has been used to decrease these uncertainties. In Bayesian statistics, parameters and models are updated with known values and information. It is similar to machine learning models, which use data to train and refine the model.

A Bayesian model for S. cerevisiae was used as it is the most abundantly used organism in industry and has many GEMs. The GEM used was the **enzyme-constrained GEM** (**ecGEM**). It was then further developed into the **enzyme-- and temperature-constrained GEM** (**etcGEM),** which also incorporates the temperature dependence of the native enzyme (EN) concentration and kcat. For each enzyme, the melting point (T_M), the change in heat capacity (ΔCp) for the transition state, and the optimal temperature (T_{opt}) were included. We discussed both (T_M) and the change in heat capacity (ΔCp) for proteins in Chapter 4.9. In addition, another term for **non-growth-associated maintenance (NGAM)** of the cells, which is also temperature-dependent, was included. Examples of non-growth-associated maintenance include maintaining membrane potential, turgor pressure, normal protein refolding, and DNA repair.

The Bayesian models reproduced the datasets well. Using the models, key enzymes that control the flux through metabolic pathways were determined at each temperature. The most rate-limiting enzyme at a superoptimal temperature in yeast was squalene epoxidase (ERG1), which is involved in sterol metabolism. Replacing the S. cerevisiae enzyme with one from a thermotolerant yeast strain resulted in better growth than in wild-type cells.

Figure **12.15** below shows the complexity and extent of the metabolic proteins and pathways of the enzyme-constrained GEM (ecGEM).

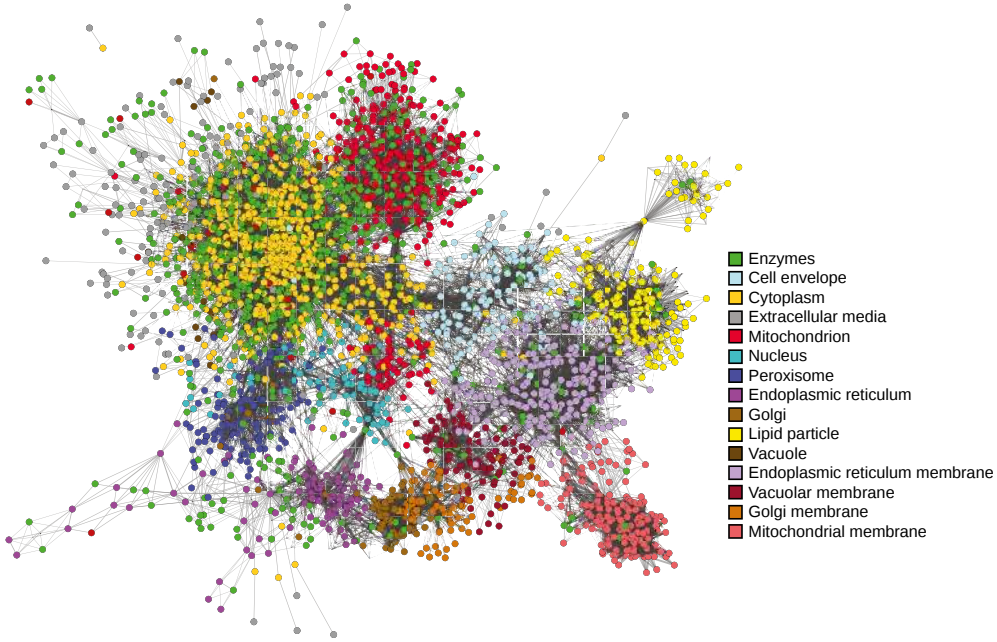


Figure \(\PageIndex{15}\): Metabolic proteins and pathways included in the enzyme-constrained GEM. Benjamín J Sánchez et al., Molecular Systems Biology (2017)13:935. https://doi.org/10.15252/msb.20167411. Creative Commons CC BY

Now, let's explore some of the results of the study. Figure **12.16** below shows how the temperature dependencies of proteins were incorporated into the enzyme-constrained GEMs.

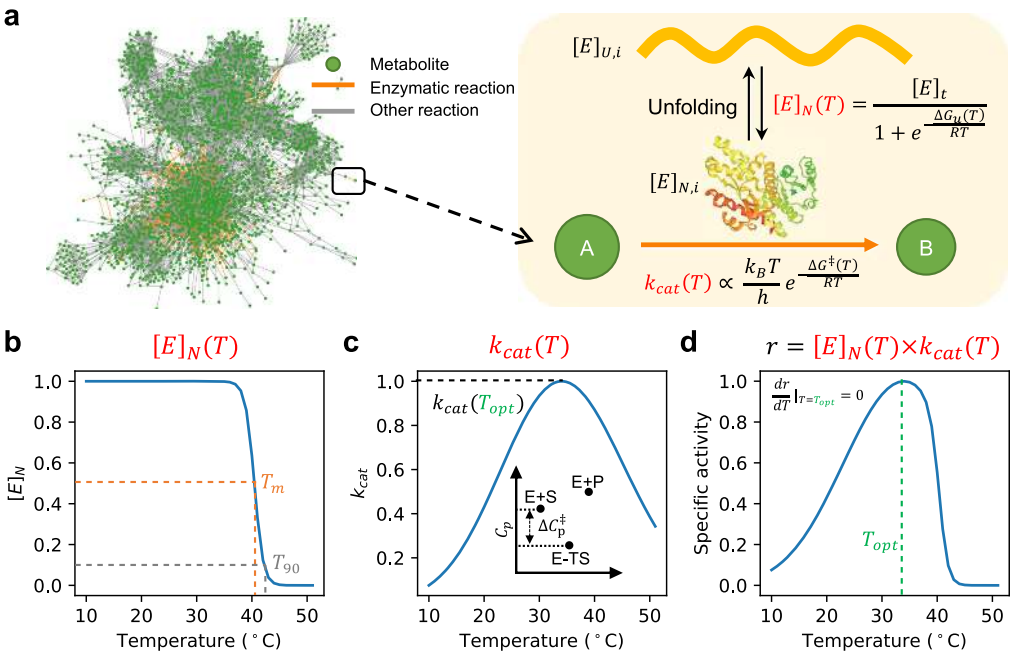


Figure **12.16**: **Using Bayesian statistical learning to integrate temperature dependence in enzyme-constrained GEMs.** Li, G et al., *Nat Commun* **12**, 190 (2021). https://doi.org/10.1038/s41467-020-20338-2. Creative Commons Attribution 4.0 International License. http://creativecommons.org/licenses/by/4.0/.

Panel a shows the complexity of the metabolic network used to produce the ecYeast7.6, shown in greater detail in Fig. 13 above, and how E_N and k_{cat} depend on temperature.

Panel b shows how a two-state denaturation model was used. $[E]_N$ is the enzyme concentration in the native state; T_{opt} is the optimal temperature at which the specific activity is maximized; T_m and T_{90} are temperatures at which there is a 50% and 90% probability that an enzyme is in the denatured state, respectively. In Chapter 4.4, we indicated that for a reversible two-state transition, T_M is the temperature at which half of the enzyme is native and half denatured, giving a Keq for the N ↔ D equilibrium of 1.

Panel c shows how k_{cat} depends on temperature. The insert shows how the heat capacity changes from E + S to the E-transition state. We have previously observed that $\Delta C_P > 0$ for protein unfolding, and this positive ΔC_P value is a signature of the hydrophobic effect that occurs when nonpolar groups become more solvent-exposed. We previously showed that enzymes bind the transition state more tightly than they bind the substrate. This $-\Delta C_P$ is more in line with the latter.

Panel d shows the temperature dependence of the enzyme's **specific activity, r**, as a function of temperature, which is determined by E_N (panel B) and k_{cat} (panel C).

Now we can explore the outputs of the ecGEM run with the separate added effects of temperature on NGAM, k_{cat}, and E_N (denaturation). Finally, the combined etcGEM was run. The combined etcGEM produced the observed outcomes in yeast growth. Given that the contributions of each of the three factors, NGAM, k_{cat}, and protein denaturation, to whole-cell growth could be modeled. The outcomes from these models as a function of temperature are shown in Figure **12.17**. They support the notion that temperature effects on yeast enzymes explain yeast growth rate.

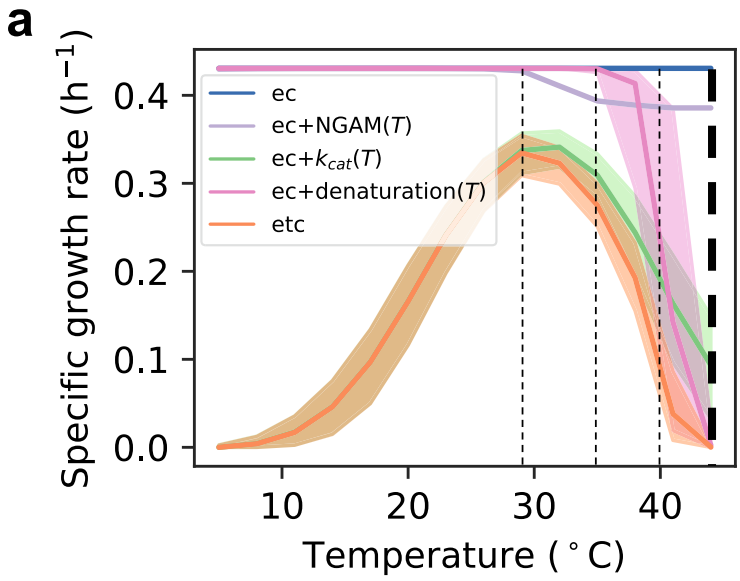


Figure 12.17: **Fig. 3: Yeast growth rate is explained by temperature effects on its enzymes.** Li, G et al., ibid

This figure shows how the temperature dependence of different processes combines to affect the growth rate. EC is the prediction from the enzyme contained GEM, —predictions with the enzyme-constrained model; ec+NGAM includes temperature effects on nongrowth-associated maintenance; ec+$k_{cat}(T)$ incorporates the temperature effects on enzyme k_{cat} values; ec+denaturation(T) incorporates the temperature effects on enzyme denaturation. Finally, in the etc model, the enzyme and temperature-constrained model incorporates temperature effects on all three (NGAM, k_{cat} and enzyme denaturation) into the ec model. The solid lines indicate median values, and the shaded areas indicate the region between the 5th and 95th percentiles (n = 100).

Here are some summarized results:

- <29 °C, only temperature-dependent k_{cat} affected the cell growth rate (green line under the orange etc line <29 °C;
- at 29 °C <T < 35 °C, both k_{cat} and NGAM (gray line) determined the growth rate;
- at T > 35 °C, enzyme denaturation at major effects and by 40 °C was dominant,

Figure 12.18$d-e$ shows, using images, how the temperature dependencies of the factors E_N, k_{cat}, and r (specific activity) affect yeast growth. A phenomenal amount of data is displayed in these images.

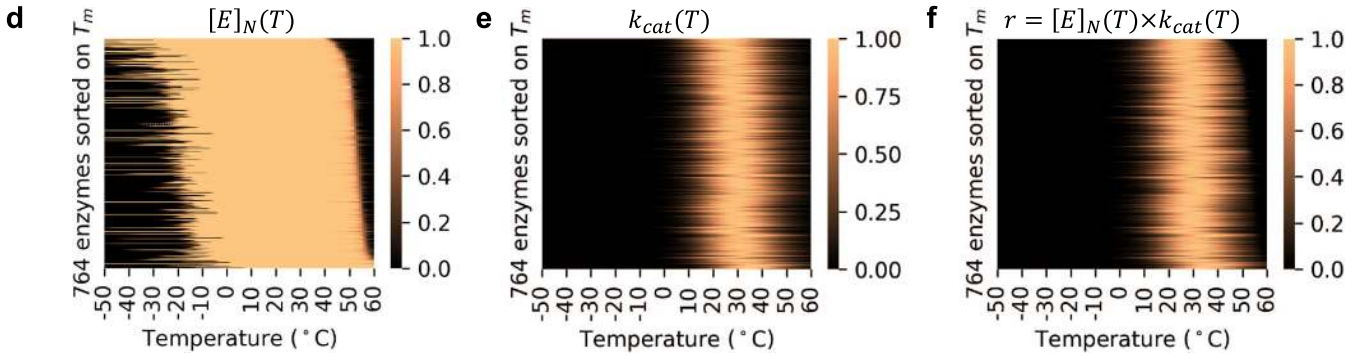


Figure 12.18$d-e$: **Fig. 3: Yeast growth rate is explained by temperature effects on its enzymes.** Li, G et al., ibid

Panel d shows the probability that a given enzyme is in the native state. Think of the y-axis as increasing 1 pixel at a time from bottom to top, with each newly added pixel representing a different enzyme for 764 enzymes along the y-axis. The x-axis shows, with each pixel (at a given y-axis value), if the enzyme is native at that temperature

The interface between bright (native) and black (denatured) on the right side of the image shows that some enzymes (top) become unfolded at 40 ºC, while some don't unfold until close to 60 ºC

Panel e shows normalized k_{cat} values of 764 enzymes at different temperatures. The brightest white pixels show the highest k_{cat} values. The image clearly shows the brightest vertical band at around 30 ºC, the optimal growth temperature of yeast.

Panel f shows the normalized specific activities (r) of 764 enzymes at different temperatures. Again, the highest specific activity is centered around 30 ^{o}C.

Note in Fig. 15d that most enzymes also denature at temperatures < -10 ^{o}C, but cells were not viable under those conditions.

The etcGEM replicated a finding that, above 37 °C, yeast cells switch from respiration to partial fermentation, accompanied by a larger flux through glycolysis. This occurred because specific enzyme activities decreased with increasing temperature, constraining metabolism. In addition, the total protein concentration reaches a limit and cannot increase further, which could have increased enzyme activity. Along with increased glycolysis, mitochondrial ATP production decreases. Respiration produces more ATP per mole of glucose, but glycolysis/fermentation produces more ATP/protein mass, so when protein concentration reaches a maximum, glycolysis is more efficient.

Lastly, the etcGEM was used to identify enzymes whose fluxes changed most at superoptimal temperatures. (We introduced the flux control coefficient in Chapter 14.3). The results of this modeling are shown in Figure **12.19** below.

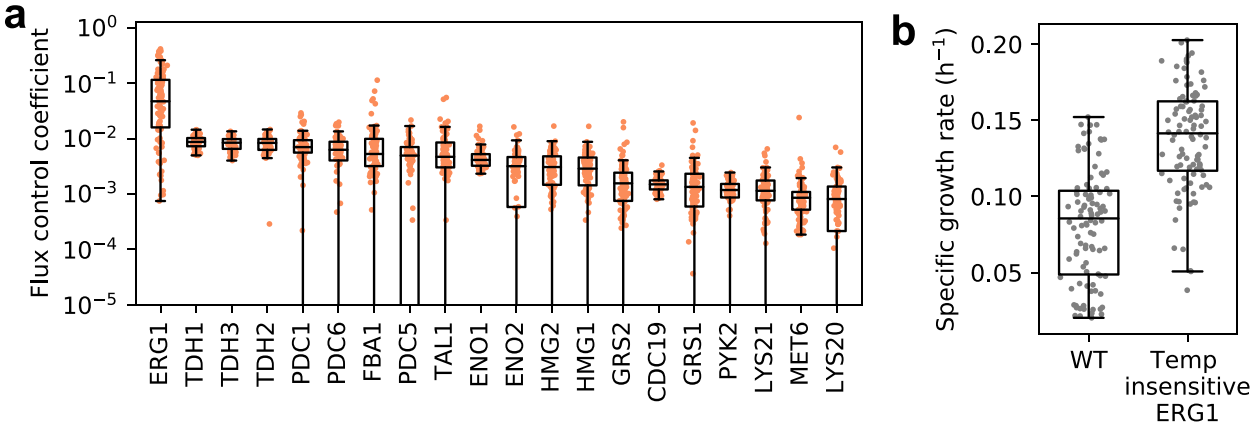


Figure **12.19**: Flux control coefficients at the superoptimal model for yeast.

One enzyme that stands out in Panel a, ERG1, is squalene epoxidase, an enzyme involved in sterol oxidation. If the wild-type enzyme was replaced with a temperature-insensitive ERG1, the specific growth rate increased significantly (over 55%).

WHAT DOES THIS HAVE TO DO WITH CLIMATE CHANGE? LIFE'S THERMAL TOLERANCE AND LIMITS

We've just explored the molecular and metabolic adaptations that allow organisms to thrive at higher temperatures. The question is how quickly the present life can adapt to global warming driven by rising greenhouse gas levels. Life on the planet will adapt, but the diversity of life forms in the biosphere will change. Five mass extinctions have occurred over the last 450 million years up until the present, as shown in Figure **12.20** below.

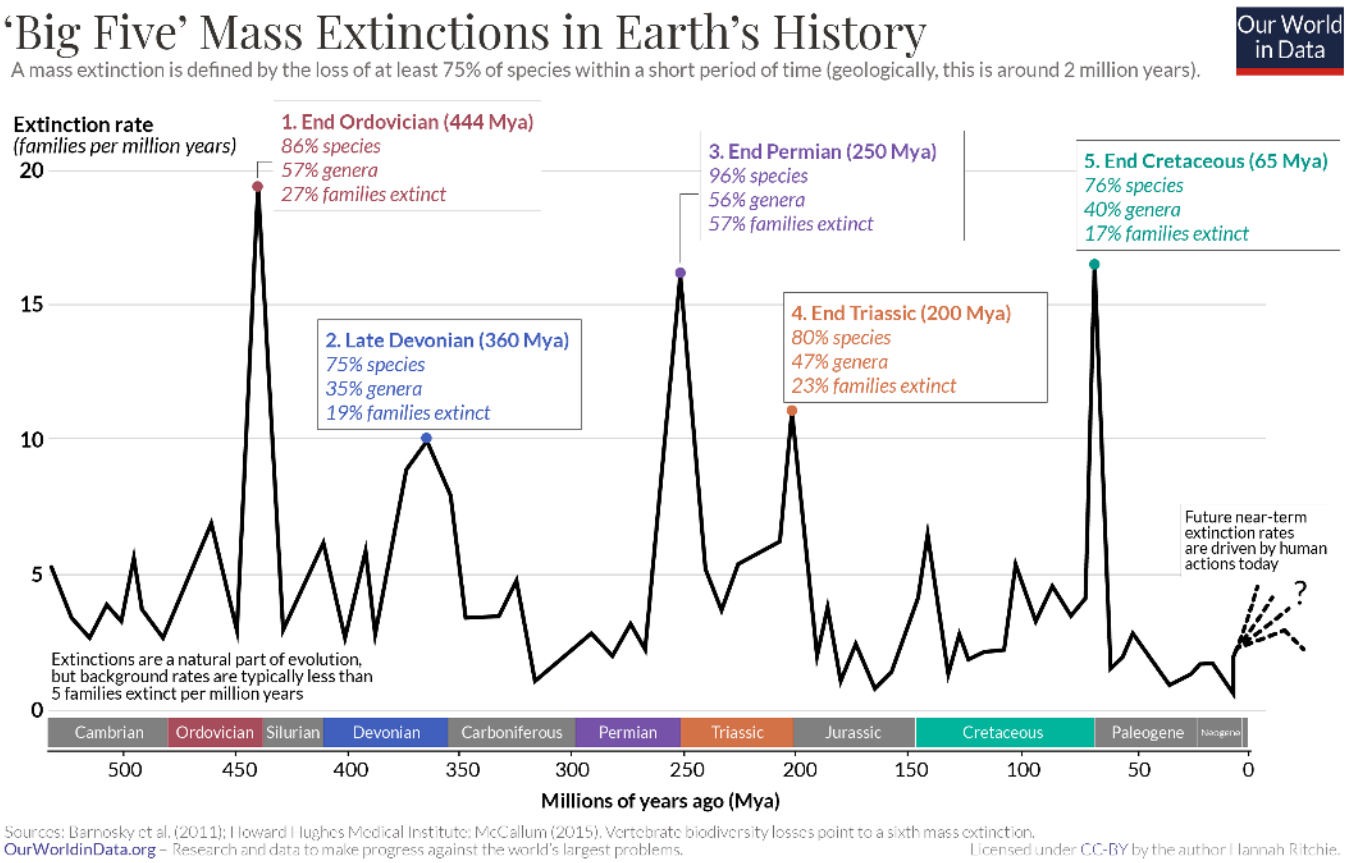


Figure **12.20**: Five mass extinctions over the last 450 million years. Hannah Ritchie. Our World in Data. https://ourworldindata.org/mass-extinctions. Creative Commons BY license.

Many factors, often interrelated, can contribute to mass extinction. These include volcanism, asteroid impact, climate change, ocean anoxia, and the release of methane from ocean hydrates and permafrost. All are associated with increased temperatures, as shown in Figure **12.21**. It documents the correlation between temperature changes and the extinction rate for marine animals over the last 450 years. The gray bars highlight the extinction cycle.

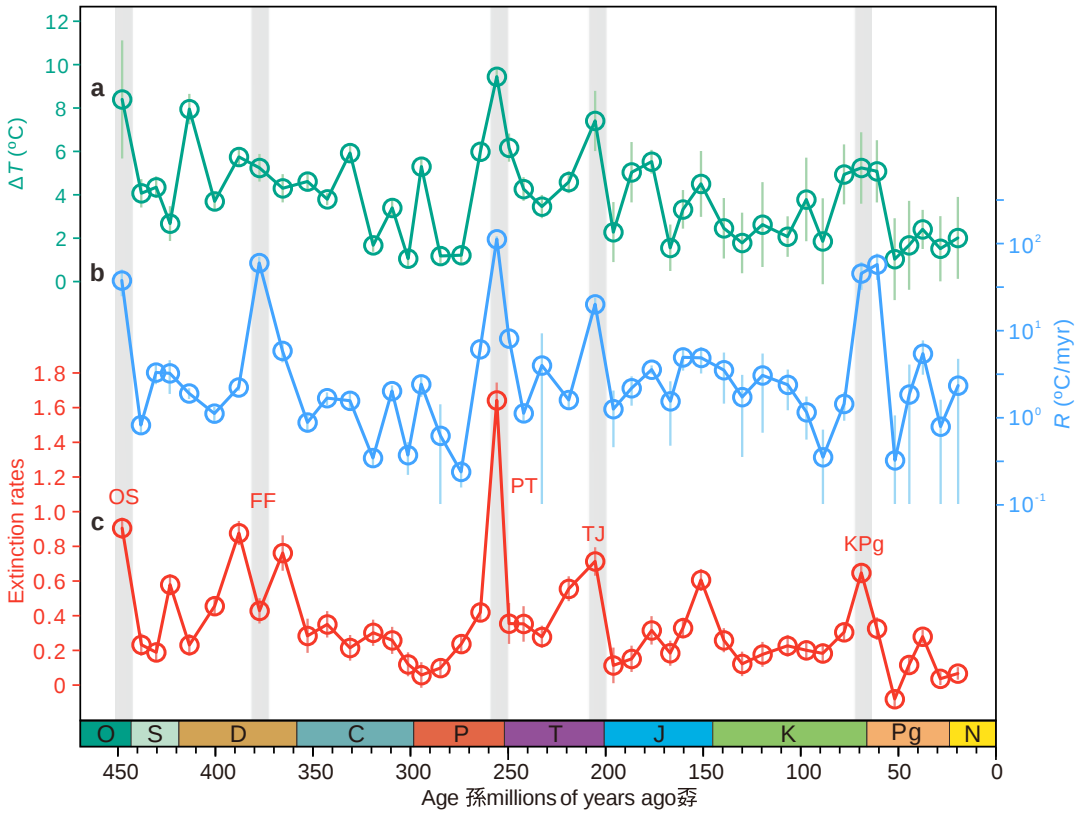


Figure **12.21**: **Temperature change and extinction rate over the past 450 million years.** Song, H., Kemp, D.B., Tian, L. *et al. Nat Commun* **12**, 4694 (2021). https://doi.org/10.1038/s41467-021-25019-2. Creative Commons Attribution 4.0 International License. http://creativecommons.org/licenses/by/4.0/.

Pane a shows the largest magnitude of temperature change (Δ*T*, absolute value) in each time interval (bin)

Panel b shows the maximum rate of change in temperature (*R*, absolute value) in each time bin, expressed at the million-year (Myr) scale.

Panel c shows the generic extinction rates of marine animals calculated using gap-filler methods using data from the Paleobiology Database. The Big Five extinctions occurred in the end-Ordovician (OS), Frasnian-Famennian transition (FF), Permian-Triassic transition (PT), Triassic-Jurassic transition (TJ), and Cretaceous-Paleogene transition (KPg). Vertical bars show mean ± 1 x standard deviation (see Methods). O Ordovician, S Silurian, D Devonian, C Carboniferous, P Permian, T Triassic, J Jurassic, K Cretaceous, Pg Paleogene, N Neogene. Dark cyan, blue, and red dots represent Δ*T*, *R*, and extinction rate, respectively.

The authors suggest that a temperature change of >5.2 °C and a rate of >10 °C/Myr would lead to a new extinction rate comparable to the "Big Five". A rise of 5.2 °C is in the upper range of the IPCC projection (but likely only with human inaction to prevent it). The current rate of temperature increase (about 2 °C per 200 years) is unprecedented over the last 3 million years. So it appears that we are headed to a 6th mass extinction caused by a combination of environmental degradation, pollution, and climate change created by humans.

Rothamn has suggested that we could tip into an "official" mass extinction depending on the magnitude and rate of change in the carbon cycle. If long-scale changes occur too quickly and organisms can't adapt, extinction follows. If the changes occur on a short time scale (as is happening now), the size of the change is a key factor. His analysis suggests that a key factor is the anthropogenically driven increase in ocean CO_2. A threshold of 310 Pg (Gt), which we could reach by 2100, could officially trigger the sixth mass extinction. However, many would argue that we are already in the 6th extinction cycle. For example, of about 30,000 terrestrial vertebrate species, about 1.7% (515 species) are on the verge of extinction (having <1000 individuals). 77 mammal and bird species have lost most of their populations.

When it comes to how organisms will adapt to our present climate change, Hochachka and Somero ask six relevant questions:

1. What is the thermal optima, and how much change leads to suboptimal or lethal conditions?
2. What mechanisms set upper limits?
3. How close do organisms live to the limits of their thermal tolerance?
4. To what extent can organisms acclimate to temperature increases?
5. When are genetic changes necessary for survival?

6. Does the acquisition of heat tolerance reduce cold tolerance?

We can ask if organisms can survive and thrive, and at what cost. Humans most assuredly can survive a warming world. Still, if temperatures become too high, they will not thrive, and parts of the world will become uninhabitable, with high economic, social, political, and cultural costs. Some organisms will become extinct. Mass migrations of all species will occur as they seek more habitable environments.

In an evolutionary sense, species occupy environments in which they can survive and adapt. Our climate has been fairly constant since the end of the last ice age, about 12,000 years ago. Climatic changes that make an environment suboptimal depend on an organism's sensitivity and how close it lives to its thermal limits. We have already documented the thermal limits of individual enzymes and whole metabolic systems.

As you learned in introductory chemistry, multiple linked reactions can only go as fast as their slowest step. An analogous insight is that a chain is only as strong as its weakest link. It may be that the membranes, not proteins, are the weakest link in temperature adaptation, as higher temperatures alter phases and subphases, such as lipid rafts, which can in turn disrupt the activity of membrane proteins. Membrane functions (permeability, endo- and exocytosis, and maintenance of transmembrane potentials) are also very important.

Temperature effects on neural communication in synapses might be key. An interesting example is a particular Antarctic fish that, after prolonged exposure to 4 °C, dies when temperatures are raised to around 9 °C. Synaptic transmission through the acetylcholine receptor is altered as the amount of acetylcholine in the synapse increases and the rate at which it is degraded by acetylcholinesterase decreases.

The lethal temperature for an organism can depend on many factors, including the rate of temperature increase, the length of exposure, previous long-term acclimatization, and, for humans, humidity. Humans can't dissipate body heat by sweating if the external temperature is >37 0C (the average body temperature). If the humidity is high enough, sweating is ineffective in dissipating heat. Since metabolism produces heat, the body temperature can increase past 37 ^{0}C even if the external temperature is lower. A lethal limit for humans can occur as low as 29 ^{0}C (84 ^{0}C) at a relative humidity of 85%. Even now, about 30% of the human population is exposed to lethal thresholds at least 20 days/yr, and this will only grow as temperatures and humidity increase.

Comparisons of similar species (congeneric) that live in intertidal regions (above the waterline at low tide and underwater at high tide) vs. subtidal regions (close to shore but always submerged) reveal significant differences. Organisms living in intertidal regions will experience a higher range of temperatures. 19 species of congeneric porcelain crabs inhabit different latitudes and vertical depths in intertidal and subtidal regions. Intertidal crabs in regions with highly variable temperatures are exposed to temperatures much closer to their lethal temperature limit, indicating that the T_{lethal} - $T_{max\ habitat}$ gets smaller. Heart function and neural activity at higher temperatures appear to be weak links in survival. Heat shock protein function is also different in congeners of marine snails. Lethal temperatures appear to be those at which protein synthesis dramatically decreases. Repair of damaged proteins is reduced, limiting vertical migration to lower temperatures and increasing organisms' susceptibility to predation. These effects can occur over a small increase in temperature (a few degrees Celsius). It becomes more important to heed the IPCC's warnings to limit global average temperature increases to 1.5 °C or, more likely, to the 2.5 °C range.

Laboratory experiments in directed evolution show that an organism's thermal tolerance can be increased, but there are limits. E. Coli can live at a variety of temperatures, and experiments to evolve them at 37 ^{0}C (human gut temperature), at 42 ^{0}C (close to their lethal limit), and in an environment with fluctuating temperatures (between 32 ^{0}C - 42 ^{0}C) have been conducted. Over 1000 generations, the rate of evolution was highest in the 42 °C group. The group that evolved at fluctuating temperatures was better adapted to both higher and lower temperatures. Under no circumstances did E. coli evolve into a thermophilic species, which would require novel gene function rather than just a small set of mutations that yield more optimal values of k_{cat} and K_M for enzyme catalysis.

SUMMARY

(Summary written by Claude, Anthropic)

This chapter examines how temperature affects enzyme structure, function, and organismal metabolism across scales from individual active sites to genome-scale metabolic networks to ecological extinction thresholds — connecting molecular biochemistry to the most urgent consequences of climate change.

Competing temperature effects on enzyme function. As temperature rises, two opposing processes determine enzyme fate. First, kcat and VM increase with temperature following the Arrhenius equation. Second, the rate of thermal inactivation (kinact) also increases — generally more steeply than kcat — producing a bell-shaped VM curve with an optimal temperature. KM simultaneously increases with temperature, reflecting weaker substrate binding at higher conformational entropy. The ratio kcat/kinact, termed catalytic power, therefore declines as temperatures rise above the optimum. Evolution has responded to this tension in opposite directions: thermophiles evolve greater structural stability (sacrificing some activity at moderate temperatures), while psychrophiles evolve higher kcat and greater flexibility to maintain catalytic rates in the cold. Both represent trade-offs between stability and activity.

Soil enzymes and SOC dynamics. Soil stores approximately 1,500 Gt of organic carbon — more than the atmosphere and all vegetation combined — making microbial enzyme activity a critical lever in the global carbon budget. SOC is high at northern latitudes because low temperatures suppress microbial respiration; warming accelerates decomposition and threatens to release large amounts of stored CO_2 in a positive feedback loop. Studies of three extracellular enzymes (β-1,4-glucosidase, N-acetylglucosaminidase, acid phosphatase) in Mount Kilimanjaro soil samples reveal a critical phenomenon: at a single elevation, increasing temperature from 10°C to 20°C raises both KM and VM by approximately equal proportions, causing their effects on reaction rate to cancel at low substrate concentrations. This defines a critical substrate threshold (Scrit) below which temperature has no net effect on polymer degradation rate. Above Scrit, warming accelerates decomposition. Intracellular glucose oxidation (mineralization) shows no such cancellation — rates increase at all substrate concentrations — suggesting qualitatively different adaptive responses for extracellular versus intracellular enzyme systems. Comparing enzymes from organisms at 2,010 m versus 3,020 m elevation shows that cold-adapted organisms have lower Q_{10}KM and Q_{10}VM values and substantially higher Scrit — demonstrating that organisms experiencing wider temperature ranges have evolved stronger compensatory thermal buffering. Thermal adaptation appears driven more by the breadth of temperature fluctuation than by mean temperature alone.

Structural mechanisms of thermal adaptation in KSI. Ketosteroid isomerase (KSI), one of the fastest enzymes known, provides a detailed molecular case study. Comparing orthologs from *Pseudomonas putida* (mesoKSI) and *Mycobacterium hassiacum* (thermoKSI) — which share only 33% sequence identity — reveals how modest structural changes produce large differences in stability and activity. The key substitution is D103S: Asp 103 in mesoKSI participates directly in oxyanion hole stabilization; Ser 103 in thermoKSI bridges to the oxyanion intermediate via a water molecule with a weaker hydrogen bond, reducing kcat ~10-fold at low temperatures. However, Asp 103 deprotonates upon solvent exposure during unfolding (its pKa drops from >9 in the buried native state to ~3.7 when solvent-exposed), thermodynamically stabilizing the unfolded state and making mesoKSI less thermally stable. Ser 103 does not deprotonate upon unfolding, leaving the native thermoKSI relatively more stable ($\Delta\Delta G° \approx +6.8$ kcal/mol). Conservative substitutions at positions 86, 88, and 101 (F86W, V88L, V101I) further stabilize thermoKSI. Analysis of 1,140 KSI sequences confirms a global trend: the D103 fraction decreases as optimal growth temperature increases, with S103 correspondingly rising. This pattern extends to other enzyme families where protonated active-site Glu and Asp residues are replaced in thermophiles.

Computational analysis of thermophilic adaptations. A large-scale computational analysis of 2,194 enzyme families from 5,582 bacterial species identifies broadly applicable principles of thermal adaptation. Thermophiles preferentially contain Ile, Glu, Tyr, and Lys, while mesophiles favor Ala, Gln, and Asp. The most frequent temperature-associated change is Leu/Val → Ile (occurring 2–3× more than the reverse), because Ile better fills interior cavities and has greater conformational flexibility than Leu while maintaining branched-chain hydrophobic packing. Ile-Ile contact pairs are the most strongly thermophile-associated interacting pair. For charged residues, Arg → Lys and Asp → Glu changes are characteristic of thermophiles: Lys and Glu have greater conformational flexibility and Lys additionally has larger hydrophobic surface area than Arg and Asp respectively. Lys-Glu salt bridges are most strongly associated with thermophilic proteins, while Arg-Asp pairs dominate in mesophilic ones. The results challenge simple earlier models attributing thermostability solely to increased salt bridges or hydrophobic packing, showing instead that the identity — not just the presence — of interacting pairs matters critically.

Allosterism and genome-scale metabolic modeling. Temperature affects not just individual active sites but also allosteric communication between them. In imidazole glycerol phosphate synthase (IGPS) from *Thermotoga maritima*, molecular dynamics simulations show that increasing temperature from 30°C to 50°C produces conformational changes in the apoenzyme that closely resemble those induced by the allosteric effector at room temperature — effectively mimicking allosteric activation. This demonstrates that climate warming can subtly reconfigure protein dynamics with functional consequences throughout the metabolome.

Genome-scale modeling of *S. cerevisiae* using the enzyme-and-temperature-constrained GEM (etcGEM) — incorporating temperature dependences of enzyme native concentration (EN), kcat, and non-growth-associated maintenance (NGAM) — reproduces the observed yeast growth curve including sharply reduced growth above 37°C and no growth at 42°C. Modeling reveals that below 29°C, kcat alone limits growth; from 29–35°C, both kcat and NGAM are rate-limiting; above 35°C, enzyme denaturation dominates and is essentially the sole constraint by 40°C. The model also reproduces the metabolic switch from respiration to fermentation at supraoptimal temperatures: as specific enzyme activities fall and total protein concentration saturates, glycolysis becomes more ATP-efficient per unit protein mass than oxidative phosphorylation. Flux control analysis identifies squalene epoxidase (ERG1) as the key bottleneck at supraoptimal temperatures; replacing it with a thermotolerant ortholog increases growth rate by over 55%.

Ecological thermal limits and mass extinction. Temperature increases of >5.2°C and rates of change of >10°C per million years correlate with each of the five major mass extinctions over the past 450 million years. Current human-driven warming (~2°C/200 years) is orders of magnitude faster than any geological rate of change in the 3-million-year record, and Rothman's analysis suggests that anthropogenic CO_2 additions approaching 310 Gt (possibly reached by 2100) could officially trigger a sixth mass extinction — though many argue this cycle has already begun. Mechanistically, the weakest thermal links in organisms are not necessarily enzymes but membranes (phase disruption, lipid raft dissolution), synaptic transmission (as in Antarctic fish dying at 9°C from acetylcholine receptor dysfunction), and protein synthesis (which declines dramatically near lethal temperatures). Lethal thermal limits in humans depend critically on humidity: at 85%

relative humidity, 29°C can be lethal because sweating cannot dissipate metabolically generated heat. Approximately 30% of the global human population already experiences exposure to lethal thermal thresholds at least 20 days per year. Directed evolution experiments with *E. coli* confirm that organisms can adapt to higher temperatures through gradual mutation accumulation, but cannot transform into thermophilic species — the magnitude of genetic change required is too great for the pace of current climate warming.

12: A Warmer World- Temperature Effects On Proteins is shared under a CC BY-NC-SA 4.0 license and was authored, remixed, and/or curated by LibreTexts.

13: BIOCHEMISTRY, CLIMATE CHANGE AND HUMAN HEALTH

Search Fundamentals of Biochemistry

LEARNING GOALS

(Learning goals written by Claude, Anthropic)

By the end of this chapter, students should be able to:

One Health, Heat Illness, and Kidney Disease

- Explain the One Health framework and describe the spectrum of heat-related illness (cramps, exhaustion, syncope, heat stroke), connect increasing heat wave frequency and severity to mortality data from major events (2003 Europe: 70,000; 2010 Russia: 55,000; 2022 Europe: 60,000), and explain why cardiovascular strain develops at 34°C in humid versus 41°C in dry conditions.
- Describe the clinical presentation, geographic distribution, and proposed mechanism of CKDu — connecting occupational heat/humidity exposure to renal inflammation and fibrosis in the absence of traditional risk factors — and identify its global expansion from Mesoamerica to Sri Lanka, India, Florida, and California.

Necroptosis, ZBP1, and Heat Stroke Mechanisms

- Describe the necroptosis pathway from receptor activation through RIPK3 autophosphorylation (pT224, pS227) to MLKL membrane translocation, calcium influx, and membrane permeabilization, contrasting this caspase-independent pathway with classical apoptosis and identifying the regulatory phosphorylation sites (pS164, pT165) that divert signaling toward apoptosis.
- Explain how ZBP1 activates RIPK3 through its RHIM domain during heat stress — independently of its Zα nucleic acid-binding domain — citing the experimental evidence (RHIM mutations prevent death; Zα mutations do not; ZBP1-GFP aggregation through RHIM), and distinguish this from viral Z-RNA/Z-DNA sensing.
- Distinguish necroptosis, pyroptosis (gasdermin pore formation, IL-1β/IL-18 release), and PANoptosis, and explain how heat stroke-induced epigenetic changes in monocyte DNA methylation patterns persist for 30+ days and are inherited by daughter cells, providing a mechanism for reduced heat tolerance after prior illness.

PM2.5: Sources, Entry, and Cellular Toxicity

- Define PM10, PM2.5, and PM0.1, describe the chemical composition of PM2.5 particles (black carbon, PAHs, transition metals, sulfate/nitrate/ammonium), and explain how secondary pollutants form — including tropospheric ozone from NOx/hydrocarbons and secondary organic aerosols from α-pinene/limonene terpene photochemical oxidation.
- Describe the three entry routes for PM2.5 (phagocytosis, pinocytosis, clathrin/caveolin endocytosis), explain how nanoscale PM0.1 protein coronas (hemoglobin, albumin, fibrinogen) amplify lung fibroblast proliferation and fibrosis, and explain the chemistry of the 1952 London Fog (SO_2 + NO_2 → sulfate in aqueous droplets, concentrated by evaporation) that killed ~12,000 people in two weeks.
- Explain the NRF2/Keap1/p62 antioxidant axis — how electrophilic PM2.5 metabolites modify Keap1 Cys residues releasing NRF2, how p62 accumulation creates a positive feedback loop, and how PM2.5 lysosomal membrane permeabilization and organelle damage ultimately activate apoptosis, necroptosis, and pyroptosis — and connect long-term PM2.5 exposure to neural damage (increased phospho-tau, malondialdehyde in hippocampus) and to epithelial-mesenchymal transition (EMT) via TGF-β/SMAD, PI3K/Akt, Wnt/β-catenin, and NF-κB signaling as a mechanism for lung cancer.

INTRODUCTION

Climate change affects human and biospheric health, which are inextricably linked. Many, including the US CDC, define One Health as "a collaborative, multisectoral, and transdisciplinary approach—working at the local, regional, national, and global levels—to achieve optimal health outcomes recognizing the interconnection between people, animals, plants, and their shared environment."

We all know that pollution from the use of fossil fuels also has severe health consequences independent of effects mediated more directly by climate change. A solution to both is to dramatically decrease the use of fossil fuels and mitigate pollution from their use. People most likely do not understand the extent to which climate change and fossil fuel use are linked to human health. If they did, they might become advocates for climate action. This section will cover how climate change and fossil fuel use affect human health and diseases. This section will focus on heat-related illnesses and pulmonary/cardiovascular diseases. The next chapter will address climate change, emerging diseases, and pandemics.

Fossil fuel use and climate change affect other diseases, including some indirectly. For instance, increases in cancer deaths will occur due to lower availability of health care arising from extreme weather disasters that impact health facilities and people's access to them. An

increase in cancer deaths occurred during the COVID pandemic, since people deferred preventive healthcare treatments as well as cancer surgeries during the pandemic. Allergic illness will increase as growing seasons lengthen and species that cause allergic reactions shift to new growth regions.

HEAT-RELATED ILLNESS

Heat illnesses include cramps, exhaustion, syncope (fainting), and heat stroke, the latter of which can quickly become fatal. Heat affects normal physiology and health. About 1% of all cardiovascular deaths are estimated to be linked to extreme temperatures. We know the number of warm days and heat waves has increased with climate change.

Figure **13.1** below shows how heat waves have changed in the US in the decades from 960 to 2022 using data from 50 large metropolitan areas. The 2020s are on track to continue the trend of increasing heat waves.

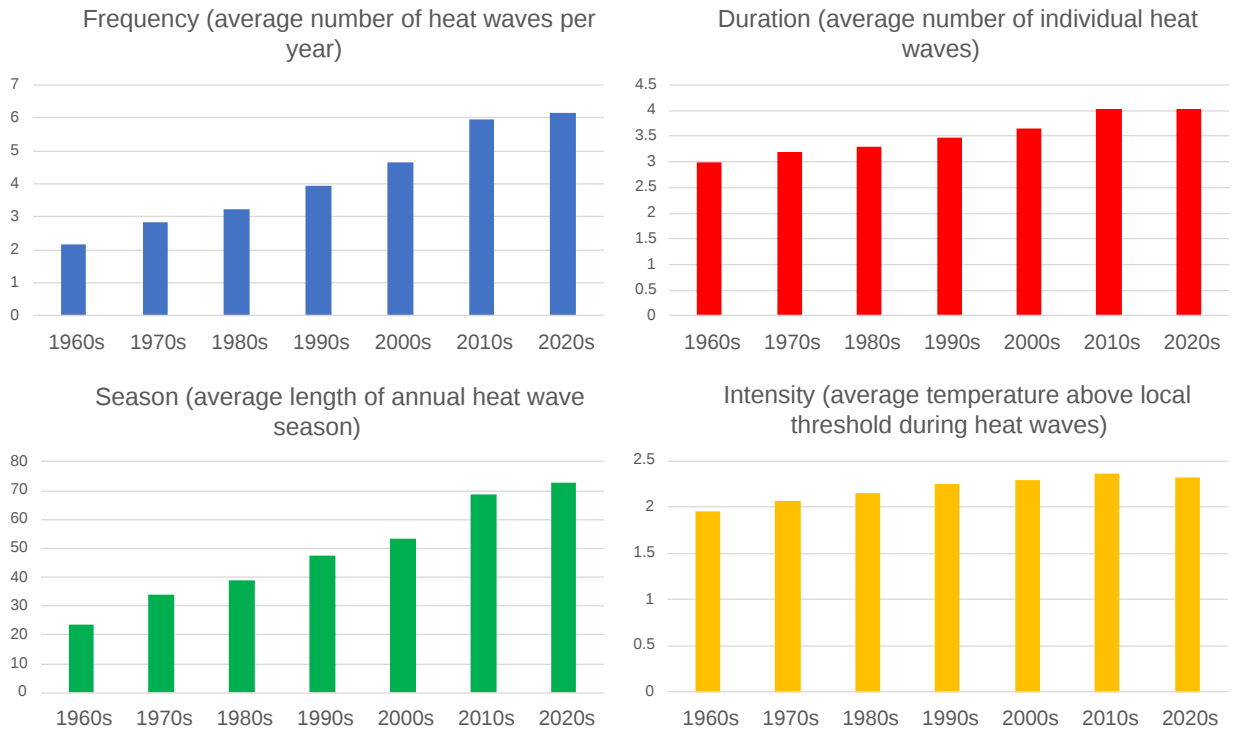


Figure **13.1**: Climate Change Indicators: Heat Waves. EPA. https://www.epa.gov/climate-indicato...ors-heat-waves. Data source: NOAA (2022)

Many recent historical heat waves have occurred. A heat wave in Europe in 2003 caused 15,000 heat-exposure-related deaths in France and 70,000 throughout Europe. On June 28, 2019, France recorded a temperature of 45.9 °C (115 °F). In 2022, China experienced a two-month heat wave and drought, with a record temperature of 45 °C (113 °F) in Chongqing. The Chicago Heat Wave of 1995, with a maximal temperature of 106 °F, caused by high temperatures and humidity, killed over 500 people. The worst might be the Russian Heat Wave of 2010, when temperatures were 5 °C (9 °F) higher than normal and reached 40 °C (104 °F). Around 55,000 people died.

Figure **13.2** shows temperature and excess mortality from the 2022 heat wave in Europe, during which 60,000 people died from heat-related causes.

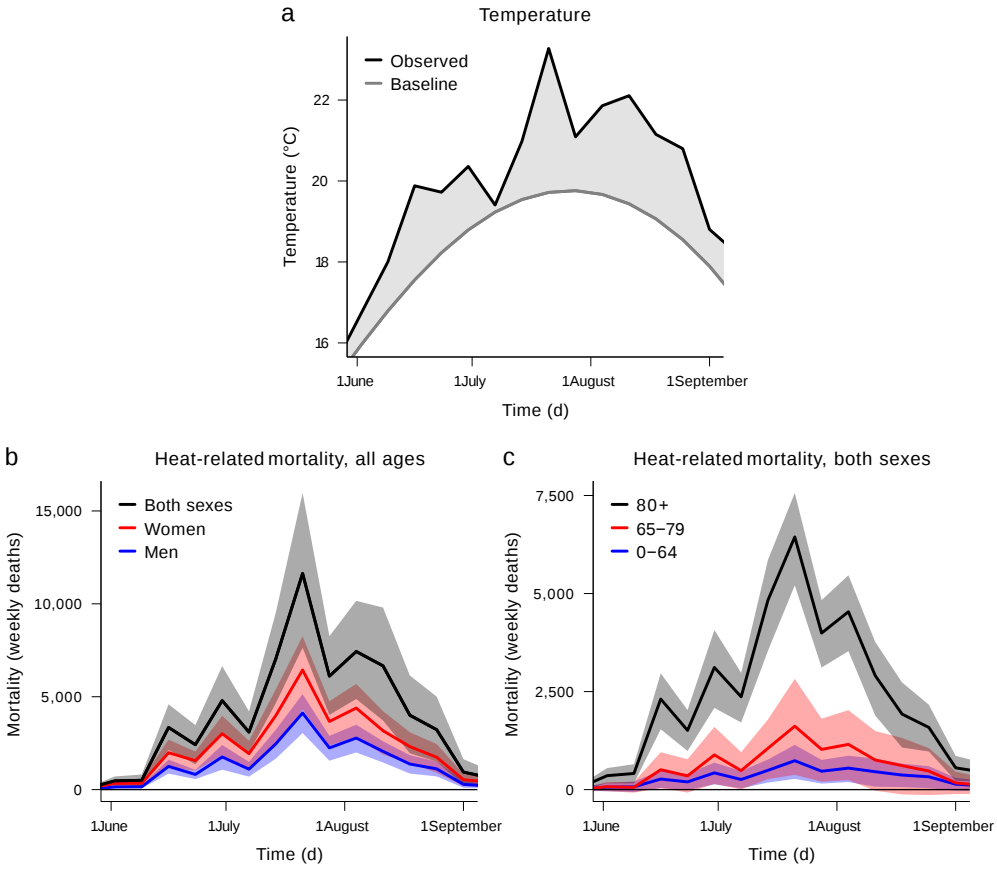


Figure **13.2**: **Weekly temperature and heat-related mortality numbers in Europe during the summer of 2022.** Ballester, J., Quijal-Zamorano, M., Méndez Turrubiates, R.F. *et al.* Heat-related mortality in Europe during the summer of 2022. *Nat Med* (2023). https://doi.org/10.1038/s41591-023-02419-z. Creative Commons Attribution 4.0 International License. http://creativecommons.org/licenses/by/4.0/

Panel a shows the weekly baseline (gray line) and observed (black line) temperature (°C) averaged over Europe. Temperature anomalies are the differences between observed and baseline temperatures (gray shading). Baseline temperatures were computed as the mean annual cycle of observed temperatures in the reference period 1991–2020.

Panels b and c show weekly heat-related mortality (weekly deaths) aggregated over Europe for the overall population (black), women (red), and men (blue) (**b**) and people aged 0–64 (blue), 65–79 (red), and 80+ (black) years (**c**), together with their 95% CIs (shadings). The numbers for women and men in **b** do not include the United Kingdom; values for the age groups in **c** do not include Germany, Ireland, and the United Kingdom.

Figure **13.3** below shows the steady increase in deaths as the average summer temperature in Europe has increased. The 2022 outlier is shown as a red dot.

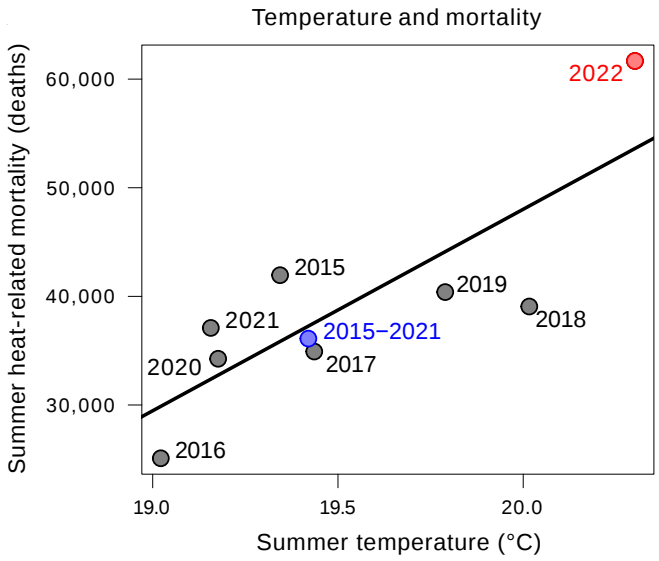


Figure **13.3**: **The summer of 2022 within the context of rising temperatures in Europe.** Relationship between summer mean temperature (°C) and summer heat-related mortality (summer deaths) in the analyzed European countries. The straight line shows the linear fitting for the 2015–2022 period. Ballester et al., ibid.

In exercise studies under controlled conditions, the heart rate increases and plateaus after a temperature increase. If the temperature increases further, the heart rate increases with less plateauing, a sign of cardiovascular strain. In humid conditions, cardiovascular strain develops even on slow walking at 34 °C (93.2 °F). Under dry conditions, the strain develops at around 41 °C (106 °F). The strain (as indicated by an increasing heart rate) proceeds for about 20 minutes, resulting in a rise in core temperature.

The annual probably of heat waves with apparent temperatures of 40 °C/104 °F (dangerous with a high incidence of heat cramps, heat exhaustion, and heat strokes) and 55 °C./131 °F (very dangerous with heat stoke very likely) increases as the average global temperatures increase from the pre-Industrial Revolution values by 1.5 - 4 °C (y-axis), as shown in Figure **13.4** below.

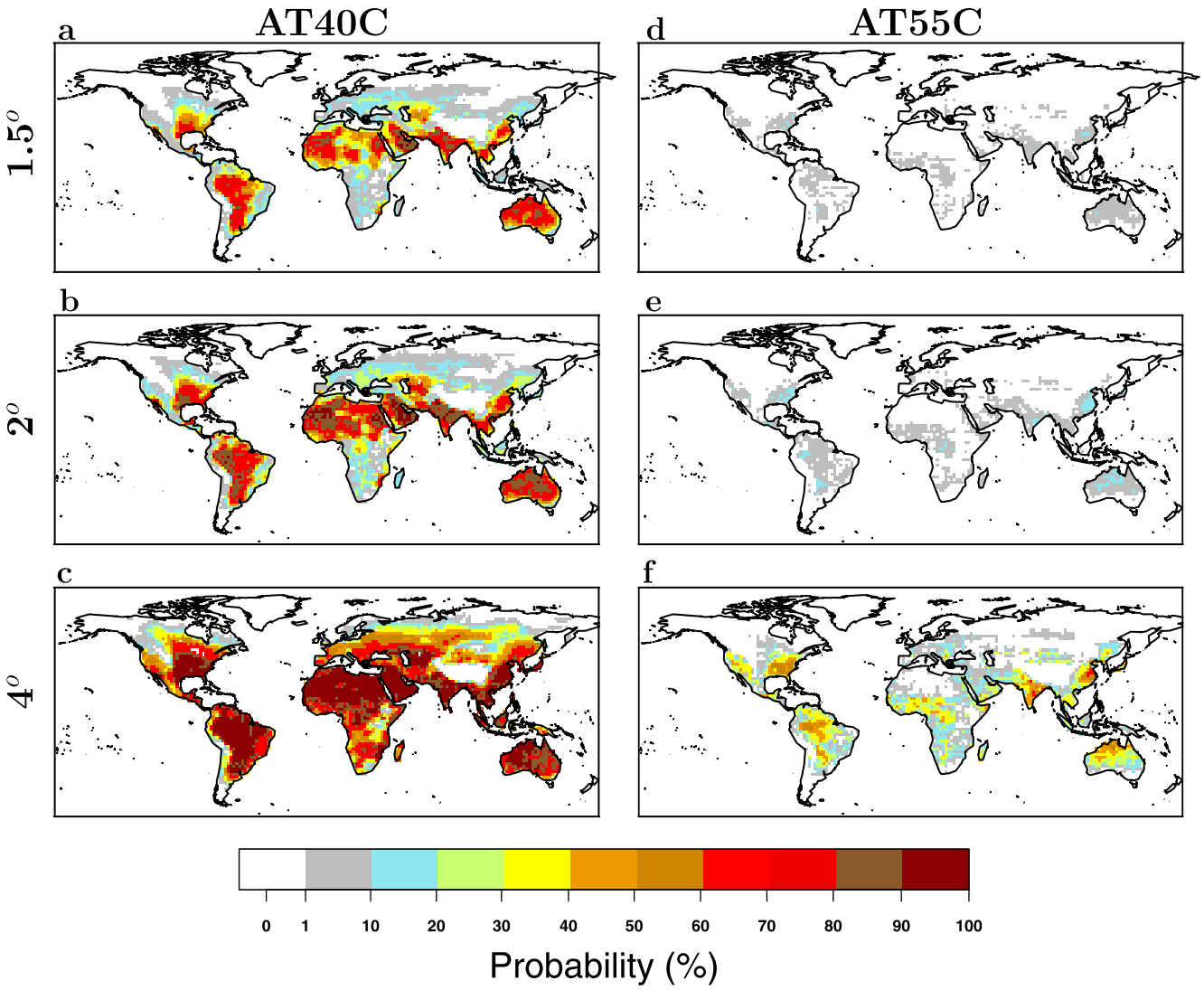


Figure **13.4**: Annual probability of occurrence of heat waves with apparent temperature (with contributions from humidity) peaks greater than 40 °C and 55 °C. Russo, S., Sillmann, J. & Sterl, A. Humid heat waves at different warming levels. *Sci Rep* **7**, 7477 (2017). https://doi.org/10.1038/s41598-017-07536-7. Creative Commons Attribution 4.0 International License. http://creativecommons.org/licenses/by/4.0/.

Panels (**a**–**c**) show the probability of occurrence of heat waves with $AT_{peak} \geq 40$ (AT40C) calculated at each grid point for all model years with global mean temperature anomaly relative to 1861–1880 at 1.5, 2, and 4 degrees warming (see Fig. 2), respectively.

Panels (**d**–**f**) are similar to panels (**a**–**c**) but show the occurrence of heat waves with $AT_{peak} \geq 55$ (AT55C).

The USA released the 5th National Climate Assessment in 2023, which presents current and projected climate change and its effects. One set of predictions is the change in number of days above 100 ^{0}F (38 ^{0}C) for different increases in the average global temperature since the pre-industrial revolution time, which is illustrated in Figure **13.5** below.

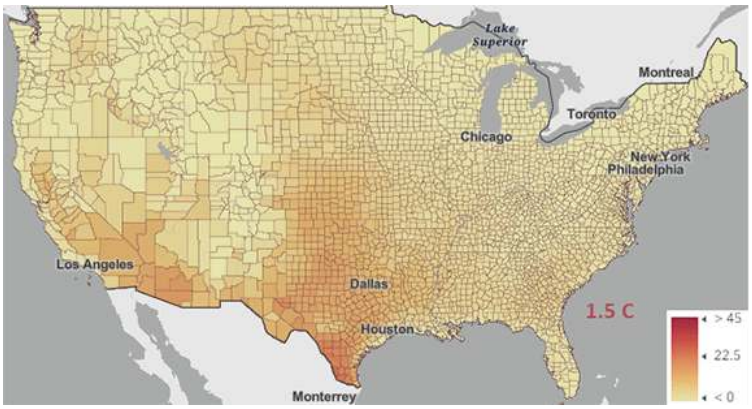


Figure **13.5**: Change in number of days above 100 ^{0}F (38 ^{0}C) for different increases in the average global temperature since the pre-industrial revolution time. https://www.arcgis.com/apps/mapviewe...3fa3e8bd1fd086

The world reached a net increase of 1.5 ^{0}C (2.7 ^{0}F) in 2024, shown in the map with the lightest red coloration. The other maps are for 2 ^{0}C (3.6 ^{0}F), 3 ^{0}C (5.4 ^{0}F), and 4 ^{0}C (7.2 ^{0}F). Note the significant change from 1.5 ^{0}C (2.7 ^{0}F) to 2 ^{0}C (3.6 ^{0}F).

The USA Weather Service offers a map (still in development) showing the current heat risk.

HEAT EXPOSURE AND KIDNEY DISEASE

Cumulative exposure to high effective temperatures caused by sublethal combinations of heat and humidity leads to chronic kidney disease. This is happening with increasing frequency to workers in poor agricultural areas and others who work in such hot conditions in industry and outdoors. This type of kidney disease is not caused by diabetes, hypertension, or other known glomerular diseases. Chronic kidney disease in such workers was noted in El Salvador and elsewhere in Central America. The disease has a high mortality rate. In El Salvador, the death rate from kidney disease is ten times higher than in the US. Initially, the disease was called Mesoamerican nephropathy.

Biochemical correlates of the diseases are yet unclear. Serum creatinine levels are increased, which might affect renal perfusion and lead to kidney damage. The effects might be generally cumulative or from repetitive episodes of exposure. Sugarcane field workers who report nausea, vomiting, headaches, muscle weakness, back pain, and fevers have high levels of creatinine. Kidney biopsies show inflammation and kidney fibrosis.

Similar diseases in other parts of the world with the same presentation include Sri Lankan nephropathy and Uddanam nephropathy (in the Indian state of Andhra Pradesh). Some have categorized them as CKDu, Chronic Kidney Disease of Unknown Etiology/Uncertain Cause, or chronic kidney disease of non-traditional origin (CKDnt).

Figure **13.6** below shows the distribution of kidney disease in the Western Hemisphere in 2019.

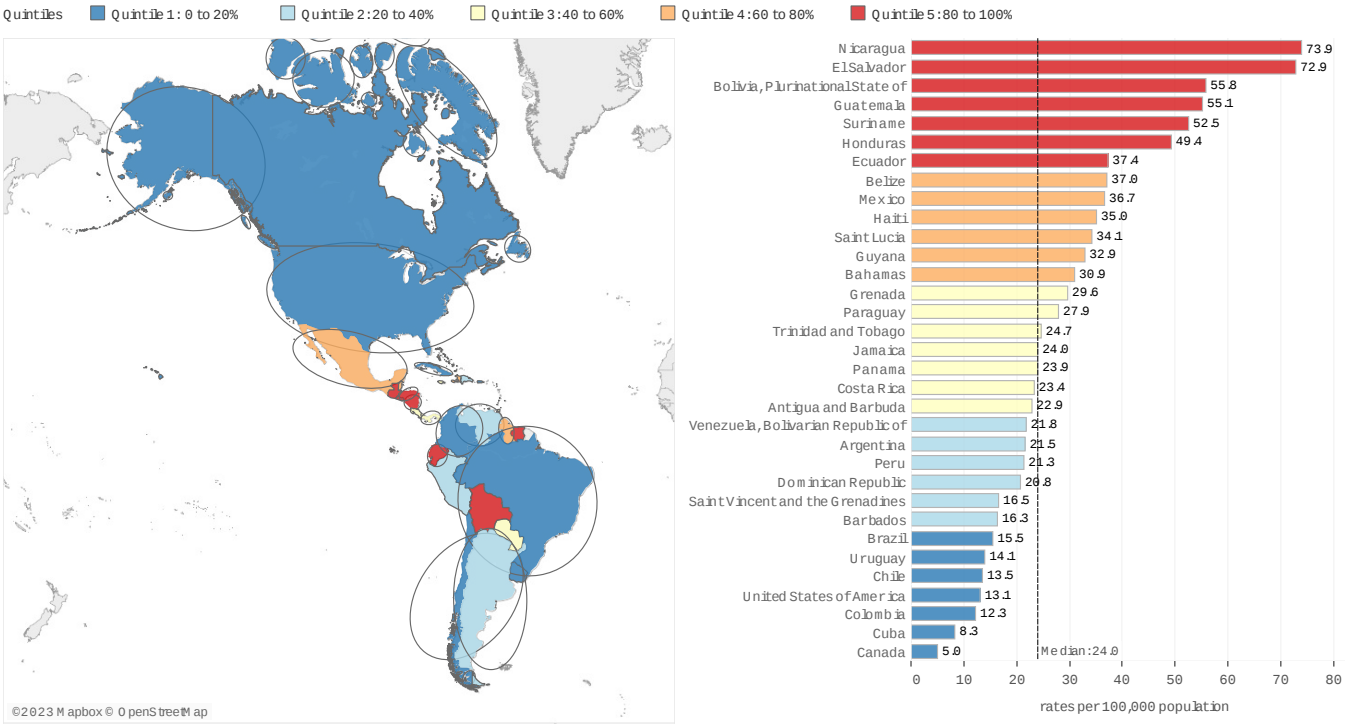


Figure 13.6: Burden of Kidney Disease. 2019. Men and Women. Pan American Health Organization/WHO.

Other factors, such as increased exposure to herbicides, heavy metals, and microbial agents, might also cause or contribute to the disease. The disease is most prevalent in the hotter regions of affected countries, with a lower incidence in workers at high altitudes. An increased incidence of chronic kidney disease also appears to be occurring in workers in Florida and California.

BIOCHEMICAL MECHANISM FOR HEAT STROKE

The actual biochemical mechanisms of heat stroke effects (circulatory failure, organ injury, uncontrolled clotting, death) are not fully understood. Certainly, cell death plays a significant role, but not via the classical apoptotic pathway, which depends on caspase activation (see Chapter 28.14). Rather, cell death occurs through **necroptosis**, a caspase-independent pathway. In necroptosis, an upstream protein kinase **RIPK3** (receptor-interacting serine/threonine protein kinase 1) activates the effector protein **MLKL** (mixed lineage kinase domain-like protein) through phosphorylation. Phosphorylated-MLKL then translocates to the cell membrane, leading to calcium influx and plasma membrane damage in the final "execution" phase of cell necrosis.

The activation of RIPK3 and MLKL through other receptors, including the toll-like receptors (TLR3 and TLR4), and tumor necrosis factor receptor 1 (TNF-R1), is shown in Figure **13.7** below.

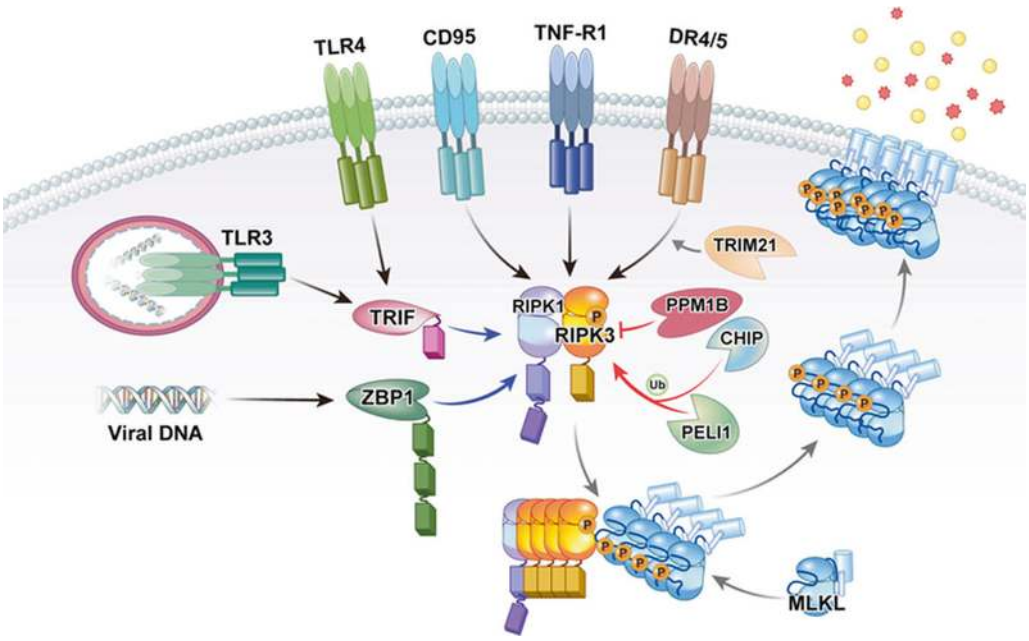


Figure **13.7**: **Activation of RIPK3 by multiple stimuli.** Morgan MJ, Kim YS. Roles of RIPK3 in necroptosis, cell signaling, and disease. Exp Mol Med. 2022 Oct;54(10):1695-1704. doi: 10.1038/s12276-022-00868-z. Epub 2022 Oct 12. PMID: 36224345; PMCID: PMC9636380. Creative Commons Attribution 4.0 International License. http://creativecommons.org/licenses/by/4.0/

RIPK3 can be activated by various receptors upon binding their respective ligands. These are TNF receptor 1 (TNF-R1), CD95, death receptors (DR4/5), Toll-like receptors (TLR3/4), and Z-DNA-binding protein-1 (ZBP1)/DAI. In the first three of these pathways (but not TLR3/4 or ZBP1), RIPK1 is required and binds to RIPK3 through its receptor-interacting protein homotypic interaction motif (RHIM). In the case of ZBP1, RIPK3 is recruited directly via the ZBP1 RHIM domain, whereas for TLR3/4, RIPK3 is recruited indirectly via the TRIF RHIM domain. Once activated, RIPK3 autophosphorylates itself, then phosphorylates and activates MLKL, inducing a conformational change and translocation to the membrane, leading to membrane permeabilization. During this process, post-translational modifications positively and negatively regulate the necroptosis pathway. Two E3 ligases, Pellino-1 (PELI1) and carboxy terminus of HSC70-interacting protein (CHIP), may control the basal threshold of necroptosis. Another E3 ubiquitin ligase, TRIM21, is proposed to regulate necroptotic cell death in response to TRAIL. PPM1B suppresses necroptosis by dephosphorylating RIPK3.

The domain structure and phosphorylation sites on human RIPK3 are shown in Figure **13.8*a*** below.

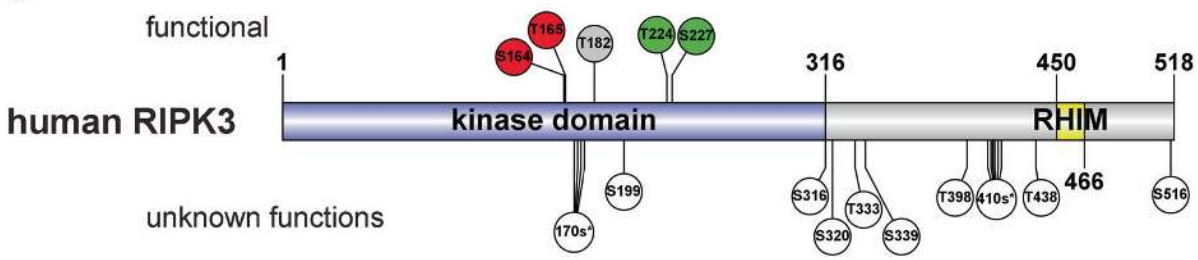


Figure **13.8*a***: Schematic of human RIPK3 domain architecture and the phosphorylation sites identified. Meng, Y., Horne, C.R., Samson, A.L. *et al.* Human RIPK3 C-lobe phosphorylation is essential for necroptotic signaling. *Cell Death Dis* **13**, 565 (2022). https://doi.org/10.1038/s41419-022-05009-y. Creative Commons Attribution 4.0 International License. http://creativecommons.org/licenses/by/4.0/

Phosphorylation sites with proposed functions are shown at the top. pT224 and pS227 positively regulate necroptosis (green) by recruiting MLKL. pS164 and pT165 negatively regulate necroptosis by inhibiting RIPK3 kinase activity (red). Phosphorylation of T182 (grey) was proposed to promote RIPK3 kinase activity and to recruit PELI1 to mediate proteasomal degradation of RIPK3. Phosphorylation sites with unknown functions are shown on the bottom (white). Asterisks (*) denote multiple serine/threonine on the same peptide, as the exact phosphorylation site could not be unambiguously identified.

Figure **13.8*b*** shows **necrosome,** a complex containing multiple activated RIPK3s and RIPK1. Aggregation of RIPK3 occurs through the **RHIM** (RIP homotypic interaction motifs) domain through the formation of amyloid fibers. The necrosome then phosphorylates MLKL, which forms oligomers and traffics to the membrane.

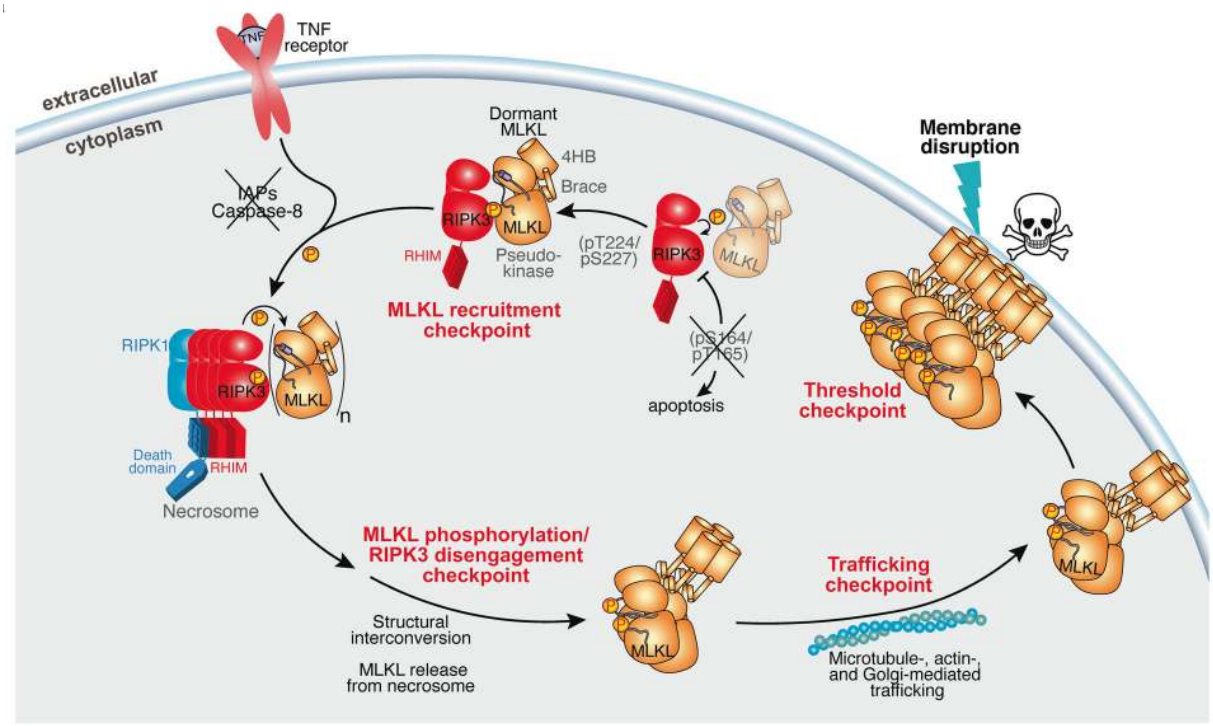


Figure **13.8*b***: A schematic diagram of the current model of necroptosis signaling. Meng, Y. et al., ibid.

RIPK3 kinase activity is negatively regulated by pS164/pT165, which promotes apoptotic pathways. Under basal conditions, in the absence of inhibitory pS164/pT165, RIPK3 autophosphorylates T224/S227 in a MLKL-dependent manner, allowing MLKL to be recruited to the kinase domain of RIPK3. Upon TNF signaling in the absence of cIAPs and Caspase-8 activity, MLKL is phosphorylated in the necrosome before disengaging from the RIPK3 kinase domain, undergoing a structural transition, and assembling into active oligomers, which are then trafficked to the plasma membrane, where they accumulate as hotspots to enact cell death.

Figure 8b above also shows that an internal viral DNA sensor protein can activate RIPK3. That protein is **ZBP1**, or Z-DNA-Binding Protein 1, which also binds Z-RNA. Nuclear Z-RNA can be derived from viruses like influenza A, leading to activation of the same pathway. Cytokine expression then produces a systemic inflammatory response.

In addition to apoptosis and necroptosis, another type of programmed cell death caused by inflammation is called **pyroptosis**. Usually occurring in macrophages infected with bacteria, pyroptosis activates intracellular inflammasomes, leading to the production of inflammatory cytokines via caspase-mediated proteolysis. In pyroptosis, proteins called gasdermins are cleaved by caspases, and their N-terminal sections self-assemble at the cell membrane to form pores, releasing the inflammatory cytokines IL-1β and IL-18.

A final programmed cell death pathway for virally infected cells is called PANoptosis, which uses the PANoptosome complex and has downstream results not explained by the other three programmed cell death pathways (pyroptosis, apoptosis, and necroptosis). ZBP-1 leads to the activation of RIPK3, caspase-8 (a key player in the apoptosis pathway), and the NLRP3 inflammasome.

ZBP-1 seems to play a key role in heat stroke. Its concentration increases under heat stress, mediated by the heat shock transcription factor 1 (HSF1), which is induced by cellular stress. HSF1 induces a heat shock response, leading to increased transcription of chaperones and heat shock proteins (HSPs), such as ZBP-1. Deletion/inactivation of ZBP-1, RIPK3, MLKL, or caspase 8 reduces heat stroke. The main role of ZBP-1 in cell death from heat stroke arises from the RIPK3/MLKL pathway and, to a lesser extent, through cross-talk with the classical apoptosis pathway through caspase 8.

How does ZBP-1 activate cell death during heat stroke without binding to and activating dsDNA or RNA derived from a viral infection? Does ZBP-1 have an endogenous ligand other than viral Z-RNA or Z-DNA? First, explore the domain structures of key proteins in the RIPK3 activation pathway. Figure 1 above shows three key proteins, RIPK1, TRIFF, and ZBP1, that interact with RIPK3. These proteins, including RIPK3, have an RHIM domain that mediates protein-protein interactions. Figure **13.9** shows the domain structure of our key protein, ZBP-1, the cytosolic Z-DNA/Z-RNA sensor.

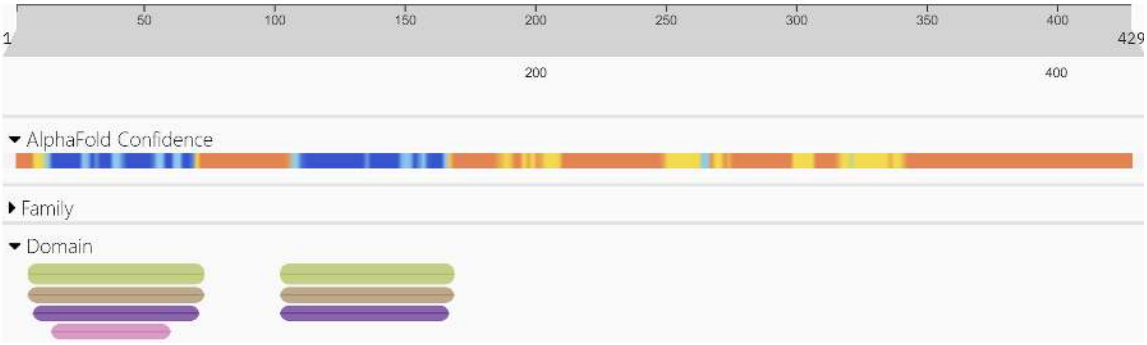


Figure 13.9: Domain structure of ZBP-1 (http://www.ebi.ac.uk/interpro/protein/UniProt/Q9H171/)

The green bars in the N-terminal part of the protein are the Z-DNA binding domain. These are also called Zα domains. These regions are the most ordered in the protein, as indicated by the blue in the AlphaFold confidence bar.

Figure 13.10 shows an interactive iCn3D models of the AlphaFold-predicted model of human Z-DNA-Binding Protein 1 (ZBP1), (Q9H171)

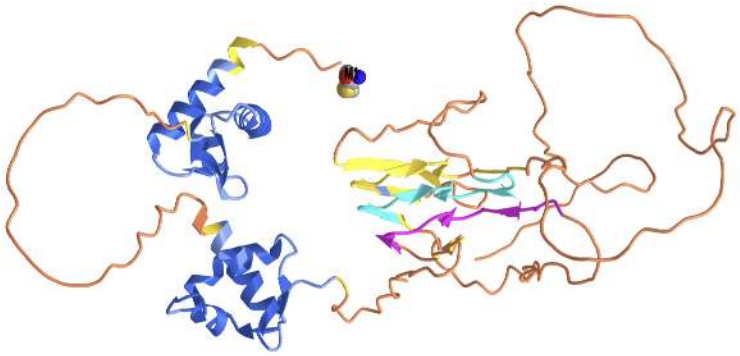


Figure 13.10: AlphaFold-predicted model of human Z-DNA-Binding Protein 1 (ZBP1), (Q9H171). (Copyright; author via source). Click the image for a popup or use this external link: https://structure.ncbi.nlm.nih.gov/i...FMCRhJwHFVb1X7

The spacefill atoms labeled M1 represent the N-terminal methionine of the protein. The two Z-DNA binding domains are well-ordered and are shown as blue cartoons. Much of the protein can't be predicted as it is most likely intrinsically disordered. Two fairly well-structured motifs, shown in magenta and cyan, are the RHIM1 and RHIM2 protein interaction motifs, which can self-associate via their amyloid-like structures. These motifs allow ZBP1 to bind to other proteins with RHIM motifs, leading to cell death via necrosis. The C-terminal domain appears to be involved in type I interferon-mediated signal transduction in response to DNA.

Figure 13.11 shows an interactive iCn3D model of the second Z-DNA binding domain of human DAI (ZBP1) in complex with Z-DNA (3EYI)

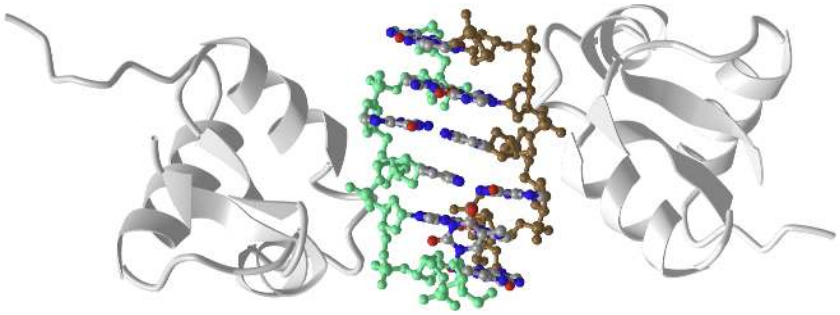


Figure 13.11: Second Z-DNA binding domain of human DAI (ZBP1) in complex with Z-DNA (3EYI). (Copyright; author via source). Click the image for a popup or use this external link: https://structure.ncbi.nlm.nih.gov/i...SLBmo2xqV1WpS6

Without viral DNA or RNA, the Zα domain can bind endogenous ligands. Moreover, a deficiency in RIPK1 or RHIM in RIPK1 also triggers ZBP1-mediated necroptosis and inflammation, and its Zα domain is required. If nuclear export is stopped, ZBP1 activates nuclear RIPK3 and then necroptosis. This suggests that nuclear ZBP1 interacts with endogenous nuclear Z-nucleic acids, likely Z-RNA from retroelements, to activate RIPK3-dependent necroptosis and may contribute to some forms of chronic inflammation.

Here are a series of findings on RIPK3-dependent cell death on heat stress in mouse fibroblasts that show that Z-nucleic acid binding to ZBP1 is not required for heat stress effects:

- Heat (43°C for 2 hr) induces phosphorylation of RIPK3 and MLKL within 2 hours and cleavage of pro-caspases and GSDME within 6 hours, but none occurs if RIPK3 is deleted.
- Deletion of ZBP1, but not RIPK1, affects heat-induced death, indicating that heat stress acts through ZBP1 and RIPK3.
- In ZBP1-deficient mice, the effects of heat stress (clotting, inflammation, organ injury, and death) were prevented.
- Mutations in the RHIM domain, but **not** the Zα domains (made to prevent Z-nucleic acid binding) or in the C-terminal signaling region (to stop signaling), prevented death from heat stress. Hence, Z-nucleic acid binding is **not** required, but it may contribute to heat-stress-induced cell death.
- Heat stress caused the aggregation of a ZBP1-GFP (green fluorescent protein) fusion protein through the RHIM domains of ZBP-1.

Hence, ZBP1 is an innate pathogen sensor and an initiator of heat-related death in the absence of pathogens.

HEAT STROKE-INDUCED EPIGENETIC CHANGES

Short of death, heat stroke can also cause long-term health issues. Increasing global temperatures are forcing people to work in more dangerous temperatures and at night to reduce heat exposure. Data suggest that people with heat-related illnesses are more susceptible to health consequences from additional heat exposure. This has been noted in exertional heat illnesses. (such as in athletes). Additional long-term effects on immune regulation have been observed. Epigenetics may play a role in long-term effects such as greater vulnerability to additional heat challenges. Studies show that a single episode of exceptional heat stroke changes DNA methylation patterns in bone marrow-derived monocytes from mice. Monocytes become immunosuppressed, leading to increased microbial disease and reduced heat shock responses. Epigenetic changes are passed on to progeny monocytes, leading to compromised function. The epigenetic changes persist for 30 days or more, and we noted them in inflammatory cell signaling pathways. This suggests a mechanism for the reduced tolerance to those with previous heat-related illnesses.

CARDIOVASCULAR, PULMONARY DISEASES AND CANCER

Many factors can cause these diseases and lead to mortality. For example, cancer mortality can increase due to the lower availability of health care arising from extreme weather disasters that impact health facilities and access to them. Early detection of many cancers is key to survival. Instead of discussing climate change's links to cancer, we will focus on pollution, particularly small particles.

PM2.5 PARTICULATE POLLUTION EFFECTS ON CARDIOVASCULAR AND PULMONARY HEALTH

Pollution from the combustion of fossil fuels contributes to many chronic diseases. Here, we will focus on one type of pollutant, particulate matter, which can be inhaled. These particles can be liquids, solids, or combinations of both. They are classified according to size with common categories, including:

- PM10: diameters $\leq$ 10 uM = 10,000 nm;
- PM2.5: fine particles with diameters $\leq$ 2.5 um = 2500 nm
- PM0.1: ultra-fine particles with diameters $\leq$ 0.1 µm = 100 nm (also called nanoscopic particulate matter or NPM)

Figure **13.12** below shows the relative sizes of PM10 and PM2.5 particles compared to other biological structures.

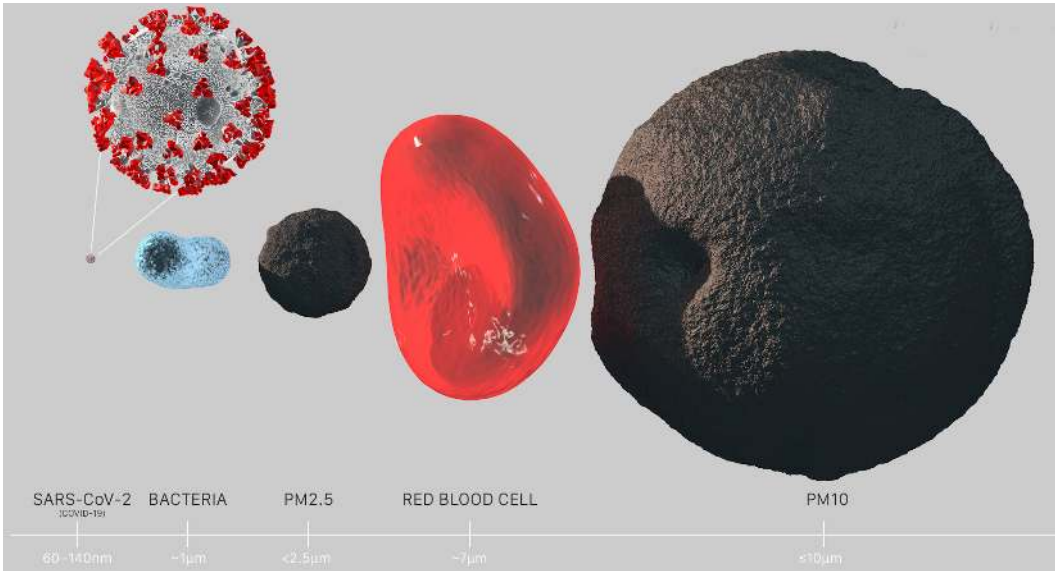


Figure **13.12**: Relative sizes of PM particles compared to biological structures. Sotirios Papathanasiou. Particulate Matter (PM2.5) Mega Guide. With Permission. https://seetheair.org/2022/05/16/par...-5-mega-guide/

Figure **13.13** below shows the relative sizes of PM0.1 particles compared to a PM2.5 particle.



Figure **13.13**: Relative sizes of PM01 particles compared to a PM2.5 particle.Sotirios Papathanasiou, ibid.

COMPOSITION OF PM2.5 PARTICLES

PM2.5 particles collected from polluted city air can be purchased from the National Institute of Standards and Technology (NIST, SRM 1648a) and used in experimental studies of living cells. It is typically added to water, and a suspension is produced through sonication. PM2.5 particles are derived from human sources, such as vehicle and industrial emissions, and from natural processes, such as biomass burning and windblown dust. They can also include salts from land and ocean sources.

They arise from burning fossil fuels and the wear and tear of products such as automobiles (including tires). PM2.5 particles contain mainly black carbon, polycyclic aromatic hydrocarbons (PAH), aryl hydrocarbons, volatile organic compounds (VOCs), as well as minerals, ions (sulfate, nitrate, ammonium), and general biological materials. The metal composition includes Group 1A (K, Na, Fr), Group 2A (Ca, Mg), Group 3A (Al), transition metals (Al, As, Cr, Fr, Mn, Pb, Ti, Zn), and counter ions Br and Cl. They also contain silicon and silicates. Of course, particles in the air, including dust, also derive from non-anthropogenic sources. Atmospheric dust is also produced from land by winds and volcanic eruptions. In homes, dust contains a high concentration of dead skin cells. along with pollens, hair, fur, and fibers from

clothes and paper. Humans have evolved with particulates in the air, but large increases in their abundance, driven by human activities in many parts of the world, pose serious health consequences.

In addition, reactions among atmospheric pollutants produce "secondary" pollutants. One, the tropospheric gas ozone (O_3), produced by hydrocarbons and nitrogen oxides, is a known health risk, and its levels are higher in cities on sunny, hot, and humid days. Secondary organic carbon (SOC) is generated from primary organic carbon, typically volatile organic compounds (VOCs), through photochemical oxidation. These VOCs (like m-xylene and 1,2,4-trimethylbenzene) can produce aerosols (larger particles, called secondary organic aerosols by reacting with each other to produce larger structures. Terpenes containing isoprene units like α-pinene and limonene (a monoterpene found in large abundance in fruit peels) are reactants for the products of much larger structures. (See Chapter 10.1 and Chapter 21.6 for a review of isoprene and terpenes). Figure **13.14** below shows generalized pathways for forming particulate SOCs from smaller terpenes.

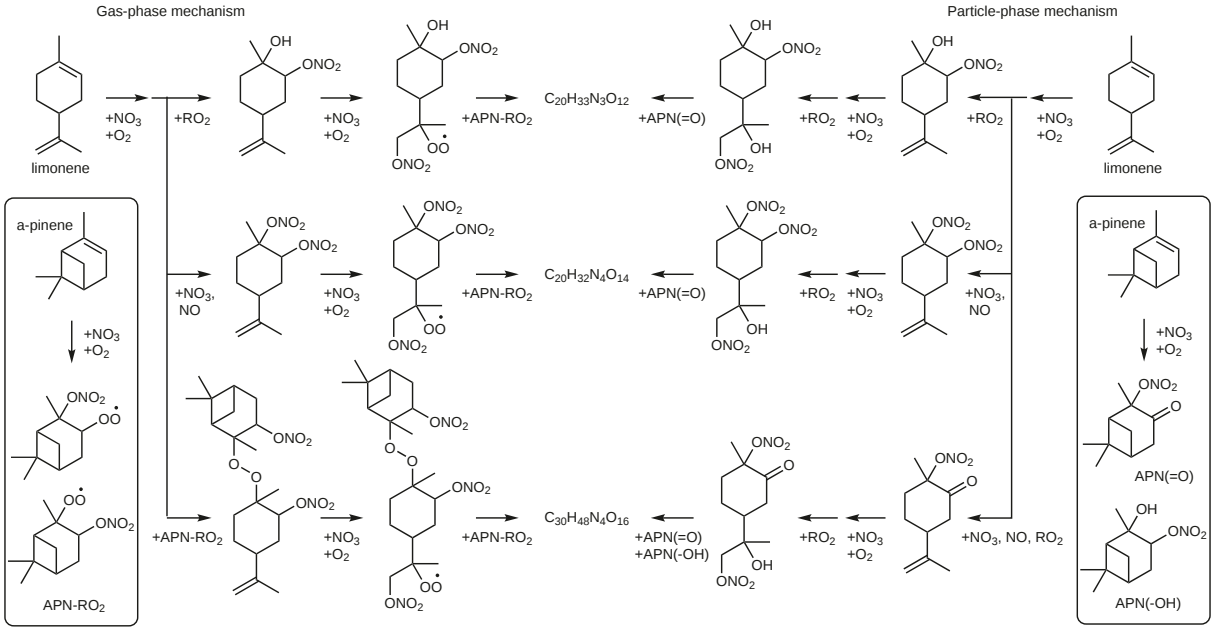


Figure **13.14**: **Proposed mechanisms for the formation of $C_{20}H_{33}N_3O_{12}$, $C_{20}H_{32}N_4O_{14}$, and $C_{30}H_{48}N_4O_{16}$ in the simultaneous oxidation (MIX) experiment.** Takeuchi, M., Berkemeier, T., Eris, G. *et al.* Non-linear effects of secondary organic aerosol formation and properties in multi-precursor systems. *Nat Commun* **13**, 7883 (2022). https://doi.org/10.1038/s41467-022-35546-1. Creative Commons Attribution 4.0 International License. http://creativecommons.org/licenses/by/4.0/.

The gas-phase mechanism via cross-reactions of α-pinene and limonene peroxy radicals (RO_2·), and the particle-phase mechanism via hemiacetal formation involving α-pinene and limonene oxidation products. APN-RO_2, APN(=O), and APN(-OH) represent α-pinene oxidation intermediates (i.e., RO_2·), α-pinene oxidation products containing carbonyl groups, and α-pinene oxidation products containing hydroxyl groups, respectively.

Figure **13.15** below shows the morphology of PM2.5 particles.

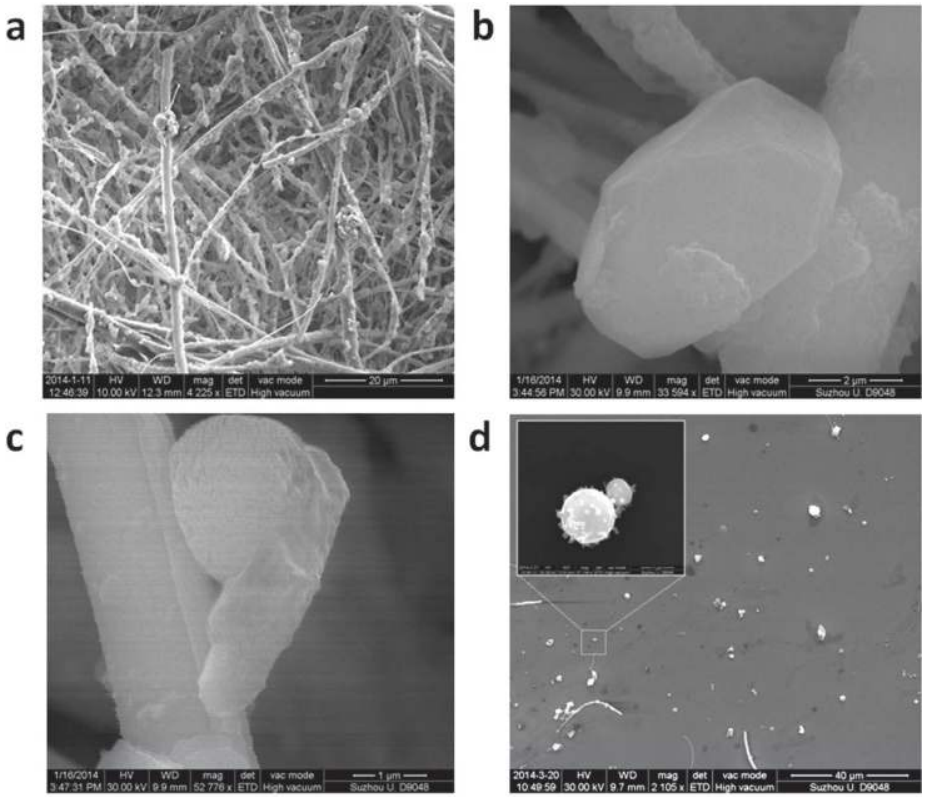


Figure **13.15**: Morphology of PM2.5 particles. The scale bars are 20 μm for image (a) 2 μm for image (b) 1 μm for image (c) 40 μm for image (d). Shi, Y., Ji, Y., Sun, H. *et al.* Nanoscale characterization of $PM_{2.5}$ airborne pollutants reveals high adhesiveness and aggregation capability of soot particles. *Sci Rep* **5**, 11232 (2015). https://doi.org/10.1038/srep11232. Creative Commons Attribution 4.0 International License. http://creativecommons.org/licenses/by/4.0/.

Panel (a) shows a large area image of collected PM2.5 on the filamentary filter.

Panels (b) and (c) show SEM images of particles with flat and rough top surfaces, respectively.

Panel (d) shows an SEM image of the PM2.5 transferred to a silicon substrate. Inset, zoom-in SEM image of an Iron-rich particle.

Many PM2.5 particles have rough surfaces that can deform and interact more readily with (i.e., stick to) other particles through noncovalent interactions, forming even larger particles.

Figure **13.16** below shows the elemental composition of rough, semi-rough, and flat PM2.5 particles.

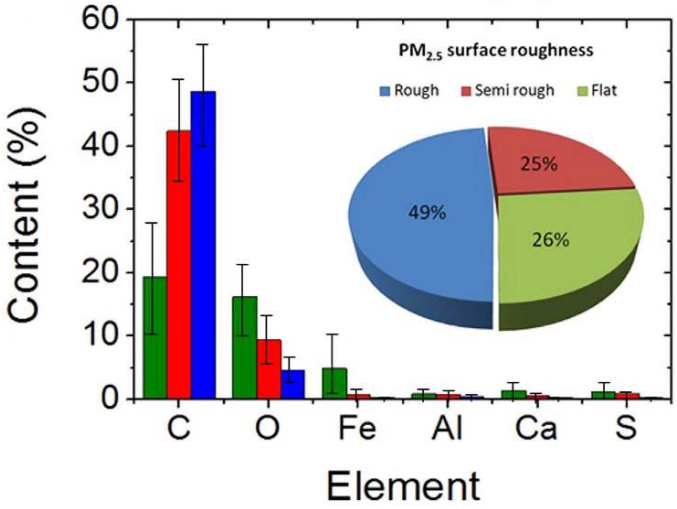


Figure **13.16**: EDAX Chemical composition histogram of the particles collected with SEM/EDAX classified by surface roughness; a larger surface roughness (and therefore, stickiness and deformation) is linked to a larger content of carbon while particles with a flat surface (low stickiness and viscosity) are richer in oxygen and metals. Shi, Y. et al., ibid.

Figure **13.17** below shows electron micrographs of actual airborne particles. Most are PM2.5 particles with diameters $\leq$ 2.5 uM = 2500 nm.

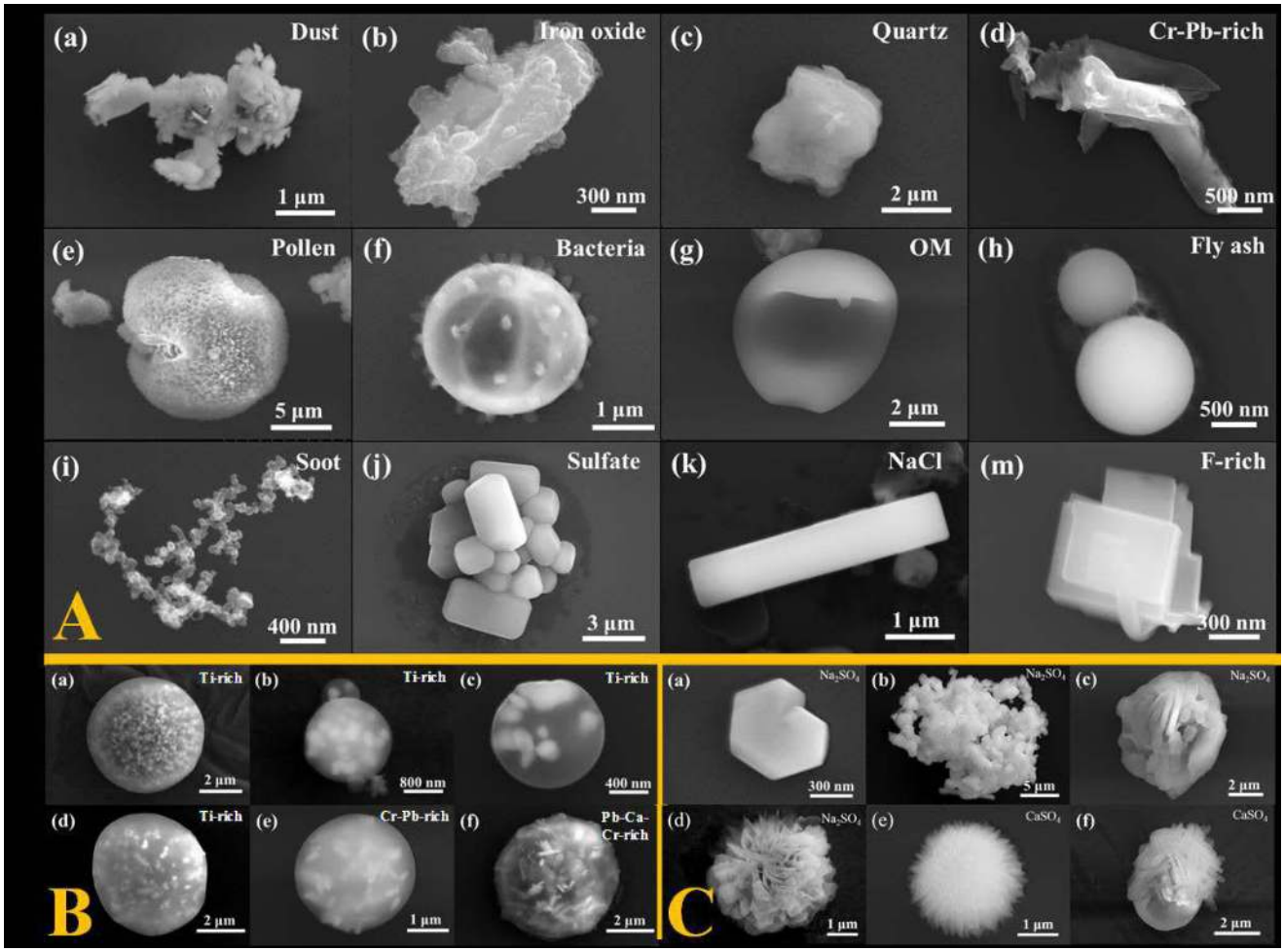


Figure **13.17**: A collage of SEM images for airborne particulates. (A) General classification of airborne particulates: (B) particulates with seed-coating composite morphology; (C) sulfate particulates with different morphologies. Clara Yuan Li et al, Journal of Environmental Protection, Vol.7 No.10, 2016. https://www.scirp.org/journal/paperi...?paperid=71021. Creative Commons Attribution 4.0 International License.

Given their composition and structures, it doesn't take much thought to realize that the particles must cause significant health effects. Would you want to breathe these particles routinely?

HEALTH EFFECTS OF PM2.5 PARTICLES

PM2.5 particles are associated with many types of illness, including cardiovascular and pulmonary diseases (including asthma) and cancer. Since they are small, they can be easily inhaled and deposited in the lung alveoli, where they can enter the bloodstream and be deposited in tissues. Particles up to 240 nm (0.25 µm) can cross the placenta, and black carbon particles have been found to cross the placenta. PM2.5 particles can cause inflammation, DNA damage, and organelle dysfunction, and generate free radicals, most likely involved in these toxic health effects.

THE GREAT LONDON FOG OF 1952

Aerosol particles can even have acute and lethal effects. During the Great London Smog in December 1952, around 12,000 people died in two weeks from its effects. Figure **13.1** shows people in the thick smog from that event. The smog consisted of acidified water droplets from SO_2 and NO_2 released by burning coal containing sulfur. This gas can be oxidized to sulfate in gas-phase reactions, probably through the ·OH free radical or in aqueous phase reactions using O_3, peroxides, and NO_2 as reactants/catalysts.

The reaction of SO_2 with NO_2 in aqueous droplets is shown below:

$$SO_2(g) + 2NO_2(g) + 2H_2O(aq) \rightarrow 2H^+(aq) + SO_4^{2-}(aq) + 2HONO(g) \quad (13.1)$$

Given the stoichiometry of the reaction with NO_2, the reaction proceeds significantly only in the presence of high NO_2. The reaction is favored under high relative humidity. In large water droplets in clouds, the droplets are not very acidic, but as water evaporates from them, the sulfate concentration and acidity increase dramatically. However, the oxidation rate and solubility decrease as the acidity increases.

Major cities in China, including Beijing and Xi'an, have experienced high levels of haze and particulate matter in the atmosphere until recently. Yet these smogs were not as lethal (very acidic) as those in London because NH_3 added to the droplets neutralized the acidic particles. Atmospheric ammonia is derived from large amounts of agricultural fertilizers that are aerosolized, from vehicles that produce NH_3 in catalytic converters, and from urea used in the catalytic reduction in diesel engines. The relevant production of sulfates in the presence of NH_3 is shown in the equation below.

$$2NH_3(g) + SO_2(g) + 2NO_2(g) + 2H_2O(aq) \rightarrow 2NH_4^+(aq) + SO_4^{2-}(aq) + 2HONO(g) \quad (13.2)$$

Figure **13.18** below shows a ghostly image of pedestrians in London during the Great Fog.



Figure **13.18**: Ghost-like pedestrians going through the smog. https://heritagecalling.com/2022/12/...f-london-1952/. Public Domain

The prevailing weather conditions (cold temperatures) increased emissions from coal use. A stalled high-pressure system and resulting low winds led to stagnant air, allowing increasingly acidic PMs to build up. The appalling death toll led politicians to pass the Clean Air Act in 1954, which, over many years, led to huge improvements in air quality in London and dramatically reduced negative health effects and deaths. This was a prelude to the US Clean Air Act, which dramatically improved air quality.

High levels of PM2.5 remain prevalent worldwide, though there have been dramatic decreases in the US. The notable exceptions occur during forest fires that are exacerbated by climate change. In the US, the Air Quality Index (AQI) is one indicator of health risk. It measures the value of 5 pollutants: fine particles (PM2.5 and PM10), ground-level ozone, SO_2, NO_2, and CO. The AQI at a given time is determined by the highest pollutant. In haze from smoke, the reported AQI reflects PM2.5 particles. AQI values < 50 represent good air quality, while an AQI value over 300 represents hazardous air quality. Western forest fires in Oregon in September 2020 led to an AQI of 611 in Madras, Oregon. Forest fires in Eastern Canada and a slow-moving weather system temporarily led to PM2.5 levels over 800 (mg/m3) in New York City on June 7, 2023. No place is immune to PM2.5 particles from wildfires and human-caused pollution.

Severe forest fires in Canada in 2023 led to significant health consequences in the US. On 19 smoke days (Air Quality Index ≥101, which is unhealthy for sensitive groups) between April 30–August 4, 2023), there was a 17% increase in visits to emergency departments for asthma-associated conditions. In counties affected by California wildfires in 2015-2017, there was a large increase in "out-of-the-

hospital coronary arrest". In the first 3 months after the 2025 fires in Los Angeles, there was a 46% increase in heart-attack-related emergency room visits at Cedars-Sinai Hospital.

- AirNow - gives present pollution data, primarily PM2.5 levels, based on US zip codes.

The following interactive graphs show the changes in PM2.5 particles over time (from Hannah Ritchie and Max Roser (2019), OurWorldInData.org/outdoor-air-pollution • CC BY. Source: Brauer et al. (2017) via World Bank).

Figure **13.19** shows the share of the population exposed to PM2.5 levels higher than the World Health Organization's suggestions.

Figure **13.19**: Share of the population exposed to PM2.5 levels higher than those suggested by the World Health Organization.OurWorldInData.org/outdoor-air-pollution • CC BY. Source: Brauer et al. (2017) via World Bank

Figure **13.20** below shows the death rate from PM2.5/100,000 people in 2017 in countries worldwide.

Figure 13.20: Death rate from PM2.5/100,000 people in 2017 in countries worldwide.

Recent estimates based on WHO guidelines suggest that, in India, an average of 16.6 million annual deaths (13-22 million) from 2009 to 2019 were attributable to PM2.5 (about 25% of total mortality), far above the estimates shown in the graph above.

MECHANISMS FOR PM2.5 HEALTH EFFECTS

In Chapter 5.4, we discussed how solids such as silica, cholesterol crystals, uric acid crystals, and even aggregated proteins such as prions can be engulfed by monocytes/macrophages (much as they engulf bacteria as part of their immune function) in a process called phagocytosis. The particles are enveloped in a plasma bilayer-derived membrane, which buds into the cell. This vesicle merges with a lysosome, which gets damaged in the process. They then release ATP into the cytoplasm, which acts as a damage signal, activating inflammation.

PM2.5 particles can also be taken up by phagocytosis to produce intracellular phagosomes. Pinocytosis and caveolin/clathrin-mediated endocytosis can also take them up. The resulting endosome fuses with lysosomes and mitochondria, causing damage. The heavy metals from PM2.5 particles released into the cell also contribute to damage.

Smaller particles with diameters less than 0.1 μm (100 nM), sometimes called **nanoscale particulate matter (NPM)**, offer large surface areas for protein adsorption. The adsorbed proteins form a "crown" called a protein **corona**. The corona is larger than the NPM. Proteins bound to the particles include hemoglobin, albumin, and fibrinogen. The corona also mediates cellular interactions and participates in the

mechanisms that lead to inflammation and cellular dysfunction. Because the extracellular matrix includes proteins such as collagen and fibrin, the interaction of PM2.5 with fibrin has been studied as a model for how particles might interact with cells. In particular, lung fibroblasts embedded in a 3D fibrin matrix (i.e., a 3D organotypic culture) were exposed to NPM particles with protein coronas, and the effects of these particles on cell proliferation, oxidative stress, and other parameters were monitored. Figure \(\PageIndex{21}\) below characterizes the interaction of the NPMs with the fibroblast in the 3D culture.

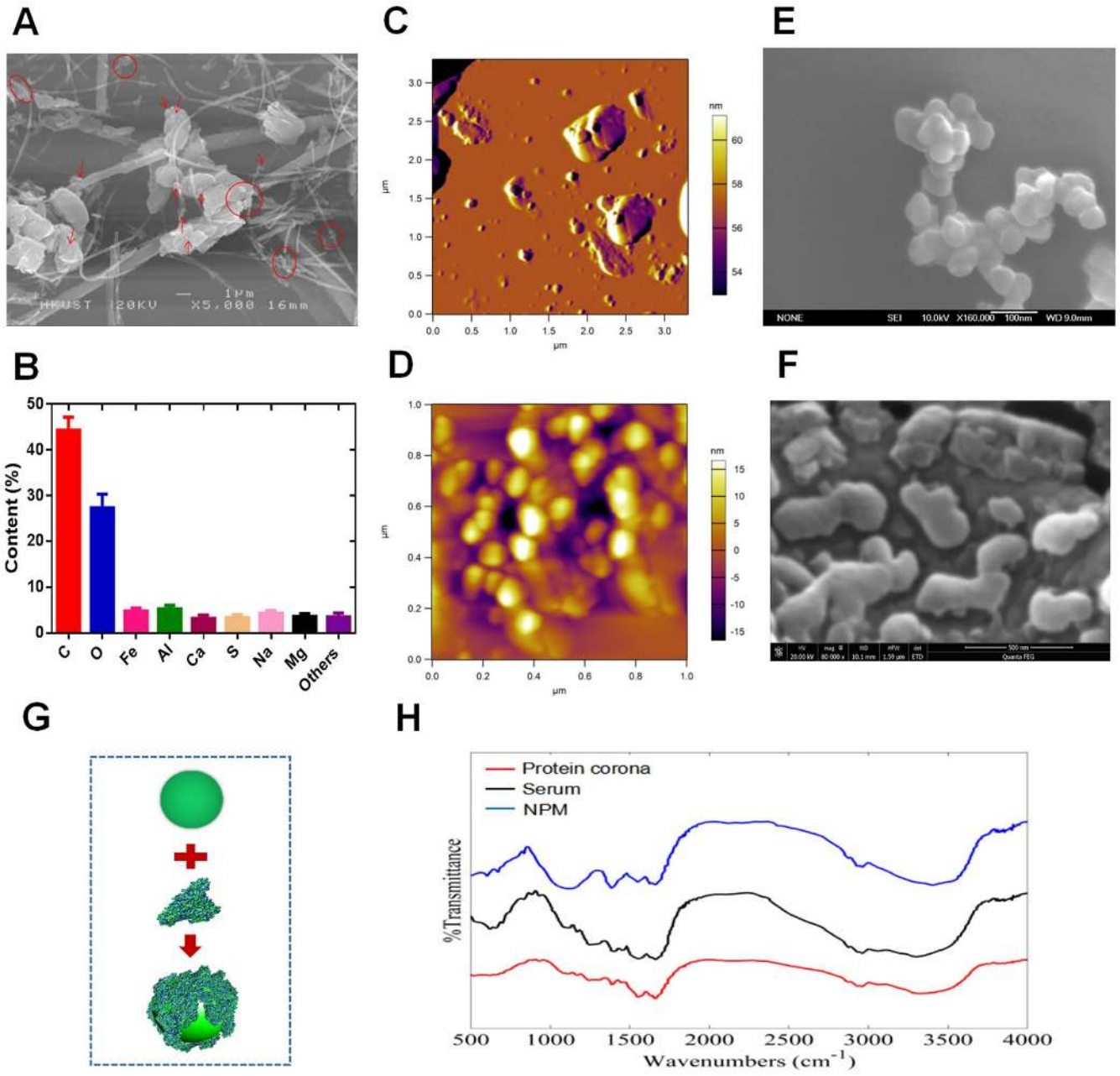


Figure **13.21**: Physicochemical characterization of airborne particulate matter. Li, Y., Wang, P., Hu, C. *et al.* Protein corona of airborne nanoscale PM2.5 induces aberrant proliferation of human lung fibroblasts based on a 3D organotypic culture. *Sci Rep* **8**, 1939 (2018). https://doi.org/10.1038/s41598-018-20445-7. Creative Commons Attribution 4.0 International License. http://creativecommons.org/licenses/by/4.0/.

Panel (**A**) shows SEM images of airborne PM2.5 (nanoscale PM2.5 is marked in red).

Panel (**B**) shows an EDX (Energy-dispersive X-ray spectroscopy) analysis of PM2.5.

Panel (**C**) shows an atomic force microscopy (AFM) image of nanoscale PM2.5 (NPM) from air pollutant samples (scale 3.5 μm).

Panel (**D**) AFM image of airborne NPM from air pollutant samples (scale 1 μm).

Panel (**E**) shows an SEM image of airborne NPM from air pollutant samples.

Panel (**F**) shows an SEM image of an NPM-protein corona.

Panel (**G**) shows a schematic diagram of the biological interaction between NPM and the protein.

Panel (**H**) shows an FTIR spectrum of NPM, serum, and NPM-protein corona.

The NPM-protein corona particle leads to the proliferation of 3D-cultured human lung fibroblast cells beyond stimulation with NPMs or serum alone. The bigger the size of the corona, the greater the proliferative effect. This is consistent with the extensive lung fibrosis observed after chronic exposure to PM2.5 particles. Reactive oxygen species also increased in the presence of NPM-corona particles. These data suggest that the NPM-protein corona is important in PM2.5-induced lung fibrosis and pulmonary disease.

NEURAL EFFECTS OF PMS

PM particles, particularly the ultrafine PM0.1 particles (UFP), can enter the brain and affect neural function. Exposure to PM2.5 over long periods is associated with an increased incidence of dementia and Alzheimer's Disease (AD). Four particular components of PMs (SO_4^{2-}, NH_4^+, black carbon, and organic matter) were most associated with a higher risk of dementia and AD. In the US, the first admission to a hospital for Parkinson's, Alzheimer's, and other dementias is "significantly" associated with the average annual mean PM2.5 exposure.

Even low levels of exposure pose risks. Transgenic mice expressing mutant forms of human presenilin 1, amyloid precursor protein, and tau were exposed to subchronic, "real-world" levels of PM2.5 via inhalation for 3 months. Neuronal loss was observed in the cortex, but no motor or cognitive impairment was noted. Increased levels of phosphorylated Tau and free radical formation, as evidenced by malondialdehyde (a marker of oxidative stress), were observed in the hippocampus and olfactory centers, consistent with inhalation of PM2.5 through the noise. No abnormal amyloid plaques were observed in this short exposure time.

PM-induced neuronal damage occurs through the generation of reactive oxygen species, increased inflammatory responses, and organelle damage (all of which are interrelated). Even in skin cells (keratinocytes), exposure to PM2.5 particles led to increased ROS and malondialdehyde levels, decreased superoxide dismutase levels, and increased DNA damage. Inflammatory Caspase levels also increased.

Cells have mechanisms to detect and eliminate aberrant species before they cause more severe biological effects. One process is **autophagy,** which degrades misfolded proteins and damaged organelles, both of which are important for normal neural function. Aberrant autophagy is a key player in the pathogenesis of dementia. A second pathway is **ferroptosis**, an apoptotic pathway that kills cells that have accumulated large amounts of iron ions, which are themselves free radicals. Through the Fenton reaction and other mechanisms, iron ions can generate damaging reactive oxygen species and oxidize lipids, proteins, and nucleic acids (see Chapter 12.3).

Several key proteins are involved in antioxidant defense and autophagy:

- NRF2 (Nuclear factor erythroid 2-related factor 2): This transcription factor binds to antioxidant response elements (ARE) in protective genes.
- Keap1 (Kelch-like ECH-associated protein 1): An adapter protein that targets NRF2 for ubiquitination and, as such, is a sensor for oxidative stress. Under those conditions, electrophilic metabolites post-translationally modify reactive Cys side chains, inactivating ubiquitin ligase activity. This increases NRF2 and subsequent transcription of antioxidant genes.
- SQSTM1 aka p62 (Sequestosome-1): This protein bridges autophagosomes and polyubiquitinated proteins (cargo for degradation).

Hence, under low oxidative stress, NRF2 is degraded by KEAP1, keeping its concentration low. If SQSTM1 (p62), increases, and reduced autophagy, p62 biding to the NRF2 sites on KEAP1, leading to the release of NRF2, its transfer to the nucleus, and activation of gene transcription of protective genes. These three proteins also protect cells from ferroptosis. In the long term, neural cell death occurs during dementia. Hence, apoptosis, necroptosis, and pyroptosis (from activation of the inflammatory response mediators caspase, Gasdermin, and key cytokines like IL-1β and IL-18) do "win out" to eventually kill cells.

Figure **13.22** below shows the domain structure of SQSTM1 (panel A) and the signaling process described above.

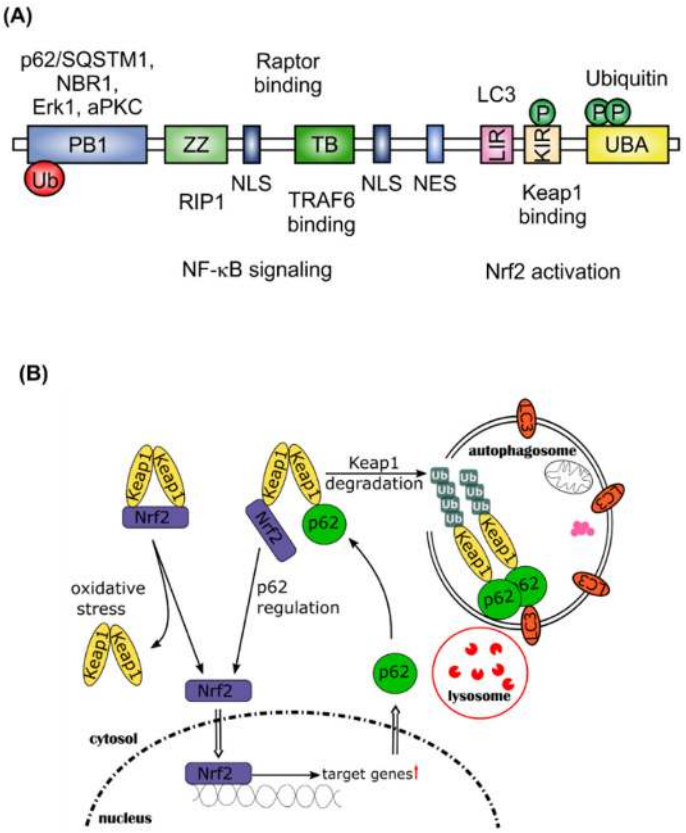


Figure **13.22**: Positive feedback-loop of Nrf2 activation by *p62/SQSTM1*. Vomund S, Schäfer A, Parnham MJ, Brüne B, von Knethen A. Nrf2, the Master Regulator of Anti-Oxidative Responses. Int J Mol Sci. 2017 Dec 20;18(12):2772. doi: 10.3390/ijms18122772. PMID: 29261130; PMCID: PMC5751370. Creative Commons Attribution (CC BY) license (http://creativecommons.org/licenses/by/4.0/).

Panel (**A**) shows the domain structure of p62/SQSTM1;

Panel (**B**) shows p62/SQSTM1 as an important protein in selective autophagy, as it binds to Keap1 and other long-lived proteins, forming polyubiquitinated protein aggregates. Furthermore, it binds to the autophagy marker LC3 within the autophagosome, thereby leading the aggregated proteins into the autophagosome. After fusion with a lysosome, proteins and organelles, such as mitochondria, are degraded within the autophagosome. By binding to Keap1, p62/SQSTM1 stabilizes Nrf2 and enhances its nuclear translocation, leading to the activation of Nrf2 target genes (↑ = upregulation of Nrf2 target genes). One of these genes is *p62/SQSTM1*

PM2.5 particles interfere with the protective autophagy and ferroptosis pathways, leading to increased NRF2 activity and the expression of antioxidant genes. These processes are beneficial for ridding cells of aberrant particles and killing damaged cells in normal conditions, but not when neuronal cells are exposed to PM2.5 particles.

Lysosomal membrane permeabilization (LMP), as well as mitochondrial and ER damage, may be a likely mechanism for initiating ultimate neuronal death on long-term exposure to PM2.5 particles. PM2.5 particles inhibit lysosomal activity and increase permeability, releasing degradative enzymes into the cytoplasm. Ultimately, increased or decreased Nrf2 activation leads to disease states.

PMS AND CANCER

Long-term exposure can also cause lung cancer. This is associated with the conversion of lung cells from normal epithelial to mesenchymal cells (the EMT transition). Phenotypically, mesenchymal cells can migrate, invade other tissues, and cause enhanced extracellular matrix production, all hallmarks of tumor cells. This EMT transition is associated with significant changes in cell signaling and transcription factor production. These changes are documented in Figure **13.23** below and its caption.

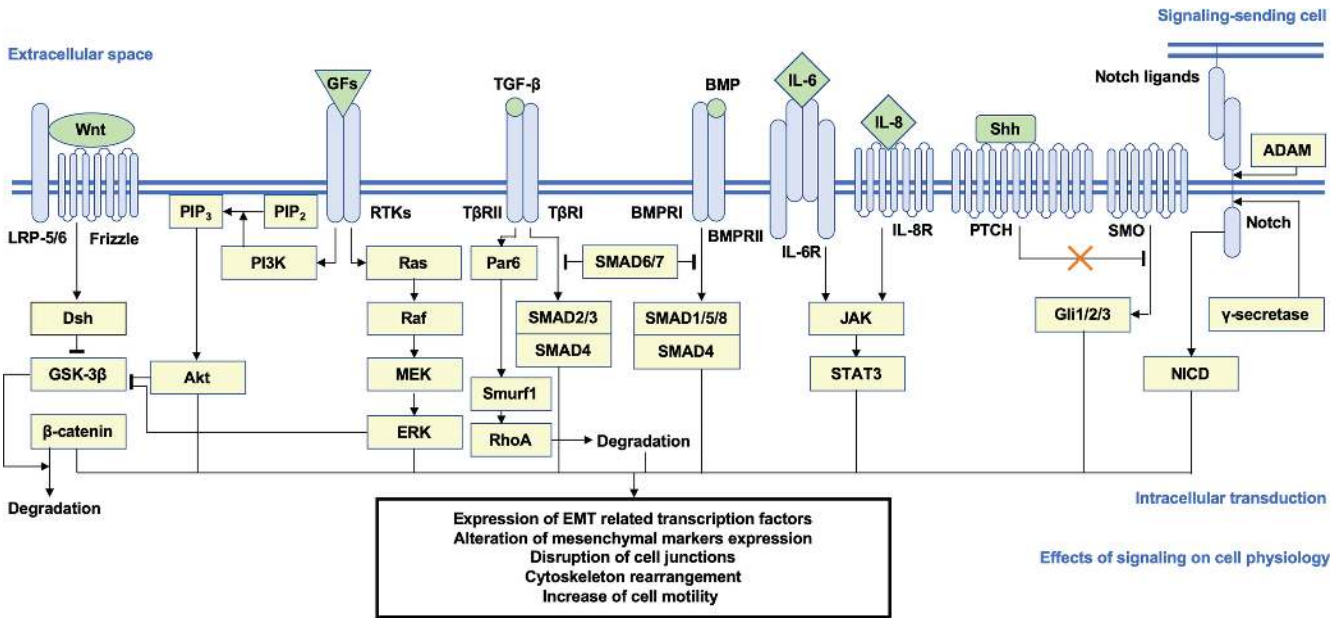


Figure **13.23**: Brief schema of the putative signaling transduction mechanisms underlying EMT. Xu et al., **Front. Physiol., 29 November 2019. Sec. Renal Physiology and Pathophysiology.** Volume 10 - 2019 | https://doi.org/10.3389/fphys.2019.01404. **Creative Commons Attribution License (CC BY)**

Activation of the Wnt/β-catenin, PI3K/Akt, Ras/ERK, TGF-β/SMAD2/3, BMP/SMAD1/5/8, JAK/STAT3, Shh, and Notch pathways is highly correlated with EMT. After ligand-receptor binding, intracellular secondary messengers are activated and initiate downstream transduction, which generally induces the nuclear translocation of signaling-specific TFs and the transcriptional regulation of EMT-related genes, such as CDH1 and CDH2, EMT TFs, and mesenchymal markers, accompanied by a series of alterations in cellular physiological or pathological activities (e.g., dysjunction of adherin junctions, cytoskeleton remodeling, and increase of cellular motility). Arrows represent the molecular interactions in which downstream messengers are activated; T-shaped arrows represent inhibitive molecular interactions. EMT, epithelial-mesenchymal transition; PI3K, phosphoinositide 3-kinase; ERK, extracellular signal-regulated protein kinase; TGF-β, transforming growth factor β; JAK, Janus kinase; Shh, sonic hedgehog; TFs, transcription factors.

PM2.5 particles, their deleterious contents (heavy metal ions, PAHs, etc.), and the ROS generated are associated with the changes seen in the EMT transition. These include activation of transforming growth factor β (TGF-β)/SMADs, NF-κB, growth factor (GF)/extracellular signal-regulated protein kinase (ERK), GF/phosphatidylinositol 3-kinase (PI3K)/Akt, wingless/integrated (Wnt)/β-catenin, Notch, Hedgehog, high mobility group box B1 (HMGB1)-receptor for advanced glycation end-products (RAGE), and aryl hydrocarbon receptor (AHR) signaling cascades, and to cytoskeleton rearrangement.

SUMMARY

(Summary written by Claude, Anthropic)

This chapter examines how climate change and fossil fuel combustion damage human health at the molecular level, organized around the One Health framework — the recognition that human, animal, plant, and environmental health are inseparably linked. Two major topics are covered: heat-related illness and particulate matter (PM) pollution.

Heat-Related Illness and Kidney Disease. Heat waves are increasing in frequency, duration, and severity globally. Major events — the 2003 European heat wave (70,000 deaths), the 2010 Russian heat wave (55,000 deaths), and the 2022 European heat wave (60,000 deaths) — establish extreme heat as a leading cause of climate-attributable mortality, with a clear linear relationship between rising summer mean temperatures and heat-related deaths. The elderly and women are disproportionately affected. Physiologically, heat imposes cardiovascular strain through sustained heart rate elevation; under humid conditions this develops at temperatures as low as 34°C. US National Climate Assessment projections show a dramatic increase in days above 100°F between 1.5°C and 2°C of warming — a threshold the world crossed in 2024 — with the difference between these two warming scenarios being especially stark.

Cumulative occupational heat exposure also causes CKDu (chronic kidney disease of uncertain etiology), first identified as Mesoamerican nephropathy in Central American sugarcane workers and subsequently recognized in Sri Lanka, India, and now among agricultural workers in Florida and California. CKDu presents with elevated serum creatinine, renal inflammation, and fibrosis in the absence of traditional risk

factors (diabetes, hypertension, glomerular disease), correlates strongly with regional heat exposure, and carries high mortality rates — ten times higher than in the US in El Salvador.

Biochemical Mechanisms of Heat Stroke. Heat stroke kills cells primarily through **necroptosis** rather than classical apoptosis. The central pathway runs through **RIPK3**, which first autophosphorylates (at pT224 and pS227) and then phosphorylates **MLKL**; phosphorylated MLKL undergoes a conformational change, oligomerizes, traffics to the plasma membrane, and causes membrane permeabilization, calcium influx, and cell lysis. Negative regulatory phosphorylation of RIPK3 at pS164 and pT165 diverts signaling toward apoptosis. Multiple activated RIPK3 molecules assemble via their RHIM domains into amyloid-like **necrosome** complexes that amplify MLKL phosphorylation. E3 ligases PELI1 and TRIM21 regulate pathway thresholds.

Under heat stress, **ZBP1** (Z-DNA Binding Protein 1) is upregulated by the heat shock transcription factor HSF1 and activates RIPK3 through its **RHIM domain** — not its Zα nucleic acid-binding domain. This is mechanistically distinct from viral Z-RNA sensing: mutations in ZBP1's RHIM domain prevent heat-stroke pathology, while Zα domain mutations do not. ZBP1 aggregates through its RHIM domains under heat stress, driving RIPK3 activation in the absence of any pathogen. Mouse knockouts of ZBP1, RIPK3, or MLKL dramatically reduce heat-stroke clotting, inflammation, organ injury, and death. The chapter also introduces **pyroptosis** (gasdermin cleavage by caspases produces membrane pores releasing IL-1β and IL-18) and **PANoptosis** (a convergent death program integrating necroptosis, apoptosis, and pyroptosis via ZBP1 and the NLRP3 inflammasome) as additional heat injury mechanisms.

Beyond acute cell death, heat stroke induces lasting **epigenetic changes**: a single episode alters DNA methylation patterns in bone marrow monocytes, causing immunosuppression and reduced heat shock responses that persist for 30+ days and are inherited by daughter cells. This provides a molecular basis for the clinically observed reduced heat tolerance in individuals with prior heat illness.

PM2.5: Sources, Composition, and Health Effects. PM2.5 particles (≤2.5 μm diameter) from fossil fuel combustion carry a complex toxic cargo: black carbon, polycyclic aromatic hydrocarbons, transition metals (Mn, Pb, Zn, Fe, Cr, As), sulfate, nitrate, ammonium, and VOCs. Secondary atmospheric reactions among these pollutants generate additional hazards — tropospheric ozone from NOx/hydrocarbon reactions, and secondary organic aerosols from terpene (α-pinene, limonene) photochemical oxidation. The Great London Fog of 1952 — which killed ~12,000 people in two weeks from highly acidic sulfate aerosols formed by SO_2 oxidation in aqueous droplets catalyzed by NO_2 — established the lethal potential of PM pollution and directly prompted the UK Clean Air Act. Today, wildfire smoke (worsened by climate change) creates acute PM2.5 spikes of global reach, with Canadian fires driving AQI readings over 800 in New York City in 2023 and the 2025 Los Angeles fires producing a 46% spike in cardiac emergency visits.

PM2.5 particles enter cells via phagocytosis, pinocytosis, and clathrin/caveolin-mediated endocytosis. Nanoscale PM0.1 particles acquire a **protein corona** — adsorbing hemoglobin, albumin, and fibrinogen — that amplifies inflammatory signaling and drives lung fibroblast proliferation in 3D culture models, consistent with the extensive pulmonary fibrosis seen in chronic PM2.5 exposure. The primary toxicity mechanisms are **oxidative stress** and **inflammation**. The transcription factor **NRF2**, normally targeted for ubiquitination by Keap1, is released when electrophilic PM2.5 metabolites modify Keap1 cysteine residues, upregulating antioxidant genes. The scaffold protein **p62/SQSTM1** bridges autophagosomes to polyubiquitinated cargo and creates a positive feedback loop by displacing NRF2 from Keap1 when autophagy is overwhelmed. When these defenses fail, lysosomal membrane permeabilization releases digestive enzymes into the cytoplasm, and mitochondrial and ER damage trigger apoptosis, necroptosis, and pyroptosis.

In the **nervous system**, PM0.1 ultrafine particles cross the blood-brain barrier and accumulate in neural tissue. Long-term PM2.5 exposure is significantly associated with Alzheimer's disease, Parkinson's disease, and other dementias. In transgenic mouse models, subchronic real-world PM2.5 exposure increases phosphorylated tau and hippocampal oxidative stress (measured as malondialdehyde) and causes cortical neuronal loss — even without frank cognitive impairment in the short term. Ferroptosis — iron-driven, ROS-mediated cell death dependent on the NRF2/Keap1/p62 axis — is an additional PM-relevant death mechanism in neurons.

In the **lung**, chronic PM2.5 exposure drives **epithelial-mesenchymal transition (EMT)** — converting epithelial cells into migratory, invasive, matrix-producing mesenchymal cells through coordinated activation of TGF-β/SMAD, PI3K/Akt, Wnt/β-catenin, NF-κB, ERK, JAK/STAT3, Notch, Hedgehog, HMGB1/RAGE, and aryl hydrocarbon receptor signaling — with PM2.5 components (heavy metal ions, PAHs, ROS) driving each of these oncogenic cascades and the cytoskeletal rearrangements that define malignant transformation. PM2.5 is thus both a promoter of pulmonary fibrosis and a lung carcinogen, acting through convergent molecular mechanisms that connect oxidative stress, inflammation, and epigenetic reprogramming to the hallmarks of cancer.

13: Biochemistry, Climate Change and Human Health is shared under a CC BY-NC-SA 4.0 license and was authored, remixed, and/or curated by LibreTexts.

14: Pandemic Diseases and Drug Discovery - Under Construction

How can I use this chapter?

Many might think that biochemistry and climate change are unrelated. They are with respect to causation. However, the effects of climate change on the biosphere need to be understood for many reasons. Knowing these effects might convince people to support actions to mitigate the worst effects of climate change. Understanding biochemical responses to climate change gives us an opportunity to make the biosphere more resilient to increased temperatures and conditions such as drought and floods. We could develop strategies to reduce the potential for future pandemics, which are likely with a changing climate.

The primary cause of current climate change is the burning of fossil fuels and the release of CO_2 into the atmosphere, which warms the planet and causes collateral climate effects. Other causes include CO_2 released from cement production and methane, another greenhouse gas, released from fossil fuel production. Burning fossil fuels also causes pollution, which sickens and kills millions each year. Other human activities, such as corporate farming, deforestation, habitat changes, production of plastics, and widespread use of herbicides and pesticides, all synergize to have negative effects on what is now called "One Health", the collective health of humans, animals, and the biosphere. We know and need to act on the fact that harm to any part of the biosphere affects us all.

This chapter is divided into four main parts.

- Part 1 (Sections 01A, 01B, 2, and 3) offers a deep dive into the causes of climate change and how we construct past and predict future CO_2 and temperature values. These sections contain little biochemistry per se. They are presented so students can understand how we know the relationships between climate, CO_2, and temperature. A second goal is to allow students to rebut common misconceptions and disinformation that minimize the causes and extent of climate change. In reality, people are not moved by mere data and information, so Part 1 can be presented just as background for interested readers. The rest of the sections focus on using biochemistry to understand the biological effects of climate change on organisms and ways to mitigate its worst effects.
- Part 2 (Sections 4-10) focuses on the production and use of biofuels to decrease our reliance on fossil fuels. The basic hope for many forms of biofuel is that CO_2 can be removed from the atmosphere (by organisms or chemical means) as a feedstock for biofuels and then converted to fuels (like ethanol), which, on burning, return an equivalent amount of CO_2 to the atmosphere. 1 CO_2 is removed, and 1 CO_2 is returned to the atmosphere with net zero emission! Unfortunately, this accounting is inadequate, as the net CO_2 emissions over the whole life-cycle of biofuel production and combustion must be considered, and when that happens, it may be that corn bioethanol (for example) is not much better, and possibly even worse, than burning fossil fuels. Of course, it would cause zero net emissions if the CO_2 emitted from burning is captured, but this would apply to fossil fuels as well. In addition, opportunity costs, such as the loss of potential cropland to feed people, are often not considered. These "applied" sections have a great deal of biochemistry as well as some organic chemistry that students have previously encountered.
- Part 3 (Sections 11-14) focuses more on the biological effects of higher temperatures, pollution from fossil fuel use, and other climate effects on biomolecules, organisms, and, ultimately, human health.
- Part 4 (Sections 16-18) explains how we can use biochemistry, molecular biology, genetic engineering, and synthetic biology to capture more carbon, use less fertilizer, make plants more resilient to climate change, and make manufacturing greener.

This text complements the material presented in Chapter 32: Biochemistry and Climate Change, which illustrates the need for interdisciplinary solutions.



To facilitate access for both instructors and students to climate change-relevant examples in Chapter 32, this clickable Climate Change and Biochemistry icon will be placed throughout Fundamentals of Biochemistry by climate change-relevant topics.

Other important climate change books

Bending the Curve: Climate Change Solutions by et al. Ramanathan, Veerabhadran et al. is a text that presents 10 climate change mitigation strategies using science, societal transformation, governance, economics, technology, and ecosystem management. "Bending the curve" was first used during the early years of the COVID pandemic. In climate change, it means bending the CO2 atmospheric curve and the resulting global temperature curve after a peak value is reached to reach values less detrimental to human and biosphere life. Key themes emerge from the book:

- *"There is still time to bend the curve.*
- *Bending the curve will require interdisciplinary solutions.*
- *Bending the curve requires a radical shift in attitude.*
- *Technology, market mechanisms, and policy need to be a part of the solution"*

Books by Hannah Ritchie from Our World in Data:

- Clearing the Air: A Hopeful Guide to Solving Climate Change in 50 Questions and Answers: Clear, simple answers to the most common and vexing questions about climate change that we can take action on right now.
- Not the End of the World: How We Can Be the First Generation to Build a Sustainable Planet: A pragmatic guide on focusing action, such as transitioning energy and reducing food waste, to build a livable future for all.

Key Climate Change Graphs from Chapter 32

(Last update: 2/22/26)

1. Science of Climate Change

- CO_2 in the atmosphere: 800,000 BCE to Now - Interactive graph from Our World in Data
- Methane (CH_4) concentration in the atmosphere: 800,000 BCE to Now - Interactive graph from Our World in Data
- CO_2 and Temperature over the last 800,000 Years - LibreText. Data from Antarctic Ice Cores Revised 800K YrCO2 Data. Bereiter, B. et al, J. http://ncdc.noaa.gov/paleo/study/17975
- Combo CO_2 and Temperature - 1000 to present (Data and data sources from the 2 Degrees Institute)
- Temperature of the planet over the last 500 million years - Wikimedia
- Simulated northern hemisphere temperature changes, smoothed with an 11-year running mean, relative to AD 950–1250 - J. Space Weather Space Climate, 7, 2017
- Total GHG emissions from fuel combustion by product, World: IEA
- Greenhouse gases by economic sector in the US - Pie Chart: EPA
- Greenhouse gas emissions by sector, World, 2023: Our World in Data
- ExxonMobil's Global Warming Projection Hidden from the World: Science Magazine
- CO_2 concentration (black circles) and the $\delta^{13}C$ (brown circles) from 1000 to 2010 - Proof that post-industrial rise in CO_2 from burning fossil fuels: Rubino et al., JGR: Atmospheres, 2013.
- Climate Shift For Today - Land: Probabilities that anomalies in land temperature can be attributed to climate change. Climate Central (Attribution Science
- Mapped: How climate change affects extreme weather around the world. (Attribution Science). CarbonBrief
- Maps and Data: NOAA

2. Future Projections for Earth's Climate: What a difference a degree makes!

- Climate Interactive Lab Interactive Map - See worldwide temperature and precipitation projections for different levels of temperature increase. IPCC Working Group I (WGI): Sixth Assessment Report
- University of Chicago Climate Impact Map for future warming. Temperature increases with different emissions scenarios
- University of Chicago Climate Impact Map - Future Deaths with increasing temperature

- CalAdapt Climate Tools: projections for two possible climate futures for California, one in which emissions peak around 2040 and then decline (RCP 4.5) and another in which emissions continue to rise throughout the 21st century (RCP 8.50
- CalAdapt - Extreme Precipitation Events - Specific for California
- Climate Map for Probable Futures: non-profit climate literacy initiative - effects of heat, cold, humidity, precipitation, dryness
- Tipping Points: Carbon Brief
- Earth System Tipping Points: Global Tipping Points
- Positive Tipping Points: Global Tipping Points
- How long would it take for the Earth to cool if we stopped emitting CO_2 now: IPCC 6th Assessment Report. CO_2 would fall from the present value of around 430 ppm to 330 ppm, a value last seen around 1900, yet the temperature change (since the Industrial Revolution) drops from the present increase of about 1.5 ^{0}C (2.7 ^{0}F) to a value of about 1.3 ^{0}C (2.34 ^{0}F) above the preindustrial level. Hence elevated temperatures are "baked" into the system for at least 100 years even if we stop emitting now!
- Copernicus Climate Data with Projections with rotating globe
  - Climate Pulse: Present, Monthly and Yearly Data
  - Copernicus Interactive Climate Atlas: Climate Data from 1850 to now and projections for future changes by ^{0}C, and by climate model
  - ERA Explorer: access to over 85 years of global climate data

3. Climate Change and the Oceans

- Climate Shift For Today - Oceans: Probabilities that anomalies in ocean temperature can be attributed to climate change. Climate Central
- Heat Content in the top 700 meters of the ocean - Our World in Data
- Global sea level rise from 1900 to now -
- Ocean acidification: mean seawater pH, Hawaii - Our World in Data
- Arctic Yearly Mean Sea Ice Extent (million km²) - Copernicus Marine Service
- Antarctic Yearly Mean Sea Ice Extent (million km²) - Copernicus Marine Service
- Global Yearly Ocean CO2 Uptake (PgC) - Copernicus Marine Service
- Climate impacts of a collapsed Atlantic Meridional Overturning Circulation (AMOC) under different global warming scenarios (link not working 2/25/26)
- Land below 3 feet of water: Climate Central

4. CO_2 Emissions - US vs China

- Annual CO_2 emissions from fossil fuels and industry: US, China, et al. - Our World in Data
- CO_2 emissions per capita: US, China, et al. - Our World in Data
- Cumulative CO_2 emissions since the Industrial Revolution: US, China, et al. - Our World in Data

5. Agricultural Effects

- Food: greenhouse gas emissions across the supply chain: Our World in Data
- Greenhouse Gases per 100 grams of protein: Our World in Data

6. Biofuels

- Bioenergy Fuel Production - World: Our World in Data
- Biofuels vs Solar Panels: Our World in Data
- Shares of cereals aliquoted for food, animal feed, or fuel: Our World in Data
- GHG emission intensities for corn ethanol compared to before the RFS. PNAS
- Changes in corn agriculture and pollution after the adoption of the Renewable Fuel Standards in the US. PNAS

7. Climate Change, Fossil Fuels, and Biosphere/Human Health

- Loss of 3 billion or 29% birds in North America since 1970: Science. https://www.science.org/doi/10.1126/science.aaw1313

- Living Planet Index, World
- What are the safest and cleanest forms of energy? Our World in Data
- Death Rate Per Unit of Electricity Production. Our World in Data
- Death rate from particulate matter air pollution vs. PM2.5 concentration: Our World in Data
- Air pollution deaths from fossil fuels: Our World in Data
- Sources of air pollutants: Our World in Data. Scroll to see pollutant sources

8. Power from Electricity vs Fossil Fuels: The Energy Transition

- Electricity Generated from Different Power Supply: Total and Capacity from Claude. (Download and open file)
- Total electricity generated in each country or region, measured in terawatt-hours: Our World in Data
- Electricity production by source (terawatt-hours): US, China, India, EU
- Share of electricity production by source: US | China | India | Europe
- Share of electricity from low-carbon sources - US, China, India, EU
- Share of electricity from coal: Our World in data
- The Energy Transition in 5 Charts: RMI

9. Internal Combustion Engines vs Battery Electric Vehicles

- Efficiency Internal Combustion Engine (ICE) vs Battery Electric Vehicles (BEV) - IEA
- Comparative life-cycle greenhouse gas emissions of a mid-size BEV and ICE vehicle
- Efficiency of ICE vs BEV - Graphic from Yale Climate Communication
- Global electric car stock, 2013-2023: IEA 2024
- Electric car registrations and sales share in China, United States and Europe, 2018-2023. IEA

10. Economics

- Explicit Fossil Fuel Subsidies for World, 2010-2023: Our World in Data
- Worldwide subsidies in US $billion and in % global GDP. The bar graphs are for US $biillons, and the circles and triangles are for % global GDP. IMF.
- 7 trillion fossil fuel subsidies total 2022: Our World in Data
- Energy Subsidies and Climate Change: En-Roads
- U.S. Billion-Dollar Weather and Climate Disasters
- Crude Oil Prices (1946-2026) | Crude Oil Prices (annotated) 1968-2022
- Solar Photovoltaics Prices US 1975-2024: Our World in Data
- Levelised Cost of Solar, World: Our World in Data
- Price of lithium-ion battery cells, 1991 to 2024: Our World in Data
- Combined learning curves for electric motors, computing all needed for transitions to a country driven by electricity and not fossil fuels
- Recycling as mining: Recycling Batteries as a source of critical minerals | Cyclic Materials
- Recycling Solar panels as a source of materials
- Solar cells photovoltaics panels: Background, Manufacture - IEA

11. Climate Solutions

- En-Roads: Climate Solutions Simulator
- Energy Policy Simulator

12. Solar Energy - Rooftop

- Australia leads the way
- Simplify Solar from Third Act: Bring the solar revolution home, with smarter local rules to make rooftop & plug-in power easy, fast, and affordable
- SolarApp+: Developed in collaboration with local governments and the solar industry to advance clean energy technologies to speeds solar permitting

13. Plugin (balcony) Solar

- SB-868 Electricity: portable solar generation devices (aka Plug and Play Solar Act) for California
- Bright Saver - Mission is to build a movement where plug-in solar is affordable and accessible to all
- Solar Rights Alliance - Informs about threats or opportunities to solar investment, and provides people with simple ways you can make their voice heard
- Solar United Neighbors - a national organization dedicated to representing the needs and interests of solar owners and clean energy supporters
- California Solar and Storage Association - works to put in place and defend solar and storage policies and programs that have made California one of the biggest and most successful solar markets in the world.
- Examples: Utah Clean Energy | Utah H.B. 340 Solar Power Amendments | Germany's balcony (plugin) solar boom | Plug-In Solar Info

14. Additional National and California Legislative Climate and Clean Energy Initiatives

- SB-222 Residential heat pump systems: water heaters and HVAC: installations (CA)

15. Citizens' Climate Lobby

- Monterey Chapter
- Clean Energy Permitting Reform

Return to

- Chapter 32: Biochemistry and Climate Change - Table of Contents
- Fundamentals of Biochemistry - Main Page

14: Pandemic Diseases and Drug Discovery - Under Construction is shared under a CC BY-NC-SA 4.0 license and was authored, remixed, and/or curated by LibreTexts.

15: FIXING CARBON FIXATION

Search Fundamentals of Biochemistry

LEARNING GOALS

(Learning goals written by Claude, Anthropic)

By the end of this chapter, students should be able to:

RuBisCO Limitations and Natural Carbon Fixation Pathways

- Explain why RuBisCO is both essential and problematic — describing its slow kcat (2–10 CO_2/sec), large hetero-16-mer structure requiring chaperonin folding, competing oxygenase activity driving photorespiration, and why planting trees cannot solve near-term atmospheric CO_2 problems.
- Compare the six naturally occurring carbon fixation pathways (CBB, reverse TCA, Wood–Ljungdahl, 3-HP, HP/HB, DC/HB) using the summary table, identifying the organisms, energy sources, key enzymes, and products of each, and distinguish photoautotrophic, chemolithoautotrophic, and chemoorganotrophic modes.

Engineered Carbon Fixation: CETCH, rGPS–MCG, and Autotrophic *E. coli*

- Describe how carbonic anhydrase (kcat/KM up to 8×10^7 $M^{-1}s^{-1}$) could be engineered for CO_2 capture by addressing reversibility, HCO_3^- product inhibition, and thermal instability, and explain how CO_2 mineralization as carbonate precipitate with divalent cations achieves carbon sequestration.
- Describe the CETCH pathway's overall reaction ($2CO_2$ + 3NAD(P)H + 2ATP + FAD → glycolate + cofactors), explain how it was computationally designed from known CoA-dependent carboxylases, and compare its in vitro CO_2 fixation rate to the Calvin cycle.
- Explain how Gleizer et al. converted *E. coli* from a heterotroph to a complete autotroph — identifying the genes knocked out (phosphofructokinase, glucose-6-phosphate dehydrogenase), the enzymes added (RuBisCO, phosphoribulokinase, carbonic anhydrase, formate dehydrogenase), the role of formate as an electron donor, and how $^{13}CO_2$ isotopic labeling confirmed that all biomass carbon derived from CO_2.
- Describe the rGPS–MCG cell-free pathway, explain why a cell-free system offers advantages over living cells (oxygen insensitivity, freedom from growth regulation, continuous operation), and identify its primary products (acetyl-CoA, pyruvate, malate).

Microbial Electrosynthesis and Marine Geoengineering

- Explain microbial electrosynthesis (MES) — how electrons from water oxidation at an anode reduce CO_2 at a biocathode biofilm — identify the oxidation state change required to convert CO_2 to formate (2 electrons), and explain what would make pathways like CETCH truly carbon-neutral.
- Describe the ocean alkalinity enhancement approach (adding crushed limestone to rivers → HCO_3^- → marine shell formation → $CaCO_3$ sinking) and ocean iron fertilization (OIF) (adding $FeSO_4$ to stimulate phytoplankton CO_2 uptake), and identify the key practical and ecological challenges that make both approaches controversial.

BIOLOGICAL CARBON FIXATION

Nature has produced many enzymes that can fix atmospheric CO_2, and, of course, everyone knows that photosynthesis is the source of most fixed CO_2 in the biosphere. Plankton, cyanobacteria, algae, and plants are key in removing atmospheric CO_2 through photosynthesis. Yet, we can't plant enough trees to reduce CO_2 in the atmosphere in the next decade to avoid some of the worst consequences of anthropogenic climate change. Old-growth trees (mostly gone or under significant stress) are best at removing CO_2. New trees would take decades of growth before their effect on carbon drawdown would be consequential. We must also fix carbon dioxide to decrease atmospheric CO_2 and make more food!

Carbon (about 100 petagrams) is sequestered yearly in net primary production (carbon fixation into biomolecules). This is split almost equally between land and ocean organisms. The key enzyme in this process is Rubisco in the C3 (Chapter 20.4) and C4/CAM (Chapter 20.5) pathways. The enzyme is large, containing many large subunits and an equivalent number of small ones. A chaperonin is required for folding. It is also a very slow enzyme with a k_{cat} of around 2-10 CO_2/sec. In addition, it can bind another substrate, O_2, and engage in a competing reaction, photorespiration, as described in Chapter 20.4.

Figure 15.1 shows an interactive iCn3D model of ribulose 1,5-bisphosphate carboxylase/oxygenase from Synechococcus PCC6301 (1RBL)

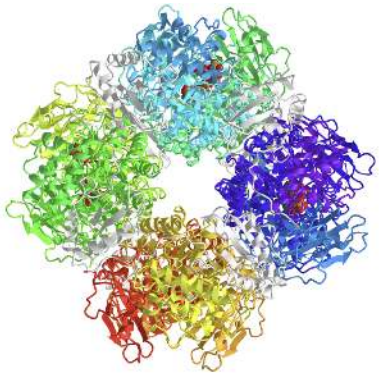


Figure **15.1**: Ribulose 1,5-bisphosphate carboxylase/oxygenase from Synechococcus PCC6301 (1RBL) (Copyright; author via source). Click the image for a popup or use this external link (long load time): https://structure.ncbi.nlm.nih.gov/i...pxLGgEKR5gCYK8

This structure is a hetero 16-mer consisting of 8 small and 8 large chains. The small chains are gray, and the large ones are different colors. Each large subunit contains a bound reaction intermediate analog, 2-carboxyarabinitol 1,5-bisphosphate.

This chapter will focus on improving and designing new ways to capture carbon dioxide and reduce its atmospheric concentration. Remember that the best way to address anthropogenic climate change is to drastically reduce the burning of fossil fuels.

NATURALLY OCCURRING PATHWAYS TO FIX CARBON

(Much of this immediate section derives from the following reference: Natural carbon fixation. Sulamita Santos et al., Natural carbon fixation and advances in synthetic engineering for redesigning and creating new fixation pathways, Journal of Advanced Research, Volume 47, 2023, Pages 75-92, ISSN 2090-1232, https://doi.org/10.1016/j.jare. Creative Commons license

Six naturally occurring pathways fix carbon. These are illustrated in Figure **15.2** below.

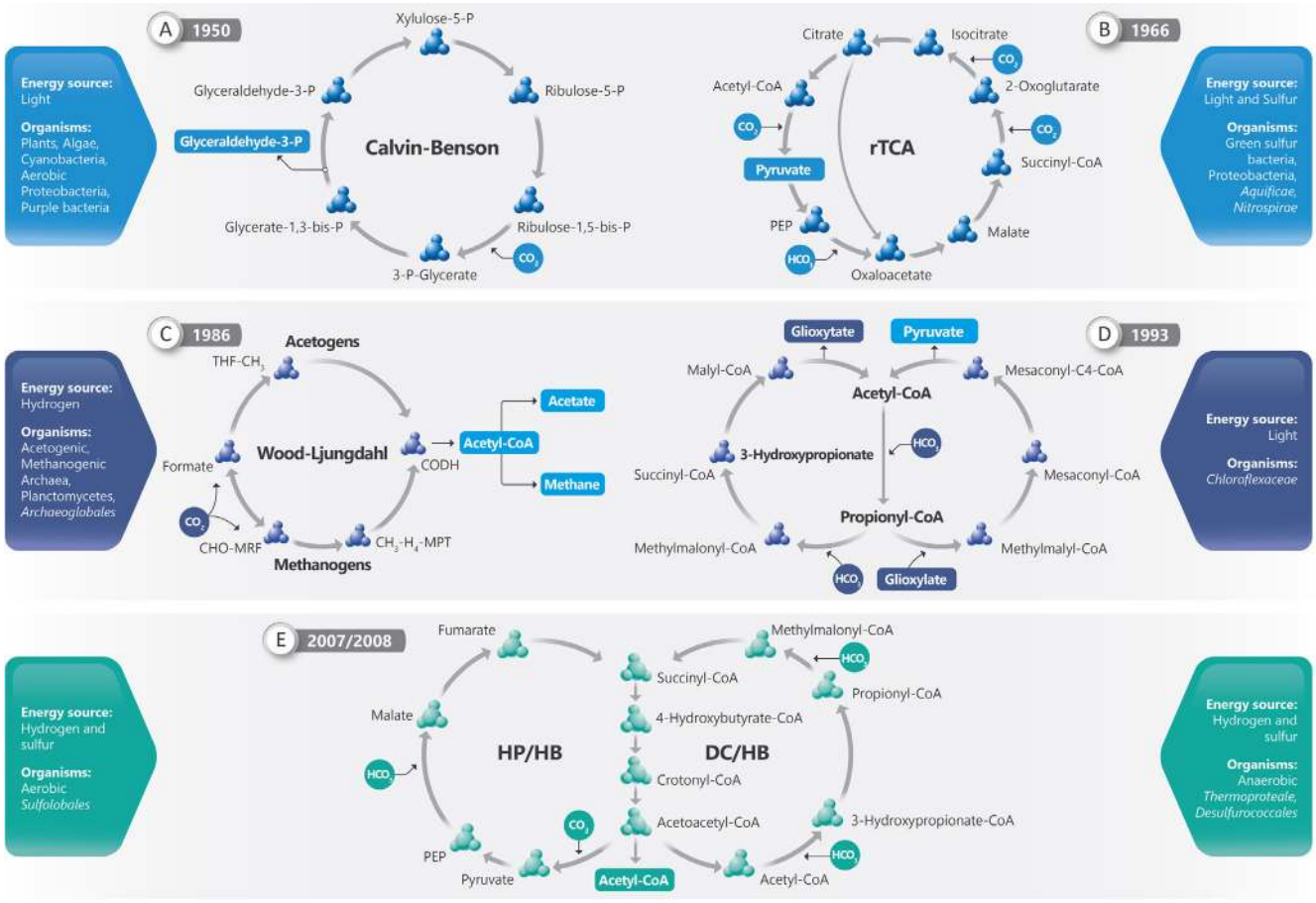


Figure **15.2**: Natural carbon fixation. Sulamita Santos et al.,ibid.

Panel (A) shows the CBB cycle, which we discussed in great detail in Chapter 20.4. The enzymes involved are ribulose-1,5-bisphosphate carboxylase/oxygenase, 3-phosphoglycerate kinase, glyceraldehyde-3-phosphate dehydrogenase, and ribulose-phosphate epimerase.

Panel (B) shows the reverse (reductive) TCA cycle, which we discussed in Chapter 16.4 in the section on the α-ketoacid pathway—a primordial, prebiotic anabolic "TCA-like" pathway. The enzymes include ATP-citrate lyase, malate dehydrogenase, succinyl-CoA synthetase, ferredoxin (Fd)- dependent 2-oxoglutarate synthase, isocitrate dehydrogenase, and PEP carboxylase.

Panel (C) shows the Wood–Ljungdahl (or reductive Acetyl-CoA) cycle, which we discussed in Chapter 30.1. At the top of the pathway are the acetogens Archaea, and at the bottom are the methanogens Archaea. The enzymes include MPT-methylene tetrahydromethopterin, MFR-methanofuran, THF, tetrahydrofolate.

Panel (D) shows the 3-hydroxypropionate (3HP) cycle. The enzymes include acetyl-CoA carboxylase, propionyl-CoA carboxylase, methylmalonyl-CoA epimerase, succinyl-CoA:(*S*)-malate-CoA transferase, trifunctional (*S*)-malyl-CoA, -methylmalyl-CoA, mesaconyl-CoA transferase, mesaconyl-C4-CoA hydratase.

Panel (E) shows the hydroxypropionate/4-hydroxybutyrate (HP/HB) and the dicarboxylate/4-hydroxybutyrate (DC/HB) cycles. The enzymes include pyruvate synthase, PEP-carboxylase, malate dehydrogenase, fumarate hydratase/reductase, acetyl-CoA/propionyl-CoA carboxylase, 3-hydroxypropionate-CoA ligase/dehydratase, methylmalonyl-CoA mutase, succinyl-CoA reductase, 4-hydroxybutyrate-CoA ligase, crotonyl-CoA hydratase, and acetoacetyl-CoA-ketothiolase.

Table **15.1** below shows a comparative description of the natural and synthetic carbon fixation pathways.

Pathway	Organisms	Energy Source	Input	Output	Reductants	Key Enzyme
Calvin-Benson (N)	Plants, Algae, Cyanobacteria, Aerobic Proteobacteria, Purple bacteria	Light	3 CO_2, 9 ATP,6 NAD(P)H	Glyceraldehyde-3-phosphate	NAD(P)H	RuBisCO
rTCA (N) *	Green sulfur bacteria, Proteobacteria, Aquificae, Nitrospirae	Light and Sulfur	2 CO_2, 2 ATP,4 NAD(P)H	Pyruvate	NAD(P)H & ferredoxin	2-Oxoglutarate synthase, Isocitrate dehydrogenase
Wood–Ljungdahl (N) *	Acetogenic, Methanogenic Archaea, Planctomycetes, Sulfate. Archaeoglobales,	Hydrogen	2 CO_2, 1 ATP, 4 NAD(P)H	Acetyl-CoA	Ferredoxin	NAD-independent formate dehydrogenase, Acetyl-CoA synthase-CO dehydrogenase
3-HP (N)	Chloroflexaceae	Light	3 HCO, 5 ATP, 5 NAD(P)H	Pyruvate	NAD(P)H	Acetyl-CoA carboxylase, Propionyl-CoA carboxylase
HP/HB (N)	Aerobic Sulfolobales	Hydrogen/sulfur	2 HCO, 4 ATP, 4NAD(P)H	Acetyl-CoA	NAD(P)H	Acetyl-CoA-Propionyl-CoA carboxylase
DC/HB (N) *	Anaerobic Thermoproteale,Desulfurococcales	Hydrogen/sulfur	1 CO_2, 1 HCO, 3ATP, 4 NAD(P)H	Acetyl-CoA	NAD(PH &Ferredoxi	Pyruvate synthase, PEP carboxylase
RHP (CN)	Methanospirillum hungatei	Hydrogen	CO_2, 3 ATP, 2 NAD(P)H	Gluconeogenesis and glycolysis	NAD(P)H	RuBisCO
Natural Reductive Glycine (CD)	Candidatus phosphitivorax, anaerolimiDesulfovibrio desulfuricans	Phosphite	CO_2, ATP, NAD(P), H	Formate/ Pyruvate	NAD(P)H &Ferredoxi	CO_2-reducing formate dehydrogenase(fdhAB)
Reverse Otca (CD)	Desulfurella acetivorans	Hydrogen	CO_2, ATP, NAD(P) H	Acetyl-CoA	Ferredoxin	Citrate synthase
CETCH (S)	Theoretical	–	2 CO_2, 2 ATP, 3 NAD(P)H	Glyoxylate	NAD(P)H	CoA- dependent carboxylase
Reductive Glycine (S)	Demonstrated in E. coli as host	–	CO_2, NADH	Pyruvate	Ferredoxin	Glycine cleavage system
Synthetic malyl-CoA-glycerate (S)	Demonstrated in E. coli and Synechococcus elongatus PCC7942 host	–	CO_2, 3 ATP, 3 NADH	Acetyl-CoA	NAD(P)H	PEP-carboxylase, RuBisCO
SACA Pathway (S)	Demonstrated in E. coli as host	–	CO_2	Acetyl-CoA	–	NAD-independent formate dehydrogenase
Formolase pathway (S)	Theoretical	–	CO_2, NADH, ATP	Dihydroxyacetone-phosphate	NADH	NAD-independent formate dehydrogenase

Sulamita Santos et al., Natural carbon fixation and advances in synthetic engineering for redesigning and creating new fixation pathways, Journal of Advanced Research,
Volume 47, 2023, Pages 75-92, ISSN 2090-1232, https://doi.org/10.1016/j.jare. Creative Commons license

Plants and photoautotrophic microorganisms fix CO_2 by the Calvin cycle using NADPH and ATP, producing O_2. Some anaerobic photosynthetic bacteria don't produce O_2. In **chemolithoautotrophic** microorganisms, energy sources (i.e., electron donors like H_2, H_2S, sulfur, Fe^{2+}, nitrite, and NH_3 found in bedrock - the lithosphere) other than NADPH, ATP, and light can be used to drive CO_2 uptake. For **chemoorganotrophic** microbes, reduced organic molecules such as sugars and amino acids serve as electron (donor) sources.

Genetic engineering and synthetic biology are now employed to improve preexisting enzymes and create new pathways for carbon capture.

As a simple example, people are trying to engineer carbonic anhydrase, which converts CO_2 to HCO_3^-, for transport to the lungs, where it is converted back to CO_2 and released. It is a diffusion-controlled enzyme with a k_{cat}/K_M reported as high as 8×10^7 $M^{-1}s^{-1}$, so how can it be made better? One way is to engineer thermal stability into the enzyme. A critical problem for the forward reaction is that the enzyme is readily reversible; thus, bicarbonate, HCO_3^-, is a competitive inhibitor of the forward reaction. In addition, the enzyme can be engineered to be more stable at higher pH to allow product (HCO_3^-) removal by the addition of OH^- in the process of mineralization, as shown in the equation below,

$$HCO_3^- + OH^- \rightarrow CO_3^{2-} + H_2O$$

where the carbonate anion can precipitate in the presence of divalent cations like Ca^{2+}, Mg^{2+}, and Fe^{2+}. Here is a link to a Literature-based Guided Assessment on thermoengineering of carbonic anhydrase.

Now, let's explore using new pathways created by synthetic biology to capture carbon. Some of these pathways are engineered to produce reactants (feedstocks) for biofuels, which we discussed in depth in Chapter 32, the section on chemical synthesis. We'll focus on the CETCH pathway, the reductive glyoxylate and pyruvate synthesis (rGPS) cycle, and the malyl-CoA-glycerate (MCG) pathway.

CETCH (Crotonyl-CoA-EThylmalonyl-CoA-4Hydorxybutyl-CoA) pathway

To engineer a new pathway, Swander et al identified efficient carboxylases from known ones (acetyl-CoA carboxylase, Rubisco, propionyl-CoA carboxylase, PEP carboxykinase, 2-oxoglutarate carboxylase, and pyruvate carboxylase), all of which we have discussed in previous chapters. They created new pathways, calculated free energy and ATP/NADPH requirements, and optimized the pathways. They chose CoASH–dependent carboxylases and enoyl-CoA carboxylases/reductases. Figure **15.3** below shows the reaction of one key carboxylase.

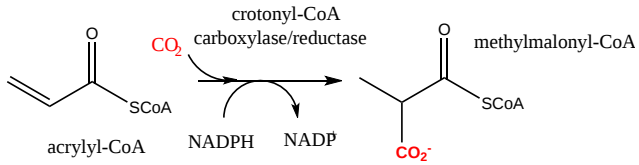


Figure **15.3**: Carboxylase used in the CETCH pathways to fix CO_2

The pathway was named CETCH (**C**rotonyl-CoA-**ET**hylmalonyl-**C**oA-4**H**ydorxybutyl-CoA) which catalyzes this next reaction in cell lysates (in vitro):

$2CO_2 + 3NAD(P)H + 2ATP + FAD \rightarrow$ glycolate $+ 3NAD(P) + 2ADP + 2P_i + FADH_2$

The rate of CO_2 fixation by the CETCH pathways was similar to the rate of the Calvin cycle rates in cell lysates.

In a more expansive approach, Gleizer used synthetic biology to convert E. coli from a heterotroph to an autotroph, with its biomass (carbon reservoir) derived from CO_2. Formate (HCO_2^-) was used as a source of reducing power (electrons), as it was oxidized by an added formate dehydrogenase to produce NADH, which was then used to support the autotrophic fixation of CO_2 via the Calvin cycle enzymes. Using isotopically labeled $^{13}CO_2$ to track carbon flow, after 10 generations of evolution, the cells were completely autotrophic, fixing CO_2. To accomplish this, they knocked out genes for phosphofructokinase (glycolysis) and glucose-6-phosphate dehydrogenase (pentose phosphate pathway) to impair these main metabolic pathways. They added carbonic anhydrase (to interconvert CO_2 and HCO_3^-), and Rubisco and phosphoribulokinase. As formate was ultimately converted to CO_2, the net effect was not carbon neutral, but could be if atmospheric CO_2 was used to make formate (for a feedstock) by electrochemical reduction.

Figure **15.4** below shows the next synthetic E. Coli autotroph reactions.

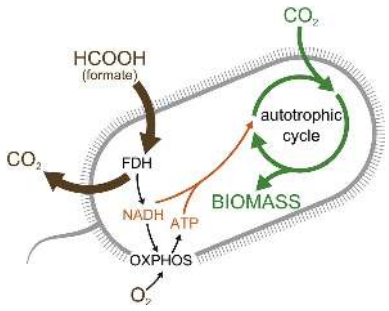


Figure 15.4: Schematic Representation of the Engineered Synthetic Chemo-autotrophic *E. coli*. Shmuel Gleizer et al., Conversion of Escherichia coli to Generate All Biomass Carbon from CO2, Cell, 179 (2019). https://doi.org/10.1016/j.cell.2019.11.009. Creative Commons license.

CO_2 (green) is the only carbon source for all the generated biomass. CO_2 fixation occurs via an autotrophic carbon assimilation cycle. Formate is oxidized by a recombinant formate dehydrogenase (FDH) to produce CO_2 (brown) and NADH. NADH provides the reducing power to drive carbon fixation and serves as the substrate for ATP generation via oxidative phosphorylation (OXPHOS in black). The formate oxidation arrow is thicker than the CO_2 fixation arrow, indicating a net CO_2 emission even under autotrophic conditions.

Figure 15.5 shows that almost 100% of carbon atoms after many generations are labeled with ^{13}C (detected by mass spec analysis) derived from $^{13}CO_2$.

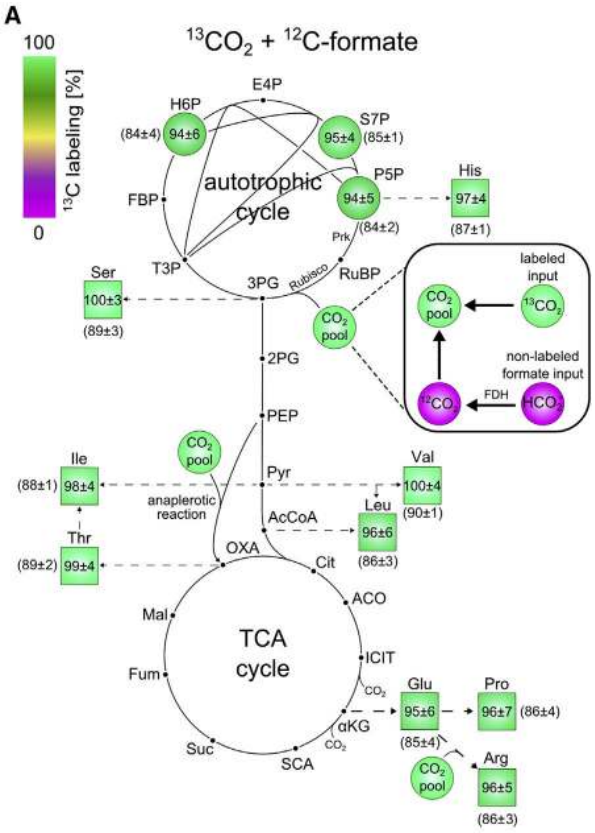


Figure 15.5: Isotopic Labeling Experiments Using ^{13}C Show that All Biomass Components Are Generated from CO_2 as the Sole Carbon Source. Gleizer et al., ibid.

(A) Values are based on LC-MS analysis of stable amino acids and sugar-phosphates. The fractional contribution of $^{13}CO_2$ to various protein-bound amino acids and sugar phosphates in evolved cells grown on $^{13}CO_2$ and naturally labeled formate was almost complete, indicating full ^{13}C labeling of biosynthesized amino acids. The reported numbers are the ^{13}C fractions of each metabolite, calculated as the effective $^{13}CO_2$ fraction out of the total inorganic carbon (which decreases due to unlabeled formate oxidation to CO_2). The numbers in parentheses are the uncorrected measured values of the ^{13}C fraction of the metabolites.

Synthetic reductive glyoxylate and pyruvate synthesis (rGPS) cycle and the malyl-CoA-glycerate (MCG) pathways

These pathways were created to synthesize acetyl-CoA, pyruvate, and malate from CO_2 in cell-free systems, freeing the system from cell growth and regulatory requirements and making it insensitive to oxygen. These molecules are also intermediates in the created cycle, which could operate continuously for hours at the same or greater rates of CO_2 fixation compared to photosynthesis. The cycle is shown in Figure **15.6** below.

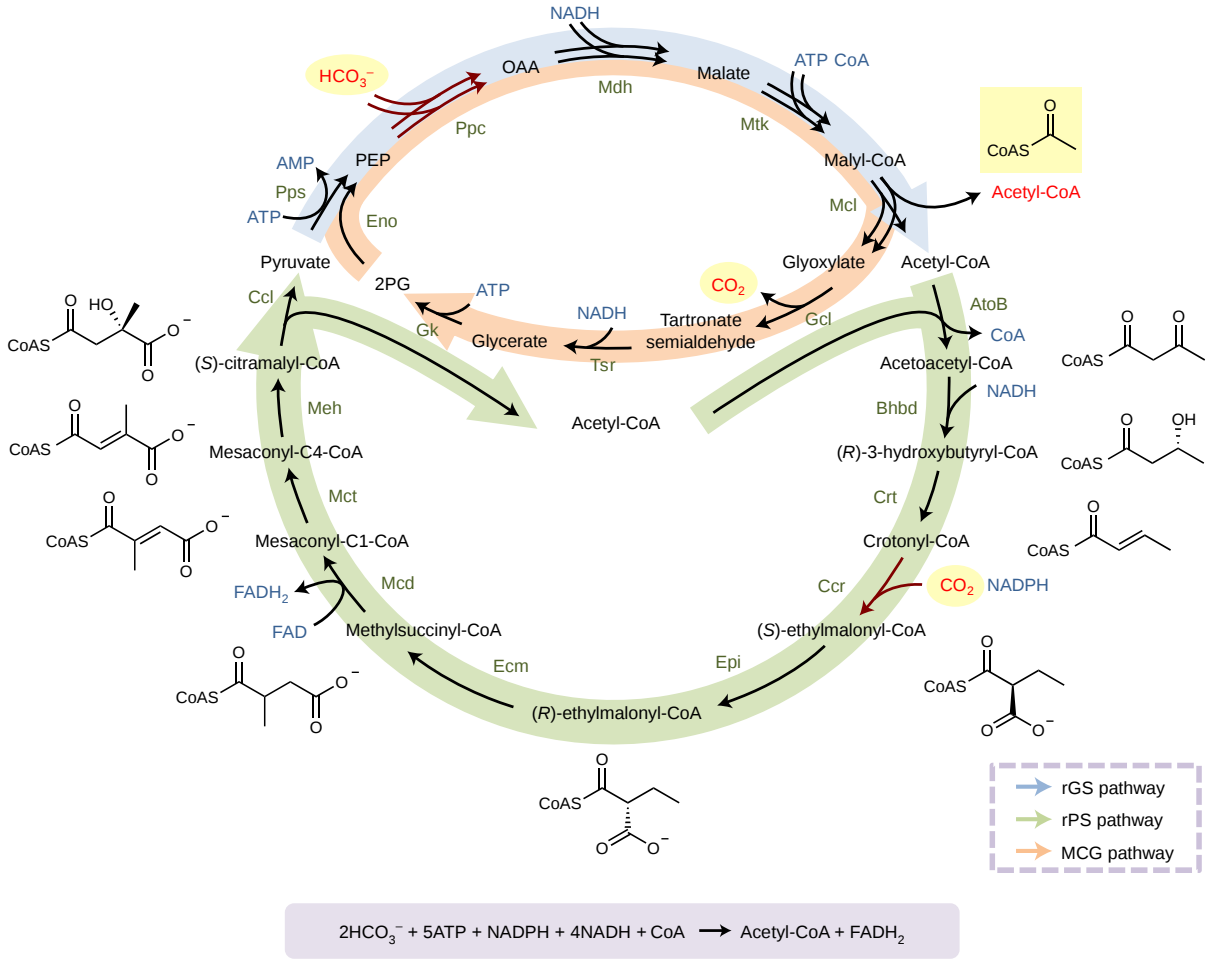


Figure **15.6**: The rGPS–MCG cycle with acetyl-CoA as the end product. Luo, S., Lin, P.P., Nieh, LY. *et al.* A cell-free self-replenishing CO_2-fixing system. *Nat Catal* **5**, 154–162 (2022). https://doi.org/10.1038/s41929-022-00746-x . Creative Commons Attribution 4.0 International License, http://creativecommons.org/licenses/by/4.0/

The rGPS cycle consists of the reductive glyoxylate synthesis (rGS) pathway (blue) and the reductive pyruvate synthesis (rPS) pathway (green). The malyl-CoA-glycerate (MCG) pathway (orange) consists of the rGS and glycerate pathways. The red arrow indicates the carboxylation reaction. Gcl, glyoxylate carboligase; Tsr, tartronate semialdehyde reductase; Gk, glycerate 2-kinase; Eno, enolase and 2PG, 2-phospho-d-glycerate

Microbial electrosynthesis from CO_2

We mentioned above that if the formate used in the CETCH pathway could be synthesized electrochemically from CO_2, the pathway would be truly carbon-neutral. New microbial electrochemical methods are being developed to synthesize various small molecules that could serve as feedstocks for industrial chemical synthesis. The carbon in CO_2 has an oxidation number of +4, while the carbon in formic acid has an oxidation number of +2. Hence, two electrons must be added electrochemically to make the CETCH pathway truly carbon neutral. Bigger electrochemical reductants of CO_2 require more electrons. Figure **15.7** below shows how key feedstocks could be made electrochemically from CO_2 and how they are usually made in industry.

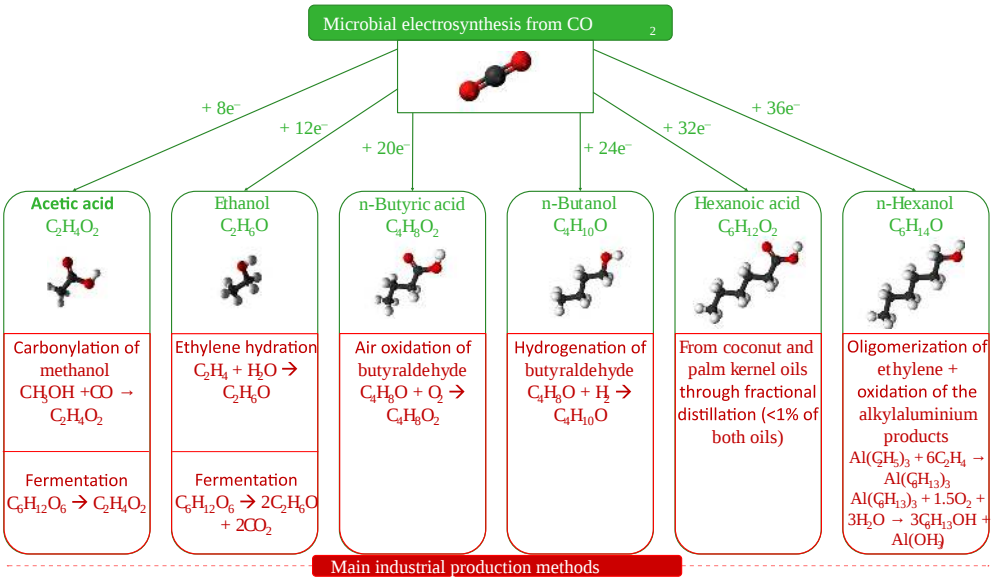


Figure 15.7 : **Overview of the Main Products Formed from Microbial Electrosynthesis (MES) From CO_2, Along With the Main Industrial Methods to Manufacture These Products.** Jourdin et al., Trends in Biotechnology, April 2021, Vol. 39, No. 4 https://doi.org/10.1016/j.tibtech.2020.10.014. Creative Commons Attribution (CC BY 4.0)

These feedstocks could be produced by reductive electrosynthesis using electrons generated by water oxidation via electrolysis. Released electrons (oxidation number of O in water is -2 and 0 in O_2) move to a biocathode to reduce CO_2, as illustrated in Figure **15.8** below.

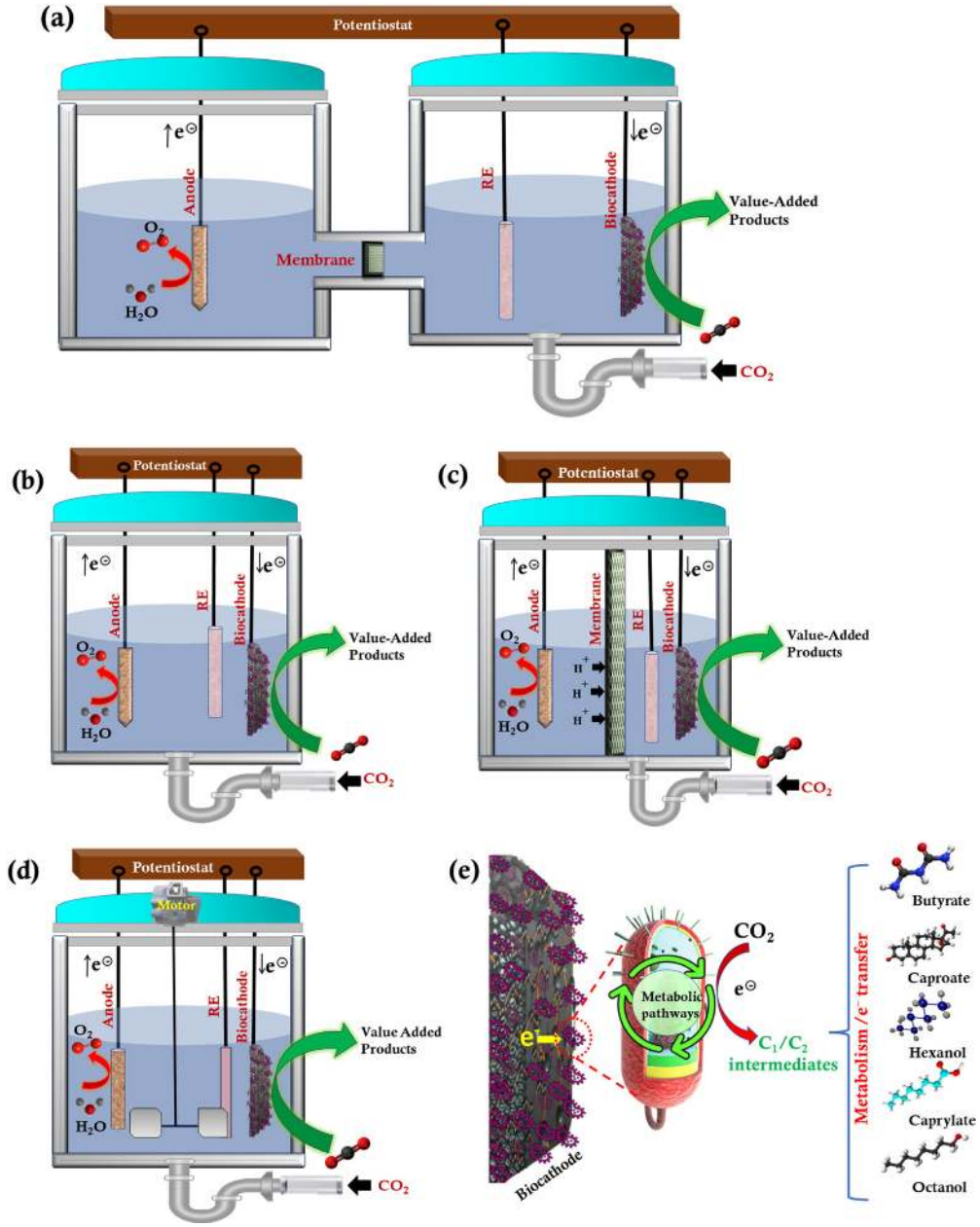


Figure 15.8: Reactor configurations for MES-based CO_2 conversion: (a) H-type, (b) single chamber, (c) dual chamber, (d) continuous stirred tank, and (e) schematic of the electron transfer mechanism. **G. S. Lekshmi et al., Microbial electrosynthesis: carbonaceous electrode materials for CO_2 conversion.** *Mater. Horiz.*, 2023, **10**, 292-312. DOI: 10.1039/D2MH01178F. Creative Commons Attribution-Non Commercial 3.0 Unported Licence

The biocathode consists of a biofilm of cells printed onto a carbon support (graphene, graphite, or carbon nanotubes).

MARINE CO_2 REMOVAL THROUGH GEOENGINEERING

As the climate worsens, more climate scientists are considering ways to improve the oceans' ability to capture CO_2. Both inorganic and biological methods have been proposed. These methods will likely have unintended consequences, affecting biodiversity and the natural mechanisms for carbon sequestration. Hence, they are both controversial.

Inorganic:

Here is a review from Chapter 32.3: The Carbon Cycle and Carbon Chemistry

The reversible movement of CO_2 from the atmosphere to the oceans, $CO_{2\ atm} \leftrightarrow CO_{2\ ocean}$, depends on the difference in the partial pressures of CO_2 (ΔpCO_2) in the atmosphere and surface waters. The reaction is also driven to the right by the removal of CO_2 (aq) as it forms carbonic acid (H_2CO_3), which then forms bicarbonate (HCO_3^-) and carbonate (CO_3^{2-}). These coupled reactions chemically buffer ocean water, thus regulating ocean pCO_2 and pH.

pCO_2 is not homogeneous in ocean surface waters and varies with current and temperature conditions. CO_2 can be more readily released from upwellings of nutrient-rich and warm waters, especially in the tropics. In cold Northern waters and the Southern Ocean, where water sinks, it is taken up from the atmosphere (again, CO_2 is more soluble in cold water).

As we discussed in Chapter 31.1, **ocean chemistry of CO_2 largely determines atmospheric CO_2 levels**. The coupled reactions of CO_2 in the oceans are shown below.

$$CO_2(g,\ atm) \leftrightarrow CO_2(aq,\ ocean) \tag{15.1}$$

$$CO_2(aq,\ ocean) + H_2O(I,\ ocean) \leftrightarrow H_3O^+(aq) + HCO_3^-(aq) \tag{15.2}$$

$$H_2O(I) + HCO_3^-(aq) \leftrightarrow H_3O^+(aq) + CO_3^{2-}(aq,\ sparingly\ soluble) \tag{15.3}$$

These reactions should be familiar to all chemistry students and were presented previously in Chapter 31.1 and Chapter 2. A significant source of oceanic bicarbonate is the **weathering** of rocks such as limestone and marble, both forms of $CaCO_3$. The relevant reactions are shown below.

$$\begin{aligned} CaCO_3(s) + H_2O &\leftrightarrow Ca^{2+}(aq) + CO_3^{2-}(aq) \\ CO_3^{2-}(aq) + H_2O &\leftrightarrow HCO_3^-(aq) + OH^-(aq) \end{aligned} \tag{15.4}$$

CO_2 is nonpolar and not very soluble in water. Either is CO_3^{2-} in the presence of divalent cations like Ca^{2+}. However, HCO_3^- is and can be considered a "soluble" form of carbon. This soluble form from terrestrial weathering enters rivers and eventually reaches the ocean. It is also the form of carbonate that is transferred into cells by anion transporters for eventual shell formation. HCO_3^- is also a chief regulator of both blood and ocean pH. Weathering is slow compared to anthropogenic CO_2 emissions from fossil fuel use, but it is nevertheless a key player in the carbon cycle and in regulating ocean pH.

The same weathering reactions on silicate rocks release silicate ions into rivers and the ocean, where they can be used by diatoms to form $CaSiO_4$ shells. As the oceans take up more CO_2, they become more acidic, mimicking "weathering" of the shells of living organisms and potentially leading to their death. Silicon is directly underneath carbon in the periodic table, so this simplified reaction is analogous to those we see with CO2 and its inorganic ions.

$$H_4SiO_4 = SiO_2 + 2H_2O \tag{15.5}$$

H_4SiO_4 is silicic acid.

With this background in mind, you can understand the proposed method of adding crushed limestone ($CaCO_3$) to the rivers (which drain into the oceans) to remove atmospheric CO_2. As the solid crushed limestone dilutes, it becomes more soluble. As CO_3^{2-} is a reasonable base, the water would become more alkaline. It would mostly get converted to HCO_3^- which can be transported into river shell-forming organisms. The rest enters the oceans, where it can be transported into organisms and used to make $CaCO_3$ shells, eventually sinking to the depths where the carbon would be sequestered for 1000s of years. This would also reduce river acidification. Whether this process could be run at the scale needed to reduce atmospheric CO2 significantly is unclear.

Biological

This method involves adding Fe^{2+}, usually iron (II) sulfate ($FeSO_4$), to the oceans to promote phytoplankton growth. This process has been called ocean iron fertilization (OIF). One problem with $FeSO_4$ is that it rapidly oxidizes to insoluble iron(III) species at elevated temperatures. It must be transported to sufficient depths so it doesn't return to the surface. Another problem is the adverse effects of nutrient removal on other marine organisms.

SUMMARY

(Summary written by Claude, Anthropic)

Carbon fixation — converting atmospheric CO_2 into organic biomolecules — removes approximately 100 petagrams of carbon per year through net primary production, split roughly equally between land and ocean organisms. The dominant enzyme is **RuBisCO**, which despite its global importance is remarkably slow (kcat ≈ 2–10 CO_2/sec), requires a chaperonin for assembly, and is compromised by a competing oxygenase reaction that drives wasteful photorespiration. While planting trees is widely proposed as a climate solution, old-growth forests

are far more effective carbon sinks than new plantings, which require decades before contributing meaningfully to drawdown. The chapter therefore focuses on engineering improved and entirely new carbon fixation strategies.

Natural carbon fixation pathways. Six naturally occurring pathways fix CO_2 beyond the Calvin-Benson-Bassham (CBB) cycle. The **reverse TCA cycle** fixes CO_2 into pyruvate in green sulfur bacteria using ferredoxin and NAD(P)H. The **Wood–Ljungdahl pathway**, used by acetogenic and methanogenic Archaea, is one of the most energy-efficient routes, producing acetyl-CoA from two CO_2 molecules using hydrogen as the energy source. The **3-hydroxypropionate cycle** (Chloroflexaceae) uses acetyl-CoA and propionyl-CoA carboxylases to fix bicarbonate. The **HP/HB** and **DC/HB cycles** (thermophilic Archaea) use hydrogen and sulfur to produce acetyl-CoA under anaerobic conditions. These pathways collectively demonstrate the metabolic diversity available for CO_2 capture and provide a toolkit for synthetic biology.

Engineered carbonic anhydrase. As an entry point to synthetic carbon capture, carbonic anhydrase — which interconverts CO_2 and HCO_3^- at near-diffusion-controlled rates (kcat/KM up to 8×10^7 $M^{-1}s^{-1}$) — is being engineered for greater thermal stability and higher pH tolerance. The key challenge is product inhibition: HCO_3^- competitively inhibits the forward reaction. Engineering the enzyme to function at higher pH allows OH^- addition to drive HCO_3^- to CO_3^{2-}, which precipitates with Ca^{2+}, Mg^{2+}, or Fe^{2+} as insoluble carbonate minerals — permanently sequestering the captured carbon.

Synthetic carbon fixation pathways. The **CETCH pathway** (Crotonyl-CoA/EThylmalonyl-CoA/4-Hydroxybutyryl-CoA) was designed computationally by selecting efficient CoA-dependent carboxylases and enoyl-CoA carboxylases/reductases from known enzymes and optimizing the pathway for thermodynamic feasibility and cofactor balance. Operating in cell lysates, it fixes 2 CO_2 per cycle to produce glyoxylate: $2CO_2$ + 3NAD(P)H + 2ATP + FAD → glycolate + cofactors, at rates comparable to the Calvin cycle in vitro. In a more ambitious approach, Gleizer et al. converted *E. coli* from a heterotroph into a fully autotrophic organism by knocking out phosphofructokinase and glucose-6-phosphate dehydrogenase (disabling glycolysis and the pentose phosphate pathway), and adding RuBisCO, phosphoribulokinase, and carbonic anhydrase. Formate served as the electron donor, oxidized by formate dehydrogenase to generate NADH for CO_2 fixation. After directed evolution over 10 generations, $^{13}CO_2$ isotopic labeling confirmed that virtually 100% of cellular carbon derived from CO_2. The **rGPS–MCG cell-free pathway** (reductive glyoxylate/pyruvate synthesis + malyl-CoA-glycerate) takes this further by operating entirely outside living cells — avoiding regulatory constraints, oxygen sensitivity, and competition with cellular metabolism — while fixing CO_2 into acetyl-CoA, pyruvate, and malate at rates matching or exceeding photosynthesis continuously for hours.

Microbial electrosynthesis. To make pathways like CETCH truly carbon-neutral, formate feedstocks must themselves be produced from atmospheric CO_2. Microbial electrosynthesis (MES) achieves this by delivering electrons from water electrolysis to a biocathode — a biofilm of microorganisms on graphene, graphite, or carbon nanotube supports — where CO_2 is reduced. Converting CO_2 (+4 oxidation state) to formate (+2) requires two electrons; larger products require more. This electrochemical approach, powered by renewable electricity, could close the carbon loop for synthetic fixation pathways.

Marine CO_2 removal by geoengineering. As biological and synthetic approaches develop, ocean-based geoengineering is also being explored, though both proposed approaches are controversial due to potential unintended ecological consequences. The **inorganic approach** (ocean alkalinity enhancement) involves adding crushed limestone ($CaCO_3$) to rivers; as it dissolves, it raises water alkalinity, converting CO_2 to HCO_3^-, which eventually enters marine organisms as shell material ($CaCO_3$), sinks to the ocean floor, and sequesters carbon for thousands of years — also mitigating river and coastal acidification. Whether this is scalable to climatically meaningful levels remains uncertain. The **biological approach** — ocean iron fertilization (OIF) — adds $FeSO_4$ to iron-limited surface waters to stimulate phytoplankton blooms and biological CO_2 uptake. Practical challenges include rapid oxidation of Fe^{2+} to insoluble Fe^{3+} at the surface, the need to deliver iron to depth, and disruption of marine nutrient cycles and biodiversity.

Throughout, the chapter emphasizes that all carbon capture strategies complement but cannot substitute for the primary imperative: drastically reducing fossil fuel combustion.

15: Fixing Carbon Fixation is shared under a CC BY-NC-SA 4.0 license and was authored, remixed, and/or curated by LibreTexts.

16: FIXING NITROGEN FIXATION

Search Fundamentals of Biochemistry

LEARNING GOALS

(Learning goals written by Claude, Anthropic)

By the end of this chapter, students should be able to:

Environmental Costs and Nitrogenase O_2 Sensitivity

- Describe the environmental consequences of excess Haber-Bosch fertilizer — N_2O production (GWP 300× CO_2, nitrogen oxidation state change from −3 in NH_3 to +1) and eutrophication — and explain why reducing dependence on the Haber process is both an agricultural and a climate priority.
- Explain why nitrogenase FeS clusters are destroyed by O_2 using reduction potential calculations — showing that nitrogenase Em (−420 to −500 mV) makes reaction with $O_2/O_2^{\bullet-}$ (Em ≈ −330 mV) thermodynamically favorable ($\Delta G \approx -16.4$ kJ/mol) — and trace the subsequent superoxide → peroxide → hydroxyl radical Fenton chemistry that irreversibly inactivates the enzyme.
- Describe the symbiotic rhizobium–legume relationship, explain the role of leghemoglobin as an O_2 buffer (P50 ≈ 0.01–0.05 μM vs. ≈4–5 μM for myoglobin) keeping nodules microaerobic, and list the advantages of root-nodule nitrogen fixation over dependence on soil microbes.

Engineering Nitrogenase into Crop Plants

- Identify the minimum nif gene set required for functional nitrogenase (nifH, nifD, nifK encoding structural subunits with [4Fe-4S], [8Fe-7S], and FeMo cofactors; nifA/nifL regulation; nifB/nifE for FeMo cofactor maturation; NifM chaperone), and explain why expressing this complex in cereal crops is technically daunting.
- Explain why mitochondria are a better target than chloroplasts for nitrogenase expression in eukaryotes, summarize progress in yeast (NifDK tetramer) and transgenic rice (NifH targeted to mitochondria, acetylene reduction demonstrated), and identify remaining obstacles including low FeS cluster occupancy, mitochondrial protease cleavage of NifD, and poor electron transfer to NifDK.
- Describe how the corn-root bacterium Kv137 was engineered into strain Kv137-1036 by replacing nifL with an independent promoter to uncouple nitrogenase expression from nitrogen availability, and explain the resulting agricultural and environmental benefits (−25 lb chemical fertilizer/acre, no N_2O production, no waterway runoff, deployed on 3 million acres in 2021).

Controlling Plant Immune Response to Enable Symbiosis

- Describe the structure of lipo-chitooligosaccharides (LCOs/Nod factors) — β(1,4)-linked N-acetylglucosamine polymer with a fatty acid at the non-reducing end — explain how LysM receptor kinases (CERK1, NFR1) recognize chitin-based signals through their extracellular LysM1–3 domains, and describe the structure of CERK1 including its three LysM domains, single transmembrane helix, and intracellular Ser/Thr kinase domain.
- Explain how two point mutations in the Symbiosis Determinant 1 juxtamembrane region of NFR1 (T304M, D306A) shift signaling from immune defense to symbiotic acceptance, and describe what happens when this region is swapped into CERK6 — converting it into a symbiosis receptor enabling root nodule formation even in barley — connecting these findings to the evolutionary origin of nitrogen-fixing symbiosis from ancestral immune receptors and to the possibility of engineering nodulation into cereal crops.

NITROGEN FIXATION

We spent most of Chapter 22.1 discussing the biochemistry of nitrogenase, which converts the stable molecule N_2 into NH_3/NH_4^+. It's a highly complex reaction conducted by symbiotic microbes (prokaryotes) that fix N_2 for plants. Modern agriculture needs more than nitrogenase can provide. The world uses the Haber-Bosch process to produce over 100 million metric tons of nitrogen fertilizer, which supports half of the world's food supply. Only about half of the ammonium added to the soil is taken up by plants. The rest is released into waterways or used by microbes, which can convert it to the potent greenhouse gas nitrous oxide (N_2O). It has a 300x greater effect per unit of climate-warming potential than CO_2. The oxidation number of N in NH_3 is -3, and in N_2O it is +1, indicating that NH_3 can be oxidized for energy production by the microbes. Also, excess NH_4^+ goes into waterways and leads to eutrophication, the overproduction of algae and plankton, which depletes O_2 from the waters and kills other organisms.

N_2O emissions have increased dramatically since 1850, as shown in the interactive graph from Our World in Data in Figure **16.9** below.

Figure 16.9: Our World in Data. https://ourworldindata.org/grapher/n...ions?tab=chart

So, what can we do to "fix" nitrogen fixation to reduce reliance on the Haber process and its collateral climate effects? Perhaps we could use mutagenesis to improve nitrogenase efficiency. That would not be easy given the complexity of both the enzyme and the mechanism of N_2 conversion to NH_3, which requires many metal-ion cofactors. A better alternative would be to express nitrogenase in plants so they could synthesize their own nitrogen fertilizer! Also, maybe we can convert more food crops into species that can host nitrogen-fixing bacteria in their roots, forming a symbiotic relationship. Then nitrogen can be fixed directly in the roots.

Before we discuss ways to "fix" nitrogen fixation, we will present a brief introduction to how all plants acquire fixed nitrogen. Then we will explore ways to enhance that process to reduce the need for the Haber process and for fertilizers.

Recent Updates: 12/16/25

HOW DO PLANTS ACQUIRE FIXED NITROGEN?

All plants need fixed nitrogen, but none have nitrogenase. Seems like an evolutionary mismatch! We presented nitrogenase in great detail in Chapter 22, but didn't mention that the enzyme can't function in the presence of much oxygen. Aerobic plants don't have nitrogenase, so they must acquire fixed nitrogen elsewhere. How are these quandaries resolved?

All plants obtain fixed nitrogen from two sources: soil microbes that produce NH_4^+, which can diffuse into plants, and leguminous plants that harbor symbiotic bacteria in root nodules, which produce NH_4^+ within the plant. Without microbes, no nitrogen would be fixed or made available to the plant. The bacteria in these nodules include the flagellated, Gram-negative, diazotrophic genus Rhizobia (rhiza means "root" in Greek, and bios means "life"). In this symbiotic relationship, rhizobia acquire carbohydrates and other nutrients from plants and, in turn, provide NH_4^+ to them. Figure 16.*cc* below shows root nodules, which contain the nitrogen-fixing bacteria.



Figure **16.10**: Root nodules containing rhizobia. https://milnepublishing.geneseo.edu/...ter/rhizobium/.

fgfgf

The advantages to plants and the environment from using nitrogen-fixing bacteria in root nodules are many:

- They make their own NH_4^+, so it doesn't have to diffuse through the soil from soil microbes
- The plant highly controls uptake
- Competition for NH_4^+ by other species is eliminated
- Losses of NH_4^+ are very low
- There are low levels of environmentally deleterious nitrogen products, including NO_3^- and N_2O.

Hence, producing fixed nitrogen in root nodules of legumes is highly efficient compared to non-leguminous plants.

Oxygen remains a potential problem because it can greatly interfere with nitrogenase in bacteria. Nitrogenase is so sensitive to oxygen because it contains **iron–sulfur clusters** with relatively low reduction potentials.

Let's review reduction potentials. Remember that O_2 has a **standard reduction potential** $E^{0'}$ = 0.816 (see Table 12.4.2) and is a powerful oxidant, causing the loss of electrons in substrates that act as reducing agents for O_2 as it forms water. Remember than $\Delta G^{0'} = -nFE^{0,}$ for the reaction $1/2O_2 + 2H^+ \rightarrow H_2O$.

For the reaction of oxygen to form the reactive oxygen species, superoxide, instead of water (which doesn't require protons):

$$O_2 + e^- \rightleftharpoons O_2^{\bullet -} \tag{16.1}$$

The standard reduction potential for superoxide formation (at pH 7) is about -0.33 V.

When we consider enzymes with FeS centers, each has a different $E^{0'}$ value, as the geometry and electrostatics at the FeS centers can vary widely. We discussed this in Chapter 19.1: Electron-Transfer Reactions in Mitochondria.

Instead of using $E^{0'}$ values (analogous to pKa values for acid/base reaction), an alternative, $\mathbf{E_m}$ is often used for reactions involving complicated metal ion centers. $\mathbf{E_m}$ is the **midpoint reduction potential**, measured not under standard conditions, but in a given set of experimental or physiological conditions. It's analogous to pKa, which occurs at the midpoint of an acid/base titration curve. We know that pKas for proton-donating groups in proteins vary widely for different local environments.

The approximate Em values for the FeS clusters of nitrogenase and the citric acid cycle enzyme aconitase (which also has an FeS cluster), compared to that of superoxide formation, are shown below:

- Nitrogenase FeS protein ~ **−420 to −500 mV**
- Aconitase ~ **−200 to −350 mV**
- $O_2/O_2^{\bullet -}$ ~ **−330 mV**

Comparing these negative values shows that the nitrogenase FeS centers are a stronger reductant than the FeS center in aconitase. Let's do some quick calculations based on this equation from introductory chemistry.

$$\Delta G = -nF\Delta E \tag{16.2}$$

Let's say the Em value of nitrogenase is around -0.5 V. Using the equation:

$$\Delta E = E_{\text{acceptor}} - E_{\text{donor}} \tag{16.3}$$

We can show that $\Delta E_{\text{nitrogenase}}$ ~ -0.33 V - (-0.5 V) = +0.17V so $\Delta G = -nF\Delta E$ = -16.4 kJ/mol or -3.9 kcal/mol. The same calculations for aconitase give a $\Delta G > 0$. These quick calculations show that the FeS centers of nitrogenase readily react with O_2 to form O_2^- (superoxide), a

reactive oxygen species.

In catalysis, these clusters spend significant time in reduced states (electron-loaded). O_2 can approach/bind weakly near exposed Fe sites or react to produce reactive oxygen species (see Chapter 12.3: The Chemistry and Biochemistry of Dioxygen). These reactions are summarized below.

The bound O_2 can react with iron to form superoxide, as shown in the reaction below.

$$\mathrm{Fe-S(\ reduced\ )} + O_2 \rightarrow \mathrm{Fe-S(\ oxidized\ )} + O_2^{\bullet -} \tag{16.4}$$

The superoxide can produce peroxides through a dismutation reaction without or with the enzyme superoxide dismutase to from peroxides as shown below:

$$2O_2^{\bullet -} + 2H^+ \rightarrow H_2O_2 + O_2 \tag{16.5}$$

The peroxide can then react through the Fenton reaction to produce the hydroxy free radical as shown below:

$$Fe^{2+} + H_2O_2 \rightarrow Fe^{3+} + OH^- + \bullet OH \tag{16.6}$$

Locally produced ROS can oxidize sulfur and iron in nitrogenase, thereby inactivating it. So O_2 doesn't just inhibit the enzyme, it **destroys it**, requiring new synthesis to replace it.

Rhizobium is mainly aerobic in the soil outside of the root nodules, as it uses O_2 for respiration. However, inside the nodules, it is functionally microaerobic since O_2 is so low. Even then, O_2 is still a problem for N_2 fixation. Rhizobia solve this oxygen problem through a protein called leghemoglobin (a better name for it would be legmyoglobin!). This cytosolic protein acts as an O_2 buffer (much like myoglobin in skeletal and cardiac muscles) to keep free O_2 low and nitrogenase active. It also binds O_2 much more tightly than myoglobin. The P_{50} of leghemoglobin is about 0.01-0.05 μM compared to 4-5 μM for myoglobin.

Figure **16.2** shows an interactive iCn3D model showing the alignment of sperm whale myoglobin (1MBN) and soybean leghemoglobin (1BIN).

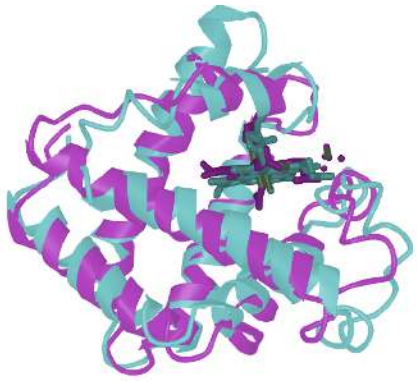


Figure **16.2**: Alignment of sperm whale myoglobin (1MBN, cyan) and soybean leghemoglobin (1BIN, magenta). (Copyright; author via source). Click the image for a popup or use this external link: https://www.ncbi.nlm.nih.gov/Structu...6ec85ef13b1a77

After viewing the initial alignment, toggle the "a" key to see each structure separately.

GENES OF NITROGEN FIXATION - CAN THEY BE PUT INTO PLANTS?

Inserting bacterial genes encoding nitrogenase into plants would allow them to produce their own NH_4^+. It's a complex endeavor, though.

Three genes encode the catalytic nitrogenase enzyme complex:

- nifH gene for the subunit **Nitrogenase iron protein 1** (also called Nitrogenase component II, and Nitrogenase reductase). It is a homodimer that binds one [4Fe-4S] cluster per dimer.
- nifD gene for the subunit **Nitrogenase molybdenum-iron protein alpha chain** (also called Dinitrogenase and Nitrogenase component I). It catalyzes the key enzymatic reactions along with its partner nifK as part of a heterodimer. It binds one [8Fe-7S] cluster per heterodimer with nifK and 1 [7Fe-Mo-9S-C-homocitryl] cluster per subunit.
- nifK gene for the subunit **Nitrogenase molybdenum-iron protein beta chain** (also called Dinitrogenase and Nitrogenase component I). In its heterodimeric partner, nifD, it catalyzes key enzymatic reactions. It binds one [8Fe-7S] cluster per heterodimer with nifD and 1 [7Fe-Mo-9S-C-homocitryl] cluster per subunit.

The nitrogenase enzyme complex has regulatory proteins as well:

- nifA - **Nif-specific regulatory protein** required for activation of most nif operons. It senses N_2. If N_2 is insufficient, the protein NtrC activates NifA expression, which in turn activates the remaining genes.
- nifB - **FeMo cofactor biosynthesis protein NifB** (also called FeMo-cofactor maturase NifB, Nitrogenase cofactor maturase NifB, and radical SAM assemblase NifB).
- nifL - **Nitrogen fixation regulatory protein** required for inhibiting NifA activity (i.e., nitrogenase formation) in response to oxygen and low levels of fixed nitrogen.
- nifE - **Periplasmic [NiFe] hydrogenase small subunit**.
- NifM - a possible peptidyl-prolyl *cis-trans* isomerase (i.e., a protein chaperone) that helps fold NifH.

Figure **16.10** below summarizes these gene products.

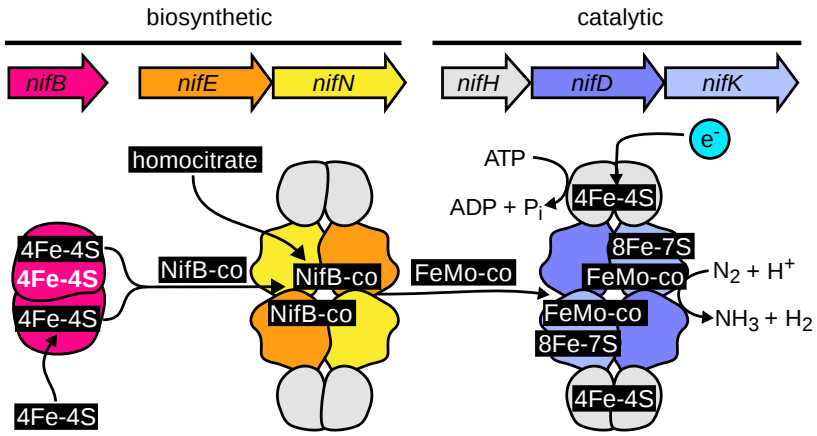


Figure **16.10**: Minimum set of *nif* genes essential for nitrogen fixation with molybdenum-iron nitrogenase. EMILY M. BENNETT et al., ***BIODESIGN RESEARCH.*** 10 Jan 2023, Vol 5, https://spj.science.org/doi/10.34133/bdr.0005 . Creative Commons Attribution License 4.0 (CC BY 4.0).https://doi.org/10.34133/bdr.0005

The stoichiometry depicted has not been adjusted. NifB contains one catalytic cluster (shown in white) and two substrate [4Fe-4S] clusters that react to produce the NifB cofactor. NifEN matures the NifB cofactor, producing the FeMo cofactor. The molybdenum-iron (MoFe) nitrogenase (NifHDK) contains the FeMo cofactor at its active site. Electron donors transfer single electrons to the [4Fe-4S] cluster at the interface of the NifH homodimer. Electrons are moved from the [4Fe-4S] cluster into the active site of nitrogenase using energy produced by ATP hydrolysis by NifH. A minimum of 8 electrons is required to reduce each N_2 molecule.

It would be especially important to express nitrogenase in the main cereal food crops (rice, corn, and wheat), which get their nitrogen from soil microbes (in contrast to legumes, which contain nitrogen-fixing bacteria in nodules in their roots). It's a daunting task given the complexity of the protein complex, its metal cofactors, their inhibition by O_2, and the multiple genes required for nitrogenase regulation. Ideally, the relevant gene clusters could be moved into a chloroplast, which is evolutionarily derived from bacteria, so the gene regulation system might be more suitable. It also has low O_2 levels at night. However, O_2 is produced in chloroplasts, which is problematic given nitrogenase's sensitivity to O_2.

Saccharomyces cerevisiae has been engineered using synthetic biology to express the NifDK nitrogenase tetramer in its mitochondria (via post-translational import). Yeast is a model organism, and tools have been developed for synthetic biology experiments with it. Much can be learned and applied to other eukaryotic organisms, such as plants. Mitochondria have high O_2 consumption (as opposed to production as in the chloroplast) and the ability to synthesize bacterial-type iron-sulfur clusters. The Nif gene clusters were engineered into the XV chromosome as shown below in Figure **16.11**.

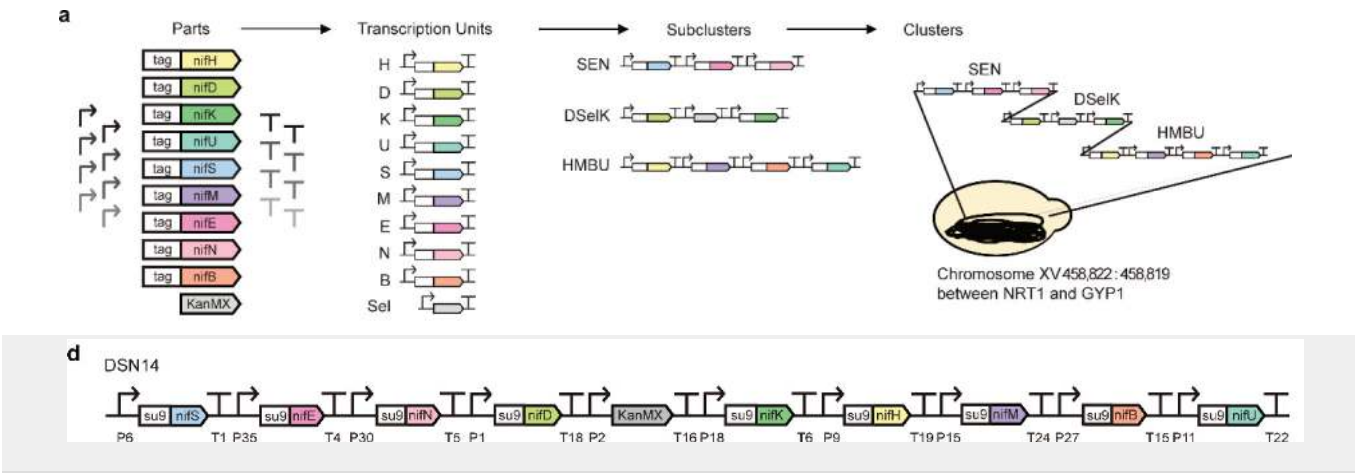


Figure **16.11**: nif gene assembly in yeast. *Buren et al., ACS Synth. Biol.* 2017, 6, 6, 1043–1055. https://doi.org/10.1021/acssynbio.6b00371. **CC-BY license**

Panel (a) shows the assembly strategy for transcription units, subclusters, and full clusters inserted by homologous recombination in the genome of *S. cerevisiae*. Panel (d) shows a diagram of *nif* gene organization in DSN14, a strain of *S. cerevisiae.*

Nitrogenase activity has also been functionally expressed in transgenic rice containing the NifH with a [4Fe-4S] cluster from *Hydrogenobacter thermophilus* and NifM (a peptidyl-prolyl *cis-trans* isomerase from *Azotobacter vinelandii)*, which helps NifH fold. They were correctly targeted to mitochondria, thereby minimizing O_2-induced oxidative damage to metal-ion cofactors. The purified protein could transfer electrons to the MoFe protein (NfiDK dimer), but did so poorly. It also assisted in the assembly of the FeMo cofactor. However, the [4Fe-4S] cluster occupancy in the protein was poor. However, the purified protein could also reduce acetylene, HC=CH (an alternative substrate similar to N=N), upon addition of purified NifDK.

Many steps must be optimized to create a functional nitrogenase in rice, corn, and wheat plants. For example, mitochondrial-expressed NifD is readily cleaved by a mitochondrial endoprotease. Some NifD subunits are more resistant to proteolysis, and a single amino acid change (Y100Q) leads to enhanced protein stability. AI will likely be extremely useful for maximizing nitrogen use efficiency in crop plants.

INTERACTION OF NITROGEN-FIXING BACTERIA WITH NONLEGUMINOUS PLANTS

Bacteria can express nitrogenase that can fix atmospheric N_2. Still, they won't work with the critical cereal crops unless the bacteria can interact with roots in the "rhizosphere", the layers of dirt intimately in contact with roots. This life in this area is often called a **holobiont**, which consists of the plant host and all species that interact with it in a symbiotic relationship. The metabolism in the holobiont is complex. For example, plant carbohydrates are used by other organisms in the holobiont. It's similar to the gut biome, which consists of an ecosystem of human and microbial cells.

Bacteria have now been engineered to express nitrogenase AND interact with corn roots to fix N_2. The cells are derived from a γ-proteobacterium (KV137) found on corn roots that fixes N_2. They have been engineered to turn nitrogenase genes on when N_2 fixation is needed. The engineered bacteria are added to liquid fertilizer, reducing the need for chemical fertilizer by 25 lb/acre while increasing yields. This bacterial-based fertilizer does not wash into waterways with its negative environmental effects. Likewise, no N_2O is produced during microbial metabolism of excess fertilizers, thereby decreasing the release of this potent greenhouse gas. In 2021, it was used on 3 million acres of corn.

One problem with using biological N_2 microbes in agricultural settings is that high levels of chemical fertilizers can effectively inhibit microbial N_2 fixation, which is regulated (as mentioned above) to shut down if nitrogen is bioavailable. Still, bacteria that fix N_2 can produce up to 10% of the nitrogen requirement. Genetic engineering is needed to overcome this inhibition. Such bacteria are **diazotrophs,** as they can fix N2 and grow without exogenous N_2 sources. Rhizobia is one example of a bacterium that can fix N_2 in legume nodules. The diazotroph isolated from corn roots and described above, Kv137, was gene-edited to produce a modified strain (Kv137-1036) that fixes N2 without being inhibited by applied nitrogen fertilizers.

The Kv137 strain has the nifA and nifL genes and proteins, which, as described above, regulate nitrogenase expression in response to nitrogen availability. These two genes are on one operon under the control of a single promoter. nifL was replaced with another promoter, thereby removing the nifA downregulation, since nifL was absent. This allowed nitrogenase to be expressed and active even in the presence of exogenous fertilizer.

Figure **16.12** below shows that the Kv137-1036 strain (red dots) colonizes corn roots.

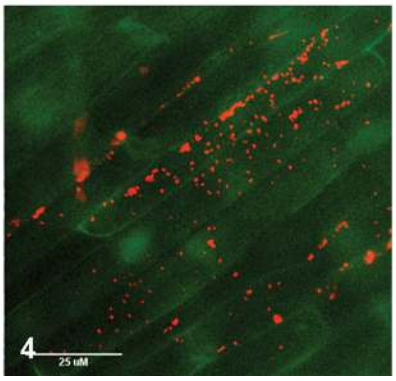


Figure **16.12**: Commercial efficacy of strain Kv137-1036 - Colonization of corn roots by microbes (red) after germination. Wen et al., Enabling Biological Nitrogen Fixation for Cereal Crops in Fertilized Fields. *ACS Synth. Biol.* 2021, 10, 12, 3264–3277. December 2021. https://doi.org/10.1021/acssynbio.1c00049. **Attribution 4.0 International (CC BY 4.0)**

Recent Updates: 1/6/26

CONTROLLING PLANT IMMUNE RESPONSE TO ALLOW SYMBIOSIS AND NITROGEN FIXATION

Another approach to enable plants to synthesize fixed nitrogen is to allow them to harbor nitrogen-fixing bacteria in their root hairs (as in legumes). This would require engineering the plant to take up soil bacteria to enable a symbiotic relationship, while also disabling any plant immune response to the symbiotic pathogen. A detailed knowledge of the signaling pathways for bacterial uptake and the plant's immune response is required.

Signaling molecules are required for both symbiosis and an immune response. **Lipo-chitooligosaccharides (LCOs)**, most commonly known in agriculture and biology as **Nod factors** (**Nod**ulation **factors**), are complex signaling molecules used by soil bacteria and fungi to communicate with plant roots. An example of an LCO is shown in Figure **16.*xx*** below.

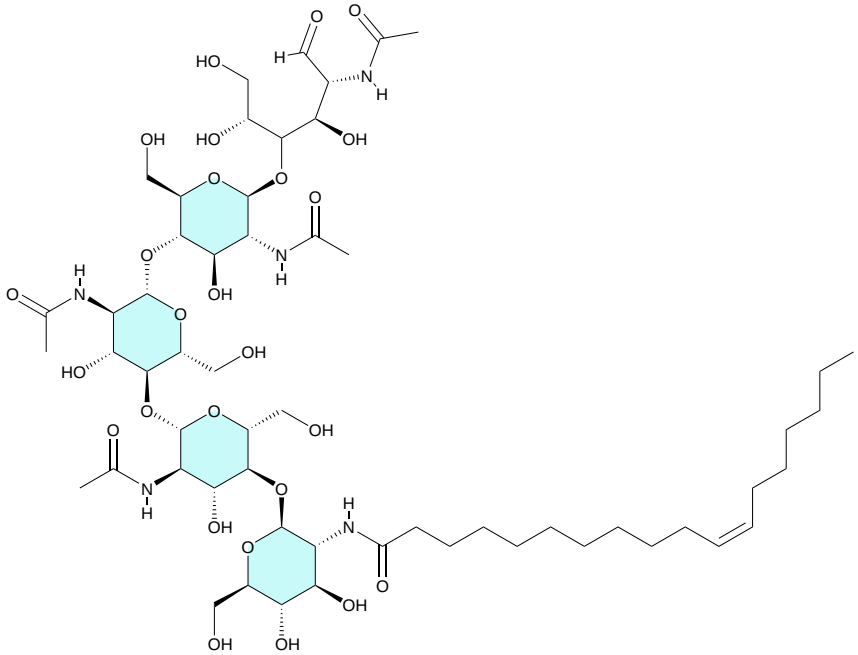


Figure **16.*xx***: An example of an **Lipo-chitooligosaccharides (LCOs)**

It is a β 1,4-linked polymer of N-acetylglucosamine (GlcNAc, blue ring). An elongated polymer of β-1,4-linked N-acetylglucosamine, known as chitin (which we explored in Chapter 7.2: Polysaccharides), is found in insect shells and fungal cell walls. In this particular LCO, an $18{:}1^{\Delta 11}$ fatty acid in amide replaces the usual acetyl group.

LCOs are signaling molecules produced primarily by two types of soil microorganisms:

- **Rhizobia Bacteria:** These nitrogen-fixing bacteria release LCOs called **Nod factors** that are recognized by legumes and lead to root nodule formation;
- **Mycorrhizal Fungi:** These fungi produce LCO-like **Myc factors** that allow plants to absorb phosphorus through a symbiotic relationship with the plant.

Specificity in plant root recognition and the ultimate uptake of specific bacteria into plant roots is based on the length of their chitin and lipid chains and on signaling processes that follow.

A key protein in the immune response towards LCOs and other chitin derivatives is the **Lysin motif (LysM) receptor kinase**. It is a monotopic (single membrane pass) protein with an intracellular Ser/Thr protein kinase domain and an extracellular mltD domain which binds chitin derivative. It acts as a pathogen-associated molecular pattern (PAMP) receptor. (We discussed PAMPs in Chapter 5.04: B. The Innate Immune System, PAMPs and DAMPs, and Inflammation). The PAMP in this case is the LCO. The chitin PAMP is recognized by lysine motif (LysM) domains in the extracellular mltD domain of the receptor kinase.

Figure **16.*xx*** shows an interactive iCn3D model of the ectodomain (extracellular) of the cell surface receptor **chitin elicitor receptor kinase 1 (CERK1)** of the plant Arabidopsis bound to $(NAG)_4$, a short chitin fragment (4EBZ).

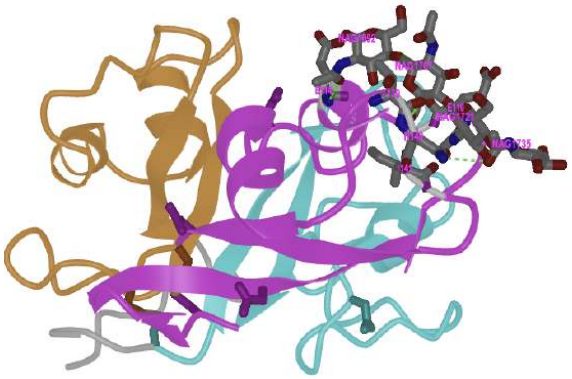


Figure **16.*xx***: Ectodomain of the cell surface receptor chitin elicitor receptor kinase 1 of Arabidopsis bound to $(NAG)_4$ (4EBZ). (Copyright; author via source). Click the image for a popup or use this external link: https://www.ncbi.nlm.nih.gov/Structu...47cfed55bec523

The ecto (extracellular) domain has three lysine motifs (LysM1-LysM3) domains (cyan, magenta, and gold), that can bind chitin. In the above model, only the magenta LysM2 interacts with a short chitin chain, $(NAG)_4$. Side chains in LysM2 that are involved in binding are shown as sticks and labeled.

Figure **16.*xx*** shows an interactive iCn3D model of the AlphaFold predicted structure of the Arabidopsis chitin elicitor receptor kinase 1(CERK1) involved in the immune response (CERK1, A8R7E6 · CERK1_ARATH)to pathogens (fungi, bacteria)

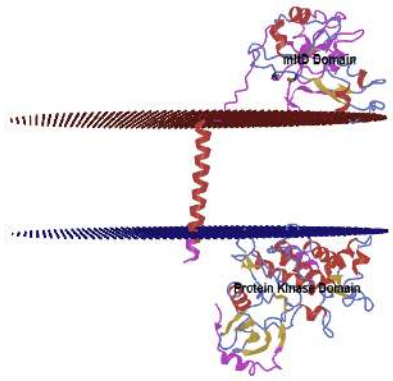


Figure **16.*xx***: AlphaFold model of the Arabidopsis chitin elicitor receptor kinase 1 (CERK1, A8R7E6 · CERK1_ARATH). (Copyright; author via source). Click the image for a popup or use this external link: https://www.ncbi.nlm.nih.gov/Structu...db9d41e1f20f2d

The disconnect between the intracellular part of the transmembrane helix and the kinase domain results from a poor AlphaFold-predicted structure for amino acids Ser 262 to Lys 306. If larger chitin fragments are used (e.g., an octamer), the protein dimerizes.

This PAMP receptor, when bound to a chitin derivative, induces innate immune signaling and resistance to pathogenic fungi. However, the same receptor also facilitates symbiosis with arbuscular mycorrhizal fungi. This soil fungus lives in symbiosis with most land plants. They

enter roots and create **arbuscules** (tree-like structures) instead of root nodules like those found in legumes. Images of a arbuscular mycorrhizal fungus in colonizing roots are shown in Figure **16.*xx*** below.

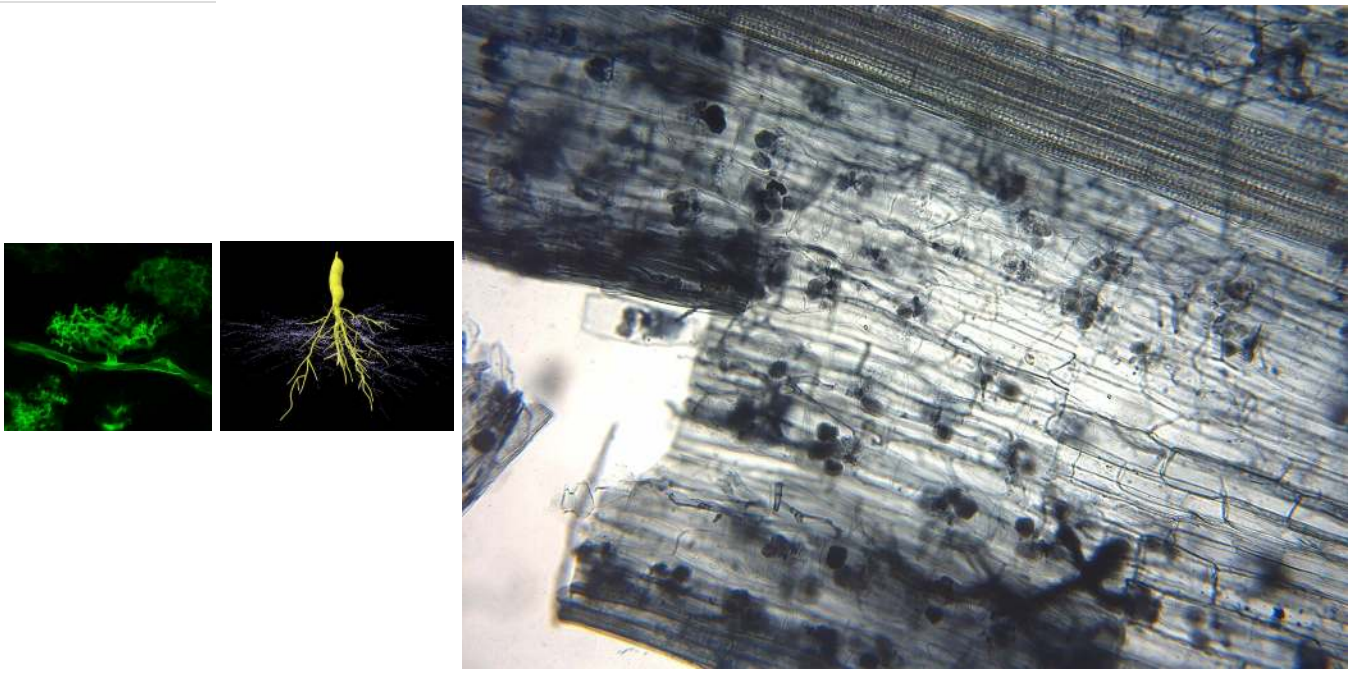


Figure **16.*xx***: Arbuscular mycorrhizal fungus colonizing roots. Left: Arbuscule of Rhizophagus irregularis colonizing a maize root observed under confocal microscope. Hector Montero. WikiCommons. https://commons.wikimedia.org/wiki/F...AArbuscule.png. Middle: Root tuber colonized by an arbuscular mycorrhizal fungus. WikiCommons. https://commons.wikimedia.org/wiki/F...ce=chatgpt.com. Right: Microscopic image of arbuscular mycorrhiza. MS Turmel, University of Manitoba, Plant Science Department, Public Domain, https://commons.wikimedia.org/w/inde...?curid=7553044.

The root hairs on a root are not the fungi, as the fungal hyphae are too fine to see without a microscope unless they are clumped together. The fungi are mostly inside the root and appear like a little tree (left and right image above). They are not visible as hairs, but the hyphae do extend into the soil (middle image). Arbuscules facilitate nutrient exchange and increase the transfer of water, phosphorus, and nitrogen into plants, while plants send fixed carbon to the fungus.

Resistance to such fungi in legume root cells must be overcome for symbiosis to occur via immune tolerance. The symbiotic pathway in legumes is activated by Nod receptors. The CERK6 receptor, involved in an immune response, and the Nod Factor Receptor 1 (NFR1), involved in symbiosis, are highly similar in structure across their extracellular and intracellular domains, as well as in their interactions with chitin ligands.

The NFR1 receptor (for symbiosis) from Lotus japonicus has a LysM receptor-like kinase that binds Nod factors from rhizobial bacteria. The intracellular part of the Nod factor receptor one (NFR1) can be mutated at two residues (T304M and D306A) to shift signaling from an immune response to a symbiotic response. These mutations occur in the Symbiosis Determinant 1, located in the juxtamembrane section, a flexible region of 40 or more amino acids between the C-terminal part of the transmembrane helix and the kinase domain.

Comparing the structures of CERK6 and an ortholog of NFR1, LYK3, shows that symbiosis determinant 1 is exposed internally in the cell and can mediate protein:protein interactions and hence signaling (i.e., not binding to the chitin ligand). If the symbiosis determinant 1 sequence of NFR1 is swapped into the immune receptor CERK6, it is converted into one that allows bacterial infection and the formation of root nodules, even in non-legume plant receptors (such as barley)!

These experiments suggest a way in which nitrogen-fixing symbiosis evolved from earlier immune receptors.

The LysM receptor kinase from Medicago is an ortholog of NFR1 from Lotus japonicus. It is a chitin-ligand-symbiosis receptor and contains Met and Ala at positions 303 and 305, respectively. Figure **16.*xx*** shows an interactive iCn3D model of the Medicago Truncatula LYK3 kinase domain with M304 and A306 (9GFZ).

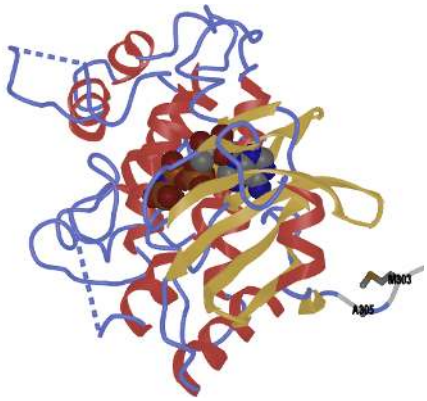


Figure **16.*xx***: Medicago Truncatula LYK3 kinase domain with M304 and A306 (9GFZ). (Copyright; author via source). Click the image for a popup or use this external link: https://www.ncbi.nlm.nih.gov/Structu...83af4acd1333b1

SUMMARY

(Summary written by Claude, Anthropic)

The Haber-Bosch process produces over 100 million metric tons of nitrogen fertilizer annually — supporting roughly half of the world's food supply — but only about half of this applied nitrogen reaches plants. The rest enters waterways (causing eutrophication and O_2 depletion) or is converted by soil microbes to nitrous oxide (N_2O), a greenhouse gas with 300 times the warming potential of CO_2 per unit mass. N_2O emissions have risen dramatically since 1850. This chapter explores three strategies to reduce dependence on the Haber process by improving or extending biological nitrogen fixation.

Why nitrogenase is O_2-sensitive. Nitrogenase contains iron-sulfur clusters with very negative midpoint reduction potentials (Em ≈ −420 to −500 mV), making them thermodynamically spontaneous reductants of O_2 (Em for $O_2/O_2^{\bullet -}$ ≈ −330 mV; ΔG ≈ −16.4 kJ/mol). The resulting superoxide dismutates to H_2O_2, which generates the hydroxyl radical via the Fenton reaction, oxidizing and destroying the enzyme's FeS centers. Unlike reversible inhibition, O_2 destroys nitrogenase outright, requiring new enzyme synthesis.

The root-nodule solution. Legumes solve the O_2 problem by housing rhizobial bacteria in root nodules, where the protein **leghemoglobin** buffers free O_2 at extraordinarily low levels. Its P50 (≈0.01–0.05 μM) is 100–500 times tighter than myoglobin (≈4–5 μM), keeping the nodule interior near-anoxic while still supplying O_2 for rhizobial respiration. This symbiosis delivers NH_4^+ directly within the plant with minimal N_2O production, no soil runoff, and tight control of nitrogen uptake — advantages that make it far more efficient than relying on soil microbes.

Engineering nitrogenase into crop plants. Transferring nitrogen fixation into cereal crops requires at minimum three structural genes (nifH, nifD, nifK) encoding subunits with elaborate FeS and FeMo cofactors, plus regulatory and maturation genes (nifA, nifB, nifL, nifM). Mitochondria are preferred over chloroplasts as a target organelle because they consume O_2 rather than producing it, and they can synthesize bacterial-type FeS clusters. The full nif gene cluster has been expressed in *S. cerevisiae* mitochondria (assembled by homologous recombination on chromosome XV). In transgenic rice, NifH targeted to mitochondria can transfer electrons to purified NifDK and reduce acetylene (an N_2 analog). Key obstacles remain: FeS cluster occupancy is poor, mitochondrial proteases cleave NifD (a Y100Q mutation improves stability), and full N_2 reduction in planta has not yet been achieved.

Engineering root-colonizing bacteria. A complementary approach uses naturally occurring diazotrophic bacteria. The corn-root bacterium Kv137 was engineered into strain Kv137-1036 by replacing the nifL gene (which normally shuts down nitrogenase when fixed nitrogen is available) with an independent promoter, thereby uncoupling nitrogenase expression from nitrogen availability. The strain colonizes corn roots, reduces chemical fertilizer requirements by ~25 lb/acre, increases yield, produces no N_2O, and causes no waterway runoff. By 2021 it was deployed on 3 million acres of corn — a real-world demonstration of synthetic biology improving agricultural sustainability.

Controlling plant immune responses to enable symbiosis. A third strategy — engineering non-legume plants to accept nitrogen-fixing bacteria directly into their root hairs — requires understanding how plants distinguish symbiotic microbes from pathogens. Both relationships are initiated by **lipo-chitooligosaccharides (LCOs)**: Nod factors from rhizobia and Myc factors from mycorrhizal fungi, recognized by **LysM receptor kinases** on root cells. The immune receptor CERK1 and the symbiosis receptor NFR1 are structurally similar and bind the same chitin-based ligands; the difference between immune and symbiotic outcomes is determined by a short juxtamembrane region called **Symbiosis Determinant 1**. Two point mutations in this region of NFR1 (T304M, D306A) shift signaling from immune defense to symbiotic acceptance. Swapping the Symbiosis Determinant 1 sequence from NFR1 into CERK6 converts it into a symbiosis receptor that enables root nodule formation even in non-legumes such as barley — suggesting that nitrogen-fixing symbiosis evolved from

ancestral immune receptors through modification of intracellular signaling, and pointing toward a tractable path for engineering this capability into cereal crops.

16: Fixing Nitrogen Fixation is shared under a CC BY-NC-SA 4.0 license and was authored, remixed, and/or curated by LibreTexts.

17: TURNING TREES INTO PLEXIGLASS - SYNTHETIC BIOLOGY FOR PRODUCTION OF GREEN FOODS AND PRODUCTS

Search Fundamentals of Biochemistry

LEARNING GOALS

(Learning goals written by Claude, Anthropic)

By the end of this chapter, students should be able to:

Food Production, Climate, and Alternative Proteins

- Quantify the climate impact of food production (~25% of global GHG emissions, ~35% from agriculture), explain why cattle require the most land per 1,000 kcal of any food source, and connect dietary choices to climate outcomes.
- Explain why soy leghemoglobin gives plant-based burgers a meat-like taste, describe its high O_2 affinity (kon ≈ 2×10^8 s^{-1}, koff ≈ 20 s^{-1}) and structural similarity to myoglobin, and distinguish the C4 (succinyl-CoA → ALA, in fungi and animals) from the C5 (α-ketoglutarate → ALA, in bacteria and plants) heme biosynthesis pathways, identifying ALA as the critical shared precursor and describing the synthetic biology strategies (gene upregulation, downregulation, knockout) used to maximize heme production in *Pichia pastoris* under the AOX1 promoter.
- Describe at least four alternative protein sources under development through synthetic biology or sustainable agriculture (β-lactoglobulin from *Trichoderma reesei*, casein/egg-white proteins from *Pichia pastoris*, fungal fermentation using *Fusarium venenatum*, duckweed), and explain why duckweed is particularly promising — containing up to 50% protein (primarily RuBisCO), all essential amino acids, aquaculture compatibility, and no farmland requirement.

Biosourced Industrial Materials

- Explain the environmental significance of replacing fossil-fuel-based acrylic acid production (~4,000 kg CO_2/metric ton) with biological feedstocks, describe the free radical polymerization mechanism by which MMA and MBL form PMMA and PMBL respectively, and outline the six key steps Arzeda used to engineer a fermentation pathway from lignocellulosic hydrolysate to MBL using Scylax™ (computational pathway design) and Archytas™ (enzyme engineering).
- Compare the physical properties of biosourced PMBL to fossil-fuel-derived PMBL and PMMA — including superior thermal stability (Tg = 195°C vs. 105°C for PMMA), tensile strength, elasticity, and solvent resistance — and explain why achieving ~5 g/L (approaching the ~20 g/L commercial threshold) represents a significant milestone for sustainable materials.

INTRODUCTION

Manufacturing is energy-consuming, environmentally damaging, and contributes to climate change by releasing CO_2 and other pollutants. A manufactured item has a lifetime after which it must be disposed of, often in a manner that involves little recycling. A circular economy in which a used product is always recycled for further use would be highly beneficial for the environment if done well.

Synthetic biology seeks to genetically alter and redesign organisms to produce traditional or novel products more sustainably with less energy input and polluting output. Although it is a nascent field, well-known products are being produced through its use. We will explore several products made through synthetic biology, as well as those in which novel cells are the products.

PRODUCTS FROM CELLS

Burgers by Impossible Foods

Agriculture has transformed the planet. About 50% of all land (excluding deserts and ice sheets, and comprising an area equal to the Americas) is used for agriculture, most of which is for animal production. In 2015, the US accounted for about 8% of the world's total greenhouse gas emissions from food, while China accounted for around 14%. Contributions to food production include agriculture, land-use change, and supply-chain emissions (transport, packaging, food processing, retail, cooking, and waste).

Estimates indicate that wild mammals account for only about 6% of the total mass of all mammals (including people, livestock, and pets) on Earth. In a parallel finding, the mass of "stuff" (plastics, metals, asphalt, concrete, etc) created by humans now exceeds the entire biomass of the planet!

Most of the agricultural land is used to produce meat and milk for human consumption. Collectively, cattle by far require the most land use, as shown in the interactive graph of Our World In Data in Figure 17.1 below, which shows how many square meters are required to produce 1000 kcals (1000 cal in the dietary sense) of food from each food type listed. The graph is similar when the measure is land use per 100 grams of protein produced.

Figure 17.1: Land use of foods/1000 kcals. https://ourworldindata.org/land-use-diets

The number of animals slaughtered **daily** worldwide is unbelievably high, as shown in Table 17.1.

cows	goats	sheep	pigs	ducks	chickens	fish
900,000	1.4 million	1.7 million	3.8 million	11.8 million	202 million	100's of millions

Table 17.1: Animals slaughtered daily for food. Max Roser (2023) - "How many animals get slaughtered every day?" Published online at OurWorldInData.org. Retrieved from: 'https://ourworldindata.org/how-many-...ered-every-day' [Online Resource]

The global percentage of all GHG emissions from the agricultural sector is about 35%, as illustrated in Figure 17.2 below. Averages for some specific countries are also shown.

Figure 17.2: https://ourworldindata.org/grapher/f...SA~IND~RUS~POL

The percentage of greenhouse gas emissions from all aspects of food products through the entire food chain is about 25%. Figure 17.3 below shows the best estimate of global greenhouse gas per sector in 2016. The number today would probably differ little from these.

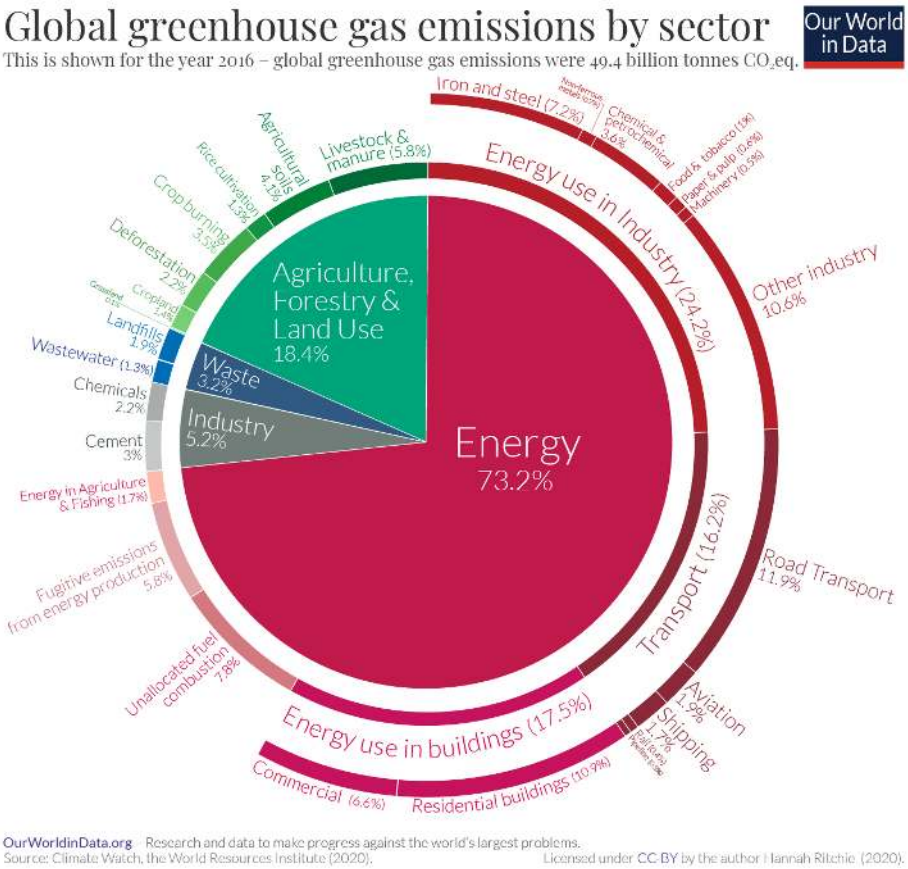


Figure **17.3**: Breakdown of global greenhouse gas emissions in 2016. Hannah Ritchie (2020) - "Sector by sector: where do global greenhouse gas emissions come from?" Published online at OurWorldInData.org. Retrieved from: 'https://ourworldindata.org/ghg-emissions-by-sector' [Online Resource].

An expanded analysis of the approximate 25% of global emissions that arise from food is shown in Figure **17.4** below.

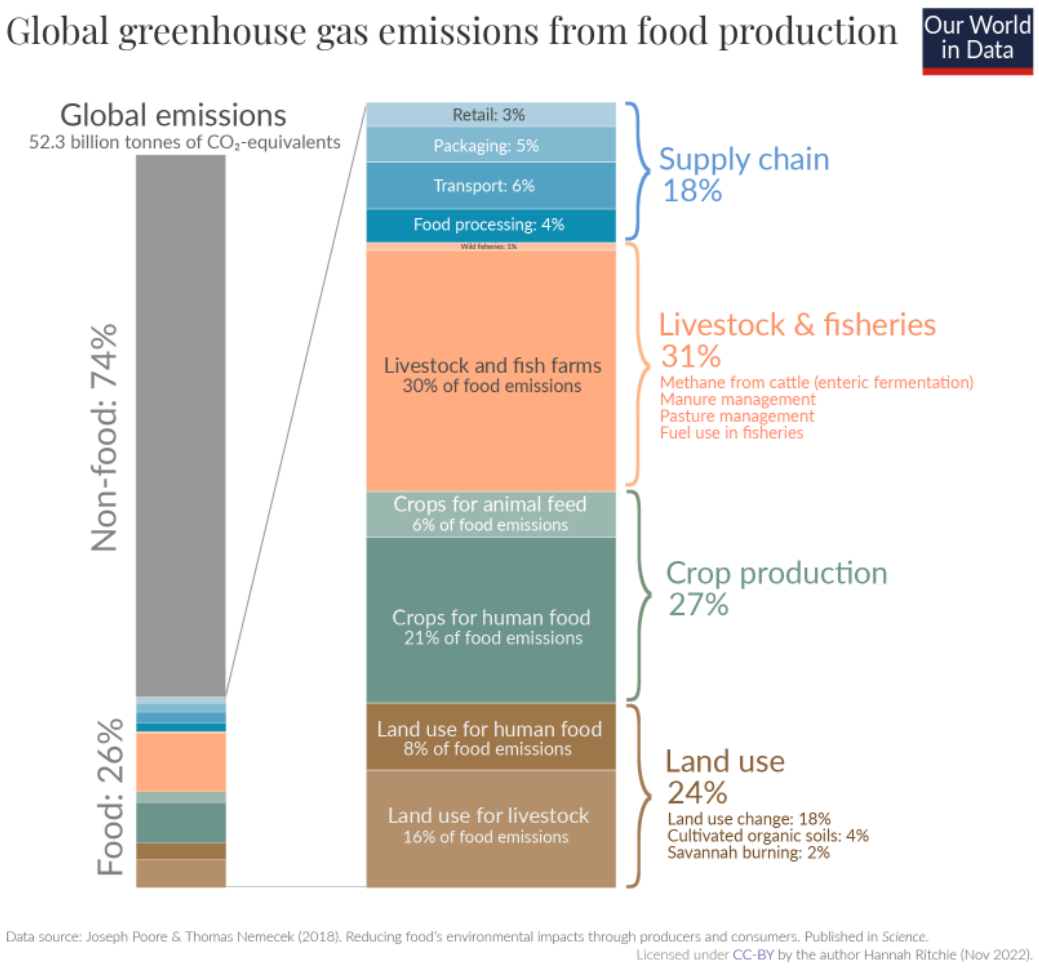
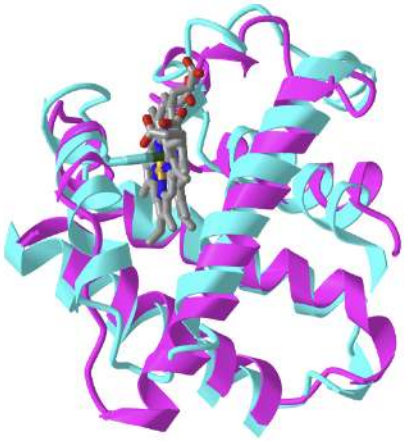


Figure **17.4**: Global greenhouse gas emissions from food production. Hannah Ritchie (2019) - "Food production is responsible for one-quarter of the world's greenhouse gas emissions," Published online at OurWorldInData.org. Retrieved from: 'https://ourworldindata.org/food-ghg-emissions' [Online Resource]

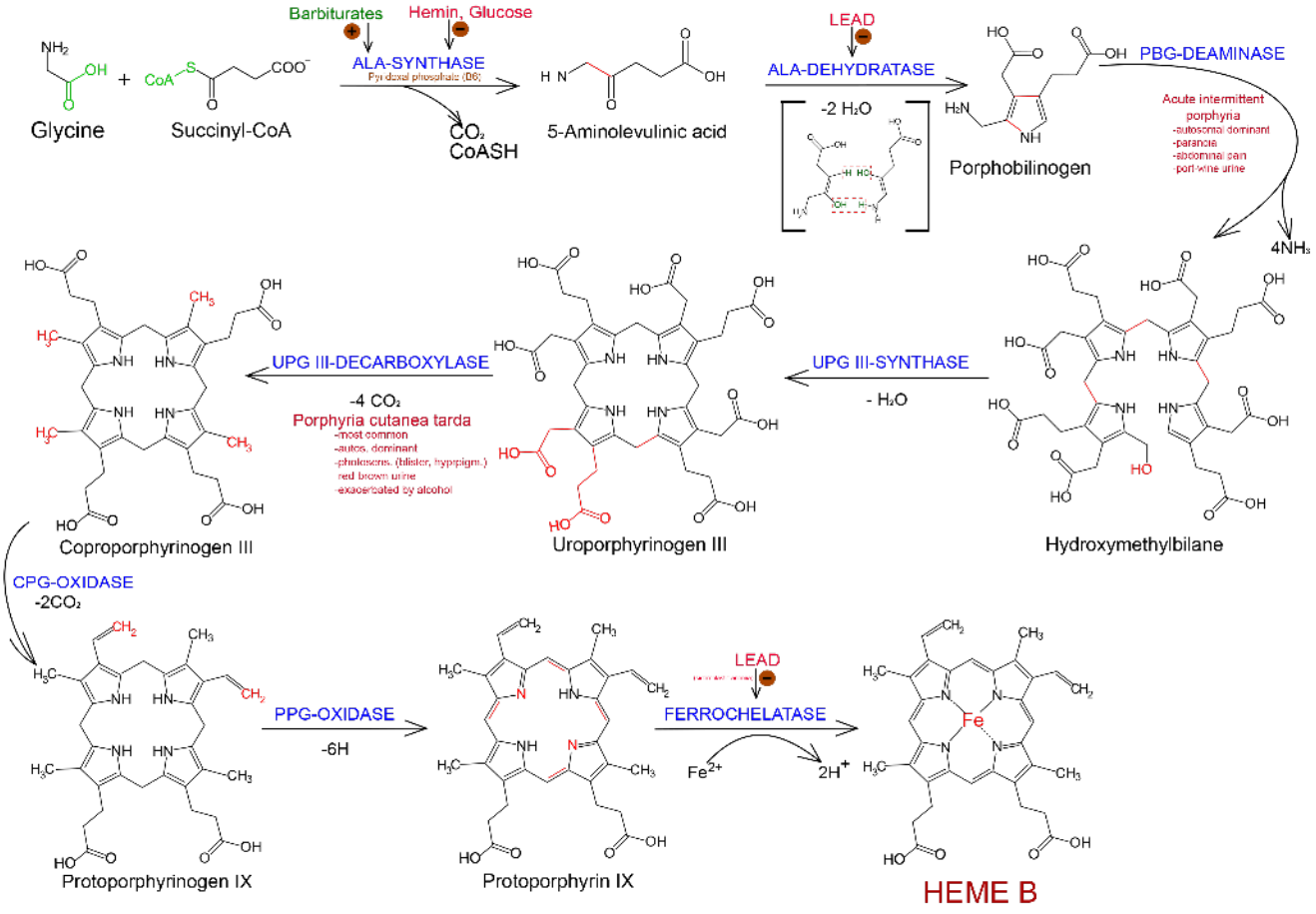
Making plant-based foods that taste more like meat, if people would eat them, could have a large effect on greenhouse gas emissions and climate change. One example is Impossible Burgers and similar products from Impossible Foods. They use soy **leghemoglobin**, a monomeric heme-binding protein found in legume root nodules, to give meat a blood-like appearance and taste. As a single-chain heme-binding protein, it has a high affinity for O_2, similar to animal myoglobin. The high affinity derives from very high on-rates for binding O_2 (almost diffusion-controlled at around $2x10^8$ s^{-1}, and an off rate of around 20 s^{-1}. This high affinity keeps O_2 bound, preventing it from inhibiting nitrogenase and nitrogen fixation by root-associated microbes. Heme is important for the positive taste of red meat. Plant-based burgers containing leghemoglobin require much less land and lead to far lower greenhouse gas emissions.

Figure **17.5** shows an interactive iCn3D model of the alignment of sperm whale myoglobin (1MBO) and soy leghemoglobin (1BIN).



NCBI iCn3D Figure 17.5: Alignment of sperm whale myoglobin (1MBO, cyan) and soy leghemoglobin (1BIN, magenta). (Copyright; author via source). Click the image for a popup or use this external link: https://structure.ncbi.nlm.nih.gov/i...4pUi1S6qFtGn4A

The leghemoglobin in the Impossible burgers is produced in yeast. Large amounts of heme are required to produce leghemoglobin in yeast, which is also produced in the engineered cells by introducing the appropriate genes. The C4 pathway (humans, animals, fungi, and purple non-sulfur phototrophic bacteria top) and C5 pathway (archaea, plants, and other bacteria) for heme synthesis are shown in Figure 17.6 below (heme synthesis described more detail in Chapter 22.3). The succinyl-CoA is derived from the citric acid cycle.



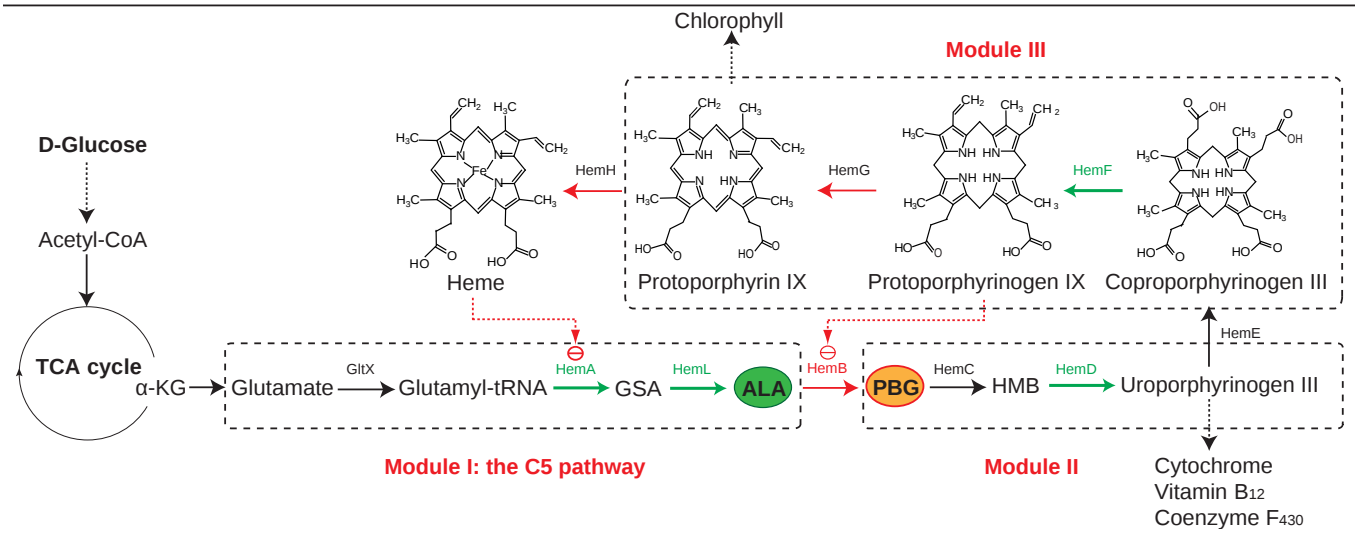


Figure **17.6**: Top - C4 heme synthesis pathway (humans, animals, fungi, and purple non-sulfur phototrophic bacteria top). Bottom-heme synthesis C5 pathway (archaea, plants, and other bacteria). Heme biosynthetic pathway. Wikimedia Commons: Heme-Synthesis-Chemical-Details-Mirror (top) and Heme pathway in *E. coli*. Zhang, J., Kang, Z., Chen, J. *et al.* Optimization of the heme biosynthesis pathway for producing 5-aminolevulinic acid in *Escherichia coli*. *Sci Rep* **5,** 8584 (2015). https://doi.org/10.1038/srep08584. Creative Commons Attribution 4.0 International License. http://creativecommons.org/licenses/by/4.0/ (bottom).

Succinyl-CoA (C4 pathway) and α-ketoglutarate (C5 pathway) are derived from the citric acid cycle. The key precursor 5-aminolevulinate, ALA, needs to be elevated by engineering the C4 or C5 pathways, with the C5 pathways generally producing more ALA in engineered E. Coli.

Leghemoglobin from soy (species name Glycine max) can also be synthesized in the methylotrophic (uses methanol as a sole carbon source) yeast Pichia pastoris, which is often used for recombinant protein expression. Three groups of enzymes are needed.

- group 1: porphobilinogen synthase (PBGS)
- group 2: uroporphyrinogen III synthase (UROS), uroporphyrinogen III decarboxylase (UROD), coproporphyrinogen III oxidase (CPO)
- group 3: Ala synthase (ALAS), protoporphyrinogen oxidase (PPO), and ferrochelatase (FECH)

Transcription of these genes in P. pastoris can be controlled by using the methanol-induced alcohol oxidase (AOX1) promoter, which is often used to achieve high expression of recombinant proteins.

Figure **17.7** below shows a more detailed representation of the heme synthesis pathway.

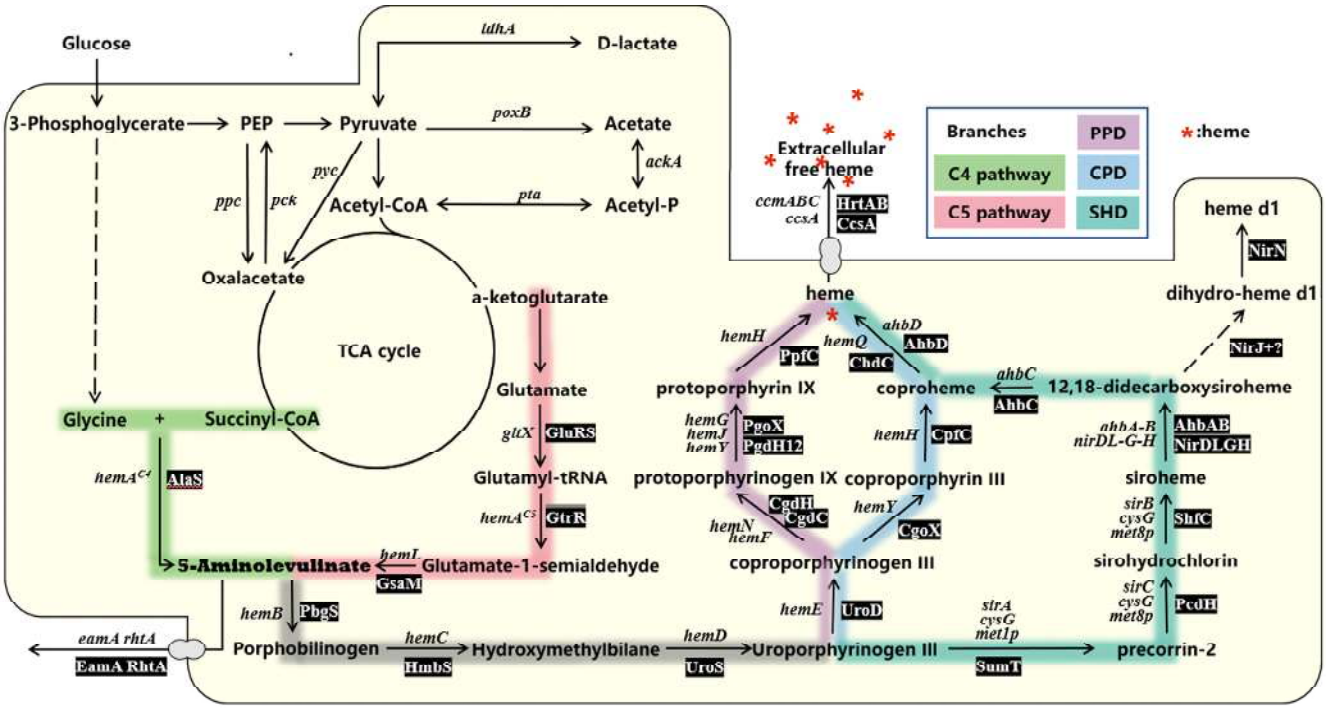


Figure 17.7: The biosynthetic pathway of heme. Su, H.; Chen, X.; Chen, S.; Guo, M.; Liu, H. Applications of the Whole-Cell System in the Efficient Biosynthesis of Heme. *Int. J. Mol. Sci.* **2023**, *24*, 8384. https://doi.org/10.3390/ijms24098384. Creative Commons Attribution (CC BY) license (**https://creativecommons.org/licenses/by/4.0/**)

The two biosynthetic pathways of 5-aminolevulinic acid (bolded to indicate its importance) are shown in green (C4 pathway) and red (C5 pathway). The three downstream synthetic pathways of heme are marked with blue (CPD), indigo (SHD), and purple (PPD). Solid lines indicate single reactions, and dashed lines indicate more than two. The names of genes encoding the individual enzymes are in italics, and some reactions have alternative genes. The abbreviations of the corresponding enzymes are shown in the grey rectangle.

Figure 17.8 below complements this figure and shows the synthetic biology strategies to enhance heme production.

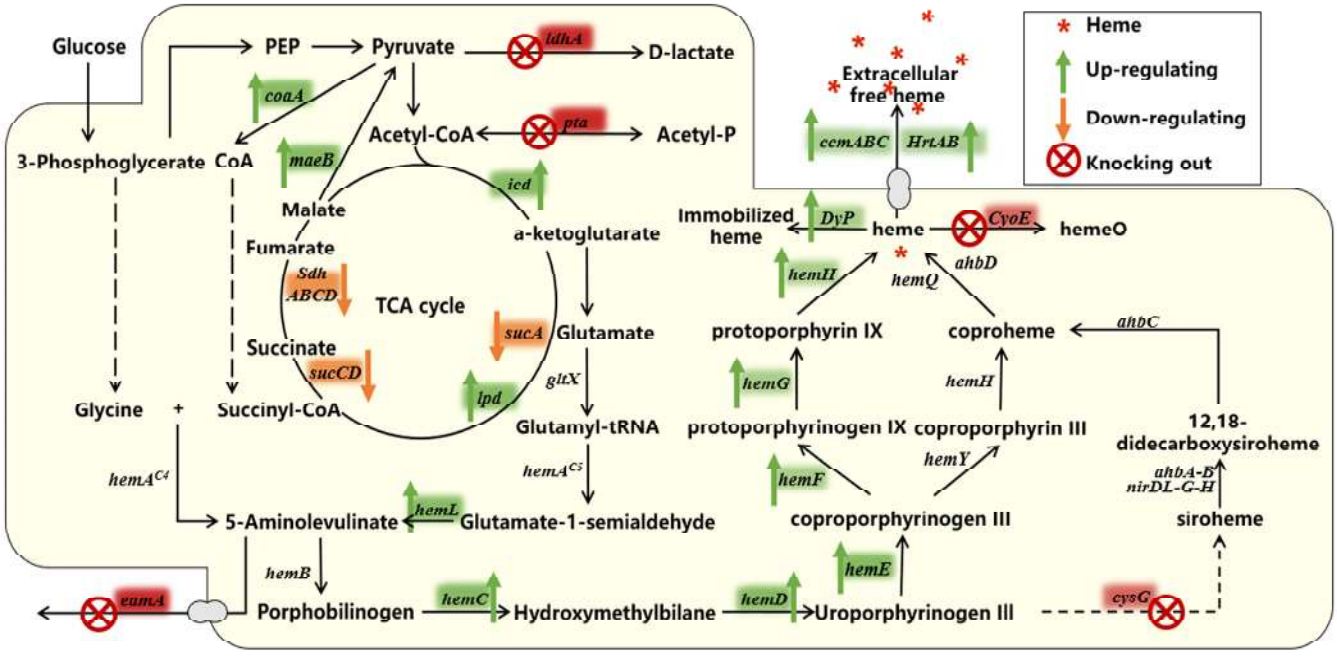


Figure 17.8: Synthetic biology strategies to enhance heme production. Green, orange, and red color blocks indicate genes that need to be up-regulated, down-regulated, and knocked out, respectively. See Table 1 for a list of names and abbreviations for heme synthesis

enzymes. Su, H. et al., ibid.

Computational tools such as AI can help design new pathways and novel enzymes to enhance production. It is becoming easier to transfer large pathways into yeast.

The sales of alternative meat products have decreased recently. This decrease probably stems from more vocal opposition from the meat industry and people's reticence to eat what many consider ultra-processed foods. High-protein and nutritious burgers can be made very simply with beans and grains.

OTHER FOOD PRODUCTS FROM MICROBES AND SUSTAINABLE PLANTS

Significant effort is being devoted to growing meat in the lab using cell culture. This nascent field faces many challenges, including consumer resistance to eating lab-grown meat. At present, meat grown in tissue culture is very expensive. Three key steps in growing meat are finding the best cells, determining the nutrient conditions that maximize their growth, and adjusting conditions to make the lab-grown meat taste like meat.

Muscle stem cells have been used as they can multiply many times, but these have growth limits. Alternatively, immortal cells, such as those derived from chicken fibroblasts, could be used. They can also be converted into fat cells. Yet they could accrue mutations with possible but unlikely health consequences. Animal cells grown in culture often use fetal cow serum for its rich composition of growth factors and nutrients. However, it is expensive and has ethical concerns since it's derived from animals. Synthetic growth medium can be used, but it is also expensive. Whether lab-grown meat can overcome high costs and consumer resistance will determine its potential as a substitute.

More simply, people can increase their intake of peas, soy, grains, and nuts in their diet (i.e., being a vegan or vegetarian is the best approach to reducing their carbon footprint). Soy products have an extensive history of use as a source of protein but contain potential allergens (significant in babies who use soy formulas) and isoflavones, which mimic human estrogen derivatives. Pea-based infant formula is increasingly used as a substitute.

Expressed recombinant proteins made in genetically modified bacteria and yeast are also becoming more popular. Examples (other than leghemoglobin) include the production in the fungus Trichoderma reesei of β-lactoglobulin, a cow whey protein, for dairy and animal-free milk products. The genetically modified yeast Pichia pastoris has also been engineered to make milk casein proteins, egg-white proteins, muscle myoglobin, and human breast milk proteins. Enzymes used to manufacture cheese (derived from calves' stomachs) can be replaced by chymosin made in yeast. Production of many of these proteins is linked to fermentation. Filamentous proteins with a texture similar to chicken fiber can be made through fermentation in the filamentous fungi *Fusarium venenatum*. Macroalgae, such as seaweed, can provide a high-protein food and have long been used in many cultures. Kelp farming can help not only provide protein but also capture carbon. Finally, long eaten in many cultures, insects could become more climate-friendly protein sources.

If humans are in search of non-animal sources of protein to fight climate change, why not produce and eat the most abundant protein in the biosphere, Rubisco? New products derived from the duckweed plant (genus Lemna) are coming to market. Figure **17.9**:



Figure **17.9**: Duckweed (and a frog). https://commons.wikimedia.org/wiki/F...7678481%29.jpg

Duckweed is high in nutrients, fast-growing, and a great source of Rubisco. It can be grown in aquaculture and does not require farmland. It contains up to 50% protein. After harvesting, the plants are filtered, milled, and dried using very simple technologies. Proteins, the most

abundant of which is Rubisco, are then extracted. Duckweed can be used in baked goods and as a meat and dairy substitute. It is equal to eggs and meat because it supplies all the essential amino acids humans require.

New methods are needed to make environmentally sustainable foods that minimize damage to our climate and biosphere. Over 150 Nobel and World Food Prize Laureates have signed a letter (January 2025) urging political and financial institutions to fund the development of new food technologies to prevent "an estimated 700 million people going hungry today and an additional 1.5 billion people to feed by 2050".

GENETIC MANUFACTURING OF INDUSTRIAL FEEDSTOCKS

Let's look at one example of how synthetic biology and computational techniques are used to create products such as plexiglass from biological acrylate sources. Acrylates are esters of acrylic acid (typically made from propylene) synthesized by reacting it with alcohols like methanol. Life cycle analyses show that almost 4,000 kg of CO_2 are emitted per metric ton of acrylic acid. Biological feedstocks like glycerol and 3-hydroxypropanoic acid can be used to reduce the climate effect, but large-scale supplies are needed. Figure 17.10 overviews acrylate production from fossil and biological feedstocks.

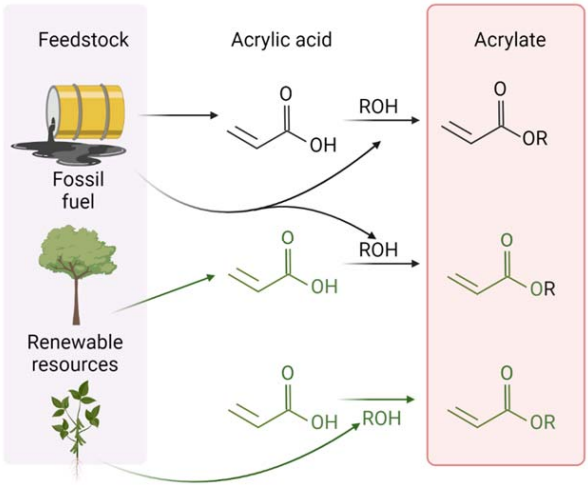


Figure 17.10: Production pathway of acrylates using fossil fuel and renewable resources. Souza, L.R.d.; Whitfield, B.; Al-Tabbaa, A. Biobased Acrylate Shells for Microcapsules Used in Self-Healing of Cementitious Materials. *Sustainability* **2022**, *14*, 13556. https://doi.org/10.3390/su142013556. Creative Commons Attribution (CC BY) license (**https://creativecommons.org/licenses/by/4.0/**)

When the alcohol is methanol, the final product is methylacrylate (MA). The structure of the cyclic acrylate monomer feedstock used to polymerize plexiglass (lucite) is methylene-butyrolactone (MBL), whose structure is shown in Figure 17.11 below.

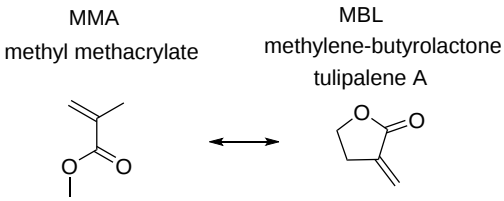


Figure 17.11: Structure of methyl methacrylate and its lactone (a cyclic ester)

Methyl methacrylate can undergo a free radical polymerization in the presence of an initiator (In·), as shown below in Figure 17.12.

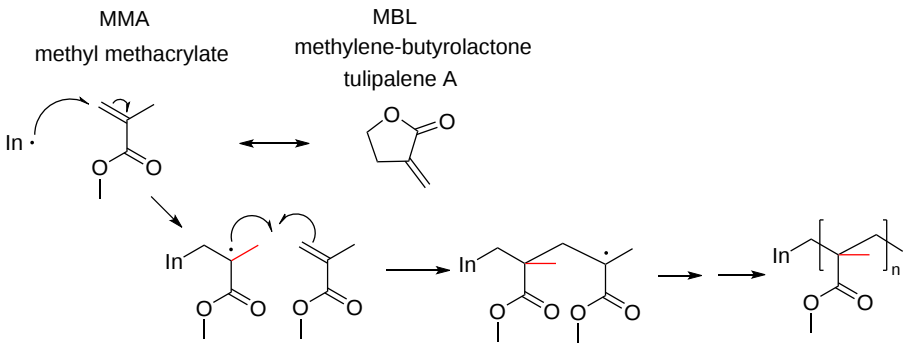


Figure 17.12: Mechanism of free radical polymerization of MMA

This reaction can form large polymers, such as plexiglass. The market for acrylic acid, the feedstock for plexiglass, is estimated to reach 12 million metric tons by 2030.

MBL, the lactone of MMA, is made in tulips from pathways that are not completely elucidated. It can also be used as a feedstock for the polymerization of plexiglass. Figure 17.13 shows the polymerization products from MMA and MBL.

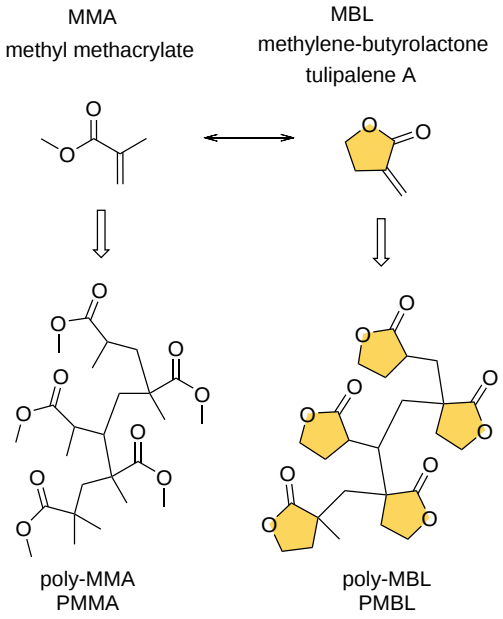


Figure 17.13: Structure of poly-MMA and poly-MBL

Using synthetic biology and advanced computational methods, plexiglass can be produced from biological sources rather than fossil fuels. To accomplish this, Azerda has designed synthetic pathways from millions of potential metabolic pathways (using a software package called Scylax™) and intelligently redesigned key enzymes to maximize their catalytic potential for the synthesis of MBL (using the software Archytas™). They used high-throughput DNA and protein analyses to maximize expression. Finally, they engineered expression strains and downstream purification processes to maximize the final output of MBL. In summary, the key steps in the process were:

- identifying a pathway from millions of reactions in databases of pathways that could produce MBL from simple sugars through a fermentation process;
- engineering pathway enzymes to significantly increase catalytic efficiency and decrease inhibition;
- producing test quantities of the products in cell strains;
- scaling up production to levels needed for purification and reactions of the MBL
- purifying sufficient amounts of MBL from large fermentation broths
- making the desired product (plexiglass, for example) from the feedstock.

Strains of bacteria, yeast, and filamentous fungi were modified to meet the criteria outlined above. The ultimate substrate for the process was a lignocellulosic hydrolysate, so in the end, the process converts trees into plexiglass (incredible to think about)! Of course, it is also amazing that CO_2 from the air, water, and minerals/ions from the soil can become a tree!

Starting with a detectable product level, the process was continually improved and scaled to yield 5 g/L in broth, which is close to the 20 g/L required for commercial viability. Figure **17.14** below shows plexiglass created from the lignocellulosic stock!

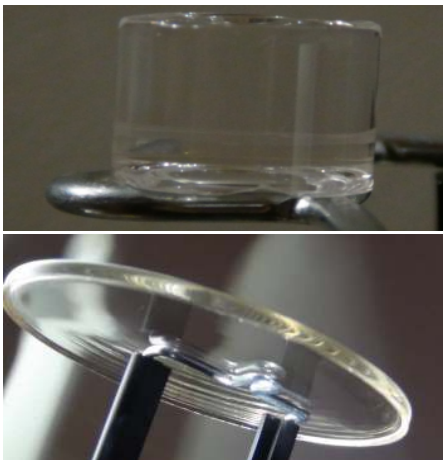


Figure **17.14**: Plexiglass made from biosourced MBL.

Table **17.2** below compares the key physical properties of the polymers from Arzeda's PMBL compared to literature values for fossil-fuel-based PMBL and PMMA.

Property	Measure	Lit PMBL	Arzeda PMBL	PMMA
Thermal	Glass transition pt T_g (^oC)	194-195	195	105
Mechanical	Elasticity (mPa)	1999/3439	5972	2855
	Tensile strength (mPa)	36.7/62.7	72.7	70
	Elongation at break	1.3%.6.5%	1.3%	2.5
Optical	Light transmission	NA	>88%	92%
Solvent resistance	toluene, 30 days, 20 ^oC	NA	Pass	Fail

Table **17.2**: https://www.energy.gov/sites/default...-korkegian.pdf

SUMMARY

(Summary written by Claude, Anthropic)

Manufacturing and food production together are responsible for a substantial fraction of global greenhouse gas emissions. This chapter examines how synthetic biology can produce foods and industrial materials from biological rather than fossil fuel sources — contributing to a more sustainable, circular economy.

The climate cost of food. Food production accounts for approximately 25% of global GHG emissions, with the agricultural sector alone contributing ~35%. Animal agriculture is the dominant driver: cattle require the most land of any food source per 1,000 kcal or per 100 g of protein, and over 200 million chickens and nearly 4 million pigs are slaughtered globally every day. Wild mammals now represent only ~6% of all mammalian biomass on Earth, and the mass of human-made materials now exceeds the entire biomass of the planet. Shifting toward plant-based diets is one of the most impactful individual responses to climate change.

Leghemoglobin and Impossible Burgers. Impossible Foods uses soy leghemoglobin — a monomeric heme-binding protein from legume root nodules, structurally homologous to myoglobin — to give plant-based burgers their meat-like taste, appearance, and aroma. Heme is a key contributor to the flavor of red meat. Leghemoglobin's extremely high O_2 affinity (kon ≈ 2×10^8 s^{-1}, koff ≈ 20 s^{-1}) normally serves to buffer free O_2 away from nitrogenase in root nodules. For commercial production, the protein is expressed in the methylotrophic yeast *Pichia pastoris* under the methanol-inducible AOX1 promoter. Sufficient heme must also be produced in the engineered yeast; this requires co-expression of three groups of enzymes spanning both the C4 (succinyl-CoA → ALA, in animals and fungi) and C5 (α-ketoglutarate → ALA, in bacteria and plants) heme biosynthesis pathways, with synthetic biology strategies including targeted gene upregulation, downregulation, and knockout to maximize flux through the pathway. AI-assisted pathway design is increasingly used for this optimization.

Other alternative proteins. A wide range of sustainable protein sources is under development. Recombinant proteins produced by engineered microbes include β-lactoglobulin (cow whey protein) from *Trichoderma reesei*, casein and egg-white proteins from *Pichia*

pastoris, and chymosin (replacing calf-stomach rennet for cheese making). Filamentous fungi (*Fusarium venenatum*) produce fibrous proteins with chicken-like texture through fermentation. Lab-grown meat from muscle stem cells or immortalized cell lines (e.g., chicken fibroblasts) remains technically challenging and expensive, with fetal bovine serum dependence, high costs, and consumer resistance as major barriers. More immediately, veganism and vegetarianism — increasing intake of peas, soy, grains, and nuts — remain the most effective individual dietary strategies for reducing carbon footprint. Duckweed (*Lemna* spp.) is an especially promising emerging source: it grows rapidly in aquaculture without farmland, contains up to 50% protein (primarily RuBisCO), requires minimal processing, and provides all essential amino acids. Macroalgae, insects, and other non-animal protein sources complete the portfolio of lower-impact alternatives.

Biosourced industrial materials: plexiglass from trees. Beyond food, synthetic biology can replace fossil fuels in manufacturing. Acrylic acid — the feedstock for plexiglass (PMMA) — currently generates nearly 4,000 kg CO_2 per metric ton produced from propylene. Arzeda used computational tools (Scylax™ for pathway design from millions of metabolic reactions; Archytas™ for enzyme engineering) to identify and optimize a fermentation pathway from lignocellulosic hydrolysate (wood) to methylene-butyrolactone (MBL), a cyclic lactone that polymerizes into a plexiglass-like material (PMBL). Key steps included computational pathway selection, enzyme engineering to increase catalytic efficiency and reduce product inhibition, strain construction in bacteria, yeast, and filamentous fungi, and scale-up from initial detection to 5 g/L in fermentation broth — approaching the ~20 g/L threshold for commercial viability. The resulting biosourced PMBL matches or exceeds fossil-fuel-derived PMBL and PMMA in thermal stability (Tg = 195°C vs. 105°C for PMMA), tensile strength, elasticity, and optical clarity, and outperforms PMMA in solvent resistance. In essence, the process converts atmospheric CO_2 (fixed by trees) into a durable plastic — demonstrating the potential for synthetic biology to close the carbon loop in industrial materials production.

17: Turning Trees into Plexiglass - Synthetic Biology For Production of Green Foods and Products is shared under a CC BY-NC-SA 4.0 license and was authored, remixed, and/or curated by LibreTexts.

Index

Glossary

Sample Word 1 | Sample Definition 1

Detailed Licensing

Overview

Title: Biochemistry and Climate Change

Webpages: 28

Applicable Restrictions: Noncommercial

All licenses found:

- CC BY-NC-SA 4.0: 96.4% (27 pages)
- Undeclared: 3.6% (1 page)

By Page

- Biochemistry and Climate Change - *CC BY-NC-SA 4.0*
  - Front Matter - *CC BY-NC-SA 4.0*
    - TitlePage - *CC BY-NC-SA 4.0*
    - InfoPage - *CC BY-NC-SA 4.0*
    - Table of Contents - *Undeclared*
    - Licensing - *CC BY-NC-SA 4.0*
  - 1: The Basics of Climate Change - *CC BY-NC-SA 4.0*
  - 2: Back to the Present and Future of Climate Change - *CC BY-NC-SA 4.0*
  - 3: Use of Isotope Analysis in Measuring Climate Change - *CC BY-NC-SA 4.0*
  - 4: Climate Change - The Carbon Cycle and Carbon Chemistry - *CC BY-NC-SA 4.0*
  - 5: Biofuels A - Corn and Sugar Cane Ethanol - *CC BY-NC-SA 4.0*
  - 6: Biofuels B - Cellulosic Ethanol - *CC BY-NC-SA 4.0*
  - 7: Algae - an Introduction - *CC BY-NC-SA 4.0*
  - 8: Biodiesel, Syngas and Bioaviation fuels - *CC BY-NC-SA 4.0*
  - 9: Biohydrogen - An Introduction - *CC BY-NC-SA 4.0*
  - 10: Biohydrogen - Hydrogenases - *CC BY-NC-SA 4.0*
  - 11: A Warmer World- Temperature Effects On Chemical Reactions - *CC BY-NC-SA 4.0*
  - 12: A Warmer World- Temperature Effects On Proteins - *CC BY-NC-SA 4.0*
  - 13: Biochemistry, Climate Change and Human Health - *CC BY-NC-SA 4.0*
  - 14: Pandemic Diseases and Drug Discovery - Under Construction - *CC BY-NC-SA 4.0*
  - 15: Fixing Carbon Fixation - *CC BY-NC-SA 4.0*
  - 16: Fixing Nitrogen Fixation - *CC BY-NC-SA 4.0*
  - 17: Turning Trees into Plexiglass - Synthetic Biology For Production of Green Foods and Products - *CC BY-NC-SA 4.0*
  - Back Matter - *CC BY-NC-SA 4.0*
    - Index - *CC BY-NC-SA 4.0*
    - Glossary - *CC BY-NC-SA 4.0*
    - Detailed Licensing - *CC BY-NC-SA 4.0*
    - Detailed Licensing - *CC BY-NC-SA 4.0*

Detailed Licensing

Overview

Title: Biochemistry and Climate Change

Webpages: 28

Applicable Restrictions: Noncommercial

All licenses found:

- CC BY-NC-SA 4.0: 96.4% (27 pages)
- Undeclared: 3.6% (1 page)

By Page

- Biochemistry and Climate Change - *CC BY-NC-SA 4.0*
  - Front Matter - *CC BY-NC-SA 4.0*
    - TitlePage - *CC BY-NC-SA 4.0*
    - InfoPage - *CC BY-NC-SA 4.0*
    - Table of Contents - *Undeclared*
    - Licensing - *CC BY-NC-SA 4.0*
  - 1: The Basics of Climate Change - *CC BY-NC-SA 4.0*
  - 2: Back to the Present and Future of Climate Change - *CC BY-NC-SA 4.0*
  - 3: Use of Isotope Analysis in Measuring Climate Change - *CC BY-NC-SA 4.0*
  - 4: Climate Change - The Carbon Cycle and Carbon Chemistry - *CC BY-NC-SA 4.0*
  - 5: Biofuels A - Corn and Sugar Cane Ethanol - *CC BY-NC-SA 4.0*
  - 6: Biofuels B - Cellulosic Ethanol - *CC BY-NC-SA 4.0*
  - 7: Algae - an Introduction - *CC BY-NC-SA 4.0*
  - 8: Biodiesel, Syngas and Bioaviation fuels - *CC BY-NC-SA 4.0*
  - 9: Biohydrogen - An Introduction - *CC BY-NC-SA 4.0*
  - 10: Biohydrogen - Hydrogenases - *CC BY-NC-SA 4.0*
  - 11: A Warmer World- Temperature Effects On Chemical Reactions - *CC BY-NC-SA 4.0*
  - 12: A Warmer World- Temperature Effects On Proteins - *CC BY-NC-SA 4.0*
  - 13: Biochemistry, Climate Change and Human Health - *CC BY-NC-SA 4.0*
  - 14: Pandemic Diseases and Drug Discovery - Under Construction - *CC BY-NC-SA 4.0*
  - 15: Fixing Carbon Fixation - *CC BY-NC-SA 4.0*
  - 16: Fixing Nitrogen Fixation - *CC BY-NC-SA 4.0*
  - 17: Turning Trees into Plexiglass - Synthetic Biology For Production of Green Foods and Products - *CC BY-NC-SA 4.0*
  - Back Matter - *CC BY-NC-SA 4.0*
    - Index - *CC BY-NC-SA 4.0*
    - Glossary - *CC BY-NC-SA 4.0*
    - Detailed Licensing - *CC BY-NC-SA 4.0*
    - Detailed Licensing - *CC BY-NC-SA 4.0*